STRUCTURAL AND SMART MATERIALS ANALYSIS IN RESPONSIVE ARCHITECTURAL AND TEXTILE MECHANICAL APPLICATIONS

by

Shane J. Yates

Submitted in partial fulfilment of the requirements
for the degree of Master of Applied Science

at

Dalhousie University
Halifax, Nova Scotia
June 2012

DALHOUSIE UNIVERSITY

DEPARTMENT OF MECHANICAL ENGINEERING

The undersigned hereby certify that they have read and recommend to the Faculty of Graduate Studies for acceptance a thesis entitled "STRUCTURAL AND SMART MATERIALS ANALYSIS IN RESPONSIVE ARCHITECTURAL AND TEXTILE MECHANICAL APPLICATIONS" by Shane J. Yates in partial fulfillment of the requirements for the degree of Master of Applied Science.

Dated: June 12, 2012

Supervisor: _____

Readers: _____

_____

DALHOUSIE UNIVERSITY

DATE: June 12, 2012

AUTHOR: Shane J. Yates

TITLE: STRUCTURAL AND SMART MATERIALS ANALYSIS IN RESPONSIVE ARCHITECTURAL AND TEXTILE MECHANICAL APPLICATIONS

DEPARTMENT OR SCHOOL: Department of Mechanical Engineering

DEGREE: MASc. CONVOCATION: October YEAR: 2012

_____

Signature of Author

DEDICATION PAGE

I dedicate this thesis to my mother and father, Rev. Linda Yates and Carl Yates, P.Eng., for their constant encouragement, support, and for being the best parents a child could possibly have; and to my wonderful fiancé, Enrique, for being my love and keeping me together throughout this process. Whenever I was in a tight spot, all I needed to do was think of you, Enrique, and everything became much clearer. I could not have completed this thesis without the love from all of you. I love you all.

Sincerely,

Shane Yates

TABLE OF CONTENTS

LIST OF TABLES

LIST OF FIGURES

ABSTRACT

The @lab is a group dedicated to the research and development of electronic textiles for architectural applications; this thesis presents the structural analyses performed by the author to improve the @lab's projects. Also included are three investigations performed by the author that pertain to smart material applications in responsive architecture and textiles. The first investigation evaluated the feasibility of using piezoelectric materials to harvest power from human foot traffic; overall, it was determined to not be feasible. The second investigation experimentally tested how six parameters of shape memory alloy spring actuators affect their reaction times and stroke; all six parameters affected the reaction times and/or stroke. The third investigation experimentally tested how three parameters of superelastic SMA springs influence their stiffness and resonant frequencies; overall, it was found that traditional spring mechanics can be used to predict their behavior providing the internal stress does not reach the upper plateau stress.

LIST OF ABBREVIATIONS AND SYMBOLS USED

Abbreviations	Description
@lab	ArchiTextile Lab
1D	One-dimensional
2D	Two-dimensional
3D	Three-dimensional
ABS	Acrylonitrile-butadiene-styrene
AC	Alternating Current
ACI	Advanced Cerametrics, Inc.
ACOA	Atlantic Canada Opportunities Agency
Ag	Silver
AGS	Automatic Generating System
Al	Aluminum
AM Transformation	Austenite to Martensite Transformation
$BaTiO_3$	Barium Titanate
Bi_2Te_3	Bismuth Telluride
C	Carbon
CA	California
CFL	Compact Fluorescent
CFC	Carbon Fibre Composite
Cl	Clamped
Co	Cobalt
COH	Cost of Harvesting
Cr	Chromium
CS	Cross-Sectional Stiffness
CTI	Chromatic Technologies, Inc.
Cu	Copper
DC	Direct Current

DSC	Differential Scanning Calorimeter
e^-	Electron
EAP	Electroactive Polymer
ECG, EKG	Electrocardiograph
EDG	Electrodermograph
EEG	Electroencephalograph
EL	Electroluminescent
EMG	Electromyograph
ER	Electrorheological
Fcr	Fully covered and regrouped
Fe	Iron
FEA	Finite Element Analysis
FFT	Fast Fourier Transform
H	Hydrogen
H_2SO_4	Hydro Sulfuric Acid
HPLED	Human Powered LED
HRM	Halifax Regional Municipality
HVAC	Heat, Ventilation, and Air Conditioning
I^+	Single Charged Ion
IR	Infrared
ITO	Indium Tin Oxide
JR East	East Japan Railway Company
K	Potassium
La	Lanthanum
LC	Liquid Crystals
LCD	Liquid Crystal Display
LED	Light Emitting Diode
Li	Lithium

LVDT	Linear Variable Differential Transducer
MA Transformation	Martensite to Austenite Transformation
Me	Metal Atom
MEMS	Microelectromechanical Systems
MIT	Massachusetts Institute of Technology
Mn	Manganese
MR	Magnetorheological
MS	Material Stiffness
N	Nitrogen
Na	Sodium
Nb	Niobium
Ni	Nickel
NiMH	Nickel Metal Hydride
NiTi	Nickel-Titanium
NRC	Noise Reduction coefficient
NSCAD	Nova Scotia College for Art and Design
NTT	Nippon Telegraph and Telephone
O	Oxygen
OLED	Organic Light Emitting Diode
P	Polarization Direction
Pb	Lead
PC	Polycarbonate
pce	Partially covered electrode
PCM	Phase Change Material
PDLC	Polymer Dispersed Liquid Crystals
PE	Piezoelectric
pH	Potential of Hydrogen
PLZT	Lead Lanthanum Zirconate Titanate

PMN:PT	Lead Manganese Niobate:Lead Titanate
PS	Particle Suspension
PVDF	Polyvinylidene Fluoride
PZT	Lead Zirconate Titanate
PZT 4	Hard PZT
PZT 5H	Soft PZT
RBG	Red-Blue-Green
Sb	Antimony
SCE	Synchronous Charge Extraction
SE	Superelastic
SIM	Stress-Induced Martensite
SMA	Shape Memory Alloy
SONAR	Sound Navigation Ranging
SP	Suspended Particles
ss	Simply-supported
SSHI	Synchronized Switch Harvesting using an Inductor
SSHRC	Social Science and Humanities Research Council
Ti	Titanium
TTT	Time-Temperature Transformation Diagram
UTS	Ultimate Tensile Strength
UV	Ultraviolet
UVA	Ultraviolet-alpha
V	Vanadium
VAR	Vacuum Arc Melting
VIM	Vacuum Induction Melting
WO_3	Tungsten Trioxide
WS	Total Wire Stiffness
Zr	Zircon

Symbols Used in Chapters 1 to 3	Description	Units
B	Magnetic Flux Density, Induction Field	T
C	Magnetorheological carrier fluid constant	-
c	Speed of light	3.0×10^8 m/s
D	Piezomagnetic constant	m/A
E	Electromagnetic Wave Amplitude	
E	Electric Field	V/m
F	Frequency	Hz
h	Height	m
H	Magnetic Field Strength	A/m
i, j, k, l, m, n	Direction indices	-
k	Magnetic Coupling Coefficient	-
k_p	Pyroelectric Sensitivity Constant	C/K
L, l	Length	m
M	Electrorestrictive Coefficient	m^2/V^2
NA	Numerical Aperture	-
n_c	Cladding index of refraction	-
n_{eff}	Effective Refractive Index of Bragg Grating Core	-
n_f	Fibre index of refraction	-
n_i	Incident index of refraction	-
P	Pressure	Pa
P	Induced Polarization	$F*V/m^2$
P	Point Load	N
Q	Flow Rate	m^3/s
Q	The Polarization Electrostriction Coefficient	m^4/F^2V^2
Q, q	Charge	C
S	Maximum Velocity of a linear velocity distribution	m/s

s^H	Compliance Tensor under constant magnetic field	Pa^{-1}
t	Time	s
T	Temperature	K
T_v	Visible Transmission	-
w	Width	m
$\dot{\gamma}$	Shear Strain Rate	s^{-1}
ε	Strain	-
ε_0	The Permittivity of a vacuum	(8 .854 x 10^{-12} F/m)
ε_r	Relative Dielectric Constant	-
η	Viscosity	Pa*s
η_{pl}	Plastic Viscosity	Pa*s
θ_a	Incident Angle	rad or deg
θ_{amax}	Maximum Incident Angle	rad or deg
θ_c	Reflected Angle	rad or deg
θ_{cmax}	Maximum Reflected Angle	rad or deg
θ_{crit}	Critical Angle	rad or deg
θ_t	Refracted Angle	rad or deg
Λ	Bragg Grating Period	m
λ_B	Bragg wave	m
μ_0	Permeability of Free Space	4π x 10^{-7} H/m
μ^σ	Permeability Tensor under constant stress	H/m
σ	Stress	Pa
τ	Shear Stress	Pa
$\tau_y(F)$	Dynamic Shear Yield Stress as a function of electric or magnetic yield strength	Pa
$\boldsymbol{\varphi}$	Phase	(rad or degrees)
ω	Radial frequency	rad/s

Symbols Used in Chapter 4	Description	Units
A	Area	m^2
a (subscript)	Belonging to Section A	
A (subscript)	Pertaining to ply A	
ab (subscript)	Belonging to AB overlap	
b (subscript)	Belonging to Section B	
B (subscript)	Pertaining to ply B	
bc (subscript)	Belonging to BC overlap	
c	Maximum Distance from Bending Axis	m
c	Cosine	
c (subscript)	Belonging to Section C	
C (subscript)	Pertaining to the circumferential direction	
C_1, C_2	Boundary Condition Coefficients	
C_D	Drag Coefficient	
C_{Ux}	Compressive Strength along the fibre direction	Pa
C_{Uy}	Compressive Strength along the transverse direction	Pa
D	Diameter	m
E	Modulus of Elasticity	Pa
F	Flexibility Matrix	Pa^{-1}
F_D	Drag Force	N
F_s	Safety Factor Matrix	
G	Modulus of Rigidity	Pa
G (subscript)	Pertaining to the global composite properties	
I	Bending Moment of Inertia	m^4
i (subscript)	Signifies Inner	
I_{box}	Mass Moment of Inertia of a box	m^2

I_M	Mass Moment of Inertia	m^2
I_{tube}	Mass Moment of Inertia of a tube	m^2
K	Composite Stiffness Matrix	Pa
L	Length along x-axis	M
L (subscript)	Pertaining to the longitudinal direction	
M	Moment	N*m
o (subscript)	Signifies Outer	
P	Point Load	N
R	Radius of Curvature	m
r_1	Inner radius of a tube	m
r_2	Outer radius of a tube	m
s	Sine	
S_{Ux}	Tensile Strength along the fibre direction	Pa
S_{Uy}	Tensile Strength along the transverse direction	Pa
$S_{U\tau}$	Shear Strength	Pa
T	Transformation Matrix	
T	Simulated Tension	N
T_o	Torque	N*m
v	Velocity	m/s
v(x)	Deflection with respect to the x-axis	m
x (subscript)	Pertaining to the x-axis	
y (subscript)	Pertaining to the y-axis	
α	Angular Acceleration	rad/s^2
θ	Slope	
θ_1	Cable angle with reference to a panel's face	Degrees
θ_2	Cable angle with reference to the x-axis	Degrees
ν	Poisson's Ratio	

ρ	Density	kg/m^3
σ	Stress	Pa
τ	Shear Stress	Pa

Symbols Used in Chapter 5	Description	Units
1 (subscript)	Occurs in the poling direction	-
15 (subscript)	Indicating that the corresponding electric field and deformation are in the transverse direction, and shear direction	-
3 (subscript)	Occurs in the transverse direction	-
31 (subscript)	Indicating that the corresponding electric field and deformation are in the poling direction and transverse direction, respectively	-
33 (subscript)	Indicating that the corresponding electric field and deformation are in the poling direction	-
5 (subscript)	Occurs in a shear direction	-
A	Area of Section	m^2
a	Lower limit of a function	-
A, B	Boundary Condition Constants	-
A_{cs}	Cross-Sectional Area	m^2
A_p	Cross-sectional area of one piezoelectric layer	m^2
A_s	Cross-sectional area of the substrate layer	m^2
b	Upper limit of a function	-
C	Stiffness Tensor	Pa
c	Maximum distance from bending neutral axis	m
C	Capacitance	F
C_p	Piezoelectric Parallel Capacitance	F
C_s	Piezoelectric Series Capacitance	F
d	Piezoelectric Strain Constant (“d” coefficient)	m/V or C/N
D	Electric Displacement	C/m^2
D (superscript)	Constant Electrical Displacement, Open Circuit	-

dx	Derivative of x	m
dz	Derivative of z	m
E	Electric Field	V/m
e	Piezoelectric constant tensor	C/m^2
E (superscript)	Constant Electric Field, Short Circuit	-
e_t	Transposed matrix of the piezoelectric constant tensor	m*Pa/V
f	Applied force	N
f(x)	Function of x	
F_{33}	Total force applied onto a piezoelectric transducer in the poling direction	N
f_{ave}	Average value of a function	
f_{bl}	Blocked Force	N
F_G	Geometry Factor	
f_{Hz}	Frequency of Excitation	Hz
F_I	Input Factor	
f_p	Piezoelectric parallel resonant frequency	Hz
F_P	Force on one piezoelectric layer	N
f_s	Piezoelectric series resonant frequency	Hz
F_S	Force on substrate layer	N
F_Z	Piezo Factor	
g	Piezoelectric Voltage Constant (“g” coefficient)	V/(Nm) or m^2/C
G	Modulus of Rigidity	Pa
h_m	Thickness of the substrate layer on a piezoelectric disc	m
h_p	Thickness of the piezoelectric layer on a piezoelectric disc	m
I	Moment of inertia	m^4
I (s)	Current with reference to complex conjugate	A
i,	Current	A
j	Imaginary Number	-

k	Electromechanical Coupling Coefficient	-
k_p	Electromechanical coupling coefficient in a thin round disk, polarized in thickness and vibrating in radial expansion and contraction	-
L	Length	m
L_s	Piezoelectric Series Inductance	H
m	Distance Between the center of mass of a section and the neutral axis	m
M (x)	Bending moment with reference to the x-axis	N*m
n	Number of piezoelectric layers	-
P	Vertical Point Load	N
P_0	Air Pressure	Pa
P_{33}	Power from a piezoelectric transducer succumbing to periodic deformation in the poling direction	W
P_c	Power from a capacitor	W
P_{cant}	Power from a piezoelectric cantilevered bimorph	W
P_{Disc31}	Power from a piezoelectric disc succumbing to 31-deformation by a pressure load	W
P_{Disc33}	Power from a piezoelectric disc succumbing to periodic deformation in the poling direction	W
P_{ext}	Power from a piezoelectric extension bimorph	W
P_{mid}	Power from a simply supported bimorph experiencing a load at its midpoint	W
P_{Rect33}	Power from a piezoelectric rectangular transducer succumbing to periodic deformation in the poling direction	W
q	Charge	C
q_{33}	Total charge developed in a piezoelectric transducer succumbing to deformation in the poling direction	C
q_{cant}	Total charge developed in a cantilevered bimorph	C
q_{ext}	Total charge developed in an extension bimorph	C
q_{mid}	Total charge developed in a simply-supported bimorph with a midpoint load	C
q_s	Total displacement of a piezoelectric stack	m
R	Radius of Curvature	m
r	Radius	m

R_1	Radius of the piezoelectric layer on a piezoelectric disc	m
R_2	Radius of the substrate layer on a piezoelectric disc	m
R_L	Load Resistance	Ω
R_S	Source Resistance	Ω
R_s	Piezoelectric Series Resistance	Ω
S	Compliance Tensor	Pa^{-1}
s	Complex Conjugate	-
S (superscript)	Constant Strain	-
t	Thickness	m
t_s	Substrate Layer Thickness	m
u	Displacement	m
U_c	Energy in a capacitor	J
U_e	Electrical Energy	J
u_s	Total displacement of a piezoelectric stack	m
V	Voltage	V
V_{ol}	Volume	m^3
w	Width	m
w_s	Equivalent substrate width	m
x, y, z	Coordinate Axis Directions	-
X_L	Load Reactance	Ω
X_S	Source Reactance	Ω
Y	Modulus of Elasticity	Pa
y_m	Maximum deflection in a simply supported plate from a pressure load	M
Y_s	Modulus of Elasticity of the substrate Layer	Pa
Z_{eq}	Equivalent Impedance	Ω
Z_L	Load Impedance	Ω
Z_S	Source Impedance	Ω
γ	Shear Strain	-

δ	Deflection	m
δ_0	Free Displacement	m
ϵ	Dielectric permittivity	F/m
ε	Strain	-
ϵ_0	Dielectric permittivity of a vacuum	(8.854×10^{-12} F/m)
ε_{ave}	Average Strain	-
ϵ_r	Relative Dielectric Permittivity	-
ν	Poisson's Ratio	-
σ	Stress	Pa
σ (superscript)	Constant Mechanical Stress, Mechanically Free	-
σ_{33}	Internal stress experience in the poling direction	Pa
σ_m	Maximum stress in a simply supported plate from a pressure load	Pa
σ_{max}	Maximum Stress	Pa
τ	Shear Stress	Pa
ω	Angular Frequency	rad/s

Symbols Used in Chapters 6 and 7	Description	Units
0 (subscript)	Initial Value	-
A (superscript or subscript)	Pertaining to the Austenite Phase	-
A_{CS}	Cross-sectional Area	m^2
A_f	Finishing Temperature of Martensite to Austenite Transformation	K
A_f^{σ}	Stress-Induced Finishing Temperature of Martensite to Austenite Transformation	K
A_f^{τ}	Shear Stress-Induced Finishing Temperature of Martensite to Austenite Transformation	K
AM (subscript)	Pertaining to the austenite to martensite transformation	-
A_s	Starting Temperature of Martensite to Austenite Transformation	K

A_s^{σ}	Stress-Induced Starting Temperature of Martensite to Austenite Transformation	K
A_s^{τ}	Shear Stress-Induced Starting Temperature of Martensite to Austenite Transformation	K
A_w	Wire's Surface Area	m^2
C	Stress Influence Coefficient	Pa/K
c	Specific Heat Capacity	J/(kg*K)
C	Spring Factor	-
c_A	Austenitic Specific Heat Capacity	J/(kg*K)
C_A	Austenite Stress Influence Coefficient	Pa/K
c_M	Martensitic Specific Heat Capacity	J/(kg*K)
C_M	Martensite Stress Influence Coefficient	Pa/K
D	Effective Modulus of Elasticity	Pa
d	Wire Diameter	m
D	Spring Diameter	m
D_{eff}	Effective Spring Diameter	m
dT	Derivative of Temperature	K
dx	Derivative of x	M
$d\gamma$	Derivative of Shear Strain	Pa
$d\xi$	Derivative of Martensite Fraction	-
$d\tau$	Derivative of Shear Stress	Pa
E	Modulus of Elasticity	Pa
$\dot{E}_{conv}$	Convection Energy Rate	J/s
$\dot{E}_g$	Energy Generation Rate	J/s
$\dot{E}_{in}$	Input Energy Rate	J/s
$\dot{E}_{out}$	Output Energy Rate	J/s
$\dot{E}_{rad}$	Radiation Energy Rate	J/s
$\dot{E}_{st}$	Energy Storage Rate	J/s
F	Force	N
F_{Af}	Force at which Stress-Induced Martensite has	N

	completely turned back into Austenite	
F_{As}	Force at which Stress-Induced Martensite begins to turn back into Austenite	N
F_{Mf}	Force at which the alloy has completely changed into Stress-Induced Martensite	N
F_{Ms}	Force at which Stress-Induced Martensite begins to form	N
f_n	Spring-mass Resonant Frequency	Hz
f_n^{τ}	Spring-mass Resonant Frequency for a superelastic spring at a particular shear stress	Hz
F_{rec}	Recovery Force	N
F_{upl}	Force Needed to Reach the Upper Plateau Stress	N
G	Modulus of Rigidity	Pa
g	Gravitational Acceleration	9.8 m/s^2
G_{τ}	Modulus of Rigidity at a particular shear stress	Pa
h	Convection Coefficient	$W/(m^2*K)$
$H^{cur}(\sigma)$	Maximum Transformation Strain at a specific stress level	-
I	Current	A
I	Moment of Inertia	m^4
k	Stiffness	N/m
K	Superelastic Spring Stiffness	N/m
K_s	Static loading factor	-
L	Length	m
m	Mass	kg
M (superscript or subscript)	Pertaining to the Martensite Phase	-
MA (subscript)	Pertaining to the martensite to austenite transformation	-
M_f	Finish Temperature of Austenite to Martensite Transformation	K
M_f^{σ}	Stress-Induced Finishing Temperature of Austenite to Martensite Transformation	K
M_f^{τ}	Shear Stress-Induced Finishing Temperature of Austenite to Martensite Transformation	K
M_s	Starting Temperature of Austenite to Martensite Transformation	K

M_s^{σ}	Stress-Induced Starting Temperature of Austenite to Martensite Transformation	K
M_s^{τ}	Shear Stress-Induced Starting Temperature of Austenite to Martensite Transformation	K
N	Number of Turns	-
r	Radius of Wire	m
R	Spring Radius	m
r_{crit}	Critical Radius	m
R_e	Electrical Resistance	Ω
R_e'	Resistance per unit Length	Ω/m
s_p	Pooled Standard Deviation	-
T	Temperature	K
t	Time	s
T_1	Start Temperature	K
T_2	Final Temperature	K
T_∞	Ambient Temperature	K
T_A	Represents a Temperature in the Austenite Phase	K
T_M	Represents a Temperature in the Martensite Phase	K
U_t	Internal Energy Stored	J
V	Volume	m^3
W	Gravitational Force	N
X	Transformation Enthalpy	J/kg
x	Position along x-axis	m
α	Coefficient of Thermal Expansion	K^{-1}
α	Slope of Martensite Transformation Temperatures	-
α_{def}	Angular Deflection	rad
β	Slope of Austenite Transformation Temperatures	-
γ_d	Shear Strain from De-twinning Martensite	-
γ^e	Elastic Shear Strain	-
γ_{max}^{tr}	Maximum Shear Strain during a Stress-Induced Phase	-

	Transformation	
γ^{rec}	Recovery Shear Strain	-
γ^{th}	Thermal Shear Strain	-
δ	Spring Deflection	m
δ_{Af}	Force at which Stress-Induced Martensite has completely turned back into Austenite	m
δ_{As}	Force at which Stress-Induced Martensite begins to turn back into Austenite	m
δ_d	Deflection from detwinning martensite	m
δ_{eff}	Effective Stroke	m
δ_L	Elastic Deflection of De-twinned Martensite	m
δ_{max}^{tr}	Maximum Deflection during a Stress-Induced Phase Transformation	m
δ_{Mf}	Force at which the alloy has completely changed into Stress-Induced Martensite	m
δ_{Ms}	Deflection at which Stress-Induced Martensite begins to form	m
Δt_{cool}	Cooling Time	s
Δt_{heat}	Heating Time	s
δ^{TM}	Twinned Martensite Deflection	m
δ^{tr}	Deflection during a stress-induced transformation	m
δ_{upl}	Deflection Needed to Reach the Upper Plateau Stress	m
$\Delta\delta$	Stroke	m
δ^{τ}	Total Deflection for a Superelastic Spring	m
ε	Strain	-
ε^e	Elastic Strain	-
ε_L	Maximum Recoverable Strain	-
ε^t	Transformation Strain	-
ε^{th}	Thermal Strain	-
Θ	Thermoelastic Tensor	Pa/K
θ	Angle	rad or deg
ν	Poisson's Ratio	-

ξ	Martensitic Faction	-
$\xi_{S\tau}$	Stress-Induced Martensitic Fraction	-
ρ	Density	kg/m^3
σ	Stress	Pa
σ^{Af}	Finishing Stress of Stress-Induced Martensite to Austenite Transformation	Pa
σ_{align}	Minimum Stress needed to completely deform the shape memory alloy into martensite	Pa
σ^{As}	Starting Stress of Stress-Induced Martensite to Austenite Transformation	Pa
σ_{max}	Maximum Stress	Pa
σ^{Mf}	Finishing Stress of Austenite to Stress-Induced Martensite Transformation	Pa
σ^{Ms}	Starting Stress of Austenite to Stress-Induced Martensite Transformation	Pa
σ_{upl}	Upper Plateau Stress	Pa
σ^{y}	Yield Strength	Pa
τ	Shear Stress	Pa
τ_{max}	Maximum Shear Stress	Pa
τ_{max}^{Af}	Finishing Maximum Shear Stress of Stress-Induced Martensite to Austenite Transformation	Pa
τ_{max}^{As}	Starting Maximum Shear Stress of Stress-Induced Martensite to Austenite Transformation	Pa
τ_{max}^{Mf}	Finishing Maximum Shear Stress of Stress-Induced Martensite Transformation	Pa
τ_{max}^{Ms}	Starting Maximum Shear Stress of Austenite to Stress-Induced Martensite Transformation	Pa
Ω	Transformation Tensor	Pa
ω_n	Radial Frequency	Ra/s
Ω_τ	Shear Transformation Tensor	Pa

ACKNOWLEDGEMENTS

There are so many people to thank and acknowledge for the completion of this thesis. First and foremost, the author wants to acknowledge the @lab's Principle Investigators: Dr. Sarah Bonnemaison and Robin Muller; and the @lab's staff: Greg Sims, Stephen Kelly, Anke Fox, Pam Gaines, Melissa Schwegmann, and Adam Read. The @lab was a one-of-a-kind experience and I have learned so much from all of you. I am very thankful for this opportunity to work and collaborate with you all. I would also like to acknowledge Dr. Andrew Warkentin who first informed me of this opportunity, and the Atlantic Innovation Fund from the Atlantic Canada Opportunities Agency which committed more than $1 million toward the @lab's research and paid for my internship.

The author would also like to acknowledge those who helped with the experimental preparations and procedures including Dr. George Jarjoura for the use of the Materials Department's heat treatment lab, Greg Delbridge for his correspondence when learning Hyperworks™ software, Dr. Craig Lake for the use of the Civil Department's Instron® machine, and Peter Jones for his help with Labview™ and the resonant frequency testing.

Last but not least, the author wishes to acknowledge the members of his supervisory committee: Dr. Darrel Doman, Dr. Sarah Bonnemaison, and Dr. Alex Kalamkarov. Dr. Doman for his encouragement, humanity, and knowledge; when asking for help I always come out with a greater and deeper understanding of the concepts. Dr. Bonnemaison for her creative and compassionate mind and for her desire to integrate design, art, and science into something that is greater than the sum of their parts; your mentorship has changed the way I think about the world. Dr. Alex Kalamkarov for my introduction to the world of smart materials: a world that I never knew existed, but am now completely fascinated by. I thank you all for your involvement and your willingness to cross-examine a 600+ page document. Cheers.

CHAPTER 1. INTRODUCTION

1.1 OVERALL OBJECTIVES

Responsive technology can be defined as systems that instinctively respond to external stimuli in a programmed manner. Responsive systems are generally made of three components: sensors, processors, and actuators. Sensors act as the responsive system's somatic nervous system; they detect certain triggers or environmental stimuli for the system to respond to. Also known as the control system, processors act as the responsive system's central nervous system; they analyze and evaluate the sensory inputs, creating instructions for an appropriate response. Actuators act as the responsive system's muscles; they carry out the programmed response by either acting directly from the sensors' inputs or by instructions set by the control system. The benefits of designing responsive systems include saving time and money, improving accuracy, and the fact that they can be multifunctional and reprogrammable. Responsive technology is present in virtually every field of science; in electronics, examples include smart phones and MP3 players; in architecture, examples include structural monitoring, temperature sensing for HVAC systems, and proximity activated lighting; in medicine, examples include electroencephalograph monitoring and artificial limbs; in automotive engineering, examples include global positioning systems and cruise control.

Smart materials are generally viewed as materials that can change one or more of its properties in reaction to an external stimulus. As smart materials are responsive in their own right, they are often used in responsive systems either as sensors, processors, actuators, or sometimes all three combined. Examples of smart materials used in responsive technology include shape memory alloys in heat activated heart stents, fibre optics used to monitor the structural integrity of bridges and buildings, magnetorheological fluids used as dampers with adjustable damping coefficients, piezoelectric sensors that directly act as stress-electricity transducers, liquid crystals used for electronic display screens, and thermochromic leukodyes on clothes that change colour with human contact.

Recently there has been an increased interest in the use of responsive technology in architecture and textiles. Books such as Michelle Addington and David Schodek's *Smart Materials and Technologies for the Architecture and Design Professions (2005)* and Axel Ritter's *Smart Materials in Architecture, Interior Architecture and Design (2007)* showcase smart materials from an architect's perspective giving insight to how they work and how they can be used to add to a building's function and aesthetic. Likewise, books such as Brian Culshaw's *Smart Structures and Materials (1996)* and Wagg, Bond, Weaver, & Friswell's *Adaptive Structures: Engineering Applications (2007)* showcase smart materials from the perspective of a structural engineer and how they can be used on buildings, bridges, and modes of transport to not only monitor their structural integrity, but also intelligently respond to environmental stimuli such as wind loading and tremors. In textiles, books like H. R. Mattila's *Intelligent Textiles and Clothing (2006)* and Gilsoo Cho's *Smart Clothing: Technology and Applications (2009)* showcase how smart materials and other forms of responsive technology can be integrated into textiles and clothing along with their associated applications. Likewise, books like Tao's *Smart Fibres, Fabrics and Clothing (2001)* goes deep into the science of smart materials in textiles, presenting engineering models that integrates the mechanical properties of textiles with the responsive properties of smart materials. IntertechPira's Smart Fabrics Conference, held since 2005, focuses on the evolution of smart fabrics, where the industry stands today, and the projected next steps in technology implementation (Pira International, 2012).

In 2008, Sarah Bonnemaison, an architecture Professor at Dalhousie University's Faculty of Architecture, and Robin Muller, a textiles Professor at Nova Scotia's College of Art and Design (NSCAD), founded the Architextile Lab (also known as the @lab). Mainly funded by the Atlantic Innovation Fund by the Atlantic Canadian Opportunity Agency and a Research in Creation grant by the Social Sciences and Humanities Research Council, the @lab was established as a centre for the design and development of electronic textiles for architectural applications (Bonnemaison, 2008). Although electronic textiles are not necessarily a new phenomenon, they are generally limited to the field of wearable fashion; the architextile lab aims to integrate electronic textiles onto

larger scale applications to "focus on the built environment rather than the body" (Bonnemaison, Berzowska, Macy, & Muller, 2011). These environments would include walls, ceilings, and architectural enclosures. The first two prototypes designed and built by the @lab were an electronic curtain and shoji screen room divider. Using a loom, electroluminescent wire (EL wire) was woven into a traditional textile to produce a luminous certain; using traditional origami paper folding techniques, fiber optic lighting was integrated into a traditional shoji screen room divider to provide an additional lighting aesthetic. Both the EL wire and fiber optics are smart materials, an EL wire responds to an electric current by luminescing and fiber optics are designed to carry light with minimal diffusion. Although these two projects successfully incorporated smart materials into their functional design, they are generally not classified as responsive systems. Responsive systems require sensors to detect certain environmental stimuli and actuators to produce a programmed response to said stimuli; the EL wire panel and shoji screen do not have sensors that trigger a reaction as they only follow a programmed response by activating a manual on/off switch. Although it's debatable that the on/off switch could count as a sensor, manual on/off switches are generally not viewed as sensors in the responsive technology community. Having successfully incorporated smart materials and smart technology into fabrics, the architextile lab would then set out to create prototypes that are truly responsive to an environmental stimulus; the environmental stimulus being generated by the user.

As the @lab's projects have responsive elements and are larger scale, ensuring their structural integrity, mechanical functionality, and electrical reliability can be quite challenging. Several challenges include minimizing deflection, optimizing strength to weight ratios, efficiently integrating the smart materials and electronics into the prototype's structure or textile skin, collapsibility and dynamic mechanism design, as well as sensor and actuator selection. Using analytical methods such as traditional static and dynamic analyses, finite element analysis, and small scale model testing, one can better foresee impending structural and mechanical complications in one's design. When incorporating smart materials into one's design, one must not only understand the science behind their responsiveness, but also understand their material properties and constitutive

models to effectively predict their responsiveness. As smart materials are still relatively new and not completely understood, often times experimental testing is needed in addition to their predictive models to decide what parameters to use in your responsive system. With a focus on the @lab's responsive projects along with an additional project performed by undergraduate students that was supervised by the author, this thesis will present the structural analyses used to assess their integrity, the smart materials analyses used to predict their responsive behaviour, and the experimental testing performed to evaluate the smart materials' analyses.

1.2 THESIS LAYOUT

To give the reader an understanding of what smart materials are, Chapter 2 will go over what is signified by the term smart and will present several examples of smart materials, highlighting the science behind their responsiveness and applications. Chapter 3 will then give the reader a closer look at responsive architecture and textiles that respond to the user, followed by descriptions of the @lab's responsive projects as well as the project undertaken by undergraduate students and supervised by the author: the Human Powered LED Jogging Suit. Chapter 4 presents the structural analyses undertaken by the author to evaluate the structural integrity of the responsive structures designed by the architextile lab. Chapter 5 will take a closer look at piezoelectric materials and how they can be used to harvest power through human foot traffic. For one of the @lab's projects (*i.e.* the Flamenco Backdrop), helical shape memory alloy spring actuators were used as part of its responsive nature; Chapter 6 presents models for calculating their reaction times and strokes as well as the experimental testing performed by the author to validate or contest these models. Chapter 7 again focuses on shape memory alloy springs, but in their superelastic form. Superelastic nitinol springs were proposed by the author to be used on the HPLED jogging suit as their low stiffness would be well suited for low resonance frequencies; Chapter 7 presents the mechanical models proposed by the author along with the experimental testing performed by the author to better understand the stiffness and resonance behavior of superelastic nitinol springs. Finally, Chapter 8 gives an overall summary of the thesis, outlining its accomplishments and future prospects.

CHAPTER 2. SMART MATERIALS AND SMART TECHNOLOGY

2.1 SMART MATERIALS: AN OVERVIEW

The term, "smart", has been used quite liberally nowadays. Many use the term "smart" without fully comprehending what it signifies. Smart by definition implies notions of an informed or knowledgeable response, with associated qualities of alertness and quickness. In common usage, there is also frequently an association with shrewdness, connoting an intuitive or intrinsic response (Addington & Schodek, 2005). Worden *et al.* point out that the words intelligent and smart are often used as tools to market new products, but this is often done with little thought to what this should mean (Worden, Bullough, & Haywood, 2003). Smart phones and smart boards are examples of this kind of marketing as they can perform many roles other than their main function. A smart phone allows you to not only communicate with someone, but can act as your day planner, electronic mailbox, video game console, cookbook, calculator, and the other thousands of applications one can download. Used in educational classrooms, smart boards not only act as white boards, but can project videos, browse the internet, and essentially act as an interactive monitor for your computer. These products certainly sound smart as they can perform multiple duties other than their targeted main purpose, but does their smartness adhere to the definition presented earlier. The response of a smart phone or smart board is indeed quick and informed, but is not intrinsic. Using a variety of electronic components, engineers and technicians designed smart phones and smart boards to perform their functions; they do not naturally possess this "wisdom". Nonetheless, marketers as well as the general public have labeled these products "smart" despite the fact that they do not inherently possess their "smartness". As the definition of smart is quite vague in modern day use, it is important to define a "smart material" as the term will be used consistently throughout this thesis. Akin to smart phones and smart boards, many engineers disagree with the use of the term "smart" to describe "smart materials", but these materials have nonetheless adopted this term to describe their exclusivity.

Given the frequent use of the term "smart" in everyday use, it is unsurprising that there has been much debate toward what constitutes a smart material. This debate is illustrated through the variety of smart material definitions amalgamated in Table 2-1. Although these definitions vary, they seem to adhere to a common principle in that a smart material has the ability to alter one or more of its properties in reaction to an external stimulus.

Table 2-1: Definitions of Smart Materials from various sources

Definition	Source
"Materials that "remember" configurations and can conform to them when given a specific stimulus"	Quoted by NASA in (Addington & Schodek, 2005)
"Smart materials and structures are those objects that sense environmental events, process that sensory information, and then act on the environment"	(Kroschwitz, 1992)
"Smart materials respond to environmental stimuli with particular changes in some variables"	(Reece, 2007)
The concept of a smart material is all about materials that can react to the world within which they operate and thereby enhance their functionality or survivability. The implication within the term "smart material" is that something synthetic possesses the ability to respond to its environment using deductive rather than instinctive reactions	(Culshaw, 1996)
Functional materials are materials that can perform certain functions when triggered by environmental changes, such as stress, electric field, magnetic field, temperature variations, or when stimulated by control signals, such as electric or magnetic signals from a control center	(Cao, 2007)
Sometimes materials are called smart because they have unusual properties, but perhaps most often smart materials are considered to be materials where multi-functionality is a key attribute	(Lloyd, 2007)
Materials and products that have changeable properties and are able to reversibly change their shape or colour in response to physical and/or chemical influences, *e.g.* light, temperature or the application of an electric field	(Ritter, 2007)
Materials that exhibit coupling between multiple physical domains	Engineering analysis of smart materials (2007)

The external stimulus acting on the smart material can vary from an applied pressure, light radiation, electric fields, or even moisture for example. The reactions are equally diverse ranging from shape deformation, electric potential production, colour changes, and light production. Many of the definitions in Table 2-1 also contain an environmental element suggesting that a change in their environment or surroundings induces said reaction. One can therefore take advantage of the intrinsic properties of smart materials by altering the material's environment to induce its reaction (known as actuation) or allowing the material to detect changes in its respective environment to inform an observer about an environmental alteration (known as sensation). Smart materials have found a variety of uses in many disciplines be it the use of superelastic nitinol in orthodontic braces, fiber optic sensors to monitor strains in aircrafts, ships, and bridges, piezoelectric materials to sense, control, and impede structural vibrations, or electrorheological fluids used for dampers and clutches. Smart materials encompass a variety of subjects including materials science (metallurgy, composites), applied mechanics (vibrations, fracture mechanics, elasticity, aerodynamics), electronics (sensors, actuators, controls), photonics (fiber optics), manufacturing (processing, microstructure), and biomimetics (strategies adopted by natural structures). Smart materials have also found multiple uses in architecture and fabrics.

Materials are the elements, constituents, or substances of which something is made of, but what makes a material smart? Although a smart material has now been identified as a material that can respond to an external stimulus, what makes it different from traditional "dumb" materials? For example, all metals expand (or shrink) when subjected to heat. This metallic property was key in the invention of thermostats as well as compensating for thermal shrinkage and expansion in bridges. All metals thus respond to an environmental stimulus (*i.e.* heat) through expansion (or sometimes contraction) so why aren't all metals classified as smart? The key to "smart materials" is that they possess a property change that is absent in most traditional materials. As all metals go through volume changes through heat applications, this phenomenon is far from distinctive. When a smart material responds to an external stimulus, it undergoes a property or energy transformation that is typically absent from most materials.

There are other traits a material must have for it to be deemed "smart". In their book, *Smart Materials and Technologies*, Michelle Addington and Daniel Schodek (2005) provide five key characteristics that all smart materials and technologies exhibit. These characteristics include: immediacy, transiency, self-actuation, selectivity, and directness (Addington & Schodek, 2005). These characteristics dictate that a smart material will:

- Respond in real time (known as Immediacy)
- Respond to more than one environmental state (known as Transiency)
- Have an internal mechanism responsible for its responsive transition (known as Self-actuation)
- Respond discretely and predictably (known as Selectivity)
- Have a response that is local to the associated external stimulus (known as Directness)

Applying these criteria to an actual material that exhibit unusual phenomena, one can make an assessment towards whether or not the material can be deemed "smart". Thermochromic materials are materials that undergo colour changes when thermally activated by heat. Thermochromism is generally absent in most materials therefore it certainly passes the first test towards being designated a smart material, but it must also possess the five characteristics outlined by Addington and Schodek. Going through the criteria, one can see that thermochromics:

- Change colour once passed its transition temperature (Immediacy)
- Have different colour properties below and above their transition temperature (Transiency),
- Will go through a change in molecular structure in response to thermal activation causing the material to undergo changes in absorptance characteristics (Self-actuation),
- Predictably change colour at its associated transition temperature (Selectivity)
- Undergo colour changes only on locations that are heat activated (Directness)

As thermochromics possess immediacy, transiency, self-actuation, selectivity, and directness, they most certainly can be classified as "smart".

2.1.1 Smart Materials vs. Smart Technology

This thesis will also cover some smart technologies as well as smart materials. The term, "smart technology" is linked to smart materials in concept, but nonetheless has differences that set it apart. A smart material is essentially a material that can intrinsically respond to an environmental stimulus in a unique fashion; a smart technology, however, consists of many components that work together to sense an environmental stimulus in a unique fashion. An example of smart technology would be fiber optic sensors. Fiber optic sensors consist of a light source, a light detector, an interpretation system, and fiber optic cables to transport and sense the environmental stimulus. Through the phenomenon of total internal reflection, the fiber optic cables can sense strain, deflection, and even temperature by altering the input light signal in phase and intensity. These phase and intensity changes are in turn detected by the light detector and are translated by the interpretation system to associate these light property changes with the detected input stimulus. Measurands of the input stimuli (*i.e.* strain, pressure, temperature, etc.) are therefore calculated through variations in the transmitted light properties. Some associate fiber optics as smart materials, however, this relationship is somewhat misleading as the fiber optics themselves do not sense and respond to an environmental stimulus. The fiber optics simply act as a conduit that interprets an external stimulus into a measurable arrangement. For fiber optic sensors to function, additional hardware (*i.e.* the light emitter and light detector) and software (the interpretation system) are needed. A key attribute to smart materials, is that they independently act as transducers to transform the external stimulus into its associated response. Piezoelectric materials independently respond to strain through producing an electric potential and vice versa, shape memory alloys independently respond to heat through shape deformation, and magnetorheological fluids independently respond to magnetic fields by altering its viscosity properties. As more than one component is needed to transform the input stimulus (strain, pressure, temperature, etc.) into a measurable form (light variation), fiber optics are deemed a smart technology as opposed to a smart material.

2.1.2 Are Smart Materials Needed to Make Something Smart?

With smart materials being able to respond to their respective environment, must one always require smart materials to add "smartness" to a system? With the variety of electronic controls available, there is essentially nothing that a smart material can do that traditional electronics cannot. For example, with the ability to directly transform mechanical strain into an electric potential, piezoelectric materials are commonly used as strain, touch, and pressure sensors. However, there are many other ways to measure strain, pressure, and sense touch which include strain gauges, potentiometers, and various electric switches. Although traditional circuitry tends to be less expensive than piezoelectric sensors or actuators, given a particular setting piezoelectric materials can outweigh traditional circuitry with their intrinsic advantages. What sets piezoelectric materials apart from traditional electronic sensors, for example, is that they can be retrofitted so that no power supply is required. The mechanical strain caused from the applied pressure, strain, or touch is directly transduced into an electric current which in turn is used to interpret the sensed action and provide a signal to induce an appropriate action. With sensors derived from traditional circuitry, one must constantly provide a power supply to detect changes in electrical properties such as resistance, capacitance, or inductance. Using piezoelectric materials can decrease the amount of power and hardware needed in selected situations. Although one can most certainly use traditional circuitry instead of smart materials to perform the same function, smart materials can be advantageous in certain circumstances.

2.1.3 Do Smart Materials Actually Perform Intrinsically?

It has been mentioned already that smart materials intrinsically perform their functions. Although many smart materials naturally possess their ability to react to their surrounding environment, most smart materials are enhanced by man to better exploit their smartness. The use of the word, "intrinsic" can therefore be somewhat misleading as most smart materials are synthetically created or altered through the use of applied science. Take piezoelectric materials for example. Piezoelectricity is exhibited naturally in materials such as Rochelle salt and quartz; however, their piezoelectric properties typically cancel

out in nature as their atomic dipoles are randomly oriented. To align the atomic dipoles in parallel, a procedure known as "poling" is used. With all the dipoles parallel, the piezoelectric effect is maximized in a net direction thus amplifying their voltage output when stimulated through strain and likewise enhancing their deformation properties when electrically stimulated. Shape memory alloys are another example. Using nitinol as an example, the shape memory effect is only present in binary NiTi alloys over a very narrow compositional range based around 50 atomic percent, *i.e.* 50% nickel and 50% titanium. William J. Buehler and coworkers at the Naval Ordnance Laboratory discovered that by adding a slight extra amount of nickel, they could change the transformation temperature from near 100°C down to below 0°C (Srinivasan & McFarland, Smart Structures: Analysis and Design, 2001). Differences of just 0.1 atomic percent can easily change transformation temperatures by 20°C or more (Morgan & Friend, 2003). For this reason production and processing of NiTi alloys must be very strictly controlled. Induction melting is often used to produce the final ingot, ensuring good homogeneity of the alloy, and enabling transformation temperatures to be controlled to within 5°C (Morgan & Friend, 2003). A shape memory alloy's properties can also be altered by adding a third impurity. With regards to nitinol, third impurity examples include iron to provide a lower transition temperature, copper for their smaller transformation hysteresis and improved cyclic stability, and palladium to increase the transition temperature (Morgan & Friend, 2003). Nearly all smart materials have been altered in some regard to fully exploit their smartness. Although the end product is a material that independently reacts to an external stimulus and is therefore deemed intrinsic, the final product was realized through engineering and human ingenuity. It is quite ironic that the material is given most of the credit by labeling it "smart" when it was the labor from engineers, scientists, and technicians that crafted its smartness.

2.2 INPUT RESPONSE CLASSIFICATION

As previously discussed, smart materials have a variety of diverse reactions to environmental stimuli. These responsive actions can be categorized as passive, active, or intelligent. Likewise, smart materials are often directly described as passive, active, and

intelligent based on how they contribute to the overall smart system. This section will briefly describe these categories.

2.2.1 Passive Smart Materials

Passive materials essentially can only sense an external stimulus. Passive smart materials have the ability to provide information to a smart system with regards to an environmental stimulus, but cannot appropriately react to the external stimulus on its own. Good examples of passive smart technology are fiber optics. Fibre optics have the ability to sense deformation, strain, pressure, or temperature, but that is all they can do for a smart system. Fibre optics can be used to passively detect cracks in buildings for example, and the information gathered can be interpreted by a computer or an engineer to analyze the building's structural integrity and call for maintenance only when necessary. This system eliminates the need for routine maintenance as one will know in advance when it's required. Passive smart materials could also be used in conjunction with actuators and a control system to instinctively react to an environmental stimulus. For an example, a fibre optics system can measure how a tall building sways from seismic activity and send this information to a control system which in turn can activate an active mass driver on the top of the building to dampen the seismic vibrations. To summarize, passive smart materials sense an external stimulus, but additional hardware is required to fittingly respond to the stimulus.

2.2.2 Active Smart Materials

Active smart materials not only can sense an external stimulus, but can react to it as well. Active materials convert energy from one form (the external stimulus) to another form (the reaction output). Piezoelectric materials and shape memory alloys are generally used as active smart materials. Piezoelectric materials react to pressure or strain by producing an electric potential which in turn can be used to generate an electric signal or even generate power for microelectronics. Piezoelectric materials also react to an electric current through shape deformation which can be used for mechanical actuation. In both of these cases, the piezoelectric material senses an environmental stimulus and also

provides the output reaction. In both of these examples, the piezoelectric material actively responds to the environmental stimulus. Likewise, shape memory alloys respond to an increase in temperature from the environment through morphing into its programmed shape. The shape deformation in turn can be used for mechanical actuation. The shape memory alloy actively reacts to the input stimulus (heat) with an actuation mechanism (the shape deformation).

It should be noted, however, that active smart materials do not necessarily have to sense the external stimulus. A control system or energy transducer can be used to link the environmental stimulus to activate an active smart material. The main attribute to an active smart material is its ability to react to the external stimulus, generally through actuation. For instance, shape memory alloys can be heated electrically and therefore can be activated by electricity. Say if you had an electric circuit consisting of an electric power source, a shape memory alloy, and a switch. The aim of the circuit is to cause the shape memory alloy to deform when the switch is pressed. When the switch is pressed, electricity will flow through the shape memory alloy, heat the alloy past its transition temperature through resistive heating, and thus activate the alloy to deform to its programmed shape. The sensor in this system is the switch as it sensed someone's touch, but the actuator is the shape memory alloy changing shape as a result of the switch being closed. The shape memory alloy actively responded to the touch, but did not sense the touch directly. The switch provided the link between the environmental stimulus (pressure from the touch) and the active smart material (the shape memory alloy). This example demonstrates that an active smart material does not need to sense the environmental stimulus for activation, but nonetheless needs a mechanism to transform the environmental stimulus to a form that enables the material's activation.

2.2.3 Intelligent Materials

Intelligent materials are materials that have been programmed to operate in a manual or pre-programmed manner. In this case, the material itself must act as the sensor, control system, and actuator. The material must be able to sense the environmental stimulus,

analyze the environmental stimulus, and appropriately react to the environmental stimulus based on said analysis. In summary, the material itself must be a smart system, but the control system (in the author's opinion) should be in analog format without any electronic components. An example of an intelligent material would be photochromic glass or plastic found in modern day eyewear. In response to electromagnetic radiation in the ultraviolet (UV) spectrum induced by sunlight, photochromic materials undergo a property change that changes the hue of the material to a darkened state based on the amount of UV radiation. In this system, the photochromic material acts as sensor, control system, and actuator. The photochromic material detects UV radiation from sunlight (sensor), goes through a property change proportional to the amount of UV radiation (control system), and proportionally darkens its hue from the induced property change (actuator). The photochromic glass thus acts as a smart system through the use of analog control.

There are several commercial fabrics that act as smart systems using analog control and can therefore be classified as intelligent materials. Two of these "smart fabrics" are anti-microbrial fabrics and temperature regulation fabrics.

Agion®'s customized antimicrobrial solutions incorporate silver ions in a zeolite carrier (Agion Technologies, 2006). As the humidity increases, the environment becomes ideal for bacteria growth. The silver ions exchange with other positive ions (often sodium) from the moisture in the environment, affecting a release of silver. The amount of silver released is proportional to ambient moisture levels. The silver in turn fights bacterial microbes through inhibiting cell division, disrupting cell metabolism, and preventing respiration by inhibiting transport functions in the cell wall (Agion Technologies, 2006). These anti-microbrial fabrics act as: a sensor as they detect the presence of ambient moisture, the control system as they respond to the amount of ambient moisture through releasing silver ions in a concentration that is proportional to the amount of moisture, and as an actuator by releasing the silver ions. As anti-microbrial fabrics act as all the components of a smart system, they can be labeled as intelligent materials.

Temperature regulation fabrics use phase change materials (PCMs) to regulate temperature in winter coats by storing and releasing latent heat. PCMs are materials that can absorb, store, and release heat while the material alternates from its liquid and solid phases. Outlast® uses a paraffin wax compound which is micro-encapsulated into thousands of miniscule, impenetrable, had shells called thermocules (Outlast Technologies, Inc., 2010). These thermocules recycle body heat by absorbing, storing, distributing, and releasing heat on a continuous basis acting as a temperature buffer. Say if one wore a coat with temperature regulation fabrics while skiing. During the act of skiing, one's body would produce excess heat. The thermocules would absorb some of this excess heat effectively cooling the skier in the process. When resting on the chairlift afterwards, one's body temperature would decrease and activate the thermocules to release the energy stored earlier to warm up the skier. The thermocules are designed to regulate one's body to be at a comfortable temperature through recycling latent heat buildup. Temperature regulation fabrics act as a smart system operating as: a sensor through sensing body, a control system by storing and releasing latent body heat based on one's body temperature, and an actuator by absorbing or releasing heat to one's body.

2.3 SMART MATERIAL CATEGORIES

Smart materials can be divided into two categories based on their reaction to environmental stimuli. Materials that respond to the environment by changing one of its physical properties are appropriately known as property-changing materials, while materials that respond to the environment through exchanging energy from one form to another are appropriately called energy-exchanging materials. Many energy-exchanging materials are bidirectional meaning that the two energy exchanges can occur either way. An example of reversible energy-exchanging materials are piezoelectric materials: they respond to deformation by producing an electric potential and respond to an electric potential by deforming. Table 2-2 gives a list of various smart materials assorted by their type. This section aims to introduce the reader to a variety of smart materials along with the science used to predict their behavior.

Table 2-2: List of Smart Materials with Corresponding Inputs and Outputs

TYPE OF SMART MATERIAL	INPUT	OUTPUT
Type 1 Property-changing		
Thermochromics	Temperature Difference	Colour Change
Photochromics	Radiation (Light)	Colour Change
Mechanochromics	Deformation	Colour Change
Chemochromics	Chemical Concentration	Colour Change
Electrochromics	Electric Potential Difference	Colour Change
Liquid Crystals	Electric Potential Difference	Colour Change
Suspended Particle	Electric Potential Difference	Colour Change
Electrorheological	Electric Potential Difference	Stiffness/Viscosity Change
Magnetoreheological	Electric Potential Difference	Stiffness/Viscosity Change
Shape Memory Alloys	Temperature Difference	Deformation
Type 2 Energy-exchanging		
Electroluminescents	Electric Potential Difference	Light
Photoluminescents	Radiation	Light
Chemoluminescents	Chemical concentration	Light
Thermoluminescents	Temperature Difference	Light
Light-emitting Diodes	Electric Potential Difference	Light
Photovoltaics	Radiation (Light)	Electric Potential Difference
Fiber Optics	Deformation	Light/Electric Potential Difference
Phase Change Materials	Temperature	Phase Change
Type 2 Energy-exchanging (reversible)		
Piezoelectric	Deformation	Electric Potential Difference
Pyroelectric	Temperature Difference	Electric Potential Difference
Thermoelectric	Temperature Difference	Electric Potential Difference
Electrorestrictive	Electric Potential Difference	Deformation
Magnetorestrictive	Magnetic Field	Deformation

2.3.1 Type 1: Property Changing

If the response of a smart material alters the internal energy of the material by altering either the material's molecular structure or microstructure, then the input results in a property change of the material (Addington & Schodek, 2005). These properties can be either intrinsic, meaning that they result from the material's internal structure and composition, or extrinsic, meaning that they are dependent on additional environmental factors. An example of an extrinsic factor would be the viewing angle for liquid crystals as the colour may change in relation to the angle of incident light. Property changing materials include colour changing materials such as photochromics and suspended particle systems, viscosity changing materials such as electrorheological and magnetorheological fluids, and shape memory alloys which are part of this thesis's

experimental investigations. This section will present to the reader several property-changing smart materials along with their responsive internal mechanisms.

2.3.1.1 COLOUR AND OPTICALLY CHANGING MATERIALS

For colour and optically changing materials, an external stimulus from the surrounding environment induces a property change in the smart material which in turn alters the material's optical properties. We (living creatures with eyes) perceive these optical alterations as a colour change. Fundamentally, the input energy produces an altered molecular structure or orientation on the surface of the material on which light is incident. These changes in turn affect the material's absorptance or reflectance characteristics and hence its perceived colour. To adhere to the repeatability criterion of a smart material, these responses must be reversible.

Several different environmental stimuli have the potential to alter a material's surface molecular structure. Some examples include electromagnetic energy, thermal energy, mechanical energy, chemical energy, and electrical energy. The optically changing materials that respectively respond to each energy source are thus further categorized into photochromics, thermochromics, mechanochromics, chemochromics, hydrochromics, and electrochromics; also classified as optically changing materials are liquid crystals and suspended particles.

2.3.1.1.1 Photochromic Materials

Photochromism is defined as a reversible transformation in a chemical species between two forms having different absorption spectra by photoirradiation (Tsivgoulis, 1995). Most commercial photochromic materials tend to focus on reacting to photoirradiation derived directly from sunlight. These materials are therefore engineered to respond to electromagnetic energy in the ultraviolet (UV) region as UV radiation is traditionally absent from artificial lighting but present in sunlight. After absorbing UV electromagnetic energy, the material's molecular structure is altered, causing its reflective wavelength to change in the visible spectrum. Most photochromic materials exhibit

positive photochromism, when its stable form is colourless of slightly yellow and the transformed state is coloured (See Figure 2-1 for an example). Negative photochromism is less common, when a material's colour is bleached by incident sunlight.

Figure 2-1: Visionaire in collaboration with Calvin Klein produced a limited edition solar issue using Photochromic Plastisol Ink. The photo turns from black and white to a full spectrum of colour when exposed to sunlight or UV radiation. Photo Extracted from (Barberich, 2009)

Photochromic materials can be derived from inorganic and organic compounds. Inorganic compounds include silver halides (*e.g.* silver bromide (AgBr), silver chloride (AgCl), & silver iodide (AgI)) while organic compounds include napthopyranes, spiropyranes, and bacteriorhodopsin: a protein isolated from halobaterium salinarum that reacts to the influence of light by undergoing a reversible colour change from violet to yellow (Ritter, 2007). These compounds can be placed into paints, dyes, and plastics among other things and can produce a variety of colours. These materials can also be used for data storage and if they respond rapidly, they could be useful for random access memory components of an optical computer. Results from Ted Burkey suggest a potential writing speed of 10^7 MHz (Burkey, 2004).

The most well known use of photochromic materials is their use in reactive eyewear (See Figure 2-3). Photochromic lenses will darken upon exposure to sunlight, thus acting as sunglasses when needed. There's no need to continuously alternate between regular eyeglasses and sunglasses and one's prescription will be identical between transitions. Photochromic lenses generally use either naphthopyrane dye or silver halide crystals for

the photochromic reaction. In the case of naphthopyrane dye (as shown in Figure 2-2), when exposed to UV radiation, a weak chemical bond breaks and the molecule rearranges into a form that absorbs light at longer wavelengths (Erickson, 2009). For lenses with embedded silver halide crystals, electrons from the glass combine with the colourless silver cations upon the presence of UVA rays (wavelength of 320-400 nm) to form elemental silver (Erickson, 2009). As elemental silver is visible, the lenses appear darker. When sunlight is absent, photochromic lenses will return to their clear, transparent state.

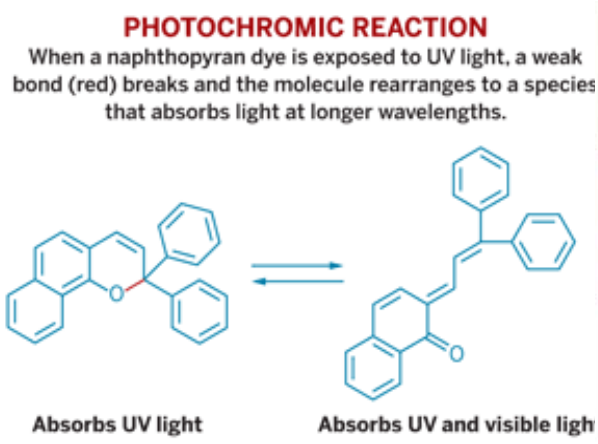

Figure 2-2: Some plastic photochromic lenses use naphthopyran dye as its photochromic material. When exposed to UV light, a weak bond (highlighted in red) breaks and the molecule rearranges into a form that absorbs light at longer wavelengths. Photo extracted from (Erickson, 2009)

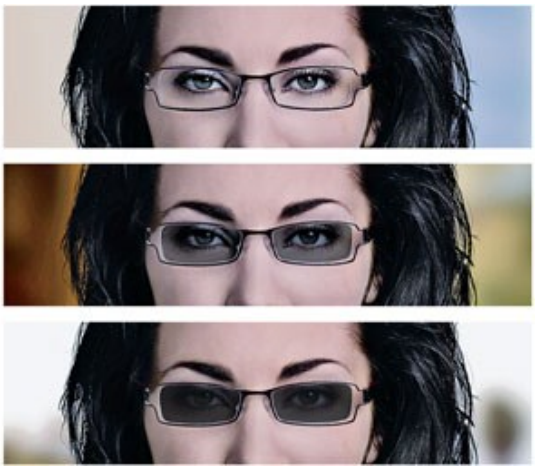

Figure 2-3: Photochromic lenses darken when they are exposed to sunlight. Photo extracted from (Erickson, 2009)

2.3.1.1.2 Thermochromic Materials

Thermochromics absorb heat, which leads to a thermally induced chemical reaction or phase transformation. Thermochromics have properties that undergo reversible changes upon changes in the surrounding temperature. The new molecular structure (or phase structure) resulting from the temperature change has a different spectral reflectivity than the original structure; as a result, the electromagnetic radiation reflected from the material changes, which we perceive as a colour change.

Thermochromic colours are derived fundamentally from liquid crystals and leucodyes, both of which are organic compounds. Thermochromic pigments or materials are formed using an organic dye, an acid activator, and a low melting solid such as an ester or alcohol that acts as a solvent when liquefied (Pariyasamy & Khanna, 2010). Thermochromic paints and dyes are widely used to provide a colour change indicator of the temperature level of a product. Thermochromic ink designed and manufactured by Chromatic Technologies, Inc. is used on cold certified cans and bottles by Coors® Light as shown in Figure 2-4; when the beer inside is at its optimum drinking temperature (4°C or lower), the white mountains turn blue (Coors Light, 2008). This transformation is performed using leuco dyes as the organic compound. Leuco dyes are also used on the Duracell battery tester. A thermochromic ink layer derived from leuco dyes is placed on top of a conductive ink layer that has a small resistance to electric current (HowStuffWorks, Inc., 2000). When conducting electric current, resistive heat is generated through the conductive ink and transfers to the leuco dye through thermal conduction. The heat activates the leuco dye to turn clear, showcasing to the viewer the colour of the conductive ink. Leuco dyes are less expensive than liquid crystals, but can only be used for one colour transformation: coloured when below the transformation temperature and clear when above the transformation temperature (Color Change Corporation, 2002). Leuco dyes can therefore only be used to indicate if the temperature is above or below the transformation temperature, but the specific transformation temperatures can be engineered. CTI can provide custom activation temperatures as low as -8°C and as high as 69°C (Chromatic Technologies, Inc. (CTI), 2009). Exposure to ultraviolet wavelengths (like sunlight) may cause the material to degrade and lose its colour-changing capabilities thus limiting their use in architecture (Addington & Schodek, 2005). Although widely used in applications, the mechanism underlying a leuco dye's thermochromism has yet to be fully understood (Tang, MacLaren, & White, 2010).

Figure 2-4: The infamous cold activated can by Coors® Light, uses thermochromic inks to let the drinker know when the beer is at its optimum drinking temperature. When the mountains turn blue, the beer is deemed, "certified cold". Photo extracted from (Chromatic Technologies, Inc. (CTI), 2009).

Liquid crystals are more expensive than leucodyes, but are highly sensitive to temperature fluctuation. Known as calamitic liquid crystals, liquid crystal molecule aggregates are typically rod shaped with flexible ends to allow ease of flow (University of Cambridge, 2007). An Austrian botanist named Friedrich Reinitzer is often credited with discovering the liquid crystal phase. In 1888, Reinitzer observed that cholesteryl benzoate had two distinct melting points, one point where the compound transitioned between a solid sample and a hazy liquid, and another point where the hazy liquid transitioned into a clear, transparent liquid (What are Liquid Crystals, 2003).

Thermochromic liquid crystals have been employed as a flow visualization tool for over four decades (Smith, Sabatino, & Praisner, 2001). Liquid crystals (LCs) have the ability to reflect a wavelength of light that is dependent on the LC's temperature. The dominant wavelength (or hue) of the reflected light varies monotonically with temperature within a specific temperature bandwidth. This monotonic relationship between colour and temperature has allowed researchers to quantitively map surface and flow-field temperature distributions with high spatial resolution and more recently, high accuracy (Smith, Sabatino, & Praisner, 2001). Liquid crystals are initially translucent below their temperature range as they reflect light with wavelengths longer than those in the visible spectrum. When heated to the lower boundary of its temperature bandwidth, a liquid

crystal will reflect light closer to the lower energy end of the visible spectrum (*i.e.* red). As temperature increases, the liquid crystals will reflect shorter wavelengths passing through orange, yellow, green, and blue, and finally violet at the higher boundary of the temperature bandwidth. Once past the upper boundary of its temperature range, a liquid crystal will once again turn translucent indicating that it reflects wavelengths shorter than those in the visible spectrum. A black substrate is normally applied beneath liquid crystals to absorb and prevent reflection of unmodified light passing through the liquid crystal layer; making the liquid crystals appear black when outside of their activation boundaries (Smith, Sabatino, & Praisner, 2001).

The temperature influenced colour changes of liquid crystals are a result of changes in their spacing and orientation. A liquid crystal exhibits its crystallic (or solid) phase below the lower boundary temperature, its anisotropic nematic phase (or liquid crystal phase) in between boundary temperatures where they reflect light in the visible spectrum, and isotropic liquid phase above its higher boundary temperature. While transitioning from its crystal to liquid phase through a temperature change, a crystal's molecule aggregates change orientation from pointing towards a common axis (*i.e.* crystallic phase structure) to no intrinsic orientation (*i.e.* liquid phase structure) thus affecting the periodic spacing between aggregates (What are Liquid Crystals, 2003). The molecular alignment respective to each phase is shown in Figure 2-5. The intermediate phase, the liquid crystal phase, is present during the transition from solid to liquid and vice versa. The liquid crystal phase is not as ordered as the crystal/solid phase, but nonetheless has some degree of alignment that distinguishes itself from liquid phase. Molecules in the liquid crystal phase tend to retain their orientation akin to a crystal, but allow themselves to switch positions with other molecules akin to a liquid (Tyson, 2011). The liquid crystal phase thus exhibits characteristics of crystals and liquids, hence the term liquid crystals.

White light passing through these liquid crystals in turn gets defracted and the wavelength with the greatest constructive interference is reflected back. Through the control of temperature, one can control the liquid crystals orientation and periodic spacing to influence the wavelength of the reflected light. For example, a temperature

closer to the upper boundary will reduce the space between molecules and therefore reflect a shorter wavelength: a wavelength closer to the blue-violet side of the colour spectrum.

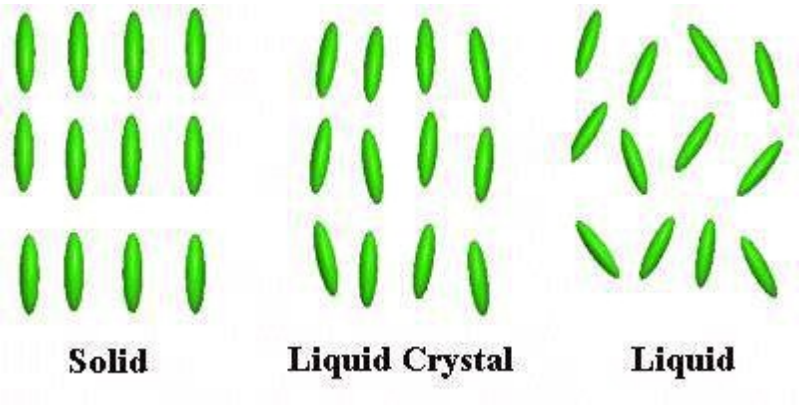

Figure 2-5: The molecular alignment of a crystal, liquid crystal, and liquid. The solid (or crystal) phase has molecules with an orientation pointing towards a common axis, the liquid phase has molecules with no orientational order, and the liquid crystal molecules exhibits an orientation that has characteristics from both the solid and liquid phases. Image extracted from (What are Liquid Crystals, 2003)

Another type of liquid crystal phase is the chiral nematic liquid crystal phase. The term, chiral nematic is often mistakenly interchangeable with the term, cholesteric (another type of liquid crystal phase) despite that both phases have distinct chemical (chiral nematic phases are non-sterol based) and physical properties (Smith, Sabatino, & Praisner, 2001). The chiral nematic phase is typically composed of nematic molecules with a chiral center that produces intermolecular forces to favour an alignment at an angle with respect to each subsequent molecule. The rod-shaped molecules in each layer are twisted with respect to the molecules above and below in succession. The molecular orientations in turn follow a helical pattern that is characterized by pitch. Pitch is defined the distance between layers that exhibit the same orientation, *i.e.* the distance where the molecules collectively rotate 360 degrees in succession. Figure 2-6 illustrates a group of chiral nematic liquid crystals along a length of ½ pitch. The pitch of the chiral nematic phase is quite important as it influences the colour of reflective wavelengths. Essentially, the pitch acts similar to a filter, allowing only wavelengths equal to pitch length to travel through the liquid crystals. Additionally, the pitch length can be altered through

temperature. An increase in temperature increases the angle between successive layers of molecules, therefore decreasing the pitch. Likewise, a decrease in temperature causes the angle between successive layers to decrease, therefore increasing the pitch. An increase in temperature will therefore shorten the wavelength of light reflected from the liquid crystal and a decrease in temperature will increase the wavelength of reflected light. This feature allows liquid to act as colour thermometers.

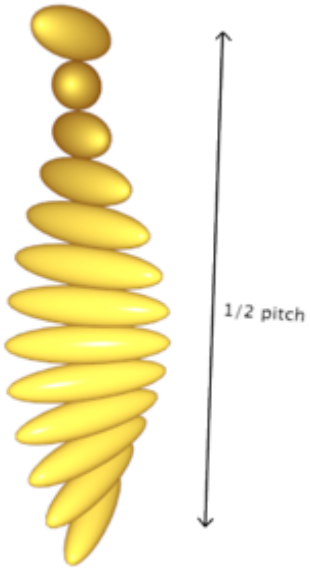

Figure 2-6: Rod-shaped chiral nematic liquid crystals are oriented in a helical patern that is characterized by pitch. Image extracted from (University of Cambridge, 2007)

Thermochromic liquid crystals are commercially available in a variety of forms, but the micro-encapsulating chiral nematic liquid crystals have become the choice for most research applications as the perceived colour displays the lowest sensitivity to lighting and viewing angle variations (Smith, Sabatino, & Praisner, 2001). Manufactured in 10-15 micron packets encased in a protective clear polymer coating, encapsulated liquid crystals are the least sensitive to contaminants such as dust or moisture with reference to other thermochromic liquid crystal technologies (Smith, Sabatino, & Praisner, 2001).

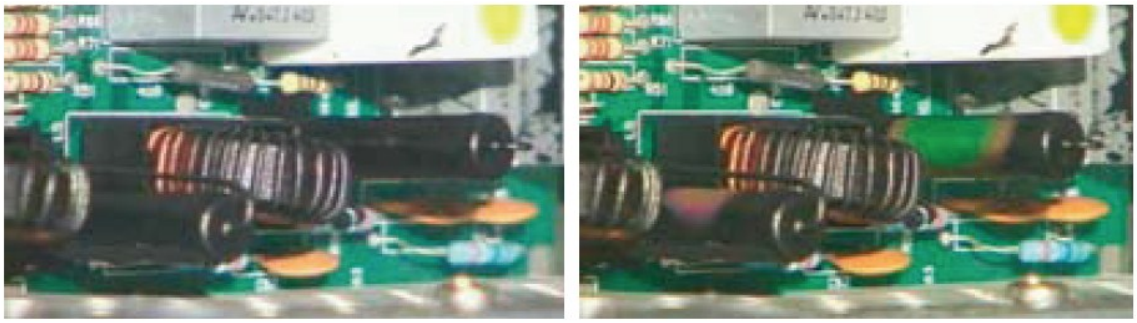

Figure 2-7: The before (left) and after (right) images of an electronic device that has been sprayed with thermochromic liquid crystals. Colours closer to the violet spectrum indicate hotter spots, while colours closer to the red spectrum indicate cooler spots. Image extracted from (Advanced Thermal Solutions, Inc., 2010)

Liquid crystals can be engineered to change temperature from -30°C to 120°C and can be sensitive enough to detect changes as small as 0.2°F (Color Change Corporation, 2002). Because of their sensitivity to temperature fluctuations, they are often used for heat transfer studies and mapping temperature fields on electronic components or boards. Shown in Figure 2-7, Advanced Thermal Solutions, Inc. offers a thermochromic liquid crystal kit for these heat transfer studies allowing the experimenter to pinpoint locations of hotspots on a device with temperature ranges from 12°C to 120°C, each one with a particular bandwidth from 1°C to 20°C (Advanced Thermal Solutions, Inc., 2010).

2.3.1.1.3 Mechanochromic Materials

Mechanochromic materials have altered optical properties when excited by the effects of compression, tension, or friction. Essentially, the material will undergo a colour change when subjected to stresses and deformations with external forces.

One of the few compounds to exhibit reversible mechanochromism is difluoroboron avobenzone. When let crystallize, difluoroavobenzone packs according to three different morphologies: prism-like crystals, needle-like crystals, and dendritic crystals which respectively fluoresce a green, cyan, and blue glow. Professor Cassandra Fraser at the University of Virginia reports that a thermally annealed film of the dendritric flue-emitting crystal glows yellow when slightly touched with a cotton swab (The Light

Touch of a Cottom Swab, 2010). The yellow emission, which is likely due to an amorphous solid form, reverts back to green with time (a matter of a few minutes at room temperature, faster if heated).

The gold(I) compound [$(C6F5Au)_2$(μ-1,4-Diisocyanobenzene)] has also shown reversible mechanochromism. After gently pressing the compound in its powder form, a team from Hokkaido University discovered that the subtle changes in the molecular arrangement caused a change in luminescent properties (NPG Asia Materials, 2008). Under UV light, the compound changes from a grey-yellowish appearance to yellow (See Figure 2-8. The change is fully reversible through the addition of a solvent. Despite these findings, mechanochromic materials have yet to make their mark commercially. This is most likely from a variety of factors that include cost, availability, demand, and use. From the information gathered, it appears that most mechanochromism occurs under luminescence, a property that has limited demand commercially.

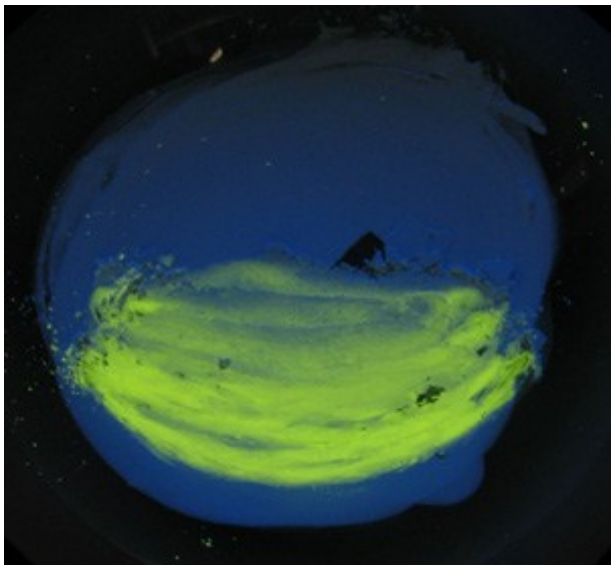

Figure 2-8: Photograph showing the gold(I) compound material under UV light illumination. The part of the powder that was crushed shows yellow luminescence, contrasting with the blue luminescence from the original compound. Image extracted from (NPG Asia Materials, 2008)

2.3.1.1.4 Chemochromic Materials

Chemochromic materials react to a change in their surrounding chemical environment. Akin to the production of heat in an exothermic reaction or the onset of an odour, a

change in colour is a sensual clue to a chemist that a chemical reaction has taken place. For example, if one places a copper penny in a solution of nitric acid, the induced redox reaction will cause the penny to turn greenish-blue. In acid-base titration experiments, acid-base indicator dyes are used to visually let the chemist know when a pH level has been reached. Phenolphthalein is used to indicate when a pH of seven has been reached by transitioning the liquid from pink to clear or vice versa. One of the most common ways to test a solutions pH paper is through litmus paper; a strong acid makes a red stain while a strong base makes a blue stain. Colour is so prevalent in chemistry, that chemists measure the intensity and hue of colour to determine the extent that a chemical reaction has taken place. The art of spectrometry allows chemists to measure colour in intensity and wavelength to determine not only the concentration of chemical solutions, but also the molecular makeup of the chemical compound itself. Spectrometry is also performed outside of the visible spectrum for aqueous solutions that do not absorb wavelengths in the visible spectrum.

As colour change plays a major role in chemical reactions, the author believes the term chemochromism is unfit for use. Almost all compounds in one form or another can change colour through a chemical manipulation. As already mentioned, elemental copper turns greenish-blue once oxidized, but copper is certainly not considered smart as many metals degrade when in an acidic solution; often with colour changes. As almost every material in some regard, can be optically altered through the use of a particular chemical reaction, the author believes that this term is not fit to be used.

2.3.1.1.5 Hydrochromic Materials

Hydrochromic materials are materials that undergo optical property alterations in reaction to the presence of water. Currently, all hydrochromic materials such as inks, fabrics, or paints transform from white to transparent when wetted with water and likewise changes back to white when dried. Matsui International Company, Inc. has produced a special binder known as Hydro-Chromic White, a special binder that can be screen printed over a fabric design (Matsui International Company, Inc., 2008). When screen printed over a

coloured design, the design will appear white when dry, but after the medium is wetted, the binder will become transparent to showcase the design hidden underneath. After drying, the binder will return to its opaque, white state and once again hide the coloured design. The product is commonly used in reactive diapers and umbrellas (See Figure 2-9).

Figure 2-9: SquidLondon's Squidarella Umbrella. Image extracted from (SquidLondon, 2010)

2.3.1.1.6 Electrochromic Materials

In the broadest sense, electrochromism is defined as a reversible colour change caused by an application of electric current or potential. Electrochromism was first noted in the 1930s when colouration was noted in bulk tungsten oxide (WO_3). In 1953, Kraus studied electrochromism of thin films of tungsten trioxide when he discovered that a WO_3 vapour layer deposited on a semitransparent metal layer (Cr, Ag) was intensively blue when cathodically polarized in 0.1N H_2SO_4 (Aegerter, Avellaneda, Pawlicka, & Atik, 1997). In 1969 and 1973, S.K. Deb published his research work on thin films of molybdenum and tungsten trioxide, which established the principles of modern electrochromism (Ritter, 2007). Several inorganic and organic materials have been shown to exhibit electrochromism, most of which are transition metal oxides. Organic electrochromic materials tend to suffer from problems with secondary reactions during switching, but more stable organic systems have been developed (Lampert, 2004). An electrochromic

material's colouration and bleaching under cathodic or anodic polarization is usually described by Equation 2-1:

$$MeO_n + xI^+ + xe^- \leftrightarrow I_xMeO_n \qquad 2\text{-}1$$

where Me is a metal atom, I^+ is a singly charged ion usually H^+ or Li^+, e^- is an electron and n depends on the particular type of oxide (Aegerter, Avellaneda, Pawlicka, & Atik, 1997). Among all of the materials studied so far, the one material that remains the most researched has been WO_3 (Deb, Opportunities and challenges in science and technology of WO3 for, 2008).

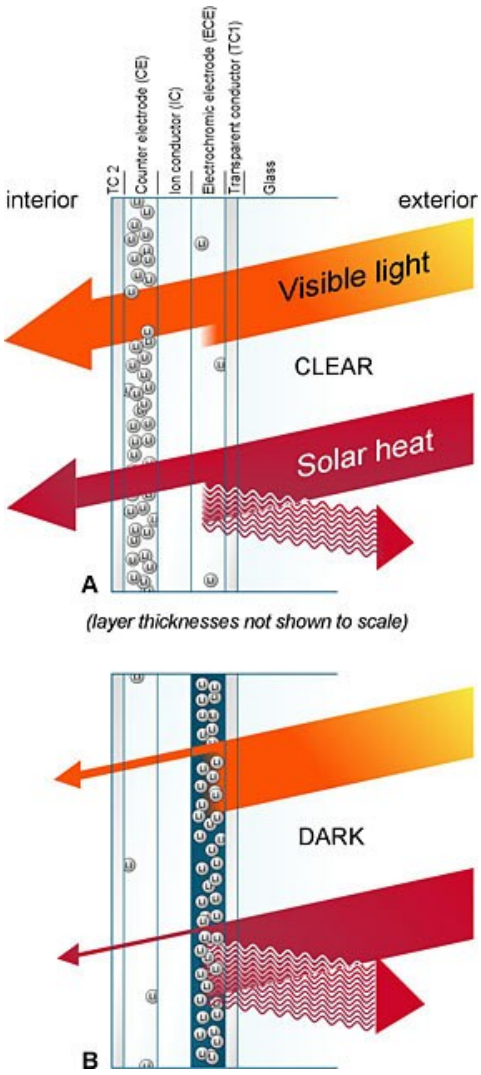

Figure 2-10: An illustration showing how Sage Glass technology works to limit both light and heat transmission. When an electric potential is applied the glass turns from clear (above) to a dark blue (below). Image extracted from (Sage Electrochromics, Inc., 2010)

Electrochromic devices are the most popular technology for large area switching devices (Lampert, 2004). Technological developments in electrochromic materials have led to a number of advancements, most notably the first available electrochromic "smart window", which has the potential to make a significant impact in energy conservation. An electrochromic window darkens and lightens depending on the induced electric potential. A small voltage (1-5V) causes the electrochromic material to darken while reversing the voltage causes the material to lighten. Fundamentally, the colour change in an electrochromic material is induced from a chemical molecular change caused by redox reactions. Several layers are needed for electrochromic reactions to take place. An electrochromic window for example needs seven layers: two glass layers, two conductive layers, an ion storage layer, an ion

conductor/electrolyte layer, and the electrochromic layer. Figure 2-10 and Figure 2-11 illustrate how these layers are organized in an electrochromic window.

Essentially, hydrogen or lithium ions (cations) along with their associated electrons are situated in the ion storage layer when inactive. When the proper electric potential is applied across the conductive layers, both the cations and associated electrons are transported to the electrochromic layer. The electric potential propels the cations to the electrochromic layer via the ion conductor layer while the electrons are propelled to the electrochromic layer through the conducting oxide layers and external circuit. The positive portion of the electrical potential must be connected to the conductive layer adjacent to the ion storage layer for these transports to occur. Once amalgamated in the electrochromic layer, the cations and electrons react with the electrochromic film through the redox reaction previously shown in Equation 2-1. The compound to the right of the equation exhibits a darkened state while the compounds on the left of the equation are relatively colourless.

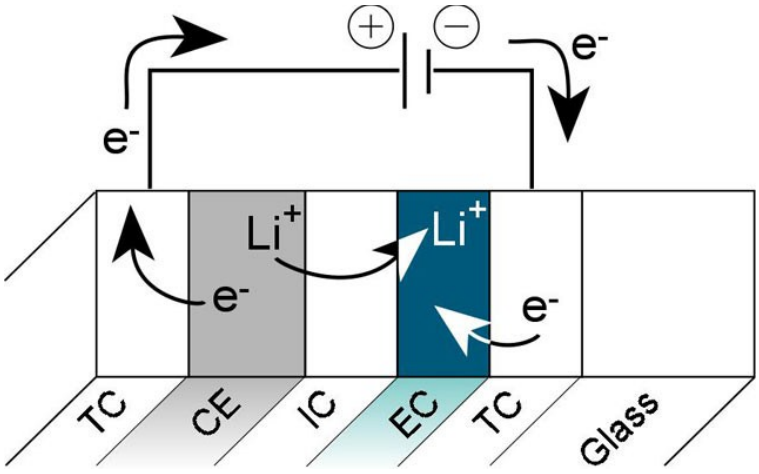

Figure 2-11: An illustration demonstrating showing the direction of electron transport upon an application of an electric field. Image extracted from (SAGE Electrochromics, Inc., 2009)

In glass assemblies (such as the ones shown in Figure 2-12), the electrochromic layer is often WO_3. Using lithium (Li+) and WO_3 to represent the cations and electrochromic material, equation 2-1 can be rewritten as follows:

$$WO_3 \text{ (colourless)} + xLi^+ + xe^- \leftrightarrow Li_xWO_3 \text{ (blue)} \qquad 2\text{-}2$$

Before the electric potential is applied, the electrochromic layer (WO_3) is colourless, but changes to a dark blue hue once the electric potential is applied as a result a the associated redox reaction. When ionically bonded with lithium ions, WO_3 exhibits a dark blue hue. The reaction thus changes the electrochromic material's light reflective properties. It is generally believed that the colouration occurs as a result of the injection and trapping of a large density of electrons in the electrochromic oxide layer (Deb, 1994).

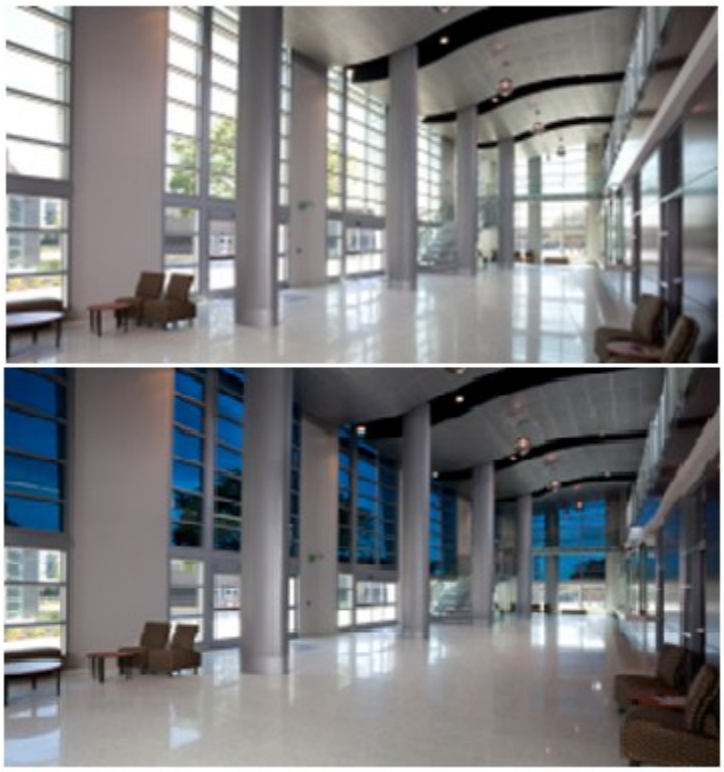

Figure 2-12: Sage Glass in the transparent and tinted state in Chabot's Student Service Center. Image extracted from (Sage Glass, 2010)

Electrochromics have several major advantages including a small switching voltage (1-5V), specular reflection, a gray scale (the darkened hue can vary with respect to applied voltage), and the fact that power is only needed during switching (Lampert, 2004). According to Sage Electrochromics, Inc., it takes less electricity to power and control 1,500 square feet of their electrochromic smart windows per day than it does to power a 60-Watt light bulb (Sage Electrochromics, Inc., 2010). Typical electrochromic devices have upper visible transmission of T_V = 70-50 and fully coloured transmission of T_V = 25-10% (Lampert, 2004). Levels of transmittance as low as 1% are possible. Switching time, however, is not instantaneous. The electrochromic smart windows offered from

Sage Electrochromics, Inc. take 3-5 minutes to change tints (Sage Electrochromics, Inc., 2010). Saint-Gobain uses electrochromic glass for automotive sunroof glazing where the switching time between the darkest and lightest shades is about 30 seconds (Saint-Gobain, 2010).

2.3.1.1.7 Liquid Crystals and Suspended Particles

Like electrochromic materials, liquid crystals and suspended particles respond to an electric potential resulting in a change in their optical properties. However, the mechanism underlying the optical property changes does not involve a chemical redox reaction. In both liquid crystals and suspended particles, the electric potential induces shifts in respective particle orientations which in turn alters the material's reflective and absorptance properties.

As mentioned previously in Section 2.3.1.1.2, liquid crystals respond to temperature with a change in their orientation. The change in orientation can be exploited to alter the reflective properties of liquid crystals in the form of a colour change. More commonly, however, liquid crystals are used to filter light through the application of an electric or magnetic field. These fields change liquid crystals' orientations, but in a way in which their light transmissive properties are altered macroscopically.

Calamitic (rod-shaped) crystal molecules typically possess an electric dipole where one end of the dipole has a net positive charge while the other end has a net negative charge (Electric and Magnetic Field Effects, 2004). Applying a sufficient electric field to a liquid crystal, the dipole molecules will reorient themselves towards the electric field's net direction. The electric field will exert a torque on the molecule's electric dipole, and will rotate in the direction of the electric field as a result. For example, take the situation where liquid crystal molecules are aligned parallel to a surface and an increasing electric field is applied perpendicular to the surface. Initially, the electric field will not cause any change in alignment, but once the threshold magnitude is reached, the molecule will begin to rotate in the direction of the electric field. After reaching a sufficient electric field, the liquid crystal molecular aggregate will be in complete alignment with the

induced electric field. The induced change in orientation of a liquid crystal's molecules through inducing an electric field is known as a Freedericksz transition and is illustrated in Figure 2-13. (Electric and Magnetic Field Effects, 2004).

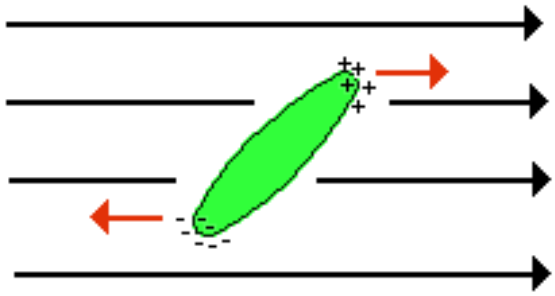

Figure 2-13: An electric field (the direction of which is shown by the arrows) causes calamitic crystal molecules to rotate in the direction of the applied field. Image extracted from (Electric and Magnetic Field Effects, 2004)

Feedericksz transitions are most commonly exploited in liquid crystal displays (LCDs); an illustration of an LCD's filtering mechanism is shown in Figure 2-14. LCDs consist of a nematic liquid crystal layer sandwiched by layers of polymer substrate, followed by transparent electrodes, sheets of glass, and polarizing films. The polymer substrate layer undergoes a rubbing process which leaves a series of parallel microscopic grooves in the layer. The polymer substrate layers are 90 degrees out of phase of each other. The grooves will cause the first layer of molecules to align with the filter's orientation (Tyson, 2011). These grooves in turn, help align the nematic liquid crystals in a 90 degree twist into the bulk of the crystal, quite similar to the chiral nematic phase (Twisted Nematic (TN) Displays, 2004).

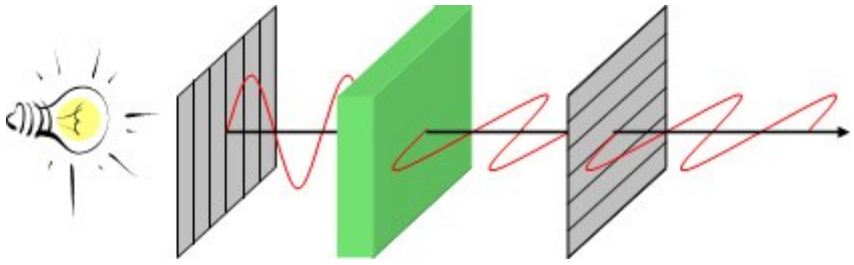

Figure 2-14: An illustration showcasing how an LCD screen works. The white light is first polarized via a polarizing film, is twisted by the liquid crystal layer, and goes through the final polarizing film. (Desimpel, 2006)

As external white light passes through the LCD via the first polarizing film, it is polarized and transports through the first glass and electrode layers providing that an electric field as not been induced. As light travels through the first polymer substrate layer and enters the liquid crystal layer, the light's polarization state twists with the direction of the liquid crystal molecules (Twisted Nematic (TN) Displays, 2004). Once at the second polymer substrate layer, the light's plane of vibration thus vibrates at the same angle as the final layer of liquid crystal molecules, 90 degrees out of phase from the initial layer of liquid crystal molecules. The light then travels through the second electrode, the second glass layer, and to the second polarizing film. As the second polarizing film has filter slots that are rotated 90 degrees akin to the nematic crystal layer, the polarized light goes through unhindered. The resultant light on the other end of the LCD is thus pure white light (See Figure 2-15.

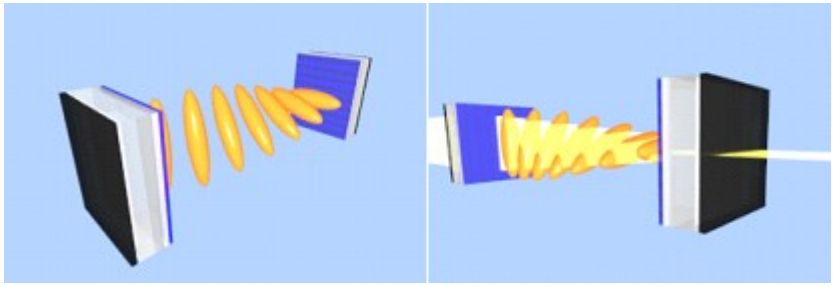

Figure 2-15: An illustration of how the nematic crystal layer twists the polarized light across the polarizing films. There is no applied electric potential across the liquid crystals in this state. Image extracted from (University of Cambridge, 2007)

If one would apply an electric field across the liquid crystal layer, one would observe something different. After applying an electric field across the liquid crystal layer through the electrode layers, the liquid crystal molecules would undergo the Freederickz transition discussed earlier. The liquid crystal molecules will thus reorient themselves in the direction of the electric field. The induced angle change depends on the magnitude of the applied electric field. The new orientation of nematic liquid crystals no longer induces the polarized light to rotate. The polarized external light source will therefore enter and leave the liquid crystal layer in the same plane (See Figure 2-16). As the

second polarized slots are at a right angle to the first polarized film, the polarized light will not pass through, and the LCD will appear dark.

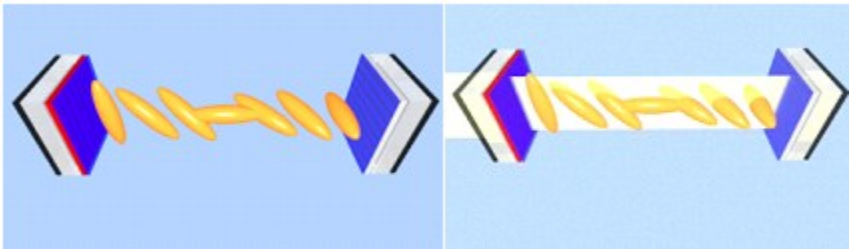

Figure 2-16: Illustration of how an electric potential rotates the nematic crystals and prevents the light from transmitting through the second polarizing film. Image extracted from (University of Cambridge, 2007)

One drawback of LCD screens is the need of a light source, which can be either internal or external. Using reflective mediums, an external light can be used to showcase pixels whose nematic liquid crystals have been reoriented through an applied voltage. Reflective LCD screens are often used in calculators, digital wristwatches, and electronic readers. To relieve an LCD screen's dependence on external light sources, many LCD screens have an internal light source. The internal light source is located at the back of the liquid crystal display and is hence known as a backlight. Most computer and television screens are backlit using fluorescent tubes above, beside, and occasionally behind the LCD screen while a white diffusion panel behind the LCD redirects and scatters the lights evenly to ensure a uniform display. (Tyson, 2011). As the liquid crystal layer filters much of the backlight's emissions, the light showcased on the LCD screen is much more diffuse; often more than half of original light source is lost (Tyson, 2011).

Through careful control of the voltages applied to the electrodes, one can vary the orientation of the nematic liquid crystals to vary the filtration of light. Manipulating the voltage magnitude allows the pixel to have a variety of shades. For light/dark LCD screens, the pixels can have a variety of grey shades, typically 256 shades in modern LCD screens.

Liquid crystals are often used for colour displays. As illustrated in Figure 2-17, colour LCD screens contain pixels with three subpixels: one green, one blue, and one red. As shown in Figure 2-17 each subpixel contains a filter that filters the light source into its respective red, blue, or green colour. The liquid crystals in turn can be oriented through voltage manipulation to control the amount of red, blue, and green light being passed through the pixel, thus being able to create almost any colour imaginable. As each subpixel can produce 256 different shades, the pixel as a whole can produce one of 16.8 million colours (256 shades of red x 256 shade of blue x 256 shades of green). As LCD monitors are thinner, lighter, and draw much less power, they have all but replaced cathode ray tube monitors. Liquid crystals have also been applied to smart window technology as "privacy" glass. Privacy glass allows windows to transform from its traditional transparent state to an opaque state. The opaque state tends to have a milky white hue. The liquid crystals used in this application are known as polymer dispersed

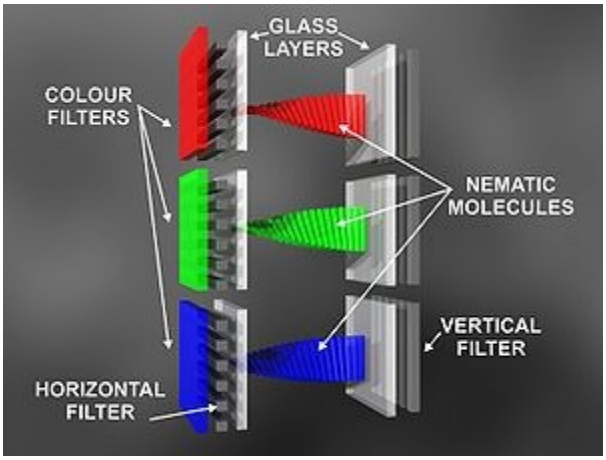

Figure 2-17: LCD screens contain three subpixels: one to filter red light, one to filter green light, and one to filter blue light. Image extracted from (Liquid Crystal Display, 2010)

liquid crystal as the liquid crystals are encased within polymer vesicles. Polymer and liquid crystals are initially mixed together in liquid form and as the polymer is cured, phase separation occurs resulting in the formation of liquid crystal droplets. The concentration of polymer is typically within the range of 30%-50% and the liquid crystal droplets are typically of the micron size scale (Polymer Dispersed Liquid Crystals (PDLCs), 2007). The polymer/liquid crystal mixture is sandwiched between two conductive films (such as indium tin oxide (ITO)) and two glass sheets.

The liquid crystal molecules in each droplet have directional order in orientation, but each droplet can be randomly aligned relative to other droplets. The combination of droplet size and isotropic orientation of droplets leads to a highly optically scattering state which gives the cell an opaque, milky state (Polymer Dispersed Liquid Crystals (PDLCs), 2007). After an alternating voltage is applied to the conductive films, an electric field is induced across the polymer/liquid crystal layer, causing the liquid crystals to align themselves parallel to the electric field (See Figure 2-18). The shift in orientation greatly reduces the degree of optical scattering, allowing the incident light to be optimally transmissible in the direction of the applied electric field. As shown in Figure 2-19, the glass windows become transparent after inducing the electric field across the polymer/liquid crystal layer. When transitioning between its off and on state, the integrated hemispherical visible transmission values for a PDLC device increases from 50% to 80% while the shading coefficient increases from 0.63 to 0.79. Using 100V AC, Switch Lite Privacy Glass consumes 3.5 W/m^2 (Pulp Studio, Inc., 2001) when turned on in its transparent state, but the major drawback of PDLC smart windows is the fact that a continuous current is necessary for the smart window to be in its transparent state, *i.e.* open circuit memory is generally not possible with dispersed liquid crystals. The overall power consumption is therefore typically higher than electrochromic smart windows. The main advantage of PDLC smart windows, however, is its reaction time. Switch Lite's Privacy Glass transitions from a transparent to opaque and vice versa in

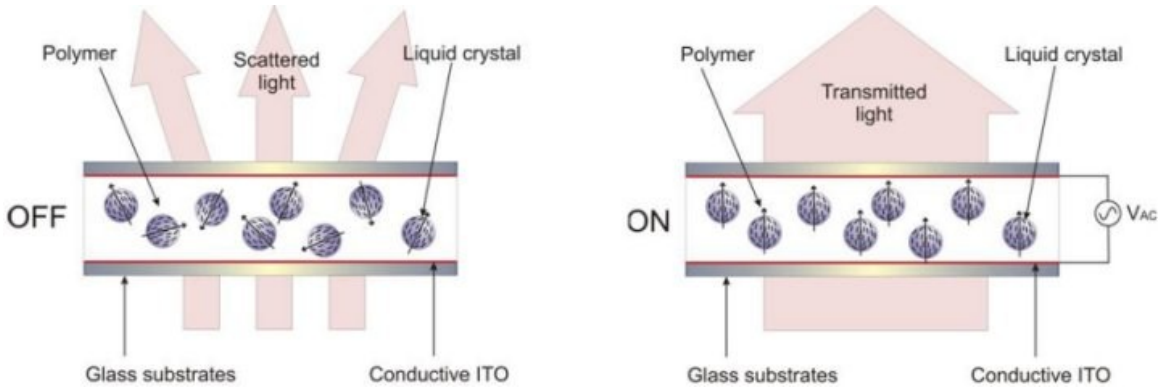

Figure 2-18: In a privacy glass' off state (Left), the liquid crystals are randomly oriented, scattering the light as it passes through the glass, creating an opaque state. An applied potential across the conductive layers (right) induces the liquid crystal droplets to rotate towards the electric field and light is fully transmitted, making the glass transparent. Image extracted from (Centre of Molecular Materials for Photonics and Electronics, 2007)

approximately one millisecond (Pulp Studio, Inc., 2001). Also, the polymeric nature makes the technology possible to employ in plastic substrates, making the production of flexible and lightweight devices foreseeable (Galvañ, et al., 2011).

Figure 2-19: Smart Privacy Glass uses Liquid crystals to change the glass' naturally opaque state (left) to transparent (right) and vice versa. Image extracted from (Fehrenbacher, 2006)

Another form of privacy glass uses suspended particles (SP) to transition the glass from an opaque state to a transparent state. Like PDLC devices, SP devices were initially developed for displays which is why they are relatively fast in comparison to other technologies. Both also rely on an electronic field to align its active elements to let light through undisturbed. Also known as electrophoretic windows, smart windows with suspended particle technology typically have 5 layers similar to a PDLC makeup: an active layer sandwiched between two conductive sheets (like indium tin oxide) and two glass layers. When first introduced, the active layer was composed of needle-shape dipole particles of polyiodides or parapathite approximately 1 µm long, suspended in an organic liquid, but in current devices, methods have been developed to encapsulate microdroplets (<1mm long) containing the suspended particles in a polymer matrix (Bell J. , 2009). While in the off position, these particles are randomly oriented and block light resulting in a darkened state similar to electrochromic windows. Akin to PDLC smart windows, when an alternating current is applied to the conductive sheets, an electric field across the active layer is induced, forcing the particles to align parallel to the electric field. The reorientation allows incident light to pass through the smart glass resulting in an overall transparent state. When the electric field is suppressed, the particles reverse back to their original random orientation and the glass returns to its dark state. Due to patents held by Research Frontiers, Inc., little information has been found on recent

developments of suspended particles (Baetens, Jelle, & Gustavsen, 2010). Figure 2-20 shows SPD smartglass in an office setting in both its on and off states.

Figure 2-20: SPD Smartglass has the ability to instantly darken from 50% down to 1% light transmission for video conferences and presentations and can also regulate the amount of heat coming into the building while blocking 99% of harmful UV rays as well. Photo extracted from (Innovative Glass Corporation, 2006)

Like electrochromic smart windows, SP smart glass can be fine tuned as a gray scale to vary the amount of light transmission and they can also control heat transfer resulting in a decreased need for air conditioning during summer months and heating during winter. SP devices have fast response times of 100-200ms, require 65-220V of alternating current to operate, and have typical transmission ranges of 0.79-0.49 and 0.5-0.04 (Baetens, Jelle, & Gustavsen, 2010). SP products are also quite energy efficient; at line voltage, SP display film typically uses a maximum of approximately 0.06 watts per square foot (0.65 watts/m^2) (Research Frontiers Inc., 2011). SPD products are also quite durable; Research Frontiers, Inc. has tested their SPD-films at millions of on/off cycles (Research Frontiers, Inc., 2011). It should be noted that like PDLC smart glass, SPD smart glass requires a continuous current when in it's "on", transparent state resulting in an overall higher energy consumption in comparison to electrochromic windows as electrochromic windows only require power when switching. Unlike PDLC devices, however, SP devices have a high viewing angle.

2.3.1.2 ELECTRORHEOLOGICAL AND MAGNETORHEOLOGICAL FLUIDS

Electrorheological (ER) and Magnetorheological (MR) fluids are fluids whose properties change upon the application of an electric or magnetic field, respectively. Primarily, the

respective field change significantly increases the fluid's ability to support shear stress in particle suspension systems and increases the fluid's viscous properties in homogeneous systems. The effect is fully reversible once the respective field is removed. Most engineering applications of ER and MR fluids exploit their controllable yield stress to vary the coupling or load transfer between moving parts in mechanisms such as dampers and clutches.

ER fluids are generally classified into two types: particle suspension (PS) systems and homogeneous systems. To the author's knowledge, MR fluids are only classified as PS systems. PS systems consist of particles in an insulating liquid while a homogenous system consists of miscible blends of more than one liquid. The most popular homogeneous ER system is liquid crystal polymer solution (Zhao, Yin, & Tang, 2007).

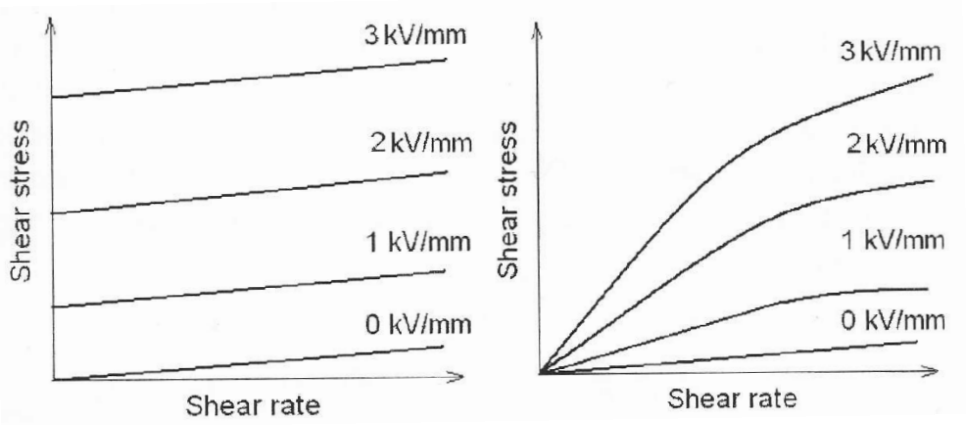

Figure 2-21: The shear stress/shear rate relationships between ER particle suspension systems (left) and ER homogenous systems. Image extracted from (Zhao, Yin, & Tang, 2007)

Both systems respond differently to increasing the field strength. Figure 2-21 showcases the shear stress vs. shear rate plots of both PS and homogeneous ER systems at varying electric field strengths. Looking at Figure 2-21, one would notice two key differences between the two plots; the change in slope and vertical intercept as one increases the electric field. For PS systems, the slope remains constant while the vertical intercept increases, and for homogeneous systems, the y-intercept remains at zero while the slope increases. As the slope is the measure of the fluid's viscosity (See Equation 2-3), the plots suggest that as the electric field is increased, the viscosity of a PS system remains constant while the viscosity of a homogeneous system increases. The constant vertical

intercept of zero on the homogeneous plot indicates that the system will exhibit flow after inducing a shear stress of any magnitude while the increasing vertical intercept on the PS plot indicates that a shear stress greater than the vertical intercept is needed to induce flow and the magnitude of this minimum shear stress positively correlates to a change in the induced field's magnitude.

It should also be noted that the shear stress vs. shear rate plot for PS and homogeneous systems are respectively linear and non-linear. Because the shear stress/shear rate relationship is linear for PS systems, PS systems have been less complicated to model and engineer. It is therefore not surprising that more research has been performed on particle suspension systems in comparison to homogeneous systems. The remainder of this section will thus focus on particle suspension systems as they are more prevalently used in industry.

Both ER and MR PS systems essentially consist of suspensions of particles in inert carrier liquids. Typically 1-10μm in diameter, these particles are added to fluids such as mineral or silicone oils in weight fractions as large as 50%, but weight fractions around 30% are most common (Srinivasan & McFarland, Smart Structures: Analysis and Design, 2001). For ER fluids, the particles must possess a high dielectric constant while MR fluids require the particles to be ferromagnetic. Most ER and MR fluids also contain minute quantities of additives that can affect the polarization of the particles or stabilize the structure of the suspension against settling, but these additives can generally be neglected when modeling the fluid's behavior.

In the fluid's neutral state, the particles are uniformly distributed through the fluid, generally resulting in Newtonian characterization which states that the shear stress (τ) is the product of the fluid's viscosity (η) and the strain rate ($\dot{\gamma}$):

$$\tau = \eta\dot{\gamma} \qquad 2\text{-}3$$

However, once an electric or magnetic field is respectively applied to an ER or MR fluid, the particles will form chains called fibrils in the field's direction, milliseconds after the field's application (Srinivasan & McFarland, Smart Structures: Analysis and Design, 2001). After applying a magnetic field across an MR fluid, the ferromagnetic particles become magnetically polarized in the magnetic field's direction, subsequently attracting the neighbouring particles to form fibrils in the magnetic field's direction (See Figure 2-22). For ER fluids, the relatively high dielectric constant of the suspended particles captures the electric field, redistributes the charge densities within the particles, and causes them to attract to other particles thus forming fibrils (See Figure 2-23) (Culshaw, 1996).

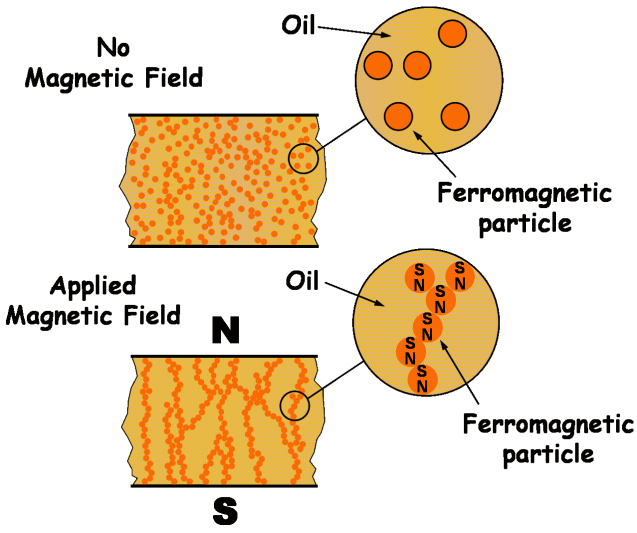

Figure 2-22: Naturally, the MR particles are uniformly distributed and randomly oriented in the suspension fluid (top). After applying a magnetic field across the gradient, the particles rotate in the magnetic field's direction and form fibrils (bottom). Image extracted from (Bell R. C., 2006)

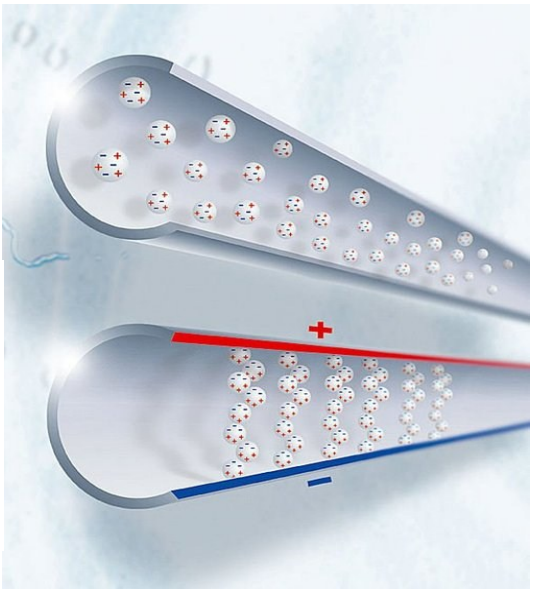

Figure 2-23: Naturally, the ER particles are uniformly distributed and randomly oriented in the ER suspension fluid (top). After applying an electric field across the gradient, the particles rotate in the direction of electric field and form fibrils (bottom). Image extracted from (Fludicon, 2010)

When there is relative motion between the walls of an ER or MR fluid's container, shear strain is induced in the fluid, resulting in a shear stress distribution across the fluid. When a sufficient shear strain is applied perpendicular to the electric or magnetic field's direction, the bonds that hold the fibrils are broken and must reform. The continual

breaking and reforming of these particle chains results in a force that resists the motion between walls (Srinivasan & McFarland, Smart Structures: Analysis and Design, 2001).

When a particle suspension ER or MR fluid is "turned on" through the application of a respective electric or magnetic field, its yield stress and flow properties are analogous to overcoming friction when moving an object horizontally along a surface. To move an object horizontally along a surface, you must first exert a force to overcome the associated static friction. Once the static friction has been overcome, a smaller force is needed to overcome the dynamic friction to continuously move the object. Like the static friction force, a significant shear stress (known as the static yield stress) is needed to induce flow on an ER or MR fluid in its "on" state. Once the static yield stress has been surpassed, one must surpass a smaller yield stress (known as the dynamic yield stress) to continuously induce flow. Both the static and dynamic yield stresses increase with increasing field strength and are typically proportional to the field strength raised to a power between 1 and 2 (Srinivasan & McFarland, Smart Structures: Analysis and Design, 2001). For ER fluids, the power is 2 for low to moderate electric field strengths, but decreases below 2 for large field strengths (Zhao, Yin, & Tang, 2007). The field strengths needed to activate ER and MR fluids are typically on the order of 1kV/mm and 100A/mm respectively. The upper limit on the induced shear stress occurs when the MR fluid reaches magnetic saturation (around 250 A/mm) or when the ER fluid breaks down electrically (around 4kV/mm) (Srinivasan & McFarland, Smart Structures: Analysis and Design, 2001).

It has commonly been suggested that an ER or MR fluid's viscosity increases after inducing its respective field, however, this statement is somewhat misleading for particle suspension systems as previously illustrated in Figure 2-21. As defined previously in Equation 2-3, the viscosity is equal to the shear stress divided by the shear rate; hence if one plots the shear stress vs. the shear rate graphically, the slope would be equivalent to the viscosity. Figure 2-21 showcases how the shear stress varies with shear rate at increasing field strengths. If one adds a respective field to the fluid, one would notice that the viscosity changes very little. Inducing a field does not affect the slope of the

plot, but affects the intercept along the vertical axis, the shear stress axis. This intercept corresponds to the fluid's dynamic yield stress and increases with an increasing field strength. This linear relationship, known as the Bingham Plastic Model, is presented below as Equation 2-4.

$$\tau = \tau_y(F) + \eta_{pl}\dot{\gamma} \qquad 2\text{-}4$$

Where: τ = shear stress, τ_y = dynamic yield stress, $\dot{\gamma}$ = shear rate, η_{pl} = plastic viscosity, and F = the electric or magnetic field strength

Note that the dynamic yield stress is a function of the field strength, be it electric field strength for ER fluids or magnetic field strength for MR fluids. As previously mentioned, the dynamic yield stress is proportional to the field strength as shown in Equation 2-5 where a is somewhere between 1 and 2 depending on the field strength

$$\tau_y \propto F^a \qquad 2\text{-}5$$

The dynamic yield stress is most often determined through experimentation at specific field strengths for accuracy. The Bingham plastic model is generally used at high strain rates, where the static yield stress is not a factor. However, one should once again note that the Bingham plastic model is only used in particle suspension systems, not homogenous systems.

ER and MR fluids are generally applied in one of two modes: valve mode or direct-shear modes. In the valve mode, shear is modeled as a fixed-plate configuration where a pressure is applied to the fluid, inducing flow. The valve mode is applicable for hydraulic controls, servo valves, dampers, and shock absorbers (LORD Corporation, 2010). In the direct-shear mode, shear is modeled as a sliding-plate configuration where shear is induced by moving one plate relative to another. The direct-shear mode is applicable for clutches, brakes, chucking and locking devices, and some dampers. Both modes are illustrated in Figure 2-24.

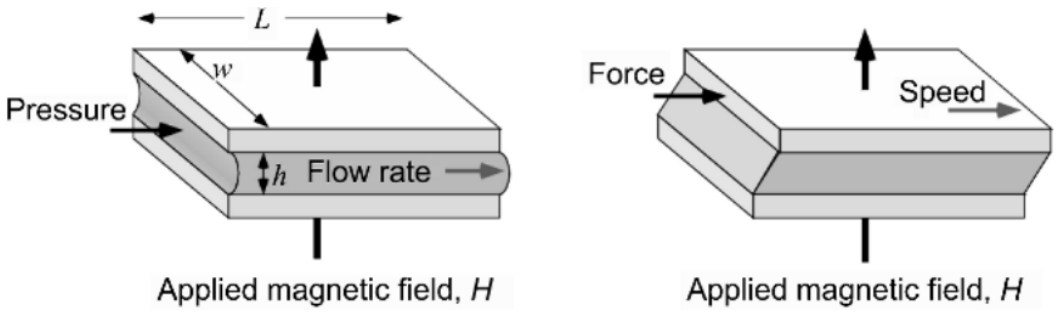

Figure 2-24: The two modes of MR fluid operation: Valve-Mode (Left) and Direct-Shear Mode. Figure extracted from (Carlson J. D., 2007)

In valve mode, the total pressure drop is the summation of the pressure drop due to the viscosity of the MR fluid (ΔP_η) and the pressure drop due to the magnetic field-induced yield (ΔP_{τ_y}) as shown below in Equation 2-6

$$\Delta P = \Delta P_\eta + \Delta P_{\tau_y} \tag{2-6}$$

Equation 2-6 can be derived further depending on the flow conditions. To determine whether the fluid is experiencing low or high flow conditions, one must use the following parameter using the volumetric flow rate (Q) along with other fluid properties and shape boundaries shown in Figure 2-24:

$$T^* = \frac{wh^2\tau_y}{12Q\eta} \tag{2-7}$$

When T^*<0.5, the fluid is said to be in high flow (HF) conditions and Equation 2-7 is equivalent to Equation 2-8, accurate within 5% (Srinivasan & McFarland, Smart Structures: Analysis and Design, 2001).

$$\Delta P = \Delta P_{\eta,HF} + \Delta P_{\tau_{y,HF}} = \frac{12\eta QL}{wh^3} + \frac{3L\tau_y}{h} \tag{2-8}$$

Likewise, when T*>200, the fluid is said to be in low flow conditions and 2-8 is equivalent to Equation 2-9.

$$\Delta P = \Delta P_{\eta,LF} + \Delta P_{\tau_{y,LF}} = \frac{8\eta QL}{wh^3} + \frac{2L\tau_y}{h} \tag{2-9}$$

Comparing the limiting cases, one may conclude that Equation 2-9 can be simplified to Equation 2-10 where B and C and respectively within ranges of 8-12 and 2-3 for any given steady-state flow conditions.

$$\Delta P = \Delta P_{\eta,LF} + \Delta P_{\tau_{y,LF}} = \frac{B\eta QL}{wh^3} + \frac{CL\tau_y}{h} \qquad 2\text{-}10$$

For the damping force, one would simply multiply the total pressure force by the cross-sectional area of the valve. It is important to understand, however, that Equations 2-7 to 2-10 are derived for fixed plate applications. As most dampers are cylindrical (like the one shown in Figure 2-25), separate equations need to be derived for better accuracy. For the derived equations for cylindrical dampers, refer to (Spencer, Yang, Carlson, & Sain, 1998).

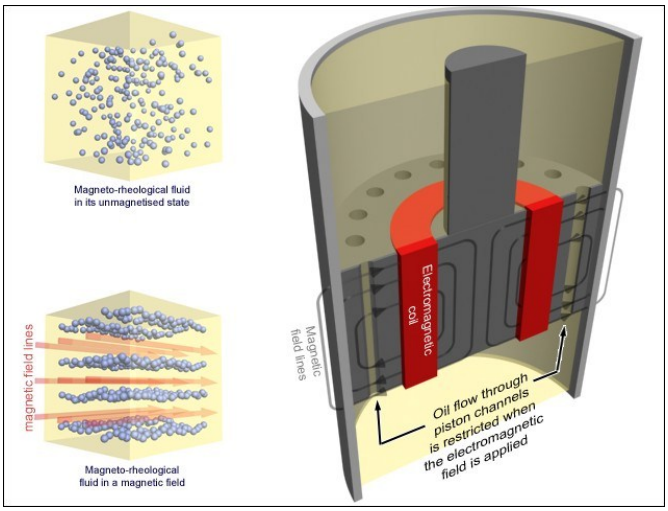

Figure 2-25: Illustration showing the mechanism of an MR cylindrical damper. Figure extracted from (Longhurst, 2011)

Like valve mode, the direct-shear mode has two components in its model equations: one for the viscous properties of the fluid and the other for the magnetorheological induced dynamic shear yield stress. The total force is the summation of the viscous force from the fluid and the force emitted from the dynamic yield stress

$$F = F_\eta + F_{\tau_y} \qquad 2\text{-}11$$

As the plates have a linear velocity distribution ($\dot{\gamma} = \frac{S}{h}$,where S is the maximum velocity and h is the plate thickness), and the total force from the induced shear stress is equivalent to the shear stress multiplied by the plate area (Lw), Equation 2-11 can be rewritten as below:

$$F = \frac{SLw\eta}{h} + Lw\tau_y \qquad 2\text{-}12$$

Again, one should note that Equations 2-11 and 2-12 are for the sliding plate configuration as illustrated in Figure 2-24. For alternative situations, the force equations must be derived accordingly with the vessel's geometry.

2.3.1.2.1 Electrorheological Particle System Components, Properties and Mechanisms

Since the discovery of the ER effect, several mechanisms have been proposed to explain the phenomenon. These mechanisms include the electro polarization model, electric double layers model, water bridges model, and conduction model. Out of all of the proposed mechanisms, the electrostatic polarization model appears to adhere to most experimental results. Essentially, the electrostatic polarization model states that once the electric field has been applied, each particle's charge distribution leads to a dipole formation and consequently is attracted to neighbouring dipole particles. This attraction leads to the formation of particle chains or fibrils along the direction of the electric field. It should be noted, however, that in different environmental conditions, other phenomena are likely to influence the electrorheological effect; there are therefore no sound mechanisms that can interpret all ER phenomenon as one (Zhao, Yin, & Tang, 2007).

As previously stated, an ER particle suspension system consists of micrometer-size leaking dielectric particles in insulating liquid. The electrorheological behavior of the fluid strongly depends on the size and shape of these particles as well as their volume fraction in the fluid. When the volume fraction is too high, the ER fluid may lose its flow behaviors, rapid response, and possibly even its reversibility (Zhao, Yin, & Tang, 2007). On the other hand, a low volume fraction will hinder the electrorheological effect resulting in a weaker dynamic yield stress. For good ER performance, the particle volume fraction is between 0.05 and 0.50 (Hao, 2001) The ER effect is expected to be weak if the particles are too small as Brownian motion tends to compete with the particle interaction, but the ER effect is also expected to be weak for particles that are too large as

sedimentation will prevent the particles from forming fibrils when activated by an electric field (Zhao, Yin, & Tang, 2007). It has also been shown that an ER fluid's dynamic yield stress increases with respect to an increasing particle size. With regards to the shape of the particles, ellipsoidal particles are expected to have a stronger ER effect than spherical particles as ellipsoidal particles strength chain formation due to a greater electric-field induced moment (Zhao, Yin, & Tang, 2007).

The liquid carrier in an ER particle suspension is typically oil or another liquid with low conductivity. Examples include silicone oil, vegetable oil, mineral oil, and paraffin among others. An ideal dispersing liquid material should have a high boiling point (over 200 °C), a low viscosity (mPas), a high breakdown strength (greater than 7 kV/mm), and a relatively high density (Zhao, Yin, & Tang, 2007). The ER effect can also be greatly enhanced if one kind of particulate materials is mixed with a liquid that is also ER active.

There are two different formations of ER materials: extrinsic (water-containing) and intrinsic (water-free). Extrinsic materials, such as silica gel and starch poly(lithium methacrylate) require the presence of a polar liquid, such as water to produce an ER effect. The water is adsorbed around the particle's surface to provide a bridge for ion attraction between particles. However, adsorbed water or other polar liquids greatly increases the current density of ER fluid and limits working temperature stability thus making extrinsic ER materials unfavourable for practical applications (Zhao, Yin, & Tang, 2007). In light of this, several anhydrous ER materials (intrinsic materials) have been developed such as aluminosilicate and carbonaceous. These materials inherently have polar groups and intrinsic charge carriers, liberating the need for water.

In comparison to magnetorheological fluids, particular ER fluids have several advantages including improved speed, simpler control as an electric field is more readily available than a magnetic field, heavy ferrous components are not required, and steady-state currents can be low, but at a very high voltage (kV) (Bullough W. A., 2007). Besides the need for a very strong electric field, electrorheological fluids have other disadvantages, mainly concerning its performance. The dynamic yield stresses of ER fluids are

typically two orders of magnitude smaller than that of MR fluids (Bell R. C., 2006). Also, a much greater volume of ER fluid (typically of the order of 100 to 1000) is needed to perform the same function of an MR fluid (Srinivasan & McFarland, Smart Structures: Analysis and Design, 2001). Unfortunately, ER fluids can be sensitive to temperature changes, moisture, and contamination which makes their use outside the laboratory difficult and costly (Carlson J. D., 2009). These limitations have greatly inhibited the technological development of ER fluid systems. Table 2-3 below presents typical properties of ER fluids.

Table 2-3: General Properties of Electrorheological Fluids. Extracted from (Culshaw, 1996)

Property	Normal Range
Particle Size Range	1μ to 100μ
Suspended Particle Content	15% to 40% volume fraction
Voltage Requirement	Several kV/mm
Power Density	Several mW/cm^2
Response Time	ms
Viscosity (at E=0)	1000 mPa.s (at 25°C)
Maximum increase in viscosity	Factor of 10
Shear Stress	500 Pa (at 1kV/mm)
Operating Temperature	-30°C to 300°C
Fluid Dielectric Constant	~1.5
Particle Dielectric Constant	~10

2.3.1.2.2 Magnetorheological Particle System Components, Properties & Mechanisms

Contrasting ER fluids, MR fluids do not require the application of a high voltage enabling them to achieve very high yield strengths without encountering the problem of dielectric breakdown. MR fluids can routinely achieve dynamic yield strengths of 50 kPa or more with magnetic field magnitudes that can readily be achieved through electromagnets (Carlson J. D., 2009). MR fluids can also operate at both high and low temperatures. Overall, MR fluids trump ER fluids in performance and applicability and have therefore found greater use in industrial applications.

MR fluids generally consist of micron-sized, nearly pure elemental iron particles suspended in hydrocarbon-based oil. Upon the application of a magnetic field, the iron particles polarize and chain together along the magnetic field's direction. The most widely used MR fluid particles are carbonyl iron particles. Having a spherical shape (1-10μm in diameter), carbonyl iron particles are formed from the thermal decomposition of iron pentacarbonyl. The volume fraction of these particles is generally around 20-45%. Like ER suspended particles, there are tradeoffs in having significantly large or small volume fractions of iron particles in MR fluids. Increasing the iron particle volume fraction will proportionally increase the dynamic yield stress; however, the off-state viscosity will also unfavourably increase at an even faster rate (Carlson J. D., 2009). Although nearly all magnetically polarisable particles in an MR fluid are iron derived, any magnetically polarisable particle can be used to produce an MR fluid, but the MR effect will be generally weaker.

As for the inert carrier liquid, hydrocarbon oils are the vehicle of choice as they have good lubricity, durability, and availability and also have a library of well understood additives to enhance the MR effect. The hydrocarbon oils can be derived from mineral oils, synthetic oils, or mixture of the two oil types, but 99% of all commercial MR fluids are based on synthetic hydrocarbon oils (Carlson J. D., 2009). Water-based fluids are also used as MR fluids as they have the highest on-state yield strength and lowest off-state viscosity (Carlson J. D., 2009). However, due to their high vapour pressure, water-based MR fluids are prone to evaporative loss. In light of this, water-based MR fluids can only be used in situations where the system is completely sealed.

Additives are added to the MR fluid to discourage sedimentation, prevent agglomeration, enhance lubricity, prevent oxidation, modify the viscosity, and inhibit wear. For example, organic and inorganic thixotropic agents and surfactants are used to discourage sedimentation (Carlson J. D., 2009).

With regards to an MR fluid's field strength, the maximum dynamic yield strengths are typically on the order of 25-100 kPa. Figure 2-26 gives a plot of the dynamic yield stress with reference to the applied magnetic field at three different particle volume fractions: 22%, 32%, and 40%. From the plot, it is evident that the dynamic yield strength increases as the particle volume fraction increases. For magnetic fields below about 100 A/mm, the plots demonstrates that the dynamic yield strength increases in an approximate linear fashion with respect to an increasing magnetic field. After 100 A/mm, the relationship begins to progressively roll off before settling at its maximum dynamic yield strength at approximately 400 A/mm. Carlson states that the magnetic field strength that is practically useful is usually about 250 A/mm (Carlson J. D., 2009).

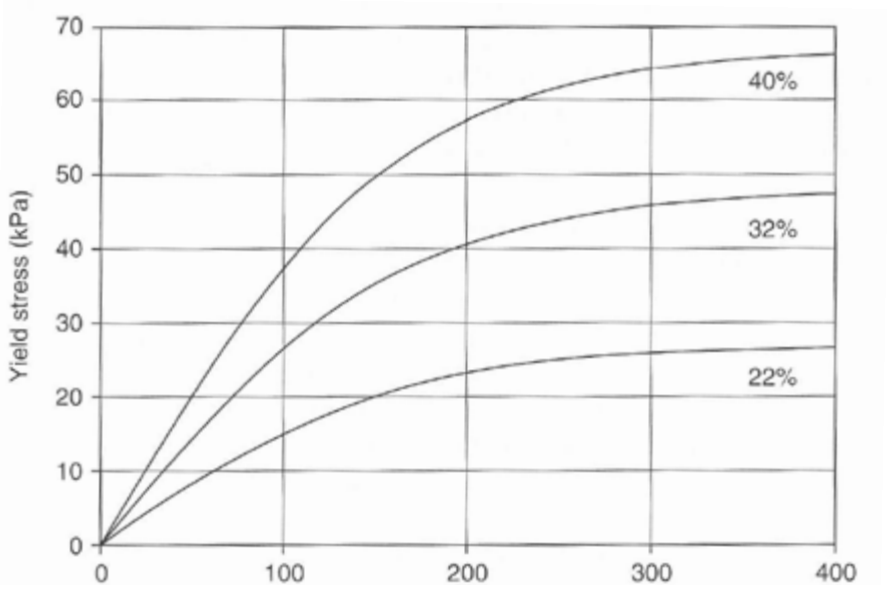

Figure 2-26: The dynamic yield stress/magnetic strength relationship at different particle volume fractions . Image extracted by (Carlson J. D., 2009)

In his journal article entitled, "MR fluids and devices in the real world", Carlson describes the relationship of dynamic yield stress and magnetic field strength through the following formula:

$$\tau(H) = C * 271{,}700 * \phi^{1.5239} * \tanh(6.33x10^{-6}H) \qquad 2\text{-}13$$

Where: $\tau(H)$ = dynamic yield stress (Pa),
H = Magnetic Field Strength (A/m),
μ_0 = magnetic constant equal to 4π x 10^{-7} Henry/m
C = 1.0, 1.16, or 0.95 depending on whether the carrier fluid is hydrocarbon oil, water, or silicone oil

Typical properties of MR fluids are shown below in Table 2-4.

Table 2-4: General Properties of Magnetorheological Fluids. Extracted from (Carlson J. D., 2007)

Property	Normal Range
Particle volume fraction, ϕ	0.20 to 0.45
Particle weight fraction	0.70 to 0.9
Density	2 to 4 g/cm^3
Yield Strength, τ_{MR} @ 100kA/m	10 to 55 kPa
Yield Strength, τ_{MR} @ saturation	25 to 100 kPa
Plastic viscosity, η_p @ 40°C, $\dot{\gamma}$>500s^{-1}	50 to 200 mPa*s
Temperature Range	-40 to +150 °C
Magnetic Permeability, relative @ low field	3.5 to 10
Fig. of merit, τ_{MR}^2/η_p	10^{10} to 10^{11} Pa/s
Response Time	Less than 10 ms

MR fluids have found more applications in many industrial markets. In 2002, General Motors Corporation unveiled their Cadillac Seville with MagneRide suspension. Made by Delphi Corporation, the MagneRide suspension (shown in Figure 2-27) has real-time

Figure 2-27: The Magneride Suspension made by Delpi Corporation has real-time controllable MR fluid shock absorbers and has since been installed in several car models. Image extracted from (Patrascu, 2009)

controllable MR fluid shock absorbers and has since been installed in other car models including the Corvette sports car, the Cadillac XLR sport utility vehicle, the Buick Lucerne, the Audi R8, and the Ferrari 599 GTB. What sets it apart from other systems is the lack of moving parts and its sense of control. The electronic control unit adjusts the MR system once every millisecond in accordance to the driver's desired riding style and

road monitoring sensors (Patrascu, 2009). This ensures the smoothest ride possible. The biggest disadvantage is the cost and as a result, only about half a million suspension systems are on the road (Patrascu, 2009). Other successful applications of MR fluids include seismic dampers on civil engineered structures. Several large MR fluid dampers weigh 280 kg, contain 15 liters of MR fluid, and are capable of controllable forces up to 200 kN (Carlson J. D., 2007). Japan's National Museum of Emergin Science and Innovation have MR fluid dampers capable of withstanding 300 kN to control seismic activity (Carlson J. D., 2007). MR fluids have even made their way into biokinetics. Developed by Biedermann Motech and Lord Corp., a smart, artificial knee has been developed using MR fluid dampers to semi-actively control the knee's motion (vl Henkel, 2009). Shown in Figure 2-28, sensors and microprocessors sense and process data gathered from changes in the wearer's walking speed, uphill and downhill motion, high and low loads, ramps, stairs, and uneven terrain, to adapt the knee motion appropriately within milliseconds (vl Henkel, 2009).

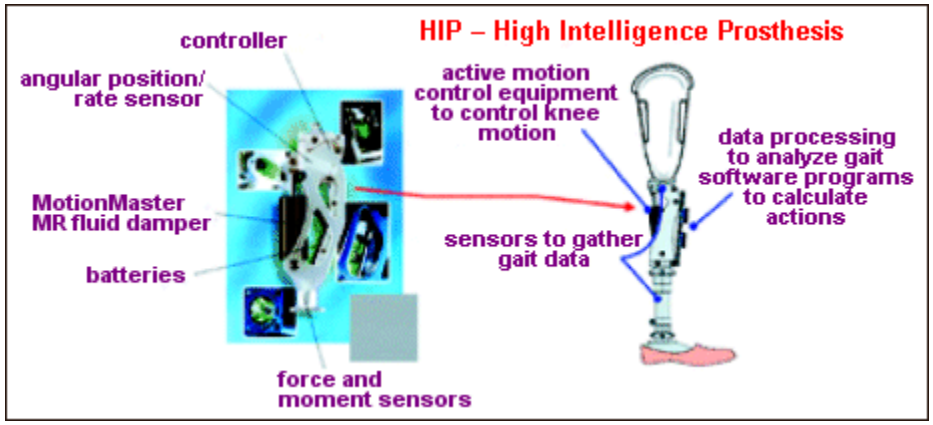

Figure 2-28: The High Intelligence Prosthesis (HIP) uses MR fluid dampers to adapt knee motion when crossing terrain (vl Henkel, 2009)

2.3.1.3 PHASE CHANGING MATERIALS

Phase change materials (PCM) respond to ambient temperature by absorbing or releasing latent heat, resulting in a solid to liquid phase change or liquid to solid phase change, respectively. Materials generally have a set temperature when changing phase. Using ice/water as an example, ice melts at 0°C and remains at 0°C until it has completely

transformed into water, likewise water freezes at 0°C and remains at 0°C until it has completely transformed into ice. During these transformations, latent energy is absorbed during a solid to liquid phase transformation and released during a liquid to solid phase transformation. This ability to store and release heat at a specific temperature has been exploited in various areas in architecture and textiles.

In textiles, PCMs are used to regulate body temperature in winter clothing. As already mentioned in Section 2.2.3, Outlast® Adaptive Comfort ® fabric uses a paraffin wax compound that absorbs excess heat when the user is warm, but then releases said stored energy when the user is cold. Figure 2-29 shows a visual of Outlast® technology works.

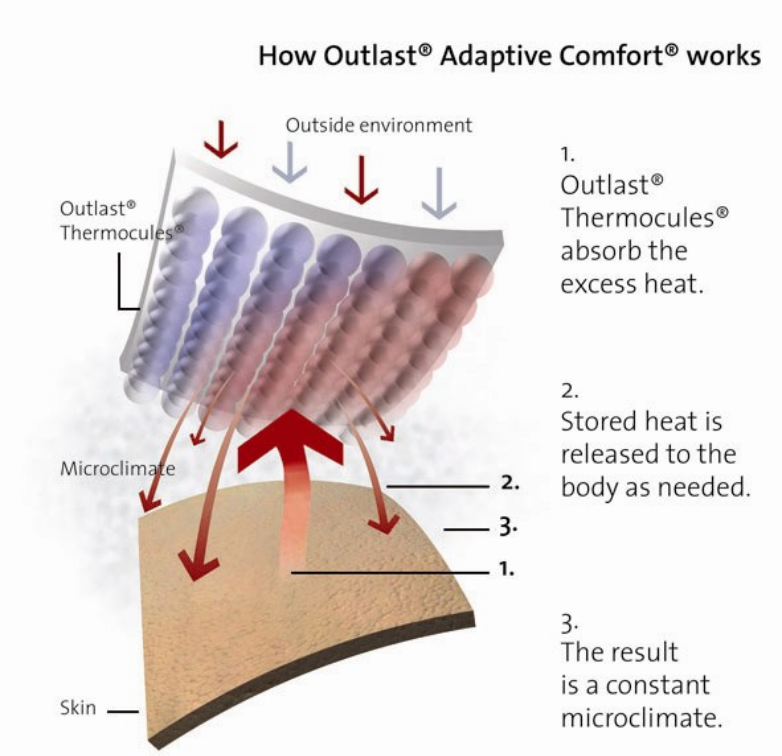

Figure 2-29: A visual of how Outlast® Adaptive Comfort® works. Extracted from (Orchard Farm Ltd., 2012)

Phase-changing materials can also be used in architecture to regulate room temperature. Known as "phase change wallboard", walls are embedded with phase change materials such as salt hydrates, paraffins, and fatty acids that melt at comfortable room temperature. When the room temperature is surpassed, the wallboard will absorb the excess heat and regulate the room temperature; afterwards when the room temperature cools, the previously absorbed heat will be released to regulate the room temperature. Generally, transition temperatures are designed to be around 65-72°F for heating dominated climates with primary heating needs and 72-79°F for climates with primary cooling needs. One of the most referenced phase change wallboards is the GlassX, shown in Figure 2-30. Glass X not only uses phase changing materials to absorb and release latent heat, it has a suspended prismatic filter between panes of glass that reflect higher-angle sunlight back out while transmitting low angle sunlight. The low angle

Figure 2-30: The GlassX, a smart window that uses phase change materials to extract solar energy and regulate room temperature. Image extracted from (Wilson, 2010)

sunlight then goes to the PCM layer to absorb the heat and transfer it to the inside room. Two separate low-emissivity coatings and low-conductivity gas filled in the outer two sealed glass spaces help push heat from the PCM layer inward while slowing outward heat loss (Wilson, 2010).

2.3.1.4 SHAPE MEMORY ALLOYS

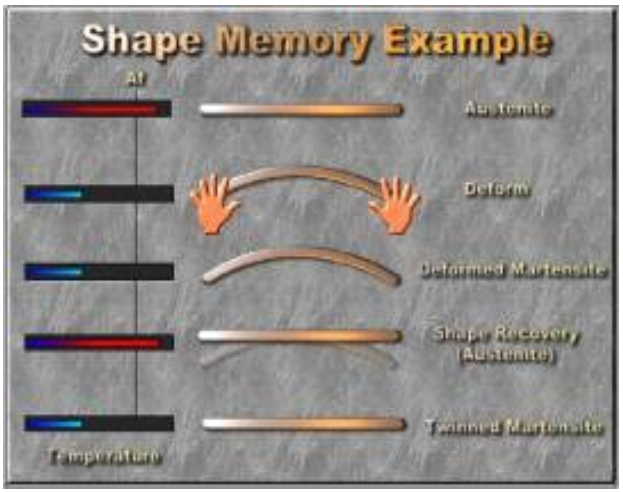

Figure 2-31: Transformation Cycle for a one-way shape memory alloy. Extracted from (Shenzhen Star Spring Materials Co.)

Shape memory alloys (SMAs) got their name from their intrinsic ability to remember their shape. This is due to an underlying phase change that is activated upon heating the alloy beyond a certain temperature. Above this characteristic temperature, the SMA is in its austenite phase (See the top portion of Figure 2-31). The cubic crystal arrangement of this phase make the material quite stiff making it comparable to stainless steel. When cooled below this temperature, the material goes through a phase transformation to its corresponding martensite phase. The SMA is quite pliable at its martensitic phase due to its twinned crystal arrangement. Should one deform the SMA at its martensitic phase followed by adding heat in succession, the shape memory will not only transform back into austenite, but will transform into its previous austenitic shape. This talent has enabled shape memory alloys to be used in electronics, vibration control, biomedicine, and fashion among other areas.

Although they can be somewhat used as temperature sensors as they react to a specific temperature, they are mostly used as actuators. Advantages over other actuators are their high power to volume ratio, their silence, and their variable shapes among other things. Their main drawbacks, however, are their poor efficiency, low bandwidth, and relatively

low velocity. Table 2-5 lists several advantages and disadvantages of SMAs as actuators.

Table 2-5: The Advantages and Disadvantages of Shape Memory Alloys (SMAs). Extracted from (Hesselback, 2007)

Advantages	Disadvantages
+ Large Energy Density +Small & Compact +Simple Mechanisms +Variable Shapes +Linear or Rotational Motion +Miniaturisable +Usable in clean room environment +Good Corrosion Resistance +Low Voltage (<40V) +Silent +Intrinsic Sensor Effect	-Uncertainty about duration and stability of the effect -Relatively low velocity -Very low efficiency (below 2%) -Limited Range of Transformation Temperatures -Low Bandwidth

An SMA's efficiency is determined by thermodynamics; most of the input energy is transformed to heat the alloy rather than displace an object. Additionally, this heat is lost to the surrounding environment and cannot be converted back to a reusable form of energy. Due to the low efficiency, limited effect duration, and low speed, it must be understood that shape memory actuators are not intended for applications where electrical motors or pneumatic actuators are well established (Hesselback, 2007).

Despite its drawbacks, Hesselback (2007) argues that the very high work-per volume ratio of approximately 4J/cm^3 is highly values if space is limited, making SMA actuators favourable in certain circumstances in electronics. Hesselback (2007) notes that a piezoelectric actuator with the same force and stroke would need up to 10 times the space in comparison to an SMA actuator. The low efficiency is less important in this circumstance because the overall energy consumption is low. The shape memory effect will be further explained and explored in Chapter 6.

Another form of SMAs are superelastic SMAs (also known as pseudoelastic SMAs). These alloys have transition temperatures below the temperature of the ambient environment and are thus naturally in their austenite phase. However, the martensite phase can be induced by stress meaning that the alloy is quite deformable, but will easily

return back to its programmed shape when the applied stress is removed. Its deformation is therefore "super" elastic. There is of course a limit to magnitude of applied stress before plastic deformation starts to occur. The superelastic mechanism will further be explained and explored in Chapter 7.

SMAs are commonly used in various fields of practice such as optometry, medicine, and electronics among others. NiTiNOL is frequently used for medical stents like the one shown in Figure 2-32. These stents are made from NiTiNOL that is programmed to fully expand at body temperature. They are placed inside blood vessels such as arteries, and are set to expand once inside. The stents increase blood flow through widening the arteries thus decreasing overall blood pressure. Superelastic NiTiNOL is used for eyeglass frames that continually revert back to their original shape when bent (Figure 2-33 and for orthodontic braces. Other notable uses for shape memory alloys include Braille characters that pop up from shape memory actuators and can be rewritten (Haga, Makishi, Iwami, Totsu, Nakamura, & Esashi, 2005), wires and staples for scoliosis braces (Sanders, Sanders, More, & Ashman, 1993), digital storage devices (Srinivasan & McFarland, Smart Structures: Analysis and Design, 2001), microvalves (Piccini & Towe, 2012), and the HiTAEIH robot hand (Baz, Iman, & Mccoy, 1990).

Figure 2-32: SMAs are used to make medical stents that expand when inside the human body. Photo from (Nixon, 2008)

Figure 2-33: Superelastic NiTiNOL is used on eyeglass frames, enabling them to bend without permanent plastic deformation. Photo from (Rakuten Global Market, 2012)

2.3.2 Type 2: Energy Exchanging

What sets energy exchanging materials from property changing materials is their ability to transform energy from one form to another, something that is governed by the first law of thermodynamics. The input energy is associated with the smart material's input stimulus while the output energy is associated with the smart material's response. The input energy can vary from a mechanical deformation as is seen in piezoelectric materials, a thermal difference as is seen in thermoluminescent materials, or magnetic field as is seen in magnetorestrictive materials; likewise these materials have output energies that vary from an electric potential, light, and mechanical deformation, respectively. When the energy state of a given material is equivalent to the energy state of its surrounding environment, then that material is said to be in equilibrium where no further energy can be exchanged.

Addington & Schodek (2005) point out that all materials must conserve energy and the internal energy of a material must increase when energy is added. However, the increase in internal energy is most often manifests itself as heat. Energy exchanging smart materials distinguish themselves in their ability to use their internal energy in a unique fashion that can often be exploited. Many of the energy-exchanging materials are bi-reversible meaning that the input and outputs can be switched, *i.e.* the input can sense the output and vice versa. Generally, the energy exchanging smart materials that are not bidirectional are ones that exchange radiation energy as the high inefficiency of radiant energy exchange increases thermodynamic irreversibility (Addington & Schodek, 2005). This subsection will present the energy exchanging materials that are not bidirectional, while Section 2.3.3 will present the energy exchanging materials that are bidirectional.

2.3.2.1 LUMINESCENT MATERIALS

Generally speaking, luminescent materials can be thought of as materials that emit light that is not reflected by traditional incandescence. Rather, energy is exchanged in the material to produce light by another means. The input energy can be electrical, thermal, light radiation, and chemical among others. This section will focus on materials that are

part of the luminescence family. Smart materials that produce light via semiconductors will be presented in the next subsection, Section 2.3.2.2.

Luminescence refers to the emission of light due to incident energy; the light is caused by the re-emission of energy in wavelengths in the visible spectrum and is associated with the reversion of electrons from a higher energy state to a lower energy state. Most materials that are luminescent are solids that contain small impurities, *e.g.* zinc sulfates with tiny amounts of copper (Addington & Schodek, 2005). When exposed to incident energy, the electrons or photos associated with said incident energy are absorbed by the material which whose internal electrons rise to a higher level as a result. Via the photoelectric effect, photons are produced as the material's internal electrons drop back down to a lower level. These photons are in turn observed by a bystander as light, providing that the light is within the visible spectrum. The wavelength of the light is dependent upon the materials internal structure with emphasis on its impurities. Among the smart materials in the luminescence family are photoluminescent materials, electroluminescent materials, chemoluminscent materials, and thermoluminescent materials.

Photoluminescent materials absorb electromagnetic waves which in turn are transformed into electromagnetic waves in the visible spectrum. The incident electromagnetic rays are absorbed by the material's electrons which are excited to a higher state. When later transferring to a lower energy state, photons are emitted as light in the visible spectrum. These photons are at lower wavelengths due to energy conversion. There are two types of photoluminescent materials: fluorescent materials and phosphorescent materials. Fluorescent materials emit visible light instantaneously when incident light (ultraviolet/black light in particular) is projected onto the material. Alternatively, phosphorescent materials can absorb both visible and UV light, but there is a slight delay in its responsive light emission. However, phosphorescent materials can keep their luminescence after the incident light source has been removed. Photoluminescent materials can come in a variety of colours with high brilliance and intensity, are inexpensive, have a large market presence, and come in both natural and synthetic forms

including paints and dyes (See Figure 2-34 and Figure 2-35), but a light source is always needed for activation and they can become bleached over time (Ritter, 2007).

Figure 2-34: Japenese artist Que Houxo does live performances where he paints images using fluorescent paints under a blacklight. Image extracted from (Roth, 2009)

Figure 2-35: As an art project, Katharina Sieverding painted a Smart Car™ with phosphorescent paint. Image extracted from (Spinelli, 2007)

Electroluminescent materials absorb electrical energy (via applied voltage or electric field) which is then transformed into radiation energy in the visible spectrum. Electroluminescence occurs via two methods. The first method uses phosphorous compound materials with scattered impurities. A high electric field forces electrons to move through the phosphor medium and react with the impurities. The impurities' electrons are in turn raised to a higher level; when said electrons jump back down to a lower level, photons are released as visible radiation. The colour emitted depends on the medium's composition. Electroluminescent materials are used as backlights in electronic watches and are available in wire form known as EL wire (See Figure 2-36), films known as EL film, ink known as EL ink, and even lamps such as compact fluorescence lamps (CFLs). Electroluminscent materials tend to have a long replacement life and low power consumption. Although CFLs provide high brightness, EL film and EL wire are not as noticeably bright. Electroluminscent materials also require an alternating current.

Figure 2-36: Designed by Marcus Tremento, this lamp is completely made with electroluminescent (EL) wire. Image extracted from (Technabob, 2008)

Chemoluminescent materials absorb energy from a chemical reaction which is in turn transformed into visible radiation. Like the other luminescent materials, light is produced as electrons are excited to a higher energy state, producing photons in the visible spectrum when returning to a lower state. Unlike the other luminescent materials, a chemoluminscent material's electrons are excited via a chemical reaction. Generally, chemoluminescent materials produce light without a significant heat output. A glowstick is an example of a device containing chemoluminescent materials. Deforming the glowstick breaks the seal between two chemicals which subsequently react with one another and produce light in the process. Another example of chemoluminescence is Luminol. Luminol reacts with the hemoglobin in blood, producing a compound that luminesces in the dark. Luminol is therefore often used in forensic science to detect blood after it's been cleaned by the perpetrator.

Thermoluminescent materials transform thermal energy (*i.e.* heat or temperature differences) into electromagnetic energy in the visible spectrum. Figure 2-37 shows an image of chlorophane before and after exposure to hear. The light energy released is derived from the electron displacements within the crystal lattice caused from a previous exposure to high-energy radiation. The previous radiation exposure excited the material's electrons to a high state of which some are metastable over long periods of time. If the temperature is high enough (around 400°C or higher), the thermal energy is

sufficient to cause the electrons to relax to its ground state (Richter, 2007). The state transition results in the emission of photons in the visible spectrum. The intensity of the luminescence can be correlated to the length of time at which the material was exposed to the previous radiation source. It has been used to date Paleolithic flint to date when it was first ignited by prehistoric man (Richter, 2007).

Figure 2-37: Thermoluminescence of a fluorite (chlorophane) that emits light when heated. Image extracted from (Encyclopædia Britannica Inc., 2012)

2.3.2.2 SEMICONDUCTOR LIGHT EMITTING MATERIALS

Semiconductors are widely used in electronics as they behave like conductors under certain conditions and insulators under other conditions. They are most widely used in diodes and transistors. Semiconductor diodes allow current to flow in one direction while blocking its flow in the opposing direction, while transistors enables to switch current on and off as well as control the strength of an amplifying current. Diodes and transistors work by combining P and N type semiconductors. With a medium that is usually composed of silicon or germanium, N and P types are made by adding impurities known as dopants, arsenic and boron being the most popular dopants. Donor dopants, usually pentavalent impurities such as arsenic, are used to make N-type semiconductors, giving the extra valence electrons to the silicon medium, making the semiconductor more

negatively charged. The extra electrons in N-type semiconductors can be lost easily, thus increasing the material's conductivity. Acceptor dopants, usually trivalent impurities such as boron, are used in P-type semiconductors which compensate for their electron deficiency of one valence electron by acquiring an electron from its neighbor. If you apply a voltage to either type of semiconductor, electrons will flow from the negative to positive voltage, as expected. Alternatively, if N-type and P-type semiconductors are placed back to back as a PN-junction across an applied voltage, electronics will only flow if junction is forward biased, *i.e.* the positive and negative terminals are connected to the P-type and N-type semiconductors, respectively. If the positive and negative terminals are respectively connected to the N-type and P-type terminals (*i.e.* reverse biased), no current will flow (providing the breakdown voltage is not exceeded). Figure 2-38 illustrates the current flow when the voltage is forward or reverse biased.

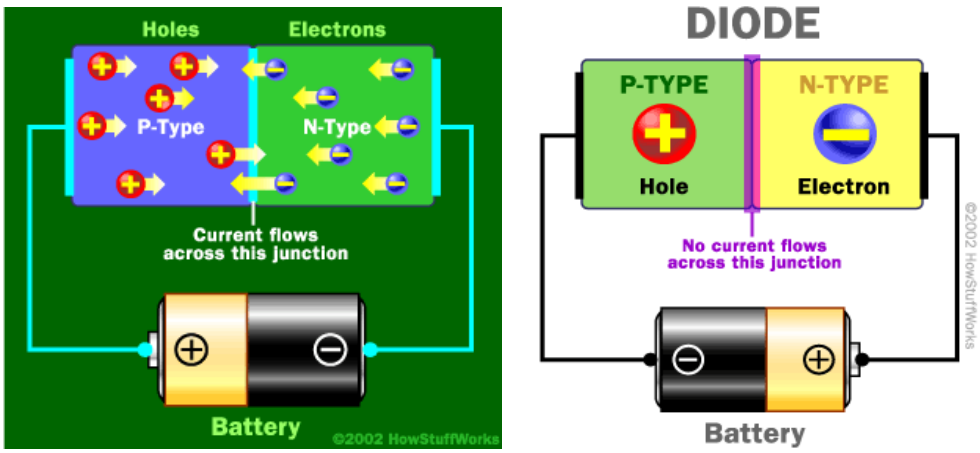

Figure 2-38: (Left) When the positive and negative terminals are connected to the P-Type and N-type diode semiconductors, respectively, electrons flow from the negative to positive terminals. (Right) When the positive and negative terminals are connected to the N-type and P-type diode semiconductors, respectively, no current is allowed to flow, providing that the breakdown voltage has not been exceeded. Image Extracted from (Harris & Fenlon, 2002)

A diode is simply one PN-junction: it allows current to flow in only one direction. All diodes, when forward biased, release energy as electromagnetic radiation, *i.e.* light. The light released by standard silicon is in the infrared range. Infrared light emitting diodes (LEDs) are commonly used in remote-control devices. Visible LEDs are designed to emit copious amounts of visible light. Visible LEDs can be designed to be many colours including red, green, blue, yellow, white or in combinations via red-blue-green (RBG) LEDs. The colour of the LED is dependent on the semiconductors' makeup. Compared

to standard incandescent bulbs, LEDs are more durable and energy efficient, run cooler, achieve full brightness faster, and last much longer. Although the efficacy is low at 20-30 lumens per watt, it is still better than incandescent lighting (Addington & Schodek, 2005).

Other light emitting semiconductors that have been getting a lot of focus recently are organic light emitting diodes (OLEDs). An OLED is essentially an LED whose emissive electroluminescent layer is composed of organic compounds. Generally 100 to 500 nanometers thick or about 200 times smaller than a human hair (Freudenrich, How OLEDs Work, 2010), an OLED is composed of five layers: the substrate, the anode, the conducting layer, the emissive layer, and the cathode. Figure 2-39 illustrates how the layers are situated in an OLED. The substrate is generally composed of glass or clear plastic and supports the OLED; the anode, which is transparent, is connected to the negative voltage terminal; the conducting layer acts as the N-type semiconductor, an example of a conductive layer material is polyaniline; the emissive layer acts as the P-type semiconductor, an example of an emissive layer material is polyfluorene; the cathode, which may or may not be transparent, is connected to the positive voltage terminal (Freudenrich, How OLEDs Work, 2010).

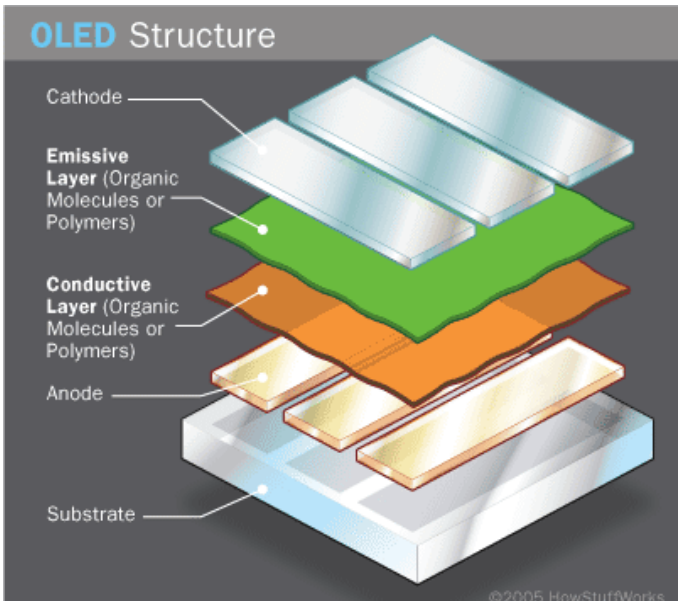

Figure 2-39: The Components of an OLED. Image extracted from (Freudenrich, How OLEDs Work, 2010)

Screens consisting of OLEDs are replacing LCD screens as they do not require a backlight, draw far less power, can be printed on plastic, provide an amazing contrast with a near 180° viewing angle, have a fast response time of 0.01ms, and can be much thinner (less than 1cm) and brighter (Ritter, 2007). Active Matrix OLED screens are currently used in several cell phone, music player, and game console models. The technology has allowed OLEDs to be printed on very flexible substrates (See Figure 2-40). Although television OLED screens are currently available, LCD and plasma screen televisions are selling better at present due to their lower cost.

Figure 2-40: At the 2009 Society for Information Display in San Antonio, Samsung showcased their prototype Active Matrix OLED (AMOLED) screen. The new screen is much more flexible than its predecessors and has a response time that is 1000 times faster than a standard LCD. Since then, this technology has been used in more than 50 cell phone, music player, and game console models (Snegidhi.com, 2009)

2.3.2.3 PHOTOVOLTAICS

In the previous subsection it was revealed how semiconductors can be used to emit photons from electrons via an electric potential, in this subsection it will be showed how semiconductors can be used to produce electron flow using photons from incident light; this technology is known as photovoltaics. In typical photovoltaic cells, like the ones illustrated in Figure 2-41, the N-type semiconductor layer is facing the incident light while the P-type layer is on the opposing side of the PN junction. The incident light energy causes the excessive electrons in the N-type semiconductor to raise their energy

levels causing them to move towards a load such as a battery, resistor, or mechanical device and subsequently move to the P-type semiconductor. The incident sunlight therefore induces an electric current. Series connections between cells are often needed for adequate voltage, but this arrangement leaves a connection vulnerability as one broken link will force all panels to cease functioning. The amount of energy production is proportional to the sunlight intensity; photovoltaic cells are therefore not able to function at night. Despite the drawbacks of light intensity, photovoltaics have made significant gains in efficiency; a consortium led by the University of Delaware has achieved an efficiency of 42.8% compared to an efficiency of 10% as seen in the mid 1970s (Parker, 2007). Commercially, typical modules have a rated power output of around 75-120 Watts peak (Wp) each. A typical domestic system of 1.5-2kWp may therefore comprise around 12 to 24 modules covering an area between 12 to 40 m^2 depending on the technology, sun intensity, and orientation (The Electricity Forum, 2012).

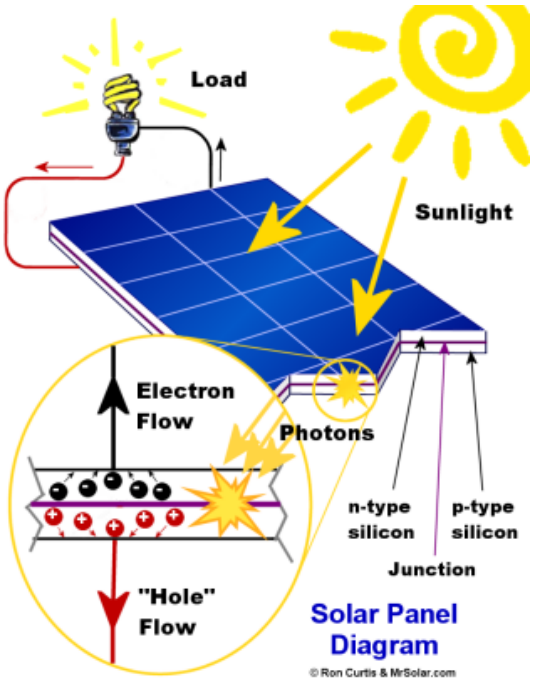

Figure 2-41: Photovoltaic cells generally have the N-type semiconductors facing the incident light to excite their electron abundance. The incident light excites the electrons to move to a load and subsequently towards the P-type semiconductor. Image extracted from (Green Energy. Green Home, 2012)

2.3.2.4 FIBRE OPTICS

Fibre optics are generally not considered smart materials, but smart material systems as they require several components to sense and respond to an environmental stimulus. The fibre optics themselves, only act as a conduit for light. External components are needed to interpret the light for analysis.

Made out of glass or plastic, optical fibres can be divided into three sections: the core, cladding, and buffer coating. Figure 2-42 gives a visual of an optical fiber's components. The core's function is to transmit the light, the cladding's function is to reflect the light back into the core, and the buffer coating's function is to provide protection against environmental damage such as moisture. The diameter of the cladding is typically 125µm, while the core tends to be about 9µm for single mode fibres and 50µm to 110µm for multimode fibres. The principle of operation lies within the concept of total internal reflection, a phenomenon that is illustrated in Figure 2-43.

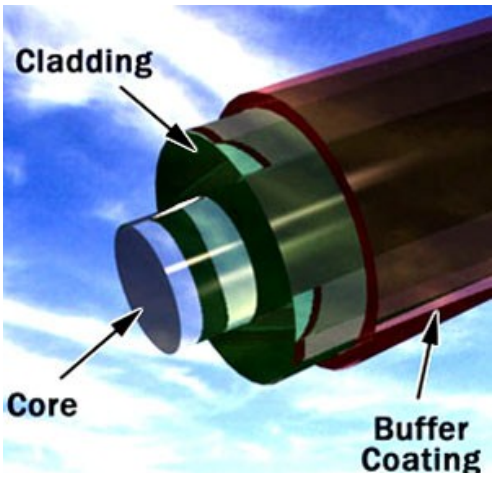

Figure 2-42: Fibre Optics Consist of a core, cladding, and buffer coating

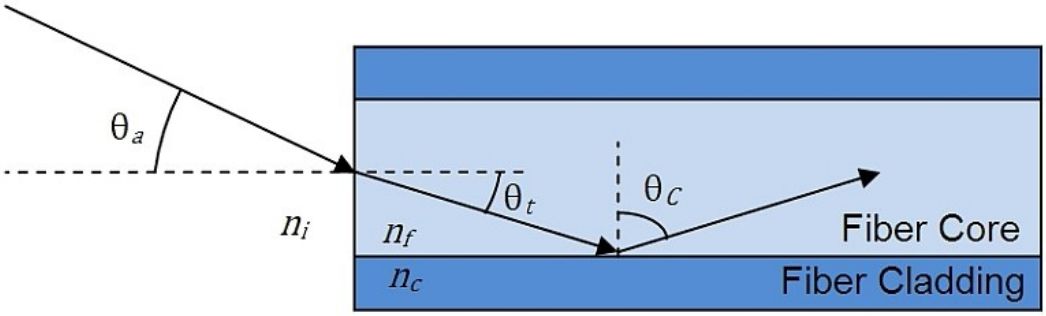

Figure 2-43: The incident angle (θ_a) is refracted to its transmission angle (θ_t) when entering the fibre core, and is consequently reflected by the fiber cladding at an angle equal to 90°-θ_t (i.e. θ_c=90°-θ_t). Image extracted from (ThorLabs, 2012)

The outside environment, core, and cladding all have different indexes of refraction: n_i, n_f, and n_c as labelled in Figure 2-43. In terms of value, the indexes of refraction increase from n_i, to n_f, and to n_c. In the event that the outside environment is air or other gases, n_i is generally assumed to be equivalent to 1. As light enters the core from the environment, the increase in refraction index causes the incident angle to bend with respect to the fiber's longitudinal axis. The new angle is calculated using Snell's law where θ_a is the incident angle and θ_t is the refracted angle inside the core:

$$n_i \sin\theta_a = n_f \sin\theta_t \qquad 2\text{-}14$$

Assuming that n_i is less than n_f, θ_t must therefore be smaller than θ_a. As the light travels along the core at the new angle, it will eventually reach the core/cladding junction. As the cladding's index of refraction is lower than the core's, the angle will refract a second time but at an angle that is greater than θ_t. However, if the supposed refracted angle is higher than 90°, the light will no longer refract, but completely reflect, hence the term total internal deflection. During total internal reflection, the reflected angle (θ_c) will be the equivalent of 90° minus the core refraction angle:

$$\sin\theta_t = \sin(90 - \theta_c) = \cos\theta_c \qquad 2\text{-}15$$

The critical angle (θ_{crit}), is the angle at which total internal reflection begins to take place. It can be found using Equation 2-16:

$$\theta_{crit} = \sin^{-1}\frac{n_c}{n_f} \qquad 2\text{-}16$$

Substituting the critical angle into Equation 2-15 and then Equation 2-16, the maximum incident angle (θ_{amax}) for total internal reflection can be found in terms of indexes of reflection and the critical angle:

$$\frac{n_i}{n_f}\sin\theta_{amax} = \cos\theta_{cmax} \qquad 2\text{-}17$$

Squaring both sides and rearranging, the numerical aperture (NA) of the optical fiber is found:

$$n_i \sin\theta_{amax} = \sqrt{n_f^2 - n_c^2} = NA \qquad 2\text{-}18$$

The numerical aperture is a measure commonly provided by the manufacturers to allow the user to easily calculate the maximum incident angle. The light will go through total internal reflection providing that the angle is less than the maximum incident angle.

Fiber optics are widely used in the field of telecommunications as they are excellent conduits for transmitting light pulses over long distances. However, the light signal can degrade within the fiber, mostly due to impurities in the glass. The extent of the signal degradation depends on the purity of the glass and the wavelength of the transmitted light. For example; at a wavelength of 850nm, the degration is generally 60-75%/km; at a wavelength of 1300nm, the degradation is generally 50-60%/km; and at 1550nm, the degradation is generally greater than 50%/km. However, some premium optical fibers tend to show much less signal degradation, less than 10%/km at 1550nm (Freudenrich, 2001) .

With regards to smart material systems, fibre optics can be used as sensors to sense various stimuli including rotation, acceleration, electric and magnetic field, temperature, pressure, acoustics, vibration, linear and angular position, strain, humidity, viscosity, and chemical measurements (Udd, 2002). The inherent advantages of fiber optic sensors include their ability to be lightweight, of very small size, passive, low power, resistant to electromagnetic interference, high sensitivity, wide bandwidth, and environmental ruggedness (Udd, 2002). Fibre optic sensors can be intrinsic or extrinsic, the former indicating that the optical fibres themselves sense the environmental stimulus while the latter requires a light modulator to sense the environmental stimulus (See Figure 2-44).

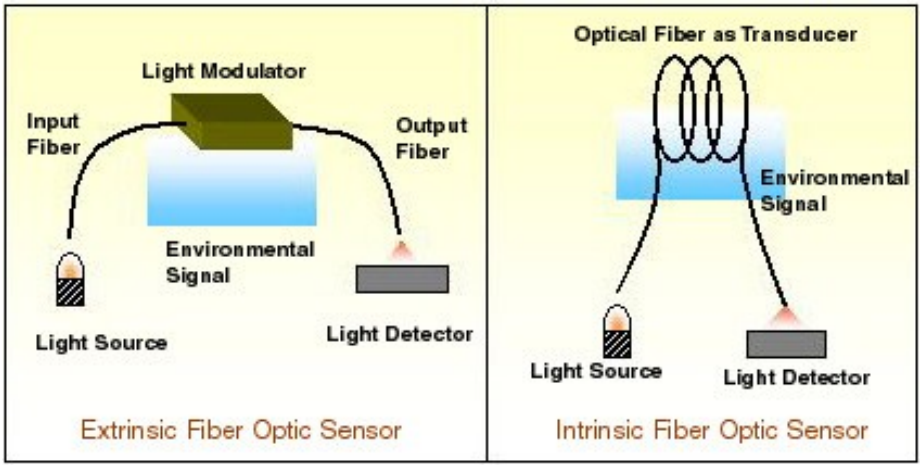

Figure 2-44: Extrinsic Fibre Optic Sensors (Left) have a light modulater that responds to an environmental stimulus; the optical fibres simply act as conduits that transfer light. Intrinsic Fibre Optic Sensors (Right) contain optical fibres that directly respond to the environment. Image Extracted from (International Shool of Photonics)

The optical fibres in extrinsic fiber optic sensors merely act as conduits for light signals. Both sensors have a light source to provide a reference input, and a light detector to sense and decode how the reference input light source has changed from exposure to an environmental stimulus. There are advantages and disadvantages to both intrinsic and extrinsic fibre optic sensors. Extrinsic sensors are less sensitive, more easily multiplexed, easier to use, and exhibit ingress/egress connection problems with the light modulator. Alternatively, intrinsic sensors are more sensitive, more difficult to shield from unwanted external perturbations, have no ingress/egress connection problems as there is no light modulator, require more single demodulation, are significantly more expensive than extrinsic sensors, and are more versatile and robust (Fuhr P. , 2000). The elementary description of an electromagnetic wave is governed by Equation 2-19 where E(t), ω, and φ(t) are the wave's amplitude, frequency ($\omega = {}^{2\pi c}/_{\lambda}$), and phase, respectively.

$$E(t)\cos[\omega t + \varphi(t)] \qquad 2\text{-}19$$

To effectively measure an environmental stimulus, said environmental stimulus must change one or more of the three terms in Equation 2-19. Fibre optic sensors have been installed in bridges (Casas & Cruz, 2003), buildings (Measures, 2001), sailboats (Michael, 2001), ice (Zhou, Huang, He, Chen, & Ou, 2010), textiles (Rothmaier, Luong, & Clemens, 2008), and even parachutes (El-Sherif, et al., 2000). Several different fiber optic sensor technologies exist, three of which are Microbend Sensors, Fabry Perot Sensors, and Bragg Grating Sensors.

Microbend sensors are based on coupling and leakage of modes that are propagating in a deformed fibre (International Shool of Photonics). As shown in Figure 2-45, this can generally be achieved by sandwiching the fibers in between plates with complementing grooves. When a force or pressure is applied across these plates, the optic fibre deforms from a straight wire to a wave-like form. Consequently, less light will be able to experience total internal deflection, resulting in a decrease in light intensity, *i.e.* amplitude in Equation 2-19. The greater the degree of applied force or pressure, the greater the attenuation of light intensity.

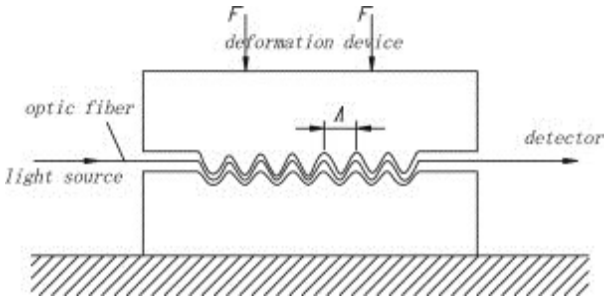

Figure 2-45: The Principle of Operation of Microbend Sensors. Image Extracted from (Zhu, Liu, Yuan, Liu, & Liu, 2010)

Pictured in Figure 2-46, a Fabry-Perot fibre optic sensor relies on changes of the effective length of an optical fibre. A Fabry-Perot sensor is composed of two fibres: one that is connected to the light source/light detector (the fibre optic lead) and another that is simply a segment with a reflective end. There is an air gap between the two fibres, allowing an interference pattern to be reflected back to the light detector. When a light wave is sent down the fibre optic lead, part of the wave is reflected back when it reaches the end of the fibre optic lead. The remainder travels across the air gap where it is reflected by the other fibre segment with a reflective end. The resultant light wave that travels back to the light detector is a combination of both reflected light waves known as an interference pattern. When the air gap is increased, through applied strain or temperature change as examples, the interference pattern will change as the second wave will have to travel a longer distance. The interference pattern will therefore be more out

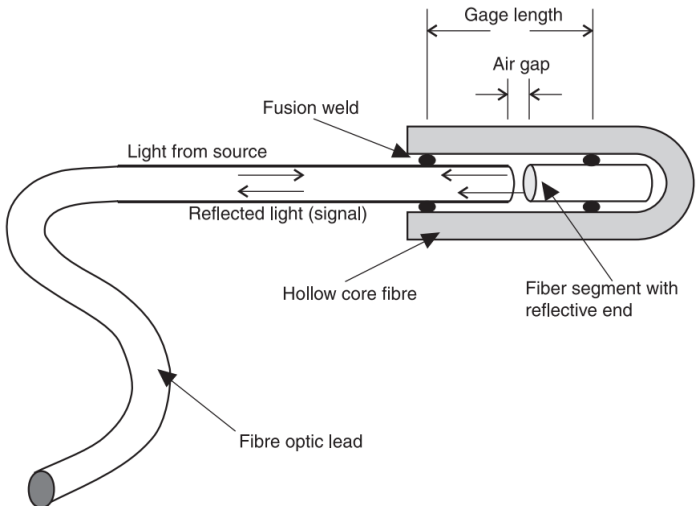

Figure 2-46: The Components of a Fabry-Perot Sensor. Extracted from (Kalamkarov, Georgiades, MacDonald, & Fitzgerald, 2000)

of phase. The light detector can then translate the phase change into the corresponding change in the air gap. Strain and displacement can therefore be directly interpreted from the change in air gap distance. To sense temperature, the air gap is surrounded by a metal such as stainless steel (See Figure 2-47). When the core expands or contracts due to temperature, the air gap expands or contracts, thus affecting the interference pattern.

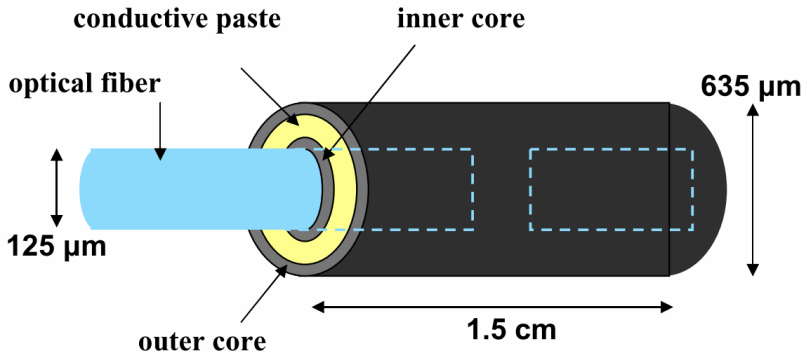

Figure 2-47: A Fabry-Perot can sense temperature change when attached inside metal hollow core, the inner core. In this particular example, the outer core is used to mechanically decouple the sensor from a composite's matrix material. Extracted from (Active Materials Lab, UCLA, 2002)

Bragg Grating fibre optic sensors use diffraction gratings to change the wavelength of a light source. Diffraction gratings are etched into the core by high-power lasers. This often requires the removal of the fibre's buffer coating, exposing the core to a bright light field, and then recoating the fibre with polyimide to restore its durability; this process often reduces the fibre's structural strength by at least a factor of 4 (Fuhr, Huston, Ambrose, & Barker, 1995). The pattern essentially damages the core by locally changing the index of refraction in the high-intensity dark band of the fibre (Fuhr P. , 2000). The spacing of the diffraction grating is known as the Bragg grating period. As light (with a broad spectrum) travels down the Bragg gratings, light is partially reflected back with a wavelength that corresponds with the Bragg grating period (See Figure 2-48). The wavelength reflected by the Bragg grating is referred to as the Bragg wave (λ_B) and can be presented as Equation 2-20 where n_{eff} is the effective refractive index of the fiber core and Λ is the Bragg grating period.

$$\lambda_B = 2n_{eff}\Lambda \qquad 2\text{-}20$$

The light that isn't reflected by the Bragg gratings, exits the optical fibre with the Bragg wave absent from the original broad light spectrum (See Figure 2-48). When a fibre is strained due to deformation or change in temperature, the grating spacing expands or contracts causing a different Bragg wave to be reflected, *i.e.* a different colour. The change in colour is then picked up by a light detector to appropriately measure the change in strain. The response of a typical fibre optic Bragg grating sensor in the 1300nm range yields a wavelength variation of around 1nm/1000mstrain (Fuhr P. , 2000). The wavelength strain sensitivity of a 1.55mm Bragg grating is 1.15pm/mstrain and its temperature sensitivity is 1.3 pm/°C (Ramsey, 1990).

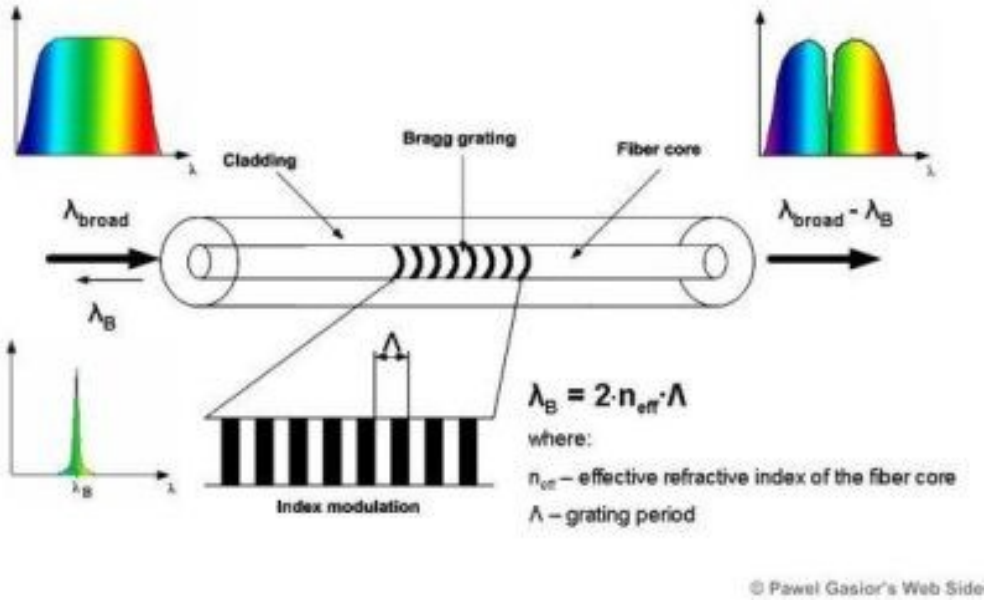

Figure 2-48: The Principle of Operation of a Bragg Grating Fibre optic Sensor. Image extracted from (Fiber Bragg Gratings, 2002)

Not all optical fibres are used for sensing. As optical fibres provide an excellent conduit of light, they are often used in aesthetic lighting. For lighting purposes, plastic optical fibres are generally used for safety reasons. The plastic fibres are also quite bendable and are small enough in diameter to weave into fabrics. Aesthetic optical fibres are also quite inexpensive compared to fibre optic sensors. Figure 2-49 and Figure 2-50 showcase how fibre optic lighting has been integrated into textiles and aesthetic lighting.

Figure 2-49: Fibre Optics have been integrated into fabrics. Lumigram© has used these fabrics on various things such as clothing, pillows, and table cloths. Image extracted from (Lumigram©, 2010)

Figure 2-50: Fibre Optics have been used for aesthetic lighting including chandeliers. Image extracted from (DMAC Electric, 2012)

2.3.3 Type 2: Energy Exchanging (Reversible)

Some energy exchanging smart materials are bidirectional, meaning that a smart material's energy transfer can occur in either direction. Among the smart materials that have this trait are piezoelectric materials, pyroelectric materials, thermoelectric materials, magnetostrictives, electrostrictives, and electroactive polymers. This subsection will go over each one of these materials along with the phenomena they make them smart materials.

2.3.3.1 PIEZOELECTRIC MATERIALS

Piezoelectric materials are one of the most documented smart materials. Known as the direct piezoelectric effect, piezoelectric materials have the ability to respond to deformation by inducing an electric displacement. Known as the converse piezoelectric effect, piezoelectric materials also respond to an electric field through deformation. What sets them apart from other smart materials is that their responsive relationships are generally linear; for the direct piezoelectric effect, the induced electric field is linearly proportional to the applied stress whereas for the converse piezoelectric effect, the induced strain is linearly proportional to the applied electric field. The piezoelectric material's linear response provides simplicity to a system's design as opposed to smart materials that possess quadratic or exponential responses to environmental stimuli.

Although piezoelectricity happens naturally in some materials such as quartz and Rochelle salt, generally the piezoelectric effect is not strong enough to be used in practical situations. This is because their dipole moments are randomly oriented. The piezoelectric effect is maximized by reorienting all dipole moments in a uniform direction; this is accomplished by poling. Poling is a process in which the piezoelectric material is heated around its Curie temperature followed by the application of a strong electric field on the order of 1MV/m. The piezoelectric material is then cooled while maintaining the electric field. The end result is a piezoelectric material with dipole moments in line with the direction of the applied electric field.

Figure 2-51 illustrates the sensing and actuating mechanisms with respect to the poling direction and electrode charges. The poling direction (a downwards arrow) indicates the direction of the electric field during poling while the red positive and negative signs indicate the charge on each of the piezoelectric material's electrodes. During the converse piezoelectric effect, if the applied electric field is in the poling direction, the material will elongate and the electrodes' charges will be of the same sign as that during the poling process. Alternatively, if the applied electric field is in the opposite direction as the poling field's direction, the piezoelectric material will contract and the electrodes' charges will be of the opposite sign as that during poling. During the piezoelectric effect, if the material is strained through tension, the resultant charges on the electrodes are the same as they were during the poling process; however, the induced electric field will be in the opposite direction of the poling direction. Alternatively, if the material is strained through compression, the resultant electrode charges will be opposite to the original poling charges while the induced electric field will be in the poling direction.

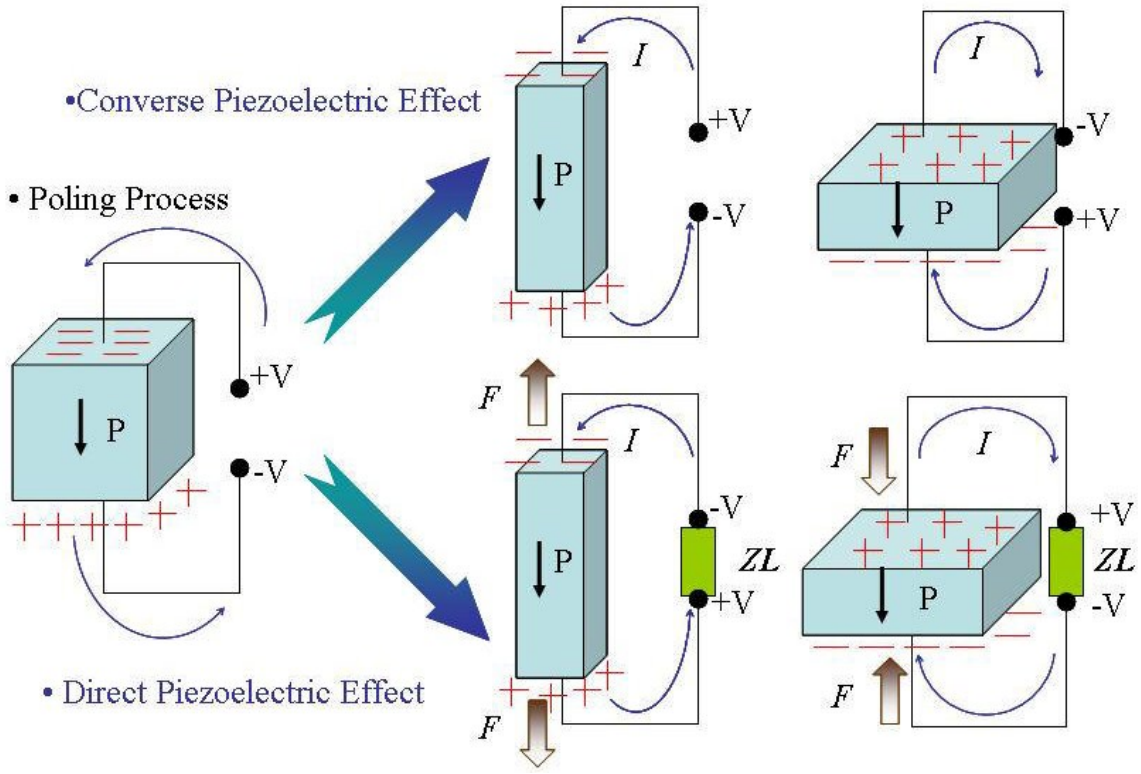

Figure 2-51: Piezoelectric materials respond to an electric potential via deformation (known as the converse piezoelectric effect) and respond to deformation via an electric potential (known as the direct piezoelectric effect). The arrows with a P denote the original direction of the poling field, while the red (-) and (+) signs denote the charge on the piezoelectric material's electrodes. Image Extracted from (Hsu, 2006)

Piezoelectric materials are used both as actuators and sensors. As an actuator, piezoelectric materials can be very precisely controlled to move objects in microelectromechanical systems (MEMS), but are generally limited to moving in the sub millimeter range. For larger deformations, mechanical amplification mechanisms need to be made at the expense of output force. As a sensor, piezoelectric materials can translate various stimuli into an electric potential via the converse piezoelectric effect. These stimuli include force, strain, pressure, acceleration, and sound. The converse piezoelectric effect can also be used to generate sparks or convert mechanical energy into small amounts of power, the latter being known as piezoelectric harvesting. The science behind piezoelectric materials along with an investigation into the effectiveness of piezoelectric harvesting will be later presented in Chapter 5.

2.3.3.2 PYROELECTRIC MATERIALS

Pyroelectric materials, such as lithium tantalite, have the ability to sense a temperature change or heat flow with a responsive temporary voltage. Like piezoelectric materials, pyroelectric materials are generally sandwiched between electrodes and have electric dipoles that have been polarized through poling. As mentioned, during poling the material is heated around its Curie temperature where it is more easily influenced by an electric field. An electric field is then applied, causing the dipoles to align, and is maintained while the material is cooled. Once polarized, if one began to heat the pyroelectric material without an electric field, the dipoles' polarization will begin to decrease, losing all of its polarization if returned to the Curie temperature. If the heat was applied suddenly, this would cause a temporary voltage across the pyroelectric material due to the sudden shift in polarity. Pyroelectric materials are often used to detect sudden changes in temperature as a result of incidence of infrared radiation as the temperature change from said radiation (ΔT) is linearly proportional to the change in the charge developed (Δq) between the pyroelectric material's electrodes:

$$\Delta q = k_p \Delta T \qquad 2\text{-}21$$

The k_p in Equation 2-21 is the sensitivity constant of the crystal. Pyroelectric sensors are often used to detect the motion of a human or other heat sources (Bolton, 2008). As a

reversible energy exchanging material, an induced electric field will produce a change in temperature, but this effect is seldom used.

2.3.3.3 THERMOELECTRIC MATERIALS

Thermoelectric materials have the ability to produce electricity from a temperature gradient. It was first discovered by the German physicist, Thomas Johann Seebeck, and was first published in 1826 (Duckworth, 1960). Seebeck discovered that an electrical current is present in a series circuit of two dissimilar metals with two junctions, an electrical current that increases when the temperature gradient between junctions is increased. This phenomenon is known as the Seebeck effect. Figure 2-52 illustrates the Seebeck effect between a copper wire and two iron wires; at a temperature difference of 100K between the hot and cold junctions, a 1.22 mV voltage is produced (Duckworth, 1960). The Seebeck effect is most often exploited in thermocouples for temperature measurements.

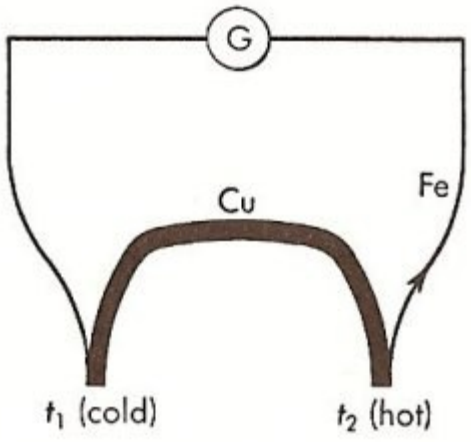

Figure 2-52: The Seebeck effect was observed when two dissimilar metals (like copper and iron) are joined in series. The Seebeck effect is greater when the junctions have a greater heat differential. Image extracted from (Duckworth, 1960)

The Seebeck effect can be reversed, meaning that a direct current applied to a series connection of dissimilar metals (like the connection shown in Figure 2-52) can cause a heat differential between the two junctions. This phenomenon is known as the Peltier effect, named after the French physicist Jean-Charles-Athanase Peltier, who discovered it in 1934 (Encyclopaedia Britannica Inc., 2012).

Thermoelectric materials can also be used to generate small amounts of electricity. To maximize the amount of power generated, metal junctions have been replaced with semiconductors. A common semiconductor used in thermoelectric generators is bismuth telluride (Bi_2Te_3) (ADV Engineering, 2012). As pictured in Figure 2-53a, the P-type and N-type semiconductors are electrically connected in series. Both semiconductors are

connected to the same heat junction electrode, but separate cold junction electrodes; the cold junctions are connected to each other through an electrical load. One could say that the N-type and P-type semiconductors are electrically connected in series, but thermally connected in parallel (Snyder, 2008). As the heat flows from the hot junction to cold junction, electrons in the N-type semiconductor are excited by the thermal energy and are encouraged to move towards the cold junction where they are further encouraged to move towards the P-type semiconductor thus creating an electric current. The power output is proportional to the thermal differential's magnitude: the larger the temperature different between the hot and cold junctions the larger the power output. At the hot junction, as electrons are transitioning from a low to high energy state, heat is absorbed. Likewise at the cold junction, as electrons are transitioning from a higher energy state to a lower energy state, heat is released. To increase the power output, several thermoelectric cells are electrically connected in series as shown in Figure 2-53c. Devices requiring low power consumption such as wristwatches have used thermoelectricity as a power source; the temperature differential is between the wearer's body temperature and the environment's ambient temperature (Torfs, Lennov, Van Hoof, & Gyselinckx, 2006). However, the ambient temperature must be significantly less than body temperature; the wristwatches would no doubt work better an Antarctica than Ecuador.

Semiconductor materials are also used to create thermal generators via the Peltier effect. As shown as Figure 2-53b, thermoelectric devices will produce a heat differential when an electric potential is applied across the P- and N-type semiconductors. The electric potential forces the electrons in the N-type semiconductor to move to the P-type semiconductor, ejecting heat across the connection due to the fact that electrons are going from a higher energy state to a lower energy state. When the electrons in turn travel from the P-type semiconductor to the N-type semiconductor, where they are directly connected through a common electrode, the electrons absorb heat from their surroundings to obtain the energy needed to go back to its higher state of energy. The cold junction previously defined in the thermoelectric generator is thus now the hot junction and vice versa.

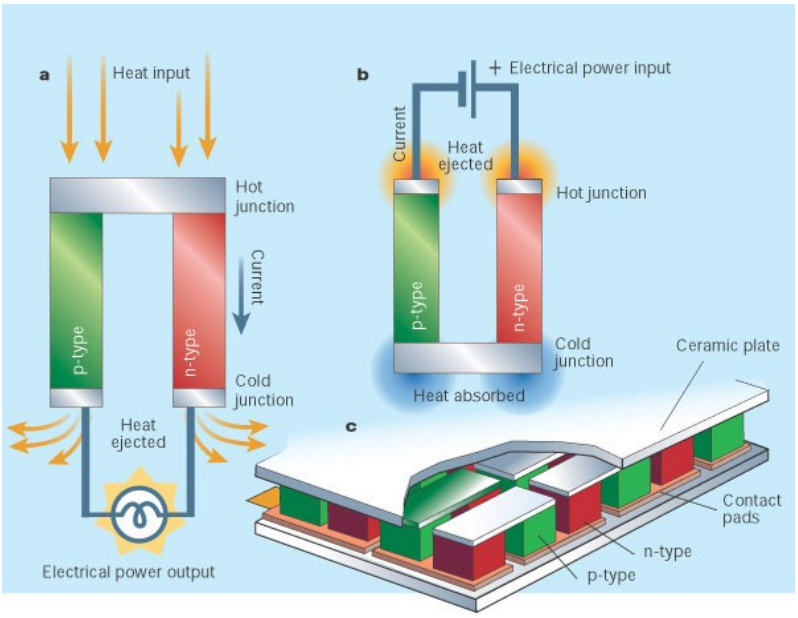

Figure 2-53: P and N type semiconductors are used in thermoelectric power generators (a) and heat generators (b). To obtain larger power generation and temperature gradients, several thermoelectric cells are electrically connected in series. Image extracted from (Metallurgy for Dummies, 2011)

2.3.3.4 MAGNETOSTRICTIVES

The magnetostrictive effect is commonly known as the Joule effect as it was first observed by James Prescott Joule in 1842. Joule observed that applying a magnetic field to iron bar causes the iron bar to increase in length in the magnetic field's direction and likewise contract at respective right angles (Jenner & Lord, 2003). Essentially, magnetostrictives react to a magnetic field through shape deformation, generally in contraction or elongation. Likewise known as the Villari effect, a deformation caused by an applied stress will change a magnetostrictive's magnetic susceptibility, the material's response to a magnetic field. Magnetostriction only occurs in materials with ferromagnetic properties (*e.g.* iron, nickel, and cobalt). These materials have an incomplete 3d electron shell which forms a magnetic dipole. Magnetostrictive materials are internally divided into domains, *i.e.* areas of uniform magnetic polarization which encompass several atoms. These domains may be thought of as ellipsoids with their magnetic dipoles being running along the longest axis. Without a magnetic field, these domains along with their respective magnetic dipoles are randomly oriented. However, once a magnetic field has been applied, the domain walls migrate and the domain rotates

parallel with the magnetic field's direction due to the induced moment on the domain's magnetic dipole. As a result of these magnetic domain shifts and rotations, the material elongates in the magnetic field's direction. The change in length is depicted in Figure 2-55 as length "e" or as length ΔL in Figure 2-54. The material will elongate (or contract) parallel to the magnetic field regardless of the magnetic field's direction (Claeyssen & Engdahl, 2007). If one was to apply a magnetic field to a cylindrical rod made of magnetostrictive material, the cylindrical will appear to only expand or contract along the longitudinal axis as the strain induced by the magnetic field will be more noticeable along the direction of the longest length. The maximum strain will occur when the magnetic field is along the rod's longitudinal axis (See Figure 2-54). Increasing the magnetic field's magnitude will increase the magnetostrictive strain up to its saturation magnetostriction, the strain at which the material has become magnetically saturated

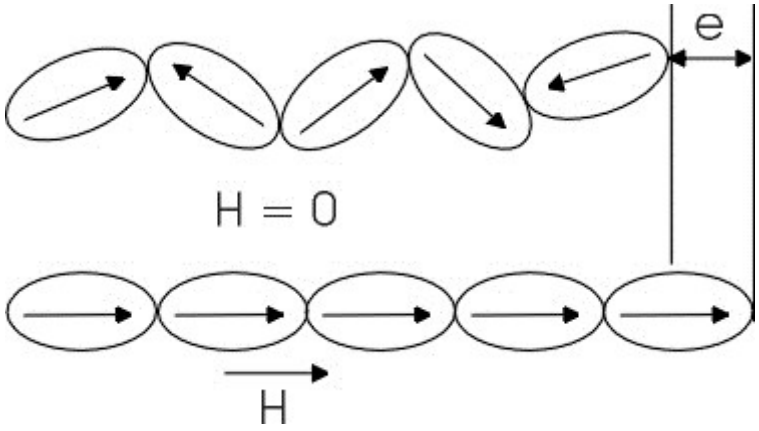

Figure 2-55: Applying a magnetic field causes magnetic domains to rotate in the field's direction, resulting in an a change of length, e. Image extracted from (Active Materials Laboratory UCLA)

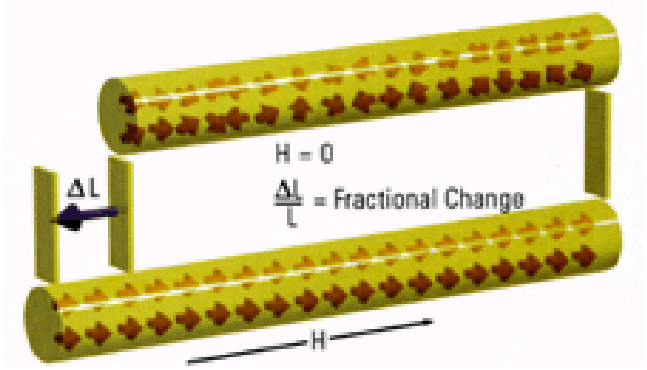

Figure 2-54: The magnetorestrictive effect is most effect across a rod if the applied magnetic field is applied longitudinally along the rod. Image extracted from (MTS Systems Corp.)

The most effective magnetostrictive is most likely Terfenol-D ($Tb_{0.3}Dy_{0.7}Fe_{1.9}$) as it has the best compromise (at room temperature) between a large magnetostrain and a low magnetic field (Claeyssen & Engdahl, 2007). However, with a dynamic strain coefficient of 15-20 nm/A at low magnetic fields, the magnetostrictive strain is still quite small. To better its actuation abilities, magnetostrictives are often prestressed to produce more strain. Fundamentally, the prestress biases the domain's original rotation to allow the domain to rotate further when magnetically polarized by a magnetic field which in turn produces a greater strain. Although simplified (the domains should be in random unpolarized rotations as opposed to all being along the same direction), the effect of prestressing to increase the magnetorestrictive strain is illustrated in Figure 2-56. If the stress is compressive, the induced magnetic field to lengthen the material needs to be parallel to the magnetic field direction. If the stress is in tension, the induced magnetic field needs to be perpendicular to the magnetic field direction. One should note, however, that prestressing in tension is rarely used as magnetostrictives are generally brittle materials, materials that easily break under tension.

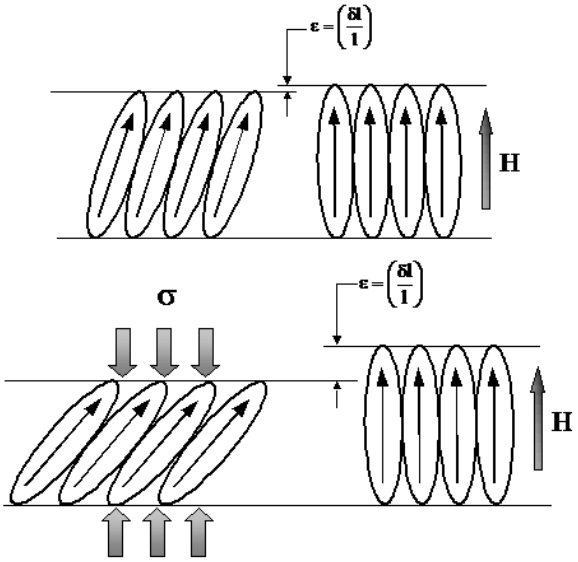

Figure 2-56: Magnetorestrictive materials can be prestressed to produce more strain. Image extracted from (McKnight, 2002)

Magnetostrictive materials generally have nonlinear behavior in relation to the magnetic field and resultant magnetostrictive strain. However, under compressive loading, experimental results show that linear models can give good predictions even with large excitation fields and large dynamic strains (Claeyssen & Engdahl, 2007). The

constitutive equations for magnetostrictive materials are presented below in Equations 2-22 and 2-23 where ε and σ represent tensors of varying strain and stress while B and H represent vectors of varying induction and magnetic fields. Known as magneto-elastic coefficients, the constants s^H, d, and μ^σ are the tensors of constant-H compliance, piezomagnetic constants, and constant-σ permeabilities, respectively. As the prestress is usually compressive due to the brittleness of magnetostrictives, compression is usually represented as positive in magnitude when using Equations.

$$\varepsilon_i = s_{ij}^H \sigma_j + d_{ni} H_n \quad (i,j = 1, \dots 6) \tag{2-22}$$

$$B_m = d_{mj}\, \sigma_j + \mu_{mn}^\sigma H_n \quad (m,n = 1, \dots ,3) \tag{2-23}$$

The subscripts in Equations 2-22 and 2-23 pertain to the directions of the induced conditions (*i.e.* prestress or magnetic field direction) and the axis direction that the constant represents. The subscripts "i", "j", "m", and "n" respectively represent the axis of the strain tensor, the axis of the applied prestress, the axis of the magnetic induction, and the axis of the applied magnetic field. In the case of long rods, the rod's longitudinal axis is defined as axis "3" while the two transverse directions are defined as axes 1 and 2. When these long rods that are subjected to magnetic fields and prestressed conditions along the rod's axis, Equations 2-22 and 2-23 can be further simplified. In this particular situation, it is presumed that the magnetic fields and prestresses induced in the transverse direction are negligible ($H_1 = H_2 = 0$ and $\sigma_1 = \sigma_2 = 0$); it is also assumed that there are no shear elements in the induced stress ($\sigma_4 = \sigma_5 = \sigma_6$). The equations can thus be simplified into equations 2-24, 2-25, and 2-26:

$$\varepsilon_1 = \varepsilon_2 = s_{13}^H \sigma_3 + d_{31} H_3 \tag{2-24}$$

$$\varepsilon_3 = s_{33}^H \sigma_3 + d_{33} H_3 \tag{2-25}$$

$$B_3 = d_{33} \sigma_3 + \mu_{33}^\sigma H_3 \tag{2-26}$$

With the 33-mode coupling, comes an associated coefficient, k_{33}, that represents the magnetostrictive's ability to convert magnetic energy into elastic energy or vice versa (Jenner & Lord, 2003):

$$k_{33}^2 = \frac{d_{33}^2}{s_{33}^H \mu_{33}^\sigma} \tag{2-27}$$

The combination of a high coupling, a high prestress, and a high magnetic field is required to obtain large dynamic strains and very high output powers (Claeyssen & Engdahl, 2007).

Table 2-6 gives typical values of the magnetostrictive, Terfenol-D, at a 90kA/m bias magnetic field at various prestress magnitudes.

Prestress value- σ_0 (MPa)	**Y^H (GPa)**	**s_{33}^H (1/GPa)**	**μ_{33}^T/μ_o**	**d_{33} (nm/A)**	**k_{33} (%)**
30	29	0.034	3.7	8.0	63.1
35	21	0.048	4.2	11.0	69.3
40	23	0.043	3.8	9.7	67.4
50	40	0.025	3.0	5.0	52.0

Table 2-6: Values of Terfenol-D at a 90 kA/m magnetic field with varying compressive prestresses (σ_0)

Prestress value- σ_0 (MPa)	**Y^H (GPa)**	**s_{33}^H (1/GPa)**	**μ_{33}^T/μ_o**	**d_{33} (nm/A)**	**k_{33} (%)**
30	29	0.034	3.7	8.0	63.1
35	21	0.048	4.2	11.0	69.3
40	23	0.043	3.8	9.7	67.4
50	40	0.025	3.0	5.0	52.0

2.3.3.5 ELECTROSTRICTIVES

Electrostrictives are similar to piezoelectric materials in that they deform under electric fields, the key difference being that electrostrictives have non-linear constitutive equations. Electrostriction occurs in any material as every material is composed of randomly-aligned electrical domains, but the effect is generally low with the exception of ferroelectric materials. Like magnetostrictives, electrostrictives deform parallel to the induced field regardless of the field's direction, however, electrostrictives generally compress upon the application of an electric field. The electric field in essence, causes the dipoles to attract one another, thus resulting in compression in the electric field's

direction. Like piezoelectric materials, electrostrictive materials will produce an electric potential when stretched (Kholkin, Kiselev, Kholkine, & Safari, 2009).

Electrostrictive ceramic materials are ferroelectrics. All ferroelectric materials fundamentally exhibit both piezoelectric and electrostrictive effects and are generally modeled under the following constitutive equation:

$$\varepsilon_{ij} = \varepsilon^{E}_{ijkl}\sigma_{kl} + d_{ijkl}E_k + M_{klij}E_kE_l \qquad 2\text{-}28$$

Where: ε_{ij} are the components of the elastic strain
ε^{E}_{ijkl} is the elastic compliance tensor measured at constant electric field
σ_{kl} is the component of stress tensor
d_{ijkl} is the piezoelectric tensor
E_k and E_l are components of the electric field vectors
M_{klij} is the electrostrictive coefficient

The first, second, and third sets of terms respectively relate to the mechanical, piezoelectric, and electrostrictive strains. Typically the electrostriction term is more than an order of magnitude smaller than the piezoelectric term (Kholkin, Kiselev, Kholkine, & Safari, 2009), but certain materials such as lead manganese niobate:lead titanate (PMN:PT) and lead lanthanum zirconate titanate (PLZT) are designed to have larger electrostrictive coefficients and smaller piezoelectric materials so that the electrostrictive effect is the dominant effect when an external electric field is applied (Hu, Du, Ling, Zhou, & Li, 2004). Materials in which the piezoelectric effect is completely absent have centrosymmetric orientation (Kholkin, Kiselev, Kholkine, & Safari, 2009).

As previously mentioned, electrostrictive behavior is quadratic. With reference to a long rod where the longitudinal axis is defined as the "3" axis, the electrostrictive term in Equation 2-28 can be approximated as follows:

$$\varepsilon_{33} = M_{11}(E_1)^2 = Q_{11}(P_3)^2 \qquad 2\text{-}29$$

Where: ε_{33} = the elastic strain along the longitudinal axis
M_{11} = the electrostrictive coefficient along the transverse direction
E_1 = the electric field in the transverse direction
Q_{11} = the polarization electrostriction coefficient along the transverse direction
P_3 = the induced polarization along the longitudinal axis

The polarization is related to the electric fields according to the following equation:

$$P_{11} = \epsilon_0 \epsilon \vec{E}_1 \quad 2\text{-}30$$

Where: ϵ_0 = the permittivity of a vacuum (8 .854 x 10^{-12} F/m)
ϵ = the dielectric constant of the material

Equation 2-28 and 2-29 models the direct electrostrictive effect. Likewise, the converse electrostrictive effect (an electrostrictive's ability to produce an electric charge density with an induced strain) can be modeled as Equation 2-31 when a stress is applied along the longitudinal axis. The resultant from Equation 2-31 has units of m^2/F.

$$\Delta\left(\frac{l}{\epsilon_0 \epsilon}\right) = 2Q_{11}\sigma_3 \quad 2\text{-}31$$

Where: Δl = the change in length along the longitudinal axis
σ_3 = the induced stress along the longitudinal axis

Because electrorestrictives are nonlinear, they are more difficult to model, control, and ultimately use. However, the key advantage of electrostrictives lies within their low hysteresis. Figure 5-11 in Section 5.1.4 compares the hysteresis between PZT (a piezoelectric ceramic) and PMN-PT (an electrostrictive ceramic) and illustrates that although the generated strain of PMN-PT is less than PZT, the hysteresis is greatly improved. The low hysteresis loss implies that these ceramics can be used to induce mechanical vibrations at higher frequencies (up to 50 kHz) (Culshaw, 1996).

2.3.3.6 ELECTROACTIVE POLYMERS

The piezoelectric phenomenon showed that deformation can be directly induced through an applied electric field. Unfortunately their low deformation limited their use as actuators. The need for large deformation rose to the synthetic creation of electroactive polymers. Like piezoelectric materials, electroactive polymers respond to deformation with the production of an electric potential across the material's thickness and also responds to an electric field through deformation. However, electroactive polymers (EAPs) are quite soft having a modulus of elasticity that vary from 0.001 to 1 GPa in comparison to piezoelectric materials which have a modulus of elasticity that ranges from 10 to 100 GPa (Leo, Electroactive Polymer Materials, 2007). With induced strains that can exceed 100%, EAPs are also deform much more than piezoelectric materials which

generally can only deform to about 0.1% strain (Leo, Electroactive Polymer Materials, 2007). In fact, EAPs can expand up to 380% (Ritter, 2007). Due to their direct response to an electric potential along with their high deformation, much research is being performed on EAPs in artificial muscles (See Figure 2-57).

EAPs are generally subdivided into two categories: electronic EAPs and ionic EAPs. Electronic EAPs are polymers that change shape or dimensions due to the migration of electrons in response of an electric field, much like piezoelectric materials. Electronic EAPs also tend to be called electric EAPs and are generally dry. Electronic EAP technologies include: dielectric EAPs, electrostrictive graft elastomers, electrostrictive paper, electro-viscoelastic elastomers, and liquid crystal elastomer materials (Bar-Cohen, 2001). Ionic EAPs change shape as the results of the migration of ions in response to an electric field. Ionic EAPs are usually wet and an electrolyte is required. Ionic EAP technologies include: ionic polymer gel, ionomeric polymer-metal composites, conductive polymers, and carbon nanotubes (Bar-Cohen, 2001). Several advantages and disadvantages for both electronic and ionic EAPs are listed in Table 2-7.

Table 2-7: Advantages and Disadvantages of Electronic and Ionic EAPs

EAP Type	Advantages	Disadvantages
Electronic	• Can operate in room conditions for long periods of time • Rapid response time (msec levels) • Can hold strains under DC activation • Induces relatively large actuation forces	• Requires high voltages (~150 MV/m) • Requires compromise between strain and stress • Glass Transition Temperature is inadequate for low temperature actuation tasks
Ionic	• Requires Low Voltage • Provides predominantly bending actuation (longitudinal mechanisms can be constructed) • Exhibits Large Bending Displacements	• Except for conductive polymers, ionic EAPs don't hold strain under DC voltage • Slow response (fraction of a second • Bending EAPs induce a relatively low actuation force • Except for conductive polymers and carbon nanotubes, it is

		difficult to produce a consistent material • In aqueous systems the material sustains hydrolysis at >1.23V

Figure 2-57: Due to their ability to directly respond to an electric field and their large deformation, researchers are looking into EAPs for artificial muscles. Image extracted from (Bar-Cohen, Artificial Muscles, 2011)

2.4 ABUSE OF THE TERM SMART

As previously mentioned, many engineers, scientists, and technologists disagree with applying the term "smart" to a material or system. Culshaw said it best by saying, "The terms "smart structures" and "smart materials" are much used and more abused" (Culshaw, 1996). The term "smart material" tends to suggest that the material is capable of cognitive reasoning of its environment followed by a response that best adapts to those environmental changes. If this were the case, no non-living material would naturally be smart. Only biological systems are capable of sensing and adapting to their surrounding environment. For example, if someone was to touch a hot stove for the first time, sense pain, and quickly remove his/her hand, he/she would associate touching the hot stove with pain and would thus learn to refrain from touching the hot stove again. Materials do not have the luxury of learning from past experience. Materials can inherently respond to external stimuli, but they cannot inherently learn to adapt themselves accordingly. Returning to the hot stove situation, if one put a metal bar on the stove, it would respond to the excessive heat by expanding. One could argue that the metal's crystal structure adapts to the excess heat through expansion, but one cannot argue that this phenomenon

was not learned and is essentially a property associated with the metal. Thermal expansion is an intrinsic property of metal. Alternatively, if one places a shape memory alloy (a smart material) like nitinol to the hot stove, one would observe a separate phenomenon. Shape memory alloys have the ability to be quite deformable at low temperatures in their martensitic phase, but if one heats the alloy past its transformation temperature, it returns to a programmed shape in its austenitic phase. Regardless of the shape of the alloy at its martensitic phase, it will "remember" its programmed shape above its transition temperature. If one deforms the nitinol in its martensitic phase followed by situating it on top of the hot stove, the nitinol would not expand, but deform to a preprogrammed shape. This "shape memory effect" is absent in most metals, but present in the select group of metals known as shape memory alloys. This phenomenon has been deemed smart do to its rareness and resourcefulness, but this phenomenon is nonetheless a property of shape memory alloys similar to the fact that most metals expand when heated. Shape memory alloys do not learn from their past experiences through adaptation, they repeatedly perform their intrinsic functions.

Frustrated from the abuse of the term "smart material", Culshaw (1996) included in alternative intellectual hierarchy of materials in his book, "Smart Structures and Materials". On top of the hierarch are "Living Materials". Living materials need to continuously dissipate energy and require suitable energy sources. They are capable of reacting to their surroundings, and these reactions may be classified into instinctive and intelligent categories. Instinctive implying a decision-making process based on past experience while intelligent implying a reaction that does not require any analysis. A living material also has the capacity to reproduce. Next on the hierarchy are "Instinctive" or "Reactive" materials. These materials are essentially what we know today as smart materials, but also include non-smart materials that still have reactive properties. Instinctive/reactive materials respond to a particular stimulus by changing its properties in a physical, chemical, electromagnetic, or another domain. It is arguable that all metals are reactive especially to temperature. "Inert Materials" are on the lowest part of the intellectual hierarchy. The functions of inert materials are usually structural or decorative and are specifically designed to give minimal response to external stimuli. Culshaw's

idealized representation of these material types are illustrated in Figure 2-58. Among the three material types already mentioned, Culshaw included an "Intelligent" type. Like a living material, intelligent materials have the ability to react to their surroundings based on sensory inputs as well as past experience, but unlike living materials, they are unable to reproduce. It should be noted however, that no intelligent material has yet been realized from a single compound whereas inert and instinctive materials are often pure compounds. Culshaw argues that it would be more appropriate to call intelligent materials, "intelligent materials systems" as they incorporate various components to sense their environment and adapt accordingly.

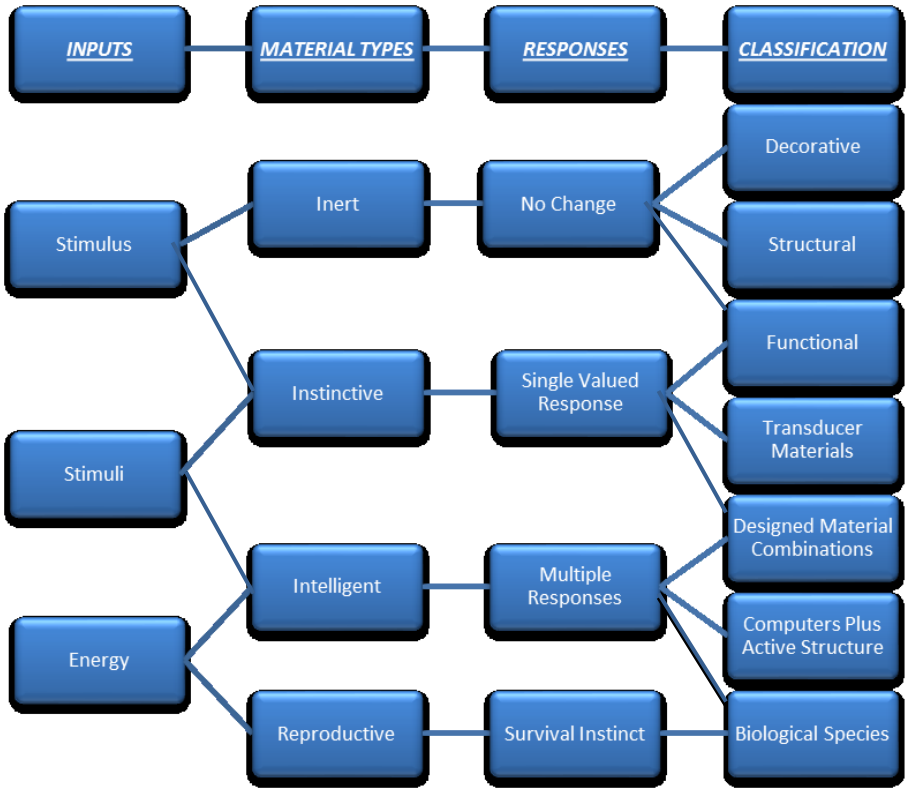

Figure 2-58: Culshaw's Idealized Representation of Material Types (Culshaw, 1996)

CHAPTER 3. RESPONSIVE ARCHITECTURE AND TEXTILES, AND THE ARCHITEXTILE LAB

3.1 RESPONSIVE AND INTERACTIVE ARCHITECTURE AND TEXTILES: AN OVERVIEW

Integrating responsiveness into architecture can very much add to its design. Sometimes the addition has a functional purpose to improve the building's structural integrity. By adding fiber optic sensors to a building's walls, for example, one can monitor structural defects including crack formation and propagation, eliminating the need for routine maintenance checks where manpower is needed to visually inspect the building. Composed of microcapsules, self-healing paint has also been developed so that when the paint is scratched, said microcapsules burst and combine to form siloxane which in turn fills in the resultant crack (Nosowitz, 2008). One can also use MR or ER fluids to actively control seismic vibrations.

Like smart structures, there are some smart textiles that can also accordingly adapt to their environment to preserve their integrity. Presented earlier in Section 2.2.3, Agion® technology inhibits bacterial growth by releasing silver ions in environments with high moisture content. Another example is impact resistant fabrics where shear thickening fluids are used. In their liquid state, shear thickening fluids are filled with tiny particles in suspension that repel each other so they remain suspended and evenly spaced; however, upon a sudden impact (*i.e.* a shear force), the energy disrupts the forces that keep them apart, making them clump together and temporarily turning the liquid into a solid. As the impact energy dissipates, the liquid returns to its previous liquid state. The impact energy thus diffuses in the fabric by breaking up suspension bonds rather than tearing the fabric apart.

Other times, responsive architecture and textiles sense environmental stimuli with a response that benefits their inhabitants or wearers. Often times these responsive systems use smart materials to respond to their environment. Extracted from Wagg et al's

Adaptive Structures: Engineering Applications (2007), Table 3-1 presents the various needs of a building and how smart materials can be used in these building systems. Most of these building systems do not help the buildings themselves, but rather their inhabitants. Thermoelectric materials can be used to control HVAC systems, phase change materials can be used to regulate room temperature, photovoltaics can be used to convert incident solar energy into electrical energy, and electrochromic windows can be installed to control the amount of sunlight entering the building. Most of these functions do not improve the structural integrity of the building, but rather improve the well-being of its inhabitants.

Like responsive architecture, most responsive textiles mainly benefit the wearer rather than the textile itself. Textiles have been made to resist water droplets from reaching the wearer while at the same time allowing water vapour from the user to exit. The SERN-TEX® hydrophobic microporous membrane fabric, for example, has a membrane aperture size that is 700 times the diameter of water vapour, but 20,000 times smaller than the smallest drop of water (SERN-TEX®, 2012); water droplets therefore cannot pass through, but water vapour can easily pass through. Fabrics have also been designed to regulate body temperature. Other than the Outlast®'s phase change jacket already mentioned in section 2.2.3, a hydrogel "SmartSkin" wetsuit has been developed to regulate the body temperature of divers by regulating water flow into and out of the suit. In the event that the diver's skin drops below a preset threshold temperature, the suit expands to cut off water flow. However, if the diver is warm, the SmartSkin allows water to flow into the material; if the water heats up past a certain transition temperature (determined by the proportion of hydrophilic to hydrophobic components), the SmartSkin releases the warmed water and contracts, allowing more cold water to enter the suit (U.S. Natick Army Systems Center, 2002). Textiles have also incorporated moisture responsive fibres to help cool down athletes. The Nike Sphere React Cool responds to sweat by instinctively opening holes within its weave, becoming more breathable to permit increased airflow across the skin, thus cooling the body with increased convection (Lim, 2002). Thermoelectric Peltier elements have also been integrated into clothing to cool down the wearer. Grado Zero Espace, a research and development firm located in

Firenze, Italy, has designed and produced underclothes with Peltier elements to actively cool racecar drivers (Ritter, 2007).

Table 3-1: Smart Material Applications for Buildings. Extracted from (Wagg, Bond, Weaver, & Friswell, 2007)

Building System Needs	Relevant Material or System Characteristics	Representative Applicable Smart Materials
Control of Solar Radiation	Spectral Absorptivity/ Transmission of envelope materials	Suspended Particle Panels Liquid Crystal Panels Photochromics Electrochromics
	Relative Position of Envelope Material	Louver or Panel Systems -Exterior and exterior radiation (light) sensors: photovoltaics, photoelectrics -Controls/actuators: Shape Memory Alloys, Electro- and Magnetorestrictives
Control of Conductive Heat Transfer Through the Building Envelope	Thermal Conductivity of Envelope Materials	Thermotropics, Phase-Change Materials
Control of Interior Heat Generation	Heat Capacity of Interior Material	Phase-Change Materials
	Relative Location of Heat Source	Thermoelectrics
	Lumen/watt energy conversion	Photoluminescents, Electroluminescents, Light-Emitting Diodes
Energy Delivery	Conversion of ambient energy to electrical energy	Photovoltaics, micro- and meso energy systems (thermoelectrics, fuel cells)
Optimization of Lighting Systems	Daylight Sensing Illuminance Measurements Occupancy Sensing	Photovoltaics Photoelectrics Pyroelectrics
	Relative Size, Location and colour of source	Light-emitting Diodes Electroluminescents
Optimization of HVAC Systems	Temperature Sensing Humidity Sensing Occupancy Sensing CO_2 and Chemical Detection	Thermoelectrics, pyroelectrics, biosensors, chemical sensors, optical MEMS
	Relative location of source and/or sink	Thermoelectrics, phase-change materials, heat pipes
Control of Structural Systems	Stress and Deformation Monitoring Crack Monitoring Stress and Deformation Control Vibration Monitoring and Control Euler Buckling Control	Fiber-Optics, Piezoelectrics, Electrorheologicals (ERs), Magnetorheologicals, Shape Memory Alloys

As mentioned, responsive systems require an environmental stimulus to react to. A branch of responsive systems in which the users themselves are the environmental stimulus is labeled by the author as interactive systems. The stimulus in interactive

systems can be movement from the user, sound from the user, or the temperature of the user among other things. The response from the interactive system can be a form of movement, lighting, sound, colour change, graphics; essentially whatever the designer wants to convey to the user. Interactive architecture and textiles not only allow the user to interact with the piece itself, but also allow the piece to interact with the user. The initial stimulus is performed by the user followed by a programmed response by the system. The user can then follow up on the response with a different stimulus and the system may then provide a different response. In a sense, interactive systems allow the user to communicate with the system and vice versa.

3.1.1 Interactive Architecture

One of the first examples of interactive architecture is the TRON intelligent house designed by Ken Sakamura in 1988 in Nishi Azuba, Japan. With an overall cost of 1 billion yen at the time, the building contained a total of 380 computers that were networked with the TRON architecture. All external information received including television, radio, and telephone, as well as all internal information exchanged via an audiovisual system, could be called up on monitors installed in every room (Tron Intelligent House). The inhabitants could thus communicate with the building and vice versa for their various needs.

The TRON intelligent house is one of the ultimate examples of interactive architecture as the building as a whole is responsive to the user, but interactive architecture does not require the whole building to be responsive. The responsive system can only consist of a segment of a building such as a floor, wall, piece of furniture, or enclosure.

Shown in Figure 3-1, an example of an interactive floor is the Power Generating Dance Floor created by Sustainable Dance Club, a company founded by Enviu Innovators and the Dutch architectural firm, Döll. First installed in 2007 at Club Watt in Rotterdam, the Netherlands, the floor generates electricity when stepped or danced on. Composed of tiles that are 75x75x20cm, each tile can compress 10mm when stepped, the mechanical energy

is then converted into electrical energy via an internal generator which will produce up to 25 Watts of power (Sustainable Dance Club, 2011). If 40 tiles are connected together, the dance floor will produce up to 1kW of power. A controller module manages the energy generated by the dance floor tiles. When possible, the energy is directly used to power LEDs embedded in the tiles as well as the controller module itself. If there is an excess of energy, the dance floor will light up to dispose of the excess power or it can be used to charge a battery system. To communicate to the users how much power they're generating, the dance floor can be accompanied with an energy meter tower or digital energy meter to motivate the users to keep dancing and convert more energy; once reaching a certain level, the energy can be used to create a "reward" light show. There are some websites that suggest that these dance floors use piezoelectricity to convert the mechanical energy to electrical energy [(Streeter, 2008), (Crocker, 2011), and (Rosenthal, 2008)] and there are videos on YouTube made by the Döll firm that suggest that piezoelectricity was indeed considered at one point of time (panxut, 2006), however, the power generating dance floor's brochure (Sustainable Dance Club, 2011) gives no indication that piezoelectricity was used and videos produced by the Döll firm showcasing the end product (gemong1, 2008) tend to suggest that rotary electromagnetic generators were used to generate power.

Figure 3-1: The Power Generating Dance Floor created by Enviu and Dutch architectural firm Döll. Image Extracted from (Zucker, 2011)

Shown in Figure 3-2, an example of an interactive wall is the HypoSurface™ wall. Composed of tetrahedral elements that are activated by thousands of pneumatic actuators, the HypoSurface™ wall "behaves like a precisely controlled liquid: waves, patterns, logos, and even text emerge and fade continuously within its dynamic surface" (Hyposurface Corp, 2011). It can act as a display screen by producing messages or logos that travel from one side to another, but can also act as an interactive piece as it can be programmed to respond to sound, light, or the movement of people. For example, it can be programmed to respond to a person's proximity by identifying the person's position when he or she comes to a certain distance, and respond with a longitudinal wave at the person's position, similar to the wave generated by a rock when dropped into a pool of water (HypoSurface Corp., 2007).

Figure 3-2: The HypoSurface Wall. Image Extracted from (HypoSurface Corp., 2007)

An example of a piece of interactive furniture is the iBar, created by Mindstorm Ltd. (Mindstorm Ltd., 2011). Designed as a stool countertop for taverns and bars, the iBar is a surface system which can project any digital visual content including still images and videos. The surface system is also highly interactive, giving customers a means to entertain themselves while waiting for drinks. As a touch screen, customers can order their drinks via interactive menus, can play games, and socially interact with other bar customers. The iBar also has intelligent apps that that can support object recognition and Bluetooth connectivity. The image shown in Figure 3-3 showcases the iBar's object

recognition capabilities by creating visual network connections between drink glasses set on the iBar.

Figure 3-3: The iBar demonstrating its object recognition abilities. Image extracted from (Weston, 2006)

As shown in Figure 3-4, an example of an interactive architectural enclosure is Phillip Beesley's Hylozoic Ground. Chosen to represent Canada at Venice Biennale 2010, Beesley describes Hylozoic Ground as an "artificial forest made of an intricate lattice of small transparent acrylic meshwork links, covered with a network of interactive mechanical fronds, filters, and whiskers" (Beesley, 2009). The mechanical fronds and whiskers are activated using lever mechanisms and straight SMA wires. When heated, the SMA wires contract, but can only contract to a maximum of 5% of their length. To increase the actuation displacement with a sacrifice in actuation force, lever mechanisms are used. The SMA wires are activated in response to a user's movement; proximity sensors are used to detect a bystander's movement and alert Arduino™ microprocessors to activate the SMA lever mechanisms which in turn cause fronds or whiskers to move. "This responsive environment functions like a giant lung that breathes in and out around its occupants and creates waves of empathic motion, luring visitors into the eerie, shimmering depths of a mythical landscape, a fragile forest of light" (Beesley, 2009).

Figure 3-4: Phillip Beesley's Hylozoic Ground. Image Extracted from (Beesley, 2009)

3.1.2 Interactive Textiles

Shown in Figure 3-6, some of the first commercial interactive textiles were the infamous Hypercolor™ T-Shirts, first manufatured by the Generra Sportsear Company of Seattle (Evans-Schultz, 2011). Popular in the early 1990s, the t-shirts were dyed using thermochromic Leucodyes, enabling them to respond to body heat by changing to a lighter hue. Unfortunately, these T-shirts very quickly went out of fashion as they responded more from persperation rather than the touch of another person. In the late 2000s, several companies such as American Apparel, Anzevino & Florence, and Puma attempted to revive thermochromic clothing, but have failed to make the same cultural impact as was previously seen in the early 1990s (Weinger, 2008).

Since the initial release of the Hypercolor™ T-shirt, most interactive textiles contain embedded electronics to sense and produce its responsive functions despite the difficulties of making electronic garments washable. In 2006, Francesca Rosella and Ryan Genz, the co-founders of CuteCircuit, invented the Hug Shirt™ (Shown in Figure 3-5). Like the Hypercolor™ T-shirt, the Hug Shirt™ senses heat, but also senses touch and heartbeat. When the user hugs him or herself, sensors embedded in the Hug Shirt™ feel the strength of the touch, the skin warmth, and the heartbeat of the user. Using

Bluetooth technology, the hug can be transferred over to a separate Hug Shirt™ user where embedded actuators recreate the sensation of touch, warmth, and emotion as sensed from the initial self-hug (Cute Circuit, 2012). If you don't have a Hug Shirt™, but know someone who does, one can still send them a hug using HugMe™ software.

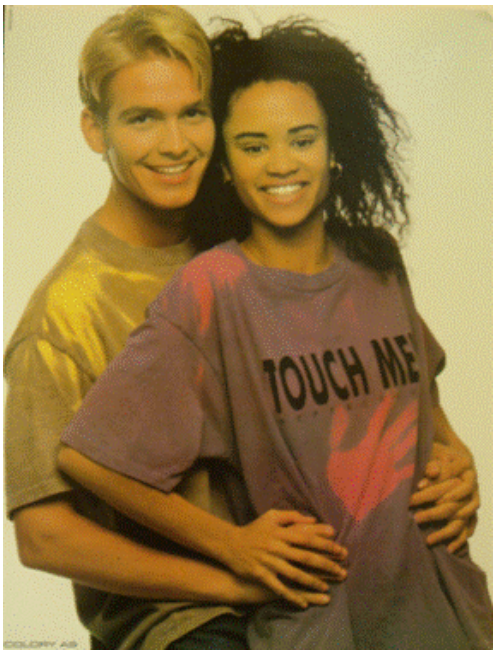

Figure 3-6: The Hypercolor T-Shirt. Image Extracted by (Evans-Schultz, 2011)

Figure 3-5: The Hug Shirt™ by Cute Circuit. Image Extracted from (Julia, 2007)

Interactive electronic T-shirts have also been made to sense sound. The T-Qualizer™, as shown in Figure 3-7, is an electronic t-shirt with an embedded equalizer like ones seen in modern stereo equipment. The embedded equalizer is attached to a module that clips on to one's garments. The module has a microphone with an adjustable amplifier to adjust the microphone's sensitivity, enabling the equalizer to react to louder sounds such as dance club music, but also softer sounds such as those found in speech. The module analyzes the magnitude of the sound, translating it into an electric current to be sent to the electroluminescent panel embedded on the T-shirt's front. Based on the magnitude of sound in relation to the amplifier setting, the EL panel will light up from bottom to top, the top being activated by the louder sounds as seen in traditional equalizers.

Wearable electronic textiles have also been getting a lot of support for medical applications. Wearable technology can detect various physiological responses including: temperature, respiration rate, heart rate, blood pressure, and blood oxygen level. Wearable technology can also be used to produce various physiological graphs such as an electrodermograph (EDG) which measures eccrine sweat gland activity, an electromyograph (EMG) which measures muscle action potentials, an electrocardiograph (ECG or EKG) which measures one's heart rate and heart rate variability, and a pneumograph which measures one's respiration rate. Shown in Figure 3-8, the HealthVest®, designed and manufactured by SmartLife has the ability to produce a full clinical standard ECG, respiratory rate, and body temperature measurement (SmartLife, 2012). In addition, the HealthVest® is mobile, washable, and has embedded sensors, eliminating the need to traditionally place the sensors on individually; the garment goes on as one piece with the sensors already in place. Although the HealthVest® is only available to medical professionals, there are other bio-monitoring garments available to the general public. For example, Numetrex Corp. has invented sports bras for women and chest straps for men that measure one's heart rate.

Figure 3-7: The T-Qualizer. Image Extracted from (Flashwear, 2012)

Figure 3-8: The SmartLife HealthVest®. Image extracted from (SmartLife, 2012)

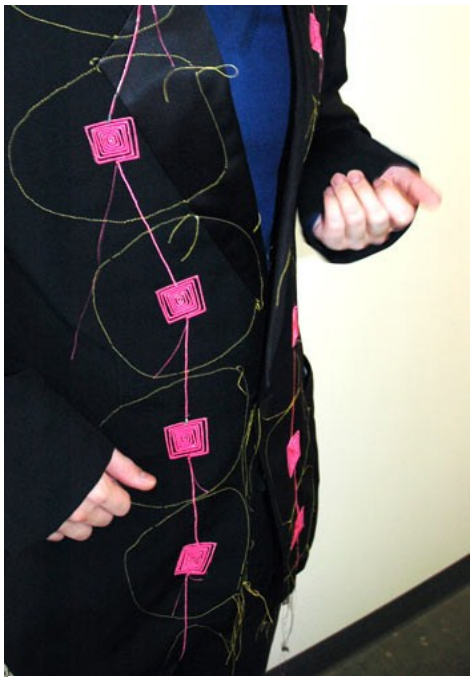

Figure 3-9: XS Lab's Accouphéne by Vincent Leclerc and Joanna Berzowska. Image Extracted from (XS Labs, 2006)

Interactive textiles have also had many developments in the art community. Directed by Joanna Berzowska, Concordia University's XSLab has made several garments that interact with the user while incorporating responsive technology. Some of their interactive works include the "Captain Electric and Battery Boy" collection which is composed of garments that harness energy from the wearer (XS Labs, 2010), the "Accouphène Tuxedo" (See Figure 3-9) which produces sounds that are controlled by hand movement (XS Labs, 2006), and the "Intimate Memory" project which is composed of garments that display their history of use and touch through light displays (XS Labs, 2005). Other examples of interactive art textiles include: the Puddle Jumper raincoat (See Figure 3-10) by Elise Co that senses water droplets (*i.e.* rain) and activates attached electroluminescent panels (Brucker-Cohen, 2005); the Reconfigurable Costume by Leah Buechley (See Figure 3-11) that is fitted with muscle flex sensors, accelerometers, bend sensors, and touch

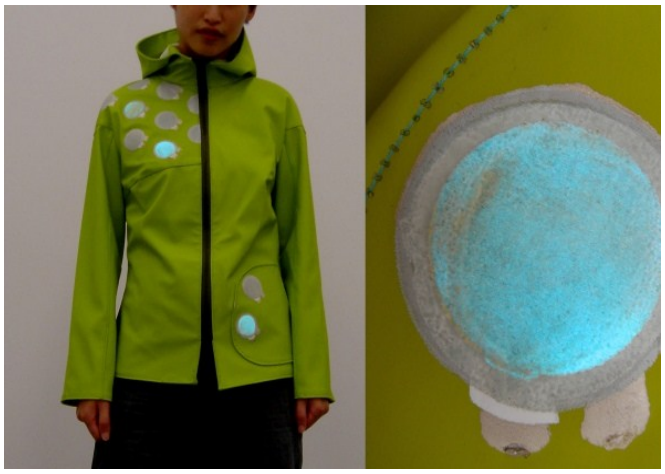

Figure 3-10: The Puddle Jumper by Elise Co. Image extracted from (Brucker-Cohen, 2005)

Figure 3-11: The Reconfigurable Costume by Leah Buechley. Image extracted from (Intelligent Clothing, 2011)

sensors to enable a performance artist to control various media such as music and video (Intelligent Clothing, 2011); and the Lullaby (See Figure 3-12) developed by Alberto Elizonda, Roberto Picemo, and Fracesca Pissutilo, which is composed of two quilts with LEDs that respond to touch on either quilt, enabling two people to communicate with each other via the quilts (TAXI : The Global Creative Network, 2011).

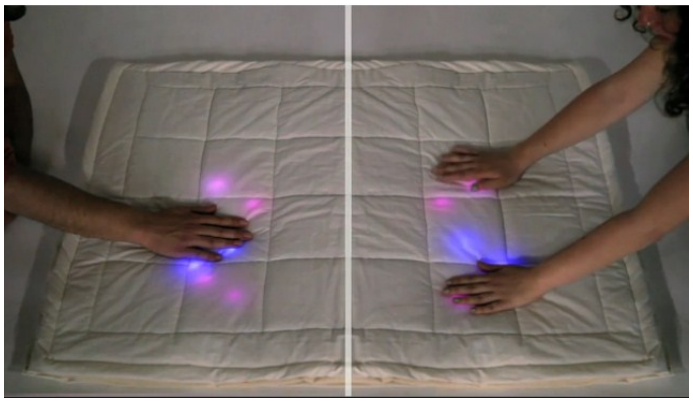

Figure 3-12: The Lullyby by Albertio Elizonda, Roberto Picemo, and Fracesca Pissutilo. Image extracted from (TAXI : The Global Creative Network, 2011)

3.2 THE ARCHITEXTILE LAB

Figure 3-13: The Architextile Lab (also known as the @lab), located at NSCAD's Port Campus

Founded as a joint project between Dalhousie University's Architecture Department and NSCAD's textile department, the architextile lab (@lab for short) sought to create electronic textiles for large scale architecture such as walls, floors, ceilings, and enclosures with an emphasis on collapsibility and responsiveness. Directed by Sarah Bonnemaison (Associate Professor of Architecture at Dalhousie University) and Robin Muller (Professor of Textiles at NSAD), the @lab had a staff of eight, integrating several disciplines to make their vision a reality. This amalgamation brought together academics, students, and professionals specializing in architecture, computer science, design & graphics, electronics, engineering, and textiles. The equipment

available at the @lab included a 3D printer, laser cutter, loom, electronics lab, and a computerized sewing machine among other equipment. The @lab used various design and analysis software programs including Adobe™ Illustrator, Rhino™, and Hyperworks™. Successfully receiving funding from various sources including the Atlantic Canada Opportunities Agency (ACOA) and the Social Science and Humanities Research Council (SSHRC), the @lab opened its doors in 2008 at NSCAD's Port campus and remained there for 3 years before moving to NSCAD's main campus under a new SSHRC grant. During those 3 years, the @lab has produced several prototypes that define the overall vision of what the lab wanted to accomplish.

The @lab's first two projects were decorative pieces. The first project, the glowing curtains (Shown in Figure 3-14), consisted of two backdrop pieces with EL wire sections. Two EL wire curtains were made: a retractable blind and a rolling curtain. The retractable blind would ravel and unravel in front of a window much like a yoga mat, while the rolling curtain would always remain open, but slide in front of and away from a window using a rolling slider mechanism that is located above the window and attached to one edge of the curtain. The curtains were made using a traditional loom, allowing the integration of EL wire with traditional loom fibres. The EL wires needed a 5V/50Hz power source, thus requiring conversion from traditional power sources. The retractable blind was powered using batteries; the batteries, converter, and switch were attached to the bottom edge of the curtain, hidden in a long flat bar. Having the parts attached to bottom of the curtain allowed the curtain to fully unravel when unrolling. The rolling curtain was powered using a regular wall outlet; the converter, transformer and switch were encased in embedded plastic parts that were rapid prototyped using the @lab's 3D printer (Bonnemaison, Berzowska, Macy, & Muller, 2011).

Like the Glowing Curtains, the @lab's second project, the folding room divider (Shown in Figure 3-15), would consist of lighting elements; however, the lighting would be delivered using optical fibres rather than EL wire. The frame of the shoji screen was built using wood, while the screen's textile was composed of organic paper that was pleated using traditional origami folding techniques. Fiber optics were embedded into

the origami textiles so that each valley had the end of an optical fibre, this required several optical fibres to be placed on each pleated column, each fibre having a different length. Each column had an LED located on the bottom, hidden within the wood frame. Each LED would turn on and off in a programmed pattern, emitting either blue or white light. The light in turn would travel along each optical fibre, concentrating its emission at the end of the fibre as a result of total internal reflection. The Shoji screen is also foldable via hinges, allowing the user to easily setup, take down, and transport the screen.

Figure 3-14: The Glowing Curtains

Figure 3-15: The Folding Room Divider

Although these projects incorporate electronics within textiles on a larger scale as part of the @lab's vision, they are programmed to respond in only one fashion. The user would turn on the EL Curtains or Shoji Screen via an on/off switch and the prototype would in turn respond in a set programmed nature. The @lab wanted to expand on what they learned from these projects by creating more complex structures and textiles that rely on input from the user. In other words, the @lab wanted to create projects that interact with their users.

3.2.1 Interactive Projects

After deciding to expand their projects to include larger structures with collapsible mechanisms and interactive elements, the @lab felt a need to hire someone with an engineering background; they hired the author. As the lab's engineer, it was the author's job to analyze the structural integrity, functionality, and smart materials as appropriate for

each prototype. The specific analyses performed for each project will be presented in Chapters 4 through 7. The rest of this subsection will give the reader some background to the various interactive projects designed, built, and tested by the @lab.

3.2.1.1 THE CRICKET

Massage therapy has become a universal tool in alleviating numerous physical and mental ailments. Massage therapist associations claim that physically, massages can relax and soften injured muscles, increase one's circulation and defense system, reduce fatigue, and lighten pain (ICBS Inc., 2007). Due to the benefits of massage in sport medicine, massage therapists are often present during public sporting events such as kayak regattas, soccer games, or swim meets. Unfortunately, public events lack privacy, an element that is generally needed for full body deep tissue massages that require one to disrobe. Massage therapists are thus limited to giving massages that do not require disrobing such as shiatsu massage therapy, body mobilization techniques, and reflexology. It would therefore be quite beneficial to have an enclosure at these public events to provide the privacy needed for a full body deep tissue massage. Inspired from the insect of the same name, the Cricket was designed to act as a massage enclosure at public events. The Cricket would also be responsive to the person receiving the massage, adding an element of interactivity to the massage enclosure.

The shape of the Cricket (shown in Figure 3-16) resembles the overall silhouette of the insect of the same name. The overall outline was oval and consisted of four-bar linkages with 6 peaks, analogous to a cricket's six knee bends, with the larger peaks closer to the door (i.e the Cricket's head) and the smaller peaks closer to the rear. Composed of aluminum tubing, each tube crisscrossed with other tubes to form connecting four-bar linkages; each tube was thus part of two four-bar mechanisms resembling diamonds: one that forms the peaks of the Cricket and another that forms the connections between adjacent peaks. One can think of the Cricket as 6 four-bar linkages connected to each other using four-bar linkages: each of the six four-bar linkages have tubes that extend past its own connection joints, ends of these extensions are then attached to the extensions from an adjacent four-bar linkage.

Figure 3-16: Clockwise from Left: The final Cricket Massage Enclosure fully set up, the final Cricket Massage Enclosure fully collapsed, the initial Cricket Massage Enclosure Prototype with reactive LED Shade Lighting on the inside

To facilitate setup and take down, the @lab felt it was important to make the structure of the Cricket one piece. Making the Cricket a single piece not only eliminated the need to keep track of several pieces, but would also ensure that the proper connections are already in place. As the Cricket was to be transportable, it was also important to make the structure collapsible. Making the Cricket one piece and collapsible was accomplished by incorporating three different collapsibility mechanisms: telescopic joints, revolute joints, and universal joints.

Each aluminum tube consists of two aluminum tubes; a smaller diameter tube is situated inside a larger diameter tube enabling the inner tube to slide along the inside of the outer tube. Each tube can therefore be manually expanded during setup, or contracted during takedown, decreasing the Cricket's space for ease of transport. The overall Cricket structure can be thought of as two sets of aluminum poles with connecting revolute joints:

one set is the top of the Cricket and the other set is the bottom of the Cricket. The revolute joints act to connect adjacent tube ends to each other while limiting the end movements to one degree of freedom. The sliding universal joints, in turn, were used to connect the top of the Cricket to the bottom of the Cricket, but also add degrees of freedom to the Cricket's collapsibility. The sliding universal joints are attached to the Cricket's outer poles and connect an outer pole to an adjacent outer pole. The sliding universal joints have three degrees of freedom: they can slide along an outer pole, rotate around an outer pole, and allow rotation relative to adjacent poles.

To further ease the setup and take-down process, the @lab added lock-and-release mechanisms to the Cricket's collapsibility mechanisms. The lock-and-release mechanisms lets the assembler know when the links are at the correct positions thus eliminating the need to measure angles or distances to ensure that the enclosure is set up correctly. A button lock-and-release mechanism was put inside the sliding universal joint to lock the rotation relative to adjacent poles, a pressure switch lock-and-release mechanism was put on the outside of the female part of the sliding universal joint to lock the position of the joint along tube, hinged latches were added to lock the revolute joints in place, and another button lock-and-release mechanism was used to secure the telescopic mechanism in place. Close up images of the revolute and universal joints along with their lock-and-release mechanisms are shown in Section 4.2.1.3. During a setup, the button mechanisms would lock in place automatically after the telescoping poles have been extended the correct length and when the universal joints have rotated to the correct angle. The pressure switches and hinged latches would then be put in place manually to lock the corresponding degrees of freedom.

The Cricket is covered using nylon based textiles due to their strength and weather resistance. These textiles would not only act as an organic mesh to add to the design's aesthetics, but would also provide shelter from the weather and act as several tensile cables to stabilize the Cricket's structure under various loading scenarios. Like the structural skeleton, the @lab also felt that it was important to make the textiles one piece

for ease of assembly. The Cricket also had a nylon fabric door that can open and close for complete privacy.

To make the Cricket interactive, it was proposed to add shade lighting to the inside of the Cricket's skin. This shade lighting would get input from the person getting the massage, *i.e.* the person's body temperature. Using IR heat sensors to measure the person's temperature, a microprocessor would use this information and translate it into a specific light color; colours closer to the red end of the color spectrum would correspond to higher amounts of body heat while colours closer to the clue end of the color spectrum would correspond to lower amounts of body heat; our electronics technician, Stephen Kelly, successfully programmed LEDs to respond to body heat in this fashion. The @lab experimented with various shade lighting shapes, some of which are shown in Figure 3-17. The shade lighting was placed onto the Cricket's initial prototype skin using conductive thread electrical connections. Although the shade lighting successfully lit up on the Cricket (as shown on the bottom right image of Figure 3-16, it failed to correctly correlate with body temperature as designed. This was likely due to the fact that the conductive thread is not insulated, leaving it vulnerable to wear and tear as well as short circuiting with adjacent connections. It was then decided that this feature should be separate from the textiles and conductive thread was not a good medium for this prototype as it is meant to be used outside (making it vulnerable to rain and moisture) and it will be accessible for people to touch which is a large safety concern.

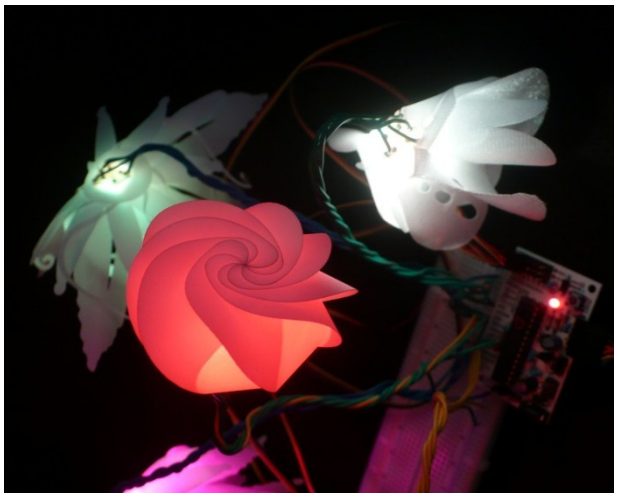

Figure 3-17: The @lab experimented with various forms of shade lighting

Overall, the Cricket was a success. One person was able to set it up in less than 30 minutes (a design requirement) and massage therapists very much liked the Cricket's

aesthetic and found it to be the right size for their line of work as they could easily access the patient 360° around the massage table to give a full-body deep tissue massage.

3.2.1.2 THE FLAMENCO DRESS AND FOLDING STAGE SET

For the next project, the @lab would work with the Halifax local flamenco dancer, Maria Osende. The @lab wanted to create two pieces that would respond to a flamenco performance: a costume that the dancer can wear and a folding stage set that would be behind the dancer.

Figure 3-18: The Flamenco Dress

For the flamenco dress, shown in Figure 3-18, the @lab created a dress inspired by Spanish culture. Traditional Spanish shapes were cut from fabric using the lab's laser cutter; the etched fabric was then made into a traditional flamenco style dress. To make the dress interactive with the user, LEDs were added to the dress and would respond to the dancer's movement.

Attached to the dancer's wrist is a case containing a microprocessor, a battery, and an accelerometer. The accelerometer would sense the wrist's angle relative to the floor as

well as any sudden movements. The microprocessor was programmed to turn the lights on from bottom to top when the dancer raises her arm, and would subsequently turn the lights off from top to bottom as the dancer lowers her arm. The dancer can also change the colour of the LEDs by quickly flicking her wrist; the LEDs will then switch from red to blue or vice versa. The dress was used during a performance at the Flamenco Valentine Show in February, 2010 at FRED Beauty Salon and Gallery. For the stage set, the @lab wanted to use more than one form of interaction. Wanting the stage set to be easily portable for on-the-road shows, it was also important to make the device collapsible enough to put in the trunk of a car and easy to set up, but large enough to have a substantial effect on the audience. The @lab also wanted the stage set to be able to transition into different shapes, allowing the dancer to choreograph different routines for different shapes.

Figure 3-19: A close up of the central axis with assembled poles. The central axis lies in the wooden platform and the backdrops structure can be disassembled to fit inside the platform for transport

To reflect Spanish culture, particularly flamenco dance, the @lab's inspiration came from a traditional flamenco fan. The end product, when set up was 15' wide, 7' high, and had a depth of 5'. The skeleton was composed of 9 telescoping poles of 3 different lengths. Seven poles had a two-pole telescopic mechanism, while the remaining two poles (the ones at 45° and 135°) had a three-pole telescoping mechanism as they were longer. A visual of the pole layout is shown in Figure 4-8 in Section 4.3. Like the Cricket, the telescoping poles had button stop-and-release mechanisms that lets the assembler know when the poles have been extended to their designed lengths. All of the poles are attached to a central rotation axis

where they can be removed through disassembly; a lock-and-release mechanism is used to secure the poles to the central axis when assembled. Figure 3-19 shows a close up of the central axis. The central axis only allows the poles to rotate around the central axis. Also attached to the central axis are hinged inserts (they are the parts in Figure 3-19 that have the silhouette of a pedaled flower) that allow every odd pole to be locked at a 0°, 45°, 90°, 135°, or 180° angle; this allows the structure to be manipulated into many different shapes like the ones shown in Figure 3-20. As seen in Figure 3-19, the central axis (and the stage set itself) lies along a wooden platform that is approximately 4' by 5'. The wooden platform is foldable and is designed to house all of the structural parts when disassembled for ease of transport. Figure 4-6 in Section 4.3 shows all of the poles disassembled and lying in the wooden platform.

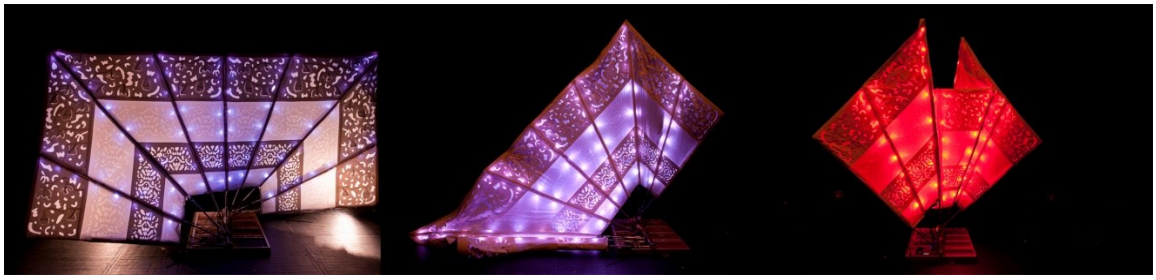

Figure 3-20: The Flamenco Stage set's central axis allows different shapes

To make the stage set interactive to the flamenco performance, the @lab decided to use light and movement as actuation. For the light actuation, RBG LEDs were placed on fabric flaps along both sides of each pole. To make the light reflective to the audience, the back of the stage set was lined with a reflection fabric while the front had a combination of translucent fabric and opaque fabric with etching. The etched patterns were the same as the flamenco dress. All fabric was white to optimally reflect all colours of light. For the movement actuation, the @lab decided to move fabric flaps via SMA Nitinol springs. On the outmost layer on the stage set's front, flaps of fabric were cut out using the laser cutter and one SMA spring was attached to the front of each flap. On the back of the flaps, the nitinol springs were crimped to electrical wire to activate the nitinol springs via resistive heating. Also on the back of each flap was a piece of superelastic nitinol wire that would act as bias force to bring the flap to its previous resting state. When activated, direct current is sent through the nitinol wire, causing the nitinol spring to compress and consequently pull the fabric and bend the superelastic nitinol wire on the

back. When the direct current is removed, the SMA nitinol spring cools down and the superelastic nitinol wire brings the flap back to its previous resting state. Figure 3-21 shows two different fabric flaps in their resting and reactive states.

Figure 3-21: Fabric Flaps are actuated by SMA Springs and bias forced using Superelastic Nitinol. The left image shows two flaps in their resting state while the right image shows the flaps in their reactive state

For stimuli, the @lab chose to again use the movement of the dancer, but also the music being played during the performance. Like the flamenco dress, an accelerometer was attached to the dancer's wrist to control the stage set's lighting. The accelerometer then communicates wirelessly with the stage set's microprocessor which translates the signals into a light show. Programs have been made where the lights can be turned on and off from one direction to another, similar to a wave, and also from inside to outside. Programs have also been made that enables the dancer to control the colour and intensity of the LEDs. To actuate the fabric flaps, the stage set was programmed to respond to instrumental music. Using microphones along with an Arduino™ microprocessor acting as a control system, the fabric flaps were successfully programmed to respond to violin music; as soon as the violin's volume surpassed a certain threshold, the fabric flaps would activate and move.

Part of this thesis was to find how the actuation times and stokes change in relation to various manipulated parameters such as the wire diameter, spring diameter, number of spring turns, direct current magnitude, bias force, and transition temperature. Predictions were made, experiments were performed, the resultant data was analyzed, and conclusions were made. For a full report on the investigation, please refer to Chapter 6.

3.2.1.3 THE WARMING HUT

The Warming Hut was the most publicized project undertaken by the @lab. For the 2011 Canada Games, the @lab was approached by HRM to design and build an enclosure for the outdoor speed skating oval to be built on the Halifax Commons. The Warming Hut would functionally act as a place where athletes or spectators can change into their skates, relax, warm up, and take shelter from the wind and cold of winter. During the previous summer, several tepees were erected on the Halifax Commons to celebrate the 400^{th} anniversary of the baptism of the great Mi'kmaq Grand Chief Membertou. The tepees were very large in height and had LED wall lighting projected on the outside canvas, creating a "rainbow" of tepees at night. The warming hut's design was partially inspired by the sights of these colourful tepees.

The final warming hut, pictured on the Halifax Commons in Figure 3-22, was 14.5' tall with a bottom diameter 146" wide, narrowing to 35" wide at the roof. The warming hut was made in eight sectioned panels that were later bolted together. Each panel was made with an aluminum frame with cross-sectioned members to prevent twisting. On the bottom and top of each section, wood panels were bolted onto the outside of the aluminum frame for further structural support and aesthetic. On every odd section (including the door section) the outside was decorated with Ferrari awning fabric and clear Lexan sheet plastic that acted as windows, enabling the users to see the skating oval from the inside; on the back of the Ferrari fabric were computer woven jacquard textiles that depicted ice crystals or skating marks. Using a palette of brown, light blue, pink, white, and black, the Ferrari pieces' colours were based on the muted colours of a Georges Braque still life. On every other section, Lexan panels were screwed into the

aluminum frame to showcase the aluminum cross-sectional members from the outside while the inside was covered with acid etched cloth to resemble skating marks. Both the Lexan and Ferrari canvas were waterproof. To make the wood panels waterproof, coats of varnish were applied to the panels. All aluminum frame connections were caulked to prevent rain leakage. The structure was erected on top of rubber mats with the door facing the opposing direction of typical winds. The hut was anchored to the ground using dog anchors that were placed into the ground months prior, before the ground was frozen.

Figure 3-22: The Warming Hut outside the Canada Games Oval in Halifax, NS. The Games were held on February 11-27, 2011

Bolted to each section's inside, excluding the door section, are aluminum framed seats with white and grey straps acting as cushions. The seats in turn were bolted together with spacers in between. The seats were heated, similar to car seats, allowing users to literally warm up when sitting down. On the top of each seat was up-lighting that would in turn illuminate the warming hut at night. On the inside of the hut's roof was a beautiful chandelier composed of laser cut organza snowflakes with embedded fiber optic lighting. The fiber optic lighting colour would consistently change, illuminating the hut's roof from the inside and outside. Pictures of the warming hut's inside are shown in Figure 3-23.

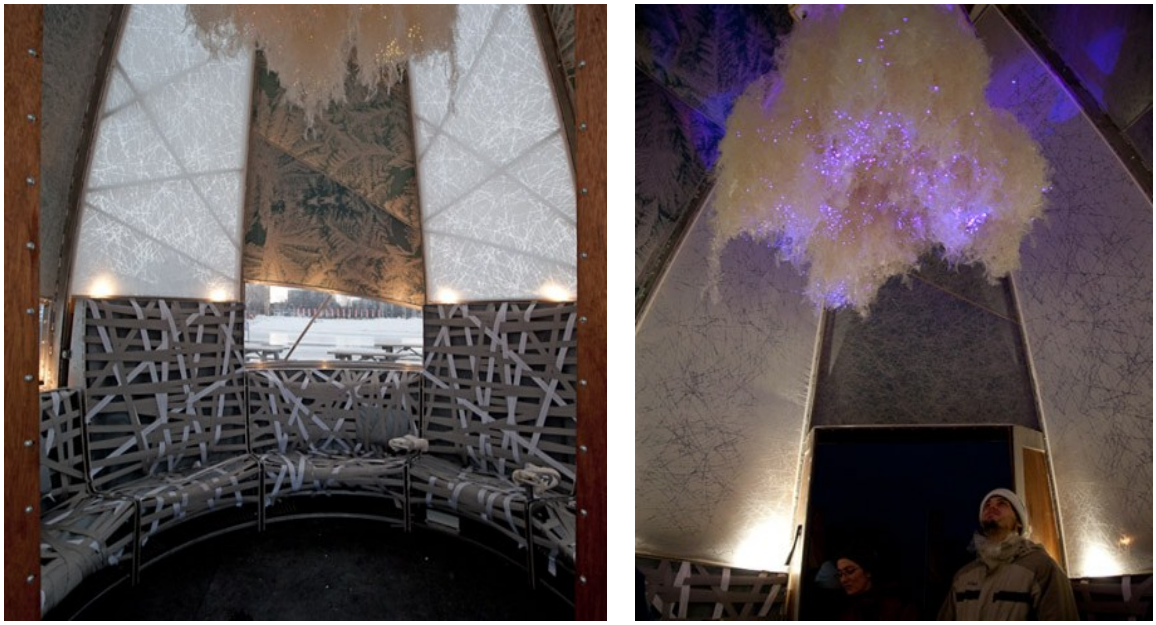

Figure 3-23: The Inside of the Warming Hut.

To make the hut interactive to the general public, the @lab would borrow a heart beat amplifier, invented by Dr. Alan Macy. Designated as the "throne" seat, one of the seats had two chair handles. On top of these chair handles were copper electrode plates, one on each handle, that were connected to the heart beat amplifier. If one placed one's hands on both electrodes, one on each electrode, the heart beat amplifier recognizes the heart beat and amplifies the electrical current associated with it in two dimensions: amplitude and frequency (Bonnemaison, Berzowska, Macy, & Muller, 2011). The @lab then used the information to amplify the sound of one's heartbeat using a subwoofer. In addition to hearing your heartbeat, you could see you heartbeat through the fibre optic chandelier. The information from the heart beat amplifier was also relayed to the chandelier to pulsate white light in syncopation with your heart beat. On January 21st, 2011, the hut was open to the public with a ribbon cutting held by the Mayor of Halifax. The hut proved to be a great success with the public with lines of people waiting to try it out.

3.2.1.4 THE ACOUSTIC CEILING

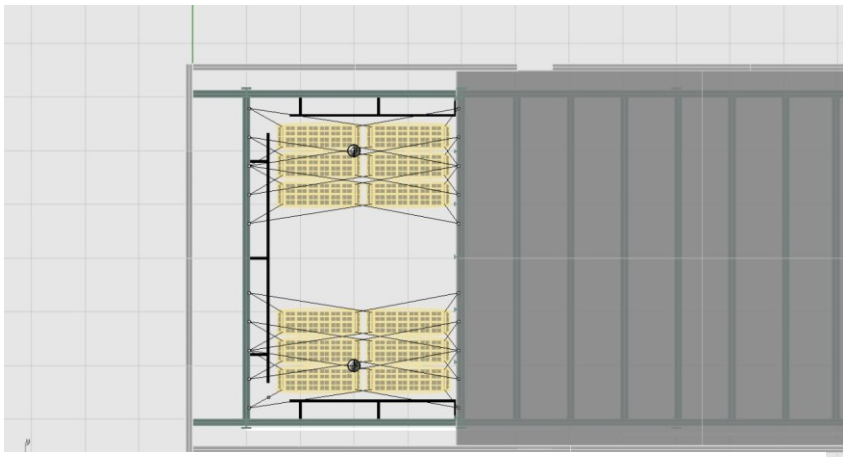

Figure 3-24: A rendered bird's eye view of the acoustic ceiling in its eventual home: the exhibition space at Dalhousie's Architecture Building

The acoustic ceiling is a ceiling that can change from a sound absorbing state to a sound reflecting state and vice versa via rotating tiles. It was desired to make the device have various levels of sound absorption/reflectance; one way to do this is to make one side of the tiles sound absorbing and the other sound reflecting. Depending on the desired reflectance, a portion of them would be on their sound absorptive side while the other would be on their sound reflective side. As one would want to change the reflectance depending on a certain situation, it would be desirable to change the overall reflectance of the ceiling, catering to said situation. The @lab proposed to make 12 panels of ceiling tiles each having 2 x 6 tiles to give a grand total of 144 tiles.

Ideally, each tile would have its own motor so that each tile can move independently to give the most variety of reflecting situations. This would require 12 motors per panel for a total of 144 motors. More simply, each panel could have only one motor where each panel's tiles would move in sync. This would require a total of 12 motors. Alternatively, each row of tiles could have its own motor so that the tiles corresponding to each row (6 tiles total) would be driven in sync by a single motor. This situation would require 2 motors per panel for a total of 24 motors. Finally, the motors could be driven in a "checkerboard" pattern; *i.e.* every odd tile on each row can be driven by one motor and every even tile can be driven by a separate motor. This would require 4 motors per panel, 48 motors total. All situations are summarized in Table 3-2 below:

Table 3-2: The Number of Motors needed for each actuation situation

Situation	Number of Tiles Driven by each Motor	Number of Motors	
		Per Panel	Total
All Independently Driven Tiles	1	12	144
All Tiles on each Panel Driven in Sync	12	1	12
One Motor per Row	6	2	24
"Checkerboard"	3	4	48

The @lab wanted to give a variety of absorbance patterns, but felt that giving each tile its own motor would over complicate things. The "Checkerboard" would therefore be the more logical choice to simplify the mechanism, but still have a wide array of reflecting situations. Figure 3-25 presents an illustration of three panels back to back with the proposed "Checkboard Mechanism".

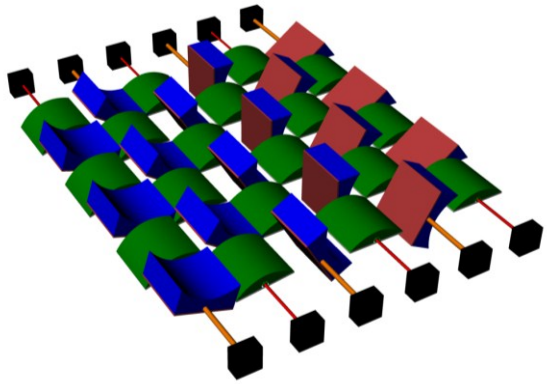

Figure 3-25: 3 panels of the proposed "Checkerboard" actuation mechanism where there are two motors along each row, one for the odd tiles and the other for the even tiles

To make the "Checkerboard" pattern work, the author came up with a double tube mechanism. Each row would consist of two tubes: an outer tube and an inner tube where the inner tube lies within the outer tube. Each tube would be driven by its own motor and the odd tiles would be connected to one tube while the even tiles would be connected to the other. Tiles can be directly attached to the outer tube, but to connect tiles to the inner tube, parts of the outer tube needed to be exposed via slits. Tiles can then be screwed into the inner tube. To keep the tube uniform (*i.e.* one piece) the slits could not be cut throughout the tubes entire circumference; this consequently limits the amount of rotation that the inner tube and outer tube can make with reference to one another. The tiles can still rotate 360 degrees, but both tubes need to be rotating to make this happen. To make

the checkerboard pattern, the tiles required to at least rotate 180 degrees, the slits were then cut to allow approximately 200 degrees of rotation.

Figure 3-26: The first reactive ceiling prototype using the proposed "Checkerboard" actuation mechanism.

Using an inertia analysis along with using a large safety factor to account for impending friction, the motor torque was estimated and appropriate motors were bought. A one-panel prototype of the reactive ceiling (shown in Figure 3-26) was produced for testing, using the proposed checkerboard double tube mechanism. The mechanism proved to function to its design specification, each motor would only turn three tiles. There was however some unwanted sound produced by the motors. In the final prototype, material will be added to dampen the unwanted noise.

As mentioned, the end prototype will be responsive to sound, making the ceiling interactive to human speech levels. The ceiling will be able to sense sound levels in the room and appropriately switch the tiles to cater to these sound levels. For example, if there is only one person speaking in front of a large audience, *e.g.* an oral presentation, it would be beneficial for ceiling to be sound reflecting to better transmit the oral presentation to the audience. Alternatively, if the room is full of groups of people carrying on separate conversations, it would be beneficial for each conversation to

remove excess noise from the surrounding conversations; a sound absorbing ceiling would be appropriate for this application. Using microphones and microprocessors, the final product will be able to sense the levels of human speech and appropriately react to these levels by making the ceiling sound absorbing, sound reflecting, or a combination of both.

Sound absorption and reflection is generally measured on a 0 to 1 scale with 0 indicating perfect reflection and 1 indicating perfect absorption; the value is known as a noise reduction coefficient (NRC) and is simply the average of the mid-frequency (i..e mid-frequency of human speech levels: 250, 500, 1000, and 2000 Hz) sound absorption coefficients rounded to the nearest 5% (NRC Ratings, 2009). Some common materials with low absorption coefficients, thus having high sound reflectivity, are brick, wood, plaster, and steel. Some common materials with high absorption coefficients, thus having high sound absorbance, are cork, carpet, cotton, and fiberglass. For the sound reflecting side of the rotating tiles, the @lab used birch plywood which has an NRC rating around 0.05 to 0.15 (NRC Ratings, 2009). For the sound absorbing side, the @lab purchased sound absorbing foam known as Sonex™One acoustical foam from Acoustical Solutions, Inc. The Sonex™One acoustical foam data sheets indicate that it is available to have NRC ratings from 0.85 to 1.10 (Acoustical Solutions, Inc., 2012), something that perplexed the author as he was led to believe that the NRC value cannot surpass a value of 1. Regardless, the foam was purchased and appears to dissipate sound quite well. It is planned to take sound measurements on the final prototype to fully address if the reactive ceiling dissipates and reflects sound as designed. It is planned to install the reactive ceiling in the summer of 2012.

To add personality to the reactive ceiling, the wood tiles were cut using the laser cutter so that three panels together (36 tiles) have a full etched picture of the outer, middle, and inner organs of a human ear. Alternatively, the foam panels will be covered in ruffled cotton fabric that has been dyed using natural dyes. Several different coloured dyes will be used so that the tiles will reveal a colourful palette.

3.3 THE HUMAN POWERED LED JOGGING SUIT

Jogging at night can be hazardous; often joggers wear reflective clothing or even lights attached to their clothes to make drivers aware of their presence. The Human Powered LED (HPLED) jogging suit not only had LEDs to alert oncoming traffic, but had LEDs that were powered from the jogging itself. The project thus required a mechanism to transform some of the mechanical energy produced while jogging into electrical energy. One senior mechanical engineering undergraduate design group at Dalhousie University had great interest in the project. The members of the group were Amanda Rogers, Devon Chandler, Richard Mills, and Marc Greencorn.

Having studied piezoelectric materials as a self-directed research course and having specifically read Shenck & Paradiso's paper, "Energy Scavenging with Shoe-Mounted Piezoelectrics" (2001) as well as Mateu & Moll's Paper, "Optimum Piezoelectric Bending Beam Structures for Energy Harvesting using Shoe Inserts" (2005), the author encouraged the group to incorporate piezoelectric harvesting into jogging shoe inserts. Using appropriate control circuits, piezoelectric materials were successfully incorporated into shoe inserts to power LEDs attached to the jogger's pants (See the left image in Figure 3-27). The LEDs were attached to the pants using Velcro and conductive thread, enabling the wearer to remove the electronics from the suit for washing. Figure 3-28 shows a picture of the piezoelectric harvesting shoes with the electric current attached to the back. The piezoelectric shoes were used as a case study by the author to test the feasibility of using piezoelectric material to harness the energy from human foot traffic. For a full report on the feasibility of harvesting energy from human foot traffic via piezoelectric harvesting, please refer to Chapter 5.

Not having confidence that the piezoelectric harvesting shoes would harness enough power to produce the 0.3W that was set as a design requirement, the design group set out to add an additional power harvesting source to the suit. Inspired by the shake flashlights one can buy in traditional hardware stores, the group and the author came up with electromagnetic inductive shakers that would harness the vertical up and down motion of

the jogging. The shakers would be placed on the jogger's hip and have a mass-spring resonance system that would resonate with the up and down motion of the jogging itself. The mass would be a rare earth magnet that would be surrounded by layers of wire coils. As the mass goes up and down, current would be induced through the coiled wire as a result of electromagnetic induction. The current generated would then be used to power LEDs located on the shirt. For optimum power generation, the mass-spring system should resonate at a jogging frequency, *i.e.* about 1 to 3 Hz, a frequency range that requires a spring with low stiffness. Having used superelastic nitinol on the flamenco stage set, the author suggested making helical springs out of superelastic wire. As superelastic nitinol can be easily bent at large strains without plastic deformation, the author figured that these properties would translate to a low stiffness helical spring. Unsure if traditional spring mechanics could be used on nitinol springs to predict their stiffness, the author made several springs of different geometries to test with the rare earth magnets to see if a resultant spring-mass system can be made to resonate at a typical jogging frequency. After manipulating the number of turns and using the larger spring diameter, the spring-mass system was built to perfectly resonate with the jogger.

Superelastic springs are therefore quite useful in attaining low frequency resonance in a spring-mass system. Figure 3-29 shows a picture of the final electromagnetic induction shakers. Successfully harnessing 0.132W each, the electromagnetic induction shakers proved to harness much more power than the piezoelectric embedded shoes which only generated about 3mW.

Wanting to know if traditional spring mechanics can be used to predict both the stiffness of a superelastic nitinol helical spring and the primary resonant frequency of a superelastic nitinol spring-mass system, the author took it upon himself by experimenting with different spring geometries. Through manipulating various spring parameters such as wire diameter, spring diameter, and the number of turns, the author conducted experiments to measure the overall spring stiffness and resonant frequencies with several masses. The results were then compared with traditional spring stiffness and resonant frequency equations along with alternative models proposed in literature that take

account of nitinol's superelastic mechanical behavior. For a full report on these superelastic nitinol springs, refer to Chapter 7.

Figure 3-27: The Human Powered LED Jogging Suit. (Left) The pants have LEDs powered by piezoelectric inserts in the shoes and are sewn into the pants using conductive thread. (Right) the sweater has LEDs powered by electromagnetic inductive shakers located on the waist.

Figure 3-28: The Piezoelectric Harvesting Shoes

Figure 3-29: The Electromagnetic Induction Shakers

CHAPTER 4. ANALYZING THE STRUCTURAL INTEGRITY OF THE @LAB'S PROJECTS

4.1 INTRODUCTION

This chapter aims to present some of the analytical and experimental methods that were performed by the author to strengthen the integrity and functionality of the @lab's projects. This chapter is divided into six subsections, one for each case study. These case studies range from analyzing the deflection in collapsible poles, to mapping the stress distribution in joints, and specifying the torque needed for rotation.

4.2 IMPROVING THE STRUCTURAL INTEGRITY OF THE CRICKET

This section is on improving the structural integrity of the Cricket. Divided into two sections, the first section goes over an attempt to model the Cricket under wind loads using Hyperworks® software, while the second section goes over the various structural recommendations made by the author to strengthen the Cricket along with the various solutions conceived by the @lab staff to address said recommendations.

4.2.1.1 COLLAPSIBILITY

The original Cricket had poles with different curvature (See Figure 4-1) to make the structure more appealing. Although curved poles can be telescopically collapsed, the curvature between the respective telescoping poles must be identical. Curved poles are also more prone to buckling, are more expensive, and are not as readily available as straight poles. To ensure the collapsibility of the Cricket, it was therefore advised that straight poles be used.

The original structural design consisted of eight diamond four-bar linkages with links that extend past their connection joints to provide connections with adjacent four-bar linkages. This way, the ends of each larger diamond form a smaller diamond, adding to the aesthetics of the architectural vision. The aim was to make each joint a pivot joint, allowing the design to uniformly collapse during the take down as an overall one degree

of freedom mechanism, similar to the concertina collapsibility mechanism shown in Figure 4-2.

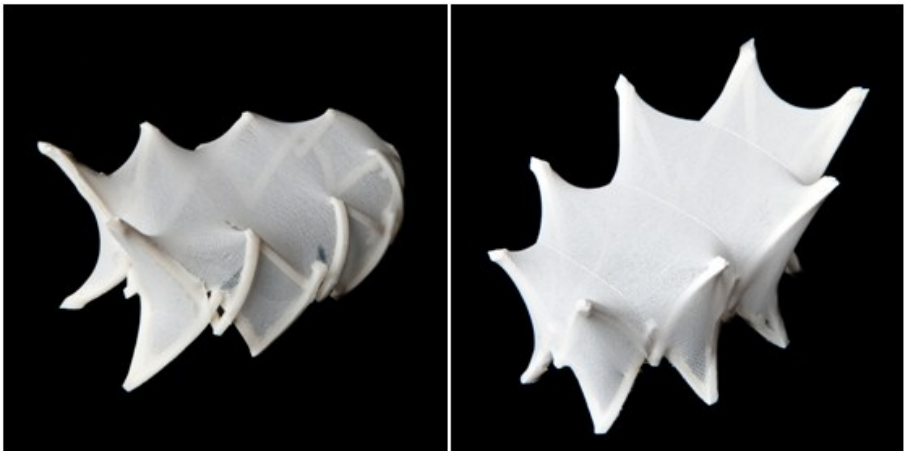

Figure 4-1: Two of the original Cricket Designs. Both designs had one degree of symmetriy, had curved links with different curvature, and had four bar mechanisms that link with neighbouring four bar mechanisms to form smaller four bar mechanisms. Photos courtesy of Greg Richardson Photography.

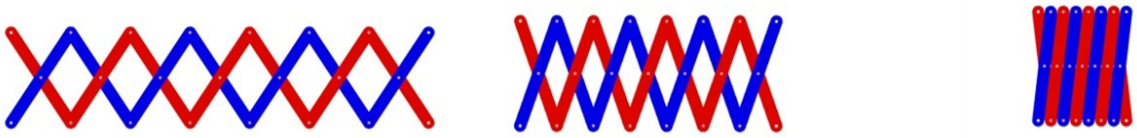

Figure 4-2: The concertina mechanism at various collapsibility stages

Although not impossible, this design would require very precise pivot angle directions in a 3D object, especially for an object that only has one plane of symmetry. Collapsible 3D objects with only revolute joints such as the Hoberman® Sphere as well as collapsible chairs and tables, generally have links with repeating lengths and repeating pivot angles; the Cricket has links with different lengths and different pivot angles. To ensure the design's collapsibility in a 3D space, it was recommended to add more degrees of freedom to some of the joints. Designed by our technician, this was accomplished by making the joints at the cross sections (*i.e.* the X-joints, See Section 4.2.1.3) universal joints that could also translate along the pole thereby increasing their mobility from one degree of freedom to 3 degrees of freedom.

4.2.1.2 MASS

As the Cricket was to be portable, it was important to keep it at a mass so that only one person is required for manual transport. Weight calculations were therefore performed on both the structural tubes and the fabric with an aim on keeping the total weight of the structure and fabric under 15 kg and 5 kg, respectively.

For the poles, the @lab considered using either steel or aluminium. Steel is known to be roughly 3 times stiffer than aluminium and more than 50% stronger than aluminium, but is 3 times denser than aluminium. Using steel tubes, the mass of the structure was estimated at 34.8 kg; while using aluminium tubes, the weight of the structure was estimated at 12.4 kg. A steel frame would produce a mass more than twice that of the design requirement; it was clear that steel would be too heavy for the intents and purposes of the Cricket. An aluminium frame, however, would produce a mass that fell within the design requirements and is therefore much more favourable to use in the final product. Although aluminium is not as stiff or as strong as steel, it is felt that aluminium will provide the Cricket with the integrity needed to serve its purpose. It is not believed that the Cricket will go through stresses large enough to cause permanent deformation on the aluminium poles.

For the fabric, the @lab considered using sailcloth or nylon ripstop, with respective masses at 0.33 kg/m^2 and 0.039 kg/m^2. Having a fabric area of 33.85 m^2, the total mass of the fabric would be 11.2 kg and 1.31 kg, respectively using sailcloth or nylon ripstop. Using the sailcloth would not only surpass the design requirement, but would almost double the total weight of the Cricket with respect to an aluminium frame. The nylon ripstop, however, proved to be quite light and strong for its weight. The nylon ripstop would therefore be used on the final product.

4.2.1.3 JOINT ALTERATIONS

One problem that the @lab noticed after making a prototype was some unwanted twisting between pivot joint links. When one shook a link back and forth away from the structure, the adjacent link would shake in the opposing direction causing unnecessary strain on the pivot joint. It was therefore recommended that a mechanism be developed so that the two links connected via a pivot joint vibrate in unison. The @lab's technician, Greg Sims, suggested and designed a hinged latch to connect the two links (See Figure 4-3) so that they can vibrate as a unit. The added latch proved successful in reducing the strain and was an additional means of letting the assembler know that the pivot joints were at their designated angles.

Figure 4-3: Adding hinged latches to the pivot joints not only locked them into place, but helped to suppress vibration and prevent twisting between adjacent links.

The first prototype also revealed a design flaw in the universal sliding joint (See Figure 4-4). A plastic lip on the female part of the joint was breaking due to an applied stress caused from the twisting of the poles. Two alterations were made to the part to strengthen the joint: the joint's material was changed to a stronger plastic and an aluminum ring was added. The original joint was rapid prototyped using ABSplus-P430 plastic by FORTUS™ which has a tensile strength of 37 MPa and an elastic modulus of 2,320 MPa. Changing the material to FORTUS™ ULTEM 9085 plastic nearly doubles the yield strength to 71.6 MPa while keeping the stiffness roughly the same at 2,200 MPa. Designed by our technician, Greg Sims, an aluminum ring was added to joint,

encasing the perimeter of the joint's female part (See Figure 4-5). The ring not only strengthens the joint, but would prevent the joint from coming apart if the plastic lip continued to break. After the aluminum rings were installed, no more universal sliding joints broke; the modification was deemed successful.

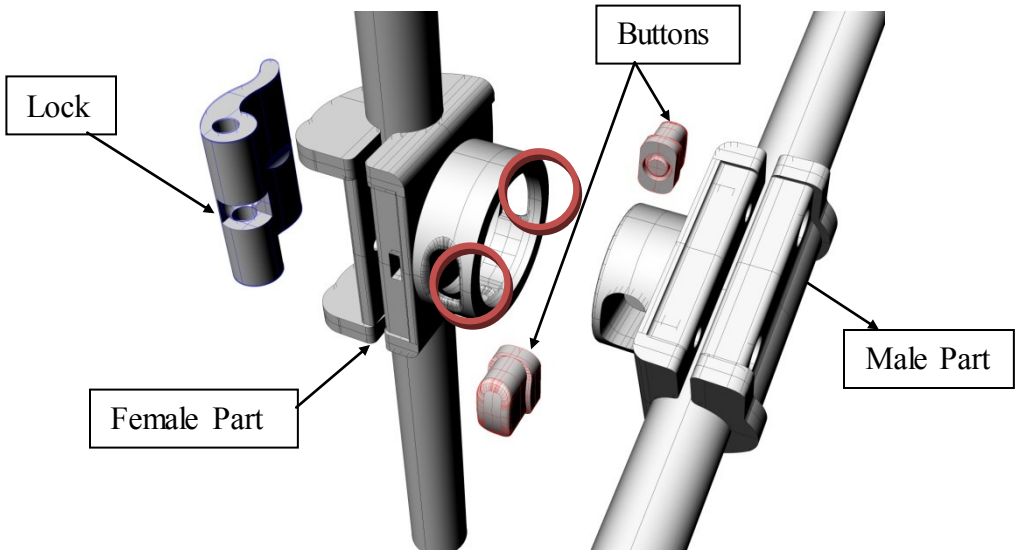

Figure 4-4: A rendered assembly drawing showcasing the various parts of the universal sliding joint. During the first prototype, the joints tended to break at the lip connected to the button. The lips are circled in red. Render and design was done by Greg Sims.

Figure 4-5: An aluminum ring was added to encase the mid section of the universal sliding joint and improve its structural integrity

4.3 THE FOLDING STAGE SET COLLAPSIBLE TUBES

Figure 4-6: The Flamenco Backdrop has poles that collapse telescopically so that they can fit inside the Backdrop's platform/carrying case

To enable a performer to efficiently setup and take down the flamenco stage set, it was important to make the stage set collapsible. It was decided that the most efficient way to do this is to have telescopically collapsing poles as a structural frame that can also detach from the center axis and be stored in a box that also serves as the stage set's platform when in use (See Figure 4-6). The fabric pieces and electronics would be put on after the stage set is erect, and taken down before the stage set is taken down. A rendering of the final design is shown in Figure 4-7.

During the design process, several design considerations were made about the poles including the length, outer diameter, thickness, and material. The flamenco stage set was to be light in weight, but it was undesirable for the poles to deflect and bend. It was the author's duty to analyze the design to foresee impending implications and make suggestions.

This project was in collaboration with a Halifax-based flamenco dance company. To make an impression on the audience, they suggested making the design bigger rather than smaller. The resultant design was then made to be roughly 2.1 m tall, 4.6 m wide with 9 sets of collapsible poles (See Figure 4-8 for rough measurements). Seven of these poles would contain two telescoping tubes while the remaining two would have three telescoping tubes. The three-tube poles would be located at the backdrop's diagonal as it is the longest member at just under 3.4 m.

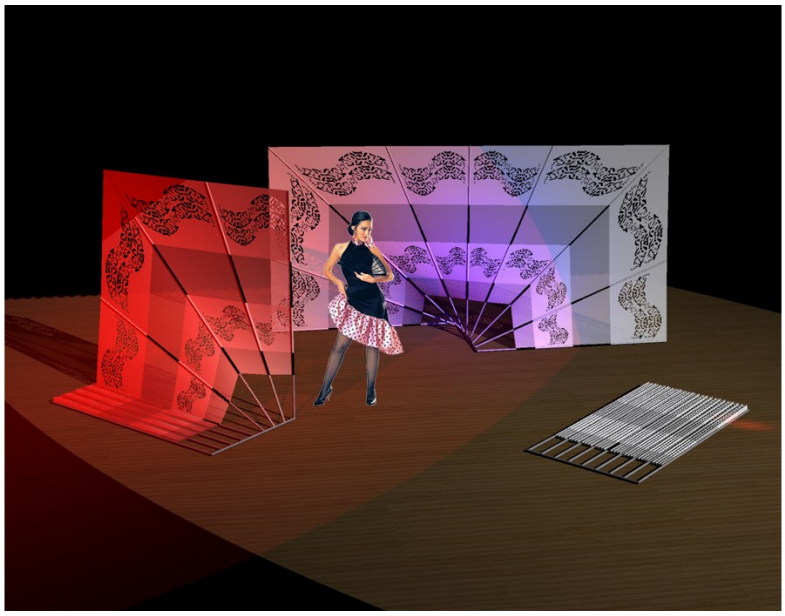

Figure 4-7: Original rendering of the flamenco stage set. Rendering done by Greg Sims

As the tubes were to be telescopic, the thickness was set at around 1.27 mm, as this thickness allows tubes with a decreased outer diameter of 0.125 mm to efficiently slide into one another with some clearance. With the length of the poles defined, pole material and outer diameters would be defined using engineering analyses. The desired outcome would be a material and tube geometry that is lightweight and strong with minimal deflection.

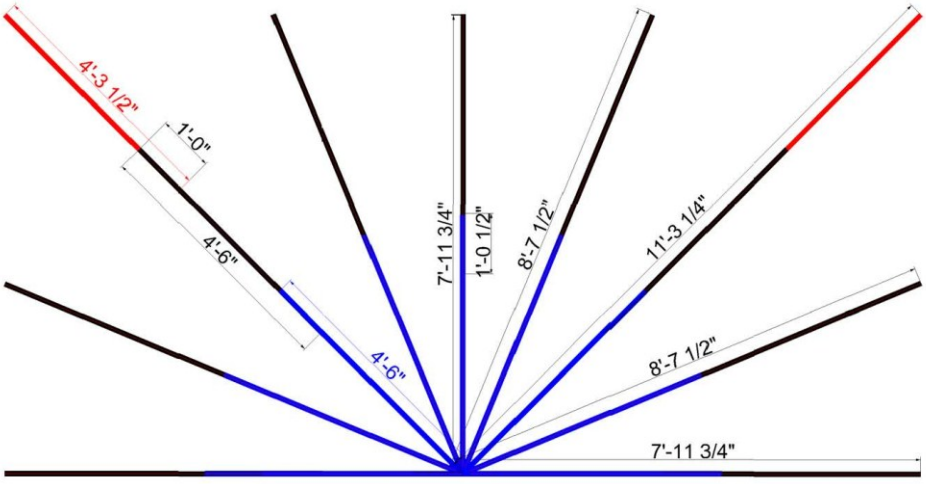

Figure 4-8: The layout for the collapsible pole mechanisms. NOTE: These are not the final dimensions for the flamenco stage set

4.3.1 Material and Outer Diameter Considerations

As already indicated, the desired outcome of the tube parameters would be a strong, light weight telescoping tube mechanism with minimal deflection. The author researched four different materials: fiber glass, carbon fibre composite (CFC), steel, and aluminum. The properties of all four are presented below in Table 4-1.

Table 4-1: Mechanical Properties of the Materials considered for the Flamenco Backdrop Collapsible Poles

	Fiber Glass (L-530)	Newport 301 Unitape (Carbon Fibre)	Stainless Steel Type 303	6061 Aluminum
Modulus of Elasticity (GPa)	24	9.0 (90deg) 131.2 (0deg)	193	68.9
Tensile Strength (MPa)	421	60.1 (90 deg) 2040 (0 deg)	415 (Yield)	269 (Yield)
Square Ply Density (kg/m^2)	0.488	0.150	N/A	N/A
Ply Thickness	0.254 mm (0.010")	0.152 mm – 0.178 mm (0.006"-0.007")	N/A	N/A
Density (kg/m^3)	1921	844-984	8000	2700
Source	(J.D. Lincoln Inc., 2010)	(Newport Adhesives and Composites, Inc., 2010)	(E-Z LOK, 2010)	(MatWeb, LLC, 2010)

Mass calculations were performed on three different sets of diameters to get a sense of how heavy the poles would be with different materials and outer diameter scenarios. The mass calculations are presented below in Table 4-2. From the results, it became apparent that steel would be too heavy for one person to comfortably lift. On the other hand, fibre glass, CFC, and aluminum all have acceptable limits for one person to lift with the maximum mass being 6.56 kg for the aluminum scenario with an outer diameter of 25.4 mm. However, fiber glass and CFC were shown to respectively have 71% and 36% of the weight of the aluminum scenarios. With excellent tensile strengths in addition to a low weight, the composites seemed like the favourable option. Having worked with aluminum before, the @lab was familiar with its use and handle, but had no prior exposure to composites such as fiber glass and CFC. The @lab wanted to thus find out how the stiffness of the composite options compared to aluminum. As carbon fiber had

about half the weight of fiber glass, the @lab wanted to focus on the CFC option to compare with aluminum.

Table 4-2: Total Mass and Volume Calculations for all Telescoping Tubes for Various Materials and Diameters

Material	Assumed Density (kg/m^3)	Total Mass with Respect to Largest Outer Diameter (kg)		
		19.1 mm (0.75")	22.2 mm (0.875")	25.4 mm (1.0")
Fiber Glass (L-530)	1921	3.46	4.06	4.67
CFC	984	1.77	2.08	2.39
Steel	8000	14.4	16.9	19.4
Aluminum	2700	4.87	5.71	6.56
Total Volume (m^3)		0.0018	0.00212	0.00243

As aluminum is generally regarded as an isotropic material while CFC is a composite material, the two materials' stiffnesses (*i.e.* modulus of elasticity) cannot be directly compared. Looking back at Table 4-1, one would notice that aluminum has one stiffness while the carbon fiber composite has two. Aluminum has only one stiffness due to its isotropy: its properties are universal no matter how you translate it in a 3D space. Carbon fiber on the other hand has two moduli of elasticity: one for along the fiber direction and another that is perpendicular to the fibre direction, *i.e.* the transverse direction. The stiffness thus depends on the direction of applied stress. In addition, layers of carbon fiber can be placed on top of one another in different directions, further affecting the overall stiffness of the material. The stiffness of carbon fiber has to be calculated using laminate theory. The next two subsections will introduce the mechanical models for isotropic and composite materials followed by a comparison of the two materials.

4.3.2 Beam Deflection and Stiffness for an Isotropic Material

Isotropic materials are materials that have the same parameters in all three directions in space. Every direction has the same modulus of elasticity, Poisson's ratio, yield strength, and modulus of rigidity among other mechanical properties. Applying these universal properties to general beam mechanics, the deflection and stiffness can easily be calculated.

From traditional beam theory, the applied moment is directly related to the modulus of elasticity, E, the moment of inertia, I, and the radius of curvature, R:

$$M = \frac{EI}{R} \tag{4-1}$$

From analytical geometry, the expression for the radius of curvature varies with the deflection, v(x):

$$\frac{1}{R(x)} = \left[\frac{d^2v}{dx^2}\right]\left[1 + \left(\frac{dv}{dx}\right)^2\right]^{-3/2} \tag{4-2}$$

In practical terms, dv/dx is considered to be much less than unity, therefore simplifying Equation 4-2 into:

$$\frac{1}{R(x)} \cong \frac{d^2v}{dx^2} \tag{4-3}$$

Combining equations 4-2 and 4-3, it can be shown that:

$$\frac{d^2v}{dx^2} = \frac{M(x)}{EI} \tag{4-4}$$

By integrating the Equation 4-4 twice, one can find the beam's slope ($\theta(x)$) and deflection

$$v'(x) = \frac{dv}{dx} = \theta(x) = \int \frac{M(x)}{EI} dx + C_1 \tag{4-5}$$

$$v(x) = \int \left[\int \frac{M(x)}{EI} dx\right] dx + C_1 x + C_2 \tag{4-6}$$

C_1 and C_2 are found by applying the appropriate boundary conditions of the system. For the flamenco telescopic tubes, one side will be completely constrained while the other will be free to move. To get a sense of how the telescopic tubes would react to an applied load such as the weight of the fabric, consider the example illustrated in Figure 4-9 where

one side of the beam is completely constrained, while the other is being deflected by a point load.

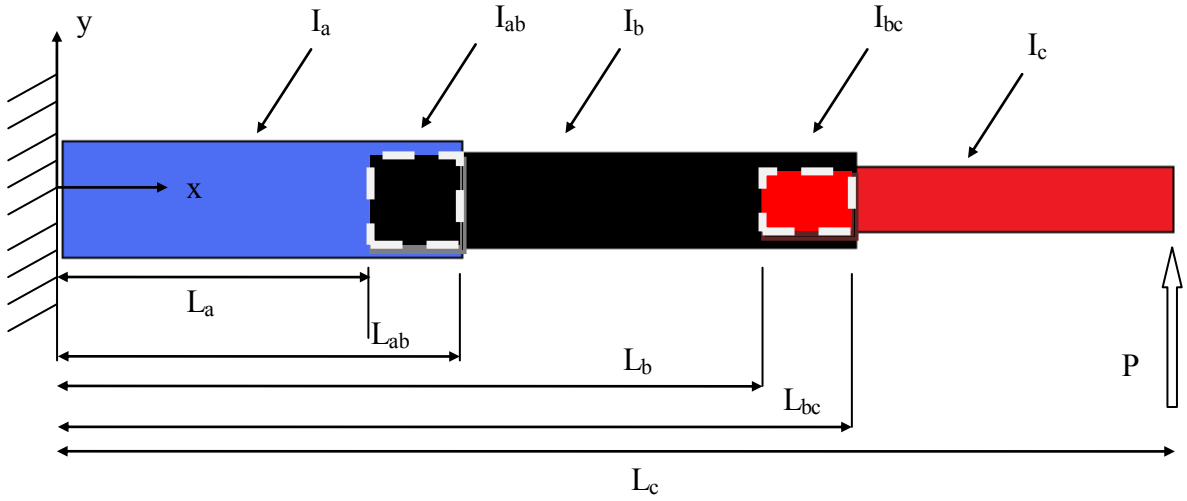

Figure 4-9: An illustration of the collapsible tube mechanism where one end is constrained and the other experiences a point load, P. The L variables represent various lengths along the x-axis, while the I variables represent the bending moments of inertia pertaining to each section. Button lock mechanisms prevent the tubes from collapsing when set up.

The internal moment at a given point on the x axis is the force, P, times the difference between the total and length at said point on the x-axis. The formula is shown in Equation 4-7 and visualized in Figure 4-10.

$$M(x) = P(L - x) \tag{4-7}$$

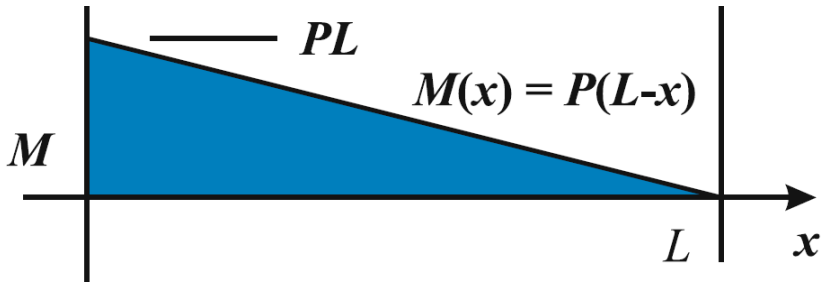

Figure 4-10: The moment diagram of the collapsible tubes

At the constrained edge (x=0), the slope and deflection are both zero. Using these boundary conditions, Equations 4-5 to 4-7, and the moments of inertia as listed in Table 4-3, one can analytically find the deflection of the tube at any point along the x-axis.

Table 4-3: Moment and Bending Moment of Inertia Formulas at various points along the x-axis

Position	Moment	Bending Moment of Inertia
x=	Formula	Formula
0	PL_c	$I_a = \frac{\pi(D_{ao}^4 - D_{ai}^4)}{64}$
L_a	$P(L_c\text{-}L_a)$	$I_{ab} = \frac{\pi(D_{ao}^4 - D_{ai}^4)}{64} + \frac{\pi(D_{bo}^4 - D_{bi}^4)}{64}$
L_{ab}	$P(L_c\text{-}L_{ab})$	$I_b = \frac{\pi(D_{bo}^4 - D_{bi}^4)}{64}$
L_b	$P(L_c\text{-}L_b)$	$I_{bc} = \frac{\pi(D_{bo}^4 - D_{bi}^4)}{64} + \frac{\pi(D_{co}^4 - D_{ci}^4)}{64}$
L_{bc}	$P(L_c\text{-}L_{bc})$	$I_c = \frac{\pi(D_{co}^4 - D_{ci}^4)}{64}$

For a stress analysis, one simply has to use the universal bending stress equation:

$$\sigma = \frac{Mc}{I} \qquad 4\text{-}8$$

where M, I, and c are respectively the induced internal moment, bending moment of inertia, and maximum distance from the respective neutral axis. The max stress would be either at the constrained end or one of the transmission points (*i.e.* a point where the moment of inertia changes). The moments and bending moments of inertia at these points are presented in Table 4-3. The resultant maximum stress would then be compared to the yield stress for a safety factor.

4.3.3 Composites Modeling in Beams and Tubes

When modeling composites in beams, it is important to note that beam theory itself does not change; all equations presented in Section 4.3.2 should still be valid. However, the modulus of elasticity, E needs to be calculated. The modulus of elasticity depends not only on both moduli of elasticity, but on the orientation of the plies. To optimize the conditions of bending, it is recommended that most plies have their longitudinal direction (the fibre direction) in line with the beam with a few perpendicular plies to resist buckling (Leckie & Dal Bello, 2009). However, the manufacturer, Sky-Pole Inc., only supplied tubes with alternating ply directions. In other words starting from the inner diameter, every odd ply would have its fibre direction in line with tube's central axis,

while every even ply would have its fibre direction along the tube's circumference. Although this orientation will not be as strong as a composite whose majority of plies are in line with the tube's central axis, it allows us to use two-ply laminate theory to calculate the composite's modulus of elasticity. Two-ply laminate theory assumes that the composite is composed of only two alternating plies with different ply-angles. The composite can be made of many plies, but as long as there are only two ply orientations, alternating between each ply layer, two-ply laminate theory can be used. It is also assumed that the thickness of each ply is small so that a two-dimensional analysis of the ply can be performed.

Each ply has its own 2D local stiffness matrix. As both plies are of the same material, both plies have the same local stiffness matrix:

$$K_A = K_B = \begin{bmatrix} \frac{E_x}{(1-\upsilon_{xy}\upsilon_{yx})} & \frac{\upsilon_{xy}E_y}{(1-\upsilon_{xy}\upsilon_{yx})} & 0 \\ \frac{\upsilon_{yx}E_x}{(1-\upsilon_{xy}\upsilon_{yx})} & \frac{E_y}{(1-\upsilon_{xy}\upsilon_{yx})} & 0 \\ 0 & 0 & 2G_{xy} \end{bmatrix}, \quad \text{4-9}$$

Note that compatibility requires that $\upsilon_{xy}E_y = \upsilon_{yx}E_x$. Both plies also have a transformation matrix to translate the ply stiffness with respect to the global coordinates where c and s represent the cosine and sine of the ply angle:

$$T = \begin{bmatrix} c^2 & s^2 & 2sc \\ s^2 & c^2 & -2sc \\ -sc & sc & c^2 - s^2 \end{bmatrix} \quad \text{4-10}$$

As the plies have equal thickness, the global stiffness matrix for the composite is

$$K_G = \frac{1}{2}(T_A K_A T_A^{-1} + T_B K_B T_B^{-1}) \quad \text{4-11}$$

With respect to the tube parameters (*i.e.* the longitudinal (L) and circumferential (C) directions), the global stiffness can also be represented as:

$$K_G = \begin{bmatrix} \frac{E_C}{(1-\upsilon_{CL}\upsilon_{LC})} & \frac{\upsilon_{CL}E_L}{(1-\upsilon_{CL}\upsilon_{LC})} & 0 \\ \frac{\upsilon_{LC}E_C}{(1-\upsilon_{CL}\upsilon_{LC})} & \frac{E_L}{(1-\upsilon_{CL}\upsilon_{LC})} & 0 \\ 0 & 0 & 2G_{CL} \end{bmatrix} \quad 4\text{-}12$$

Likewise, the global flexibility matrix can be found:

$$F_G = K_G^{-1} = \begin{bmatrix} {}^{1}/_{E_C} & -{}^{\upsilon_{LC}}/_{E_L} & 0 \\ -{}^{\upsilon_{CL}}/_{E_C} & {}^{1}/_{E_L} & 0 \\ 0 & 0 & {}^{1}/_{(2G_{CL})} \end{bmatrix} \quad 4\text{-}13$$

The elastic global properties of the composite can then be found in relation to the longitudinal and circumferential directions of the ply. As previously indicated, the two ply directions for the composite tube will be along the tube's circumference and central axes. The ply directions would thus be 0° and 90° with respect to the circumferential direction. Through assigning the A-ply and B-ply with fibre directions in the circumferential and longitudinal directions, respectively, the transformation matrices, T_A and T_B, equivalent to:

$$T_A = \begin{bmatrix} 1 & 0 & 0 \\ 0 & 1 & 0 \\ 0 & 0 & 1 \end{bmatrix}, T_B = \begin{bmatrix} 0 & 1 & 0 \\ 1 & 0 & 0 \\ 0 & 0 & -1 \end{bmatrix} \quad 4\text{-}14$$

The manufacturer, Sky-Pole, Inc., would be using Newport 301 Unitape to manufacture the poles. Using the applicable data from Newport`s material property sheet in Table 4-4, one can find the local stiffness matrices using Equation 4-9,

$$K_A = K_B = \begin{bmatrix} \frac{E_x}{(1-\upsilon_{xy}\upsilon_{yx})} & \frac{\upsilon_{xy}E_y}{(1-\upsilon_{xy}\upsilon_{yx})} & 0 \\ \frac{\upsilon_{yx}E_x}{(1-\upsilon_{xy}\upsilon_{yx})} & \frac{E_y}{(1-\upsilon_{xy}\upsilon_{yx})} & 0 \\ 0 & 0 & 2G_{xy} \end{bmatrix} = \begin{bmatrix} 1.32*10^{11} & 2.746*10^{9} & 0 \\ 2.746*10^{9} & 9.03*10^{9} & 0 \\ 0 & 0 & 1.0*10^{10} \end{bmatrix}$$

Table 4-4: Material Properties of Newport 301 Unitape from Newport Adhesives and Composites, Inc. and Performance Composites, Ltd. Extracted from (Newport Adhesives and Composites, Inc., 2010) and (Performance Composites, Ltd., 2012)

Material Property (Symbol)	Testing Method	Newport 301 Unitape	Performance Composites, Ltd. Standard Cf UD	Units
0˚ Tensile Strength, S_{Ux}	ASTM D-3039	2040	1500	MPa
0˚ Tensile Modulus, E_x		131	135	GPa
Poisson's Ratio, υ_{xy}		0.304	0.3	-
0˚ Compression Strength, C_{Ux}	SACMA SRM 1R-94	1242	1200	MPa
0˚ Short Beam Shear Stress, $S_{U\tau}$	ASTM D-2344	91.1	70	MPa
In-Plane Shear Modulus, G_{xy}		-	5	GPa
90˚ Tensile Strength, S_{Uy}	ASTM D-3039	60.1	50	MPa
90˚ Tensile Modulus, E_y		8.98	10	GPa
Poisson's Ratio, υ_{yx}		0.0208 (Calculated)	0.0222 (Calculated)	-
90˚ Compression Strength, C_{Uy}	SACMA SRM 1R-94	199	250	MPa
0˚ Short Beam Shear Strength, $S_{U\tau}$	ASTM D-2344	8.98	-	MPa

Although the in-plane shear modulus was not given in the material properties data sheet from Newport Adhesives and Composites, Inc., it should not be needed as the fibres and loads in this particular scenario are only in the longitudinal and circumferential directions along the tube. The local stresses on either laminate will therefore be in the plane of maximum stress, meaning that the resultant shear stress in the local planes will be 0 MPa. Nonetheless, a shear modulus was found from a separate supplier that offered a product with similar properties so that the complete stiffness matrix can be found and so that a finite element analysis can be performed (See Section 0).

Using Equation 4-11, K_G can be found:

$$K_G = \frac{1}{2}(T_A K_A T_A^{-1} + T_B K_B T_b^{-1}) = \begin{bmatrix} 7.05 * 10^{10} & 2.746 * 10^9 & 0 \\ 2.746 * 10^9 & 7.05 * 10^{10} & 0 \\ 0 & 0 & 1.0 * 10^{10} \end{bmatrix} \quad 4\text{-}15$$

For a stress analysis, the bending stresses are found using the same formulas derived in Section 4.3.2; however, these stresses correspond to the global properties of the tube:

$$\sigma_G = \begin{bmatrix} \sigma_C \\ \sigma_L \\ \tau \end{bmatrix} = \begin{bmatrix} 0 \\ Mc/I \\ 0 \end{bmatrix} = \begin{bmatrix} 0 \\ \frac{PLc}{I} \\ 0 \end{bmatrix} \quad 4\text{-}16$$

To get the safety factor, the local ply stresses must be determined at the point of maximum stress. To translate the global stresses into local stresses, the following translations are performed:

$$\sigma_A = K_A T_A^{-1} K_G^{-1} \sigma_G \; and \; \sigma_B = K_B T_B^{-1} K_G^{-1} \sigma_G \quad 4\text{-}17$$

The resultant local stresses will then be in a 1 x 3 matrix like the one shown in Equation 4-18 representing the stresses in the x-direction (*i.e.* the local fiber direction), local y-direction (*i.e.* the local transverse direction), and the local shear stress between axes:

$$\sigma_A = \begin{bmatrix} \sigma_{x,A} \\ \sigma_{y,A} \\ \tau_A \end{bmatrix} \text{ and } \sigma_B = \begin{bmatrix} \sigma_{x,B} \\ \sigma_{y,B} \\ \tau_B \end{bmatrix} \quad 4\text{-}18$$

The resultant local stresses along the circumferential and longitudinal directions are then compared with the tensile and compressive strengths to determine the safety factor, F_s:

$$F_s = \begin{bmatrix} S_{Ux}/\sigma_x \; or \; C_{Ux}/\sigma_x \\ S_{Uy}/\sigma_y \; or \; C_{Uy}/\sigma_y \\ S_{U\tau}/\tau \end{bmatrix} \quad 4\text{-}19$$

Equation 4-19 is used to calculate the safety factors for both A and B plies and the lowest calculated safety factor is deemed the overall safety factor.

4.3.4 Comparison between Materials and Geometries

Through using the material presented in Sections 4.3.2 and 4.3.3, this section will go over the theoretical analyses performed on the flamenco backdrop's poles. These analyses include projecting the stresses and safety factors for perpendicular point loads and tube weight loads, but also proposing methods to minimize deflection. The overall aim of this

section is to compare the projected performance between the two proposed materials (aluminum and CGC) as well as the three proposed tube geometries under consideration.

4.3.4.1 UNDER PERPENDICULAR POINT FORCE LOADING

Using Equation 4-8, the tube diameters' geometries (listed in Table A-1 in Appendix A), and the bending moments and moments of inertia formulas presented in Table 4-3, the author calculated the maximum stresses along each beam's section for the three different tube diameter situations. The total thickness for all tubes was 1.22 mm (0.048"); this thickness was chosen as it would allow the tubes to collapse into each other, but was also chosen due to the limitations indicated by the CFC's manufacturer: Sky-Pole, Inc. Sky-Pole Inc. indicated that they use a CFC unitape that is 0.152 mm (0.006") to 0.178 mm (0.007") in thickness and they recommended using 8 plies (*i.e.* layers) for our telescoping collapsible mechanism. Assuming a worst case scenario, the stress would be a maximum if all plies were the lowest thickness of 0.152 mm; using 8 plies, the total thickness for said worst case scenario would be 1.22 mm (0.048"). Although this size is not readily available for aluminum tubing, using the same geometry allowed a direct comparison with the carbon composite results. The 1.22 mm thickness was therefore used for both the aluminum and carbon composite calculations.

For each simulation, a 10 N force was applied perpendicularly to the unconstrained edge of the collapsible tubing to simulate the fabric loading on the tubing. Although this scenario does not necessarily reflect the true loading scenario on the tubing, it will give a means to compare the internal bending stresses caused between aluminum and CFC tubing. Table 4-5 presents the calculated global bending stresses with respect to the largest inner tube diameter (D_{ai}). For all three situations, the maximum stress was at the collapsible tube's constraint edge (*i.e.* at $x = 0$ with respect to Figure 4-9); as would be expected, the maximum stress increased as D_{ai} decreased. For collapsible tubing with a maximum inner diameter of 25.4 mm, 22.2 mm, and 19.1 mm, the maximum stress increased to 49.2 MPa, 63.8 MPa, and 86.0 MPa, respectively.

For aluminum tubing, the safety factor is calculated by simply taking the maximum bending stress and dividing it into aluminum's yield stress (*i.e.* 269 MPa). The safety factor is therefore calculated to be 5.46, 4.21, and 3.13 for the situations with maximum inner tube diameters of 25.4 mm, 22.2 mm, and 19.1 mm. Unsurprisingly, the safety factor increases as the tube diameter increases; larger tube diameters have larger moments of inertia which reduce the overall bending stress as indicated by Equation 4-8. However, calculating the safety factor for composite tubing is not as straight forward.

Table 4-5: Maximum Stress Calculations for Aluminum Poles at Different Longitudinal Lengths

Section Boundaries	End position (m)	Max Section Stress Location along x-axis	Maximum Stress in Respective Section (MPa)		
			D_{ai} = 25.4mm	D_{ai} = 22.2 mm	D_{ai} = 19.1 mm
0 to La	La = 1.08	0	49.2	63.8	86.0
La to Lab	Lab =1.23	La	19.4	25.7	35.6
Lab to Lb	Lb = 2.13	Lab	39.3	52.9	75.0
Lb to Lbc	Lbc =2.28	Lb	12.9	17.9	26.4
Lbc to Lc	Lc = 3.20	Lbc	24.7	35.0	53.5

To calculate the safety factor for composite tubing, one must first find the global stress matrix using Equation 4-16 for all of the three tubing situations and then substitute it into Equation 4-17 to find the local stress matrices for the A and B plies. The safety factor is then calculated by substituting the values from the local matrices into Equation 4-19 for both the A and B plies. The calculated ply stresses and safety factors are presented below in Table 4-6. As mentioned in Section 4.3.3, the true safety factor for each situation would be the lowest safety factor; for all three diameter situations, the lowest safety factor was in the transverse direction on the A-ply. The maximum inner diameters of 25.4 mm, 22.2 mm, and 19.1 mm, had safety factors of 9.63, 7.43, and 5.51, respectively. Once again, the safety factors increased as the diameters increased due to the increase in moments of inertia which cause the bending stresses to decrease.

Table 4-6: The Calculated Ply Stresses and Safety Factors for a 10N Perpendicular Edge Load

D_{ai} (mm)	Maximum Global Stress (MPa)	σ_A in MPa, (Safety Factor)			σ_B in MPa, (Safety Factor)		
		σ_x	σ_y	τ	σ_x	σ_y	τ
25.4	49.2	-1.67 (742)	6.24 (9.63)	0 (∞)	92.3 (22.1)	1.67 (35.9)	0 (∞)
22.2	63.8	-2.17 (572)	8.09 (7.43)	0 (∞)	120 (17.1)	2.17 (27.7)	0 (∞)
19.1	86.0	-2.93 (424)	10.9 (5.51)	0 (∞)	161 (12.7)	2.92 (20.6)	0 (∞)

The overall findings from the stress and weight analysis are presented in Table 4-7. Although aluminum tubing is generally more costly and readily available, the CFC tubing has been calculated to outperform the aluminum tubing in both weight and strength. With a density of 984 kg/m^3, the CFC tubing will have a weight that is 36.4% of the weight of aluminum tubing. Likewise, calculations show that CFC tubing is stronger by having safety factors that are roughly 76% greater than their aluminum counterparts. Not only would the CFC tubes be easier to carry, but would also better withstand applied stresses and strains; the strength-to-weight ratio increases by a factor of 3.6. From these results, the author concluded that the CFC tubing would be better apt than aluminum tubing for the flamenco stage set.

Table 4-7: Maximum Stress and Safety Factors for a free-edge perpendicular edge force of 10N

D_{ai} (mm)	Maximum Global Stress (MPa)	Safety Factor		Weight (kg)	
		Aluminum	CFC	Aluminum	CFC
25.4	49.2	5.46	9.63	6.56	2.39
22.2	63.8	4.21	7.43	5.71	2.08
19.1	86.0	3.13	5.51	4.87	1.77

4.3.4.2 STRESS UNDER MATERIAL'S WEIGHT

Using a similar procedure as described in the last section, the author performed calculations for the maximum internal stress when the applied force is simply the weight of the collapsible tubing mechanism. The maximum stress occurs when the collapsible tube is completely horizontal as shown in Figure 4-9. The resultant bending moment was calculated by multiplying the weight of each tube section by each section's respective midpoint along the longitudinal axis and then summing the moments; the resultant bending moment was then substituted into Equation 4-16 to calculate the global stress. Like the vertical point load calculations, the internal stresses for aluminum tubing would

be equivalent to those found via Equation 4-16; for CFC tubing, the global stress matrix is substituted into Equation 4-17 to find the local stresses for both ply directions. The aluminum safety factors are calculated by dividing the calculated maximum stress into the aluminum`s yield strength of 269 MPa; the CFC safety factors are calculated by substituting the maximum local stresses into Equation 4-19.

Similar to Table 4-6, Table A-2 in Appendix A1 shows the calculated ply stresses and safety factors for the CFC tubing. Akin to the vertical edge load calculations, the lowest safety factor was found to be in the transverse direction of the A-ply, *i.e.* the ply that has the fibres in the circumferential direction. However, said safety factor was found to be 72.9, 66.5, and 60.2 for the 25.4 mm, 22.2 mm, and 19.1 mm largest inner diameter *i.e.* D_{ai}) scenarios, respectively. As safety factors of 3 are generally acceptable, all three diameter scenarios are therefore very robust and will not fail due to the tube's weight. When analyzing the aluminum tubing scenarios, large safety factors were also found; however, these safety factors were lower than the CFC tubing. Table 4-8 shows the calculated results for both aluminum and CFC tubing including the bending moments, global stresses, and safety factors. As CFC is 36.4% the weight of aluminum, the induced bending moment and internal stress are therefore 36.4% of their aluminum counterparts. Based on the weight differences alone, one would expect a 174% increase in safety factor when comparing CFC to aluminum tubing. Based on the results from the previous section, one would also expect the CFC's safety factor to be 76% greater than aluminum. Multiplying both factors together, one would expect the CFC tubing to have a 383% increase in safety in relation to their aluminum counterparts; a 383% increase was indeed found in the calculated results.

Table 4-8: Maximum Bending Moments, Maximum Stresses and Safety Factors for Tube`s Weight

D_{ai} (mm)	Material	Maximum Bending Moment (N*m)	Maximum Global Stress (MPa)	Safety Factor
25.4	Aluminum	12.7	17.8	15.1
	CFC	4.63	6.50	72.9
22.2	Aluminum	10.9	19.6	13.8
	CFC	3.97	7.13	66.5
19.1	Aluminum	9.08	21.6	12.4
	CFC	3.31	7.88	60.2

The results show that as both materials have safety factors well above the generally acceptable safety factor of 3 under all geometry scenarios, no scenario is in danger of failing via bending under its own weight. However, the stress is considerably less in the CFC tubing with safety factors that are 383% greater than their aluminum counterparts.

4.3.4.3 MINIMIZING DEFLECTION/MODULI OF ELASTICITY COMPARISON

Although the deflection can be calculated using boundary conditions and formulas derived from Equations 4-5 and 4-6, they are quite long and extensive for beams with varying moments of inertia. However, if one wants to compare the deflections between materials such as CFC vs. aluminum, one can simply compare their moduli of elasticity. Equation 4-6 dictates that a beam's deflection is inversely proportional to the beam's deflection; a higher modulus of elasticity will therefore minimize deflection.

Generally, the moduli of elasticity of CFC cannot be directly compared to aluminum due to their different properties; aluminum is generally assumed to be isotropic while CFC is a composite material. Aluminum thus has one modulus of elasticity while CFC generally has two (three if you count the thickness direction, but this modulus of elasticity can be ignored assuming that the composite is thin). In the case of a tube, the CFC would have a modulus of elasticity in the longitudinal direction and another in the circumferential direction; usually they're different. However, composite plies can be arranged and loaded in such a way to produce moduli of elasticity that are the same in both principal directions; providing that the load is in the direction of one of the global axes, the composite's modulus of elasticity may be compared to that of an isotropic material. As the maximum strain is along the longitudinal axis during bending, if the composite's moduli of elasticity are the same in both longitudinal and circumferential directions, then said modulus of elasticity may be directly compared to aluminum's modulus of elasticity.

A composite's global moduli of elasticity and Poisson's ratios can be found by using the tube's flexibility matrix, *i.e.* Equation 4-13. As the stiffness matrix has already been calculated (*i.e.* Equation 4-15), the flexibility matrix can be found by inverting it. The

global properties can then be found by using the flexibility matrix's elements as indicated by Equation 4-13. Equation 4-20 shows the flexibility matrix calculation while Table 4-9 shows the calculated CFC global properties.

$$F_G = K_G^{-1} = \begin{bmatrix} 7.05*10^{10} & 2.746*10^{9} & 0 \\ 2.746*10^{9} & 7.05*10^{10} & 0 \\ 0 & 0 & 1.0*10^{10} \end{bmatrix}^{-1}$$
$$= \begin{bmatrix} 1.42*10^{-11} & -5.53*10^{-13} & 0 \\ -5.53*10^{-13} & 1.42*10^{-11} & 0 \\ 0 & 0 & 1.0*10^{-10} \end{bmatrix} \quad 4\text{-}20$$
$$= \begin{bmatrix} 1/E_C & -\upsilon_{LC}/E_L & 0 \\ -\nu_{CL}/E_C & 1/E_L & 0 \\ 0 & 0 & 1/(2G_{CL}) \end{bmatrix}$$

Table 4-9: Calculated Carbon Composite Global Properties

Property	E_C (GPa)	E_L (GPa)	ν_{CL}	ν_{LC}	G_{CL} (GPa)
Value	70.4	70.4	0.0389	0.0389	5

With circumferential and longitudinal values of 70.4 GPa, it has been demonstrated that the 0°/90° alternating plies have two identical global moduli of elasticity. Likewise, the global Poisson's ratios are also the same with values of 0.0389. The composite's modulus of elasticity may therefore be compared with that of an isotropic material given the circumstances.

As previously presented in Table 4-1, aluminum's modulus of elasticity is 68.9 GPa which is very close to the carbon composite's global modulus of elasticity of 70.4 GPa. Although the carbon composite tube has a modulus of elasticity that is 2.2% greater, the increase is insignificant to play a factor in choosing the material to minimize deflection. If one were to compare the deflection from similar loading scenarios, based on these results, the author predicts that both aluminum and 0°/90° ply CFC would produce similar deflections; neither material should hold an advantage to minimize deflection.

4.3.5 Finite Element Modeling

Thus far by using beam theory and composites modeling it has been shown that the carbon composite option is stronger, lighter, and slightly stiffer than their aluminum counterparts; carbon composite is therefore the material of choice. However, to validate or disprove these findings, it is beneficial to perform a finite element analysis (FEA). Beam theory only treats the tube as a 1D object and thus has limitations in its accuracy. Through FEA, the tube can be modeled as a 2D (or 3D) object to more properly showcase how the stress is distributed from an applied load. Additionally, FEA can be used to model the beam's deflection without the need to derive extensive formulas. This section will present the FEA that was performed on the flamenco collapsible tubing mechanism.

4.3.5.1 PROBLEM DEFINITION

To support or refute the findings found from the analyses performed thus far, a FEA was performed. As it was found that both materials can effectively withstand a load caused solely from the tube's weight, the FEA would thus focus on the vertical point loading scenario. In summary, the aims of this FEA are to:

- Find the maximum stresses, safety factors, and deflections in relation to the three tube size situations to observe the affect of using larger diameters
- Find the maximum stresses, safety factors, and deflections in relations to the two materials (*i.e.* aluminum vs. CFC) to see which is better suited for the flamenco backdrop
- Compare the findings with those found in Section 4.3.4 to determine if the calculations performed using beam theory and composite modeling are sufficient to predict the behavior of the collapsible tubes.

The model was setup so that the tubes' lengths are those as listed in Table 4-5; one end was completely constrained while the other supported a vertical load of 10 N as was done in the analysis performed in Section 4.3.4.1. A total of six simulations were performed,

the three geometries had two simulations each: one using aluminum material properties while the other using CFC properties.

4.3.5.2 MESH TYPE AND MATERIAL PROPERTIES

For the mesh, 2D shell elements were used as opposed to 3D elements to not only save simulation time, but to also take advantage of HyperMesh®'s composite modeling program. The tubing's geometry was set up to simulate the scenario as depicted in Figure 4-9. The lengths of the five different sections were modeled to the lengths listed in Table 4-5, while the tubes' inner and outer diameters are those as listed in Table A-1 in Appendix A1.

The total thickness for all tubes was 1.22 mm as was done in the calculated analysis performed in Section 4.3.4.1. For the aluminum simulations, the shell elements were assumed to be isotropic and a 68.9 GPa modulus of elasticity was used along with a Poisson's ratio of 0.3. For the carbon composite simulations, the shell elements were given a composite property. It was said by the manufacturer, *i.e.* Sky-Pole, Inc., that with reference to the inner diameter plies, the odd plies' fibre directions would be along the circumferential axis (*i.e.* a ply orientation of 0°) while the even plies' fibre directions would be along the longitudinal axis (*i.e.* a ply orientation of 90°). These specifications were applied to the HyperWorks® simulation. The HyperMesh® modeling software allowed one to visually see the fibre orientations in each layer via arrows (see Figure 4-11).

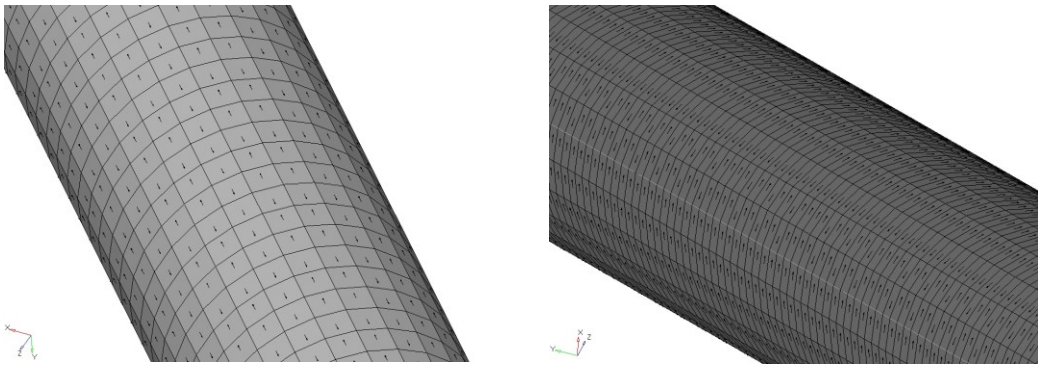

Figure 4-11: Hypermesh™'s composite modelling software allowed one to visually see where the ply orientation using arrows. (Left) A ply with a fibre orientation along the longitudinal axis. (Right) A ply with a fibre orientation along the circumferential axis.

As the collapsible tubing mechanism had five sections with different inner and outer diameters, each section was modeled to its designated diameter and then connected via adjoining material elements. For simplicity, the gap in the overlapping sections (*i.e.* L_a to L_{ab} and L_b to L_{bc}) was ignored as it is not expected to greatly affect the results. The thicknesses of the overlapping sections were modeled as having double the thickness, *i.e.* 2.44 mm (0.096"). For the simulations, each section was modeled as a thin tube with a diameter that corresponds to its respective mid-thickness. Each section was assigned a thickness property: 1.22mm for the single tube sections and 2.44" for the overlapping sections; the mid-diameters and thicknesses are listed in Table A-3 in Appendix A1. The simulations were carried out using both 0.5 cm^2 and 0.3 cm^2 elements for convergence; as all results from the 0.3 cm^2 element simulations produced results within 5% of the 0.5 cm^2 there was no need to do further simulations at smaller element sizes.

4.3.5.3 SIMULATION RESULTS

Table A-4 and Table A-5, located in Appendix A1, present the FEA results from the aluminum and CFC simulations, respectively. Figure 4-12, Figure 4-13, and Figure 4-14 visually present FEA results in terms of maximum global stress, safety factor, and maximum deflection; all three figures present the FEA results from the 0.3 cm^2 elements.

For all of the simulations, the maximum global stress was found at the constrained edge as was predicted; however, it appears that beam theory offered a conservative stress estimate at these beam geometries. Looking at Figure 4-12, the FEA results showed that both the aluminum and CFC simulations produced maximum global stresses that are lower than the predicted stresses from beam theory calculations. Beam theory predicts that the maximum stress would solely depend on the beam's geometry and applied load; there was a consistent gap between the FEA aluminum and carbon composite results thus indicating that material selection also plays a factor in the internal stress. The gap did not change much in relation to an increasing diameter; the gap only decreased from 6.5 to 6.2 MPa which leads the author to believe that the gap would continue to manifest at further increases in tube diameters. The gap is likely due to the materials' different mechanical

architectures: aluminum is an isotropic material while CFC is a transversely isotropic material that is plied in alternating directions. From the FEA, it appears that both architectures distribute the internal global stresses differently which results in a consistent gap between maximum internal stresses as opposed to the prediction that the internal stresses would be the same.

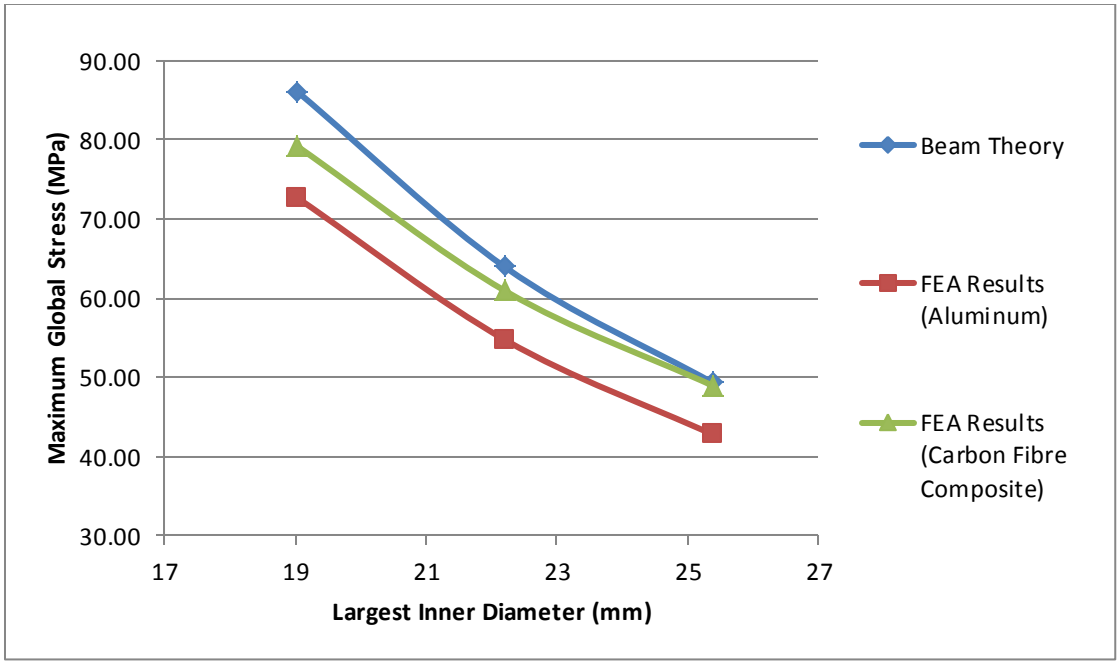

Figure 4-12: The Maximum Global Stress Values for the Three Tube Geometry Situations (with reference to the largest inner diameter) and the Two Materials using both Beam Theory and FEA

As mentioned, the beam theory calculations tended to overestimate the maximum global stresses; the beam theory calculations thus gave conservative estimates. Interestingly, looking at Figure 4-12, the beam theory stresses appear to converge to the CFC FEA results as the tube diameters increase. It is possible that the beam theory calculations may converge to the aluminum values at larger tube diameters; the author would anticipate this as the beam theory equations are generally only used for isotropic materials. The author speculates that the beam theory's convergence to the FEA results at increasing tube diameters is due to the inflicted deflection magnitudes. The beam theory stress equation (*i.e.* Equation 4-8) assumes that the beam's deflection is small. Looking at Figure 4-14, one would notice that the deflection decreases as the tube diameters increase; Equation 4-8 would thus be able to better predict the stresses at larger tube diameters which would explain the convergence to the FEA results with increasing

beam diameters. As the deflection increases, the author believes that the induced curvature would allow the beam to better disperse stress; the actual maximum stress for these increased diameters would thus be less than that predicted by Equation 4-8.

Although the beam theory calculations were not completely in line with the FEA results, they nonetheless gave an estimate that was only 15.3-18.5% and 0.7-8.7% greater than the aluminum and carbon composite FEA results. Based on the FEA results, the beam theory calculations can be used as a conservative global stress estimate.

Akin to the global stress results, the FEA results showed that using beam theory and composite modeling produced conservative safety factors. The FEA results for the aluminum simulations were more in line with the beam theory results; the beam theory calculations underestimated the aluminum safety factors by 13.3-15.6%. However, the FEA results for the CFC tubing showed much higher safety factors; the beam theory calculations underestimated the safety factors by 54.1-64.2%. Similar to the global stress results, the safety factor estimates were closer to the FEA results at larger tube diameters.

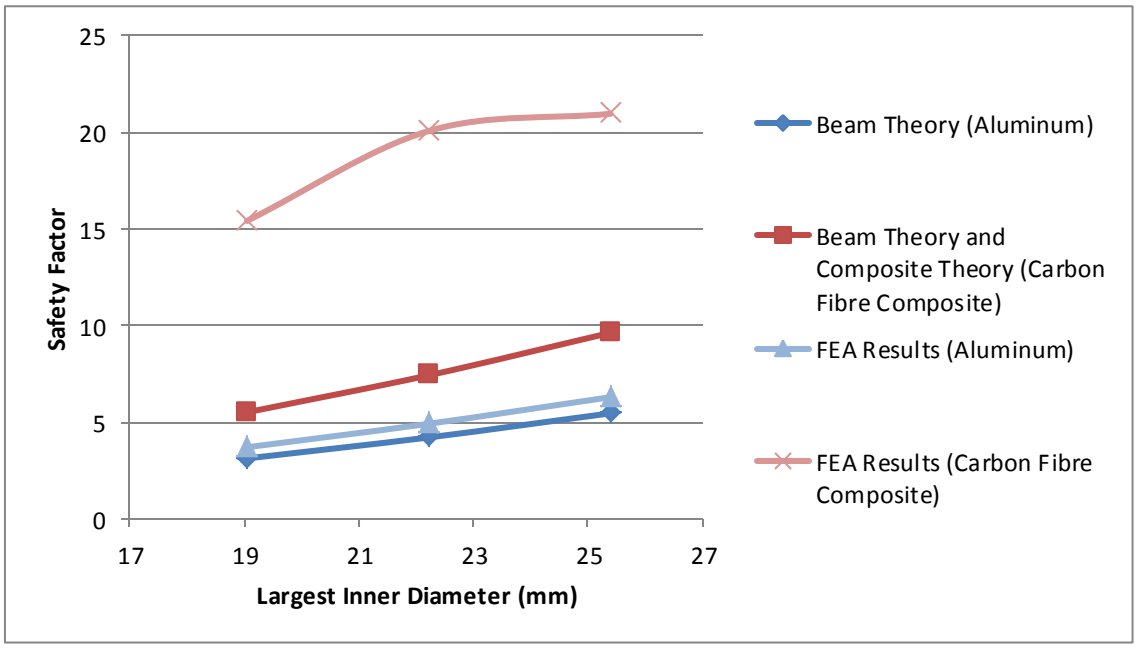

Figure 4-13: The Safety Factor for the Three Tube Geometry Situations (with reference to the largest inner diameter) and the Two Materials using Beam Theory, Composite Theory, and FEA

Like the global stress results, the author attributes the differences in beam theory calculations and FEA results on the materials' architectures. Beam theory is based on the use of isotropic materials; this explains why the aluminum FEA results are more in line with the beam theory projections. One may be tempted to blame the gross increase for the FEA CFC safety factor on human input error; however, if this were the case, one would also expect greater error in the maximum global stress FEA results. One could blame human input error in the composite calculations, but the author could not find any fault in the calculated stiffness or safety factor matrices (*i.e.* Equations 4-15 and 4-19). It is therefore believed that beam theory may not be applicable to composite modeling.

Although the safety factor calculations from beam theory were not completely in line with the FEA results, the calculations can be used as conservative estimates. For both the beam theory calculations and FEA results, it was found that the CFC is better apt for the flamenco backdrop as it produced larger safety factors.

Figure 4-14 shows the aluminum and CFC FEA results in terms of the induced deflection with reference to the largest inner diameter. As would be expected, the deflection decreases as the diameters increase; larger diameters cause the moments of inertia to increase which in turn dampen the deflection as dictated by Equation 4-6. However, the deflection trends were not as predicted. Section 4.3.4.3 showed that the global stiffnesses for the aluminum and CFC were very similar with CFC being only 2.2% stiffer. Based on these results it was predicted that there would not be much difference in deflection. As seen in Figure 4-14, at the lowest diameters, there is a significant gap between the aluminum and CFC deflections; however, this gap decreases as the diameters increase. The gap decreases from 15.9 cm, to 8.8 cm, and to 5.2 cm as the largest inner diameter respectively increases from 19.1 mm, 22.2 mm, and 25.4 mm. Based on the FEA results, the prediction of similar deflections between aluminum and CFC tubes appears to only be supported at larger tube diameters. It is unclear why the aluminum deflection appears to converge to the CFC deflection as the diameters increase, more analysis is necessary to determine the cause. Regardless, the FEA results suggest that the CFC tubing is better apt to minimize deflection.

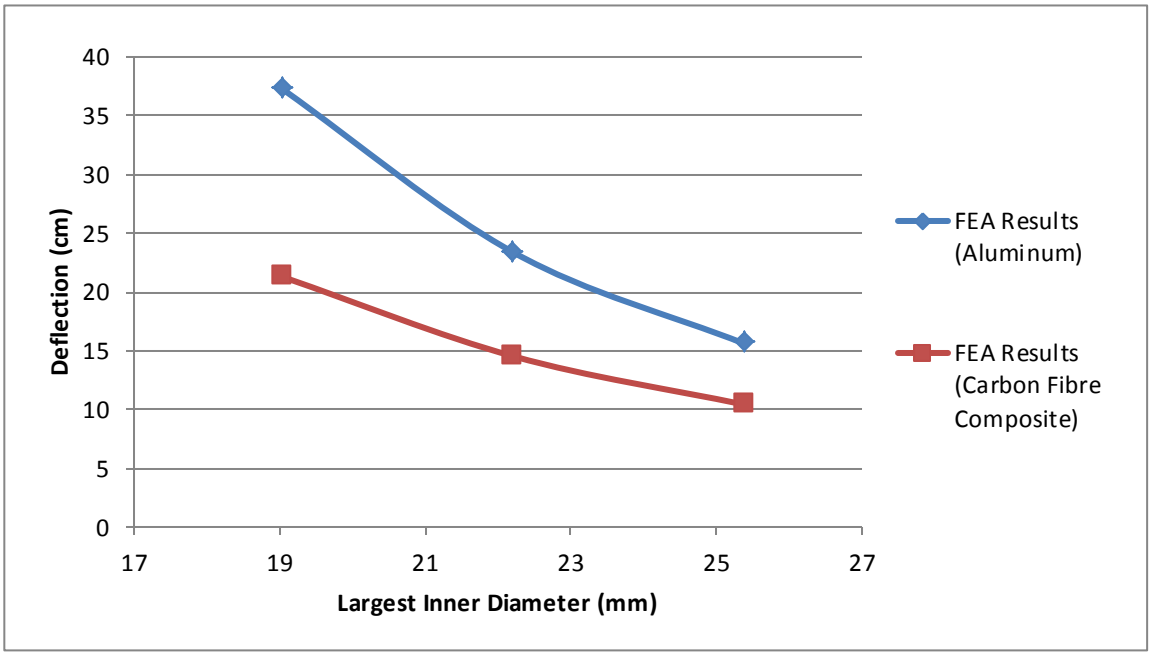

Figure 4-14: The FEA Deflection Results for the Three Tube Geometry Situations (with reference to the largest inner diameter) and the Two Materials

4.3.6 Recommendations

Based on the findings from both the beam theory calculations and FEA results, it was recommended that CFC tubing be used as opposed to aluminum on the basis that the investigation has shown the CFC option to be lighter, stronger, and would cause less deflection. In terms of diameter sizes, it was recommended to use the largest diameter (*i.e.* D_{ai} = 25.4 mm). Although the FEA revealed that there was not much difference in safety factor between the 22.2 mm and 25.4 mm largest inner diameter situations (only a 4.4% increase in safety factor was observed), the FEA did reveal a significant decrease in deflection between the two situations (a 28.2% decrease in deflection). Based on the desire to minimize deflection, the largest diameter situation was recommended. These larger tube diameters would only add an additional 0.21 kg to the weight of the backdrop; the author believes this weight would not be noticeable to the user.

4.4 THE WARMING HUT UNDER WIND LOADING

As the warming hut was to be used in a public setting for public use, it was imperative for the hut to be structurally safe and sound. With little trees and nearby buildings, the Halifax commons is known for its high winds; the hut must not only be waterproof, but be able to withstand these high winds. To get a sense of the deformation and stresses the original design would experience under high wind loads, a structural FEA was performed.

4.4.1 Problem Definition

As mentioned, the warming hut was to be used on the Halifax Commons, a place without much shelter from wind. The warming hut must therefore be able to withstand these wind loads to ensure its structural security for public use. To secure the hut to the ground, sandbags were to be placed under the seats and attached to the hut's foundation. To limit the weight of the hut's structure, the frame and seats were to be machined from aluminum. Divided into eight panels, each weighing approximately 78 kg, the panels were to be bolted together on site before bolting the seats to each panel. The original design (Shown in Figure 4-15) only consisted of the aluminum frame, and the tensile fabric to provide shelter. As fabric is quite difficult to model in FEA, the aluminum structure was modeled to withstand the entire wind load. Although the modeled loading scenario does not accurately portray the hut's true loading as the fabric would no doubt reduce the overall stress by more evenly distributing the load across the frame, the modeled scenario will give a conservative estimate towards the structure's maximum displacement and stress.

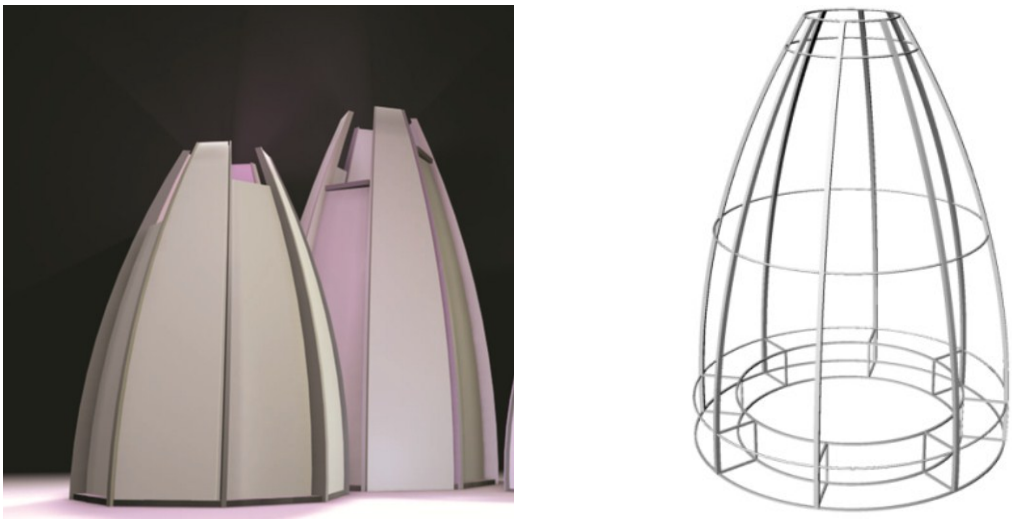

Figure 4-15: The Original Warming Hut's Design. Structure and fabric (left) and structure only (right). The structure is composed of 8 vertical members, 5 horizontal rings, and seats all made from aluminum bar.

To ensure its structural integrity under wind loading, it is desired for the hut to withstand wind loads of 35 m/s: wind speeds typical of level 1 hurricanes. Although very unlikely that the wind loading will be this excessive, it will add a sense of security to the hut's structural integrity.

4.4.2 Mesh Type and Material Properties

As the original frame was completely made from aluminum sheet metal with uniform thickness, a 2D shell mesh was used. $8mm^2$-sized elements were used. Being completely composed of aluminum, the modulus of elasticity, Poisson's ratio, and yield strength used in the analysis were 68.9 GPa, 0.3, and 269 MPa, respectively.

4.4.3 Boundary Conditions and Loads

To simulate the ground constraints of the hut's foundation, the bottom surfaces of the hut's foundation were completely constrained to the ground. The loading scenario would simulate a wind that is perpendicular to the face of the hut with one of the vertical members in the middle of said face. To simulate this loading, the drag force equation (Equation 4-21) was used. As the drag coefficient (C_D) for the warming hut is not known, it will assume to be high at a value of 2 to get conservative results although the

coefficient is more likely to be much lower. The air density (ρ) was assumed to be 1.25 kg/m^3. As mentioned previously, the simulated air velocity (v) is 35 m/s.

$$F_D = \frac{1}{2}\rho v^2 C_D A \qquad 4\text{-}21$$

With reference to the plane perpendicular to the wind load, the face area (A) of the fabric was divided into sections to more accurately distribute the drag forces. The face area was divided into five areas with cutting planes that represented the midlines between adjacent vertical members (See Figure 4-16). Known as the front area, one of these areas would be applicable to the front vertical member; known as the mid layers, two of these areas would be applicable to the vertical members adjacent to the front vertical member; known as the side area, the other two areas would be applicable to the side vertical members. These areas were further divided by 3 of the hut's structural rings for a total of 12 different section areas. The face area was found for the 12 different sections and plugged into the drag force equation to get the drag force at each area. The face areas and calculated drag forces are presented in Table 4-10.

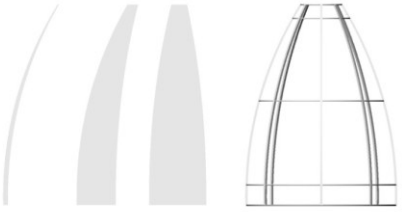

Figure 4-16: The surface area with reference to the perpendicular plane of the wind load was divided into 5 different areas: 1 front face, two middle faces, and two side faces. These faces were made using cutting planes located at the midline between adjacent vertical members. The face areas from left to right are the side area, mid area, and the front area

Table 4-10: The face areas and calculated drag forces

Sections	Front Area		Mid Area		Side Area	
	Face Area (m^2)	Estimated Drag Force (N)	Face Area (m^2)	Estimated Drag Force (N)	Face Area (m^2)	Estimated Drag Force (N)
Bottom	0.587	899	0.402	616	0.050	76
2nd from bottom	2.252	3449	1.544	2365	0.192	294
3rd from bottom	1.498	2294	1.027	1573	0.128	196
Top	0.128	196	0.088	134	0.011	17
Total	4.465	6838	3.062	4688	0.380	582

In the simulation, the vertical members were also divided into four sections using the three horizontal rings, and the corresponding drag force load was applied to each section. The load was applied to each section by taking the section`s estimated drag force and dividing it by the amount of nodes on each section. The corresponding load was then applied to the section's nodes.

4.4.4 Simulation Results

Located at the top of the front area of the hut, the maximum displacement was found to be 27.0 cm. Although most areas of the frame had stresses well below the aluminum yield strength of 269 MPa, there was a significant stress concentration where the vertical members connected to the seat frames. The maximum stress at this connection was found to be 923 MPa which is well above the material's yield strength. Although the model does not show how the fabric would distribute the stress over the frame, these results indicate that there is a strong need to better distribute the stress at these connections.

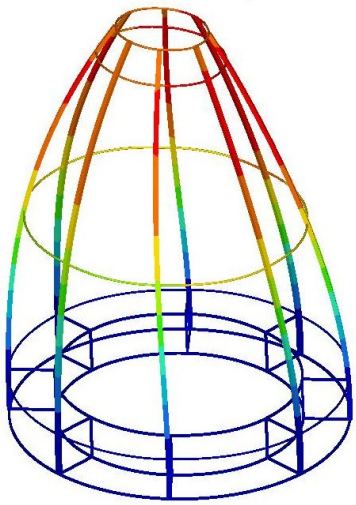

Figure 4-17: A Visual of the Displacement Results of the Simulation. Using the red-blue colour scale, red indicates areas of high displacement and blue contains areas of low displacement.

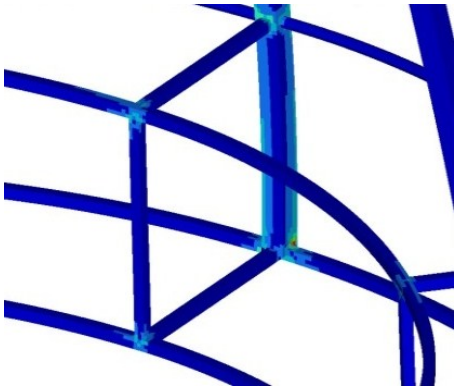

Figure 4-18: The Maximum Stress was found at the connections between the vertical members and the seats.

4.4.5 Structural Changes

As the author is not a licensed engineer; and as a public structure, the hut needed structural clearance from a practicing engineer; the structural analysis was passed on to a local engineering firm in Halifax: BMR Structural Engineering. To improve the stress distribution, BMR engineering consulted with the hut's architect, Adam Reid, to alter the hut's design. The structural changes included adding material to the seats where they connect with the vertical columns, adding more support members across the panels in many directions, adding wood panels at the bottom and top of each panel to disperse stress and prevent twisting, using ground anchors instead of sand bags to constrain the hut to the ground, and making the hut's width larger by increasing the bottom radius from 1.69 m (66.4") to 1.85 m (73"). Figure 4-19 and Figure 4-20 respectively show a rendering of the final design of the hut's structural frame and a photo of a finished seat. The warming hut was erected on January 22nd, 2011 and was up for three months without any structural problems.

Figure 4-19: A rendering of the final structural frame

Figure 4-20: Additional material was added to the seat where it connects to the structural frame

4.5 THE FLAMENCO BACKDROP ROTATIONAL JOINT

For the flamenco stage set, the @lab originally wanted a mechanism that would allow the user to rotate the poles during a performance without noisy automatic motors or manual locks. The @lab came up with an internal "spring board" mechanism, located at the rotating axis of the poles. When the mechanism is at its resting position (*i.e.* when the poles are at a designated angle), the spring boards are upright and prevent the poles from rotating around the center axis under its own weight. However, if a user applies enough force on the pole in the direction of rotation, the spring board will be forced to bend, consequently allowing the pole to rotate to its next resting position. As this mechanism relies on forcing a part to bend, a part that was to be rapid prototyped, a stress analysis was imperative to see if a rapid prototyped material could withstand this forced displacement with no plastic deformation. This problem was to be solved using FEA.

4.5.1 Problem Definition

Designed by our design & graphics technician, the mechanism consists of two parts: the spring board itself, and the wave wheel. Rendered drawings of the spring board and wave wheel are presented in Figure 4-21 and Figure 4-22, respectively. On a central hub, each spring board is sandwiched between to wave wheels and is attached to one of the collapsible tube mechanisms. Each wave wheel is completely constrained from moving, but the spring board can rotate with a pole, providing that an adequate amount of rotation torque is applied. On each side of the spring board, there are four flange extrusions that act as cantilever beams to resist an amount of rotation torque. At the end of each flange is a filleted extrusion (known as a hill), used to lock the mechanism at designated positions. The wave wheel surrounds the spring board flanges and gets its name for its wave-like circumferential outline. The wave-wheel's inner circumferential outline consists of hills and plateaus, analogous to a sine wave. At a designated resting position, the hill on the spring flange is nestled in one of the plateaus along the wave wheel which prevents the spring board and attached collapsible tube from moving; the spring force from the flanges are large enough so that the spring board and attached collapsible tube cannot rotate. However, when enough torque is applied to the pole by a user, the flanges

are forced to bend radially towards the central hub, allowing the spring board and pole to rotate to the next plateau on the wave wheel.

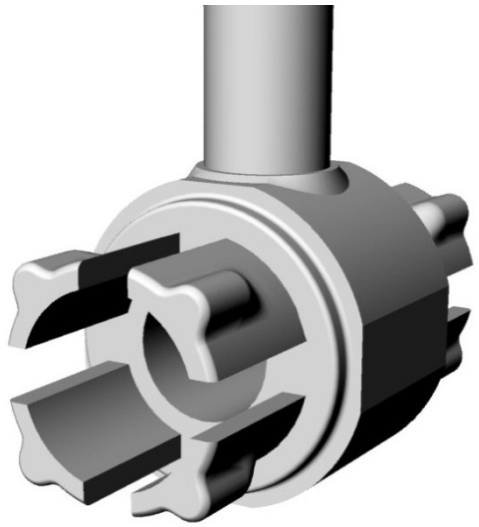

Figure 4-21: The "Spring Board" Mechanism

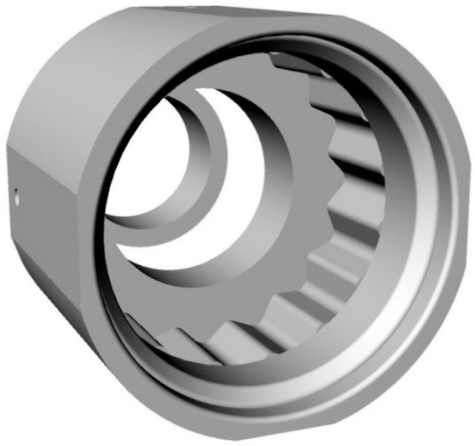

Figure 4-22: The Wave Wheel

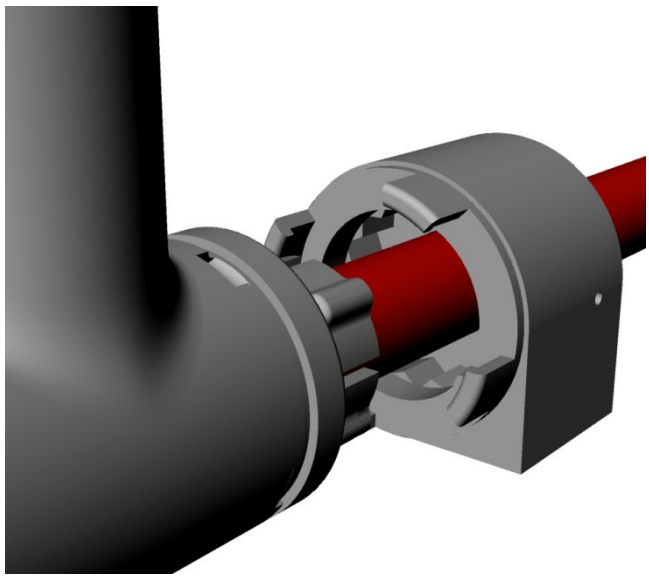

Figure 4-23: An exploded view of the spring board and wave wheel attached to the central axis

The design was to be rapid prototyped as the pieces would be quite difficult and expensive to machine or mold through dies. A prototype was made using the @lab's own 3D printer. Although the poles tended to sway somewhat from their intended angles, the mechanism initially worked. However, soon after a few uses, some of the

flanges broke. Representatives from Stratasys, Inc., the company that sells the @lab ABS plastic for the 3D printer, suggested maybe sending the part out to be rapid prototyped using a stronger plastic. To see if a stronger rapid prototyping ABS plastic could elastically withstand the forced deflection, a FEA was be performed by the author.

4.5.2 Mesh Type and Material Properties

As the part was an irregular shape, a 3D mesh was the best option. The part had fillets and non-uniform thicknesses; a 2D mesh would not have been feasible. As the part had three planes of symmetry, the part was reduced to one eighth to minimize the simulation time. Two of these planes were through the central axis in the longitudinal direction, while the other vertically splits the part in half. Each eighth represents one of the eight spring flanges. Appropriate boundary conditions were applied to the cutting planes (See Section 0). To improve the accuracy of the model, brick elements were used as opposed to tetrahedral elements or mixed elements. This was achieved using the mapping functions of Hypermesh™ software. The minimum acceptable Jacobian for each element would be 0.3 with less than 10% of the elements being less than 0.7.

The tensile strengths and tensile moduli of three different rapid prototyped materials were extracted from Fortus™ 3D production systems and are presented in Table 4-11. Their ABSplus-P430 is one of their most popular brands as it is affordable and available in a wide variety of colours. The ABSplus-P430 is what was used to make the initial prototype. The other two brands, PC (Polycarbonate) and ULTEM 9085 cost more with ULTEM 9085 costing the most, but their tensile strengths are nearly double that of the ABSplus-P430. What stands ULTEM apart from PC is its slightly higher tensile strength and its doubled impact toughness. Given that they all have similar tensile moduli, only one simulation will be performed as the tensile strength is not directly needed for the FEA, only for the safety factor calculation. The simulation will use the tensile modulus of 2,280 MPa, while the Poisson's ratio will be assumed at 0.3 as it was not given by the manufacturer. It should also be pointed out that the materials did not have a compression strength listed in their data sheets. This is likely due to the fact that rapid-prototyped materials are better at withstanding compression than tension. As a result, the simulation

will thus focus on the tensile forces being developed in the simulation. The overall aim of the case study is to see if any of the materials listed in Table 4-11 can withstand the projected displacement.

Table 4-11: Material Properties for Various Rapid Prototyped Plastics. Extracted from (Stratsys, Inc., 2011)

Mechanical Property	Test Method	ABSplus-P430	PC (Polycarbonate)	ULTEM 9085
Tensile Strength	ASTM D638	37 MPa	68 MPa	71.6 MPa
Tensile Modulus	ASTM D638	2,320 MPa	2,280 MPa	2,200 MPa
IZOD Impact, notched	ASTM D256	106 J/m	53 J/m	106 J/m

4.5.3 Boundary Conditions and Loads

As previously mentioned, the spring board part was divided into one eighth as there were three degrees of symmetry. This will save simulation time, but appropriate boundary conditions need to be applied to take account of the missing material. Essentially, it is required for all the element faces attached to these planes of symmetry to be unable to translate outside of these planes of symmetry. As an example, the rear cutting plane is in the xy-plane, so the attached nodes should not be able to move in the z direction or rotate around the x and y axes. Listed in Table 4-12, appropriate constraints were placed on all three planes of symmetry for the simulation.

Table 4-12: The Symmetrical Cutting Planes and their Boundary Conditions

Plane of Symmetry	Lies on	Constraints
1st Symmetrical Cutting Plane	xz-plane	x-axis rotation y-axis translation z-axis rotation
2nd Symmetrical Cutting Plane	yz-plane	x-axis translation y-axis rotation z-axis rotation
Rear Cutting Plane	xy-plane	x-axis rotation y-axis rotation z-axis translation

For the load, the design required the point of contact on the spring board to deflect 2.11 mm. The loading scenario would therefore be a static displacement input of 2.11 mm at the point of contact. The meshed part with labeled load and boundary conditions is shown in Figure 4-24.

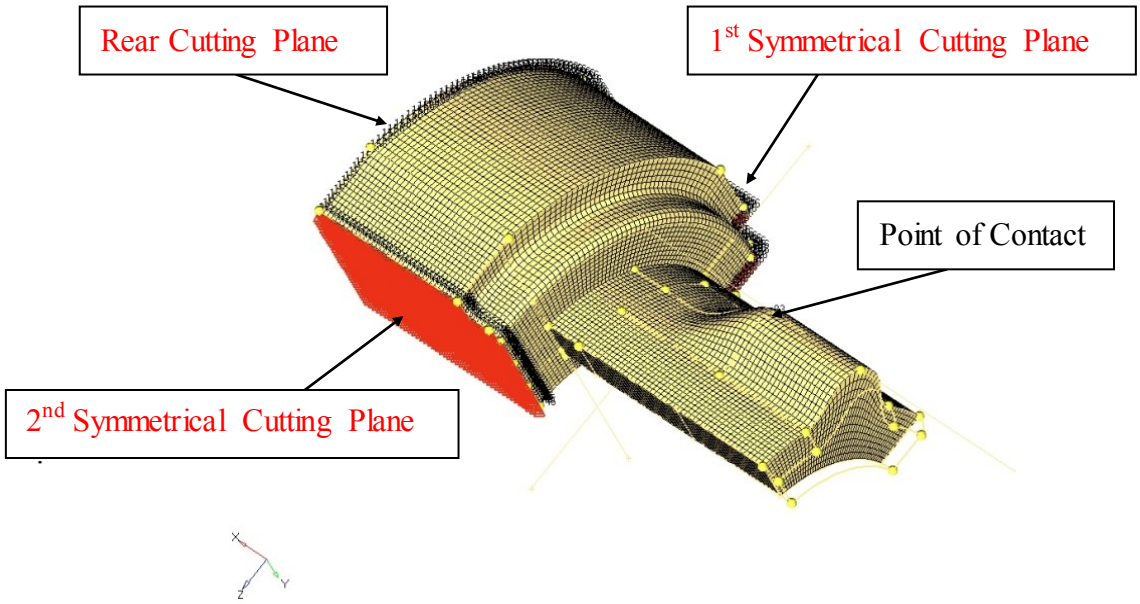

Figure 4-24: The mesh with labeled loads (in black) and boundary conditions (in red).

4.5.4 Simulation Results

The simulation was first executed with $1mm^3$ brick elements using RADIOSS™ FEA software. Using Hyperview™ software, the results were visualized. Figure 4-25 illustrates the results from Hyperview™. The visual colours represent relatively high and low stresses respectively based on the red to blue colour spectrum. The grey parts represent un-highlighted elements on the visual where relatively no stress was experienced.

Stress concentrations were found on the top and on the bottom of the spring board flange at the area where it connects to the spring board's body, which makes sense as the connection would be experiencing the highest internal moment and thus highest bending stress. The maximum stress on the top of the flange was found to be 69.1 MPa and was located at the center of the connection with body, while the maximum stress on the bottom was found to be 104 MPa and located at the corners of the flange where it connects to the body. Although the bottom has a higher maximum stress, it is experiencing compression. The stress on the top is from tension. As mentioned earlier, rapid-prototyped parts are better at handling compression than tension, so the part is therefore more likely to fail when experiencing tension. For this reason the simulation will focus on the tensile stresses on the top of the flange.

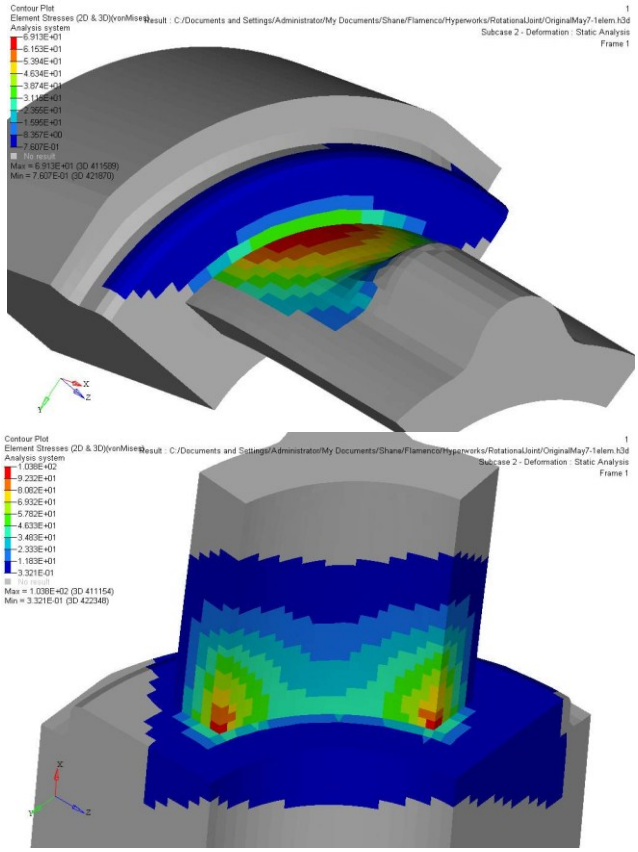

Figure 4-25: Visual Results of the 1mm^3 sized brick elements simulation. The top and bottom images respectively showcase stresses on the top and bottom sides of the springboard

Looking back at the tensile strength values of the rapid-prototyping materials in Table 4-11, one would notice that the maximum tensile stress of 69.1 MPa is very close to the tensile strength of the strongest material (71.6 MPa). The safety factor is therefore quite small at a value of 1.04, indicating that the part is on the verge of failure.

To get a more accurate prediction of the applied tensile stress, a mesh convergence study was performed using smaller brick element sizes of 0.9, 0.75, 0.6, and 0.5 mm^3. The maximum tensile stress was obtained from each simulation. The results are listed in

Table 4-13 and graphed in Figure 4-26. The simulation appears to converge at 0.5 mm^3 brick elements with a maximum stress value of 80.9 MPa, resulting in a safety factor of 0.88. Based on the mesh convergence study, the springboard mechanism will fail.

Table 4-13: The Results from the Mesh Convergence Study.

Brick Element Size (mm^3)	Maximum Tensile Stress (MPa)	Safety Factor (Based on Tensile Strength of 71.6 MPa)
1.0	69.1	1.04
0.9	69.4	1.03
0.75	73.4	0.98
0.6	79.8	0.90
0.5	80.9	0.88

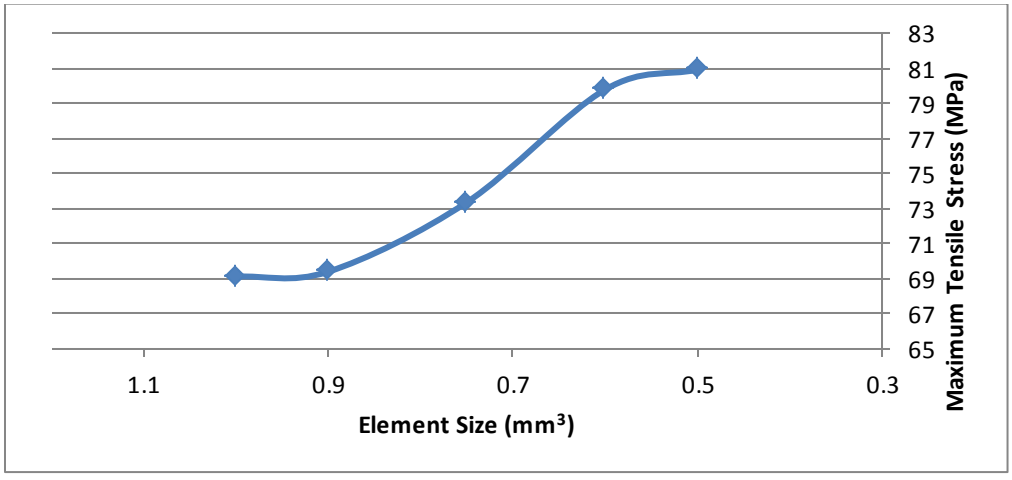

Figure 4-26: A Visual Representation of the Mesh Convergence Study

4.5.5 Investigating Possible Alternative Designs

Attempting to reduce the tensile stress in the flange, a few geometrical alterations to the flange were conceived by Greg Sims (the @lab's technician). These alternative designs included adding fillets to the flange/body connection, adding 3mm to the length of the flange, or making the flange 1 mm thicker. Figure 4-27 shows rendered drawings of the three alternative designs. To see if these three adjustments would indeed improve the tensile stress, a FEA was performed for all of them using the same conditions as

described for the original design's simulation. The analyses were performed using 0.5 mm^3 brick elements as the mesh convergence studies showed that the maximum stress converges at this size. The results are presented below in
Table 4-14.

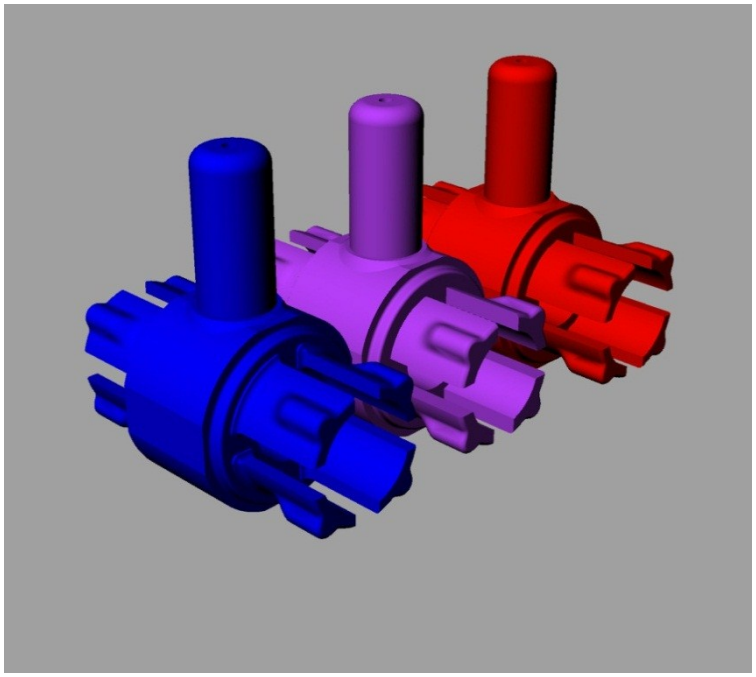

Figure 4-27: The Alternative Flange Designs. The filleted design is in blue, the 1mm in additional thickness is in purple, and the 3mm in additional length is in red

Table 4-14: The FEA Results for the Alternative Flange Designs

Alternative Flange Design	Maximum Tensile Stress	% Difference from Original Design
Fillets at the body/flange connection	77.8	-3.88
Adding 3 mm in Length	65.84	-18.7
Adding 1 mm thickness	83.9	+3.66

The fillet and 3 mm length addition scenarios reduced the maximum tensile stress by 3.88% and 18.7%, respectively, while increasing the thickness by 1 mm actually increased the stress by 3.66%. The decrease in stress from adding the fillets is expected as fillets more evenly distribute the applied stress, leading to a decrease in the internal stress. The 3mm length addition and 1mm thickness addition scenarios can be explained

by looking at the universal being stress and deflection equations. The elastic deflection of a cantilever beam is directly proportional to the force to the first power, but also to the length to the third power which implies that the deflection is more dependent on the length of the beam than the applied force. Doubling the force would double the deflection, but doubling the length would increase the deflection by a factor of 8. Akin to the simulated loading scenario, if the deflection were to stay constant, doubling the length would reduce the applied force by a factor of 8. As an increase of length would decrease the applied force, the flange's internal moment would decrease which in turn would lead to a decreased internal bending stress. It should be noted, however, that increasing the length would also decrease the spring back force from the flange which would make the poles more susceptible to rotation under their own weight. Like the cantilever's length, the deflection is also dependent on the thickness of the beam to the third power as part of the beam's bending moment of inertia. Unlike the length, however, the deflection is inversely proportional to the third power of the thickness. For the deflection to stay the same, an increased thickness will therefore require an increased applied force, leading to an increase in the internal bending stress at the flange/body connection.

Although two of the alternative designs showed an improvement over the original design, the maximum improvement only increased the safety factor to 1.09; not enough to comfortably declare that the mechanism will not break. Even if the longer beam design was used, the amount of spring force would be reduced, leaving the poles more vulnerable to sway at designated angles, or even rotate on their own at angles closer to the floor. Due to the results of this analysis along with the initial prototype failure, the spring board mechanism was discarded.

4.6 THE REACTIVE CEILING LUGS

To attach the panels to the ceiling, the @lab would be using cables. The cables would be attached to four lugs, one on each corner, that are bolted into the frame. The @lab wanted to make sure that the lugs would be able to withstand the applied stresses. As the lugs would be machined using sheet metal of uniform thickness, a 2D mesh FEA would

be performed by the author to analyze their integrity. A rendered drawing with dimensions can be found in Appendix A2.

4.6.1 Problem Definition

As mentioned previously, to hang the reactive ceiling panels in the air, cables would be used to attach the panels to the ceiling. The cables would be attached to four lugs, one on each panel's corner, that are bolted to the frame. It is desired to know if the lugs will be able to withstand the stress of a panel in the event that one or more of the cables broke. The tension in the remaining cables would therefore increase to make up for the snapped cable, increasing the stress on their respective lugs. The increase in stress would be from the combination of the decreased load distribution of the panel's weight, along with the impact caused by the momentum of the panel descent.

To simulate the situation, the mass of each panel was calculated. A summary of the parts along with their estimated weight is listed below in Table 4-15. The total mass of one panel was found to be 29.8 kg, making the weight approximately 292 N using a gravitational acceleration of 9.8 m/s^2.

Table 4-15: The Weight of One Panel as a Summation of its various parts

Part	Mass (kg)
Poles	1.36
Tiles	9.44
Frame	8.84
Additional Poplar Parts	3.03
Additional Aluminum Parts	1.48
Motors	5.6
Total	29.8

To simulate the force increase, the design required a lug that would withstand a force equivalent to double the weight of a panel, as opposed to the static load of one quarter the weight of a panel. As the cables were on angles relative to gravitational acceleration, the

angle was needed to calculate the tension in the cables. As shown in Figure 4-15, depending on position of the lug, the cable could have one of 4 different angles.

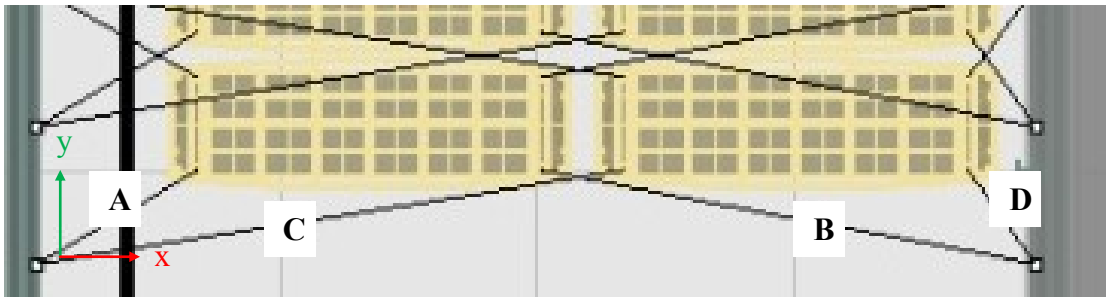

Figure 4-28: A view of the xy-plane. The reactive ceiling panels would be attached to the walls via cables. The cables could have one of 4 angles, labeled A, B, C, and D.

The simulated tension, T, on the cable can be calculated by taking the cable's angle with reference to the face of the panel (θ_1) and dividing it from double the weight of the panel, 2 W.

$$T = \frac{2W}{\sin\theta_1} \qquad 4\text{-}22$$

For the FEA simulation, 3D coordinates of the tension must be found relative to the lug; this requires a second cable angle. The angle with reference to the x-axis in the xy-plane as shown in Figure 4-15 was taken. As the lug itself is at an angle of 6.9 degrees with reference to the x-axis in the xy-plane, the total angle had to be adjusted with an increase of 6.9 degrees; the total angle being represented as θ_2. Both values for $\theta_1$and θ_2 for all four cables along with the calculated cable tension, are listed in Table 4-16.

Table 4-16: The Angles of All four Cables as labelled in Figure 4-28 along with the Simulated Tension

Property	A	B	C	D
Angle In Plane of Cable with reference to the face of the panel, θ_1	80.2	50.2	54.1	75.0
Angle of cable with reference to the x-axis in the xy-plane	55.1	9.45	11.2	31.5
Angle of the cable with reference to the x-axis in the xy-plane with the angle of the lug, θ_2	62.0	16.4	18.1	38.4
Simulated Tension (N)	591.8	759.7	720.1	603.9

It should be noted that the simulation assumes that the angles between the cable and lug will not change during the event of an adjacent cable snapping; a factor which would certainly come into play should 2 or 3 cables snap.

4.6.2 Mesh and Material Properties

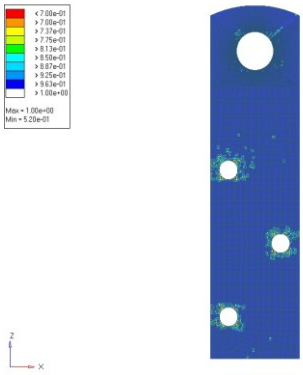

Figure 4-29: The Meshed Lug with 22720 elements and a visual representation of the Jacobian values with blue being 1.0 and red being a fail of less than 0.7. The mesh was performed using HyperMesh® software.

As the lug was to be machined out of sheet metal of uniform thickness, a 2D mesh would be used with shell elements. The meshed elements would have a minimum Jacobian value of 0.5 with less than 10% being below 0.7. Six meshes were done for the mesh convergence study. Table 4-17 lists the % of failed elements (*i.e.* elements with a Jacobian of 0.7 or less), and the minimum Jacobian for all meshes in the mesh convergence study. The last mesh in the mesh convergence study is shown in Figure 4-29. The simulations will be done with aluminum using an elastic modulus of 68.9 GPa, a Poisson's ratio of 0.3, and a yield strength of 269 MPa. The dimensions of the lug can be found in Appendix A.

Table 4-17: The Minimum Jacobian and Failed Jacobian % for all Meshes in the Mesh Convergence Study

# Elements	Failed Jacobian (<0.7)	% Failed	Minimum Jacobian
378	26	6.9	0.57
816	31	3.8	0.63
1589	4	0.25	0.65
2853	3	0.11	0.64
6059	1	0.017	0.66
22720	11	0.048	0.52

4.6.3 Boundary Conditions and Loads

As visualized in Figure 4-29, the lug has four holes: the smaller three being used to bolt the lug to the frame and the larger hole being used as the cable attachment. The smaller three holes were therefore completely constrained while the larger hole was completely free to deform under loading. As approximately three quarters of the lug is sandwiched between slabs of wood (*i.e.* the bolted section), constraints need to be made to limit this section's movement in the lug's respective plane. With reference to Figure 4-29's coordinate system, this section must be constrained to the xz-plane, *i.e.* no translation is allowed in the y-plane along with no rotation along the x and z axes.

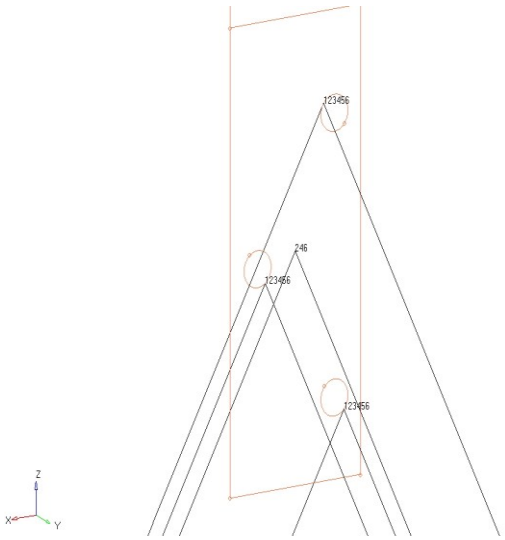

Figure 4-30: The lug with its respective boundary conditions caused from the bolts (represented by the holes), and the slabs of wood that sandwich about ¾ of the lug

For the loading conditions, two loads must be simulated: the load caused by the tension from the respective cable, and the load caused by the weight of the panel. The cable load was placed onto the large hole in the correct position of contact depending on the cable angle. The respective load calculated using Equation 4-22 was then placed at the point of contact at the correct vector directions. With reference to the face of the lug, θ_1 and θ_2 can be used to get the x, y, and z vector directions of each cable where the x-axis is along the length of the lug, the y-axis is along the thickness of the lug, and the z-axis is along the height of the lug.

$$\begin{aligned} x &= \cos\theta_1 \cos\theta_2 \\ y &= \cos\theta_1 \sin\theta_2 \\ z &= \sin\theta_1 \end{aligned} \qquad 4\text{-}23$$

A separate simulation would be done for each cable with each simulation being performed six times at smaller element sizes for the mesh convergence study. The load caused by the weight of the panel (2 W as defined earlier) was simulated by evenly distributing the weight across the nodes on the bottom edge of the lug. Figure 4-31 shows a visual of both loading scenarios.

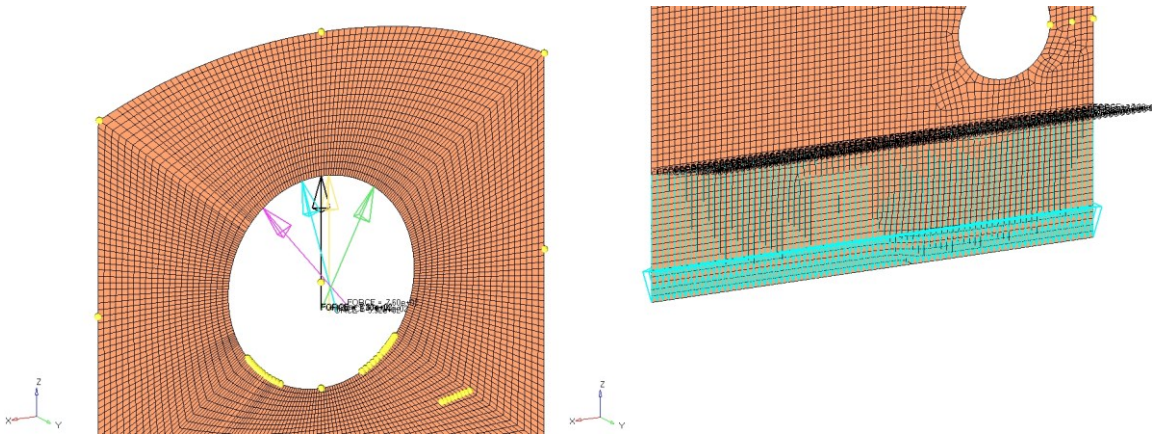

Figure 4-31: The Two Loading Conditions. Left: the loads from cables A, B, C, and D. Right: The load from double the weight of the panel distributed over the amount of nodes on the lug's bottom.

4.6.4 Simulation Results

The maximum stress and displacements were found for each cable scenario through a mesh convergence study. The stress results showed 3 areas of stress distribution: a cable contact stress, a circumferential stress, and a bending stress. A cable contact stress is located at the point of contact between the cable and lug, a circumferential stress is located along a section of the larger hole's circumference, and a bending stress is located at the junction where the lug is no longer sandwiched between the two slabs of wood. A visual of the three different stress distributions are shown in Figure 4-32. The results are tabulated in Table A-6 in Appendix A with illustrations of the maximum displacements, circumferential stresses, and bending stresses in Figure 4-33, Figure 4-34, and Figure 4-35.

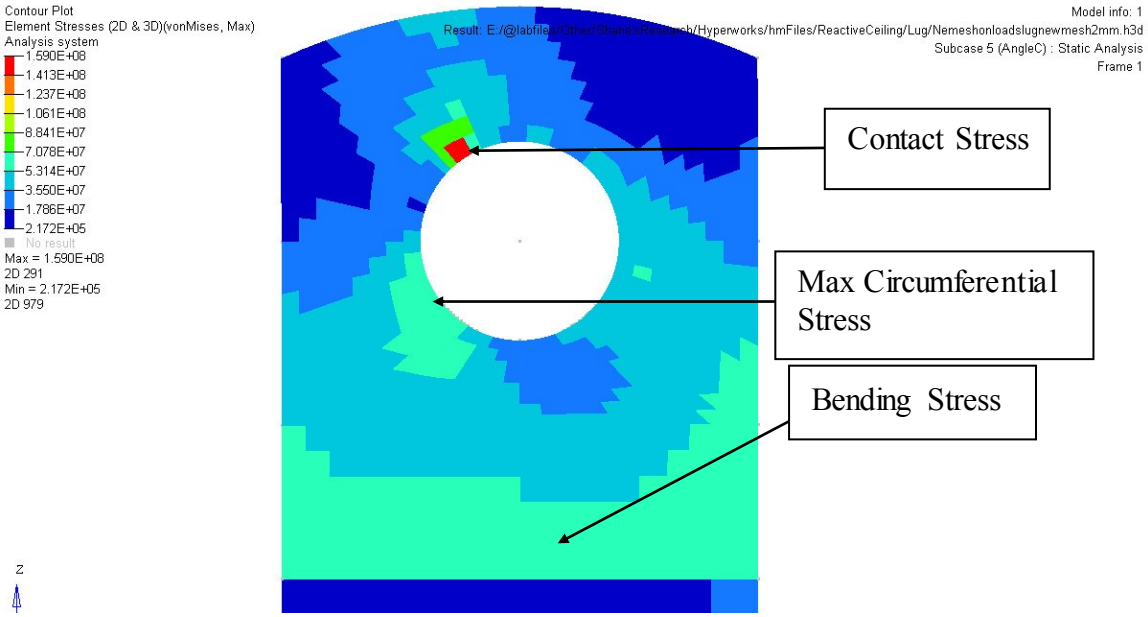

Figure 4-32: The Three Different Stress Concentrations on the Lug. This particular simulation was the C-cable at 1589 elements.

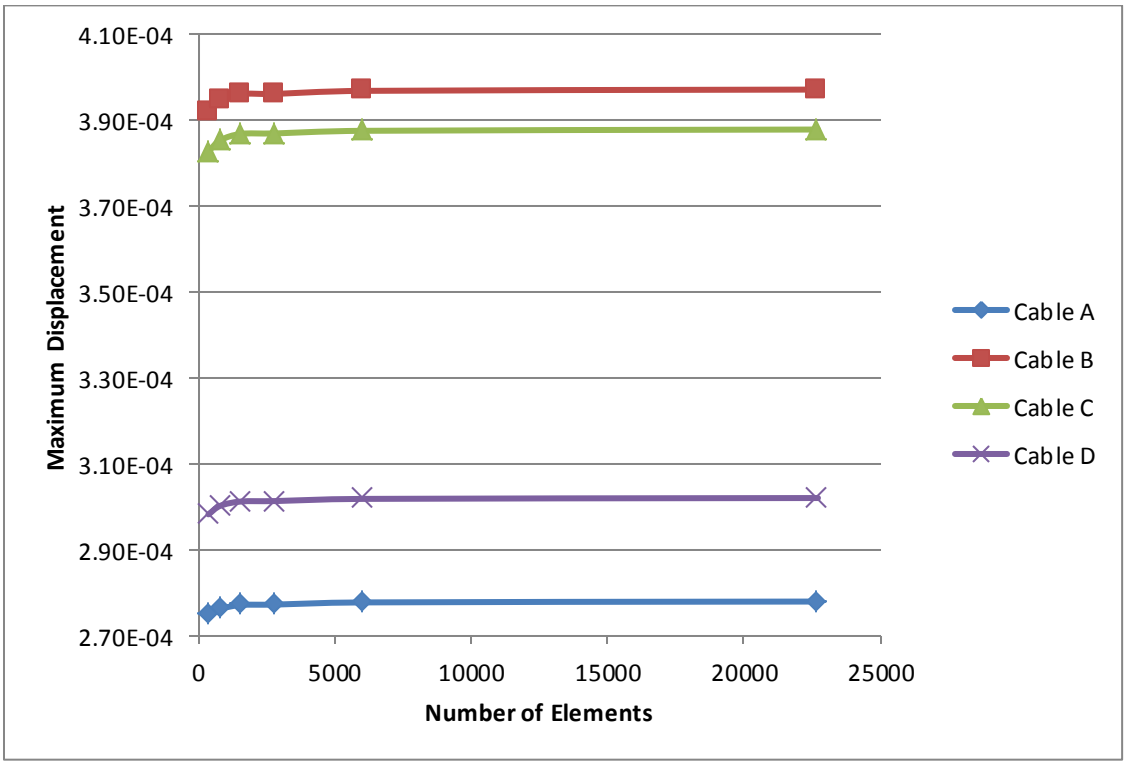

Figure 4-33: The Maximum Displacement Mesh Convergence Study of all four Cables

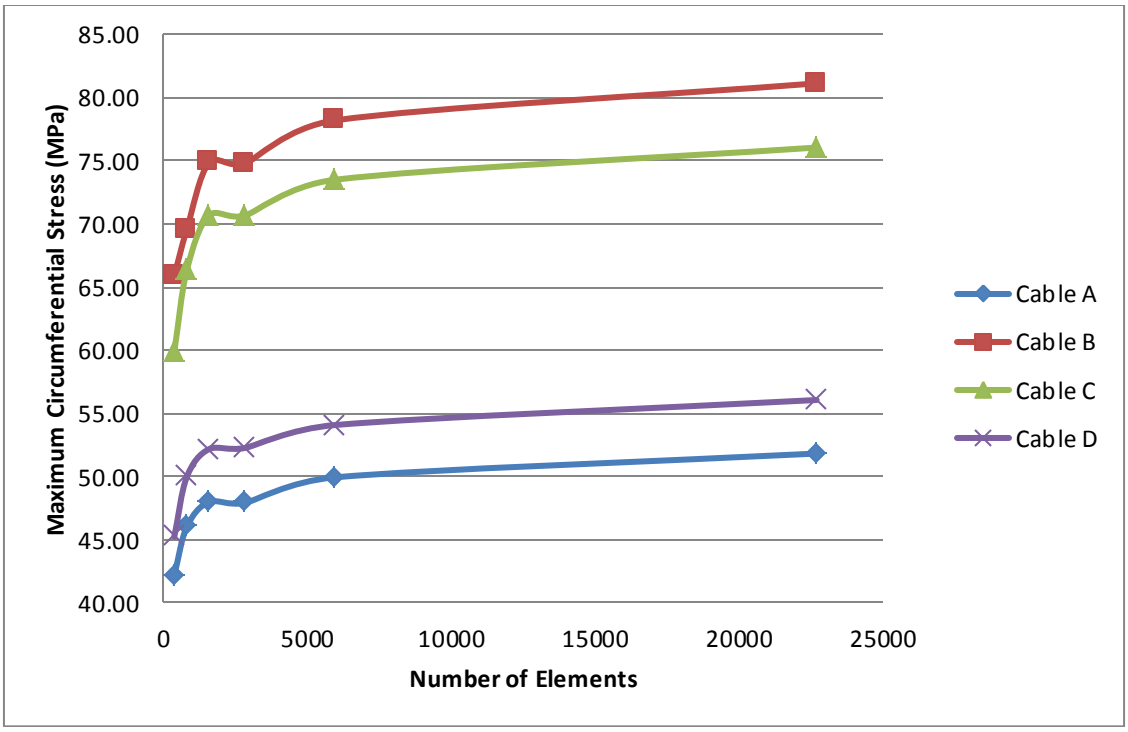

Figure 4-34: The Maximum Circumferential Stress Convergence Study of all four Cables

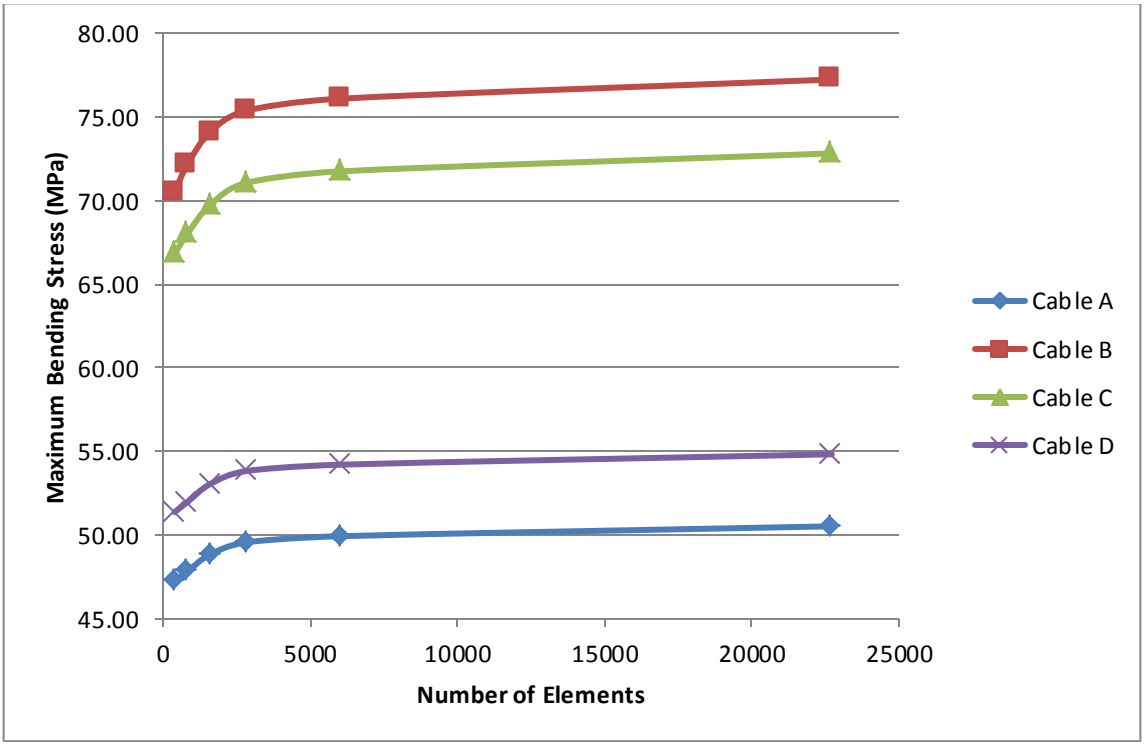

Figure 4-35: The Maximum Bending Stress Mesh Convergence Study of all four Cables

The maximum stress was always at the point of contact and continued to increase as the mesh elements got smaller. In terms of the cable scenario, the simulation assumes that the cable is the diameter of one element. A smaller element would thus have a higher stress from the same cable tension. As the diameter of the cable will be larger than the smallest element size used in the mesh convergence study, the maximum contact stress will be ignored as it will not be the true maximum stress value in the actual scenario.

The maximum displacement convergence study showed that the B cable would experience the largest displacement at 0.397 mm; the C cable is close behind at 0.388 mm, followed by the D and A cables at 0.302 mm and 0.278 mm. The maximum stress convergence studies showed similar results with the B cable experiencing the largest circumferential and bending stresses respectively at 81.1 MPa and 77.3 MPa, followed by the C cable respectively at 76.1 MPa and 72.8 MPa, the D cable respectively at 56.1 MPa and 54.8MPa, and the A cable at 51.8 MPa and 50.5 MPa. Having the highest cable tensile force, it makes sense that the B cable would have the highest bending stress and deflection. In fact, the lug order of lowest to highest bending stress and deflection (*i.e.* B, C, D, A) is the same of lowest to highest cable tension. Although the circumferential stress was 2.3-5.0% higher than the bending stress in all four cables, it should be noted that the circumferential stress is radially surrounded by material that prevents complete rupture. Although the circumferential stress is more likely to warp the material, it will only disfigure the large hole, rather than cause yielding that will plastically warp the lugs position. On the other hand, if exceeding the yield strength, the bending stress will permanently warp the lug's angle: a situation which is more undesirable than a warped hole. The bending stress should therefore be of most concern overall.

Looking back at the yield strength of aluminum (269 MPa), the maximum bending stress of 77.3 MPa produces a comfortable safety factor of 3.48. The aluminum lug design is therefore quite capable of performing its assigned duty of withstanding the weight of the panel along with the cable tension in the event of a cable failure. However, if one wants to be extra secure, one can switch the aluminum for steel as it has about 3 times the

elastic modulus, with more than a 50% increase in yield strength, and adds only about 0.33 kg to the panel's mass.

4.7 TORQUE ANALYSIS FOR THE REACTIVE CEILING MOTORS

As the reactive ceiling was to be motorized using step motors, torque calculations needed to be performed to specify what motor was needed. The motor needs to have enough torque to drive the boxes and tube or rod, but shouldn't be too heavy for safety reasons. A deflection analysis was first performed to see how much the tubes deformed under their own weight and the weight of the boxes. Although the deflection was low at around 7.5mm, it was agreed that no amount of deflection was desirable as deflection would add unnecessary strain on the motors. To prevent deflection, beams would be placed across the width of the panel to hold the poles in a level position. The torque analysis will therefore assume that there is no deflection across the double tubes.

Ignoring frictional forces, the torque needed to rotate an object is dictated by Equation 4-24 and is dependent on two variables: the mass moment of inertia of the object, I_M, and the angular acceleration of the object. This section will thus be divided into three subsections: one dedicated to the mass moment of inertia calculation, one dedicated to the angular acceleration estimation, and one discussing the needed torque specifications.

$$T_o = I_M \alpha \qquad 4\text{-}24$$

4.7.1 Mass Moment of Inertia

The mass moment of inertia is a measure of an object's resistance to rotation and is dependent on both the object's mass, and geometry in relation to the axis of rotation. In the event that there is more than one object along the axis of rotation (as is the case with the reactive ceiling), the mass moments of inertia are added. Each double tube mechanism has a total of eight objects with mass moments of inertia along same central axis of rotation: 6 boxes of equivalent dimensions, 1 outer tube, and 1 inner rod. On one side of the double tube mechanism, one motor would be attached to the end of the outer

tube to rotate the outer tube and 3 boxes; on the other side, another motor would be attached to the end of the inner rod to rotate the inner rod along with the other 3 boxes.

The mass moment of inertia equation for a box, I_{box}, is shown in Equation 4-25 with m representing the mass of the box, and a and b respectively representing the width and height of the box's face that is perpendicular to the central axis of rotation.

$$I_{box} = \frac{1}{12}m(a^2 + b^2) \quad 4\text{-}25$$

With a projected mass, width, and height of 0.454 m (1 lb), 0.305 m (12"), and 0.0762 m (3"), respectively, the total mass moment of inertia for one box was estimated at 3.74 g*m^2. The mass moment of a tube, I_{tube}, is shown in Equation 4-26 with m, r_1, and r_2 representing the mass of the tube, the inner radius of the tube, and the outer radius of the tube. If the tube is actually a rod, the equation can be accordingly adjusted by making $r_1 = 0$.

$$I_{tube} = \frac{1}{2}m(r_1^2 + r_2^2) \quad 4\text{-}26$$

With a projected mass of 0.329 kg, outside diameter of 15.9 mm (0.625"), and tube thickness of 1.47 mm (0.058"), the mass moment of inertia for the outside tube was estimated at 0.0172 g*m^2. With a projected mass of 0.352 kg and diameter of 9.53 mm (0.375"), the mass moment of inertia of the inner rod was estimated at 0.00399 g*m^2.

As mentioned, each motor will be attached to either a rod or tube: both carrying three boxes respectively. The total mass moment of inertia will therefore be the summation of 3 boxes and one tube or rod. However, as the outer tube and inner rod have mass moments of inertia that are respectively 0.15% and 0.036% of that of 3 boxes, the mass moments of inertia of the outer tube and inner rod are therefore considered negligible. The total mass moment of inertia will therefore be assumed to be that of three boxes: 11.2 g*m^2.

4.7.2 Angular Acceleration

The angular acceleration was estimated using the maximum desired angular velocities along with the desired times for the motor to reach said angular velocities. The @lab

wanted the maximum rotation speed of the boxes to be about 1 revolution per second which is equivalent to 2π rad/s. Wanting the boxes to reach this speed in 0.25 s, the maximum required angular acceleration was calculated to be 25.1 rad/s^2. It should be noted, however, that this estimation assumes that the angular acceleration is constant over the period of acceleration.

4.7.3 Final Torque Estimations

Using the estimated mass moment of inertia of 11.2 g*m^2 and estimate angular acceleration of 25.1 rad/s^2, the torque specification was estimated at 0.282 N*m. However, it is very important to note that this specification completely negates the friction between the inner rod and outer tube. Separating the tube and rod are rapid prototyped bushings made from ABS plastic. These bushings are located at the slits where the inner rod is exposed. As the tube and rod rotate relative to one another, the bushings will rub against the slits, causing a frictional force that will resist the rotation. To calculate these frictional forces, one would need the coefficient of friction between aluminum and the ABS plastic along with the normal forces being applied at the area of contact. The true coefficient of friction would need to be found through experimentation, but Elert (2005) estimates the coefficient of friction between aluminum and plastic to be 0.4 (Elert, Coefficients of Friction for Aluminum, 2005). Using this coefficient of friction along with the normal force of the rod and 3 boxes, 16.8 N, the additional frictional force was calculated to be 6.72 N. Multiplying the estimated friction force with the inner radius of the outer tube gives 0.0435 N*m: the additional torque needed to overcome the frictional force. The total torque required by the motor is therefore 0.325 N*m.

Although the total projected torque includes both inertial and frictional forces, several assumptions had to be made for its estimation. Some assumptions have already been mentioned such as constant acceleration, the value of the coefficient of friction, and negating the weight of the tube and pole when calculating the moment of inertia; however, other assumptions include presuming that the tube and rod are perfectly straight, that there is no debris between the bushings such as dust or particulate matter,

that the slits have been adequately deburred, and that the bushings are loosely positioned in the outer tube without any induced pressure. As it is quite unlikely for all of these assumptions to be valid, the estimated torque should be multiplied by a safety factor to account for unexpected increases in torque. Using a safety factor of 3.07, it was recommended to get a motor with a torque capability of at least 1.0 N*m.

CHAPTER 5. INVESTIGATING THE POTENTIAL TO HARVEST POWER FROM HUMAN FOOT TRAFFIC USING PIEZOELECTRIC MATERIALS

5.1 PIEZOELECTRIC MATERIALS: AN OVERVIEW

Pierre and Jacques Curie are widely credited for discovering piezoelectricity in 1880 (Uchino & Ito, 2009) after experimenting with Rochelle Salt. It was shown that Rochelle Salt produced an electric potential upon applying a mechanical stress. This effect was deemed the piezoelectric effect; piezo being derived from piezen: Greek for "to press". The produced electric potential was shown to be directly proportional to the applied mechanical stress. It was later demonstrated that piezoelectric materials also exhibited the converse effect, *i.e.*, they deform (strain) in proportion to an applied electric field.

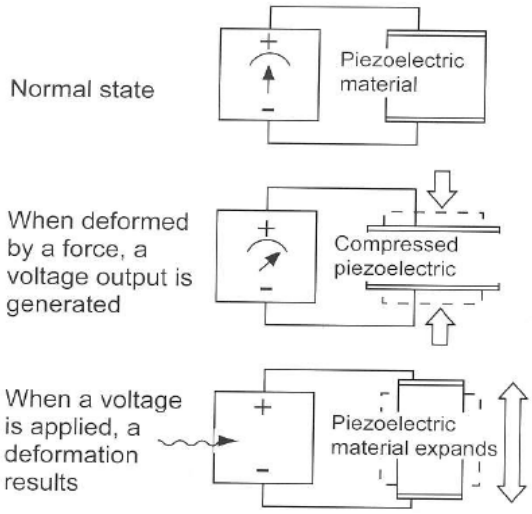

Figure 5-1: The Piezoelectric Effect and Converse Piezoelectric Effect. Known as the piezoelectric effect, a piezoelectric material produces an electric potential after applying a mechanical stress (pictured in center). The converse piezoelectric effect is a piezoelectric material's ability to deform after applying an electric field. Photo extracted from (Addington & Schodek, 2005)

Both the piezoelectric effect and converse piezoelectric effect are illustrated in Figure 5-1. Using the piezoelectric effect, one can use piezoelectric materials as pressure and touch sensors, producing a measureable voltage that is proportional to the applied pressure. Likewise, the converse piezoelectric effect can be exploited to use piezoelectric materials as actuators, producing a deformation after applying a voltage. Piezoelectric materials can experience a 4% change of volume from the piezoelectric effect (Introduction: the piezoelectric effect, 2007).

Interest in piezoelectric materials grew due to the onset of World War I when the submarine was used against Great Britain in an attempt to destroy the trade routes that supplied the nation. To combat the submarine, a Frenchman named Langevin developed a transducer that used a piezoelectric crystal to produce a mechanical signal and measure its electrical response as a means of locating submarines: work that would be the basis of SONAR (Leo, Introduction to Smart Material Systems, 2007). Further developments in piezoelectric (PE) materials occurred in the next world war with improvements in SONAR and the use of PE materials as electronic oscillators and filters. The need for better PE materials motivated the development of synthetic materials that exhibited PE properties including barium titanate and lead-zirconate-titanate. These synthetic materials were then used in various applications such as ceramic filters for communications and radio, and phonograph cartridges for record players (Leo, Introduction to Smart Material Systems, 2007). Other modern uses for piezoelectric materials include microphones, auto-focus lens drivers, speakers, charcoal grill fire starts, vibration reducing skis, doorbell pushers, position sensors, and actuators for MEMs applications (Addington & Schodek, 2005). With regards for architectural applications, PE materials are most often used as sensors; they can be used for measuring both static and dynamic phenomena. PE materials can be used for structural health monitoring including vibration monitoring as they have a wide dynamic range and can be used for measurements over a wide frequency range. Although PE materials are generally used for local measurements, they can be placed in arrays to produce more distributed measurements. Piezoelectrics have proven effective in vibration control because of their capabilities for serving both as sensors and actuators; both passive and active approaches are in use.

5.1.1 Types of piezoelectric materials

Piezoelectricity can occur in natural or synthetic materials. In general, materials that naturally possess piezoelectricity are anisotropic and include materials such as quartz, Rochelle salt, ammonium phosphate, paraffin, bone, and even wood (Jalili, 2010b). Synthetically created piezoelectric materials typically come in two forms: ceramics and polymers. Ceramics, the vast majority being part of the lead-zirconate-titanate (PZT)

family, can be regarded as randomly oriented piezoelectric crystals (Culshaw, 1996). PZT-based ceramics have two principal benefits: they furnish materials with high piezoelectric activity, and can be molded into a wide variety of shapes. The properties of PZT can also be optimized to suit special applications by adjusting the zirconate/titanate ratio. However, for many applications, PZT-based ceramics possess significantly high mechanical impedances that can null their strong piezoelectric properties. In these situations, it is favourable to use composites of piezoelectric materials with polymers to furnish the appropriate combination of impedance matching and strain field distribution sensitivity (Culshaw, 1996). The most widely used polymer is polyvinylidene fluoride, more commonly known as PVDF. The dielectric strength of PVDF polymers is about 20 times higher than that of PZT, thus allowing them to endure much higher electric field strengths in comparison to PZT materials (Jalili, 2010b). PVDF are also excellent piezoelectric sensors when flexibility and lightweight attributes are required as PZT tends to be quite brittle and heavy by comparison. Although PVDF copolymers have found uses in various applications such as ultrasonic transducers, hydrophones, microphones, and vibration damping, their low stiffness and electromechanical coupling coefficients have limited their use (Jalili, Physical Principles and Constitutive Models of Piezoelectric Materials, 2010b). Various properties for piezoelectric ceramics and polymers are shown below in Table 5-1. Many of the associated properties will be explained in later sections.

Table 5-1: Properties of Piezoelectric Materials (Extracted from) (Culshaw, 1996)

Property	Units	Ceramics				β phase Polymer PVDF (typical
		PZTA	PZTB	$Na^1/2K^1/2NbO_3$	$LiNbO_3$	
Density	$x10^3$ kg/m^3	7.9	7.7	4.5	4.64	1.78
Curie Temperature	°C	315	220	420	1210	100
Modulus of Elasticity	GPa	~70	~70	~100	~100	2
Maximum Strain	με	1000	1000	1000	1000	700
$\mathbf{d_{31}}$	pC/N	-119	-234	-50	-0.85	+20
$\mathbf{d_{33}}$	pC/N	268	480	160	160	-33
$\mathbf{d_{15}}$	pC/N	335	-	-	-	-
$\mathbf{k_{31}}$	0.33	0.39	0.27	0.02	0.12	
$\mathbf{k_{33}}$	0.68	0.72	0.53	0.17	0.19	
$\mathbf{k_{15}}$	0.68	0.65	-	0.61	-	
ε_r	-	1200	2800	500	29/85	12
Breakdown Field	V μm^{-1}	~1	~1	~	~1	~100

Recently, another form of PE materials has been developed: piezoelectric fibre composites. Like the name suggests, PE fibre composites consist of small diameter (10 to 250μm) embedded within a composite matrix. Traditionally using PZT ceramic materials, Advanced Cerametrics Inc. (ACI) produces their PE fibre composites via a patented low-cost technology called the Viscose Suspension Spinning Process (VSSP) (Advanced Cerametrics Inc., 2009). VSSP is able to form continuous fibres of virtually any ceramic material including bioceramics, structural ceramics, and electroactive ceramics such as piezoelectric and electrostrictive materials. Compared to traditional PE ceramics, ACI claims that PE fibre composites are more robust, flexible, have higher repeatability, weigh 35% less, and have much better lifetimes having demonstrated an operation of over 200 million cycles without degradation in piezoelectric properties (Advanced Cerametrics Inc., 2009). Table 5-2 lists the various properties of ACI's PZT fibres.

Table 5-2: Physical and Electrical Properties of ACI's PE fibres (PZT)

Property	Units	PZT-8 (Hard)	PZT-5A (Soft)	PZT-5H (Soft)
Density	g/cm^3	7.5	7.5	7.5
Modulus of Elasticity	$x\ 10^{10}\ N/m^2$	9.3	6.6	6.4
Curie Temperature	°C	300	350	190
Mechanical Q	-	900	100	65
Relative Dielectric Constant, ε_r (kHz)	-	1100	1725	3450
Dissipation Factor (kHz)	-	0.3	2.0	2.0
k_{31}	-	0.33	0.36	0.38
k_p	-	0.56	0.62	0.64
k_{33}	-	0.66	0.72	0.75
k_{15}	-	0.59	0.69	0.68
d_{31}	$x\ 10^{-12}$ m/V	-107	-173	-262
d_{33}	$x\ 10^{-12}$ m/V	241	380	583
d_{15}	$x\ 10^{-12}$ m/V	382	582	730
g_{31}	$x\ 10^{-3}$ Vm/N	-10.9	-11.5	-8.6
g_{33}	$x\ 10^{-3}$ Vm/N	24.8	25.0	19.1
g_{15}	$x\ 10^{-3}$ Vm/N	28.7	38.2	28.9
S_{11}^E	$x\ 10^{-12}\ m^2/N$	10.8	15.2	15.6
S_{12}^E	$x\ 10^{-12}\ m^2/N$	-3.6	-5.3	-4.7
S_{33}^E	$x\ 10^{-12}\ m^2/N$	13.7	18.3	19.8

5.1.2 Crystallographic Structure and Mechanisms

The key to the piezoelectric effect's mechanism lies within the atomic structure. A piezoelectric material has two phases, one below and the other above the corresponding Curie temperature. The phase above the Curie temperature is known as the paraelectric phase while the phase below the Curie temperature is known as the ferroelectric phase. A typical piezoceramic governed by the general formulation $A^{2+}B^{4+}O_3^{2-}$ is cubic during its paraelectric phase, but tetragonal during its ferroelectric phase (see Figure 5-2). In the general formulation, the A denotes a large divalent metal ion such as lead or barium, the B stands for a tetravalent metal ion such as zirconium or titanium, and O represents oxygen. Using PZT as an example, when at its paraelectric phase, the atom is quite stable having a net dipole moment of 0 as all the positive charged ions (Pb^{2+} and Zr^{4+}/Ti^{4+}) coincide with the negatively charged O^{2-} ions. However, as the atom cools to its ferroelectric phase, the atoms move out of alignment causing a net dipole moment. This dipole moment is what causes the piezoelectric effect and converse piezoelectric effect. If one applied an electric field to the dipole moment, the atom would want to align itself accordingly in the direction of the electric field. Likewise if one applied pressure to the dipole moment causing it to misalign, this would in turn change the net dipole moment causing an electric potential to envelope.

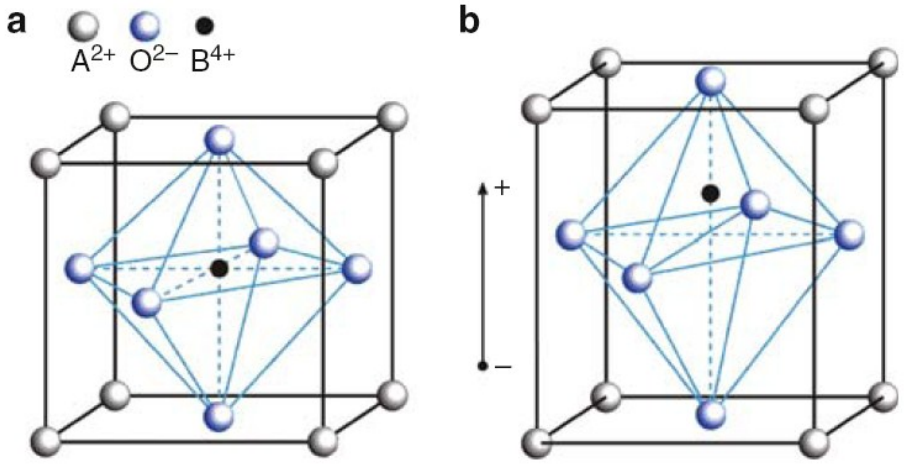

Figure 5-2: Schematic of a piezoelectric dipole in the general $A^{2+}B^{4+}O_3^{2-}$ before and during poling. Above the Curie Temperature (left) the material has a symmetric cubic crystal structure; below the Curie Temperature (right) the material becomes tetragonal resulting in an electric dipole. Photo extracted from (Jalili, An Overview of Active Materials Utilized in Smart Structures, 2010)

Figure 5-3 and Figure 5-4 respectively illustrate a piezoelectric material's extension and shear actuation mechanisms. When an electric field (denoted as E in Figure 5-3 and Figure 5-4) is applied in the poling direction (denoted P), the material elongates along the poling direction. The dipole's positive segments are attracted to the negative portion of the field while the negative segments are attracted to the positive portion of the field. The dipole thus naturally elongates as each section is attracted in opposite directions away from the dipole center. If the electric field was applied in a direction opposite to the poling direction, the dipoles would naturally contract as the dipole segments would be repelled towards the dipoles center. For a piezoelectric material to exhibit shear, the field must be applied perpendicular to the poling direction. This situation induces the positive dipole segments to rotate towards the negative portion of the electric field while simultaneously inducing the negative dipole segments to rotate towards the position portion of the electric field. The net reaction is shear displacement along the piezoelectric material.

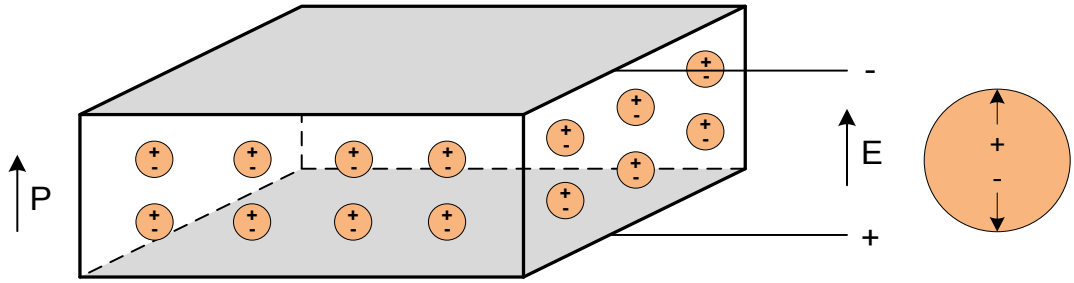

Figure 5-3: The Extension Actuation Mechanism. Extracted from (Raja, 2007)

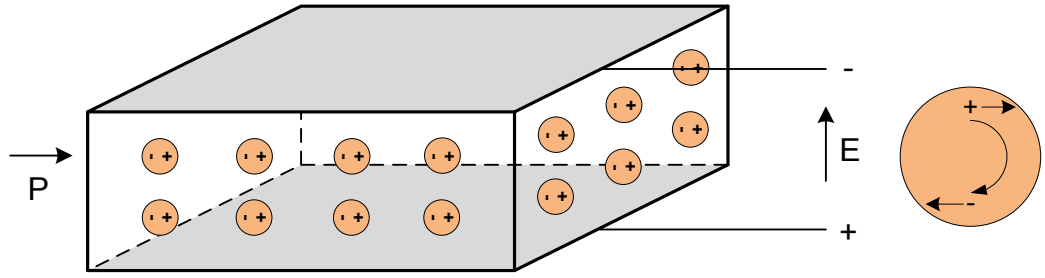

Figure 5-4: Shear Actuation Mechanism. Extracted from (Raja, 2007)

Figure 5-5 illustrates the direct piezoelectric effect when short circuited. Essentially, the direct piezoelectric effect causes a charge to envelope over the material's attached electrodes due to mechanical changes in the material's dipole moments. In the event that the force causes tension, as shown in the left image of Figure 5-5, the dipole moment will be elongated resulting in induced voltages across the materials' dipoles. The induced electric field is in the direction of the dipole's natural electric field which is opposite to the poled electric field. In an attempt to return the dipoles to a neutral state during an applied tensile stress, the negative pole's electrode attracts electrons from the surrounding environment while the positive poles force the attached electrodes to donate electrons to the surrounding environment. Similar to a capacitor, the piezoelectric material stores these built up charges on the attached electrode plates as an electric potential until it has a reason to dissipate. If the material is short circuited (as shown in Figure 5-5), the excess electrons on the negative pole electrode go to the positive pole electrode, inducing an electric current that dissipates once the charges across the electrodes have been neutralized. Once the tensile force has been released, the electrons will return to the negative pole electrode, again causing a direct electric current (in the opposite direction) that dissipates once the electrodes have been neutralized and the PE material's dipoles have returned to their un-stressed state.

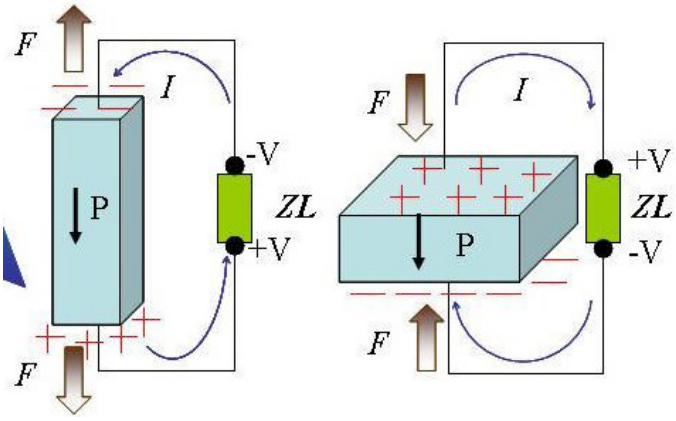

Figure 5-5: The Direct Piezoelectric Effect. Image Extracted from (Hsu, 2006)

Alternatively, if the force causes a compressive stress, as shown in the right image of Figure 5-5, the dipole moment will be shortened. When shortened, the dipole wants to return to its previous state; each pole thus attracts ions of opposing charges wanting to lengthen the dipole moment. The negative pole thus causes its associated electrode to

donate electrons to the surrounding environment while the positive pole causes its electrode to attract electrons from its surrounding environment. This results in an induced electric field across the electrodes that is in the same direction as the poling direction. If the piezoelectric material is short circuited, the excess electrons on the positive pole electrode will flow to the negative pole electrode, inducing an electric current until the electrodes' charges have been neutralized. Once the compressive force has been released, the electrons will return to the positive pole electrode, again causing a direct electric current (in the opposite direction) that dissipates once the electrodes have been neutralized and the dipoles have returned to their un-stressed state.

A piezoelectric material can lose its piezoelectric effects if a very strong electric field is applied in the opposite direction of polarization, if a high mechanical stress is applied to the material resulting in the distortion of the dipoles' alignment, or if the material is heated above its Curie temperature. In most practical applications, the working temperature of piezoceramics is kept below half of the Curie temperature to avoid permanent damage (Jalili, 2010b).

5.1.2.1 POLING

Initially, the atomic dipoles throughout a piezoelectric material are randomly oriented. This random orientation almost cancels out the piezoelectric effect as dipoles are arranged in every direction imaginable. Through a process known as poling, these dipoles can be aligned in a uniform direction to maximize the piezoelectric effect. In poling, the material is heated above or slightly below the Curie temperature where it has no dipole moment. A very strong electric field, typically on the order of 1 MV/m (Culshaw, 1996), is then applied. The dipoles then shift into alignment with the field direction known as the poling direction. While maintaining the electric field, the piezoelectric material is then cooled below the Curie point where the dipoles are permanently fixed. The material's dipoles are now "poled" in a uniform direction. Figure 5-6 shows a schematic of a piezoceramic material before and after the poling process. Before poling, the ceramic consists of regions with different orientations of

spontaneous polarization known as ferroelectric domains which amalgamate to a net zero piezoelectric effect. After poling, the polarization within the domains and grains are strongly aligned with the applied electric field enabling the material to uniformly react to an electric field or applied stress.

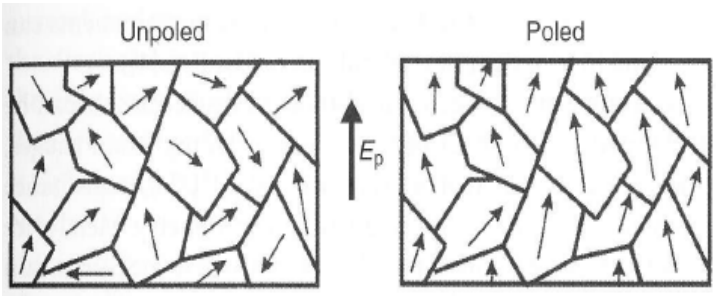

Figure 5-6: Schematic of the poling process in piezoelectric ceramics. Ceramics naturally have randomly oriented polarization (left). After poling, domains are aligned in the applied electric field direction. (Kholkin, Kiselev, Kholkine, & Safari, 2009)

5.1.2.2 DOPING

Doping refers to the adding of ions to piezoelectric ceramics to control and alter their electromechanical properties. As little as 0.1% of a dopant may be sufficient to considerably affect a material's properties (LC Ceramics Laboratory, 2009). Affected properties include switching & hysteresis behavior, leakage current, frequency dispersion, and non-linearity of electromechanical properties with respect to the driving field (LC Ceramics Laboratory, 2009). Piezoelectric ceramics are generally separated in "hard" and "soft" categories. Referring to the ABO_3 formulation presented earlier (See Figure 5-2), hard piezoceramics are doped with acceptor ions such as K^+ or Na^+ at the A site or Fe^{3+}, Al^{3+}, or Mn^{3+} at the B site; while soft piezoceramics are doped with donor ions such as La^{3+} at the A site, or Nb^{5+} or Sb^{5+} at the B site (Kholkin, Kiselev, Kholkine, & Safari, 2009). The antonyms "soft" and "hard" piezoelectric ceramics refer to the ferroelectric properties, *i.e.* the mobility of the dipoles or domains and hence also to the polarization/depolarization behaviour. Soft piezo ceramics are characterized by a comparatively high domain mobility and a resulting "ferroelectrically soft" behaviour, *i.e.* relatively easy polarization. Soft PZT materials (typically abbreviated as PZT 5H) are thus favoured for higher deformations and are advantageous in regards to their large strain constants, moderate permittivities and high coupling coefficients. Disadvantages

include greater hysteresis and susceptibility to depolarization or other forms of deterioration (APC International Ltd., 2011). Soft piezoelectrics are often used as actuators for micropositioning and nanopositioning, and as sensors for vibrational pickups, and ultrasonic transmitters and receivers for flow or level measurement (PI Ceramic GmbH, 2009). In contrast, ferroelectrically "hard" PZT materials (typically abbreviated as PZT 4) can be subjected to high electrical and mechanical stresses. The stability of their properties destines them for high-power applications (PI Ceramic GmbH, 2009). Hard piezoelectric ceramics are advantageous with regards to their moderate permittivity, large coupling coefficients, high qualities and very good stability under high mechanical loads and operating fields. They are used in ultrasonic cleaning (typically in the kHz frequency range) and ultrasonic processors (PI Ceramic GmbH, 2009). Table 5-3 below summarizes the differences between "soft" and "hard" piezoelectric ceramics.

Table 5-3: A Comparison between Soft and Hard Doped Piezoelectric Ceramics. Extracted and modified from (APC International Ltd., 2011)

Characteristic	Soft-Doped	Hard-Doped
Stain Constants (d)	Larger	Smaller
Permittivity	Higher	Lower
Dielectric Constants (ε)	Larger	Smaller
Dielectric Dissipation Factor (tanδ)	Higher	Lower
Electromechanical Coupling Coefficients (k)	Larger	Smaller
Electrical Resistance	Very High	Lower
Mechanical Quality Factors (Q_m)	Low	High
Coercive Force	Low	Higher
Linearity	Poor	Better
Polarization / Depolarization	Easier	More Difficult

5.1.3 Properties and Nomenclature

Piezoelectric materials have different properties in the poling direction in comparison to the remaining two transverse directions. These properties include traditional material properties such as moduli of elasticity but also properties exclusive to piezoelectric materials such as strain constants and electromechanical coupling constants. Both the traditional and exclusive properties are dependent on the direction of deformation and

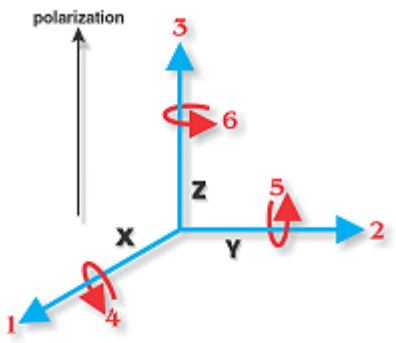

Figure 5-7: Piezoelectric Nomenclature uses a 1, 2, 3 axis system similar to the common x, y, z system. The polarization direction is always the 3-direction. Extracted from (APC International, Ltd., 2012)

electric field direction. It would therefore be beneficial in incorporating these two factors within the material constants themselves.

In light of this, researchers devised a 1, 2, 3 coordinate system that is analogous to the traditional X, Y, Z coordinate system. The coordinate system is illustrated in Figure 5-7. The polarization axis in this system is always represented as the 3-axis. Likewise, 4, 5, and 6 represent rotations around the x, y, and z axis respectively. To highlight the respective deformation and electric field directions, piezoelectric coefficients have double subscripts, the first being the electric field direction while the other being the direction of the resultant mechanical stress or strain. As an example, d_{31} represents the strain developed in the 1 direction when an electric field is applied in the poling direction. Several other piezoelectric constants have superscripts to signify the boundary conditions. The superscripts σ, E, D, and S signify the following:

σ = Constant Stress, Mechanically Free

E = Constant Field, Short Circuit

D = Constant Electrical Displacement, Open Circuit

S = Constant Strain

As an example, Y_{33}^{E} represents the modulus of elasticity in the polarization direction when a constant electric field is applied in the poled direction. This section will give an overview of four widely used piezoelectric properties: strain constants, voltage constants, moduli of elasticity, and electromechanical coupling constants. Figure 5-8 illustrates the open and closed circuit scenarios.

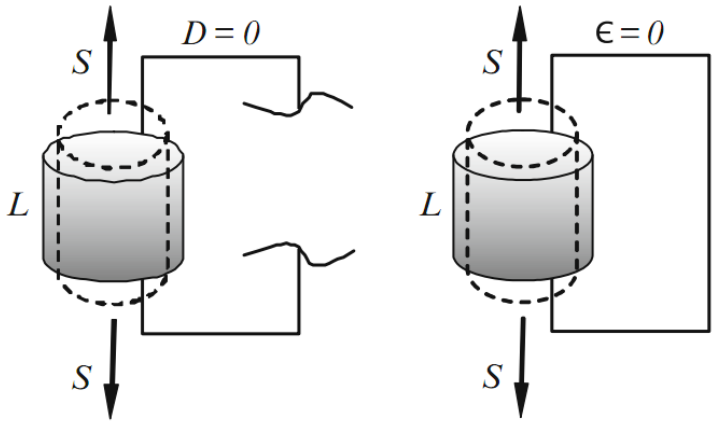

Figure 5-8: Schematic of (left) open circuit (OC or D = 0), and (right) short circuit (SC or E = 0). Extracted from (Jalili, 2010b)

5.1.3.1 STRAIN CONSTANTS ("D" COEFFICIENTS)

Having units of meters per volt, the strain constants (also known as "d" coefficients) are measurements of the converse piezoelectric effect as they relate the mechanical strain produced by an electric field. With units of coulombs per Newton, strain constants are also used to measure the piezoelectric effect through relating the charge collected by attached electrodes to an applied stress. Both relationships are presented below in Equations 5-1 and 5-2 and show that both the piezoelectric effect and converse piezoelectric represent linear relationships. However, at sufficient levels of applied stress, the relationship will be nonlinear due to the saturation of electric dipole motion (Leo, Piezoelectric Materials, 2007).

$$d\left(\frac{m}{V}\right) = \frac{strain\ developed}{applied\ electric\ field} = \frac{\varepsilon}{E} \qquad 5\text{-}1$$

$$d\left(\frac{C}{N}\right) = \frac{short\ circuit\ charge\ density}{applied\ mechanical\ stress} = \frac{D}{\sigma} \qquad 5\text{-}2$$

Table 5-4 gives various strain constants for Hard and Soft PZT materials. As already mentioned, an induced electric field in the poling direction will cause the material to expand in the poling direction. Likewise the material's length in the transverse directions will decrease due to the inflicted transverse strain. The resultant strain constants should therefore be positive for the longitudinal direction (d_{33}) and negative for the transverse

direction (d_{31}). For shear deformation to occur, the electric field must be perpendicular to the poling direction. The PE material's dipoles will consequently rotate to develop the shear deformation. As the shear strain coefficient, d_{15}, typically has the largest values among the d coefficients, this property can be exploited to produce effective shear actuators and sensors. The longitudinal/transverse and shear deformations are illustrated in Figure 5-9. In comparing hard and soft PZT, the soft PZT have higher strain constants which are to be expected as they are designed to have larger deformations.

Table 5-4: Strain Constants for Hard and Soft PZT. Data from (APC International, Ltd., 2012)

	d_{33} (m/V)	d_{31} (m/V)	d_{15} (m/V)
Hard PZT	215 e-12	-95 e-12	330 e-12
Soft PZT	600 e-12	-275 e-12	720 e-12

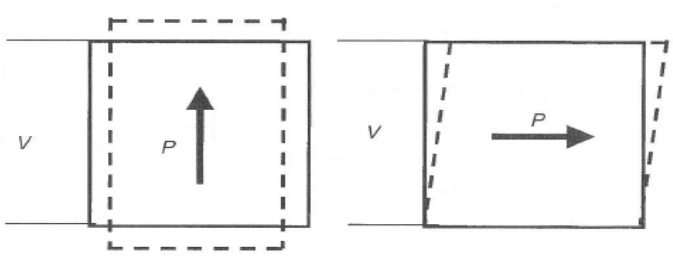

Figure 5-9: (Left) Longitudinal and Transverse Deformations under applied electric field. (Right) Shear Deformation under applied electric field.

5.1.3.2 VOLTAGE CONSTANTS ("G" COEFFICIENTS)

The voltage constants, also known as the "g" coefficients, are a measurement of the piezoelectric effect as they relate the electric field produced by an applied stress. This relationship is presented below as Equation 5-3 and has units of volts per Newton-meter. Voltage constants can also be used to model the converse piezoelectric effect as the ratio between the developed strain over an applied charge density. This relationship is presented below as Equation 5-4 and has units of square meters per coulomb. Akin to the strain constants, the voltage constants demonstrate a linear relationship between variables.

$$g\left(\frac{V}{N*m}\right) = \frac{open\ circuit\ electric\ field}{applied\ mechanical\ stress} = \frac{E}{\sigma} \quad 5\text{-}3$$

$$g\left(\frac{m^2}{C}\right) = \frac{strain\ developed}{applied\ charge\ density} = \frac{\varepsilon}{D} \quad 5\text{-}4$$

High voltage constants are favourable for large electric field outputs; essential for sensory applications. Table 5-5 shows typical voltage constants of hard and soft materials.

Table 5-5: Voltage Constants for Hard and Soft PZT. Data from (APC International, Ltd., 2012)

	g_{33} (m^2/C)	g_{31} (m^2/C)	g_{15} (m^2/C)
Hard PZT	25 e-3	-10 e-3	28 e-3
Soft PZT	21 e-3	-9 e-3	27 e-3

Equation 5 below presents how strain constants and voltage constants are related where ϵ and ϵ_0 respectively represent the relative permittivity of the piezoelectric material and the permittivity of free space (8.854e-12 F/m). Using this information, one can substitute this equation into the related constitutive equations to eliminate the need for voltage constants.

$$g_{ij} = {}^{d_{ij}}/_{\epsilon_0 \epsilon} \qquad 5\text{-}5$$

5.1.3.3 MODULI OF ELASTICITY

Like traditional materials, piezoelectric materials have moduli of elasticity. However, unlike traditional materials, piezoelectric materials have two moduli of elasticity for each direction, one for a constant field (short circuit), and one for a constant electric displacement (open circuit). Assuming that the moduli of elasticity for the 1 and 2 directions are the same, a piezoelectric material traditional has four moduli of elasticity:

Y_3^E = Ratio of stress to strain in 3-direction at constant field E (electrodes shorted)

Y_3^D = Ratio of stress to strain in 3-direction with electrodes open circuited

Y_1^E and Y_1^D are the moduli in the 1 or 2 direction

Y_5^E and Y_5^D are the ratios of shear stress to shear strain

Table 5-6 below shows typical moduli of elasticity at constant electric fields for both hard and soft PZT. Piezoelectric materials are generally stiffer in the transverse directions than the poling direction and hard PZT have greater moduli of elasticity in comparison to

soft PZT. This is to be expected as hard PZT are designed to withstand greater amounts of mechanical stress.

Table 5-6: Moduli of Elasticity for Hard and Soft PZT. Data from (APC International, Ltd., 2012)

	Y_1^E (GPa)	Y_3^E (GPa)
Hard PZT	90 e-3	72 e-3
Soft PZT	59 e-3	51 e-3

5.1.3.4 ELECTROMECHANICAL COUPLING COEFFICIENT

Shown in Equations 5-6 and 5-7, the electromechanical coupling coefficients describe the energy conversion by the piezoelectric material be it mechanical to electrical of vice versa. They essentially measure the piezoelectric material's efficiency.

$$k = \sqrt{\frac{electrical\ energy\ converted\ into\ mechanical\ energy}{electrical\ energy\ applied}} \quad 5\text{-}6$$

$$k = \sqrt{\frac{mechanical\ energy\ converted\ into\ electrical\ energy}{mechanical\ energy\ applied}} \quad 5\text{-}7$$

Subscripts denote the relative directions of electrical and mechanical quantities as well as the kind of motion involved. They can be associated with vibratory modes of certain transducer shapes. k_{33} is appropriate for a long thin bar polarized along its length, excited by an applied electric field along its length, and goes through simple expansion and contraction. k_{31} is relates to a long thin bar, electroded along is large faces, polarized in thickness, and goes through simple contraction and expansion. k_{15} describes the energy conversion in shear vibration. k_p refers to the electromechanical coupling in a thin round disk, polarized in thickness and vibrating in radial expansion and contraction. Table 5-7 below shows the various coupling coefficients for hard and soft materials. The table suggests that soft PZTs are have better efficiencies for deformation along the poling axis, but hard PZTs have better efficiencies for transverse and shear deformations.

Table 5-7: Electromechanical Coupling Constants for Hard and Soft PZT. Data from (APC International, Ltd., 2012)

	k_p	k_{33}	k_{31}	k_{15}
Hard PZT	0.50	0.62	0.30	0.55
Soft PZT	0.68	0.76	0.40	0.66

Using an equivalent circuit like the one shown in Figure 5-10, one can derive the electromechanical coupling coefficients through measuring its corresponding parallel and series resonant frequencies, f_p and f_s.

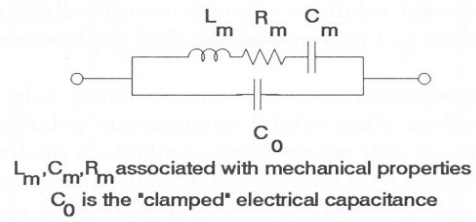

Figure 5-10: The equivalent circuit for a piezoelectric plate operating near resonance (Extracted from (Culshaw, 1996))

For example, the k_{33} electromechanical coupling constant can be calculated using the following equation (from (Kholkin, Kiselev, Kholkine, & Safari, 2009):

$$k_{33} = \pi/2 * f_s/f_p \tan\left[\frac{\pi(f_p - f_s)}{4}\right] \quad 5\text{-}8$$

For static/low frequency loading, the electromechanical coupling coefficients can be derived using the material's strain and voltage constants. k_{33} can be used to find d_{33} through Equation 5-9 where ϵ_{33} is the material's low-frequency dielectric constant and S_{33} is the elastic compliance (note that $S_{33} = (1/Y_{33})$.

$$d_{33} = k_{33}(\epsilon_{33} S_{33})^{1/2} \quad 5\text{-}9$$

Likewise, the other strain constants, d_{31} and d_{15} can be found using the other two coupling coefficients, k_{31} and k_{55}:

$$d_{31} = k_{31}(\epsilon_{33} S_{11})^{1/2} \quad 5\text{-}10$$

$$d_{15} = k_{15}(\epsilon_{11} S_{55})^{1/2} \quad 5\text{-}11$$

5.1.4 Hysteresis

Throughout this section, it has been said that a piezoelectric material's deformation linearly correlates with the associated electric field. Although this assumption is fair, it is not entirely factual. For example: the electric field-induced strain as seen in Figure 5-11. When initially applying a proportionally increasing electric field, the resultant strain is

predominantly linearly increasing as well. However, if one subsequently linearly decreases said electric field, a hysteresis loop appears. This implies that the linear relation is not apparent once the piezoelectric material relaxes from its excited state.

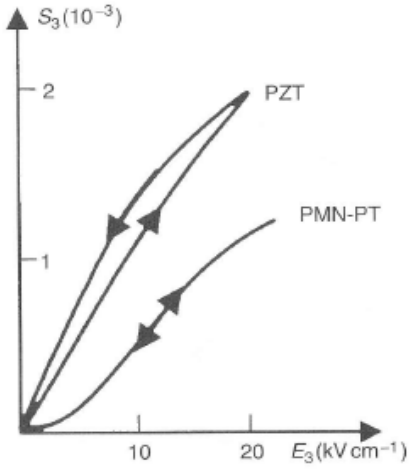

Figure 5-11: Comparison of the electric field-induced strain in typical piezoelectric (PZT) and relaxor (0.9PMN-0.1PT) ceramics. Extracted from (Kholkin, Kiselev, Kholkine, & Safari, 2009)

However, there are electrostrictive ceramics known as relaxors that have negligible hysteresis. As shown in Figure 5-11, the electric-field induced strain curve of the relaxor, PMN ($PbMg_{1/3}Nb_{2/3}O_3$), shows very little hysteresis when relaxing from its excited state, but as mentioned in Section 2.3.3.5, an electrostrictive's strain-electric field relationship is quadratic thus adding complexity in predicting their behaviour.

5.1.5 Equilibrium and Constitutive Equations

Traditional materials are stressed through an applied strain. Piezoelectric materials, however, are stressed from applied strain and an applied electric field. Likewise, piezoelectric materials develop electric charge densities after an applied strain. Traditional constitutive and equilibrium equations need to factor in these additional relationships. This section will give an overview of the constitutive and equilibrium equations of piezoelectric materials.

5.1.5.1 EQUILIBRIUM EQUATIONS

In the absence of body forces, piezoelectric materials share the traditional stress equilibrium equations presented as Equations 5-12 through 5-14. As the constitutive equations also include the calculation of the electric displacement vector, there exists an additional equilibrium equation upon which the piezoelectric material must adhere to. Shown below as Equation 5-15, the additional equilibrium equation states that the

summation of the partial derivates of the electric displacement vector in relation to their displacement along their respective axis must be equal to zero providing there are no body charges present.

$$\frac{\partial \sigma_{11}}{\partial x} + \frac{\partial \sigma_{12}}{\partial y} + \frac{\partial \sigma_{13}}{\partial z} = 0 \quad 5\text{-}12$$

$$\frac{\partial \sigma_{12}}{\partial x} + \frac{\partial \sigma_{22}}{\partial y} + \frac{\partial \sigma_{23}}{\partial z} = 0 \quad 5\text{-}13$$

$$\frac{\partial \sigma_{13}}{\partial x} + \frac{\partial \sigma_{23}}{\partial y} + \frac{\partial \sigma_{33}}{\partial z} = 0 \quad 5\text{-}14$$

$$\frac{\partial D_1}{\partial x} + \frac{\partial D_2}{\partial y} + \frac{\partial D_3}{\partial z} = 0 \quad 5\text{-}15$$

5.1.5.2 CONSTITUTIVE EQUATIONS

Working within the framework of linear piezoelectricity, two forms of constitutive equations are commonly used in engineering practice. The first set of constitutive equations calculates the strain and electric displacement in terms of the applied electric field and applied stress. The equations are presented below in matrix form:

$$\begin{Bmatrix} \varepsilon \\ D \end{Bmatrix} = \begin{bmatrix} S & d \\ d & \epsilon \end{bmatrix} \begin{Bmatrix} \sigma \\ E \end{Bmatrix} \quad 5\text{-}16$$

Inverting this equation to make stress and electric field the dependent variables and strain and electric displacement the independent variables yields:

$$\begin{Bmatrix} \sigma \\ E \end{Bmatrix} = \frac{1}{S\epsilon - d^2} \begin{bmatrix} \epsilon & -d \\ -d & S \end{bmatrix} \begin{Bmatrix} \varepsilon \\ D \end{Bmatrix} \quad 5\text{-}17$$

If one substitutes the piezoelectric coupling coefficient equation (Equation 5-9 through 5-11) into the above equation, one would get:

$$\begin{Bmatrix} \sigma \\ E \end{Bmatrix} = \frac{1}{1 - k^2} \begin{bmatrix} {}^{1}/_{S} & -{}^{k^2}/_{d} \\ -{}^{k^2}/_{d} & {}^{1}/_{\epsilon} \end{bmatrix} \begin{Bmatrix} \varepsilon \\ D \end{Bmatrix} \quad 5\text{-}18$$

The inversed compliance tensor (1/S) can be rewritten as an elastic stiffness tensor (C). Another common form (although generally less used than the former) of constitutive equations have stress and electric displacement as dependent variables, strain and electric field as the independent variables, and a new variable called the piezoelectric constant

tensor, e, that symbolizes the assumed linear relationship between the electric displacement and induced strain. These equations are presented below:

$$\sigma = \mathrm{C}^{\mathrm{E}}\varepsilon - e_t E \qquad 5\text{-}19$$

$$D = e\varepsilon + \epsilon^{s} E \qquad 5\text{-}20$$

Table 5-8 below lists all the variables associated with the constitutive equations along with what they represent.

Table 5-8: Variable Representatives for the Constitutive Equations

Symbol	Variable	Units
$\boldsymbol{\varepsilon}$	strain tensor	-
S	Mechanical Compliance Tensor	Pa^{-1}
σ	Stress Vector	Pa
D	Electric Displacement Vector	C/m^2
E	Electric Field Vector	V/m
d	Piezoelectric Strain Coefficient Tensor	C/N or m/V
ϵ^{s}	Dielectric permittivity tensor (at particular uniform strain value)	F/m
$\mathbf{C^E}$	Elastic Stiffness Tensor measured under constant electric field vector	Pa
e	Piezoelectric Constant Tensor	C/m^2
$\mathbf{e_t}$	Transposed matrix of e	m*Pa/V

With reference to the second set of constitutive equations, if one has an anisotropic solid, this would result in a total of 45 material constants for a third dimensional depiction: 21 elastic stiffnesses, 18 piezoelectric constants, and 6 dielectric permittivities.

If one assumes a transversely isotropic material, the 45 constants diminish to 10: 5 elastic stiffnesses, 3 piezoelectric constants, and 2 dielectric permittivities. The resultant constitutive equations therefore take the following form:

$$\begin{Bmatrix}\sigma_{11}\\ \sigma_{22}\\ \sigma_{33}\\ \tau_{23}\\ \tau_{13}\\ \tau_{12}\end{Bmatrix} = \begin{pmatrix} C_{11} & C_{12} & C_{13} & 0 & 0 & 0 \\ C_{12} & C_{11} & C_{13} & 0 & 0 & 0 \\ C_{13} & C_{13} & C_{33} & 0 & 0 & 0 \\ 0 & 0 & 0 & C_{44} & 0 & 0 \\ 0 & 0 & 0 & 0 & C_{44} & 0 \\ 0 & 0 & 0 & 0 & 0 & (C_{11}-C_{12})/2 \end{pmatrix} \begin{Bmatrix}\varepsilon_{11}\\ \varepsilon_{22}\\ \varepsilon_{33}\\ \gamma_{23}\\ \gamma_{13}\\ \gamma_{12}\end{Bmatrix} - \begin{pmatrix} 0 & 0 & e_{31} \\ 0 & 0 & e_{31} \\ 0 & 0 & e_{33} \\ 0 & e_{15} & 0 \\ e_{15} & 0 & 0 \\ 0 & 0 & 0 \end{pmatrix} \begin{Bmatrix}E_1\\ E_2\\ E_3\end{Bmatrix} \qquad 5\text{-}21$$

$$\begin{Bmatrix} D_1 \\ D_2 \\ D_3 \end{Bmatrix} = \begin{pmatrix} 0 & 0 & 0 & 0 & e_{15} & 0 \\ 0 & 0 & 0 & e_{15} & 0 & 0 \\ e_{31} & e_{31} & e_{33} & 0 & 0 & 0 \end{pmatrix} \begin{Bmatrix} \varepsilon_{11} \\ \varepsilon_{22} \\ \varepsilon_{33} \\ \gamma_{23} \\ \gamma_{13} \\ \gamma_{12} \end{Bmatrix} + \begin{pmatrix} \epsilon_{11} & 0 & 0 \\ 0 & \epsilon_{11} & 0 \\ 0 & 0 & \epsilon_{33} \end{pmatrix} \begin{Bmatrix} E_1 \\ E_2 \\ E_3 \end{Bmatrix} \qquad 5\text{-}22$$

or

$$\begin{gathered} \sigma_{11} = C_{11}\varepsilon_{11} + C_{12}\varepsilon_{22} + C_{13}\varepsilon_{33} - e_{31}E_3 \\ \sigma_{22} = C_{12}\varepsilon_{11} + C_{11}\varepsilon_{22} + C_{13}\varepsilon_{33} - e_{31}E_3 \\ \sigma_{33} = C_{13}\varepsilon_{11} + C_{13}\varepsilon_{22} + C_{33}\varepsilon_{33} - e_{33}E_3 \\ \tau_{23} = 2C_{44}\varepsilon_{23} - e_{15}E_2 \\ \tau_{13} = 2C_{44}\varepsilon_{13} - e_{15}E_1 \\ \tau_{12} = (C_{11} - C_{12})\varepsilon_{12} \\ D_1 = 2e_{15}\varepsilon_{13} + \epsilon_{11}E_1 \\ D_2 = 2e_{15}\varepsilon_{23} + \epsilon_{11}E_2 \\ D_3 = e_{31}\varepsilon_{11} + e_{31}\varepsilon_{22} + e_{33}\varepsilon_{33} + \epsilon_{33}E_3 \end{gathered}$$

Table 5-9 below gives the material constants for 4 piezoelectric materials.

Table 5-9: Material Properties for Various Piezoelectric Materials (Extracted from (Li, 2007))

	Elastic Stiffnesses (GPa)					**Piezoelectric Constants (C/m^2)**			**Dielectric Permittivities (nF/m)**	
	C_{11}	C_{33}	C_{44}	C_{12}	C_{13}	e_{31}	e_{33}	e_{15}	ε_{11}	ε_{33}
PZT-4	139	113	25.6	77.8	74.3	-6.98	13.84	13.44	6.0	5.47
PZT-5H	126	117	35.3	55	53	-6.5	23.3	17	15.1	13
PZT-7	130	119	25	83	83	-10.3	14.7	13.5	17.1	18.6
$BaTiO_3$	150	146	44	66	66	-4.35	17.5	11.4	12.8	15

Likewise, the first set of constitutive equations breaks down to:

$$\begin{Bmatrix} \epsilon_{11} \\ \epsilon_{22} \\ \epsilon_{33} \\ \gamma_{23} \\ \gamma_{13} \\ \gamma_{12} \end{Bmatrix} = \begin{pmatrix} S_{11} & S_{12} & S_{13} & 0 & 0 & 0 \\ S_{12} & S_{11} & S_{13} & 0 & 0 & 0 \\ S_{13} & S_{13} & S_{33} & 0 & 0 & 0 \\ 0 & 0 & 0 & S_{44} & 0 & 0 \\ 0 & 0 & 0 & 0 & S_{44} & 0 \\ 0 & 0 & 0 & 0 & 0 & 2(S_{11} - S_{12}) \end{pmatrix} \begin{Bmatrix} \sigma_{11} \\ \sigma_{22} \\ \sigma_{33} \\ \tau_{23} \\ \tau_{13} \\ \tau_{12} \end{Bmatrix} - \begin{pmatrix} 0 & 0 & d_{31} \\ 0 & 0 & d_{31} \\ 0 & 0 & d_{33} \\ 0 & d_{15} & 0 \\ d_{15} & 0 & 0 \\ 0 & 0 & 0 \end{pmatrix} \begin{Bmatrix} E_1 \\ E_2 \\ E_3 \end{Bmatrix} \qquad 5\text{-}23$$

$$\begin{Bmatrix} D_1 \\ D_2 \\ D_3 \end{Bmatrix} = \begin{pmatrix} 0 & 0 & 0 & 0 & d_{15} & 0 \\ 0 & 0 & 0 & d_{15} & 0 & 0 \\ d_{31} & d_{31} & d_{33} & 0 & 0 & 0 \end{pmatrix} \begin{Bmatrix} \sigma_{11} \\ \sigma_{22} \\ \sigma_{33} \\ \tau_{23} \\ \tau_{13} \\ \tau_{12} \end{Bmatrix} + \begin{pmatrix} \epsilon_{11} & 0 & 0 \\ 0 & \epsilon_{11} & 0 \\ 0 & 0 & \epsilon_{33} \end{pmatrix} \begin{Bmatrix} E_1 \\ E_2 \\ E_3 \end{Bmatrix} \qquad 5\text{-}24$$

Table 5-10 below lists various compliance tensors and strain coefficients for 4 different piezoelectric ceramics.

Table 5-10: Selective Material Constants for several piezoceramic types. Extracted from (Jalili, 2010b)

Constant	Units	PZT-4	PZT-5A	PZT-5H	PMN-PT
S_{11}^E	10^{-12} m^2/N	12.3	16.4	16.5	59.7
S_{12}^E	10^{-12} m^2/N	-4.05	-5.74	-	-
S_{13}^E	10^{-12} m^2/N	-5.31	-7.22	-9.1	-45.3
S_{33}^E	10^{-12} m^2/N	15.5	18.8	20.7	86.5
S_{44}^E	10^{-12} m^2/N	39.0	47.5	43.5	14.4
$\mathbf{d_{33}}$	10^{-12} C/N	289	390	650	2,285
$\mathbf{d_{31}}$	10^{-12} C/N	-123	-190	-320	-1,063
$\mathbf{d_{15}}$	10^{-12} C/N	496	584		
$\boldsymbol{\rho}$	kg/m^3	7,500	7,800	7,800	8,050
$\mathbf{k_{33}}$	-	-	0.72	0.75	0.91

Rewriting the strain tensors with reference to the moduli of elasticity, moduli of rigidity, and Poisson's ratios, one can present Equation 5-23 as:

$$\begin{Bmatrix}\epsilon_{11}\\ \epsilon_{22}\\ \epsilon_{33}\\ \gamma_{23}\\ \gamma_{13}\\ \gamma_{12}\end{Bmatrix} = \begin{pmatrix} {}^{1}/_{Y_1^E} & {}^{\nu_{21}}/_{Y_1^E} & {}^{\nu_{13}}/_{Y_1^E} & 0 & 0 & 0 \\ {}^{\nu_{12}}/_{Y_1^E} & {}^{1}/_{Y_1^E} & {}^{\nu_{23}}/_{Y_1^E} & 0 & 0 & 0 \\ {}^{\nu_{31}}/_{Y_3^E} & {}^{\nu_{32}}/_{Y_3^E} & {}^{1}/_{Y_3^E} & 0 & 0 & 0 \\ 0 & 0 & 0 & {}^{1}/_{G_{23}^E} & 0 & 0 \\ 0 & 0 & 0 & 0 & {}^{1}/_{G_{13}^E} & 0 \\ 0 & 0 & 0 & 0 & 0 & {}^{1}/_{G_{12}^E} \end{pmatrix} \begin{Bmatrix}\sigma_{11}\\ \sigma_{22}\\ \sigma_{33}\\ \tau_{23}\\ \tau_{13}\\ \tau_{12}\end{Bmatrix} - \begin{pmatrix} 0 & 0 & d_{31} \\ 0 & 0 & d_{31} \\ 0 & 0 & d_{33} \\ 0 & d_{15} & 0 \\ d_{15} & 0 & 0 \\ 0 & 0 & 0 \end{pmatrix} \begin{Bmatrix}E_1\\ E_2\\ E_3\end{Bmatrix} \qquad 5\text{-}25$$

As continuum mechanics dictate that the stress/strain tensor matrix must be symmetrical, the mechanical properties of the piezoelectric materials must hold the following relationships:

$$\nu_{12} = \nu_{21} \quad 5\text{-}26$$

$$\nu_{13}/Y_1^E = \nu_{31}/Y_3^E \quad 5\text{-}27$$

$$\nu_{32}/Y_3^E = \nu_{23}/Y_1^E \quad 5\text{-}28$$

Note that for some piezoelectric materials such as PVDF, the transversely isotropic assumptions of $d_{31} = d_{32}$, $e_{31} = e_{32}$, $d_{24} = d_{15}$, and $e_{24} = e_{15}$ are invalid. In fact, PVDF films are highly anisotropic with $d_{31} \cong 5d_{32}$ (Jalili, 2010b).

5.1.5.3 EFFECTS ON TENSORS WITH BOUNDARY CONDITIONS

Using the first set of constitutive equations, it can be shown that during a short circuit (*i.e.* E = 0), the strain and electric displacement vectors in Equation 5-16 can be reduced to:

$$\begin{Bmatrix} \varepsilon \\ D \end{Bmatrix} = \begin{bmatrix} S \\ d \end{bmatrix} \{\sigma\} \quad 5\text{-}29$$

However, during an open circuit (*i.e.* D = 0), the stress and electric field vectors in Equation 5-17 can be reduced to:

$$\begin{Bmatrix} \sigma \\ E \end{Bmatrix} = \begin{bmatrix} \frac{1}{S(1-k^2)} \\ \frac{k^2}{d(1-k^2)} \end{bmatrix} \{\varepsilon\} \quad 5\text{-}30$$

Rewriting both scenarios with only the stress-strain relationship as Equation 5-31, we notice that the compliance tensor changes from S to $S(1\text{-}k^2)$. As k^2 is always less than 1 and greater than zero; the compliance decreases during open circuit electrical boundary conditions. For this reason, it is generally improper to refer to the mechanical compliance (or stiffness) without specifying the appropriate boundary conditions.

$$\varepsilon = \begin{cases} S\sigma & Short\ Circuit\ (E = 0) \\ S(1-k^2)\sigma & Open\ Circuit\ (D = 0) \end{cases} \quad 5\text{-}31$$

Like the modulus of elasticity, the compliance and stiffness tensors have subscripts to describe the appropriate boundary conditions.

$$\varepsilon = \begin{cases} S^E\sigma Short\ Circuit \\ S^D\sigma\ Open\ Circuit \end{cases} \quad 5\text{-}32$$

$$\sigma = \begin{cases} C^E \varepsilon \; Short\ Circuit \\ C^D \varepsilon \; Open\ Circuit \end{cases} \quad 5\text{-}33$$

Where the relationship between the short circuit and open circuit compliance tensors

$$S^D = S^E(1 - k^2) \quad 5\text{-}34$$

$$C^D = C^E(1 - k^2) \quad 5\text{-}35$$

An analogous relationship exists for the dielectric permittivity tensor with reference to mechanical constraints on the piezoelectric material. A stress-free condition (σ=0) occurs when an electric field is applied without mechanical constrains, while a strain-free condition (ε=0) can be achieved by clamping both ends of the material such that there is zero motion (Leo, Piezoelectric Materials, 2007). Akin to Equations 5-34 and 5-35, the stress free and strain free dielectric permittivity relationship is:

$$\epsilon^S = \epsilon^T(1 - k^2) \quad 5\text{-}36$$

5.1.6 Transducer Configurations

Generally, transducers are in two configurations: unimorph and bimorph. The unimorph configuration consists of one layer of PE material whereas the bimorph configuration consists of two layers of PE material. The unimorph configuration usually uses the 33 operating mode to expand or contract in the poling direction. The bimorph configuration usually uses the 31 operating mode either by extending or contracting its length and width by bending. As PE materials are quite brittle, to add strength to both configurations, the PE layers are attached to metal shim layers such as brass plates. The metal shim layer can also, in turn, act as an electrode. This section will show how both configurations are traditionally modeled.

5.1.6.1 MODELING THE 33 OPERATING MODE (UNIMORPHS)

As mentioned, unimorphs have only one PE layer that is typically attached to a metal shim layer for strength. Generally, they are used to exploit the 33 operating mode by either increasing or decreasing its thickness upon the application of an electric field or by creating an electric field when stressed in the poling direction. Assuming that there is no inputs in the transverse directions (*i.e.* $\sigma_1 = \sigma_2 = \sigma_4 = \sigma_5 = \sigma_6 = 0$ and $E_1 = E_2 = 0$), the

constitutive equations previously presented in matrix form as Equations 5-24 and 5-25, can be simplified to four equations:

$$\varepsilon_1 = \frac{-\nu_{13}}{Y_1^E}\sigma_3 + d_{13}E_3 \quad 5\text{-}37$$

$$\varepsilon_2 = \frac{-\nu_{23}}{Y_1^E}\sigma_3 + d_{23}E_3 \quad 5\text{-}38$$

$$\varepsilon_3 = \frac{1}{Y_3^E}\sigma_3 + d_{33}E_3 \quad 5\text{-}39$$

$$D_3 = d_{33}\sigma_3 + \epsilon_{33}E_3 \quad 5\text{-}40$$

As the strains in the transverse directions are generally not needed for unimorph applications, the remainder of this subsection will focus on the outputs in the poling direction. Assuming that the strain in the poling direction and applied electric potential (V) are uniform across the PE material's thickness (t), and the applied stress and induced charge are uniformly distributed over the PE material's cross-sectional surface area (A_{cs}), then Equations 5-39 and 5-40 can be rearranged to find the material's displacement (u) and charge (q):

$$u_3 = \frac{t}{Y_3^E A_{cs}}F_3 + d_{33}V_3 \quad 5\text{-}41$$

$$q_{33} = d_{33}F_3 + \frac{\epsilon_{33}A_{cs}}{t}V_3 \quad 5\text{-}42$$

The variable F represents the applied force over the PE material's cross sectional area. For PE actuators, the free displacement (δ_0) (*i.e.* the displacement under no mechanical load) can thus be presented as 5-43 while the blocked force (f_{bl}) (*i.e.* the force when strain is prevented) can be presented as Equation 5-44.

$$\delta_0 = u_3|_{F=0} = d_{33}V_3 \quad 5\text{-}43$$

$$F_{bl} = -F|_{u_3=0} = \frac{d_{33}Y_3^E A_{CS}}{t}V_3 \quad 5\text{-}44$$

Likewise the total charge produced by an applied force without an induced electric potential can be represented as:

$$q_{33}|_{V=0} = d_{33}F_3 = d_{33}Y_3^E\frac{A_{cs}}{t}u_3 \quad 5\text{-}45$$

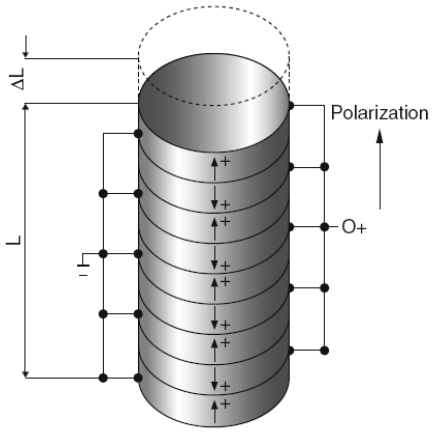

Figure 5-12: The Stack Configuration. Image Extracted from (Jalili, Physical Principles and Constitutive Models of Piezoelectric Materials, 2010b)

To increase a unimorph transducer's displacement and charge, it is common practice to arrange unimorphs in stacks. Appropriately named the stack configuration, unimorphs are layered on top of one another so that they are connected electrically in parallel, but mechanically in series. Also, the polarization direction alternates for each layer. Figure 5-12 shows the electrical and mechanical configuration of a PE stack actuator.

To find the total displacement (u_s) and charge (q_s) produced from a PE stack configuration, one simply needs to find the displacement and charge produced from one layer and multiply them by the number of layers (n):

$$u_s = nu_3 = \frac{nt}{Y_3^E A_{cs}} F_3 + nd_{33} V_3 \qquad 5\text{-}46$$

$$q_s = nq = nd_{33} F_3 + \frac{n\epsilon_{33} A_{cs}}{t} V_3 \qquad 5\text{-}47$$

However, the total blocked force for a PE stack actuator will be the same as the blocked force produced by a single layer. A multilayer PE stack actuator is a means of producing larger displacements than a single layer without a reduction in the achievable force (Leo, Piezoelectric Materials, 2007). Although stack actuators increase the overall displacement, their range is still limited, but have excellent precision. Piezoelectric actuators have been produced with precision in the subnanometer range and can produce forces up to several 10,000 N (Jalili, 2010b). They also have very low response time; NEC-TOKIN claims that their 200-300 layer PE stack actuators have a response time of 0.01 ms. Table 5-11 gives a comparison of NEC-TOKIN's stack actuators in relation to a stepping motor and voice coil motor. Although the stack actuator has an excellent accuracy, response time, and generated force, its low range typically limits its use to small scale applications.

Table 5-11: Actuator Comparison. Extracted from (NEC-TOKIN, 2004)

Drive Source	Range	Accuracy	Generated Force	Response Time
Stepping Motor	1000 mm	10 μm	30 kg	100 msec
Voice Coil Motor	1 mm	0.1 μm	20 kg	1 msec
Piezoelectric Actuator	0.05 mm	0.01 μm	3 kg/mm^2	0.01 msec

5.1.6.2 MODELING THE 31 OPERATING MODE (BIMORPHS)

As mentioned, bimorphs contain two piezoelectric layers sandwiched between an inactive substrate layer that is made from materials such as brass, aluminum, or steel. 31 operating bimorphs are used to either extend or contract a material longitudinally, or cause a material to bend. Both mechanisms rely on a PE transducer's 31 operating mode where the applied and induced electric fields remain in the poling direction, but the used displacement is in the transverse direction. Assuming that there are no applied electric fields in the transverse direction (*i.e.* $E_1 = E_2 = 0$) and that there is only one applied stress which is in one of the transverse directions (*i.e.* $\sigma_2 = \sigma_3 = \sigma_4 = \sigma_5 = \sigma_6$), then the constitutive matrices (Equations 5-24 and 5-25) reduce to:

$$\varepsilon_1 = \frac{1}{Y_1^E}\sigma_1 + d_{31}E_3 \qquad 5\text{-}48$$

$$\varepsilon_2 = \frac{-\upsilon_{21}}{Y_1^E}\sigma_1 + d_{32}E_3 \qquad 5\text{-}49$$

$$\varepsilon_3 = \frac{-\upsilon_{31}}{Y_1^E}\sigma_1 + d_{33}E_3 \qquad 5\text{-}50$$

$$D_3 = d_{31}\sigma_1 + \epsilon_{33}E_3 \qquad 5\text{-}51$$

As the 31 operating mode focuses on the strain along the 1-direction along with the electrical properties in the 3 direction, the remainder of this section will focus on Equations 5-48 and 5-51. Assuming that the strain is uniform across the material's length (L) in the 1-direction, that the stress is evenly distributed across the PE material's cross section in the 1-direction [i.e the thickness (t) multiplied by the width (w) in the case of a

rectangle], that the electric field is uniform across the PE material's thickness, and that the total charge is evenly distributed across the PE material's cross section in the 3-direction (*i.e.* the width multiplied by the length in the case of a rectangle), the total displacement and charge caused by 31-loading can be presented as Equations 5-52 and 5-53, respectively.

$$u_1 = \frac{L}{Y_1^E wt} F_3 + \frac{d_{31} L}{t} V_3 \tag{5-52}$$

$$q_{31} = \frac{d_{31} L}{t} F_3 + \frac{\epsilon_{33} wL}{t} V_3 \tag{5-53}$$

Interestingly, with an electrical load and no mechanical load (*i.e.* V≠0, f=0) the displacement is not only dependent on the strain coefficient, but also the geometry of the material; this is in contrast to the 33 loading scenario where the displacement is only dependent on the strain coefficient under electrical actuation. Likewise, the total charge under an applied mechanical loading without electrical loading (*i.e.* F≠0, V=0) is also dependent on the geometry of the material unlike the 33 loading scenario where the total charge is only dependent on the strain coefficient. Under these respective boundary conditions, the displacement and total charge are both influenced by three variables: the strain coefficient, the length of the PE material, and the thickness of the PE material. A larger strain coefficient, larger length, and smaller thickness will all increase the actuated displacement and total charge developed.

The free displacement and blocked force under 31 loading can be shown to be Equations 5-54 and 5-55, respectively, while Equation 5-56 presents the total charge produced on the material's electrodes under 31 loading.

$$\delta_0 = u_1|_{F=0} = \frac{d_{31} L}{t} V_3 \tag{5-54}$$

$$F_{bl} = -F_3|_{u_1=0} = d_{31} Y_1^E wV_3 \tag{5-55}$$

$$q_{31}|_{V=0} = \frac{d_{31} L}{t} F_3 = d_{31} Y_1^E wu_1 \tag{5-56}$$

5.1.6.3 EXTENSION CONFIGURATION

To extend a PE bimorph along its length, the two piezoelectric layers have to be laid along the substrate layer and electrically connected in such a way that both layers expand and contract simultaneously. Figure 5-13 shows one way that the layers can be setup for extension: the PE layers are electrically connected in parallel and have been attached to the substrate layer with their poling axes in opposing directions.

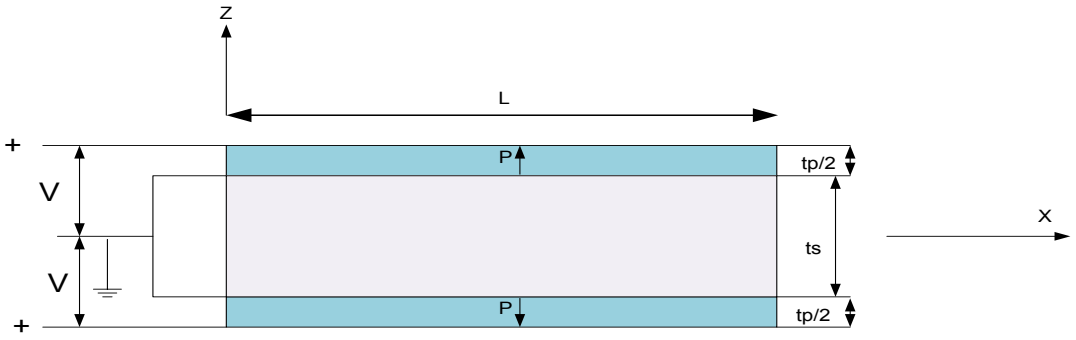

Figure 5-13: The Extension Configuration with PE Layers Electrically Connected in Parallel.

Assuming that the strain in the x-direction, ε_1, is the same for all three layers, the strain can be written as Equation 5-57 where σ_1, t_s, t_p, and Y_s are the applied stress in the transverse direction (the x-direction in Figure 5-13), substrate thickness, total PE thickness (both PE layers), and substrate modulus of elasticity, respectively.

$$\varepsilon_1 = \begin{cases} \frac{1}{Y_1^E}\sigma_1 + d_{31}E_3, & \frac{t_s}{2} \le z \le \frac{1}{2}(t_s + t_p) \\ \frac{1}{Y_s}\sigma_1, & -\frac{t_s}{2} \le z \le \frac{t_s}{2} \\ \frac{1}{Y_1^E}\sigma_1 + d_{31}E_3, & -\frac{1}{2}(t_s + t_p) \le z \le -\frac{t_s}{2} \end{cases} \qquad 5\text{-}57$$

Substituting the applied stress with the appropriate forces and cross-sectional areas (assuming a rectangular cross-section), Equation 5-57 can be rewritten as Equation 5-58 where F_p, F_s, and w represent the applied axial force on one piezoelectric layer, the applied axial force on the substrate layer, and the width of the transducer.

$$\frac{wt_p}{2}Y_1^E\varepsilon_1 = F_p + \frac{wt_p}{2}Y_1^E d_{31}E_3$$
$$wt_sY_s\varepsilon_1 = F_s \qquad 5\text{-}58$$
$$\frac{wt_p}{2}Y_1^E\varepsilon_1 = F_p + \frac{wt_p}{2}Y_1^E d_{31}E_3$$

As the total applied force is equivalent to all three forces combined, as shown in Equation 5-59, all three formulas in Equation 5-58 can be summed to get Equation 5-60:

$$F_3 = 2F_p + F_s \qquad 5\text{-}59$$

$$\left(wt_pY_1^E + wt_sY_s\right)\varepsilon_1 = F_3 + wt_pY_1^E d_{31}E_3 \qquad 5\text{-}60$$

Rearranging Equation 5-60, one can solve for the total strain (Equation 5-61) followed by the total displacement in the transverse direction (Equation 5-62).

$$\varepsilon_1 = \frac{F_3 + wt_pY_1^E d_{31}E_3}{wt_pY_1^E + wt_sY_s} \qquad 5\text{-}61$$

$$u_1 = \frac{F_3 + wt_pY_1^E d_{31}E_3}{wt_pY_1^E + wt_sY_s}L \qquad 5\text{-}62$$

Rearranging 5-62, the total force can be presented as Equation 5-63:

$$\frac{u_1 w\left(t_pY_1^E + t_sY_s\right)}{L} - wt_pY_1^E d_{31}E_3 = F_3 \qquad 5\text{-}63$$

Using a rule of mixtures approach, the total applied mechanical force on one PE layer can be presented as Equation 5-64 with A_p and A_s representing one PE layer's and substrate layer's cross-sectional areas, respectively; both with reference to the 1-axis:

$$F_p = \frac{Y_1^E A_p F_3}{2Y_1^E A_p + Y_sA_s} = \frac{Y_1^E t_p F_3}{2\left(Y_1^E t_p + Y_st_s\right)} \qquad 5\text{-}64$$

Assuming that the PE layers are electrically parallel, where their charges are added, the total charge on both plates induced by an applied force and electric field can be modeled using Equations 5-53 and 5-64 to yield Equation 5-65:

$$q_{ext} = \left(\frac{d_{31}L}{t}F_p + \frac{\epsilon_{33}wL}{t}V\right) * 2 = \left(\frac{d_{31}LY_1^E F}{\left(Y_1^E t_p + Y_st_s\right)} + \frac{2\epsilon_{33}wL}{t_p}V\right) * 2 \qquad 5\text{-}65$$

Using Equations 5-62 and 5-63, the free displacement and blocked force for a heterogeneous bimorph with an extension configuration can be modeled as Equations 5-66 and 5-67, respectively. Using Equation 5-65, the total charge produced solely from

axial mechanical loading for a heterogeneous bimorph with an extension configuration can be modeled as Equation 5-68.

$$\delta_0 = u_1|_{F=0} = \frac{t_p Y_1^E d_{31} E_3}{t_p Y_1^E + t_s Y_s} L \quad 5\text{-}66$$

$$F_{bl} = -F_3|_{u_1=0} = w t_p Y_1^E d_{31} E_3 \quad 5\text{-}67$$

$$q_{ext}|_{V=0} = \frac{2 d_{31} L Y_1^E F_3}{t_p Y_1^E + t_s Y_s} = 2 d_{31} Y_1^E u_1 w \quad 5\text{-}68$$

5.1.6.4 BENDING CONFIGURATION

A bimorph with bending configuration has its PE layers laid along the substrate layer and electrically connected so that when activated, one layer is contracting while the other is expanding simultaneously. Figure 5-14 shows one way that the layers can be setup for bending: the PE layers are electrically connected in parallel and have been attached to the substrate layer with their poling axes in the same direction.

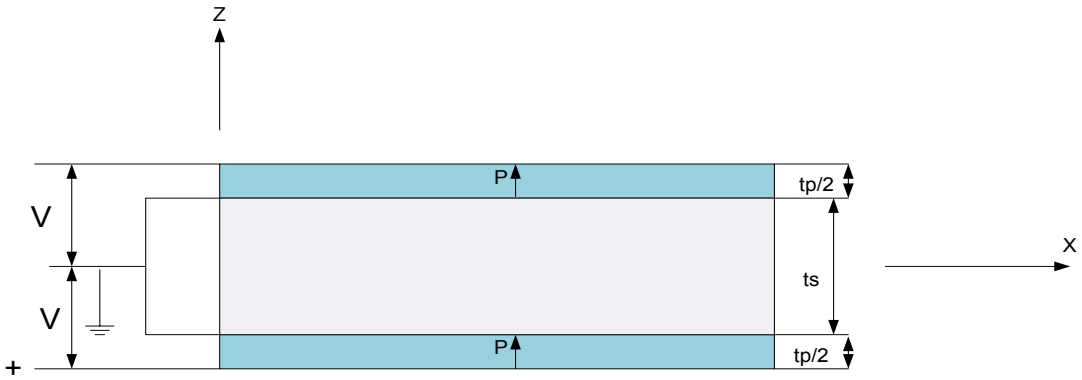

Figure 5-14: The Bending Configuration with PE Layers Electrically Connected in Parallel

As the bimorph is going through bending, the strain varies with reference to the neutral axis and depends on the bimorph's material properties. Finding a bending bimorph's outputs will therefore require an integrative approach. As the objectives (to be explained later) of this chapter only involves the direct piezoelectric effect, the author only presents models to predict the outputs solely from mechanical loading.

As a PE heterogeneous bimorph is composed of more than one material, the PE material and the substrate material, composite beam modelling must be used to predict the bimorph's behaviour under mechanical loads. To find the bimorph's strain pattern,

something that is necessary to find the bimorph's deflection and total charge, the composite's moment of inertia and modulus of elasticity must be found and defined. Both will be found using the transformed-section method.

Under composites with uniform width, the transformed-section method uses the ratio of the materials' elastic moduli and accordingly adjusts the width of one of the material's to produce an equivalent moment of inertia. Using the flexure formula ($\sigma = Mc/I$), the stresses and strains in the other material (*i.e.* the material that retained its original width) can be directly found, while the elastic moduli ratio must be used to find the associated stresses and strains with the altered-width material.

Using the transformed-section method to alter the substrate width, the equivalent substrate width (w_s) with a PE material's modulus of elasticity is:

$$w_s = \frac{Y_s}{Y_1^E} w \tag{5-69}$$

Using the new substrate width, the composite moment of inertia can be presented as Equation 5-70:

$$I = \sum (\bar{I} + Am^2) = \left[\frac{wt_s^3}{12}\frac{Y_s}{Y_1^E}\right] + 2\left[\frac{w}{12}\left(\frac{t_p}{2}\right)^3 + \frac{wt_p}{2}\left(\frac{t_s}{2} + \frac{t_p}{4}\right)^2\right] \tag{5-70}$$

Euler-Bernoulli beam theory states that a beam's bending strain is directly related to the distance from the neutral axis and the radius of curvature. The radius of curvature (R) is also a function of the internal moment, the modulus of elasticity, and the bending moment of inertia. Both relationships are shown in Equation 5-71.

$$\varepsilon(z) = -\frac{z}{R} = \frac{-M(x)z}{YI} \tag{5-71}$$

As the strain varies along the z-axis and x-axis, one cannot use a uniform strain when calculating the total charge developed from the PE layers. However, one can still use Equation 5-51 to calculate the total charge providing that one finds an averaged strain. The average value of a function, f(x), within an interval separated by values a and b can be found using the following formula:

$$f_{ave} = \frac{1}{b-a}\int_a^b f(x)dx \tag{5-72}$$

As the strain varies in the z-axis and x-axis, to find the average strain one must use Equation 5-72 twice: once for each axis. Equation 5-73 shows the double integration applied across one PE layer in a bending bimorph.

$$\varepsilon_{ave} = \frac{2}{t_p}\frac{1}{L}\int_{\frac{t_s}{2}}^{\frac{t_s+t_p}{2}}\int_0^L \frac{z}{R}dxdz = \frac{2}{t_p}\frac{1}{L}\int_{\frac{t_s}{2}}^{\frac{t_s+t_p}{2}}\int_0^L \frac{M(x)z}{Y_1^E I}dxdz = \frac{2}{t_p L Y_1^E I}\int_{\frac{t_s}{2}}^{\frac{t_s+t_p}{2}}\int_0^L M(x)z\,dxdz \qquad 5\text{-}73$$

5.1.6.4.1 Cantilever Beam Loading

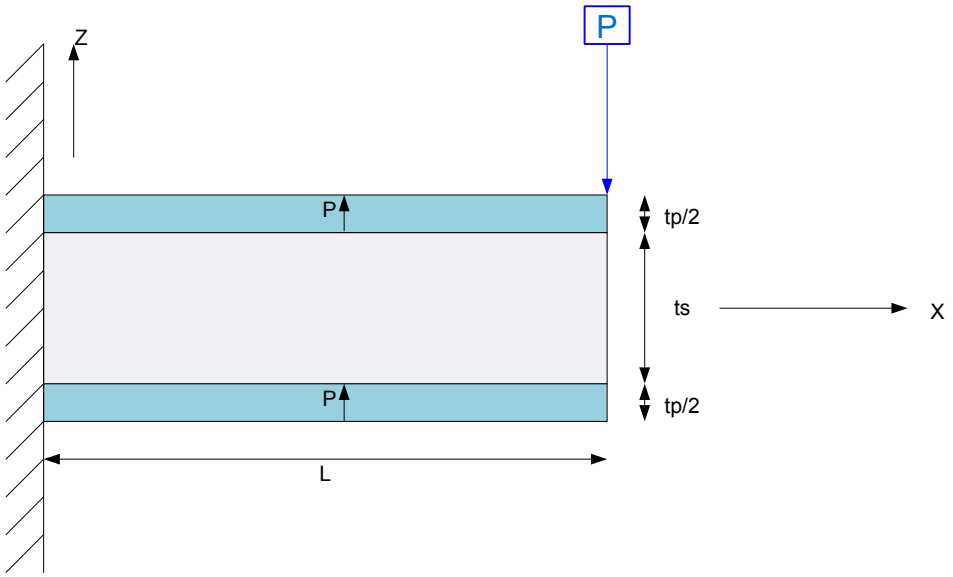

Figure 5-15: The Cantilever Beam Loading Scenario

The cantilever beam loading scenario (pictured in Figure 5-15) contains a PE heterogeneous bimorph that is constrained on one end while the other end is being deflected by a vertical point load, P. The resultant moment in the cantilever beam scenario across the x-axis is:

$$M(x) = P(L-x) \qquad 5\text{-}74$$

To get the average strain in the cantilever beam loading scenario, one simply substitutes Equation 5-74 into Equation 5-73. The integration is performed below with the final result being Equation 5-75.

$$\varepsilon_{ave} = \frac{2}{t_p L Y_1^E I}\int_{\frac{t_s}{2}}^{\frac{t_s+t_p}{2}}\int_0^L P(L-x)z\,dxdz$$

$$\varepsilon_{ave} = \frac{2P}{t_p L Y_1^E I}\int_{\frac{t_s}{2}}^{\frac{t_s+t_p}{2}}\left[Lzx - \frac{x^2 z}{2}\right]_0^L dz$$

$$\varepsilon_{ave} = \frac{PL}{t_p Y_1^E I}\int_{\frac{t_s}{2}}^{\frac{t_s+t_p}{2}} z dz = \frac{PL}{t_p Y_1^E I}\left[\frac{z^2}{2}\right]_{\frac{t_s}{2}}^{\frac{t_s+t_p}{2}} = \frac{PL}{2t_p Y_1^E I}\left[\left(\frac{t_p+t_s}{2}\right)^2 - \left(\frac{t_s}{2}\right)^2\right]$$

$$\varepsilon_{ave} = \frac{PL}{8Y_1^E I}(t_p + 2t_s) \quad 5\text{-}75$$

Assuming a parallel electrical connection, the total charge developed across the two PE layers can then be calculated by substituting Equation 5-75 into Equation 5-51 to yield:

$$q_{cant} = (d_{31}\varepsilon_{ave} Y_1^E + \epsilon_{33} E_3) 2wL \quad 5\text{-}76$$

Under no electric load, Equation 5-76 turns into:

$$q_{cant} = 2d_{31}\varepsilon_{ave} Y_1^E wL = \frac{d_{31} wL^2 (t_p + 2t_s)}{4I} P \quad 5\text{-}77$$

To get the beam's maximum deflection, one can use the following formula that relates the vertical beam displacement with the internal moment:

$$\frac{d^2 z}{dx^2} = \frac{M(x)}{Y_1^E I} = \frac{P(L-x)}{Y_1^E I} \quad 5\text{-}78$$

Integrating Equation 5-78 with respect to x twice yields Equations 5-79 and 5-80

$$Y_1^E I \frac{dz}{dx} = PLx - \frac{x^2}{2} + A \quad 5\text{-}79$$

$$Y_1^E I z = \frac{PLx^2}{2} - \frac{x^3}{6} + Ax + B \quad 5\text{-}80$$

Using boundary conditions (*i.e.* z=0 when x=0 and dz/dx=0 when x=0) one will find that both A and B are equivalent to 0; the total deflection at x=L, *i.e.* the maximum deflection (δ), is found to be:

$$\delta = z|_{x=L} = \frac{PL^3}{3Y_1^E I} = \frac{PL^3}{3Y_1^E\left\{\left[\frac{wt_s^3}{12}\frac{Y_s}{Y_1^E}\right] + 2\left[\frac{w}{12}\left(\frac{t_p}{2}\right)^3 + \frac{wt_p}{2}\left(\frac{t_s}{2} + \frac{t_p}{4}\right)^2\right]\right\}} \quad 5\text{-}81$$

The above equation can be substituted into the average strain equation to get the average strain in terms of the maximum deflection:

$$\varepsilon_{ave} = \frac{3\delta}{8L^2}(t_p + 2t_s) \quad 5\text{-}82$$

Likewise, Equation 5-82 can be substituted into Equation 5-77 to obtain the total charge in relation to the maximum deflection:

$$q_{cant} = \frac{3d_{31}Y_1^E w(t_p + 2t_s)}{4L}\delta \qquad 5\text{-}83$$

Using the flexure formula, the maximum stress on the bimorph can be found to check that it does not exceed the material's yield strength:

$$\sigma_{max} = \frac{M_{max}c}{I} = \frac{(PL)(t_p + t_s)}{2I} = \frac{3Y_1^E\delta(t_p + t_s)}{2L^2} \qquad 5\text{-}84$$

5.1.6.4.2 Simply-supported Bimorph with Mid-Point Beam Loading

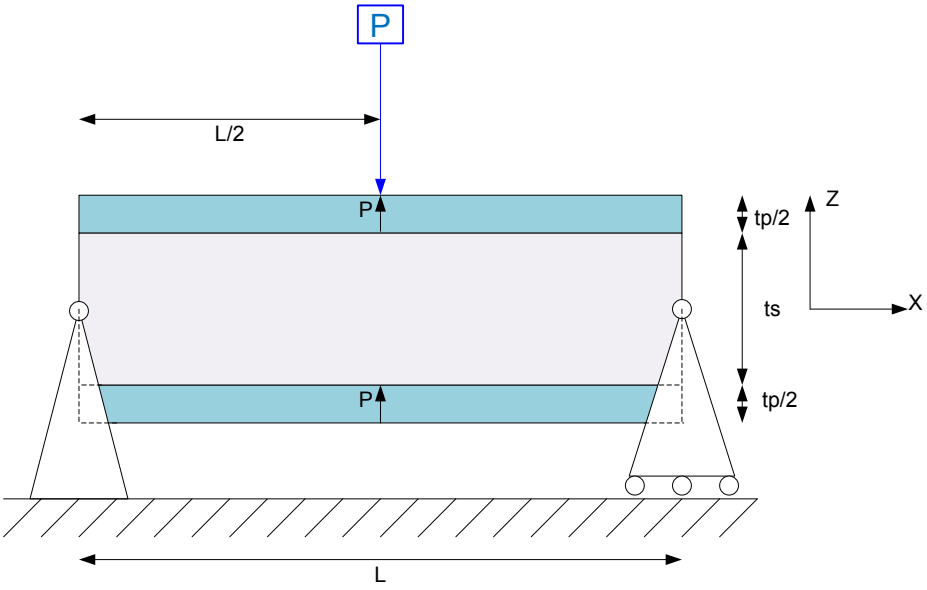

Figure 5-16: The Simply-supported Bimorph with Mid-Point Beam Loading Scenario

The simply-supported loading scenario, as illustrated in Figure 5-16, contains a PE heterogeneous bimorph that is constrained by a pin joint on one side and a roller joint on the other while a vertical point load is applied at the bimorph's middle. The pin joint allows the bottom left corner to rotate in the xz-plane but not translate in any direction while the roller joint only allows the bottom right corner to both translate and rotate, but only in the x-direction and xz-plane, respectively. As the bimorph has symmetrical loading, one can find the average strain by performing the double integration on the first half of the beam. Knowing that the moment in first half of the beam is equivalent to

Px/2, the double integration is performed below with the final solution presented as Equation 5-85.

$$\varepsilon_{ave} = \frac{4}{t_p L Y_1^E I}\int_{\frac{t_s}{2}}^{\frac{t_s+t_p}{2}}\int_0^{L/2}\left(\frac{Px}{2}\right)z\,dx\,dz = \frac{2P}{Y_1^E I L t_p}\int_{\frac{t_s}{2}}^{\frac{t_p+t_s}{2}}\int_0^{L/2} xz\;dx\,dz$$

$$\varepsilon_{ave} = \frac{2P}{Y_1^E I L t_p}\int_{\frac{t_s}{2}}^{\frac{t_p+t_s}{2}}\frac{x^2 z}{2}\Bigg]_0^{L/2} dz = \frac{P}{Y_1^E I L t_p}\int_{\frac{t_s}{2}}^{\frac{t_p+t_s}{2}}\frac{L^2 z}{4}\,dz = \frac{P}{4Y_1^E I L t_p}\int_{\frac{t_s}{2}}^{\frac{t_p+t_s}{2}} z\,dz$$

$$\varepsilon_{ave} = \frac{PL}{4Y_1^E I t_p}\left[\frac{z^2}{2}\right]_{\frac{t_s}{2}}^{\frac{t_p+t_s}{2}} = \frac{PL}{8Y_1^E I t_p}\left[\left(\frac{t_p+t_s}{2}\right)^2 - \left(\frac{t_s}{2}\right)^2\right] = \frac{PL}{32Y_1^E I}\left(t_p + 2t_s\right)$$

$$\varepsilon_{ave} = \frac{PL}{32Y_1^E I}\left(t_p + 2t_s\right) \qquad 5\text{-}85$$

By substituting Equation 5-85 into Equation 5-51, the total charge produced in the two PE layers when connected electrically in parallel can be modeled as:

$$q_{mid} = 2d_{31}\varepsilon_{ave}Y_1^E wL = \frac{d_{31}wL^2\left(t_p + 2t_s\right)}{16I}P \qquad 5\text{-}86$$

To get the beam's maximum deflection, the deflection at the point load, one would again use Equation 5-78 with the appropriate moment:

$$\frac{d^2z}{dx^2} = \frac{M(x)}{Y_1^E I} = \frac{Px}{2Y_1^E I} \qquad 5\text{-}87$$

Integrating with respect to the x-axis, one gets Equations 5-88 and 5-89

$$Y_1^E I\frac{dz}{dx} = \frac{Px^2}{4} + A \qquad 5\text{-}88$$

$$Y_1^E Iz = \frac{Px^3}{12} + Ax + B \qquad 5\text{-}89$$

Using boundary conditions (*i.e.* z = 0 at x = 0 and dz/dx=0 at x=L/2), one will find that A and B are equivalent to $-FL^2/16$ and 0, respectively. Rewriting Equation 5-89 with the newly defined coefficients, the displacement with respect to the x-axis can be defined as:

$$z = \frac{1}{Y_1^E I}\left(\frac{Px^3}{12} - \frac{PL^2x}{16}\right) \qquad 5\text{-}90$$

Knowing that the maximum deflection is at the point load (*i.e.* x = L/2), the maximum deflection can be defined as:

$$\delta = \frac{PL^3}{48Y_1^E I} = \frac{PL^3}{48Y_1^E \left\{\left[\frac{wt_s^3}{12}\frac{Y_s}{Y_1^E}\right] + 2\left[\frac{w}{12}\left(\frac{t_p}{2}\right)^3 + \frac{wt_p}{2}\left(\frac{t_s}{2} + \frac{t_p}{4}\right)^2\right]\right\}} \quad 5\text{-}91$$

Substituting Equation 5-91 into Equation 5-86, one can find the total charge with reference to the induced deflection:

$$q_{mid} = \frac{3d_{31}Y_1^E w(t_p + 2t_s)}{L}\delta \quad 5\text{-}92$$

Using the flexure formula, one can find the maximum stress on the PE layer to make sure it does not exceed its yield strength:

$$\sigma_{max} = \frac{M_{max}c}{I} = \frac{(PL)(t_p + t_s)}{8I} = \frac{(6Y_1^E\delta)(t_p + t_s)}{L^2} \quad 5\text{-}93$$

5.2 ENERGY HARVESTING

Energy harvesting refers to extracting ambient energy from the surrounding environment without compromising a system's functionality. Essentially, an energy harvesting system extracts energy that is not being used (*i.e.* "wasted" energy) and either directly uses said energy to power a device or stores it in a battery or capacitor for later use. An example of energy harvesting is adding turbines to decrease head in water piping: if head has to be decreased in water piping regardless, it would be beneficial to decrease the head by transferring the potential energy change into electrical energy for later use. Other examples include human-powered gyms such as the Green Microgym in Portland, Oregon (The Green Microgym, 2012): people go to a gym to expel energy; it would therefore be beneficial to have gym equipment that turns said expelled energy into electrical energy to power various personal devices such as cell phones, MP3 players, or digital cameras. One form of energy harvesting that has been getting a lot of attention is vibration harvesting.

Most mechanical systems have unwanted, unintended vibrations. A branch of mechanical engineering, known as vibration control, is dedicated to suppressing these unwanted vibrations. Vibration suppression is generally done by either intuitively designing the mechanical system to operate at frequencies away from their natural frequencies, or by adding mass-spring-damper systems to change the system's natural frequencies away from the system's operating frequencies. While the vibrations are suppressed as a result, the vibration energy is nonetheless transferred into a different form; the energy is wasted. Vibration energy harvesting aims to transform wasted vibration energy into useful electrical energy.

Over the past 20 years, there have been substantial improvements in computer speed and memory; largely due to MEMS technology and decreases in transistor size. Despite these improvements in computer science, battery technology has been unable to improve at an equal rate. Extracted from Anton & Sodano (2007), Figure 5-17 shows the increases in disk capacity, CPU Speed, available random active memory (RAM), and battery energy density from 1990 to 2003 in relation to 1990 levels. From Figure 5-17, one can see that

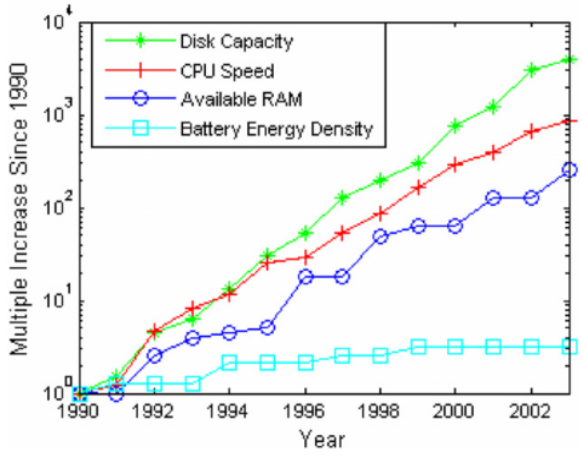

Figure 5-17: Advances in computer and battery technology from 1990 to 2003. Extracted from (Anton & Sodano, 2007)

disk capacity, CPU speed, and available RAM have improved magnitudes higher in relation to improvements in battery energy density. Although wireless systems have become more energy efficient over time, their prolonged use is still limited by their associated battery capacity; batteries must be continuously recharged or replaced. To eliminate the need for batteries for low-power systems such as wireless sensor networks,

engineers are researching the viability of harvesting vibration energy from the surrounding environment. There are several technologies that can transform vibration energy into electrical energy such as electromagnetic induction, electrostatic generation, dielectric elastomers, and piezoelectric materials. While each of these technologies can provide a useful amount of energy, piezoelectric materials have received the most attention due to their ability to directly convert applied strain energy into useable electrical energy and the ease at which they can be integrated into a system (Anton & Sodano, 2007).

The human body is also a conduit for energy harvesting. In 1996, Starner analyzed the human body and its various systems that have the potential for power recovery. These body systems included blood flow, respiration, limb movement, typing, and footfalls from walking. Table 5-12 summarizes the results from this study in terms of the mechanical power generated, the electrical power available, and the electrical energy available per movement. It has been proposed from numerous projects and studies that piezoelectric materials can be used to harness some of the wasted energy exerted from typical human activity. The human activity would stress the piezoelectric material, either directly or from induced vibrations, and in turn would produce an electric potential that can be used to store energy or directly power a device.

Table 5-12: Summary of Power and Energy Available from Everyday Human Body Activity. Data extracted from (Starner, 1996)

Activity	Mechanical Power Generated	Electrical Power Available	Electrical Energy Available per movement
Blood Flow	0.93 W	0.37 W	0.37 J
Exhalation	1.00 W	0.40 W	2.4 J
Breathing (Chest Movement)	0.83 W	0.091 – 0.42 W	0.5-2.5 J
Upper Limb Movement	3.00 W	0.33 – 1.5 W	1.5 – 6.7 J
Finger Motion	6.9-19.00 mW	0.76 – 2.1 mW	143 – 266 μJ
Footfalls	67.00 W	5-8.4 W	8.3 – 14.0 J

Looking at the available electrical power from the various activities in Table 5-12, the activity with the most potential for energy harvesting is footfalls (or heel strikes) during various activities such as walking, sprinting, or jumping. With a value of 5-8.4 W, foot falls have more than three times the available electrical power than the second highest activity, upper limb movement. It is therefore unsurprising that much research in human energy harvesting has been focused on human footfalls. One method of extracting energy from human footfalls is through using piezoelectric materials. The footfall can be used to directly stress a piezoelectric material, causing an electric potential to develop that can be used to generate electricity. Starting with Schenck (1999), several prototypes have been made using PE materials to generate electricity from foot falls. Although successful in generating electricity via PE materials, their power outputs are quite limited; generally only a few milliwatts (or microwatts) of power can be produced per transducer. Despite these research findings in peer-reviewed articles, many websites claim that piezoelectric materials can be used to efficiently transform the energy from human footfalls into electricity. Founded by Elisabeth Redmond and Andrew Katz, POWERLeap™ is a company located in Ann Arbor, Michigan that produces flooring systems that generate electricity via human foot traffic. During a presentation at the 2009 Go Green Expo in New York, Katz claimed that their piezoelectric flooring system generates 1 to 5 Watts per square foot (Power Leap, 2009). As Katz's claim was much higher than any of the peer-reviewed journals read by the author, the author was quite skeptical about the validity of said claim. Wanting to know how much electricity piezoelectric materials could conceivably be produced from human foot traffic, the author performed an investigation to calculate the maximum electrical power these smart materials can produce when used in both shoe inserts and floor tiles.

Before presenting the investigation, a review will be given on harvesting using piezoelectric materials, harvesting energy from human activity, and harvesting energy from human activity via piezoelectric materials. After formally stating the objectives of the investigation, the author will go over the components needed to harvest energy from piezoelectric materials along with the strategy used to calculate the power output at various piezoelectric geometries for both shoe inserts and floor tiles.

5.2.1 Energy Harvesting using Piezoelectric Materials: an Overview

The most common type of PE material used in power harvesting applications is PZT due to its generally high strain coefficients; however, it's extremely brittle nature causes certain limitations in the strain that it can safely withstand without being damaged. As mentioned in previous sections, PZT layers are generally applied to a substrate layer to physically strengthen the transducer. As PVDF transducers are more flexible than PZT transducers, they can be an attractive alternative for power harvesting. PVDF transducers are also less difficult to impedance match, making the energy transfer more efficient. However, PVDF strain coefficients are generally much lower than PZT materials, limiting the amount of energy that can be harvested. Alternatively, PE fibre composites have also been used for PE energy harvesting. Being derived from PZT ceramics, PE fibre composites have high strain coefficients that are typical of PZT ceramics. Additionally, PE fibre composites are more flexible, enabling them to withstand higher strains than typical PE ceramics: a feature that provides more mechanical energy available to be harvested. Extracted from (Cook-Chennault, Thambi, Bitetto, & Hameyie, 2008), Table B-1 in Appendix B1 gives an overview of several piezoelectric energy harvesting devices along with their generated power. Judging from the power outputs presented in Table B-1, the amount of energy that can be harvested from a piezoelectric transducer is generally quite low, ranging from 1 μW to 28 mW.

As mentioned, PE energy harvesting has had the most focus in harvesting the energy from ambient vibrations as ambient vibrations generally occur at frequencies closer to a PE transducer's natural frequency; maximum power output occurs at a PE transducer's natural frequency. These vibrations can occur naturally such as from seismic activity, but can also be from ambient vibrations from mechanical systems. Cook-Chennault *et al.* (2008) sought out to find the viability of PE harvesting in typical household appliances. Using two arrays of different piezoelectric transducers, the qp20w from MIDE, Inc. and the 40-0101 from APC International, Inc., Cook-Chennault *et al.* simulated their power output when cantilevered on a clothes dryer, a washing machine, and a microwave oven. For the clothes dryer, the qp20w produced 185 mW while the 40-0101 produced 68.6 mW; for the washing machine, the qp20w produced 103 mW while the 40-0101 produced

2.42 mW; and for the microwave over, the qp20w produced 5.66 mW while the 40-0101 produced 3.98 mW (Cook-Chennault, Thambi, Bitetto, & Hameyie, 2008). Although these energy levels could be used to power small electronic devices, it should be noted that the appliances were simulated having their entire surface areas covered with PE transducers. For example, to produce the projected 185 mW on the clothes dryer, more than 39,000 qp20w transducers are needed. Given that the price of one qp20w is priced at $64 (MIDE Corp., 2012), the total cost of the transducers would amount to nearly 2.5 million dollars. The PE array on the clothes dryer would not only produce a small power output of 185 mW, but would also cost a fortune to install.

PE harvesting can also be used to harvest ambient fluid flows. Priya *et al.* (2005) designed and tested a PE windmill energy device to harvest wind energy via piezoelectricity. 12 PE bimorphs were arranged in a circular array around a rotor attached to the windmill shaft. Attached to the rotor were 12 stoppers that would force each bimorph to bend 1.77 mm while rotating. A wind load was then applied so that the excitation frequency of the PE bimorphs was 6 Hz; a maximum power of 10.2 mW was obtained (Priya, Chen, Fye, & Zhand, 2005). PE harvesting has also been investigated under water currents. After calculating that PE materials could harvest 140 W/m^2 under a water current flow of 2 m/s, Pobering and Schwesinger (2004) designed and simulated the viability of using PZT cantilever bimorphs or PVDF flag generators to extract some of this ambient energy. For both types of generators, it was determined that a bluff body would need to be inserted into the river, upstream of the generators, in order to produce turbulent flow. Under simulation, the PVDF flag was calculated to generate between 11 and 32 W/m^2 of power while the power output of a PZT cantilever bimorph with 5 mm length, 3 mm width, and 60 μm thickness was reported to be 6.81 μW. Combining the PZT cantilever bimorphs into a 2D array, it was found that 100,000 units could be arranged in 1 m^2. Expanding into a 3D array, these PZT cantilever bimorphs could produce 68 W/m^3 which is approximately double the energy density of state of the art wind turbines (Pobering & Schwesinger, 2004). However, the concept was not validated, and design issues regarding the ability to generate vortices acting over each device are expected (Anton & Sodano, 2007). Additionally, the cost of materials and installation

would no doubt be much larger than current renewable energy technologies such as wind and solar power; piezoelectric harvesting would thus not be economically feasible to collect energy from ambient fluid flows.

Although the -33 coupling mode seems to be the more attractive option for energy harvesting due to its higher strain coefficient and coupling constant, the -31 mode has been used more often due to the relative ease of inducing a strain. Under the same forces and displacements, the bending bimorph configuration, which uses the -31 mode, has a greater potential to experience higher applied strains than a stack configuration, which operates in the -33 mode. When comparing a PE stack operating in the -33 mode and a cantilever beam operating in the -31 mode with equal volume, Baker *et al.* showed that the cantilever produced two orders of magnitude more power when subjected to the same force (Baker, Roundy, & Wright, 2005). The high mechanical stiffness of the stack configuration limited its strain which in turn limited its produced electric displacement. Baker *et al.* concluded that under a small force, low vibration environment, the -31 configuration is more appropriate. However, a stack configuration may be favorable under high force applications as they are more durable. Additionally, the -31 configuration is favored due to its lower resonant frequency. Roundy *et al.* concluded that the resonant frequency of a system operating in the -31 configuration has a much lower resonant frequency than a -33 configuration, making the -31 configuration more likely to resonate with ambient vibration levels and hence harvest more power (Roundy, Wright, & Rabaey, 2003).

It has also been shown that a PE transducer's shape can also greatly affect the power harvested. When comparing triangular and rectangular cantilevered bimorphs, Mateu and Moll demonstrated through mathematical derivation that the triangular bimorph will produce more power per unit area (Mateu & Moll, 2005). Similarly, Baker *et al.* experimentally tested a nearly triangular, trapezoidal cantilever bimorph versus a rectangular cantilever bimorph of the same volume and found that the trapezoidal bimorph produced 30% more power (Baker, Roundy, & Wright, 2005). Researchers have also demonstrated that prestressing a rectangular bimorph, like the one shown in

Figure 5-18 can increase a PE bimorph's power output. Danak *et al.* created a mathematical model to predict the power output of an initially curved PZT unimorph (Danak, Yoon, & Washington, 2003). The model showed the relationships between the generated charge and the initial dome height, substrate thickness, PZT thickness, and substrate stiffness. It was found that increasing the dome height gave the greatest increase followed by the substrate thickness and PZT thickness. To validate these findings, Yoon *et al.* carried out experiments on curved PZT unimorphs with varying initial dome heights, substrate thicknesses, substrate stiffnesses, beam widths, and beam lengths (Yoon, Washington, & Danak, 2005). The experiments confirmed that increasing the initial dome height, substrate thickness, and substrate stiffness all yielded higher charge outputs and also showed that charge output can be increased by increasing the length and width with the latter being more effective. Ting *et al.* also came up with a model to measure the power output of curved PZT unimorphs, but also took account of the harvesting circuitry within their proposed model (Ting, Hariyanto, Hou, Ricky, Amelia, & Wang, 2009). To validate the model, experiments were performed and gave excellent correlation with the model. As an example, at an excitation frequency of 135.59 Hz, the power output was predicted to be 46.26 mW; the experimental result was approximately 48 mW, giving a 3.6% error.

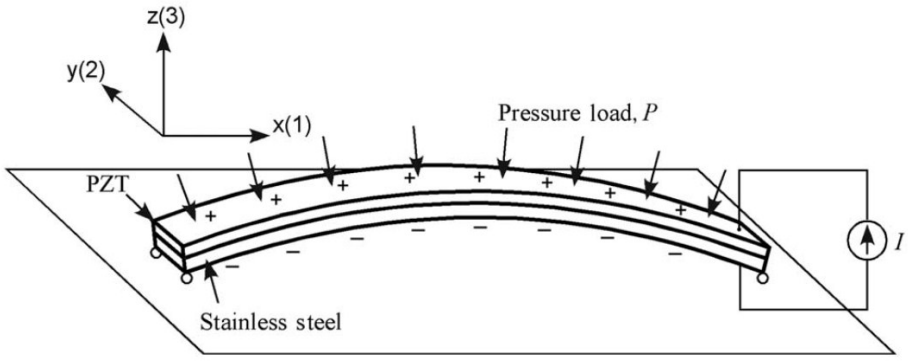

Figure 5-18: Curved PZT Unimorph Excited in 31-mode by a Normal Distributed Force. Extracted from (Yoon, Washington, & Danak, 2005)

Circular shaped PE transducers have also been investigated for energy harvesting applications but generally do not show much promise because of their -33 coupling mode operation as well as their high stiffness and resonant frequencies. Although Minazara *et*

al. found that 1.7 mW can be generated from a PE disc with a total radius of 20.5 mm, PZT radius of 12.5 mm, brass thickness of 400 μm, and PZT thickness of 230 μm, it should be noted that the disc was excited at a frequency of 1.71 kHz (Minazara, Vasic, Costa, & Poulin, 2006): a frequency that generally does not occur in a natural environment. To improve the power output of a circular discs, Kim *et al.* developed a piezoelectric cymbal transducer (Pictured in Figure 5-19) which consists of two dome-shaped steel end-caps that are bonded on both sides of a PE circular plate (Kim, Priya, Stephanou, & Uchino, 2007). The cymbal configuration uses both the 33 and 31 coupling modes to generate more power and also distributes the applied stress more evenly amongst the PZT layer. Under zero initial stress conditions, the cymbal transducer was excited by a 8N force at a 100Hz frequency; the maximum power was found to be 39 mW. However, under different conditions, Kim *et al.* improved on this power output. Under a prestressed condition (stress applied by a hydraulic press) of 67 N, the cymbal was exited by a 70N force at a 100Hz frequency and produced 52 mW. The maximum power output obtained in these experiments was nearly 100 mW at an excitation frequency of 200 Hz.

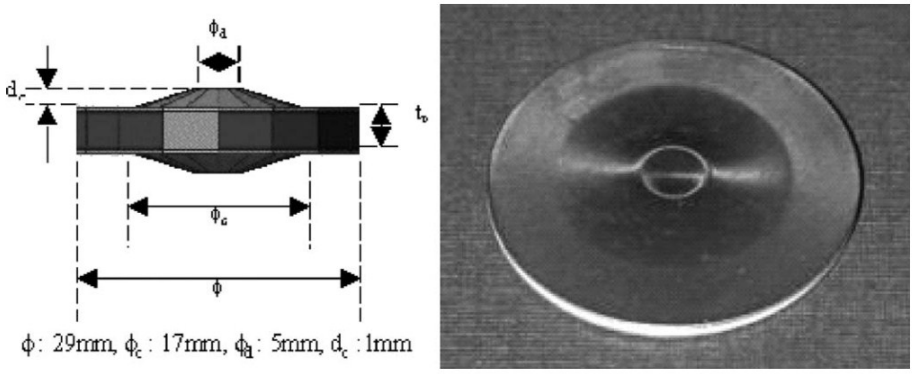

Figure 5-19: The Structure of the Cymbal Transducer developed by Kim et al. Image extracted from (Kim, Priya, Stephanou, & Uchino, 2007)

PE fibre composites have also been shown to increase power output in comparison to their heterogeneous bimorph counterparts. ACI has developed an energy harvesting system using its PE fibre composites to convert waste mechanical energy into useable electrical energy (Advanced Cerametrics Inc., 2009). The harvesting system is able to produce and store 880 mJ from a 30 Hz vibration source over a 13 second period: an

approximate power output of 68 mW. For the human powered LED jogging suit (as presented in Section 3.3), PE fibre composites, PE discs, and PE heterogeneous bimorphs were tested for energy harvesting for embedded shoe insoles. The PE fibre composites were used in the final product as they produced more power.

5.2.2 Harvesting Energy from Human Activity

In a world with ever-growing energy demands and climate change becoming more apparent, it is imperative for the human race to not only use less energy, but also tap into waste energy resources to make systems more efficient. One waste energy source that tends to be greatly overlooked is the human race itself. This concept is not new as there are several market products that rely on human energy to power electronic devices. Some of these products require a person to exert an intentional effort. Examples of these products include those that directly use the power such as shake driven flashlights or wind up radios and clocks, while other products convert the exerted mechanical energy to charge mobile devices such as the SOS Charger® Hand-Crank Emergency Cell Phone Charger. However, as an intentional effort is required, the aforementioned products do not harness wasted energy and thus generally are not viewed as energy harvesting technologies. Alternatively, there are other technologies that harvest energy from regular human activity that is generally unnoticeable. This section will give a brief review of these technologies.

One source of human power is body heat which is generally tapped by using thermoelectric technology (See 2.3.3.3). One of the first devices to tap into body heat was the Seiko SII Thermic® Heat-Powered Watch (Shown in Figure 5-20) which was brought onto the market in 1998 and only produced 500 models before being discontinued (Lee W. , 2003). In 2001, Thermo Life® Energy Corp. developed their commercial thermoelectric generator which operates at temperature differences as low as 5°C at which a matched load will have a 3 V electric potential at 10 μA and thus operates at 30 μW of power, but will be more efficient at higher temperature differences (Thermo Life® Energy Corp., 2008). Body heat harvesting technology has also been used to

power bio-monitoring devices. In 2006, Vladimir Leonov and Ruud J. M. Vullers built a working prototype of a blood oxygen sensor that was about the size of a watch and was powered by body heat. The sensor was able to generate about 100 µW or 600 µW depending if the patient was asleep or active, respectively (Ozcanli, 2010). With the success of the blood oxygen sensor, the duo then branched out to develop body-heat powered electroencephalographs (EEG) to measure brain activity and electrocardiographs (EKG) to measure heart activity. Pictured in Figure 5-21, the EEG device was in contact with 50 cm^2 of skin on the patient's forehead, harvested 3,500 µW, and wirelessly transmitted the brainwave data to a computer (Ozcanli, 2010). Photovoltaic cells were later added to the EEG device to offset some of the thermoelectric generation to reduce the cold sensation felt by the patient. Despite these breakthroughs in body heat harvesting, a thermoelectric generator can currently only convert roughly 0.4% of body heat energy into electrical power (Ozcanli, 2010). Oscanli (2010) mentions that if the whole human body were covered in thermoelectric generators, you would only be able to produce about 0.5 W. Not only would your body be quite cold, but you would not be able to power your cell phone which consumes about 1 W. Although thermoelectric generators have proven to be useful in low power applications such as wristwatches and bio-monitors, they have yet to become an efficient means of powering mobile electronics.

Figure 5-20: The Seiko SII Thermic® Heat-Powered Watch. Image extracted from (Lee W., 2003)

Figure 5-21: A Body Heat Powered Electroencephalograph Device developed by Leonov and Vullers. Image extracted from (Ozcanli, 2010)

The most popular means of harvesting human energy has been from extracting the kinetic energy from human movement. The key to harvesting this kinetic energy is to make it oblivious to the wearer. The Power Generating Dance Floor previously presented in Section 3.1.1 is an example of this concept; it harnesses the movement of the dancers without inhibiting the dancers' movements. One of the first devices to successfully operate solely from human power is the Seiko Automatic Generating System (AGS); an outline of the system is illustrated in Figure 5-22. The watch uses an oscillating weight that rotates when the user's wrist movements. The rotation then gets transferred to a 1/100 gear train where the rotation gets converted to an electric current by a rotating electromagnetic generator and charges a capacitor which in turn feeds the time circuits (Bosartis, 2010). The power output is 5 μW on average when the watch is worn, but 1mW when the watch is forcibly shaken (Paradiso, 2005). The watch first appeared under the trial name "AGM" at the Basel Fair in 1986 and was first commercially available in 1988. As of 2007, 8 million Seiko Kinetic watches have been sold worldwide (Seiko Watch Corporation, 2007).

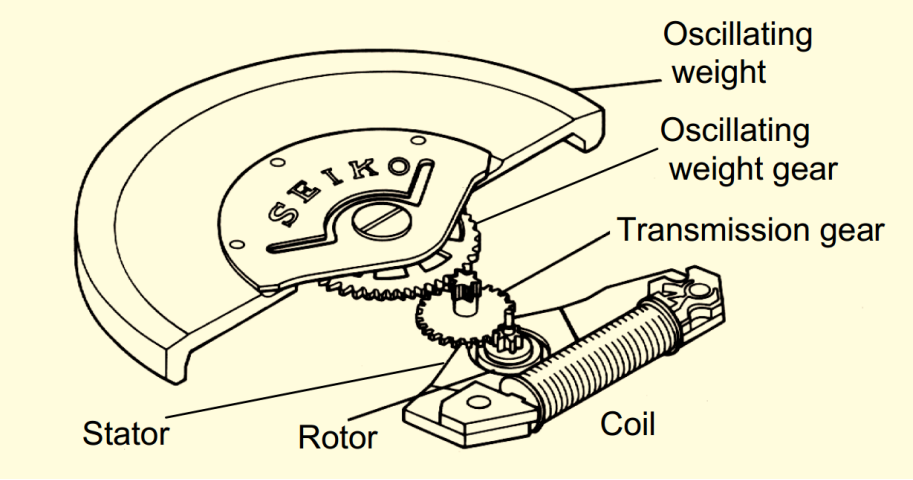

Figure 5-22: The Seiko AGS System. Extracted from (Paradiso, 2005)

Rotating electromagnetic generators have also been used to harvest energy from moving limbs. A knee-mounted brace has been developed by researchers at Simon-Fraser University that generates energy from a person's walking. Similar to regenerative braking in modern day automobiles, the device only extracts energy when the knee

swings forward; a process that relies on gravity more than muscle contraction. Results showed that effort was required by the user even with the generator disengaged. With the generator disengaged, results showed a 20% increase in effort by the wearer; with the generator engaged during the braking phase, it added fractionally more effort, and generated about 4.8 ± 0.8 W of power with a 5 ± 21 W increase in metabolic cost (Donelan, Li, Naing, Hoffer, Weber, & Kuo, 2008). The device also has the option to continuously generate power throughout the knee motion; 7.0 ± 0.7 W of electricity is generated but at an additional metabolic cost of 18 ± 24 W over that of the control condition. These results are visually shown as a histogram in Figure 5-24. Although the device is not oblivious to the wearer, it can generate enough energy to power mobile electronics. Like the human-powered gym presented in the introduction of this subsection, if the wearer intentionally exerts an effort using the knee-brace generator as a form of habitual exercise, it would be beneficial to harvest the expelled energy rather than wasting it.

Figure 5-23: The Knee-Mounted Generator by researchers at Simon Fraser University. Photo extracted from (Inman M. , 2008)

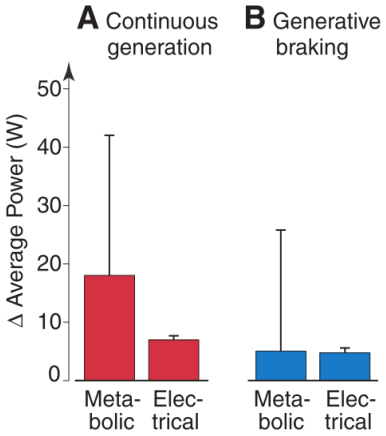

Figure 5-24: The metabolic input power and electrical output power for continuous generation and regenerative braking phase. Image extracted from (Donelan, Li, Naing, Hoffer, Weber, & Kuo, 2008)

One way of harnessing power while being oblivious to the wearer is by harvesting the vertical oscillations associated with walking. This can be accomplished via electromagnetic induction as was seen in the HPLED jogging suit (See Section 3.3) where a rare earth magnet resonates with the jogging motion when surrounded by an inductor coil. The harnessed energy from the HPLED jogging suit, 0.132 W per shaker,

was then directly used to power LEDs. Products have used electromagnetic induction to directly power mobile electronics through harnessing the power of walking. The nPower® PEG(Personal Energy Generator), shown in Figure 5-25, by Tremont Electric, Inc. claims to provide an output power of 2.5 W (5V DC at 500 mA current) and is compatible with more than 3,000 different mobile devices including the iPod®, iPhone®, and Blackberry® . Interestingly, however, you must fully charge the PEG using a USB cable before using it to charge your mobile device. Evidently, it isn't completely dependent on human motion for power. A similar product was developed by M2E Power, a product that is the size of a deck of cards and supposedly could generate 30-60 minutes of talk time on a cell phone after 6 hours of consistent walking (M2E Power, 2008). M2E Power was aiming to have their product on the commercial market in early 2009, but ended up selling its assets to Motionetics, Inc. (Caceres, 2009). Krassen Dimitrov, a Group Leader at the Australian Institute for Bioengineering and Nanotechnology at the University of Queensland, was not surprised by the company's folding stating that M2E Power's claims defied the laws of physics. Dimitrov stated, "M2E's business idea is unworkable due to simple thermodynamic constraints. This is evident using basic calculations and first-order approximations" (Fehrenbacker, 2009). As for the $8 million in external funding raised by M2E Power, Dimitrov described it as "another example of irresponsible investment decisions amidst the hype of alternative energy" (Fehrenbacker, 2009).

Another case study that harnessed the power of the vertical oscillations from walking is the Power-Generating Backpack invented by Larry Rome. With a 38 kg load, the backpack (pictured in Figure 5-26) can harvest as much as 7.4 W during brisk walking (Rome, Flynn, Goldman, & Yoo, 2005). At a value of 4.8 ± 3, the backpack also has a good cost of harvesting (COH): the additional metabolic power required to generate 1 W of power. Despite the high power output and low COH, the backpack is quite bulky and is not oblivious to the wearer.

Figure 5-25: The nPowerPEG can be used to power your mobile devices. Image Extracted from (Tremont Electric, Inc., 2011)

Figure 5-26: The Power-Generating Backpack attached to its inventor, Larry Rome. Image Etracted from (Lester, 2005)

As previously presented in Table 5-11, footfalls (also known as heel strikes) were found by Starner to have the most potential for power harvesting human activity with 5-8.4 W of electrical power available. In a similar study, Niu *et al.* analyzed the ability for several human motions to be converted into electrical energy. The results of this study are presented in Table 5-13. Although heel strike appears to not be the best option for energy harvesting as Table 5-13 suggests that joint motions such as ankle, knee, and hop movements can generate more power, Niu *et al.* argue that these power outputs are not practical as the wearer must exert extra work onto the attached generator to generate said power outputs. This excess work is known as negative work as is expressed as a percentage in Table 5-13. Niu *et al.* suggest that heel strike would still be a good candidate as it has no negative work and could be easily incorporated into a shoe.

Table 5-13: Energetic Motions for Biomechanical Electric Power. Extracted from (Niu, Chapman, Riemer, & Zhang, 2004)

Joint/Motion	Work [J/step]	Power [W]	Max Moment [Nm]	Negative Work [%]
Heel Strike	1	2		
Ankle	34.9	69.8	~140	42
Knee	24.7	49.5	~40	85.2
Hip	19.6	39.2	~40	11.5
Elbow	1.07	2.1	1-2	37
Shoulder	1.1	2.2	1-2	61
Center of Mass	0.5	1		

Several different shoes have been made in an attempt to harvest the power from footfalls. One of the most successful power output thus far (that the author knows about) was obtained by using dielectric elastomers. Kornbluh *et al.* configured the materials into the heel of the shoe such that when pressed down, it ballooned between a set of holes built into the shoe's frame, thus increasing the stress put on the material (Kornbluh, et al., 2002). The device (outlined in Figure 5-27) produced 0.8 J per step (Kornbluh, Eckerie, & McCoy, 2011), a pace of two steps per second would thus produce a power of 0.8W. Based on an 80 kg person who exerts a 3mm maximum deflection at their heel, Kornbluh *et al.* state that the shoe operates at a 33% efficiency. However, it should be noted that a very large bias voltage (generally several kilovolts) is needed to generate the power as the electric current is produced by compressing the dielectric elastomer material and changing its capacitance (Shenck & Paradiso, 2001). The energy harvesting system can thus be quite difficult to fully integrate into active footwear.

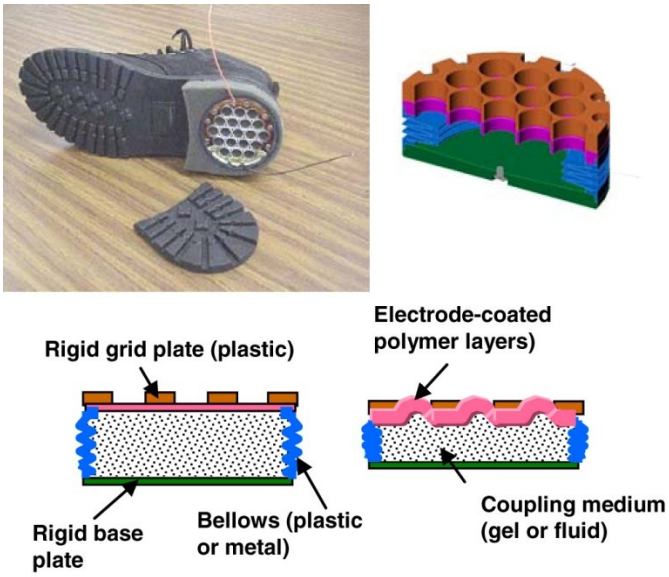

Figure 5-27: The Outline of the Shoe designed by Kornbluh et al. that harvests the energy of footfalls via dielectric elastomers. Image extracted from (Kornbluh, Eckerie, & McCoy, 2011)

Another shoe-embedded harvesting technology that is currently being researched is based on reverse electrowetting. Electrowetting is when the shape of a liquid droplet sitting on a liquid-repelling surface is changed by applying a voltage to said surface. Tom Kripenkin and Ashley Taylor, engineering researchers at the University of Wisconsin-Madison, apply this principle in reverse, converting the energy of moving said liquid into

an electrical current (Aron, 2011). After experimenting with various liquids, they settled on Galinstan: a liquid that is used in thermometers, but is non-toxic. Kripenkin and Taylor state that the device (shown in Figure 5-28) can produce between 1 and 10 Watts of power (Aron, 2011), but this value is met with skepticism. Andrew bell, who researches electronic materials at the University of Leeds, is surprised that they think they can get that much energy out of it and would like to see a demonstration that the numbers are correct (Aron, 2011). Forming a company, InStep NanoPower, LLC, Kripenkin and Taylor aim to get their product into the commercial market to provide a means of powering mobile devices and to also act as a "middleman" between mobile devices and wireless networks, a feature that reduces power consumption of wireless mobile devices (InStep NanoPower, LLC, 2010).

Conventional electricity generating technologies such as electromagnetic generators have also been integrated into shoes. Electromagnetic generators are more difficult to integrate in shoes due to their bulkiness, but they can be a better power harvesting option due to their high efficiency and well-established technology. Figure 5-29 shows a rotary magnetic generator developed by the Responsive Environments Group at MIT's media lab. The generator is a removable shoe attachment that uses a lever-driven flywheel mechanism. When worn and tested, the device generated an average of 230 mW, but significantly hampered the wearer's gait (Kymissis, Kendall, Paradiso, & Gershenfeld, 1998). The Responsive Environments Group then looked into embedding a rotary magnetic generator directly into the heal of a shoe. The prototype (shown in Figure 5-30) uses a lever and a gear train mechanism to drive to DC motors that are used as generators. When tested, the prototype generated 60 mW (Shenck & Paradiso, 2001), but the wearer's gait was again affected. It was concluded that the power output could be increased to about 1W by using a mechanical energy storage device, such as a clock spring, which would allow the generator to continuously drive between steps. Water turbines have also been integrated into shoes to harvest power from walking. Japan's Nippon Telegraph and Telephone (NTT) has developed a shoe with water-filled insoles; every time the wearer takes a step, water is forced through a small turbine which in turn generates power (Japan Probe, 2008). The prototype generates 1.2 Watts of power which

is enough to power an iPod or cell phone. Unfortunately, the prototype is quite bulky (as can be seen in Figure 5-31); NTT planned to alter the design and have it ready for the commercial market as early as 2010 (Schwartz A. , 2008), however, the author has yet to find a resource where one can buy these hydroelectric shoes.

Figure 5-28: The energy harvesting shoe concept developed by InStep Nanopower using reverse electrowetting to generate electricity from human footfalls. Image extracted from (InStep NanoPower, LLC, 2010)

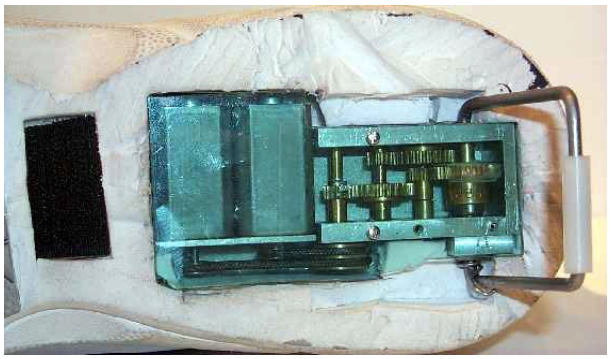

Figure 5-29: The Rotary Magnetic Generator Retrofit developed by the Reponsive Environments Group at MIT Media Lab (1998). Image extracted from (Paradiso, 2005)

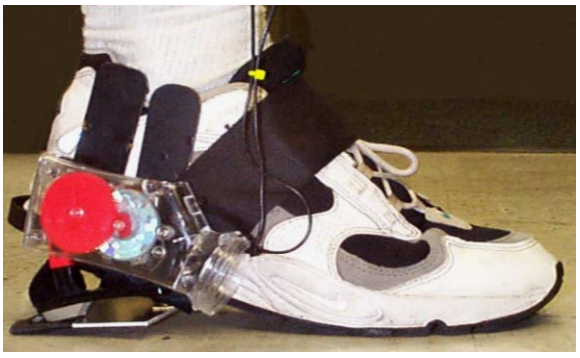

Figure 5-30: A Rotary Magnetic Generator completely embedded into the sneaker's sole (1999). Image extracted from (Responsive Environments Group-MIT, 2006)

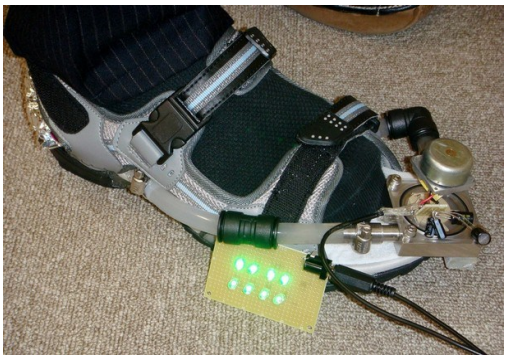

Figure 5-31: NTT Corp. developed shoes that uses water turbines to produce power. Image extracted from (Japan Probe, 2008)

5.2.3 Harvesting Human Energy using Piezoelectric Materials

As piezoelectric materials have the ability to transfer the mechanical energy from stress to a direct electric displacement, it is unsurprising that there has been much research in the use of piezoelectric materials to harness the mechanical energy from human activity. One advantage piezoelectric materials have over other human energy harnessing technologies is their ability to be oblivious to the wearer. The technologies presented earlier such as thermoelectric and electromagnetic generators tend to be bulky and affect

the wearer's comfort or gait. As piezoelectric harvesting materials and circuits tend to have fewer parts and are smaller in size, they can be more easily integrated into clothing and wearable accessories. This section will review some of the research developed for harvesting the wasted energy of human activity via piezoelectric materials.

After reading about the success of the energy harvesting backpack developed by Rome *et al.* (2005), Sodano took note that the device was rather cumbersome, can interfere with the wearer's gait, or put additional strain on the wearer. With the aim to design a system that provides no additional stress or load to that of a conventional backpack, Sodano sought out to integrate piezoelectric materials within the backpack to extract wasted human power. Sodano investigated the use of two PE systems integrated onto a backpack: PVDF films attached to the backpack's straps and PZT stacks with a mechanical amplification to induce more stress. With regards to the PVDF straps, Sodano formulated a model that would predict the power output within 13% of the actual value (Sodano, Harvesting Energy from the Straps of a Backpack Using Piezoelectric Materials, 2009). With the model validated through experimentation, it was determined that by using four straps in parallel (each strap being 1.2 m in length, 51 mm wide, and 52 μm in thickness), a total power of 45.6 mW could be harvested under a 444 N backpack load. The straps were in parallel as they generate lower voltages with higher current leads; a trait that is more beneficial for charging small batteries or supercapacitors. With regards to the PZT stacks, Sodano proposed to use the 33 coupling mode despite the fact that the 31 coupling mode is more often used in PE harvesting. As mentioned earlier, the 33 coupling mode has a larger strain coefficient and is more durable, favourable traits for energy harvesting, but the 31 coupling mode is apt to experience higher strains through bending; strains that will generally produce more power despite the lower strain coefficient. Concerned that the bending strains on the backpack loading may be excessive and induce the PZT transducers to fracture, Sodano proposed that the stress on a PZT stack be amplified via a mechanical amplification system to induce greater electric displacement on the 33 coupling mode. Consisting of lever mechanisms, the load on PZT stack was amplified by a factor of 10.8. After verifying the simulated model through experimental testing, it was determined that the

amplified stack configuration would produce a power output of ~16 mW under a backpack load of 100 lb (444 N). Although both the PVDF and PZT stack designs do not come close to the power output of Rome et al's backpack (2005), they are both sufficient to power small wireless sensors. Another proposed wearable power supply is through wrist movement, similar to the Seiko AGS system presented earlier. Renaud *et al.* (2005) proposed using PE materials to harvest the power from wrist and arm movement during walking. Although not experimentally tested, simulations showed that a maximum of 40 μW of power could be produced when attached to the wrist of a person walking

PE harvesters have also been proposed to harness human waste energy to power implantable devices. As batteries need to be replaced in implantable devices (*e.g.* pacemaker batteries generally last for 5-10 years (Tier Cardiology Group, PC, 2011)), it would be beneficial if the implantable devices could harvest the needed power from wasted energy derived from human activity. Platt *et al.* developed an in-vivo PE harvester and sensor to be used in self-powered knee replacement units. Solely powered from PE harvesting, these knee replacements are capable of sensing important phenomena associated with the knee such as abnormally high forces exerted on the joint, degradation, and misalignment. Using an applied force of 2600 N (a standard force during walking) a maximum of 4 mW of raw power and 0.85 mW of regulated power was generated (Platt, Farritor, & Haider, On low-frequency electric power generation with PZT ceramics, 2005a). In a follow-up study, Platt *et al.* showed that by subjecting the total replacement knee unit to a 900 N standard force profile, about 4.8 mW of continuous raw power was generated by combining three stacks, each of approximately 145 layers of PE materials to the unit. This output power was proven to be capable of powering many existing low-power microprocessors (Platt, Farritor, & Haider, 2005b).

To power functional electrical stimulation (FES) devices, also known as neural prostheses, it has been proposed that PE harvesting devices could be a viable alternative to batteries or transcutaneous energy transfer systems. FES devices use electrical current pulses to artificially stimulate nerves in patterns that result in muscle contractions allowing muscles to be restored to some extent. When comparing a muscle's mechanical

output power to the electrical power necessary to initiate its stimulation, one would observe that the muscle acts as a power amplifier; a small amount of power initiates the chemical reaction that converts chemical energy within the muscle to mechanical power. Based on the hypothesis that more electrical power can be converted from a muscle contraction than is needed for the initial electrical stimulation, Lewandowski *et al.* have proposed placing a PE transducer mechanically in series with a muscle-tendon unit and bone to harvest energy from stimulated muscle contractions in FES devices (Lewandowski, Kilgore, & Gustafson, 2009). A portion of the harvested energy will be used to power the nerve stimulations while the remainder will be used to power an additional application. Estimating the maximum input power needed for both the initial stimulations and the energy storage circuitry at 14 μW, it was determined that enough power could be harvested from the muscle contractions providing that the muscle produced a sustained force greater than 55 N: a force that many muscles in the human body can produce (Lewandowski, Kilgore, & Gustafson, 2009).

To investigate the feasibility of harvesting energy from blood pressure variations using PE materials, Clark & Mo investigated the use of PE unimorph diaphragms (Clark & Mo, 2009). Figure 5-32 illustrates the simulated PE unimorph under a pressure load (P_0) with arbitrary boundary conditions, the PE layer and substrate layer radii are represented by R_1 and R_2, respectively. Using three different boundary conditions, Clark & Mo sought out to find the radii ratios that would give the largest power outputs. The three different boundary conditions were a simply-supported diaphragm that is partially covered with PE material, a clamped diaphragm that is partially covered with PE material, and a clamped diaphragm with a fully covered and regrouped electrode (fcr). The fcr scenario (pictured in Figure 5-33) simulates a fully covered plate with a reversal in polarity at a radius of R_e. The reason for the reversal is due to the fact that if the disc was clamped and fully covered (*i.e.* $R_1=R_2$), the net power would be zero as a portion of the disc would generate a positive charge (the region in which the PE layer is going through tension) up to a certain radius while the remainder would generate a negative charge (the region in which the PE layer is going through compression); when integrated, the net charge would be zero. By altering the polarity at a certain radius (*i.e.* R_e), one can completely cover the

diaphragm with PE material and generate a net electric charge. For all three scenarios, Clark & Mo derived power output equations under a periodic external pressure. Table 5-14 presents the simulated results using an aluminum substrate layer radius of 1.27 cm, an applied pressure of 40 mmHg (*i.e.* the difference in systolic and diastolic blood pressure), a 1 Hz frequency, and a PE layer composed of PZT-5H from Piezo Systems, Inc. All simulations were done under their optimum PE layer to substrate layer thickness ratio. With a magnitude of 47.0 μW, the simply-supported diaphragm with an R_1/R_2 value of 0.6 generated the largest power output for continuous use. It was concluded that although the device would not likely be able to continuously power a device, it could potentially power a device at reasonable intermittent rates.

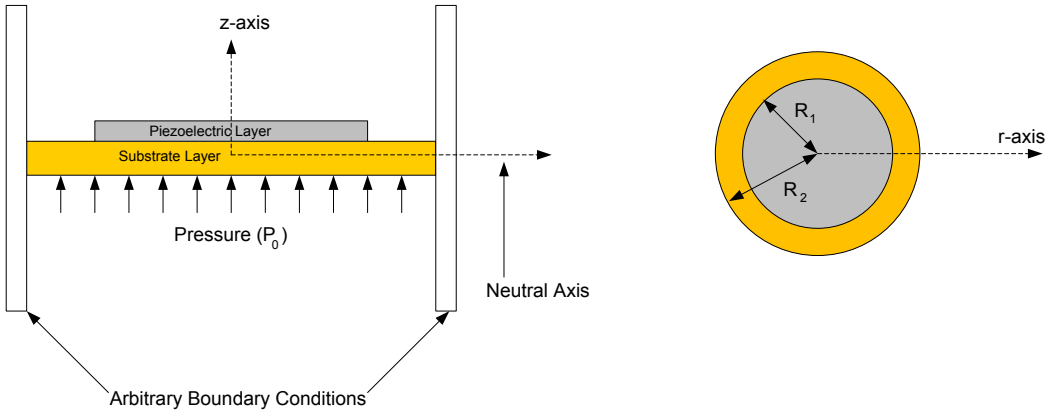

Figure 5-32: The Cross Section of a unimorph PZT circular plate with arbitrary conditions as defined by the investigation carried out by (Clark & Mo, 2009)

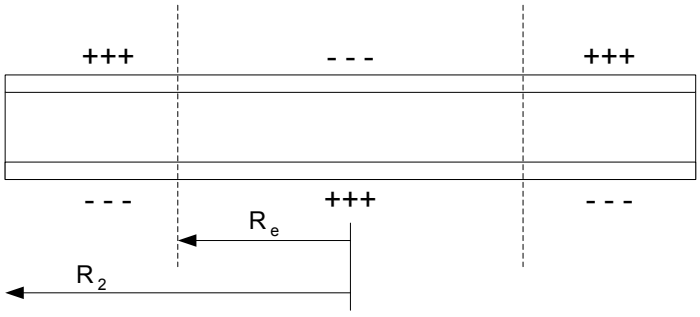

Figure 5-33: Cross section of the regrouped PZT layer showing the reversal of polarity on the charge that would be observed after regrouping the electrodes. Extracted from (Clark & Mo, 2009)

Table 5-14: Power generation for continuous and intermittent usage by blood pressure. Table extracted from (Clark & Mo, 2009)

Harvesters	Max Power @	Design Specification	Generated Power for Continuous Use (μW)	Required Time for Intermittent use of 10mW
Plate (127 μm PZT)	$R_1/R_2 = 0.6$	ss, pce	47.0	4 min
	$R_1/R_2 = 0.87$	cl, pce	18.5	9 min
	$R_e/R_2 = 0.707$	cl, fcr	2.6	64 min
ss: simply-supported, pce: partially covered electrode, cl: clamped, fcr: fully covered and regrouped electrode				

As mentioned, heel strikes have been documented as the human activity with the most potential for energy harvesting, largely due to the high energy of footfalls and the potential for assimilating energy harvesting technology directly into shoes. Most of the examples of energy harvesting footwear previously presented in Section 5.2.2 were quite bulky, affected the wearer's gait, or required many components. With regards to energy harvesting footwear, what sets PE materials apart from the other technologies is the ease of which they can be integrated into shoes as well as their ability to function with fewer, less bulky components. Both of these advantages are key to making the technology oblivious to the wearer; the gait will thus be less affected. Because of these advantages, there has been much research in PE materials and their ability to harvest energy through human foot traffic.

With the overall aim of creating self-powered radio frequency identification (RFID) tags for military applications, the investigations carried out by the MIT Media Laboratory, led by Joseph Paradiso, have been some of the most reference examples of PE embedded insoles. Two of the investigations carried out by the MIT Media Laboratory were performed by Kymissis et al (1998) and Shenck & Paradiso (2001). Capitalizing on the increased strain advantage of the 31 coupling mode, Kymissis *et al.* (1998), used two PE harvesting approaches to harvest footfalls directly in footwear. The first approach was a PVDF stave located at the ball of the foot. The stave consisted of two eight-layer stacks of 28 μm PVDF film connected electrically in parallel and sandwiching a 2 mm flexible plastic substrate bonded with epoxy. At a step frequency of approximately 1 Hz with a 250 kΩ resistive load, the stave's averaged power output was 1.1 mW. The second

approach used a curved PZT unimorph at the heel of the shoe. Using a Thunder TH-6R transducer manufactured by Face International Corp., the unimorph consisted of a 5 x 5cm, 0.015" PZT strip that was bonded to a prestressed, 5 x 8.5 cm sheet of spring steel that was neutrally curved with an eccentricity of 2.5 mm. At a step frequency of approximately 1 Hz, the curved unimorph had an averaged power output of 1.8 mW. In a follow up investigation, Shenck & Paradiso sought out to improve the power output for both approaches. Shenck & Paradiso did not change the PVDF stave design, but they did add another curved unimorph to the PZT harvesting design. The new design consisted of two Thunder-6R transducers, electrically connected in parallel, of the same dimensions as the unimorph used by Kymissis *et al.* (1998) and mounted them, one on each side, of a beryllium-copper midplate. Figure 5-34 shows an illustration of both approaches used by Shenck & Paradiso (2001). The experimental outputs from both the Kymissis *et al.* (1998) and Shenck & Paradiso (2001) are shown in Figure 5-35 and Figure 5-36 which respectively show the results from the prestressed PZT transducers and staves. The Shenck & Paradiso investigations showed improvements over both designs; the maximum averaged power outputs for the PVDF stave and PZT curved dimorph at a frequency of 0.9 Hz were found to be 1.3 mW and 8.4 mW, respectively. However, for the PVDF stave comparisons, it should be noted that the graphed power outputs for both the Kymissis *et al.* and Shenck & Paradiso investigations appear to have identical shapes; the only difference appears to be from the averaged power outputs. This leads the author

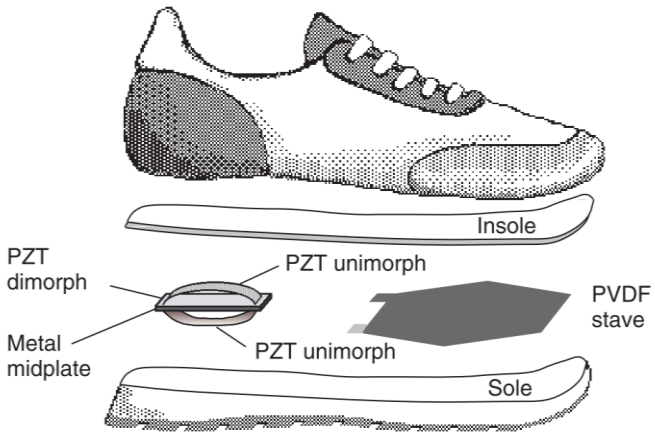

Figure 5-34: Two approaches to unobstrusive 31-mode PE energy scavenging in shoes: a PVDF stave under the ball of the foot and a PZT dimorph under the heel. Image extracted from (Shenck & Paradiso, 2001)

to believe that both PVDF power output graphs are the same graph, but one of the power outputs was mistyped; if true, there was no improvement in the PVDF stave as Shenck & Paradiso simply referenced the investigation by Kymissis *et al.* Although both studies produced power outputs two magnitudes lower than some of the energy harvesting soles presented in Section 5.2.2, both studies mentioned that the PE harvesting soles were easier to integrate within the shoe's insoles and were unobtrusive to the wearer.

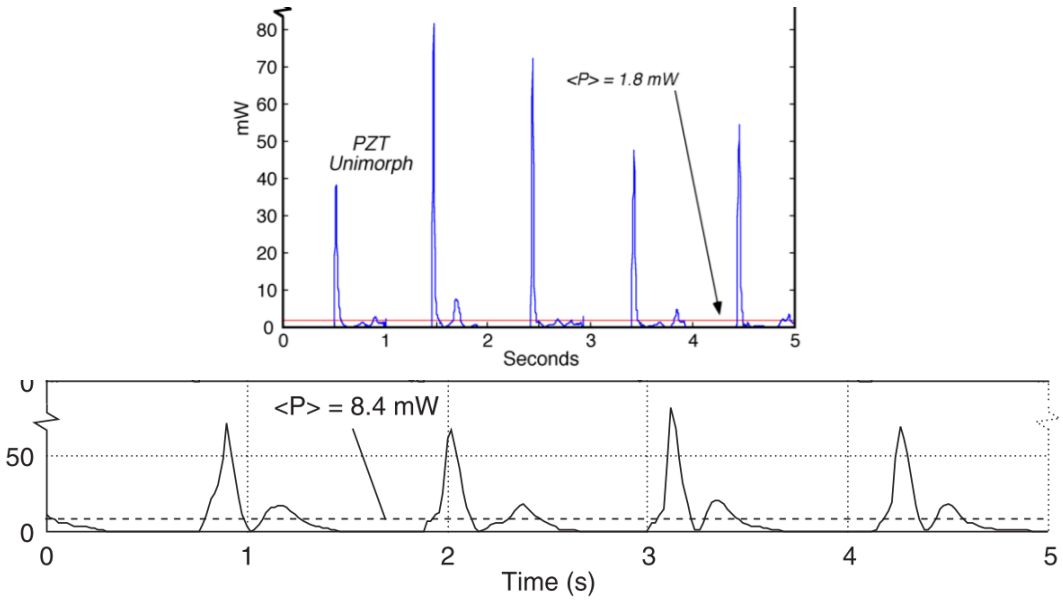

Figure 5-35: The experimental power outputs for the prestressed curved PZT (top) unimorph from Kysmissis et al. (1998) and (bottom) dimorph from Shenck & Paradiso (2001)

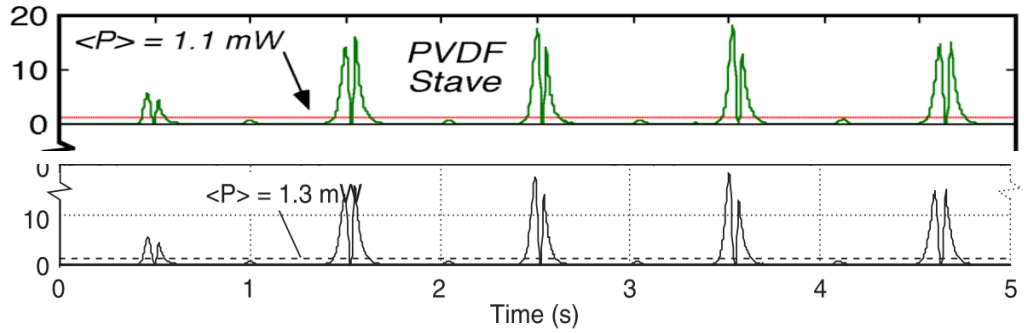

Figure 5-36: The experimental power outputs for the PVDF stave from (top) Kymissis et al. (1998) and Shenck & Paradiso (2001).

One of the most publicized stories of energy harvesting shoes via PE harvesting is with The Electric Shoe Company, founded by Trevor Baylis: inventor of the Freeplay clockwork radio: a radio that is powered by hand via a crank. With a half million pounds in startup capital from Texon (a shoe making company), Baylis successfully integrated a

PE harvesting device into a pair of boots and tested it in the Namibia Desert in June, 2000 as a fundraiser for his favourite charity: the Mines Advisory Group. After 100 miles of walking over 5 days, the boots were able to charge about half of his battery's cell phone (Drake, 2001). Baylis claimed that the boots are able to generate 100-150 mW of power (Paradiso, 2005), but to the author's knowledge, there has been no follow up on this product. A post on everything2.com claims that the company has gone out of business (Everything2 Media, LLC., 2002).

To extract more power from PE harvesting, one method is to increase the frequency of applied stress. Some researchers have used shoe embedded hydraulics to increase the applied frequency. In a study carried out by Steyn & Hagood (2003), a microhydraulic transducer (MHT) was designed and built with the goal of extracting 1 W from heel strike motion. Using discrete PE elements paired with hydraulic amplification, PE hydraulically amplified valves were produced that made it possible to create a pulsing fluid pressure on a PE piston, and hence extract more electrical power using larger excitation frequencies (Steyn & Hagood, 2003). The final device was not fully embedded into shoe insoles, but was experimentally tested at a frequency of 1 kHz at a differential pressure of 450 kPa; the maximum power output was found to be 1 mW which is 0.1% of the goaled power output.

With the aim of self-powering artificial organs, Antaki *et al.* also used hydraulics to amplify the induced stresses on shoe-embedded PE harvesting devices. The original design would use hydraulic amplification to provide a 35:1 mechanical advantage and additionally incorporate a hydraulic oscillator into the master piston to convert the constant stroke to a higher frequency (by a factor of 5) pulsed excitation of the stack (Antaki, et al., 1995). To verify the viability of PE embedded shoes, Antaki *et al.* built a smaller prototype that would have a mechanical advantage of 7.6 from a simplified hydraulic amplifier without oscillation and used a single stack of 18 PZT ceramic slugs (PZT-5A, 0.31" diameter, 0.245" thick). At a walking frequency, the predicted power outputs ranged from 421 mW to 942 mW, depending on the weight of the participant (52 kg to 75 kg). The measured power output for one shoe from four different people within

the previously defined weight range was 156 mW to 676 mW at a walking pace (roughly 1 Hz) and 676 mW to 2100 mW for simulated jogging (roughly 2 Hz with an increased heel strike force). Although the experimental results did not match the predicted values, the experimental results still harnessed a useful amount of power; the walking experiments produced an average power of 5.7 ± 2.2 mW/kg body weight while the jogging provided a higher average power level of 23.6 ± 11.6 mW/kg. However, the author (of this thesis) is quite skeptical of both the predicted values and experimental values. For example, in the paper written by Antaki *et al.* (1995), they mentioned that "for each heel/toe strike to generate 2.05 J of energy, in light of the maximum recommended stress of approximately 10 x 10^3 psi, this will require 8.5 x 10^{-7} m^3 of PZT material". The formula used to calculate this volume was presented in their paper as Equation 5-94 with U_e and V_{ol} representing the electrical energy converted by the PE transducer and the PE transducer's volume, respectively.

$$U_e = \frac{1}{2}\epsilon\sigma_{33}^2 g_{33}^2 V_{ol} \qquad 5\text{-}94$$

Using a dielectric constant of 10.5 x 10^{-9} F/m, which was listed in a table presented in the paper by Antaki *et al.*, a voltage constant of 0.311 Vm/N would be needed to produce the desired 2.05 J under the set parameters. Looking at the voltage constants previously presented in Table 5-5, the calculated voltage constant is more than 1100% larger than typical PE voltage constants; the calculated voltage constant is therefore not conceivable. Additionally, using the equations presented by Antaki *et al.* (1995), the author could not replicate the predicted values presented in their paper. For example, for a 75 kg person, Antaki *et al.* predicted a power output of 942 mW. Using the parameters of the prototype design, and assuming they used the highest g listed in their parameter table (41 x 10^{-3} Vm/N), the author calculated a maximum power output of 35.2 mW which is less than 4% of their predicted value. Based on the author's calculated predictions, it seems quite likely that Antaki *et al.* greatly overestimated their predicted values and also wrongly measured their results.

Howells (2009) also aimed at increasing the mechanical excitation frequency of PE transducers during heel strike energy harvesting; however, he would use a mechanical approach. With a goal of generating 0.5 W of power at a 1Hz step rate, Howells designed a generator (shown in Figure 5-37) that would translate the vertical displacement, using a lead screw and gear train, into a cam's rotation. As the cam rotates, it deflects four PZT-5A bimorph stacks to deflect sinusoidally. The stacks are arranged in such a way that they oscillate 90 deg out of phase with one another, recycling most of the elastic energy stored in the bimorph crystal stacks. On average, the Heel Strike Generator produced an output power of 90.3 ± 5.9 mW.

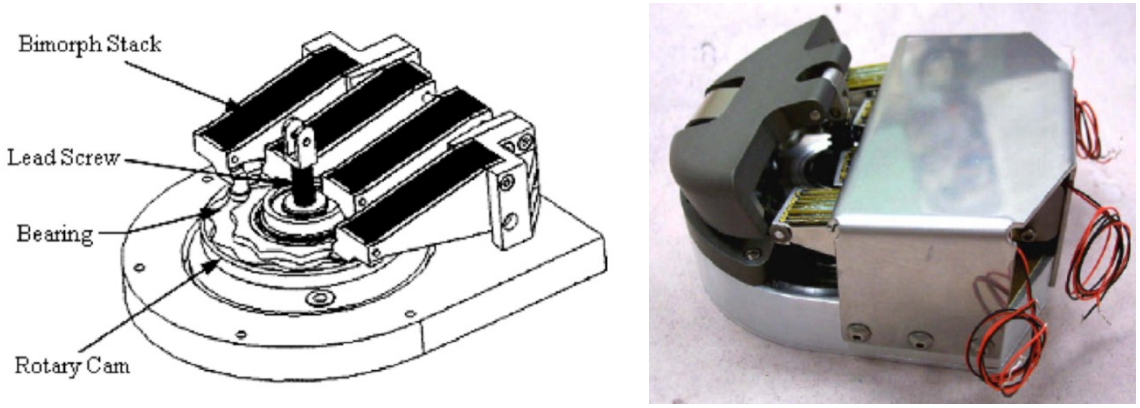

Figure 5-37: (Left) A schematic of the Heel Strike Generator and (Right) a prototype developed by Howells (2009). Images extracted from (Howells, 2009)

Aside from shoes, it has been proposed that energy from human foot traffic can be harvested by integrating PE materials into flooring. Similar to how energy harvesting shoes would supply power to the wearer to power electronics, energy harvesting flooring would alternatively supply power to the surrounding environment. Piezoelectric flooring has been installed at the ticket gates at a Tokyo train station by the East Japan Railway Company (JR East). First installed in 2006, PE flooring was installed over a 6 m^2 area and tested its power output over an eight week period (JR East Group, 2008). The flooring consisted of readily available, inexpensive PE discs and produced a maximum of 10,000 Watt-seconds per day which is about 19.3 mW/m^2 or 1.8 mW/ft^2 of continuous power. During the third week of the experimental period, after a total of 800,000 people had passed onto the flooring system, there was a decrease in power output due to durability degradation. In 2008, JR East decided to follow up on the PE flooring

experiment by installing more flooring with an aim to produce more than 10 times the values obtained from the previous experiment. Installed from January to March of 2008, the new flooring had an increased density in PE elements, improved harvesting circuits, and enhanced durability. The author could not find any resources that reports on the amount of power generated from the second flooring.

As previously reported in Section 3.1.1, the Power Generating Dance Floor by Sustainable Dance Club reported to use piezoelectric harvesting from numerous websites and there are videos on YouTube that suggest that piezoelectric harvesting was considered at one point. However, the power generating dance floor's brochure gives no indication that piezoelectricity was used and videos that showcase the final commercial product tend to suggest that rotary electromagnetic generators were used to generate power. Other than Club Watt in Rotterdam, the Netherlands, the power generating dance floor was installed at the Temple Nightclub in San Francisco, CA in March, 2011 (Hulkower, 2011). However, before collaborating with Sustainable Dance Club, the Temple Nightclub first had a consultation with another energy harvesting flooring company named POWERleap, Inc. (Adams, 2009). POWERleap, LLC claimed in 2009 that their floor tiles could generate 1-5 W of power per square foot: a claim that produces much higher results than what was found in the literature review. In comparison to the PE flooring system developed by JR East, POWERleap, LLC claims that its flooring system can produce a power output that is 3 magnitudes higher; this claim is very skeptical to the author. For a more detailed investigation of POWERleap, LLC's claims, refer to Appendix B2. Giving POWERleap, LLC the benefit of the doubt, the author sought out to investigate the maximum power output that can be harvested from human foot traffic via PE harvesting. Both the shoe and flooring scenarios will be investigated along with five different bimorph configurations and bending mechanisms.

5.3 OBJECTIVES

The overall objective of this chapter is to see if it is commercially and technically feasible to harvest the wasted energy from human foot traffic using PE harvesting. Two methods will be investigated: embedding PE materials in shoe insoles and embedding PE materials

in floor tiles. Using different PE material shapes and methods of deformation, the author will determine the maximum power output for each scenario and determine the maximum power outputs that can be obtained by applying these deformation scenarios in both energy harvesting shoes and floor tiles. The scenarios that will be investigated are:

1. PE circular discs mechanically deformed in the 33 direction by a uniform load from human weight. Both singular and stacked PE discs will be investigated. Equations from Section 5.1.6.1 will be used.
2. PE circular discs mechanically deformed in the 31 direction by a uniform hydraulic pressure induced from human weight. Results from Clark & Mo (2009) will be used.
3. Rectangular PE transducers deformed in the 31 direction by mechanically extending the transducer in the longitudinal direction by translating a force from human weight. Equations from Section 0 will be used.
4. Rectangular PE transducers constrained as a cantilever beam and deformed in the 31 direction by mechanically bending the transducer at its free end using human weight. Equations from Section 5.1.6.4.1 will be used.
5. Rectangular PE transducers that are simply constrained on both ends and deformed by applying a load at the transducers mid-point using human weight. Equations from Section 5.1.6.4.2.

5.4 REQUIRED COMPONENTS FOR PIEZOELECTRIC HARVESTING

The investigations carried out in this chapter will only account for the absolute maximum power that can be extracted from human foot traffic using PE harvesting. To calculate the maximum power that can be extracted from a PE transducer, only the material properties, geometry, constraints, and mechanical input parameters are needed. However, in order to extract this maximum energy, one must construct an effective harvesting circuit. There are several different PE harvesting circuits; some are more effective than others. A circuit that does not take account of important factors such as impedance matching or switching techniques will only be able to harvest a small fraction of the available power from a PE transducer. As the objectives of this investigation are to find the maximum power outputs that can be extracted from PE transducers, it will be

assumed that the PE harvesting circuit extracts the maximum amount of available energy. Although this investigation assumes a perfect harvesting circuit, it is still beneficial to overview the components required to harvest energy from a PE transducer. It could set the stage for researchers to experimentally examine the feasibility of harvesting wasted energy from human foot traffic via PE transducers.

5.4.1 The Basics: Full Wave Rectifier, Load, and Smoothing Capacitor

When a short circuited PE transducer is induced by a mechanical force periodically, it produces a current twice; once when pressed and once when released. When pressed, a small current flows from one side of the PE transducer to the other, when released a small current flows in the reverse direction. In other words, a PE transducer will produce an alternating current when mechanically induced. As most applications use direct current, it is usually necessary to convert an alternating current (AC) to a direct current (DC). This is often done using a full-wave bridge rectifier. Pictured in Figure 5-38, a full-wave bridge rectifier consists of four diodes that are attached to an alternating current (*e.g.* a PE transducer that is being mechanically excited sinusoidally) in such a way that an alternating signal is completed translated into a positive voltage output. Also attached to

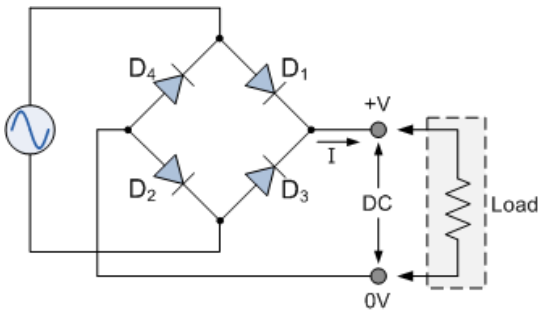

Figure 5-38: A basic AC/DC converter consists of a full-wave bridge rectifier and a resistive load. Image extracted from (Storr, 2012)

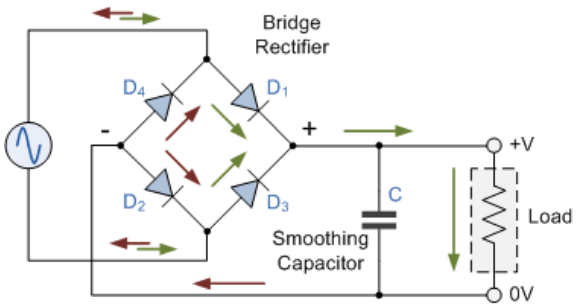

Figure 5-39: A smoothed AC/DC converted consists of a full-wave bridge rectifier, a resistive load, and a smoothing capacitor. Image extracted from (Storr, 2012)

the full-wave bridge rectifier is a resistive load that uses the translated direct current to perform work. Represented by a purple-coloured, dashed line in Figure 5-40, the voltage across the resistive load is always positive. Although the PE current has been successfully transformed into a direct current, its magnitude still changes in a sinusoidal pattern. To make the magnitude generally constant, a smoothing capacitor is used. The

schematic in Figure 5-39 shows a basic AC/DC converter with a smoothing capacitor. When using a smoothing capacitor, a ripple is generally observed resulting in some periodic variation from the direct current's magnitude. The capacitor's value is chosen so that its working voltage is higher than the PE voltage output and so that its ripple is minimal. The smooth black curve in Figure 5-40 shows a typical voltage output across a load resistor when a smoothing capacitor is used; the voltage is relatively constant with a small ripple. It should be noted that before the voltage can get to a constant level, several periods of AC are often needed to build the capacitor's voltage up to said constant level in steps.

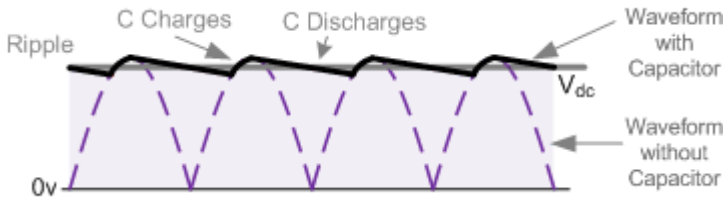

Figure 5-40: The typical resultant output waveform for a basic AC/DC converter (dashed violet curve) and an AC/DC converter with a smoothing capacitor. Image extracted from (Storr, 2012)

5.4.2 Impedance Matching Circuit

As PE transducers can generally only produce a small amount of power, it is imperative that the power transfer be maximized. This is accomplished by using the maximum power transfer theorem otherwise known as impedance matching or Jacobi's law named after its originator, Moritz von Jacobi who discovered it in 1840.

Essentially, maximum power transfer will be achieved providing that the load impedance matches the source impedance. It is generally used when the source impedance is fixed and the load impedance is variable and can be matched to the source. Essentially, the load impedance (Z_L) must be equivalent to the complex conjugate of the source impedance (Z_S); this expression is presented as Equation 5-95, with * representing a complex conjugate.

$$Z_L = Z_S^* \quad 5\text{-}95$$

For real parts, the real part on the load must be equal to the source's real part. For electrical systems, the real part is the resistance. The load resistance (R_L) must therefore equal the source resistance (R_S):

$$R_L = R_S \quad 5\text{-}96$$

For reactive components, the load reactance (X_L) must be the same magnitude of the source reactance (X_S), but of opposite phase:

$$X_L = -X_S \quad 5\text{-}97$$

For PE harvesting, the PE material is the source. To know what impedance to assign the load, one must break down the electrical components of a PE transducer into an equivalent circuit. Figure 5-41 shows the equivalent circuit of a PE transducer attached to a load of impedance Z_L. Several sources [including Culshaw (1996) and Vepa (2010)] model a PE transducer as two impedances in parallel. The first impedance consists of an inductance (L_s), resistance (R_s), and capacitance (C_s) in series. The inductance represents the inertial effect of the PE material set in vibration and is similar to the apparent mass effect of a vibrating mass of fluid, the elastic stiffness of the PE material is represented by the capacitance, and the dissipation of energy is represented by the resistance (Vepa, 2010). The second impedance consists of another capacitance (C_p) and represents the capacitive nature of a PE material and corresponds to the dielectric properties of PE material (Vepa, 2010).

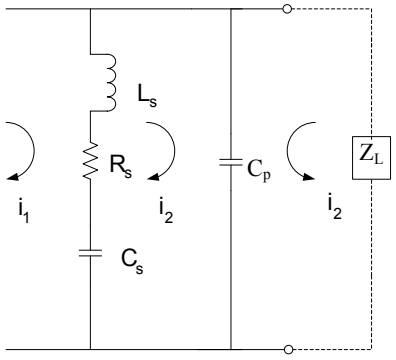

Figure 5-41: The Equivalent Circuit of a PE transducer attached to a load of impedance Z_L

To assign a load impedance that will provide maximum power transfer, one must first find the equivalent impedance for the PE material, Z_{eq}. Z_{eq} can be found by applying the

parallel formula to the series combination and the capacitance C_p. Using the parallel voltage, V, the total voltage across the series combination can be expressed as:

$$V = L_s\frac{di_1}{dt} + R_s i_1 + \frac{1}{C_s}\int i_1 dt = I_1(s)\left(L_s s + R_s + \frac{1}{C_s s}\right) \quad 5\text{-}98$$

Note that i_1 represents the current going through the series combination as shown in Figure 5-41. As impedance is defined as voltage over current, the series impedance, Z_1 is expressed as:

$$Z_1 = \frac{s^2 L_s C_s + sRC_s + 1}{sC_s} = \frac{-\omega^2 L_s C_s + j\omega R_s C_s + 1}{j\omega C_s} \quad 5\text{-}99$$

Again using the parallel voltage, V, the total voltage across the capacitance, C, is defined as:

$$V = \frac{1}{C_p}\int i_2 dt = \frac{1}{sC_p} I_2(s) \quad 5\text{-}100$$

Note that i_2 represents the current going through the capacitor as shown in Figure 5-41. The impedance over the capacitance, Z_2, can therefore be defined as Equation 5-101 where ω is angular frequency of the source:

$$Z_2 = \frac{1}{j\omega C_p} \quad 5\text{-}101$$

Using the parallel equivalent circuit theorem, Z_{eq} can be defined as:

$$Z_{eq} = \frac{Z_1 Z_2}{Z_1 + Z_2} = \frac{-\omega^2 L_s C_s + j\omega R_s C_s + 1}{-\omega^2 R_s C_p C_s + j\omega\left(-\omega^2 L_s C_s C_p + C_s + C_p\right)} \quad 5\text{-}102$$

Generally, the inertial effect is often small and may be neglected (Vepa, 2010). Assuming that the source inductance is zero, Equation 5-102 can be rearranged as:

$$Z_{eq} = \frac{j\omega R_s C_s + 1}{-\omega^2 R_s C_p C_s + j\omega\left(C_s + C_p\right)} \quad 5\text{-}103$$

Rearranging Equation 5-103 to separate the real and imaginary terms, one gets:

$$Z_{eq} = \frac{R_s C_2^2}{\omega^2 {R_s}^2 {C_p}^2 C_s^2 + \left(C_s + C_p\right)^2} - j\omega\frac{\omega^2 {R_s}^2 C_p C_s^2 + \left(C_s + C_p\right)}{\omega^2\left[\omega^2 {R_s}^2 {C_p}^2 C_s^2 + \left(C_s + C_p\right)^2\right]} \quad 5\text{-}104$$

Assuming that C_s approaches infinity (Vepa, 2010), Equation 5-104 becomes:

$$Z_{eq} = \frac{R_s}{\left[1 + \left(\omega C_p R_s\right)^2\right]} - j\omega \frac{C_p {R_s}^2}{\left[1 + \left(\omega C_p R_s\right)^2\right]} \quad 5\text{-}105$$

Applying the maximum power theorem, the impedance-matched load would be:

$$Z_L = Z_{eq}^* = \frac{R_s}{\left[1 + \left(\omega C_p R_s\right)^2\right]} + j\omega \frac{C_p {R_s}^2}{\left[1 + \left(\omega C_p R_s\right)^2\right]} \quad 5\text{-}106$$

As the impedance matched load has a positive reactance, the load would require an inductance in addition to a resistance. From Equation 5-106, the matched load resistance (R_L) and inductance (L_L) can be represented as Equations 5-107 and 5-108.

$$R_L = \frac{R_s}{\left[1 + \left(\omega C_p R\right)^2\right]} \quad 5\text{-}107$$

$$L_L = \frac{C {R_s}^2}{\left[1 + \left(\omega C_p R\right)^2\right]} \quad 5\text{-}108$$

Generally, however, the source resistance is not given by the manufacturer of the PE element as it is generally small due to the fact that PE transducers are largely capacitive due to the fact that they are dielectric materials that contain bound charge (Leo, Power Analysis for Smart Material Systems, 2007). As a result, a PE element is generally modeled as an alternating electric source with an internal capacitance. Figure 5-42 shows the equivalent Norton and Thevenin equivalent circuits for a PE transducer as an alternating electric source.

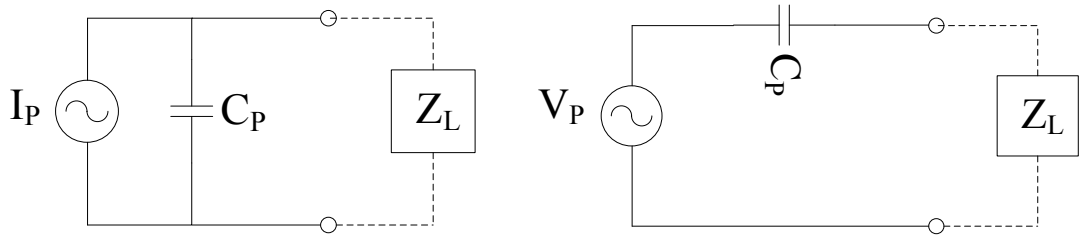

Figure 5-42: The simplified equivalent circuit attached to load. The Norton equivalent circuit is shown on the left while the Thevenin equivalent circuit in on the right

Applying the maximum power transfer theorem, one would find that the load impedance is an inductance and can be represented as:

$$Z_L = j\frac{1}{\omega C_p} \quad 5\text{-}109$$

The load impedance is thus directly proportional to the angular frequency of the source; a smaller angular frequency requires a larger impedance for maximum power transfer. As a walking frequency is quite low, a significant inductor would be required for maximum power transfer. Shenck and Paradiso (2001) point out that if PE transducer with a typical capacitance of 140 nF was mechanical induced at a typical walking frequency of 1 Hz, the impedance matched inductor would be in the order of 10^5 H (about 1.81 x 10^5 from the author's calculation). On their website, Digikey© only sells inductors with an inductance up to 150 H and that particular inductor has dimensions of about 6 cubic inches (1.5" x 1.69" x 2.38") (Hammond Manufacturing, 2012). An inductance of this magnitude is therefore not practical for harvesting energy from human foot traffic using PE materials. However, many researchers [Mateu & Moll (2005), Leo (2007), Cook-Chennault *et al.* (2008), Hande *et al.* (2009), Lewandowski *et al.* (2009), and Sodano (2009)] use an alternative approach: impedance matching using a resistor whose impedance matches that of the source:

$$R_L = \frac{1}{\omega C_p} \quad 5\text{-}110$$

Using the same PE material parameters as before (*i.e.* frequency of 1 Hz and capacitance of 140 nF) one would get a resistive load of about 1.14 MΩ: a resistance that is widely available and can be easily integrated into small circuit boards, making it easier to embed on floor tiles and shoe insoles. For the application of harvesting human foot traffic, it is therefore more practical to impedance match using a resistor.

5.4.3 Storage Devices

Most of the research in PE harvesting has been focused on extracting the maximum amount of power through a resistive load through various electronic circuitry such as impedance matching circuits and switching circuits. When using a resistive load, the harvested power must directly be used as its being harvested. As the harvested power is generally quite low in the mW or μW range, it is often desirable to store the electrical energy in an energy storing device such as a capacitor or rechargeable battery for later

use when the amount of collected energy is sufficient to operate the desired electronic device.

When comparing the use of capacitors and rechargeable batteries for PE harvesting, each device has its advantages and disadvantages. The main advantage of using a capacitor is that the energy can be used almost instantaneously. Conversely, a battery tends to take hours to charge, but the power stored does not have to be used immediately; it can be stored for later use. A battery can deliver a constant power supply while a capacitor cannot deliver a constant power supply. Also, batteries have limited life cycles whereas capacitors have virtually unlimited life cycles.

Another advantage rechargeable batteries have over capacitors is the relative simplicity associated with their harvesting circuits. For an example, when Sodano *et al.* (2005) compared the usage of capacitors and rechargeable batteries as energy storage devices for PE harvesting, there was a significant difference in harvesting circuitry. Using a 40 mm x 80 mm aluminum sheet as a substrate layer with 0.98 mm thickness, Sodano *et al.* applied a PSI-5H4E PZT layer (40 mm x 62 mm and 0.257 mm thickness) to the substrate layer using cyanoacrylate adhesive. The PZT unimorph was to be cantilevered and excited through base excitation both at its resonant frequency and a randomized vibration typically found on an automotive air compressor. Electronic schematics for the harvesting circuits for the storage capacitor and battery are respectively shown in Figure 5-43 and Figure 5-44. Based on the previous work from Kymissis *et al.* (1998), the harvesting circuit for the energy storage capacitor consisted of several components including seven resistors, three capacitors (not including the storage capacitor), a full-wave bridge rectifier, two transistors, and a Zenger diode. However, the only components required for the rechargeable nickel metal halide (NiMH) battery were a full-wave bridge rectifier and a smoothing capacitor. NiMH batteries were chosen due to their high charge density and unlike lithium ion batteries, they do not require any type of charge controller or voltage regulator to be incorporated into the circuitry (Sodano, Inman, & Park, 2005). The capacitor had a capacitance of 1000 μF or greater to accumulate charge and provide a smoother voltage. When subjected to random

vibrations, the capacitor circuit functioned as expected; however at higher frequencies, the capacitor rapidly discharged, resulting in an output of high frequency pulses. At its resonant frequency (63 Hz), it took twenty minutes to fully charge a 40 mAh NiMH battery to a 1.2 V voltage level; conversely at random vibrations, it took a few hours as the excitation bandwidth causes a significantly lower displacement in the high-frequency range, and in turn applies less strain to the PE device therefore supplying less power to the battery. The main finding from their experiment was that rechargeable batteries can be used to store energy from PE harvesting.

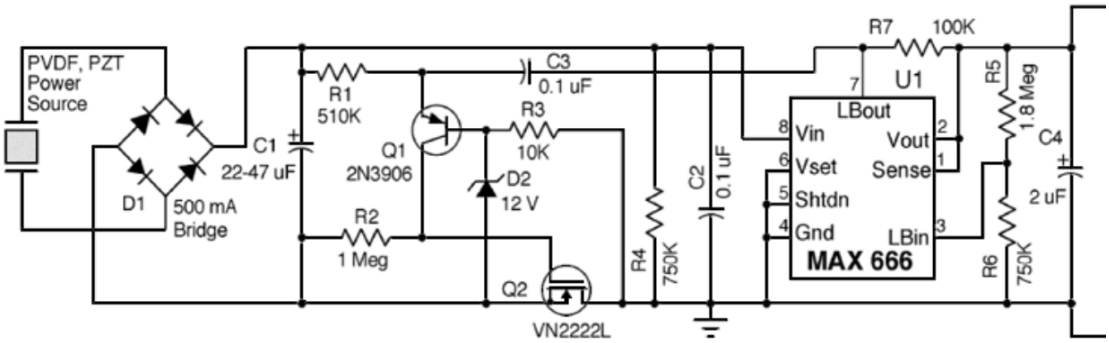

Figure 5-43: Based on the work by Kymissis et al. (1998), Sodano et al. (2005) used this harvesting circuit when using a capacitor as an energy storage device. Image extracted from (Sodano, Inman, & Park, 2005)

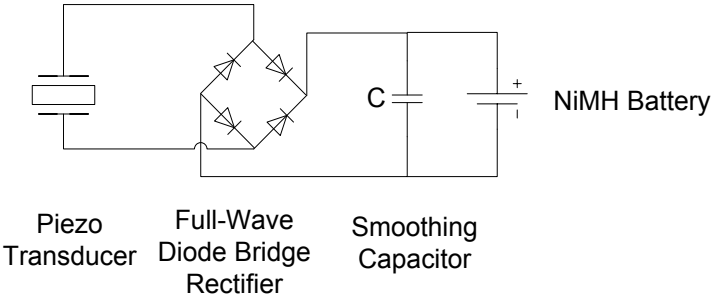

Figure 5-44: When Sodano *et al.* (2005) used a rechargeable NiMH battery as a storage device for PE harvesting, the harvesting circuit solely consisted of a full-wave bridge rectifier and a smoothing capacitor.

In 2006, Guan and Liao performed another study on energy storage devices in piezoelectric devices. They compared two rechargeable batteries, NiMH and lithium ion/polymer, with supercapacitors. Supercapacitors, also known as ultracapacitors or double-layer capacitors, are capacitors that have an energy density that is 10-100 times higher than that of traditional electrolytic capacitors. While each storage device performed more effectively at higher activation levels, the supercapacitor had the highest

charge/discharge efficiency (95%) followed by the lithium (92%) and NiMH (65%) batteries. It was also noted that both rechargeable batteries have limited life cycles, 300-500 cycles for NiMH batteries and 500-1000 cycles for lithium batteries while supercapacitors have virtually unlimited life cycles: typically more than 100,000 cycles. Supercapacitors rated 5.5 V can be continuously set from 0 V to 5.5 V via precharging to meet the optimal rectifier voltage requirement of the energy harvesting systems; conversely NiMH and lithium batteries have cell voltages rated at 1.2 V and 3.6 V with operational voltage ranges of 0.67 V-1.25 V and 3.1-3.75 V, respectively. Considering the charging protection circuit, lithium batteries need protection circuits, while NiMH batteries and supercapacitors do not. However, their high self-discharge rates and low energy densities are detrimental to the use of supercapacitors in PE harvesting. Guan and Liao pointed out that after 10 days since being fully charged, a supercapacitor's capacity drops to 85% of its full charge; the capacity falls down to 70% after 30 days. In comparison, after 30 days of being fully charged, NiMH and lithium batteries' capacities will drop to 70% and 95%, respectively. With regards to the energy density, supercapacitors have the lowest value at 1-10 Wh/kg followed by NiMH and lithium batteries with respective values of 60-80 Wh/kg and 120-140 Wh/kg. Guan and Liao concluded overall that supercapacitors are more attractive than rechargeable batteries due to their higher charge-discharge efficiencies and longer lifetimes, especially if the self-discharge rate is not significant due to constant charging.

5.4.4 Switching Techniques

To extract a larger amount of energy from PE harvesting across a resistive load, it is generally not sufficient to solely use impedance matching for maximum power transfer. Several different circuits have been proposed, many of them relying on switching techniques. Two of these switching techniques include synchronous charge extraction (SCE) and synchronized switch harvesting using an inductor (SSHI).

SCE was developed by Lefeuvre *et al.* (2005) with the aim of making a self adaptive PE harvesting circuit in which the extraction of the electric charge from a PE device

synchronizes with the system vibration to improve the efficiency of the energy transfer process. The principle of SCE is to transfer electric energy accumulated on the PE transducer to a load or storage device intermittently; the intermittent extraction of energy is synchronized with the mechanical vibration and the PE element is in the open circuit state most of the time (Qiu, Jiang, Ji, & Zhu, 2009). Shown in Figure 5-45, the circuit contains a switch in series with an inductor; the switch is turned off when the voltage on the PE element is increasing so the PE element can accumulate charge. When the voltage reaches a maximum, the switch is closed and the PE element discharges into the inductor. When completely discharged, the switch is turned back off and the PE element begins charging again in its open circuit state. As the current through the inductor cannot be suddenly stopped, it flows through to the capacitor and then the load or energy storage device due to the oscillation effect; a diode is used to block the current flow in the inverse direction (Qiu, Jiang, Ji, & Zhu, 2009). When Lefeuvre *et al.* tested the SCE interface experimentally, the converter increased power transfer by over 400%; the converter was found to have an efficiency of 70% (Lefeuvre, Badel, Richard, & Guyomar, 2005).

SSHI was investigated by Badel *et al.* (2005) and is based on nonlinear processing of the PE voltage. Shown in Figure 5-45, the SSHI circuit is quite similar to the SEC circuit, only the inductor and switch are connected in parallel with the PE element before the full-wave bridge rectifier as opposed to after. The switch is closed when the PE transducer's voltage is at a minimum or maximum; when closed, an oscillating electrical circuit is established between the inductor and PE element and the voltage across the PE element is reversed as a result (Qiu, Jiang, Ji, & Zhu, 2009). The switch is turned off once the voltage inversion is finished; because of the voltage inversion, the PE voltage increases with time as electric charges are generated by mechanical strains (Qiu, Jiang, Ji, & Zhu, 2009). Like the SCE technique, Badel et al found that the SSHI circuit is capable of delivering a 400% increase in efficiency over the standard circuit (Badel, Guyomar, Lefeuvre, & Richard, 2005).

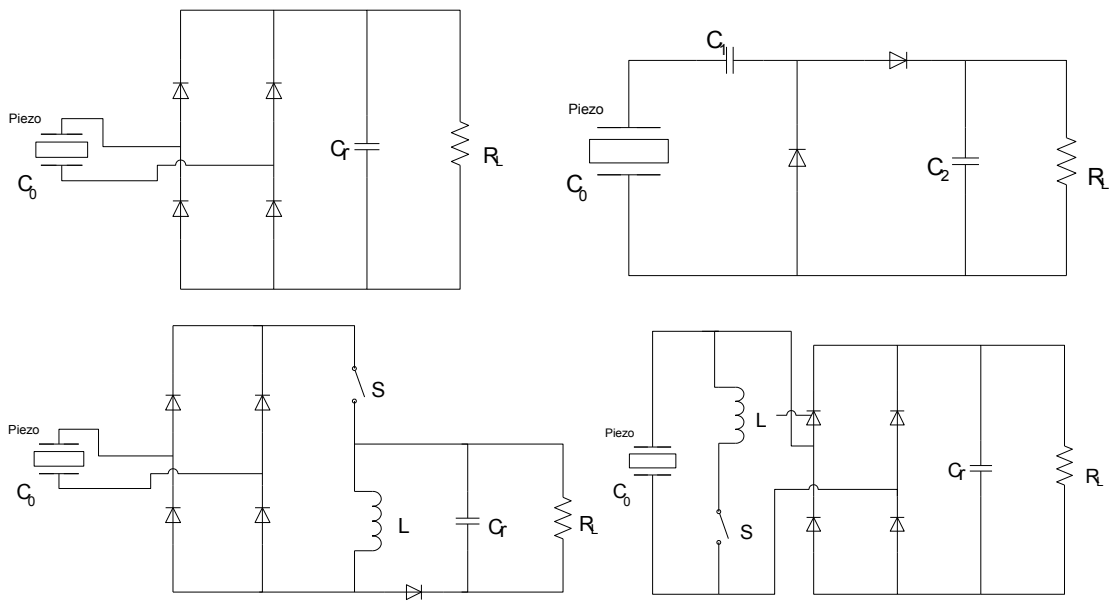

Figure 5-45: The four PE energy harvesting circuits that were compared by Qiu et al. (2009). Clockwise from top-left: Classic interface, Voltage Doubler interface, Synchronized Switch Harvesting on Inductor (SSHI) interface, and Synchronous Charge Extraction (SCE) interface. Presented as shown in (Qiu, Jiang, Ji, & Zhu, 2009)

Qiu *et al.* (2009) sought out to investigate the four different PE energy harvesting circuits to see which one would most efficiently harvest vibration energy. The four circuits are schematically drawn in Figure 5-45 and include a classic interface, a voltage doubler interface, the SCE technique, and the SSHI technique. It was experimentally shown that in comparison to both the classic and voltage doubler interfaces, the SCE and SSHI techniques can increase the harvested power by factor of 2.6 and 7, respectively, without needing an external power source (Qiu, Jiang, Ji, & Zhu, 2009). However, it was pointed out that the SCE and SSHI both consume power from the PE transducer; when comparing the theoretical and experimental power outputs, the estimated power losses were approximately 34% and 10% for the SCE and SSHI techniques, respectively.

5.4.5 The Human Powered Jogging Suit: PE Harvesting Circuitry

For the human powered jogging suit, one could have simply attached LEDs to the PE transducers in the shoe insoles and the LEDs would have lit up after stepping on the PE transducers. However, the LEDs would have only dimly lit up. For the LEDs to be visible to oncoming traffic, it is imperative that the LEDs be bright enough to see from a

distance. Taking cues from the PE embedded insoles developed by Kymissis *et al.* (1998) and Shenck & Paradiso (2001), the group would use a bucket capacitor to collect the charge over a number of steps; when the bucket capacitor's charge is sufficient, it would be discharged to a strip of LEDs in series and brightly light them up as a pulse.

The schematic for the PE harvesting circuit used in the human powered LED jogging suit is shown in Figure 5-46. From the PE transducers, the alternating current is rectified via a full-wave diode bridge rectifier and flows to the bucket capacitor (C1) as both transistors (Q1 and Q2) are not conducting. The bucket capacitor will continue to gain charge after each step until it reaches 28V: the voltage set by the Zenger diode, Z1. When this voltage is reached, Z1 begins conducting and engages the first transistor, Q1 which forms a latch with Q2, forcing it to saturate and engage as well. This latch allows the capacitor to discharge through the LED strip. However, when the voltage across the second Zenger diode (Z2) falls below its set voltage of 8.6 V, it blocks all current flow and disengages Q2 which in turn breaks the latch, disengaging Q1 as well. The charging cycle then starts again. High resistances of 500 kΩ and 1 MΩ were respectively assigned to R1 and R2 to draw less current, ensuring that more current goes to the LED strip to maximize brightness. R3 was assigned a value of 33 kΩ to control the current flow in the latch. An additional 1 MΩ resistor was later added in parallel with the LED strip to reduce the overall resistance of the circuit. The circuit was able to deliver a maximum voltage of 22 V to the LED strip: enough to pulsate nine LEDs at full brightness.

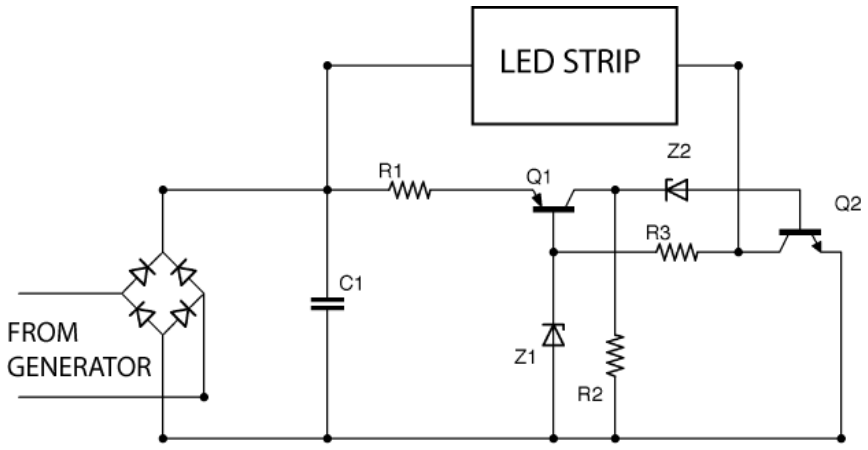

Figure 5-46: The PE harvesting circuit from the Human Powered LED Jogging Suit. Extracted from (Rogers, Chandler, Mills, & Greencorn, 2010)

5.5 ESTIMATING MAXIMUM POWER OUTPUT

At low frequencies, far from resonance, a PE plate can be assumed to behave like a parallel plate capacitor (Priya S. , 2007). From classical capacitor modeling, a parallel plate capacitor's capacitance (C) is defined by the total charge collected (q) divided by the voltage difference across the plates (V). The capacitance can also be determined from the capacitor's properties, *i.e.* its plate cross-sectional surface area (A_{cs}), the distance between plates (t), and its dielectric constant (ϵ):

$$C = \frac{q}{V} = \frac{\epsilon A_{cs}}{t} \qquad 5\text{-}111$$

The electrical energy stored by a parallel plate capacitor (U_c) can be expressed in terms of its voltage or stored charge as presented in Equations 5-112 and 5-113, respectively:

$$U_c(V) = \frac{CV^2}{2} = \frac{\epsilon A_{cs} V^2}{2t} \qquad 5\text{-}112$$

$$U_c(q) = \frac{q^2}{2C} = \frac{q^2 t}{2\epsilon A_{cs}} \qquad 5\text{-}113$$

Several researchers have used Equations 5-112 and 5-113 to describe the energy stored in a PE transducer when stressed [(Antaki, et al., 1995), (Shenck & Paradiso, 2001), (Gonzalez, Rubio, & Moll, 2001), (Niu, Chapman, Riemer, & Zhang, 2004), (Priya S. , 2007), (Cook-Chennault, Thambi, Bitetto, & Hameyie, 2008), (Ting, Hariyanto, Hou, Ricky, Amelia, & Wang, 2009), and (Wang, Yao, Laio, & Tsai, 2011)]. Shenck & Paradiso (2001) and Ting *et al.* (2009) point out that when a PE transducer is mechanically stressed, this electrical energy is available twice during its excitation cycle: once when stressed, and again when the stress is removed and the PE transducer relaxes to its neutral state. The amount of power (P_C) that can be harvested is therefore dependent on the frequency of excitation (f_{Hz}) as well as the amount of stored energy produced from each cycle (2U):

$$P_c = 2Uf_{Hz} = CV^2 f_{Hz} = \frac{q^2 f_{Hz}}{C} = \frac{\epsilon A_{cs} V^2 f_{Hz}}{t} = \frac{q^2 d f_{Hz}}{\epsilon A_{cs}} \qquad 5\text{-}114$$

In Section 5.1.6, several transducer configurations were presented, each with derived equations that represented the amount of charge developed across the PE transducer when subjected to a mechanical stress without an electric field. To find the maximum power

output for each configuration, one can simply substitute the charge equation into Equation 5-114. Using this knowledge, this section will present the power equations to be used to calculate the available power for the five scenarios presented in Section 5.3 along with their results. As will be discussed in the first subsection, the power output is determined by three sets of parameters which will be known as the piezo factor, geometry factor, and input factor.

5.5.1 33 Deformation: Circular Discs, Rectangular Transducers and the Three-Factor Strategy

Recalling Equation 5-45, the amount of charge that is accumulated across a PE transducer undergoing a uniformly distributed force in the 3-direction under zero electric field (*i.e.* $E_3 = 0$) is modeled as:

$$q_{33}|_{V=0} = d_{33}F_3$$

Substituting Equation 5-45 into Equation 5-114, one can obtain the maximum power available to be harnessed from a uniformly distributed force in the 3-direction via PE harvesting (P_{33}):

$$P_{33} = \frac{(d_{33}F_3)^2 t_p f_{Hz}}{\epsilon A_{cs}} \quad 5\text{-}115$$

To find the maximum power produced by a circular disc (P_{Disc33}), the cross-sectional surface area in Equation 5-115 can be substituted with the cross-section area of the disc's PE layer:

$$P_{Disc33} = \frac{(d_{33}F_3)^2 t_p f_{Hz}}{\epsilon \pi R_1^2} \quad 5\text{-}116$$

Likewise, to find the maximum power produced by a rectangular (or square) transducer (P_{rect33}), the plate surface area in Equation 5-115 can be substituted with the cross-sectional area of a rectangular PE layer:

$$P_{Rect33} = \frac{(d_{33}F_3)^2 t_p f_{Hz}}{\epsilon w L} \quad 5\text{-}117$$

To find the parameters that would increase power production, it would be helpful to rearrange Equation 5-115 to reflect associated parameters in groups, hence Equation 5-118 below:

$$P_{33} = \left(\frac{{d_{33}}^2}{\epsilon_{33}}\right)\left(\frac{t_p}{A_{cs}}\right)\left({F_3}^2 f_{Hz}\right) = (F_Z)(F_G)(F_I) \qquad 5\text{-}118$$

The first set of parentheses in Equation 5-118 reflects the electrical properties of the PE layer: the square of the d-coefficient over the dielectric constant; both properties are in the 33 direction. This relationship is represented as F_Z on the right side of Equation 5-118 and will be known throughout this thesis as the piezo factor. To increase power production, a PE material should have a high d_{33} and low ϵ_{33}, but as d_{33} is squared, it has a larger weight in the total power produced. To directly compare the power producing potential of PE materials with each other, one should seek out one with the highest piezo factor.

The second set of parentheses in Equation 5-118 represents the geometry of the PE layer. For optimum power production, the PE layer should have a large thickness, but small cross-section area; this factor will be known as the geometry factor and is represented as F_G on the right hand side of Equation 5-118.

The third set of parentheses in Equation 5-118 represents the physical mechanical inputs onto the mechanical transducer: the uniformly applied force onto the PE layer and the frequency of application. This parameter set will be known as the input factor throughout this thesis and is represented as F_I on the right hand side of Equation 5-118.

Table 5-15: The Power Factors for Circular Discs and Rectangular Transducers (33 Deformation)

Factor	**Values for Circular Discs (33 Deformation)**		**Values for Rectangular Transducers (33 Deformation)**	
	At constant F_3	At constant σ_3	At constant F_3	At constant σ_3
Piezo (F_Z)	$\frac{{d_{33}}^2}{\epsilon_{33}}$	$\frac{{d_{33}}^2}{\epsilon_{33}}$	$\frac{{d_{33}}^2}{\epsilon_{33}}$	$\frac{{d_{33}}^2}{\epsilon_{33}}$
Geometry (F_G)	$\frac{t_p}{\pi R_1^2}$	$t_p \pi R_1^2$	$\frac{t_p}{wL}$	$t_p wL$
Input(F_I)	${F_3}^2 f_{Hz}$	${\sigma_3}^2 f_{Hz}$	${F_3}^2 f_{Hz}$	${\sigma_3}^2 f_{Hz}$

Table 5-15 summarizes the power factors for both circular discs and rectangular transducers undergoing 33 deformation. These factors represent a consistently applied force or stress that won't damage the PE transducer. Assuming that the load is in pure compression (as it would be when being directly deformed by foot traffic), it is unlikely that the PE layer will be damaged from the input force as PE materials can withstand significant amounts of compressive stress. PI Ceramic, Ltd. states on their brochure that their PZT materials have a static compressive strength higher than 600 MPa (PI Ceramic GmbH., 2012). Additionally, when Ewart *et al.* (1999) tested the compressive strength of several PE materials, they found that poled PZT had a compressive strength of 944 ±50 MPa (Ewart, McLaughlin, & Gittings, 1999). Using the 600 MPa stated by PI Ceramics, Ltd. as a conservative compressive strength, for an 85 kg person to directly induce a plate to experience said compressive stress, the area of the plate would have to be less than 1.4 mm^2. This surface area is not realistic as it would be more difficult to wire with electronic circuitry, is not readily available from manufacturers, and would be difficult to focus the walker's entire body weight onto such a small surface area. Regardless, as traditional substrate layers have yield stresses less than 600 MPa (aluminum, brass, and stainless steel have yield strengths around 269 MPa, 124-310 MPa, and 415 MPa, respectively) the substrate layer is more likely to fail during compression than the PE layer. The compressive strength of the substrate should therefore be used to calculate the maximum compressive stress that the transducer can experience without plastic deformation. Taking the lowest yield stress listed (124 MPa), the surface area that would produce said stress under the load of an 85 kg person is approximately 6.7 mm^2: a surface area that is still too small to be realistic. Although failure in compression is unlikely when harvesting power from human foot traffic, under other environmental conditions the compressive stress may meet or exceed the compressive stress limit. As the induced compressive stress is equivalent to the induced force divided by the transducer's cross-sectional area, Equation 5-118 can be rewritten in relation to the induced stress (σ_{33}):

$$P_{33} = \left(\frac{{d_{33}}^2}{\epsilon_{33}}\right)\left(t_p A_{cs}\right)\left({\sigma_3}^2 f_{Hz}\right) \qquad 5\text{-}119$$

If one forces a transducer to experience its maximum compressive stress, one can find the absolute maximum power said transducer can produce without succumbing to plastic deformation by substituting the maximum compressive stress into Equation 5-119. What Equation 5-119 also says is that at a constant stress load, the geometry and input factors change in comparison to the constant force load scenario presented as Equation 5-118.

Unlike a constant force load, a constant stress load does not depend on the material's geometry. When a constant force load (*e.g.* a mass load) is applied across an area, the internal stress is distributed across the area; the stress decreases as the area increases. However, when a constant stress load, such as an air or hydraulic pressure load, is applied to an area, it is irrelevant what size the area is; the internal stress experienced by the transducer will be a constant stress load. In the case of an air or hydraulic pressure load, the internal stress will be equivalent to the pressure value. Under these conditions, the geometry factor changes and states that a disc with a larger radius would produce more power. Like the constant force variable in Equation 5-118, the power output is proportional to the constant stress variable squared; the larger the stress, the larger the power output.

As two different equations have been presented, one that assumes a constant force load and another that assumes a constant stress load, one must ask which equation to use when analyzing the power potential to harvest human foot traffic. The answer is dependent on the architecture of the shoe insole or floor tile. Using the shoe insole as an example, it is quite important to have a flexible insole for user comfort. If one simply placed the shoe insole directly over the transducers (like the architecture shown in Figure 5-47), the insole will likely deform to cover not only the PE transducers, but also the space between PE transducers. In this situation, one would assume a constant stress over the PE layer; the stress would be equivalent to the weight of the wearer divided by the cross-sectional area of the entire shoe insole; the cross-sectional area of the PE layer is irrelevant.

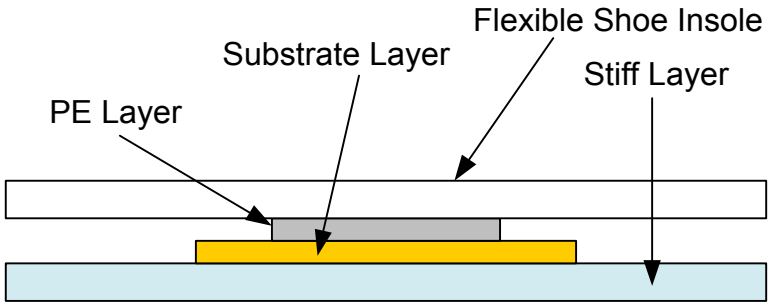

Figure 5-47: Embedded-insole architecture: PE transducers are positioned directly below the flexible shoe insole. One assumes a constant stress

However, one could redesign the shoe in such a way to concentrate the wearer's weight solely across the PE layers. Shown in Figure 5-48, one way of doing this is to sandwich the PE transducers between two stiff layers and place the shoe insole on top. The weight of the wearer would therefore be divided across the number of transducers. For example, if an 85 kg (833 N) person stepped on an insole with 16 transducers using the sandwiched architecture in Figure 5-48, each transducer would experience a force of 52.1 N applied uniformly across its cross-sectional area. The amount of force is thus only dependent on the amount of transducers, not the cross-sectional area of the transducers. However, the induced stress is directly proportional to the cross-sectional area: lower cross-section areas will increase the applied stress; a feature that is beneficial for PE harvesting. As this architecture uses a constant force, the divided force would be substituted into Equation 5-118 to obtain the amount of potential PE harvesting power for one transducer; this power output would then be multiplied by the number of transducers to get the total power output. Part of this investigation will determine which architecture is best suited to produce optimum power.

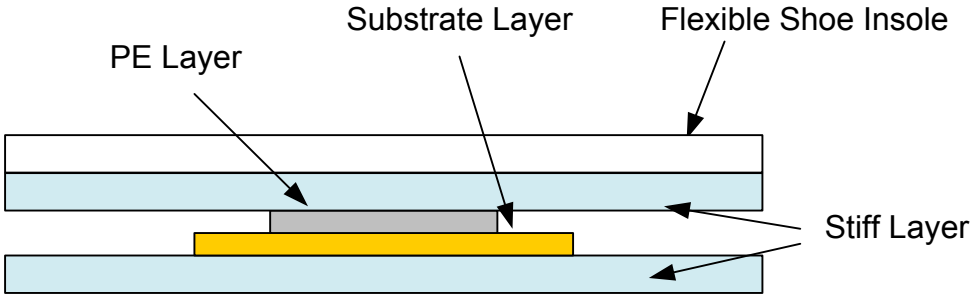

Figure 5-48: Sandwiched architecture: PE transducers are placed between two stiff layers and with the shoe insole on top. One assumes a constant force.

Recalling Equation 5-47, one can stack PE transducers to produce additional charge. Under no applied electric field, the amount of charge produced is presented as Equation 5-120 with n representing the amount of transducers in a stack:

$$q_s|_{V=0} = nd_{33}F_3 \qquad 5\text{-}120$$

Assuming that the transducers are electrically connected in parallel, the amount of power that can be harvested by a stack is presented as Equation 5-121. Note that n is not squared as one might expect by directly substituting Equation 5-120 into Equation 5-114. This is because Equation 5-114 assumes that the collected charge is from one capacitor, *i.e.* one PE transducer. As the total charge in Equation 5-120 is collected from several PE layers (and therefore several capacitors), one cannot substitute it directly into Equation 5-114. Instead, the total power is found by calculating the amount of power induced from each layer and summing the values. As each layer experiences the same force, each layer produces the same power; the total power would therefore be Equation 5-118 multiplied by the number of layers:

$$P_{33} = n\left(\frac{{d_{33}}^2}{\epsilon_{33}}\right)\left(\frac{t_p}{A_{cs}}\right)\left({F_3}^2 f_{Hz}\right) \qquad 5\text{-}121$$

Likewise, for a scenario under constant pressure, the maximum amount of power that can be harvested by a stack of PE discs is found by multiplying Equation 5-119 by the number of layers:

$$P_{33} = n\left(\frac{{d_{33}}^2}{\epsilon_{33}}\right)\left(t_p A_{cs}\right)\left({\sigma_3}^2 f_{Hz}\right) \qquad 5\text{-}122$$

5.5.1.1 MAXIMUM POWER OUTPUT CALCULATIONS: METHODS

For the maximum power output calculations, it will be assumed that the user will be 85kg (833N) and the wearer will be walking at a pace of 1 Hz, *i.e.* 1 step per second. As POWERleap, LLC stated that their floor tile could produce 1-5 W per square foot, the investigation will use one square foot as the floor tile's area to support or disprove their claim. The shoe insole cross-sectional area will be simplified as an 11 cm x 27 cm rectangle (297 cm^2): a typical area of a shoe insole. By simplifying the shoe as a rectangle, it is easier to see how many transducers of a particular size can fit within the

cross-sectional area. Using circular disc transducers as an example, one can find the total amount of discs that can fit along the width and length by dividing the disc's diameter into the respective dimension and rounding it down (as one cannot install a fraction of a disc). The amount of discs along the width and length would then be multiplied to get the total amount of transducers on the insole. Although simplifying the shoe insole to a rectangle is not realistic as it does not have the silhouette of an actual foot, the purpose of this investigation is to get an idea of how much power a PE embedded insole can produce. It will be assumed that a rectangular cross-section of 11 cm x 27 cm will provide the rough estimate needed to analyze if a PE embedded shoe insole is a viable means to harness energy from human foot traffic.

Both the constant force and constant pressure scenarios will be investigated to see if one produces more power than the other. Although decreasing the PE layer's cross-sectional area in the constant force scenario will produce higher internal stresses which is favourable for power generation, increasing the PE layer's cross-sectional area in the constant stress scenario is also favourable for power generation. Both scenarios will be investigated to see if either one has an advantage over the other. The investigation will also investigate the costs associated with purchasing the transducers as PE transducers can vary in price depending on their properties.

5.5.1.2 MAXIMIZING THE PIEZO FACTOR

As mentioned, for optimum power generation, the piezoelectric material should have properties that give it a high piezo factor. For 33 power generation, the material should have a high d_{33} and low dielectric constant. Using the formula presented in Table 5-15, the piezo factor was calculated for fifteen PE materials from three different companies; the results are summarized in Table 5-16. The PE material that had the highest piezo factor was the Type IV PE material from APC International, Ltd. with a value of 14.0 x 10^{-12} $C^2F/(N^2m)$. This piezo factor will therefore be used on the power generation analysis as it will give the highest power. Although transducer geometries that are readily available from other manufacturers will be used to calculate the maximum

geometry factor, it will be assumed that they can be manufactured using the Type IV PE material to calculate the maximum power available.

Table 5-16: The d_{33}, ϵ_{33}, and Piezo Factors for Several PE Transducer Materials

Model	Navy Type (Hard/Soft)	d_{33} (10^{-12} C/N)	ϵ_{33} (x 10^{-9} F/m)	Piezo Factor [10^{-12} $C^2F/(N^2m)$]
Piezo Systems, Inc. (Piezo Systems, Inc., 2012)				
PSI-5A4E	II (Soft)	390	15.9	9.54
PSI-5H4E	IV (Soft)	650	33.6	12.6
APC International, Ltd. (APC International, Ltd., 2012)				
840	I (Hard)	290	11.1	7.60
850	II (Soft)	400	16.8	9.51
Type IV	IV (Soft)	650	30.1	14.0
880	III (Soft)	215	8.85	5.22
PI Ceramic Gmbh (PI Ceramic GmbH., 2012)				
PIC 181	I (Hard)	265	10.6	6.61
PIC 141	I (Hard)	310	11.1	8.68
PIC 241	I (Hard)	290	14.6	5.76
PIC 300	I (Hard)	155	9.30	2.58
PIC 151	II (Soft)	500	21.3	11.76
PIC 255	II (Soft)	400	15.5	10.3
PIC 155	II (Soft)	360	12.8	10.1
PIC 153	IV (Soft)	600	37.2	9.68
PIC 152	II (Soft)	300	12.0	7.53

5.5.1.3 MAXIMIZING THE GEOMETRY AND INPUT FACTORS

For the constant stress scenario, *i.e.* the scenario in which the flexible insole is used, the total stress would be equivalent to the weight of the wearer divided by the surface area of the shoe or floor tile. With respective surface areas of 297 cm^2 and 1 ft^2, the stress induced by an 85 kg person would be equivalent to 28.05 kPa and 8.97 kPa for the shoe insole and floor tile. With an excitation frequency of 1 Hz, the remaining parameter needed to find the generated power, as shown in Equation 5-119, is the PE thickness, t_p. APC international offers PE thicknesses in their readily available circular transducers that range from 0.06 mm to 0.25 mm (APC International, Ltd., 2012). As the generated power is linearly proportional to t_p, the largest thickness would be best suited for optimal power generation. Using the 0.25mm PE thickness, the maximum power that can be extracted from this constant stress scenario is 8.2 x 10^{-8} W and 2.62 x 10^{-8} W, respectively

for the shoe insole and floor tile. It is evident that the amount of stress is insufficient to generate any useable amount of power.

Alternatively, what if the stress on a transducer was increased by limiting the contact area of the insole or shoe like the sandwiched architecture previously shown in Figure 5-48. The amount of power generated would be dictated by Equation 5-118. The geometry factor dictates that the power generated is proportional to the PE thickness but inversely proportional to the PE cross-sectional area. Larger PE thicknesses and smaller PE cross-sectional areas are thus more favorable for increased power generation.

5.5.1.4 MAXIMIZING THE INPUT FACTOR

With regards to the input factor, higher input forces are more favourable for higher power generation, but the input force has larger weight than the PE transducer's geometry as the generated power is proportional to its squared value. Because the input force is squared, one can see that embedding a single transducer would produce the maximum power output. If two identical transducers were used as opposed to one, the amount of force on each transducer would half, decreasing from 833 N to 416 N. Once the halved values are substituted into Equation 5-118 for their respective power output and added, the total power would be half of the power produced by one transducer withstanding the entire 833 N of the wearer's weight. It is therefore predicted that using one transducer would provide the maximum power output.

5.5.1.5 CALCULATED RESULTS FOR CIRCULAR DISC TRANSDUCERS

APC International, Inc. has several PE discs that are readily available. The PE disc models are presented as Table B-2 in Appendix B1. As all of the readily available PE discs have different combinations of thicknesses, the geometry factor was found for each disc to see which would produce the highest power output. With a geometry factor of 2.2 x 10^{-3} mm^{-1}, the smallest PE disc (*i.e.* the Disc with a substrate diameter of 8.9 mm) proved to have the highest geometrical factor. Using the maximum piezo factor defined earlier, the power output was calculated for all of the PE disc transducers when 1

transducer is withstanding the weight of the wearer. The power output was then calculated when the amount of transducers continuously doubled to 32 transducers. Table B-3 in Appendix B1 shows the geometry factors for all the ceramic discs along with the power calculations for 1, 2, 4, and 8 transducers. Figure 5-49 shows the total power for all PE ceramic discs with reference to the number of discs embedded in the shoe or tile while Figure 5-50 illustrates how the total power generated from one transducer varies with reference to its geometry factor.

Looking at Table B-3, one can see that doubling the amount of transducers halves the amount of power harvested as predicted in Section 5.5.1.4. This exponential relationship is illustrated in Figure 5-49. Likewise, the calculations also show that the power increases with respect to the transducer's geometry factor. If one ranked the eight transducers with respect to their generated power, the ranking would also correlate with their respective geometry factors. As presented in Equation 5-118, the amount of generated power should linearly increase with respect to the transducer's geometry factor; this linear relationship is illustrated in Figure 5-50. The disc with the highest geometry factor (the 8.9mm-diamater substrate disc) had a power generation of 20.7 μW.

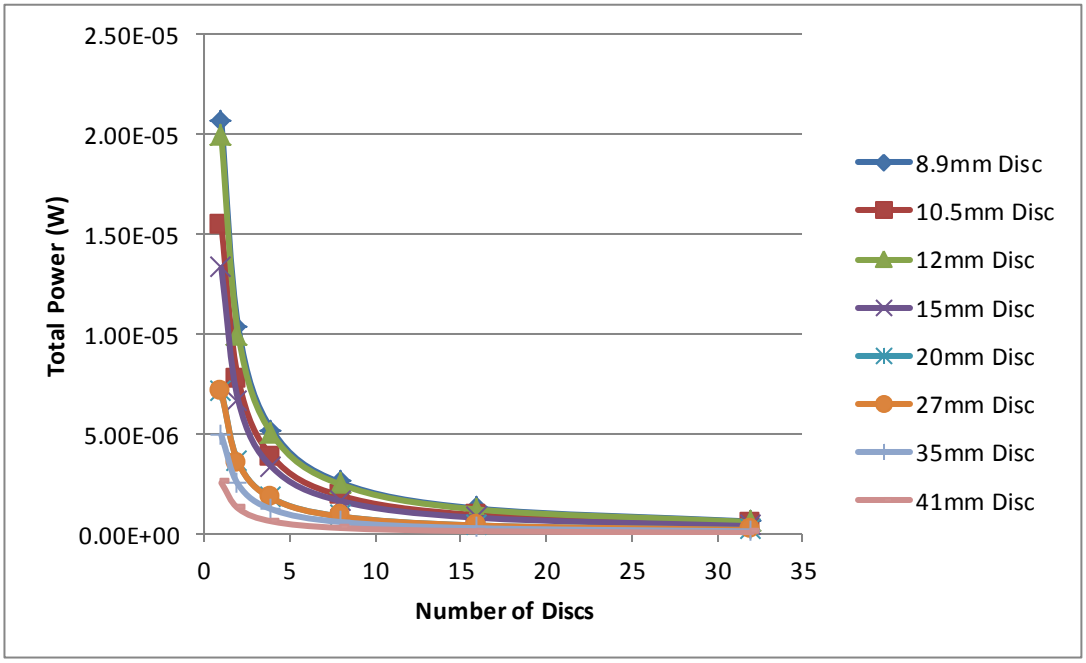

Figure 5-49: The Total Power vs. the Number of Discs for all of the PE ceramic discs available from APC International, Inc.

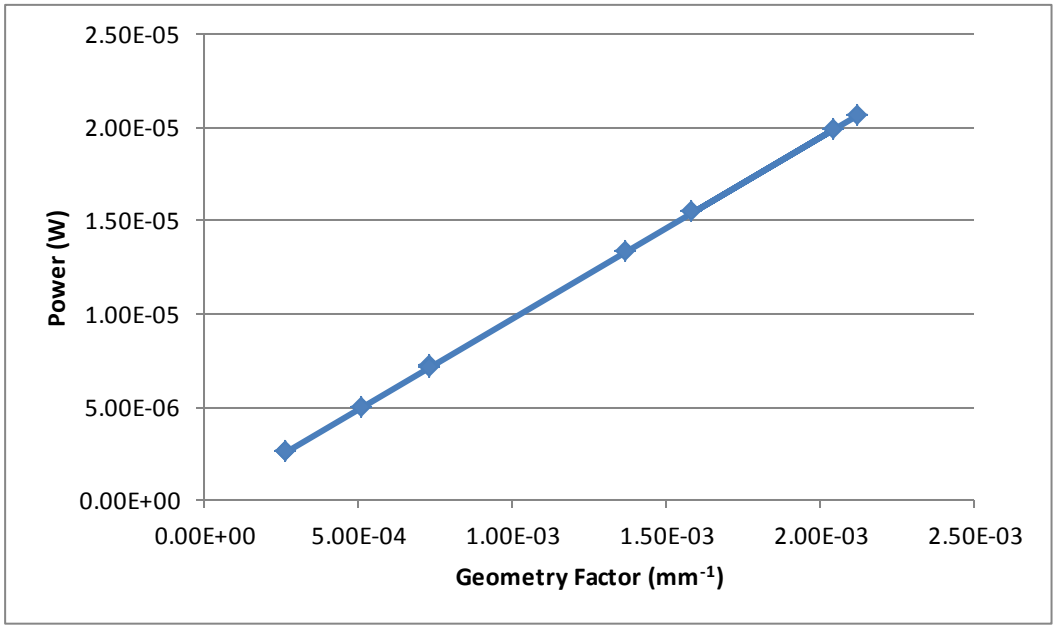

Figure 5-50: The Total Power vs. Geometry Factor for one transducer

Although the power generated from the 8.9mm disc transducer is still quite small, it should be noted that the transducers can be aligned mechanically in series and electrically in parallel to form a stack as illustrated in Figure 5-12. However, to get the output power of 1 W, as the minimal stated power output from POWERleap's energy harvesting flooring, one would need to have a stack with 48, 390 layers of the 8.9 mm discs which amounts to a stack of 5.32 m in height. Alternatively, if one assumes that the PE stack can be made with very thin electrode layers, 1W of power can be achieved using a PE stack that is 2.90 m in height. The floor tile or shoe would therefore have to be at least 2.90 m tall to harvest 1W of power directly from human foot traffic: a scenario that is not feasible for numerous reasons such as availability, cost, comfort, and buckling failure.

It should be noted, however, that the input force can be mechanically amplified to generate more power. For example, say that one used the 6mm diameter PE ceramic on the 8.9 mm disc transducer and made the PE layer(s) 1 cm thick either by using a single PE layer or several in a stack configuration (the latter would be safer and easier to harvest as its voltage output is much lower). Assuming that the substrate layer will fail at a stress of 124 MPa [the lowest brass yield strength listed by E-Z LOK (E-Z LOK, 2012)], a force amplification factor of about 4.2 can be applied. Likewise, assuming that the

substrate layer will fail at a stress of 310 MPa [the highest brass yield strength listed by E-Z LOK (E-Z LOK, 2012)] a force amplification factor of about 10.5 can be applied. Using the maximum PZT compressive stress of 600 MPa, as listed by APC, International Inc. (APC International, Ltd., 2012), and assuming that the substrate layer is made of a material that can withstand said compressive strength such as high strength steel, a mechanical amplification of 20.4 can be used. The resultant calculated power for the 4.2, 10.5, and 20.4 amplification factors are 0.0610 mW, 0.381 W, and 1.43 W respectively. If the PE thickness is increased to 2.54 cm (1 inch), the resultant calculated powers for the 4.2, 10.5, and 20.4 amplification factors increase to 0.155 W, 0.969 W, and 3.63 W respectively. These results, along with the PE layer deflections and foot displacements required to perform said deflections using a direct lever mechanism, are summarized in Table 5-17. The PE layer deflections were calculated using the listed modulus of elasticity of 51 GPa: the Type IV PE modulus of elasticity in the 33 direction as listed by APC International, Ltd. (APC International, Ltd., 2012).

Table 5-17: Power Calculations for a 6mm Disc with Mechanical Amplification

Max Stress (MPa)	Mechanical Amplification	PE Layer(s) Thickness (mm)	Maximum Power (W)	PE Layer Deflection (mm)	Foot Displacement for lever mechanism (mm)
29.5	1	10	0.00344	0.00578	0.00578
		25.4 (1")	0.00875	0.0147	0.0147
124	4.2	10	0.0610	0.0243	0.102
		25.4 (1")	0.155	0.0618	0.260
310	10.5	10	0.381	0.0608	0.640
		25.4 (1")	0.969	0.154	1.62
600	20.4	10	1.43	0.118	2.40
		25.4 (1")	3.63	0.299	6.09

The results from Table 5-17 indicate that the 1-5 W power output stated by POWERLeap, Inc. is somewhat conceivable. If one used 6mm PE disc with 25.4mm thickness, 1W can be achieved by mechanically amplifying the weight of the user by a factor of approximately 10.7. However, it should be noted that several complications arise by integrating the mechanical amplification into a shoe or tile. First of all, the calculations presented in Table 5-17 assume that the user's whole body weight is being stressed on the PE material; an assumption that is not realistic. Second of all, additional

hardware is needed to produce the needed force amplification which can be quite bulky especially for an embedded shoe. The additional hardware must also be designed to withstand significant internal stresses associated with translating the mechanical amplification. If a single lever mechanism is used for example, the arm of the lever would be subjected to a static bending stress caused by the moment of the user's weight multiplied by the lever's arm length. If a piston is used to compress the PE layer, the piston must be designed to withstand a large compressive load or risk plastic deformation. The joints associated with the amplification mechanism must also be designed to withstand significant amounts of stress. Given that PZT can withstand a compressive stresses higher than 600 MPa, failure will most likely occur in the mechanical amplification mechanism as opposed to the PE material itself. Although designing an amplification mechanism that can safely withstand these internal stresses is outside the scope of this thesis, the author believes that it is possible to design such an amplification mechanism for the floor tile; the mechanism will likely be too bulky to comfortably embed into a shoe.

5.5.2 Circular Discs: 31 Deformation via Pressure Difference

In the early design stage for the HPLED jogging suit, one of the team members expressed concern that the PE transducers would not adequately perform when directly on top of the shoe insoles as insoles are soft and flexible. Curious about his concern, the author hooked up a circular PE transducer to a full wave bridge rectifier composed of LEDs to test their brightness on hard and soft surfaces. After manually pressing the disc in its center on both a wooden table (the hard surface) and a piece of cloth (the soft surface) with the same amount of force, the author noticed that the LEDs were brighter when the transducer was on top of the piece of cloth which indicated that the induced current was larger and the transducer stored more electrical energy. The author realized that it was due to the different mode of deformation. On the hard surface, the disc was forced to uniformly deform in the axial direction and thus transduce in the 33 mode: a mode that requires large forces for adequate energy generation. However, on the soft surface, the disc was allowed to bend and thus deformed in the 31 mode; the applied force can

therefore be used to create larger internal strains and stresses: a factor that increases energy generation.

As mentioned in Section 5.2.3, Clark and Mo (2009) investigated the potential of harvesting energy from blood pressure variations using PE disc transducers. To increase the power output of readily available PE disc transducers, they postulated that operating the disc in the 31 mode would be the best option as greater strain can be induced. It was shown in earlier work by Kim *et al.* (2005) that there is an optimal radius ratio (*i.e.* R_1/R_2 with reference to Figure 5-32) of the PE layer to the substrate layer for maximum power generation. The radius ratio is dependent on the type of PE and substrate materials used as well as the transducer's thickness ratio (*i.e.* PE layer thickness to substrate thickness (h_p/h_m)). Made by Clark and Mo (2010), Figure 5-51 shows the power generated for a 127 µm PZT transducer with an aluminum substrate with reference to the radius and thickness ratios.

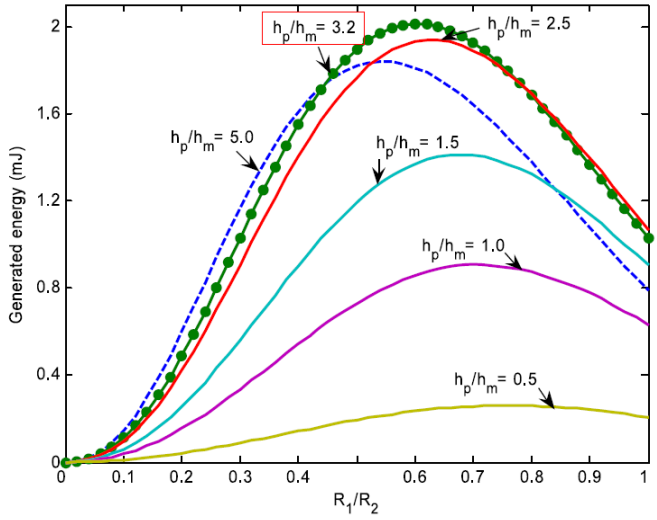

Figure 5-51: The Generated Power with reference to the diameter/radius ratio and thickness ratio for a 127 micron PZT layer with an aluminium substrate. The disc is simply-supported. Image extracted from (Mo, Radziemski, & Clark, 2010b)

As part of their initial investigation, Clark and Mo (2009) determined that for a PZT disc transducer with an aluminum substrate layer, the optimum power generation occurs when the thickness ratio is 3.2, the radius ratio is 0.6 and the disc is simply-supported. Under these optimum conditions and using a PZT thickness of 127 µm, an aluminum substrate layer diameter of 1.27 cm (0.5"), an applied pressure of 40 mmHg (5330 Pa), and a

frequency of 1 Hz, the maximum power generation was determined to be 47.0 μW. However, they did not address the structural limitations that arise when the transducer is subjected to these excitations. In a follow-up study, Mo *et al.* (2010a) addressed these structural limitations by adding three criteria to their analysis:

- The stress of the PZT must be maintained within its yield strength limit
- The thickness of the substrate layer must be above a certain limit to ensure that its yield strength is not exceeded
- The small deflection theory (deflection < thickness) limit needs to be maintained

In this study, Mo *et al.* found that the deflection limit was the most restraining factor when determining a safe substrate layer thickness. Using all three criteria, Mo *et al.* calculated that for a PE disc transducer with a PE layer radius of 12.7 mm, PE layer thickness of 127 μm, substrate layer thickness of 234 μm, undergoing a pressure of 5330 Pa, said transducer can generate 0.27 mW. This transducer was said to have an optimal design with reference to the three design criteria. The author would use this result as a reference to investigate the feasibility using pressure-loaded PE discs as a means of harvesting energy from human foot traffic.

The power generation equation used by Mo *et al.* (2010a) is very complex, requiring several parameters and constants; the author was not confident in using the equation directly. However, the author noticed that the pressure is only applied in the final equation. The derived power generation equation states that the generated power (P_{Disc31}) is proportional to the pressure's (P_0) squared value, *i.e.*:

$$P_{Disc31} \propto P_0^2 \tag{5-123}$$

This implies that providing the PE transducer's geometry and excitation frequency remain constant, one could find the power generated by a different pressure (P_{Disc31,P_0}) by calculating the pressure ratio (*i.e.* the proposed pressure divided by the simulated pressure of 5330 Pa) and multiplying the simulated power (*i.e.* 0.27 mW) by the square of said ratio:

$$P_{Disc31,P_0} = 0.27\ mW \left(\frac{P_0}{5330}\right)^2 \tag{5-124}$$

As the excitation frequency of 1 Hz is a typical walking frequency, the author used this observation to test the feasibility of using simply-supported PE discs as a means to harness the energy of human foot traffic in shoes and floor tiles. Although this limits the author's investigation to using the geometrical and material parameters used by Mo *et al.* (2010a), the author will be able to alter the applied pressure and observe if using pressure-loaded PE circular diaphragms are a viable means to harvest human foot traffic.

Table 5-18 presents the parameters used in the theoretical investigation by Mo *et al.* (2010b). The parameters in bold were extracted directly from their investigation. Unfortunately, not all of the parameters needed for the author's investigation were presented in the journal article by Mo *et al.* The author would therefore find these needed parameters by using plate theory, looking in literature, and making assumptions. The values for the missing parameters are presented in italics in Table 5-18. It is important to note that since assumptions were made in this analysis, one should not take the values of the missing parameters at face value. For the purpose of this investigation, however, these values will suffice to determine the viability of using pressure-loaded PE discs for harvesting human foot traffic.

Table 5-18: Parameters extracted from a theoretical investigation performed by Mo *et al.* (2010b). The italicized parameters were estimated by the author using theory and assumptions

Parameter (Symbol)	Value	Units
PE Layer Radius (R_1)	**12.7**	**mm**
PE Layer Thickness (h_p)	**127**	**µm**
Substrate Layer Thickness (h_m)	**234**	**µm**
Thickness Ratio (h_p/h_m)	**0.543**	**-**
Pressure	**5330**	**Pa**
Power Generated	0.27	mW
Estimated Radius Ratio (R_1/R_2) [Retrieved from Mo et al. (2010a)]	*0.75*	-
Estimated Substrate Radius	*16.9*	*mm*
Limited Deflection (i.e. Total Thickness)	*361*	*µm*
Simplified Thickness Needed to get Maximum Deflection (t)	*228*	*µm*
Estimated Stress	*36.8*	*MPa*

The first estimated parameter was the radius ratio. The radius ratio is needed to find the substrate radius: a trait that will determine how many transducers can be physically placed along a floor tile or shoe insole's surface area. Using the known thickness ratio of 0.543, the radius ratio was estimated at 0.75 by examining the peak radius ratio value on the 0.5 curve on Figure 5-51 and shifting the value slightly to the left as the thickness ratio is slightly larger than 0.5. Using the 0.75 radius ratio, the substrate radius was estimated at 16.9 mm.

The limited deflection was found using the design criteria set by Mo *et al.* The third design criterion states that the deflection will not be greater than the total thickness of the PE disc. The total thickness of the PE disc is 361 μm, the limited deflection is therefore assumed to be this value.

For the analysis, it is important to calculate the internal stress of the PE disc to ensure that it does not exceed the yield stress of the PE material or substrate as this will cause plastic deformation. As the PE disc in the investigation performed by Mo *et al.* (2010b) did not exceed the thickness of the disc, traditional circular-plate stress and deflection equations are somewhat applicable. Equations 5-125 and 5-126 respectively represent the maximum stress (σ_m) and deflection (y_m) of a simply-supported circular plate with a uniformly applied pressure load where P_0, r, t, υ, and Y represent the disc's applied pressure load, radius, thickness, Poisson's ratio, and modulus of elasticity (Beardmore, 2011):

$$\sigma_m = \frac{3(3+\upsilon)P_0 r^2}{8t^2} \qquad 5\text{-}125$$

$$y_m = \frac{(5+\nu)P_0 r^4}{64(1+\upsilon)D} = \frac{3(5+\nu)P_0 r^4(1-\nu^2)}{16(1+\nu)Yt^3} = \frac{3(5+\nu)P_0 r^4(1-\upsilon)}{16Yt^3} \qquad 5\text{-}126$$

As a PE disc is a composite material with two layers of different radii, thicknesses, and moduli of elasticity, herein lies a dilemma: Equations 5-125 and 5-126 are only applicable to a single material. The author tried finding resources for similar stress and deflection equations that catered to composite materials, but was unsuccessful. Alternatively, the author used another approach, an approach that would estimate the internal stress rather than directly solve for it. For the objectives of this thesis of

determining the viability of using pressure-loaded PE circular diaphragms for harvesting foot traffic, this estimation would suffice, but shouldn't be taken at face value.

First of all, the moduli of elasticity for aluminum and PZT are quite similar respectively being 68.9 GPa (MatWeb, LLC, 2010) and 62.0 GPa (Piezo Systems, Inc., 2012). The author therefore used the aluminum modulus of elasticity as the PE disc is composed mostly of aluminum. Using the substrate radius of 16.9mm as a simplified radius for the disc and the limited deflection of 361 μm, the author then found a simplified thickness by rearranging Equation 5-126 into Equation 5-127:

$$t = \left(\frac{3(5+\nu)P_0 r^4 (1-\upsilon)}{16 Y y_m} \right)^{1/3} \qquad 5\text{-}127$$

Using these values, the simplified thickness was found to be 228 μm which immediately set off a red flag as the substrate thickness was only 234 μm. As a composite material, one would expect the simplified thickness to be between the substrate thickness and total thickness. Nonetheless, as the author only wishes to get an estimate of the internal stress, this thickness would be satisfactory for all intents and purposes. Using the simplified thickness of 228 μm, substrate radius of 16.9 mm, Poisson's ratio of 0.33, and pressure of 5330 Pa, the estimated internal stress of the disc was calculated to be 36.8 MPa using Equation 5-125. It should be noted that if the simplified thickness was larger, as would be expected, the estimated stress would be less; 36.8 MPa may therefore be a conservative stress estimate, but one would only know for certain if a composite stress analysis is applied. Regardless, the stress value of 36.8 MPa will be used as a reference for the analysis.

The author conducted an investigation under four loading scenarios to find out which is most favourable for optimum power generation. The first two loading scenarios will focus on applying an evenly distributed pressure from the weight of the user either on the entire surface area or solely the area that consists of PE transducers. The other two scenarios focus on stressing the PE transducers to their yield strength with and without mechanical amplification mechanisms.

5.5.2.1 UNIFORMLY DISTRIBUTED PRESSURE

To force the PE transducers to deform from an applied pressure, a form of pneumatics is needed to create said pressure. When using the weight of a person, the simplest way to produce this pressure is to use a pneumatic piston/cylinder system arrangement. When an external force is applied onto the piston, the internal pressure inside the cylinder is equivalent to the force divided by the area of the piston. If the piston covers the whole area of the floor tile or shoe insole as shown in Figure 5-52, the internal pressure is equivalent to the force from the user divided by the surface area of the shoe insole or floor tile. If the piston only covers the surface area of the PE discs as shown in Figure 5-53, then the internal pressure is equivalent to the force from the user divided by the total area of the PE transducers. The maximum generated power for both scenarios will be found and compared.

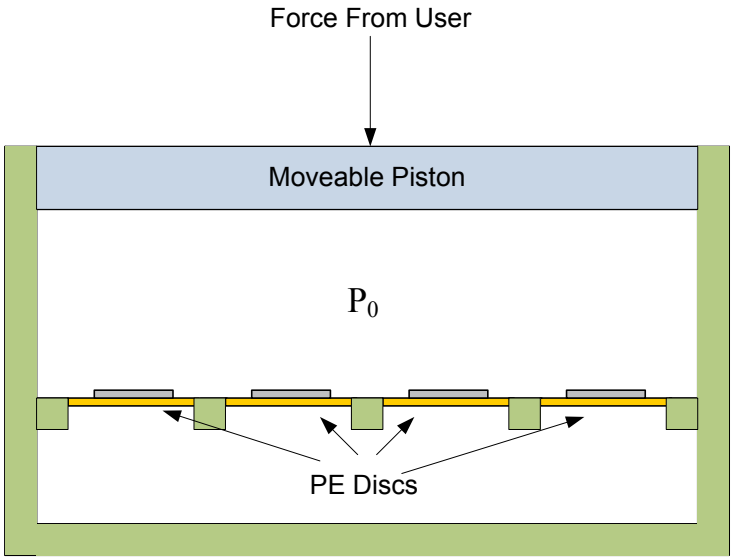

Figure 5-52: A Piston/Cylinder System that applies a uniformly distributed pressure on the entire surface area. The PE discs are simply-supported.

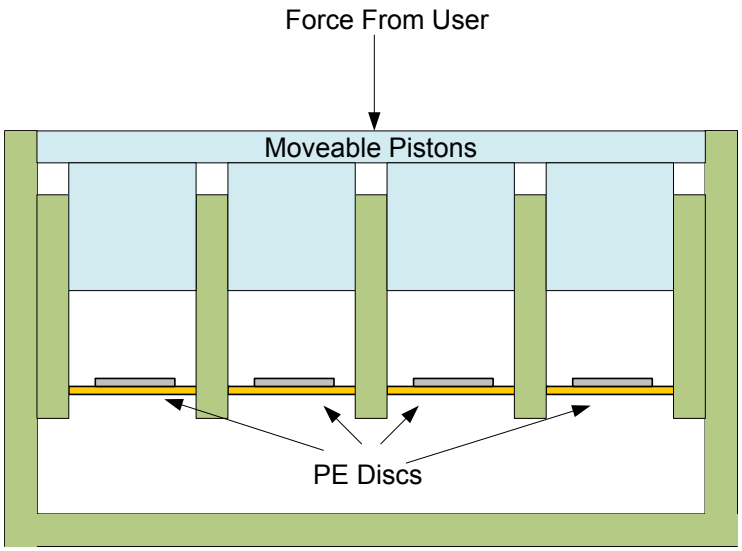

Figure 5-53: A Piston/Cylinder System that applies a uniformly distributed pressure only on the PE discs. The PE discs are simply-supported.

When calculating power output, it is also important to calculate the maximum internal stress in a transducer. It is important that the internal stress be less than the yield stress of the substrate layer as well as the PE material. Given that the PE transducers will only experience a compressive load in the setups as illustrated in Figure 5-52 and Figure 5-53, the yield strength of the PE material will be treated as 600 MPa: a conservative compressive yield strength as stated by APC International, Inc. The yield strength of the aluminum substrate layer will be treated as 269 MPa as previously presented in Table 4-1. The maximum stress and deflection are governed by Equations 5-125 and 5-126, respectively; however, it should be noted that both Equations 5-125 and 5-126 assume that the displacements are relatively small, generally less than the total plate's thickness. As will be shown, most of the displacement calculations exceed the plate's thickness, therefore it is important to note that these equations will only give rough estimates of the true stresses and displacements. These estimations are assumed to be sufficient to analyze a disc's overall power generation capabilities for piezoelectric harvesting.

For both loading scenarios, it will be assumed that the entire surface area for the floor tile or shoe insole is covered with a maximum number of PE discs. The maximum number of PE discs was determined by finding the number of discs that can fit within the respective width and length, and subsequently multiplying both values to get the total. For the floor

tile of 1 ft^2, 81 PE transducers can be used; for the shoe insole of 11 cm x 27 cm, 21 PE transducers can be used.

Table 5-19 shows the calculated results for applying a uniformly distributed stress across both the entire surface area and solely the PE transducers' collective surface area for the tile and shoe scenarios:

Table 5-19: Theoretical Outputs for Evenly Distributed Stresses across the Entire Surface Area and focusing solely on the PE Discs' Surface Area

Tile or Shoe	Pressure on Each Disc (kPa)	Total Amount of Discs	Power per Disc (mW)	Total Power (W)	Estimated Maximum Stress on Disc (MPa)	Estimated Deflection (mm)
Evenly Distributed Stress Across Insole or Floor Tile						
Tile	8.97	81	0.764	0.0489	62.0	0.607
Shoe	28.05	21	7.48	0.157	193.8	1.90
Only Discs are Supporting the Wearer's Load						
Tile	11.4	81	1.24	100	78.9	0.773
Shoe	44.0	21	18.4	387	304.3	2.98

The respective pressure was calculated for each situation by taking the gravitational force of a 185kg person (833N) and dividing it by the corresponding area of the piston. The pressure was then substituted into Equation 5-124 to get the power over one transducer; the total power was obtained by multiplying the power over one transducer by the number of transducers. As the stress is linearly proportional to the applied pressure according to Equation 5-125, the estimated stress for each scenario was found by multiplying the estimated stress of the transducer used by Mo *et al.* (2010a), 36.8 MPa, by the ratio of the scenario's pressure and the 5330 Pa pressure used by Mo *et al.* (2010a):

$$\sigma_{m,est} = 36.8MPa\left(\frac{P_0}{5330}\right) \qquad 5\text{-}128$$

When distributed across the entire surface area (as shown in Figure 5-52) the maximum generated power was found to be 0.0489 mW for the tile vs. 0.157 mW for the shoe. The shoe had the greater power as its lower surface area produces a higher pressure under the

same load; the shoe had an applied pressure that was 213% larger than the tile. Although the tile has more PE transducers, a higher pressure load (as seen in the shoe scenario) is shown to have a greater impact on the generated power. Looking at the estimated maximum stresses, the tile had a value of 62.0 MPa while the shoe insole had a value of 193.8 MPa. As both scenarios had estimated stresses below the aluminum yield stress of 269 MPa, both scenarios are deemed safe from plastic deformation.

Alternatively, when the user's load is distributed solely over the discs' surface areas (as shown in Figure 5-53), there is an increase in applied pressure as the overall surface area of the discs is less than the entire surface area of the corresponding scenarios. With calculated pressures of 11.4 kPa and 44.0 kPa respectively for the tile and shoe insole scenarios, the estimated total powers were 0.100 W and 0.387 W which are a 62% and 147% increase from the entire surface area distribution values. However, the maximum stresses also increased from the increase in pressure. The tile and shoe insole scenarios had estimated maximum stress values of 78.9 and 304.3 MPa. Although the estimated maximum disc stress for the floor tile is still well below the aluminum's yield stress of 269 MPa, the same cannot be said for the shoe insole. With a maximum stress that us 13.1% greater than the substrate layer's yield strength, the PE discs in the shoe insole will succumb to plastic deformation. It appears that the yield strength represents the upper limit of how much power a PE disc can continually produce. In other words, the maximum power output is obtained when the PE disc is periodically stressed to its maximum yield strength. Based on this principle, the next section will focus on stressing PE discs to their yield strength to improve their power output.

5.5.2.2 STRESSING THE DISCS TO THEIR YIELD STRENGTH WITH AND WITHOUT MECHANICAL AMPLIFICATION

To find the full extent of how much power can be generated from a PE disc using 31-deformation via pressure loading, one could intentionally stress a disc to its yield strength. It should be noted, however, that stressing the disc to its yield strength would not be recommended as it is custom to apply a structural safety factor to one's dessign. This section will present two situations that intentionally stress PE discs to their yield

strength. One situation will directly use the weight of the wearer and stress a limited amount of transducers to their yield strength. The other situation will cover the shoe or tile surface area with transducers, as was done in the last section, and stress all of the transducers using a mechanical amplification mechanism.

To reach the yield strength, a specific pressure needs to be applied on the PE disc. The specific pressure can be found by rearranging Equation 5-125 and substituting the center stress with the aluminum yield strength:

$$P_0 = \frac{8\sigma_y t^2}{3(3+v)r^2} \qquad 5\text{-}129$$

Without mechanical amplification, one can increase the pressure load by using the multiple piston/cylinder mechanism previously presented as Figure 5-53, but limit the amount of transducers. With fewer transducers, the collective surface area would decrease and therefore increase the applied pressure. Using the pressure found from Equation 5-129 and the known area of one disc transducer, one can multiply the two values to find the force required to stress the transducer to its yield strength. Taking this force value and dividing it into the total weight of the user (833 N for a 185 kg person), one can find the number of transducers that can be stressed to its yield strength without mechanical amplification. By substituting the simplified thickness of 228 μm, the aluminum substrate radius of 16.9mm, the aluminum yield strength of 269 MPa, and a Poisson's ratio of 0.33 into Equation 5-129, a pressure load of 38.9 kPa is needed to stress a PE disc (*i.e.* the PE disc used by Mo *et al.* (2010a)) to its yield strength. By multiplying this pressure load by the area of one PE disc, the total force on each disc is 35.1 N. Dividing this force into the total weight of the user, 23.75 discs can be stressed to their yield strength. As one cannot have a fraction of a disc, the number is rounded to 24; the resultant pressure would then be 38.5 kPa while the maximum stress will be 266 MPa: slightly lower than the yield strength. Unfortunately, 24 discs can only be installed in the floor tile, but not the shoe insole as the insole can only support 21 discs in its surface area. Substituting the pressure of 38.5 kPa into Equation 5-124, 14.1 mW can be generated by one transducer. Multiplied by 24 transducers, a maximum of 0.339 W can

be generated by a tile without the need for a mechanical amplification mechanism. These calculated results are summarized in the upper portion of Table 5-20.

Using a mechanical amplification (or attenuation) mechanism such as a lever mechanism, one can keep the maximum amount of PE discs along a surface area and force them to experience an internal stress equivalent to their yield strength. As previously calculated, the pressure needed to stress the PE disc to its yield strength is 38.9 kPa. To obtain this pressure using a piston/cylinder mechanism that covers the entire surface area (*i.e.* Figure 5-52), mechanical amplifications of 4.34 and 1.39 need to be applied to the floor tile and shoe insole mechanisms. To obtain this pressure using a piston/cylinder mechanism that covers only the transducers' surface area (*i.e.* Figure 5-53), a mechanical amplification of 3.41 is needed for the floor tile while a mechanical attenuation of 0.884 is needed for the shoe insole. At the pressure of 38.9 kPa, each transducer can produce a calculated maximum power of 14.4 mW. For the 81 PE discs in the floor tile, a maximum power of 1.167 W can be produced. For the 21 PE discs in the shoe insole, a maximum power of 0.303 W can be produced. These calculated results are summarized in the lower portion of Table 5-20.

Table 5-20: Theoretical Outputs for Stressing Discs to their Aluminum Substrate's Yield Strength with and without Mechanical Amplification. All calculations are based on the multiple piston/cylinder arrangement as showcased in Figure 5-53.

Tile or Shoe	Total Amount of Discs	Pressure on Each Disc (kPa)	Stress (MPa)	Power per Disc (mW)	Total Power (W)	Deflection (mm)	Mechanical Amplification/ Attenuation Needed
Stress is Applied over a number of Discs to reach the Aluminum Substrate's Yield Strength with no Mechanical Amplification							
Tile	24	38.5	266.2	14.1	0.339	2.61	1
Tile or Shoe is Covered with Discs and Mechanical Amplification is used to Stress all discs to reach the Aluminum Substrate's Yield Strength							
Tile	81	38.9	269	14.4	1.167	2.64	3.41
Shoe	21	38.9	269	14.4	0.303	2.64	0.884

With a calculated maximum power output of over 1 W, the floor tile scenario with mechanical amplification shows some promise for energy harvesting. It should be reiterated, however, that many assumptions were made when calculating said power

output: assumptions that may not be valid. For instance, it is unfair to assume that the internal stress equation for a circular plate undergoing a pressure load (*i.e.* Equation 5-125) remains valid when the resultant deflection is greater than the plate's thickness. It is also likely unfair to have simplified the thickness of the PE disc using Equation 5-127 in order to use the universal pressure-loaded circular plate equations. To obtain the true stress and deflection equations for pressure-loaded PE discs undergoing a deflection that surpasses its thickness, a composite material empirical analysis is necessary. The values obtained from this analysis should thus not be taken at face-value, but rather as an estimate.

It should also be noted that this investigation was limited to the PE disc size investigated by Mo *et al.* (2010a). It would be interesting to see if larger or smaller diameter discs would improve the overall power potential. Another point made by Mo *et al.* (2010a), is that they found that PMN-PT was better suited for power harvesting than PZT materials. Without considering the yield strength and small deflection limitations, the PMN-PT harvester was shown to have a power generating performance that is more than twice than that of the PE harvester. However, when the yield strength and small deflection limitations are included as design constraints, the PMN-PT further improved its projected power generating more than ten times the power generated by the PZT harvester. The difference in projected power is largely due to the difference in d_{31} coefficients. Mo *et al.* used d_{31} coefficients of -1063×10^{-12} m/V and -320×10^{-12} m/V for the PMN-PT and PZT disc investigations, respectively. As a larger d_{31} has been shown to produce larger power generations, it should be no surprise that the PMN-PT disc would produce the larger power. However, the author was a bit puzzled that a PMN-PT material can be substituted in the derived equations by Mo *et al.* (2010a). PMN-PT is an electrorestrictive material whose behavior is governed by a quadratic relationship between strain and electric field; this was previously presented in Section 2.3.3.5. As PE materials have a linear relationship between strain and electric field, it does not seem fair to be able to directly substitute the d_{31} coefficient directly into Mo *et al.*'s derived equations; the equations should be retrofitted for the quadratic relationship. However, there are some PMN-PT manufacturers that make no mention of its electrorestrictive characteristics (See (Sinocera

Corp., 2012), (H.C. Materials Corporation, 2012), and (APC International, Inc., 2012)) which could indicate that perhaps PMN-PT can be manipulated to only exhibit a linear PE effect; using the strain coefficients in the equations derived by Mo et al (2010a) would therefore be legitimate. Although Mo *et al.* (2010a) analytically showed that PMN-PT is better suited for PE harvesting, they have yet (to the author's knowledge) to experimentally test the power output of PMN-PT; most likely due to the fact that the material is still relatively new, more expensive, and not as widely available as other PE materials such as PZT. However, an experimental investigation was performed by Mo *et al.* to test the power output of PZT-5H discs under pressure loading; it was found that their derived formulas were accurate to within 6 to 15% of the experimental values (Mo, Radziemski, & Clark, 2010b)

Overall, the results from this investigation show that using pressure-loaded PZT discs in floor tiles and shoe insoles can produce a maximum power output of 1.167 W and 0.303 W, respectively, but assumptions were made that may have compromised the results. With reference to their respective surface areas, the floor tile produces a maximum power output of 1.167 W/ft^2 while the shoe insole produces a maximum power output of 0.948 W/ft^2. Experimental validation is required to confirm these maximum power outputs. From the results of Mo *et al.* (2010a), this power output could be improved by switching the PE material from PZT to PMN-PT, but as PMN-PT is not as widely available commercially and is more expensive than PZT transducers, the use of PMN-PT for harvesting foot traffic was outside the scope of this thesis.

5.5.3 Rectangular Bimorphs: 31 Extension

Recalling Equation 5-68, the amount of charge that is accumulated across a PE transducer undergoing a uniformly distributed force in the transverse direction under zero electric field is modeled as:

$$q_{ext}|_{V=0} = \frac{2d_{31}LY_1^E F_1}{t_p Y_1^E + t_s Y_s} = 2d_{31}Y_1^E u_1 w$$

Note that Equation 5-68 represents the charge developed across a bimorph whose PE layers are electrically connected in parallel. As Equation 5-114 uses a charge that is along one capacitor, *i.e.* one PE layer, the power must be calculated for each PE layer and summed to find the total power. The total charge in Equation 5-68 thus needs to be divided by 2 has it represents the charge over two PE layers. The resultant single PE layer charge is substituted into Equation 5-114 and the resultant power is doubled to find the total power developed across a bimorph when extended:

$$P_{ext} = \frac{2q_{ext}\big|_{V=0}{}^{2}\left(t_p/2\right)f_{Hz}}{4\epsilon A} = \left(\frac{d_{31}LY_1^E F_1}{Y_1^E t_p + Y_s t_s}\right)^2 \frac{t_p f_{Hz}}{\epsilon w L} \qquad 5\text{-}130$$

When Equation 5-130 is rearranged using the three factor system introduced in Section 5.5.1, the result is Equation 5-131:

$$P_{ext} = \left[\left(\frac{{d_{31}}^2}{\epsilon_{33}}\right)\left(\frac{Y_1^E}{Y_1^E t_p + Y_s t_s}\right)^2\right]\left(\frac{t_p L}{w}\right)\left({F_1}^2 f_{Hz}\right) \qquad 5\text{-}131$$

Note that the piezo factor in Equation 5-131 includes the moduli of elasticity and layer thicknesses for the PE transducer: material properties that are absent in the 33-deformation piezo factor. Equation 5-131 uses the input force as the main input factor. As the force may exceed the yield stress for the PE or substrate layer, it is advantageous to rearrange the input factor in Equation 5-131 in terms of applied stress. If one can find the maximum amount of stress the transducer can withstand, one can find its maximum power output.

As presented in Section 5.1.6.3 the entire cross-section of the bimorph experiences the same strain when deforming via extension. The stress experienced by the PE layer can then be expressed by multiplying the PE modulus of elasticity by the overall strain, ε_1:

$$\sigma_1 = Y_1^E \varepsilon_1 = \frac{Y_1^E F_1}{w t_p Y_1^E + w t_s Y_s} \qquad 5\text{-}132$$

By rearranging and substituting Equation 5-132 into Equation 5-131, one can model the power output in terms of the internal stress:

$$P_{ext} = \left(\frac{{d_{31}}^2}{\epsilon_{33}}\right)(t_p w L)({\sigma_1}^2 f_{Hz}) \quad 5\text{-}133$$

Note that Equation 5-133 dictates that the moduli of elasticity no longer determine an extension bimorph's power output with reference to an applied stress. This indicates that stiffness of the substrate and PE material are irrelevant when determining the maximum power under a given stress. Table 5-21 summarizes the power factors for an extension bimorph under constant force and constant stress.

Table 5-21: The Power Factors for Extension Bimorphs

Factor	Values for Circular Discs (33 Deformation)	
	At constant F_1	At constant σ_1
Piezo (F_Z)	$\left(\frac{{d_{31}}^2}{\epsilon_{33}}\right)\left(\frac{Y_1^E}{Y_1^E t_p + Y_s t_s}\right)^2$	$\frac{{d_{31}}^2}{\epsilon_{33}}$
Geometry (F_G)	$\frac{t_p L}{w}$	$t_p w L$
Input(F_I)	${F_1}^2 f_{Hz}$	${\sigma_1}^2 f_{Hz}$

Under extension, both the PE layer and the substrate layer are undergoing tension, unlike the modes of deformation previously presented. Unfortunately, PE materials cannot withstand large amounts of tensile stress as they are brittle materials. Guillon *et al.* (2002) performed tensile tests on four different PZT materials: two were hard PZT while the other two were soft PZT. Using a 1% probability of fracture, it was found that the two hard materials had estimated tensile strengths of 43.5 MPa and 56.5 MPa while the two soft materials had estimated tensile strengths of 34.2 MPa and 30.1 MPa (Guillon, Thiebaud, & Perreux, 2002). As substrate materials have much greater tensile yield strengths (269 MPa, 124-310 MPa, and 415 MPa respectively for aluminum, brass, and steel), it appears evident that the PE material will fail before the substrate layer. The tensile strength of the PE material will therefore be the maximum stress the extension bimorph can experience; this maximum stress will be used to determine that maximum power that the bimorph can produce.

From the results obtained from Guillon *et al.* (2002), hard materials appear to have an advantage over soft materials in that they can withstand a higher tensile strength. However, soft materials tend to have higher piezo factors. To know which PE material would be best suited for power harvesting via extension, one must not only take the piezo factor into account, but also the maximum stress it can safely withstand. According to the input factor, the power is proportional to the squared value of the stress experienced by the PE layer. One can therefore directly compare the power generating potential between PE materials by multiplying the piezo factor by the square of the maximum stress.

Table 5-22 presents the same PE materials used in the 33-deformation analysis; the piezo factors are catered to the stress-extension parameters at constant stress (*i.e.* Equation 5-133). In the final column, the piezo factors are multiplied by the square of the maximum stress that each material can safely withstand. For the hard PE materials, the maximum stress was assumed to be 55 MPa; for the soft materials the maximum stress was assumed to be 35 MPa. Both stress values were based on the upper limits of the results obtained by Guillon *et al.* (2002) as the manufacturers do not have the maximum stresses listed as part of their material properties. Guillon *et al.*'s upper limits were taken as opposed to the lower or median values to obtain the absolute maximum power that can be harvested from extension bimorphs.

Based on the results obtained in Table 5-22, the PE material best suited for power harvesting via extension is the PIC 141 material from PI Ceramic GmbH as it has the highest piezo factor-squared stress value with a magnitude of 5.36×10^3 C^2F/m^5. This material was therefore used to calculate the maximum power output for an extension bimorph.

Table 5-22: The d_{31}, ϵ_{33}, and Relevant factors for Several PE Transducer Materials Undergoing Extension Deformation

Model	Navy Type (Hard/Soft)	d_{31} (10^{-12} C/N)	ϵ_{33} (x 10^{-9} F/m)	Piezo Factor [10^{-12} $C^2F/(N^2m)$]	Piezo Factor times σ_{max}^2 (10^3 C^2F/m^5)
Piezo Systems, Inc. (Piezo Systems, Inc., 2012)					
PSI-5A4E	II (Soft)	-190	15.9	2.27	2.77
PSI-5H4E	IV (Soft)	-320	33.6	3.04	3.73
APC International, Ltd. (APC International, Ltd., 2012)					
840	I (Hard)	-125	11.1	1.41	4.27
850	II (Soft)	-175	16.8	1.82	2.23
Type IV	IV (Soft)	--	30.1	--	--
880	III (Soft)	95.0	8.85	1.02	1.25
PI Ceramic Gmbh (PI Ceramic GmbH., 2012)					
PIC 181	I (Hard)	-120	10.6	1.36	4.10
PIC 141	I (Hard)	-140	11.1	1.77	5.36
PIC 241	I (Hard)	-130	14.6	1.16	3.50
PIC 300	I (Hard)	-80	9.30	0.69	2.08
PIC 151	II (Soft)	-210	21.3	2.08	2.54
PIC 255	II (Soft)	-180	15.5	2.09	2.56
PIC 155	II (Soft)	-165	12.8	2.12	2.60
PIC 153	IV (Soft)	--	37.2	--	--
PIC 152	II (Soft)	--	12.0	--	--

With the material selected, one must then determine appropriate geometries. Unfortunately, Pi Ceramic GmbH does not appear to sell bimorphs, but rather PZT sheets and shapes. On the other hand, Piezo Systems, Inc. sells many different bimorph sizes that are readily available with brass substrates. Piezo Systems, Inc. can also custom make different size bimorphs on request. This investigation will therefore focus on the geometries available from Piezo Systems, but will use the material properties of the PIC 141 PE material available from PI Ceramic GmbH to get the maximum amount of power that can be harvested. Table B-4 in Appendix B lists the four bimorph models available from Piezo Systems, Inc. along with their respective widths, lengths, and thicknesses. Each bimorph is only readily available in one substrate thickness (0.127 mm) and three different PE layer thicknesses. Included in Table B-4 are the geometry factors for all 12 combinations of bimorph geometry and thicknesses based on Equation 5-133. It should come as no surprise that the geometry factor increases as the PE layer thickness or surface area increases, indicating that larger thicknesses and surface areas are favoured for greater power generation providing that the internal stress is the same. However,

larger forces are required to stress larger bimorphs to their maximum stress; fewer of these larger transducers can therefore be stressed by human weight.

To deform extension bimorphs via foot traffic, one can position them perpendicular or parallel to the input force. When parallel, the weight of the user can be directly used to extend the bimorph, however, the tile or insole must be large enough to accommodate the length of the transducer. Figure 5-54 shows a schematic of a mechanism that directly extends bimorphs via human foot traffic. The bimorphs are constrained on two sides to two separate parts. One part is the mechanism's frame (coloured in dark grey in Figure 5-54) and is completely constrained, the other part (coloured in light green in Figure 5-54) is a section that can move in the direction of the input force. When the user steps on the moveable section, the bimorphs are stressed in tension and in consequence produce power via the PE effect. When using the parallel system, the amount of power is limited by the input force. The input force on each bimorph is equivalent to the total weight of the user divided by the amount of bimorphs. The force should be as large as possible without causing the PE bimorphs to fracture.

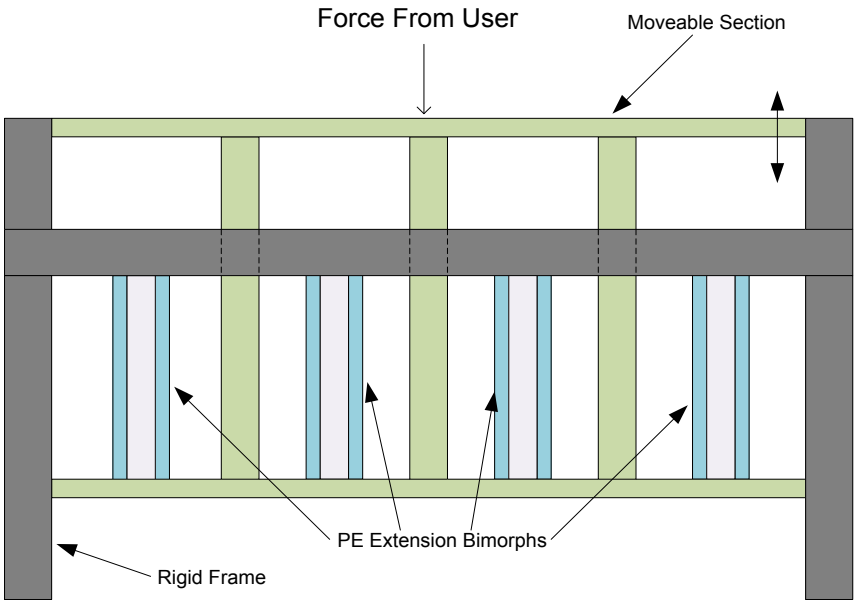

Figure 5-54: Deforming the Extension Bimorphs Parallel to the Input Force. The Bimorphs are constrained to the rigid frame (dark grey) and a section that moves (light green)

Using the parallel extension scenario, power outputs were calculated for all of the readily available geometries from Piezo Systems, Inc. As the force is the limiting factor in the mechanism proposed in Figure 5-54, Equation 5-131 was used with brass as the substrate layer as it is most widely available from Piezo Systems, Inc. The moduli of used were 97 GPa for brass (E-Z LOK, 2012) and 80.6 GPa for the PIC 141 PE material (PI Ceramic GmbH, 2009). For each bimorph geometry, the minimum amount of bimorphs was found to maximize the stress on each bimorph without surpassing the allowable PE layer stress of 55 MPa. The power generated on each bimorph was then calculated and multiplied by the minimum amount of bimorphs. Table 5-23 summarizes the results.

Table 5-23: Power Calculations for the Extension Bimorphs When Parallel to the Input force Without Mechanical Amplification

Bimorph	Total Thickness (mm)	Minimum Number of Bimorphs Needed	Force on Each Transducer (N)s	Stress on PE Layer (MPa)	Power per Bimorph (mW)	Total Power (mW)
103	0.381	12	69.4	53.8	0.131	1.57
	0.508	9	92.6	54.6	0.203	1.83
	0.6604	7	119	54.6	0.284	1.99
203	0.381	6	139	53.8	0.262	1.57
	0.508	5	167	49.2	0.329	1.64
	0.6604	4	208	47.8	0.435	1.74
303	0.381	3	278	53.8	0.524	1.57
	0.508	3	278	41.0	0.456	1.37
	0.6604	2	417	47.8	0.870	1.74
503	0.381	2	417	32.3	0.943	1.89
	0.508	1	833	49.2	3.29	3.29
	0.6604	1	833	38.2	2.78	2.78

The results indicate that the 503 bimorph with a total thickness of 0.508 mm would give the largest power output of 3.29 mW with only one bimorph. One may have expected the 0.6604 mm thickness to give the larger result as it has the largest PE layer thickness, a factor that linearly increases the power output. However, the 0.508 mm thickness experiences a larger internal stress, a factor that quadratically increases the power output.

As mentioned, the extension bimorphs can also be positioned perpendicular to the input force to for power generation. Although more parts are needed to deform the bimorphs in this manner, it makes it easier to apply mechanical amplification mechanisms to elongate bimorphs with larger surface areas. Figure 5-55 shows a mechanism using four-bar linkages that translates the input load to bimorphs placed perpendicular to said input load. The four-bar linkages are composed of rigid members with pin joints. Attached to the side pin-joints are additional rigid members with pin joints that are connected to the bimorph; attached to the top pin joint is a moveable section that can move up and down; attached to the bottom pin joint is a rigid frame that is completely constrained. When the user steps on the moveable section, the top pin joint is forced downwards, in consequence the rigid members transfer the force to the side pins which elongate the bimorph. The advantage of this mechanism is its mechanical amplification. The amount of mechanical amplification depends on the angles between rigid members. If the four-bar linkage resembled a perfect diamond [*i.e.* distance between vertical pin joints (height) and horizontal pin joints (width) are equivalent] there would be no mechanical amplification or attenuation. If the height is greater than the width, there would be mechanical attenuation; if the width is greater than the height, there would be mechanical amplification. A greater width to height ratio creates a greater amplification.

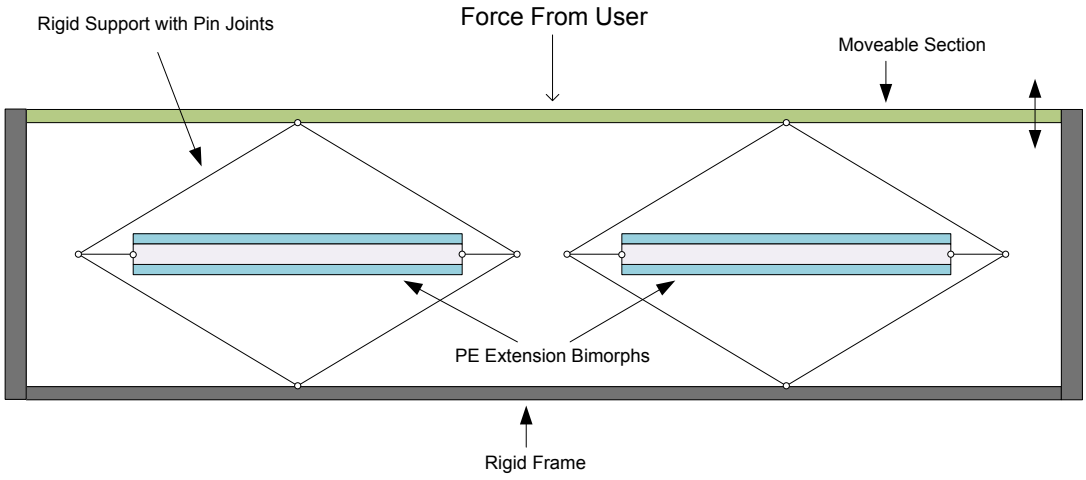

Figure 5-55: Deforming the Extension Bimorphs Perpendicular to the Input Force

To find the maximum power the mechanism illustrated in Figure 5-55 can produce, it will be assumed that the mechanical amplification can be used to stress a bimorph to its

maximum stress. As stress is the limiting factor, Equation 5-133 was used to calculate the power produced. Looking at the geometry factor in Equation 5-133, power linearly increases with an increasing PE layer thickness, width, or length. Power would thus be maximized by using a bimorph that is equivalent to the surface area of scenario, *i.e.* the floor tile or shoe insole's entire surface area. Power would also be increased by using the thickest PE layer thickness available, *i.e.* the 0.6604 mm total thickness from Piezo Systems, Inc. which has a total PE thickness of 0.533 mm. Using these geometry parameters along with the maximum stress of 55 MPa, the maximum power was found for both the shoe insole and floor tile scenarios. The required tensile force to cause this tensile stress was also calculated using Equation 5-132 which was subsequently used to calculate the required mechanical amplification. The results are summarized in Table 5-24.

Table 5-24: The Outputs for Entire Surface Area Mechanism

Scenario	Surface Area (cm^2)	Power (W)	Deflection (mm)	Tensile Force Required (N)	Mechanical Amplification Needed
Shoe	297	0.0849	0.184	4152	4.98
Floor Tile	929	0.265	0.208	11504	13.8

For a bimorph placed perpendicular to the input force, it was found that the shoe and floor tile scenarios could produce a power of 0.0849 and 0.265 W, respectively. The mechanical amplification required to produce this power output is 4.98 and 13.8 for the shoe and floor tile, respectively. Using the mechanism proposed in Figure 5-55, under these mechanical amplifications, the 833 N user would have to displace the moveable section by 0.92 mm and 2.9 mm for the shoe insole and floor tile, respectively. These displacements would likely not affect the user's gait.

Note that the same power output under the same input displacement can be achieved by using the parallel mechanism in Figure 5-54 providing that a force amplification mechanism is used. However, the amplification needed is much greater than that for the perpendicular scenario. Using the tile, for example, the same power output and input displacement is achieved by using about fourty-six 503 type bimorphs with 0.6604 mm total thickness with a force amplification of 66.3. The amplification needed for the

parallel mechanism is 380% more than the perpendicular mechanism; the perpendicular mechanism is thus easier to design and implement. Another factor is cost. When more than twenty-five 503 bimorphs with 0.6604 mm thickness are purchased, Piezo Systems, Inc. lists their price as $83 each. For 46 bimorphs, the total cost would be $3,818. Although Piezo Systems, Inc. does not have a price for a 1 square foot bimorph, the author imagines that it would be less than the total cost of 46 bimorphs.

Overall, the analysis has shown that the most efficient way of extracting power from a bimorph via extension is to use a perpendicular amplification mechanism like the one showcased in Figure 5-55, and to use a single bimorph with the largest possible surface area. When stressed to its allowable stress, the shoe insole and floor tile scenarios could generate a power of 0.0849 W and 0.265 W, respectively.

5.5.4 Rectangular Bimorphs: Cantilevered Bending

Recalling Equation 5-83, the amount of charge developed across two PE layers in a cantilevered bimorph can be modeled in relation to its deflection:

$$q_{cant} = \frac{3d_{31}Y_1^E w(t_p + 2t_s)}{4L}\delta$$

As the charge variable in the power equation (Equation 5-114) is modeled for one capacitor, the above charge equation needs to be divided by two to obtain the charge in each PE layer:

$$q_{cant} = \frac{3d_{31}Y_1^E w(t_p + 2t_s)}{8L}\delta \qquad 5\text{-}134$$

The total power from both PE layers is found by substituting Equation 5-134 into Equation 5-114 and doubling the total amount:

$$P_{Cant} = \frac{2{q_{cant}}^2\left({t_p}/{2}\right)f_{Hz}}{\epsilon_{33}wL} = \left(\frac{3d_{31}Y_1^E w(t_p + 2t_s)}{8L}\delta\right)^2 \frac{t_p f_{Hz}}{\epsilon_{33}wL} \qquad 5\text{-}135$$

Sectioning Equation 5-135 into its respective power factors yields:

$$P_{Cant} = \frac{9}{64}\left(\frac{{d_{31}}^2 {Y_1^E}^2}{\epsilon_{33}}\right)\left(\frac{w t_p \left(t_p + 2t_s\right)^2}{L^3}\right)(\delta^2 f_{Hz}) \quad 5\text{-}136$$

Likewise, the amount of power can also be modeled in terms of the applied force or maximum internal stress (*i.e.* the stress at its constrained edge along its width) which are respectively presented as Equations 5-137 and 5-138:

$$P_{Cant} = \frac{1}{64}\left(\frac{d_{31}^2}{\epsilon_{33}}\right)\left[\frac{w L^3 t_p \left(t_p + 2t_s\right)^2}{I^2}\right](F^2 f_{Hz}) \quad 5\text{-}137$$

$$P_{Cant} = \frac{1}{16}\left(\frac{{d_{31}}^2}{\epsilon_{33}}\right)\left(\frac{w L t_p \left(t_p + 2t_s\right)^2}{\left(t_p + t_s\right)^2}\right)({\sigma_{max}}^2 f_{Hz}) \quad 5\text{-}138$$

The power factors are sorted with respect to each input parameter in Table 5-25.

Table 5-25: The Power Factors for Cantilevered Beam Loading

Factor	Power Factors with Reference to Input Parameter		
	At certain δ	At certain F	At certain σ_{max}
Piezo (F_Z)	$\frac{{d_{31}}^2 {Y_1^E}^2}{\epsilon_{33}}$	$\frac{d_{31}^2}{\epsilon_{33}}$	$\frac{d_{31}^2}{\epsilon_{33}}$
Geometry (F_G)	$\frac{w t_p \left(t_p + 2t_s\right)^2}{L^3}$	$\frac{w t_p L^3 \left(t_p + 2t_s\right)^2}{I^2}$	$\frac{w t_p L \left(t_p + 2t_s\right)^2}{\left(t_p + t_s\right)^2}$
Input(F_I)	$\delta^2 f_{Hz}$	$F^2 f_{Hz}$	${\sigma_{max}}^2 f_{Hz}$

For a cantilevered beam, its power generating limit occurs when the maximum stress limit is reached. When the vertical point load is applied as illustrated previously in Figure 5-15, the upper half of the beam will go through tension while the lower half will go through compression; as PE materials are much weaker in tension, the top edge of the upper half would be expected to fail. As stress is the limiting factor for optimum power generation, Equation 5-138 will be used to calculate the power output in this investigation.

Comparing the power factors for the cantilever and extension bimorphs as shown in Table 5-21 and Table 5-25, respectively, one would notice that the piezo factors are identical while both input factors are dependent on the square of the internal stress. These observations dictate that the optimal PE material for the cantilever bimorph would be the same PE material used in the extension bimorph investigation; the PE material was

the PIC 141 model from PI Ceramic Gmbh. PIC 141's estimated tensile stress limit of 55 MPa will therefore be used as the stress limit for the cantilever beam investigation.

Looking at the geometry factor for the cantilever beam scenario, like the 33-deformation and 31 extension scenarios, the geometry factor depends on the width, length, and total PE thickness. However, a cantilever beam's geometry factor is also dependent on the substrate thickness. It will be shown that an increased substrate thickness increases the total power output; however, it will also be shown that the power output converges to a maximum value.

Using the known stress limit and piezo factor of the PIC 141 material from PI Ceramic Gmbh, the values were substituted into Equation 5-138 and the power output was found for each bimorph that is readily available from Piezo Systems, Inc. The geometry for each bimorph is listed in Table B-4 in Appendix B. The power output was also calculated for a situation where the shoe insole or floor tile was completely embedded with a single bimorph of equal dimensions, *i.e.* 11 cm x 27 cm and 1 ft^2 for the shoe insole and floor tile, respectively. Using Equations 5-81 and 5-84, the corresponding limit deflections and limit forces were calculated. Using the listed widths and lengths from each bimorph along with the designated floor tile and shoe insole widths and lengths, the maximum amount of transducers that can be implanted across the shoe insole or floor tile were calculated for each bimorph. The maximum power that can be generated from each bimorph was then multiplied by the respective maximum amount of bimorphs to find the total power in the shoe insole and floor tile scenarios.

To verify that all the transducers can be bent solely from the weight of the user, the limit force for each bimorph was multiplied by the respective number of transducers to calculate the total force needed to bend all cantilevered bimorphs to their stress limit. If the total force is less than the projected weight of the user, then the weight of the user is sufficient to bend all cantilevered bimorphs. It was found that all bimorph scenarios could be stressed to their stress limit solely from the weight of the user. However, one should note that if the bimorph is free to deflect past its maximum stress limit, the

bimorph will fracture. The deformation mechanism therefore must be retrofitted to only allow the bimorph to deflect to its deflection limit as calculated using Equation 5-84. Figure 5-56 showcases a mechanism that can bend a cantilevered bimorph to a set deflection. When the user steps on the moveable section (coloured green in Figure 5-56) the load gets transferred to the free end of the bimorph via a connector (coloured black in Figure 5-56). The connector is pin-jointed to the moveable section and bimorph, allowing the force to continually be applied perpendicular to the bimorph's free edge. The rigid frame is retrofitted to only allow the moveable section to translate vertically, but to also limit the amount of displacement via stops. The bimorph's deflection is thus limited by the distance between the moveable section and these stops: labeled as δ in Figure 5-56.

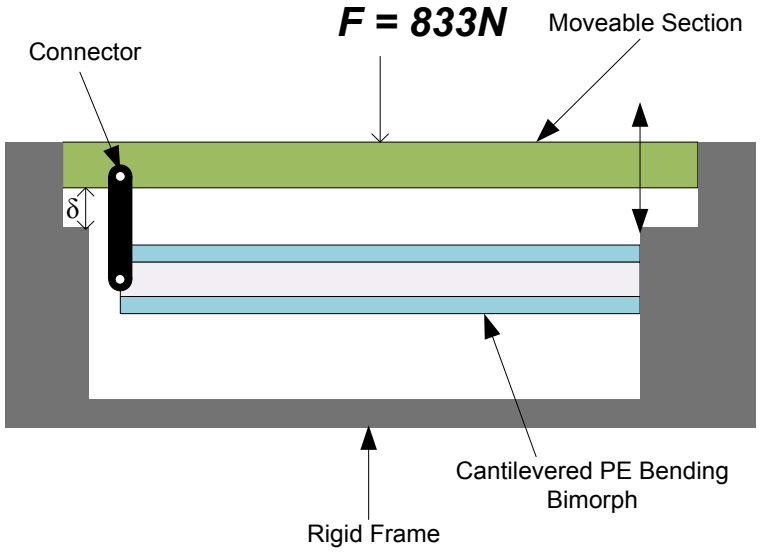

Figure 5-56: A proposed cantilevered PE bimorph deformation mechanism to harness foot traffic. The user would step on the moveable section which can only vertically translate to a set deflection, δ, to prevent the bimorph from surpassing the internal stress limit. A bias force would be needed to bring the moveable section back to its starting point.

The calculated results are presented as Table 5-26. It was found that the 0.6604 mm total thickness gave the best power outputs, therefore only the results pertaining to the 0.6604 mm total thickness are presented in Table 5-26. As all of the total-force magnitudes are less than the projected weight of the user (833 N), no mechanical amplification is necessary to stress the bimorphs to their limit. When comparing the bimorph size

scenarios to their respective total power outputs, the magnitudes are very close to one another. For the shoe insole scenario, the maximum and minimum total power outputs are within 23% of each other; for the floor tile scenario, it's 28%. For both scenarios, the maximum power output was obtained when the entire surface area was a bimorph and the minimum power output was obtained when the largest bimorph (the 503 bimorph) situation was used; the power output increased when smaller bimorphs were used, but the total power did not reach the entire surface area situation. The author attributes this pattern to the embedded bimorph surface area percentage. When larger bimorphs are used, it is more difficult to encompass the whole surface area of the shoe insole or floor tile; a lower percentage of surface area is embedded with PE bimorphs which results in a lower power output. However, as the bimorph size decreases, one can better fill the surface area with bimorphs and thus increase the total power output. The largest power output would thus be obtained when the entire surface area is embedded with one large PE bimorph. With the entire surface area embedded with one large PE bimorph, the maximum power outputs for the shoe insole and floor tile scenarios were calculated to be 7.54 mW and 23.6 mW, respectively.

Table 5-26: Power Calculations and Costs for the Cantilevered Bimorph Scenario at the Stress Limit of 55 MPa. Only the 0.6604mm total thickness situations are presented as they gave the largest power outputs.

Scenario	Bimorph	Deflection (mm)	Force on End (N)	Power/ Bimorph (W)	Maximum Amount of Transducers	Total Force (N)	Total Power (W)	Cost ($US)
Shoe	103	0.69	0.40	2.56×10^{-5}	272	108.9	0.00696	3,808
	203		0.80	5.12×10^{-5}	136	108.9	0.00696	2,448
	303		1.60	1.02×10^{-4}	64	102.5	0.00655	2,112
	503	2.78	2.00	5.12×10^{-4}	12	24.0	0.00614	1,320
	Entire Area	50.2	1.63	0.00754	1	1.63	0.00754	?
Floor Tile	103	0.69	0.40	2.56×10^{-5}	864	345.9	0.0221	12,096
	203		0.80	5.12×10^{-5}	432	345.9	0.0221	7,776
	303		1.60	1.02×10^{-4}	216	345.9	0.0221	5,616
	503	2.78	2.00	5.12×10^{-4}	36	72.1	0.0184	2,988
	Entire Area	64.0	4.00	0.0236	1	4.00	0.0236	?

Also presented in Table 5-26 are the costs associated for each bimorph situation. Although the cost for the entire area of the shoe and floor tile are not known as they need

to be custom made, it should be pointed out that the price decreases as the bimorph size increases; the cost of a bimorph covering the entire surface area will therefore likely be the cheapest option. Nonetheless, it is still projected that cheapest option will still be quite expensive. Using the tile as an example, the author imagines that it would cost about $2000 for the PE material alone. For said $2000, you would only get a 23.6 mW of maximum power. Assuming the tile is continually used and there is no degradation over time, it would take 4.83 years to produce 1 kW*hr: an amount of energy that generally costs about $0.15. It is safe to say that the tile is not a commercially viable means to generate energy.

As mentioned, the geometry factor for a cantilevered bimorph also depends on the thickness of the substrate layer. All of the bimorph thicknesses that are readily available from Piezo Systems, Inc. have the same substrate thickness of 0.127 mm, but other substrate thicknesses are available upon request. The power was therefore calculated over several substrate thicknesses assuming each one is available. Figure 5-57 graphically shows the relationship between generated power and substrate thickness for both the floor tile and shoe insole scenarios assuming that the stress limit of 55 MPa is reached. Both scenarios show that power increases with respect to substrate thickness, but converges at a point. The generated powers appear to converge to about 0.065 W and 0.021 W for the floor tile and shoe insole, respectively. If one factors in the maximum force one can exert onto the cantilevered bimorph (*i.e.* 833 N for a 185 kg person), one could calculate the substrate thickness that would stress the PE layer to its stress limit using Equation 5-84. For the shoe insole and floor tile, substrate thicknesses of 13.2 mm and 8.28 mm would respectively stress the bimorph to its stress limit of 55 MPa under an 833N force. At these respective thicknesses, the shoe insole and floor tile would produce a maximum power output of 20.4 mW and 62.4 mW, respectively. These new power outputs are respectively 171% and 165% larger than those previously presented in Table 5-26. The power output can thus be improved by increasing the substrate thickness. However, the power output is still too small for significant energy production.

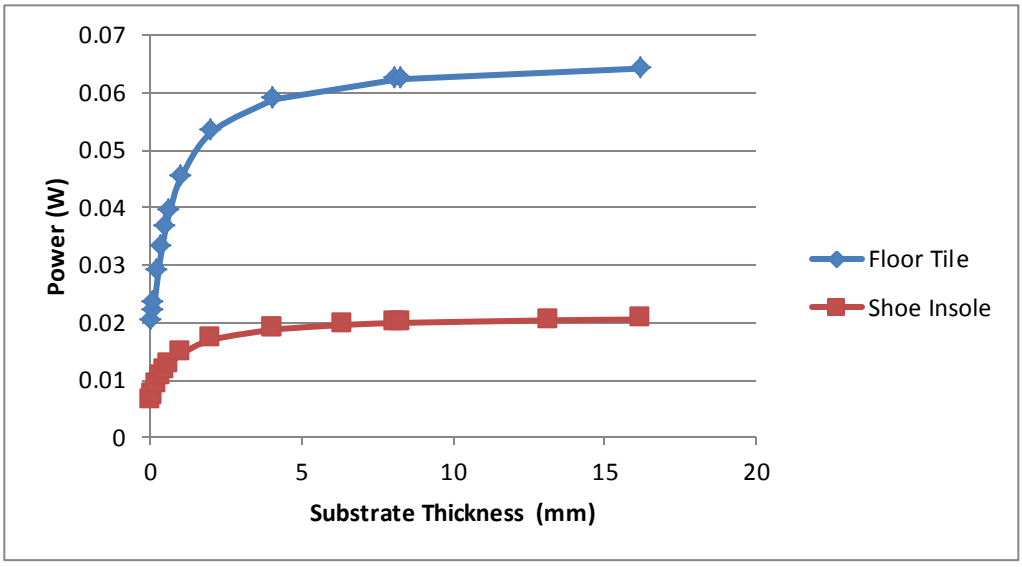

Figure 5-57: Generated power by one bimorph with reference to the substrate thickness for a cantilevered bimorph (or simply-supported bimorph). The blue and red curves represent bimorphs that encompass the entire floor tile (1 ft^2) and shoe insole (11cm x 27cm), respectively. Bimorphs have two PE layers that are 0.267mm thick and composed of PIC 141 from PI Ceramic Gmbh.

Another benefit of increasing the substrate thickness is a decrease in deflection. Previously presented in Table 5-26, if one used the readily available substrate thickness of 0.127 mm, one would need to deflect the shoe insole and floor tile bimorphs 50.2 mm and 64.0 mm: deflections that would no doubt be noticeable by the user and would affect the user's gait. However, the deflection can be significantly reduced by increasing the substrate thickness. Figure 5-58 shows the relationship between substrate thickness and deflection. The deflection appears to converge to 0mm with increasing thickness. Using the optimum substrate thicknesses found for the power output (*i.e.* 13.2 mm and 8.28 mm for the shoe insole and floor tile, respectively), the deflection would decrease to 2.41 mm and 4.79 mm for the shoe insole and floor tile, respectively. These values are respectively 4.8% and 7.5% of the deflections previously presented in Table 5-26 and may not be noticeable by the user. It has been shown that not only can the substrate thickness improve the power output, but can also improve the deflection.

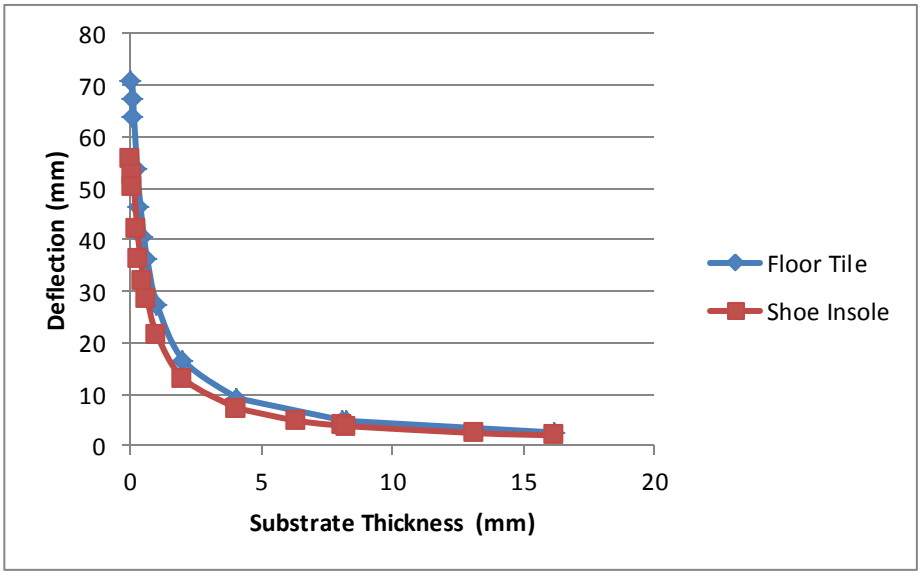

Figure 5-58: The Deflection with Reference to the Substrate Thickness. The blue and red curves represent bimorphs with the surface areas of the floor tile and shoe insole scenarios, respectively. Both bimorphs had two PE layers that are 0.267mm thick and composed of PIC 141 from PI Ceramic Gmbh

Overall, this section has shown that despite the fact that the power output can be improved by using a bimorph that covers the scenario's surface area and increasing the substrate thickness, a cantilevered bimorph's power output is still too small for practical use. The maximum power output that can be obtained from a cantilevered bimorph via human foot traffic is 20.4 mW and 62.4 mW for the shoe insole and floor tile, respectively.

5.5.5 Rectangular Bimorphs: Simply-Supported Bending with Mid-Load

Recalling Equation 5-92, the amount of charge developed across two PE layers in a simply-supported rectangular bimorph with a load at its mid-point, can be modeled in relation to its deflection:

$$q_{mid} = \frac{3d_{31}Y_1^E w\left(t_p + 2t_s\right)}{L}\delta$$

As the charge variable in the power equation (Equation 5-114) is modeled for one capacitor, the above charge equation needs to be divided by two to obtain the charge in each PE layer, as was done in cantilevered bending:

$$q_{mid} = \frac{3d_{31}Y_1^E w(t_p + 2t_s)}{2L}\delta \quad 5\text{-}139$$

The total power from both PE layers is then found by substituting Equation 5-139 into Equation 5-114 and doubling the total amount:

$$P_{Mid} = \frac{2{q_{Mid}}^2\left(t_p/2\right)f_{Hz}}{\epsilon_{33}wL} = \left(\frac{3d_{31}Y_1^E w(t_p + 2t_s)}{2L}\delta\right)^2 \frac{t_p f_{Hz}}{\epsilon wL} \quad 5\text{-}140$$

Sectioning Equation 5-140 into its respective power factors yields:

$$P_{mid} = \frac{9}{4}\left(\frac{{d_{31}}^2 {Y_1^E}^2}{\epsilon_{33}}\right)\left(\frac{wt_p(t_p + 2t_s)^2}{L^3}\right)\delta^2 f_{Hz} \quad 5\text{-}141$$

Likewise, one can model the output power in terms of the applied force and maximum internal stress (*i.e.* the stress located at the bimorph's mid-point edge) which are respectively presented as Equations 5-142 and 5-143:

$$P_{mid} = \frac{1}{1024}\left(\frac{d_{31}^2}{\epsilon_{33}}\right)\left[\frac{t_p wL^3(t_p + 2t_s)^2}{I^2}\right](F^2 f_{Hz}) \quad 5\text{-}142$$

$$P_{mid} = \frac{1}{16}\left(\frac{{d_{31}}^2}{\epsilon_{33}}\right)\left(\frac{wt_p L(t_p + 2t_s)^2}{(t_p + t_s)^2}\right)({\sigma_{max}}^2 f_{Hz}) \quad 5\text{-}143$$

The power factors are presented with respect to each input parameter in Table 5-27.

Table 5-27: Power Factors for a Simply-Supported Bimorph with a Mid-Point Load

Factor	Power Factors with Reference to Input Parameter		
	At certain δ	At certain f	At certain σ_{max}
Piezo (F_Z)	$\frac{{d_{31}}^2 {Y_1^E}^2}{\epsilon_{33}}$	$\frac{d_{31}^2}{\epsilon_{33}}$	$\frac{d_{31}^2}{\epsilon_{33}}$
Geometry (F_G)	$\frac{wt_p(t_p + 2t_s)^2}{L^3}$	$\frac{wt_p L^3(t_p + 2t_s)^2}{I^2}$	$\frac{wt_p L(t_p + 2t_s)^2}{(t_p + t_s)^2}$
Input(F_I)	$\delta^2 f_{Hz}$	$F^2 f_{Hz}$	${\sigma_{max}}^2 f_{Hz}$

When comparing Table 5-27 to the cantilever bimorph power factor table (*i.e.* Table 5-25), one would notice that they're identical. In fact, when comparing the two power equations with the maximum internal stress as its input (*i.e.* Equations 5-138 and 5-143), one would notice that they too are identical. Therefore providing the same PE material,

substrate material, and bimorph geometry are used, a simply-supported bimorph with a mid-load will produce the same amount of power as a cantilevered bimorph when the maximum internal stress is the same. However, the forces and deflections needed to cause the simply-supported bimorph to experience its maximum stress limit will be different than the cantilevered bimorph. Using Equation 5-93, the force and deflection was calculated for each bimorph available from Piezo Systems, Inc along with a custom made bimorph covering the floor tile's or shoe insole's entire surface area. To find the total force, the force on each bimorph was multiplied by the respective maximum number of transducers which was previously found in the cantilevered bimorph investigation. Table 5-28 presents the calculated results for the simply-supported bimorph under mid-loading investigation; only the 0.6604 mm total thickness results are shown as they produced the most power.

Table 5-28: Power Calculations and Costs for the Simply-Supported Bimorph with a Mid-Load

Scenario	Bimorph	Deflection (mm)	Force on End (N)	Power/ Bimorph (W)	Maximum # of Transducers	Total Force (N)	Total Power (W)	Cost ($US)
Shoe	103	0.174	1.60	2.56E-05	272	436	0.00696	3,808
	203		3.20	5.12E-05	136	436	0.00696	2,448
	303		6.41	1.02E-04	64	410	0.00655	2,112
	503	0.694	8.01	5.12E-04	12	96.1	0.00614	1,320
	Entire Area	12.5	6.52	0.0236	1	6.52	0.00754	?
Floor Tile	103	0.174	1.60	2.56E-05	864	1384	0.0221	12,096
	203		3.20	5.12E-05	432	1384	0.0221	7,776
	303		6.41	1.02E-04	216	1384	0.0221	5,616
	503	0.694	8.01	5.12E-04	36	288	0.0184	2,988
	Entire Area	16.0	16.0	7.54E-03	1	16.0	0.0236	?

As the power equations under stress loading for the cantilevered and simply-supported bimorphs were found to be identical, it was no surprise that the total power calculations were identical as well. However, the forces and deflections required to stress the simply-supported bimorphs respectively quadrupled and quartered when compared to those found in the cantilevered bimorph investigation. For the floor tile, the total force needed to deflect the 103, 203, and 303 bimorphs (*i.e.* 1384 N) surpasses the assumed weight of the user (833 N); mechanical amplification would thus be required for an 833 N person to

deform these bimorphs to their stress limit of 55 MPa. However, like the cantilevered bimorph investigation, the highest power output was achieved when one bimorph was used that covered the entire shoe insole or floor tile's surface area. Using a bimorph that covers the entire surface area, forces of 6.52 N and 16.0 N, respectively for the shoe insole and floor tile, are required to stress the bimorph to its maximum internal stress for maximum power output.

As the needed input force is much smaller than the weight of the user, it is important to limit the deflection of the bimorph, similarly to what was done in Figure 5-56 for the cantilevered bimorph, to ensure that the internal stress does not surpass the PE layers' limit stress of 55 MPa. Figure 5-59 shows a proposed mechanism that limits a simply-supported bimorph's deflection. The user steps on the moveable section (shown in green in Figure 5-59) which is connected to a wedge located at the section's midpoint. The moveable section can only translate vertically. The wedge translates the user's load to a point load at the simply-supported bimorph's mid-point. Attached to the rigid frame are stops that limit the vertical movement of the moveable section to a designated displacement, δ, which would be the maximum deflection that the simply-supported bimorph is allowed to experience.

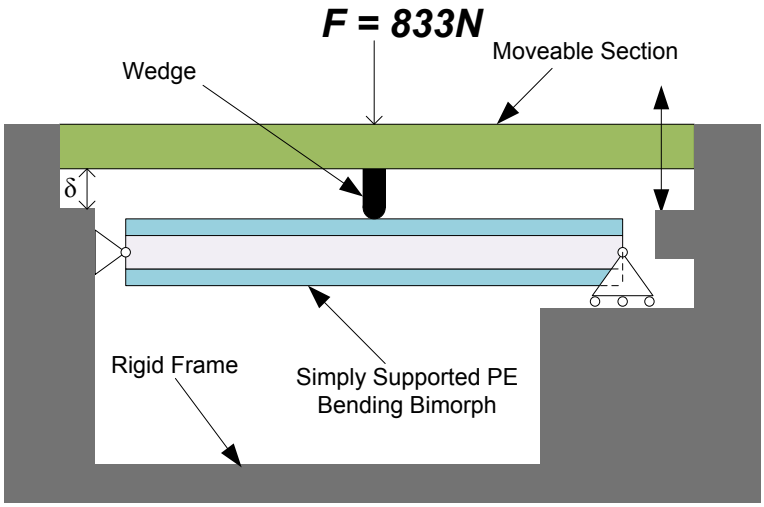

Figure 5-59: A proposed simply-supported bimorph deformation mechanism to harness foot traffic. The user would step on the moveable section which can only vertically translate to a set deflection, δ, to prevent the bimorph from surpassing its internal stress limit. A bias force would be needed to bring the moveable section back to its starting point.

Like the cantilevered bimorph, the simply-supported bimorph's power output increases with increasing substrate thickness. As both bimorph types have the same power output in relation to maximum internal stress, the relationship between substrate thickness and power output would therefore be the same as well. Figure 5-57 thus illustrates relationship between power output and substrate thickness for the simply-supported bimorph as well as the cantilevered bimorph. However, as a larger force is needed to deform the simply-supported bimorph in comparison to the cantilevered bimorph, the substrate thickness required to stress the simply-supported bimorph to its stress limit will be less than the cantilevered bimorph. As a larger substrate thickness correlates with a larger power output, the maximum power output for the simply-supported bimorph will be less than the cantilevered beam. Using the projected weight of the user (833 N) along with Equation 5-93, the substrate thickness that would stress the PE layer to its stress limit was calculated to be 6.40 mm and 4.06 mm for the shoe insole and floor tile, respectively. Substituting these optimum substrate thicknesses into Equation 5-143, the power output was calculated to be 19.6 mW and 58.9 mW resulting in a 160% and 150% increase in power output for the shoe insole and floor tile, respectively. However, this maximum power output is 3.85% and 5.7% less than the cantilever bimorph's maximum power input for the shoe insole and floor tile, respectively.

Although the power output is slightly less than the cantilevered bimorph, the simply-supported bimorph has an advantage with regards to its deflection. As mentioned, at the same internal stress at the same bimorph parameters, the simply-supported bimorph's deflection is one quarter of the deflection experienced by the cantilevered bimorph. For the floor tile for an example, using the 0.6604 mm total thickness bimorph geometry, the simply-supported and cantilevered bimorphs would experience deflections of 16.0 mm and 64.0 mm, respectively. Although both deflections would likely be noticeable by the user, the cantilevered deflection would significantly hamper the user's gait; the simply-supported deflection would be manageable. However, like the cantilevered bimorph, the deflection can be significantly decreased by increasing the substrate thickness. Using the calculated optimum substrate thicknesses (*i.e.* 6.40 mm and 4.06 mm for the shoe insole and floor tile, respectively), the induced deflections decrease to 1.20 mm and 2.30 mm

for the shoe insole and floor tile resulting in a 90.5% and 85.6% decrease in deflection, respectively. Table 5-29 summarizes the power output and deflection changes after increasing the substrate thickness from 0.127 mm to its calculated optimum value; both the cantilever and simply-supported bimorph scenarios are included.

Table 5-29: The Power Output and Deflection Changes after Increasing the Substrate Thickness to its Optimum Magnitude

Bimorph Setup	Scenario	Optimum Substrate Thickness (mm)	Power Output (W)	% Increase in Power Output	Deflection (mm)	% Decrease in Deflection
Cantilever	Shoe Insole	13.2	0.0204	171	2.41	95.2
	Floor Tile	8.28	0.0624	165	4.79	92.5
Simply-Supported with Mid Load	Shoe Insole	6.40	0.0196	160	1.20	90.5
	Floor Tile	4.06	0.0589	150	2.30	85.6

Graphically illustrated in Figure 5-60 is the relationship between a cantilevered or simply-supported bimorph with reference to the substrate thickness; both the floor tile and shoe insole scenarios are shown. Figure 5-60 shows that at low substrate thicknesses, there is a significant difference in deflection values between the floor tile and shoe insole scenarios. However, as the substrate layer increases, both scenarios' deflections converge to zero, thus making the deflection less of a determining factor for design considerations. Recalling that cantilevered and simply-supported bimorphs produce the same power under the same stress load and bimorph geometry, it would be recommended to use a simply-supported bimorph setup at low substrate thicknesses. If larger substrate thicknesses are available, the cantilevered bimorph setup would be recommended as it can use a larger substrate thickness and thus produce a larger power, albeit only 4.0% and 6.0% more than the simply-supported bimorph for the shoe insole and floor tile scenarios, respectively.

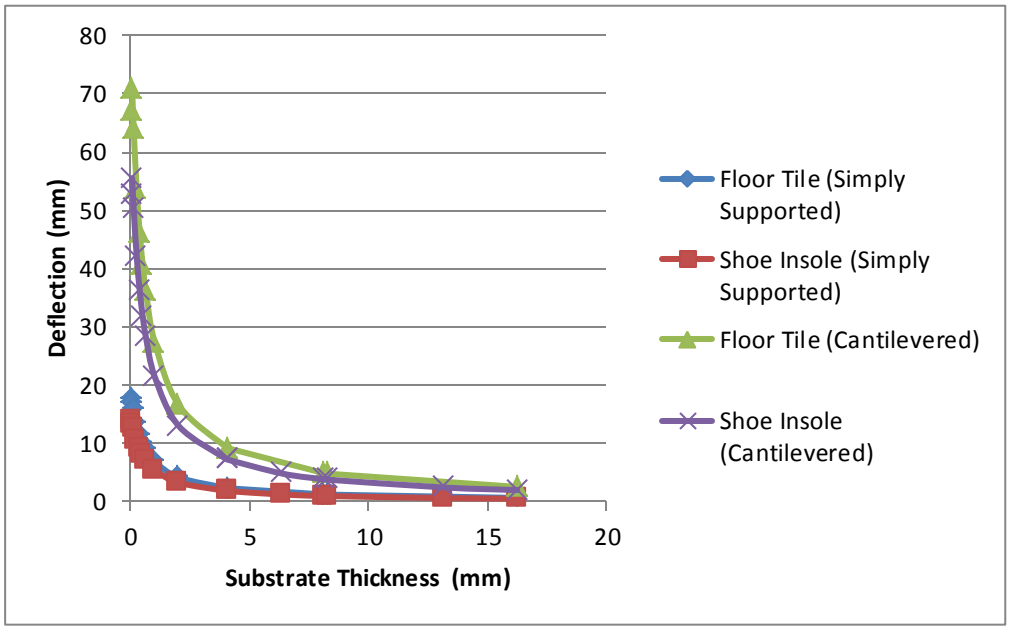

Figure 5-60: Deflection with Respect to Substrate Thickness for both the Simply-Supported and Cantilevered Bimorph Scenarios

Overall, this section has shown that despite the fact that the power output can be improved by using a bimorph that covers each scenario's surface area and increasing the substrate thickness, a simply-supported bimorph undergoing a load along its midpoint is still too small for practical use. The maximum power output that can be obtained from a simply-supported bimorph via human foot traffic is 19.6 mW and 58.9 mW. Although this power output is slightly less than the cantilevered-bimorph setup, the simply-supported bimorph experiences a smaller deflection: a factor that is favourable when considering the user's gait.

5.6 SUMMARY

As mentioned, the overall objective of this investigation was to determine if it is technically and commercially feasible to harvest the wasted energy from human foot traffic using PE harvesting either through PE embedded shoe insoles or floor tiles. Through modelling a PE transducer's power output into a three factor system, the author was able to determine the piezoelectric, geometrical, and input parameters to optimize power output for a particular setting. Five methods of PE transducer deformation were investigated: circular discs in 33-deformation, circular discs under 31-deformation via

pressure loading, rectangular bimorphs undergoing 31-deformation via extension, rectangular bimorphs undergoing 31-deformation via cantilevered bending, and simply-supported rectangular bimorphs undergoing 31-deformation upon a mid-point load. Table 5-30 summarizes the calculated power outputs obtained from all five deformation mechanisms using available transducer arrangements without any mechanical amplification mechanisms. Table 5-31 summarizes the calculated power outputs when using mechanical amplification mechanisms and thickness changes.

Table 5-30: Power Output Summary for a Single Transducer without Amplification Mechanism

Deformation Mechanism	Maximum Power [Number of Transducers for Said Max Power]		Key for Best Power Output
	Shoe (297 cm^3)	Floor Tile (1 ft^2)	
33 Deformation (Circular Disc)	0.0207 mW [1]		Minimize PE Layer Area and have all the user's weight on the disc
31 Circular Disc Through Pressure Load	157 mW [21 Discs]	339 mW [24 Discs]	Find Maximum Safe Pressure load
31 Extension	3.29 mW [1]		Find Maximum Safe Applied load, Maximize PE Layer Area
31 Cantilever End Load	7.54 mW [1] (Entire Area)	23.6 mW [1] (Entire Area)	Maximize PE Layer Area, Stress the Bimorph to its stress limit
31 Simply-Supported Mid Load	7.54mW [1] (Entire Area)	23.6mW [1] (Entire Area)	Maximize PE Layer Area, Stress the Bimorph to its stress limit

Without mechanical amplification, this investigation predicts that the most efficient method would be the circular discs going through 31-deformation via pressure loading with maximum calculated power outputs of 157 mW and 339 mW for the shoe insole and floor tile, respectively. However, it should be noted that the mechanism needed for the pressure loaded 31-deformation would transfer the user's load to the PE transducer using pneumatics; the other deformation mechanisms directly transfer the user's load to PE transducers. The pressure loaded 31-deformation thus requires a more complex deformation mechanism, but the calculated power outputs are larger than their closest contender (the cantilevered and simply-supported bimorphs) by a factor of 19.8 and 13.4 for the shoe insole and floor tile, respectively.

Table 5-31: Power Output Summary including Amplification Mechanism and Thickness Changes

Deformation Mechanism	Maximum Power [Conditions]		Key for Best Power Output
	Shoe (297 cm^3)	Floor Tile (1 ft^2)	
33 Deformation (Circular Disc)	3.62 W [6mm circular PE layer(s) with total thickness of 25.4mm (1") under a 20.4 mechanical amplification]		Use one thick PE layer or stack smaller PE layers electrically in parallel, use a substrate layer with a high yield stress, and stress the transducer to its safe stress limit
31 Circular Disc Through Pressure Load	0.303 W [21 Discs under a 0.884 mechanical attenuation]	1.167 W [81 Discs under a 3.41 mechanical amplification]	Find Maximum Safe Pressure load, use the maximum amount of transducers that can physically fit along area, use mechanical amplification to stress them all to their stress limit
31 Extension	0.0849 W [Entire area under a 4.98 mechanical amplification]	0.265 W [Entire area under a 13.8 mechanical amplification]	Find Maximum Safe Applied load, use entire surface area, use mechanical amplification to stress the bimorph to its stress limit
31 Cantilever End Load	0.0204 W [Entire Area]	0.0624 W [Entire Area]	Maximize PE Layer Area, Stress the Bimorph to its stress limit, Use a Large substrate layer thickness
31 Simply-Supported Mid Load	0.0196 W [Entire Area]	0.0589 W [Entire Area]	Maximize PE Layer Area, Stress the Bimorph to its stress limit, Use a large substrate layer thickness

If mechanical amplification is integrated into the deformation mechanisms to stress PE transducers to their stress limit, the calculated results show that the power output can be greatly increased. With mechanical amplification, the pressure loaded 31-deformation mechanism can produce a maximum power of 0.303 W and 1.167 W for the shoe insole and floor tile scenarios resulting in a 93% and 244% increase in power, respectively. However, when integrating mechanical amplification, the calculated results show that the 33 deformation mechanism can produce more power than the pressure loaded 31-deformation mechanism. Using an increased total PE layer thickness of 25.4 mm (1") along with a mechanical amplification mechanism, the power output for the 33-deformation was estimated to be 3.62 W increasing the power by a factor of 1.75×10^5. With reference to the pressure loaded 31-deformation mechanism, it has been estimated that the 33-deformation mechanism could produce 1090% and 210% more power for the shoe insole and floor tile scenarios.

Although it has been calculated that a mechanically amplified 33-deformation mechanism would produce the most power, there are several detriments that should be mentioned. First of all, the 33-deformation mechanism requires a very high mechanical amplification of 20.4. In contrast, the pressure loaded 31-deformation mechanism only requires a 3.41 mechanical amplification: a mechanical amplification that would be easier to design and integrate. Cost would also be a factor. A 25.4 mm PE transducer or stack transducer would have to be custom made which can get expensive. Circular PE discs are more widely available and generally cost effective. However, the pressure loaded 31 deformation investigation used PE discs that are generally not readily available and would have to be custom ordered as well. It would be difficult to estimate which scenario would be the most cost effective; an additional investigation would be necessary. Regardless of which scenario is the most cost effective, the author speculates that either scenario would be too expensive to make foot traffic harvesting a commercially viable solution for sustainable energy production.

It must be reiterated that many assumptions were made in this investigation; many of these assumptions would not be valid in an experimental setting. First of all, it was assumed that all of the available power could be harvested. As discussed in Section 5.4, an efficient electronic circuit is needed. The electronic circuit needs to incorporate impedance matching, switching techniques, and an efficient storage device. Regardless of what electronic circuit is used, it is unrealistic to assume that all of the available power can be harvested. The calculations made throughout this thesis represent the maximum amount of power available to be harvested, not the amount of power that will be harvested. Secondly, it was assumed that the linear relationship between deformation and electric displacement holds at large stresses; this assumption is not valid. At larger stresses (and larger applied electric fields), the deformation-electric displacement relationship is non-linear; the limits of linear behaviour vary for each ceramic composition (Helke & Lubitz, 2008) and are generally not readily available from manufacturers. Many other assumptions were made throughout this thesis; the only way of knowing if the projected power estimates are valid is to perform experiments and take measurements.

It should also be noted that there are other PE transducers that were not included in this investigation; these other transducer configurations may improve on the power output performance, but were omitted from the investigation due to their limited availability. Previously presented in Section 5.2.1, some of these configurations include curved bimorphs (See Figure 5-18) and cymbols (See Figure 5-19), but also include unimorphs. Unimorphs are like bimorphs, except only one PE layer is used as opposed to two. It would be recommended to derive equations for unimorphs in bending configurations such as the cantilevered or simply-supported scenarios as they can be positioned in such a way to only experience compression. As mentioned, bimorphs, when bent, have one PE layer in tension while the other is in compression; the PE layer in tension will break first as PE materials are quite brittle. However, if the PE layer on the unimorph is positioned on the side that experiences compression, the unimorph would be able to withstand greater stresses and thus produce more power. Figure 5-61 graphically illustrates unimorphs in the cantilevered and simply-supported deformation mechanisms; on both images the PE layer is positioned so that it only experiences compression. At the same total PE layer thickness, the author would expect the unimorph to surpass the bimorph's power output providing that the substrate thickness is thick enough to ensure the whole PE layer is experiencing compression.

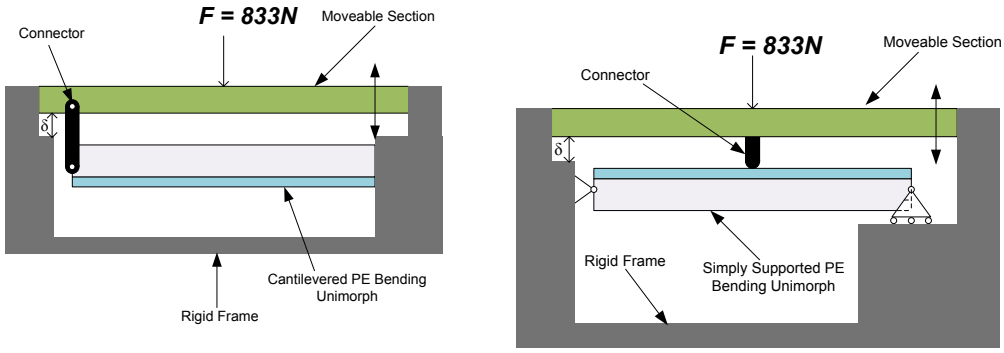

Figure 5-61: Unimorphs in the cantilevered (Left) and simply-supported (Right) deformation mechanisms. Unimorphs can be positioned so the single PE layer (in blue) can experience only compression enabling the unimorph to withstand greater stresses and thus produce more power.

One of the objectives of this investigation was to see if the 1-5 W/ft^2 power output claim made by POWERleap, LLC was conceivable. Although it has been shown that 3.62 W/ft^2 and 1.167 W/ft^2 power outputs can be achieved using the 33-deformation

mechanism or pressure loaded 31-deformation mechanism, respectively, the author reiterates these are maximum power outputs; an efficient electronic circuit is needed to harvest this power. Additionally, mechanical amplifications of 20.4 and 3.41 are needed for the 33-deformation and pressure-loaded 31-deformation mechanisms, respectively, to achieve these power outputs. When POWERleap made the claim of 1-5 W/ft^2 they were either on their 2nd or 3rd generation (most likely the third) which used two cantilevered bimorphs (judging from videos and pictures, they are no more than 1" by 2" each) and 16 PE discs (juding from pictures, they are no more than 2" in substrate diameter), respectively. This investigation has shown that even if the entire tile was covered in a bimorph with the highest PE thickness available from Piezo Systems, Inc., it would only produce a maximum power of 0.0236 W/ft^2. A power output of two 1" by 2" bimorphs therefore cannot conceivably produce 1-5 W/ft^2. Judging from photos of the 3rd generation of POWERleap^{TM} (See Figure B-4 in Appendix B), the piezo discs appear to be directly deformed from the weight of the user via 33-deformation without any mechanical amplification. From the author's investigation, it was found that the maximum power output that can be obtained via 33-deformation using readily available PE discs is 20.7 μW. Although the discs in the 3rd generation tile may be experiencing some 31-deformation, it wouldn't be close to the power output of 0.339 W/ft^2 from the pressure loaded 31-deformation scenario which is still shy of 1-5 W/ft^2. Everything considered, this investigation has shown that POWERleap's claim of 1-5W/ft^2 is false. This claim was seconded through a personal e-mail sent to the author from Daniel Inman: co-editor of *Energy Harvesting Technologies (2009)*.

Another objective was to find if harvesting human foot traffic via PE harvesting is commercially feasible. When filling out a funding application for the Buckminster Fuller Challenge, POWERleap, LLC estimated that the initial cost to create a 50 m^2 floor that generates 1 kwh of energy would be under $500 (Redmond, Katz, & Trude, 2010). From the results of this investigation, it is clear to the author that this claim not only low-balls the floor's power output output capabilities, but the floor's cost as well. Although the cost of all scenarios was not analyzed in this thesis, the author believes that it would be a challenge to create a 1 ft^2 floor tile for under $500. For the maximum power output to be

achieved for the extension and bending bimorph mechanisms, the entire floor tile would need to be covered with one giant bimorph; it is estimated that the bimorph alone would cost about $2000 US. Although the associated costs of 33-deformation disc and pressure-loaded PE disc scenarios were not analyzed in this thesis, the author projects that the cost for the transducers alone could surpass $500 US. PE stacks generally have to be custom ordered and are thus more expensive than readily available PE discs. Although PE discs are readily available and inexpensive (you can buy them in bulk for about $1 each), the readily available discs come with brass substrate layers with thicknesses that are generally one to two times the PE layer thickness. Although the investigation carried out by Mo *et al.* (2010b) used a substrate thickness that was roughly twice the thickness of the PE layer, the substrate material was aluminum. The author could not find a price for a PE disc with an aluminum substrate which lead the author to believe that they have to be custom ordered which can get expensive. More details about rejecting POWERleap, LLC's $500 cost claim can be found in Appendix B2. Everything considered, there is no possible way one can create a 50 m^2 floor that generates 1 kwh of energy using PE harvesting for under $500. Although all PE material costs for the 33-deformation and pressure loaded 31-deformation mechanisms were not realized in this investigation, the associated costs are predicted to be too high to make PE embedded flooring commercially feasible.

5.7 CONCLUSIONS AND RECOMMENDATIONS

From deriving power output equations for five different PE transducer deformation mechanisms, the author was able to evaluate each mechanism's feasibility in harvesting energy from human foot traffic. The remainder of this chapter will briefly list the conclusions made along with recommendations should this subject be pursued further.

5.7.1 Conclusions

In summary, the following conclusions were made for this investigation:

1. Without mechanical amplification, the pressure loaded 31-deformation mechanism using circular discs would be best suited for harvesting energy from human foot traffic
2. With mechanical amplification mechanisms, the 33-deformation mechanism would be best suited for harvesting energy from human foot traffic
3. The overall maximum power output is likely too small to be practically useful for significant energy generation. This applied to both PE embedded shoe insoles and floor tiles
4. The cost of PE embedded flooring is too large to be economically feasible in the commercial market as a means for sustainable energy production

5.7.2 Recommendations

Overall, based on the results from this investigation, the author recommends that PE harvesting should not be used to harvest power from human foot traffic due to its low power output and significant costs. For further investigation, the author would recommend:

1. Experimentally testing the various deformation mechanism to validate the maximum power output models
2. Conducting an assessment on the energy needed to physically make the PE materials to see how long it would take to produce a greenhouse gas rate-of-return, thus analyzing the technology's true environmental footprint
3. Analyzing the potential of using PMN-PT transducers instead of PZT transducers to improve the power output
4. Analyzing the power output potential for bending unimorphs as opposed to bimorphs as they can be arranged in a way to only experience compression
5. Analyzing the power output of PE fibre composites to improve the power output

CHAPTER 6. MODELING AND TESTING STROKE AND REACTION TIMES OF HELICAL SHAPE MEMORY ALLOY ACTUATORS

6.1 EXPERIMENTAL OBJECTIVES

6.1.1 Background

When the @lab started brainstorming ideas for the flamenco backdrop, two traits stood out: lighting and movement. It was decided that the lighting would be controlled by the movement of the dancer, but the @lab wanted moving elements in the backdrop to respond to music. Knowing Joanna Berzowska personally, we were introduced to the use of nitinol in fabrics through her work on the Kukkia, Vilkas (Berzowska & Coelho, 2005), and Skorpian (Berzowska, et al., 2007) dresses. These dresses had flaps or creases that move using nitinol helical springs. Inspired by these innovations, the @lab wanted to add similar mechanical flaps and have them programmed to respond to music.

SMA springs are not readily available. Generally, if one needs SMA helical springs, they have to be custom ordered which can be quite expensive. As the @lab did not know what parameters would be best suited for the fabric flaps (*i.e.* the amount of stroke possible, the amount of force needed, etc.), there was little point in custom ordering the SMA springs. In their article about the Kukki and Vilkas dresses, Berzowska and Coelho (2005) mentioned that they made the helical SMA springs themselves by obtaining straight nitinol wire, wrapping it around a metal bar, and heat treating it to set its shape. After testing many different wire sizes, they ended up using a wire diameter of 0.2 mm as it provided a satisfactory stroke and was sewable. Taking these cues, the author purchased 0.008" (0.2 mm) diameter nitinol wire manufactured by Dynalloy, Inc. Named Flexinol®, this particular wire had a transition temperature of 70 °C and could be activated by electric current. Experimenting with different spring lengths, spring diameters, electric currents, and using superelastic nitinol as a bias force, the SMA helical

spring flaps were successfully implemented into the backdrop's flaps using 0.008" (0.2 mm) wire diameters at a 0.09375" (2.38 mm) inner spring diameter.

From this successful implementation of SMA helical springs, the author set out to better understand how the spring parameters influence the dynamic response of the actuator. These parameters include the wire diameter, spring diameter, number of spring turns, transition temperature, electric current, and bias force. Although there have been numerous studies on the dynamic response of nitinol springs [see (Baz, Iman, & Mccoy, 1990), (Lee & Lee, 2000), (Huang, 2002), (Jee, Han, Kim, Lee, & Jang, 2008), and (Kim, Hawkes, Cho, Jolda, Foley, & Wood, 2009)], their dynamic behavior is yet to be completely understood. Also, most of these studies involve heat treating as-drawn SMA wire to be heat treated into a spring. As-drawn wire is not as readily available as Flexinol® wire and is generally more costly. Unlike as-drawn wire, Flexinol® has already been through the final annealing process and would therefore have different material properties than as-drawn wire. Although cautioned from a representative at Dynalloy, Inc. that reheating the Flexinol® wire may encourage random crystal growth and damage the material, programming the Flexinol® into helical springs proved to be quite successful for our application. Although some models do exist to predict the dynamic response of SMA nitinol spring actuators, the models all assume that the alloy has only been shape set once. As the backdrop used Flexinol® that was first shape set to be straight and then shape set again to be a helical spring, the only way to determine their dynamic response is to perform experiments with spring parameter manipulation.

6.1.2 Overall Objectives and Chapter Layout

There are two main objectives in this study. The first is to find correlations between the spring parameters and its dynamic response. Predictions will first be made using theoretical calculations and then be compared to the experimental values. As not all of the necessary information was available from the manufacturer, some values had to be assumed. The predictions are therefore only to be used as guidelines for comparison. The study will therefore concentrate more on comparisons between different parameter

values rather than an absolute comparison with the predictive values. A discussion will then be performed, giving possible explanations for the results. The second objective is to simply catalogue the stroke and reaction times at different spring parameters for reference for future projects.

6.2 SHAPE MEMORY ALLOYS: AN OVERVIEW

6.2.1 Crystal Structure and Phase Transformation Mechanism

The most common and well known shape memory alloys are nickel-titanium alloys. These alloys are more commonly referred to as NiTiNOL; Ni coming from nickel, Ti coming from titanium, and NOL coming Naval Ordance Laboratory: the lab in which they were first discovered. At its high temperature phase, austenite, nitinol along with many other shape memory alloys have a cubic structure arrangement. In nitinol, this cubic structure is composed of nickel and titanium ions. Once cooled to its low temperature phase, martensite, the crystal structure becomes heavily twinned. The twinned crystal structure gives martensite its pliability as the kinks can be deformed to a slant. After deforming the martensite, heat recovery can then be applied to the alloy to return it to its austenite form as well as its programmed shape at its austenite form. The transformation of the alloy's crystal structure throughout its phase changes is illustrated in Figure 6-1. Through heat treatment techniques, shape memory alloys can be programmed to be any shape imaginable. Figure 6-2 illustrates a nitinol spring with a deadweight for example. At its austenitic phase, the spring is programmed to be compressed. The austenite phase is quite stiff; the dead weight will not cause the spring to extend much. However, once the spring has been cooled and thus transforms into its martensitic phase, the twinned structure "detwins" in consequence of the force being applied by the weight. The detwinning allows the spring to extend. If one wanted to return to the spring's compressed state, all one would have to do is reapply heat. The heat will cause the alloy to return back to its programmed austenitic phase and at the same time lift the dead weight. In this one example of how shape memory alloys can be used to perform work.

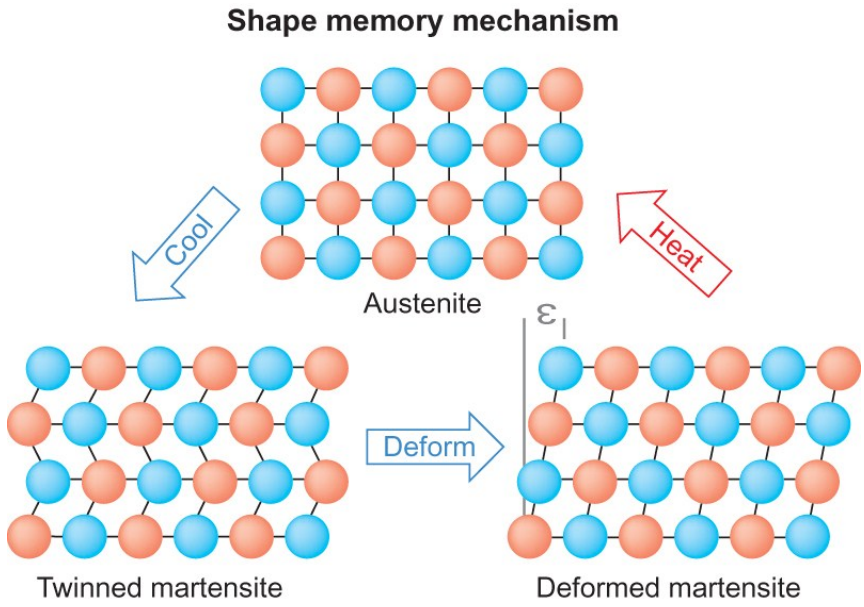

Figure 6-1: The Crystal Structures of Austenite, Twinned Martensite, and Deformed Martensite. Extracted from (Lombardi & Poncet, 2011)

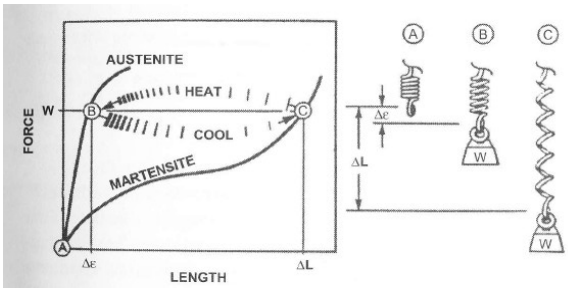

Figure 6-2: Apply a force to NiTiNOL at its austenite phase and martensite phase: a) no weight attached, b) austenite to martensite transition, c) martensite. Extracted from (Srinivasan & McFarland, Smart Structures: Analysis and Design, 2001)

Shape memory alloys have four reference temperatures. When transforming from martensite to austenite, austenite will start to form at the critical temperature, A_s, and finish its transformation at the critical temperature, A_f. Likewise for the austenite to martensite transformation, martensite will begin to form at the critical temperature M_s, and finish its transformation at temperature M_f. The complete transformation cycle is graphically shown in Figure 6-3 with reference to the alloys temperature, T and martensitic fraction, ξ. The martensitic fraction is 0 between the A_f and M_s temperatures during austenite to martensite transformation, 1 during martensite to austenite

transformation, and between 0 and 1 during a phase transformation. Most metals including steel exhibit this phase change, but at much higher temperatures (typically higher than 1500 °C), making them difficult to use as actuators. However, shape memory alloys are made to have transition temperatures closer to room temperature, enabling them to more easily transition using heat transfer techniques.

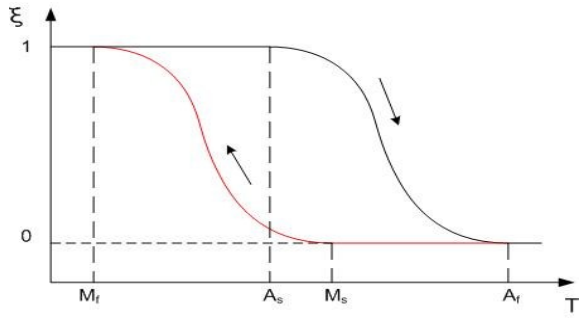

Figure 6-3: Modelling of the Martensitic Fraction (ξ) with reference to temperature. There is much thermal hysteresis after one cycle of heating/cooling. Extracted from (Sharaf, 2012)

Looking at Figure 6-3, it is evident that there is much hysteresis in the phase transformation loop. This hysteresis typically ranges from 30-40 ˚C. Although the hysteresis can be minimized through adding substrates (adding copper can reduce the hysteresis width as low as 15 ˚C (Shenzhen Star Spring Materials Co.), the hysteresis strongly plays a factor in using shape memory alloys in practice.

The transformations are associated with the release and absorption of latent heat: the martensite to austenite transformation (AM transformation) absorbs latent heat (*i.e.* endothermic) while the austenite to martensite transformation (MA transformation) releases latent heat (*i.e.* exothermic). The heat of transformation and the associated transformation temperatures are found using a differential scanning calorimeter (DSC). The principle behind a DSC is the measurement of the rate at which heat energy is supplied to a specimen to maintain a constant heating or cooling rate. Shown in Figure 6-4, a DSC curve shows the relationship of the power (mW) required to maintain a constant heating or cooling rate vs. the overall temperature of the specimen. During the AM transformation, the shape memory alloy would absorb more heat, resulting in a necessary increase in heat flow to maintain a constant heating rate; during the MA transformation, the shape memory alloy would release latent heat, resulting in a

decreased applied heat flow to maintain a constant cooling rate. These increases and decreases in heat flow are illustrated as peaks in Figure 6-4; the areas of these peaks are used to calculate the heat of transformation while the tangents are used to find the respective transition temperatures. One can also compute the specific heat capacity of the shape memory alloy by normalizing the power by the heating rate and the weight of the specimen (Kumar & Lagoudas, 2008). If a DSC is not available, one can simply use a simple "Bend and Free Recovery" test which consists of bending the alloy (initially at its martensite phase) outside of its programmed shape, heating the alloy while constantly measuring its temperature, and observing when the alloy begins and finishes changing shape. The temperature at which the alloy begins to change shape is the A_s transition temperature, while the temperature at which the shape transformation finishes is the A_f transition temperature. One can then find the remaining transition temperatures by applying a constant force on the shape memory alloy, initially at its austenite phase, while constantly decreasing the temperature; the temperature at which the alloy starts to deform is the M_s transition temperature, while the temperature at which the alloy stops deforming is the M_f transition temperature.

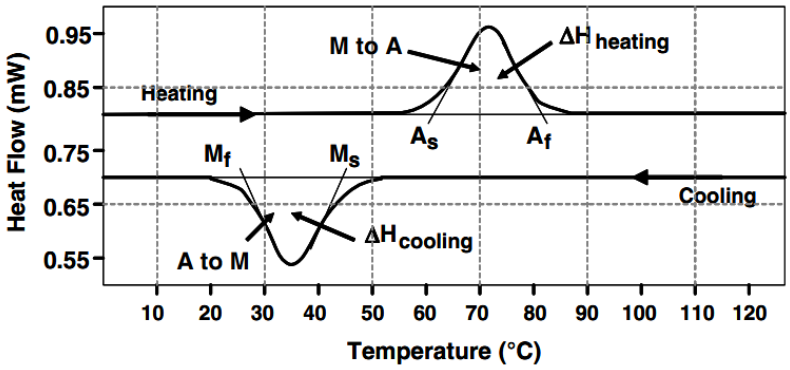

Figure 6-4: A schematic of a differential scanning calorimeter (DSC) curve for an SMA material during heating and cooling. Extracted from (Kumar & Lagoudas, 2008).

Measuring the shape memory alloy's resistivity is also generally used to measure the degree of transformation, *i.e.* the martensitic fraction (Reynaerts & Van Brussel, 1998). This is contrary to the general rule of increased resistance with increased temperature. This drop in resistance is due to the increase in thickness and decrease in length during the martensite to austenite transformation, while roughly maintaining its same volume (Dynalloy. Inc., 2011).

6.2.2 Material Properties of Shape Memory Alloys

To model the behavior of SMAs, three types of material properties are necessary: the thermoelastic properties of austenite and martensite, the critical stress and temperature states associated with the stress-strain diagrams, and the transformation strain properties.

Thermoelastic properties are the properties which apply to most structural materials, and are used to describe a material's normal response to stress, strain, and temperature. These properties include the modulus of elasticity (E), the Poisson's ratio (ν), the yield strength (σ^y), and the coefficient of thermal expansion (α). As shape memory alloys actuate by transforming from one phase to another, it is necessary to provide properties for both phases. Already mentioned; martensite and austenite are quite distinct from one another, differing in crystal structure and mechanical properties. Martensite is highly deformable while austenite is quite stiff, martensite has a rhombus atomic structure while austenite has a cubic atomic structure, and martensite first deforms through "detwinning" followed by elastic-plastic deformation while austenite only deforms through elastic-plastic deformation. Table 6-1 below highlights several mechanical properties of martensite, austenite, and stainless steel. Between martensite and austenite, it is apparent that austenite is the stronger material having a larger ultimate tensile strength, tensile yield strength, and modulus of elasticity. The mechanical properties are quite comparable with stainless steel. However, martensite can elongate several times longer than austenite before succumbing to failure. These properties need to be factored in when modeling shape memory alloys.

Table 6-1: Mechanical Properties of Martensite Nitinol, Austenite Nitinol, Stainless Steel, and Titanium. Data Extracted from (Ryhänen, 2000)

	Martensite	Austenite	Stainless Steel	Titanium
Ultimate Tensile Strength (MPa)	103-1100	800-1500	483-1850	540-740
Tensile Yield Strength (MPa)	50-300	100-800	190-1213	390
Modulus of Elasticity (GPa)	21-69	70-110	190-200	105-110
Elongation at failure (%)	Up to 60	1-20	12-40	16

When utilizing symbols to represent an SMA`s thermoelastic properties, it is common practice to use superscripts to indicate each property's respective phase. A symbol with an 'A' superscript is used to represent a thermoelastic property of an SMA's austenite phase, while an 'M' superscript is used to represent the thermoelastic property of an SMA's martensite phase. The moduli of elasticity, E^A and E^M, are found by performing a stress-strain curve at a constant temperature above A_f like the one shown on the left portion of Figure 6-5. The stress-strain curve starts with an SMA in its austenitic phase. After a certain amount of stress has been applied, the alloy begins transforming into stress-induced martensite: a phenomenon known as superelasticity. Superelasticity in SMAs will be further explained and examined in Chapter 7. The stress-strain curve is performed by loading the material to 6-8% strain and then allowing the material to return to 0% strain. When loading the material, the stress-strain relationship will initially have a linear relationship, followed by a section of constant stress, and ending with a polynomial stress-strain relationship when the material has been fully deformed into martensite and begins to plastically deform. The initial linear stress-strain relationship during loading is the austenitic elastic modulus, E^A. When unloading the material after 6-8% strain, the stress-strain relationship will start out linear, then become polynomial when approaching a separate area of constant stress, and end with another polynomial relationship. The linear relationship at the beginning of the unloading curve represents the martensitic

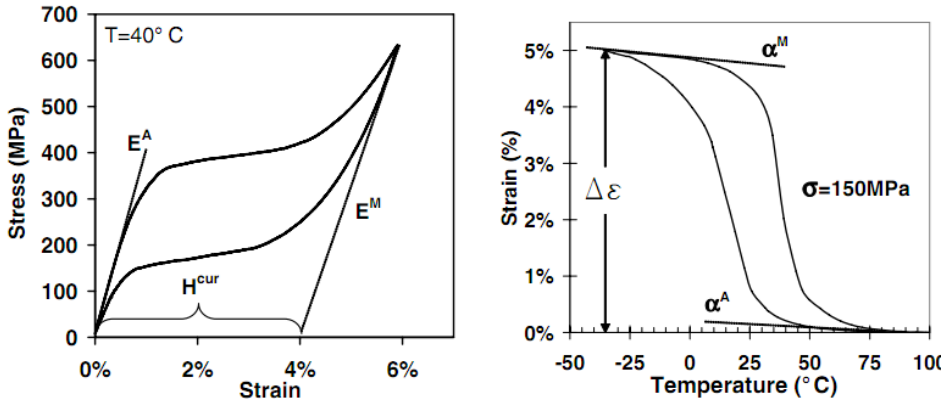

Figure 6-5: Examples of an SMA's stress-strain curve at a constant temperature above A_f (Left) and an SMA's strain-temperature curve at constant stress (Right). The left image showcases an SMA`s superelastic effect, while the right image showcases an SMA`s shape memory effect. Image extracted from (Kumar & Lagoudas, 2008)

elastic modulus, E^M. Although there appears to be two possible martensitic slopes in Figure 6-5 (the end of the loading scenario and beginning of the unloading scenario), the slope during the loading scenario is influenced by very minor continuing transformation in some parts of the specimen (Kumar & Lagoudas, 2008). The slope during unloading is therefore more representative of the truly elastic response of the SMA's martensite phase.

The coefficients of thermal expansion are found by performing a strain-temperature relationship test at constant stress. An example of a typical strain-temperature curve is shown on the right side of Figure 6-5. Starting at a temperature well above A_s, the specimen is cooled until it reaches a temperature well below M_f, and is then heated back to the starting temperature. Like most metals, the coefficient of thermal expansion is constant at pure martensite or pure austenite. The initial linear strain-temperature relationship during cooling represents the austenitic coefficient of thermal expansion, α^A, while the initial linear strain-temperature relationship during heating represents the martensitic coefficient of thermal expansion, α^M. The Poisson's ratios are found by making cross-section measurements during superelastic loading and unloading, but if the analysis and testing are for a one-dimensional case (such as a wire), the Poisson's ratios are generally not needed.

The critical stress and temperature states are parameters that help determine when a transformation will begin or end depending on the SMA's temperature and induced stress. When the SMA is under no stress loading, the transformation temperatures are M_s, M_f, A_s, and A_f as previously discusses; however, if stress is applied, these transition temperatures will increase. Likewise, at a constant temperature, a certain amount of stress is needed to induce martensitic transformation via superelasticity, but an increase in environmental temperature will increase the stress needed to produce stress-induced martensite. The relationships between these stresses and strains are generally linear and represented as stress influence coefficients, C_M and C_A. These critical stress and temperature states will be further discussed in Chapter 7.

The transformation strain properties represent the strain change during the phase transformation. It is a measure of the recoverable strain due to the transformation at a given stress level. The maximum transformation strain occurs when an SMA is cooled to its twinned martensite phase and stressed to completely transform it into its detwinned martensite phase. If stressed below this level, the recoverable strain will be a fraction of the maximum transformation strain; if stressed above or at this level, the recoverable transformation strain will still be the maximum transformation strain. The maximum recoverable strain, ε_L, is therefore represented by Equation 6-1:

$$\varepsilon_L = H^{cur}(\sigma)\big|_{\sigma \geq \sigma_{align}} \qquad 6\text{-}1$$

Where $H^{cur}(\sigma)$ is the maximum transformation strain at a specific stress level (hence H^{cur} is a function of stress) and is measured by adding a tangent line to the martensitic modulus of elasticity during a stress-strain test, and finding the resultant x-intercept (*i.e.* H^{cur} on Figure 6-5). σ_{align} denotes the minimum stress needed to completely deform the SMA into detwinned martensite. For sufficiently trained materials (*i.e.* materials that exhibit two-way memory), the value of σ_{align} may approach 0. H^{cur} is also dependent on the type of applied stress; for tensile stress, $H^{cur}(\sigma)$ is positive; for compressive stress, $H^{cur}(\sigma)$ is negative.

Table 6-2: Various material properties for four different shape memory alloys. Extracted from (Hartl & Lagoudas, 2008)

Property	NiTi	NiTiCu	NiTiPd	CuAlNi
$\mathbf{E^A}$	70 GPa	50 GPa	15 GPa	90 GPa
$\mathbf{E^M}$	30 GPa	25 GPa	25 GPa	80 GPa
$\boldsymbol{\nu}$	0.3	0.3	0.3	0.3
$\boldsymbol{\alpha}$	10 x 10^{-6}/°C	10 x 10^{-6}/°C	10 x 10^{-6}/°C	15 x 10^{-6}/°C
$\mathbf{C_A}$	7 MPa/°C	10 MPa/°C	5 MPa/°C	-
$\mathbf{C_M}$	7 MPa/°C	10 MPa/°C	5 MPa/°C	-
$\mathbf{H^{Max}}$	6 %	5 %	3 %	4 %
P	6500 kg/m^3	6500 kg/m^3	8200 kg/m^3	7500 kg/m^3
$\boldsymbol{\sigma^y}$	700 MPa	600 MPa	400 MPa	300 MPa

Table 6-2 shows some typical values of SMA material properties. Note that there is only one value for the Poisson's ratio and coefficient of thermal expansion. This is because it

is generally assumed that both the austenite and martensite phases have the same Poisson's ratios and coefficients of thermal expansion. It should also be pointed out that the stress influence coefficients for the martensite and austenite phases are the same. Although the stress influence coefficients are generally similar in value, it is generally not assumed that they are equal.

6.2.3 Constitutive and Consistency Modeling

Like the material properties, the constitutive model for shape memory alloys depends on three variables. These variables are the fraction of martensite (ξ), strain (ε), and temperature (T). The basic governing equation using all three variables is presented below in Equation 6-2.

$$\dot{\bar{\sigma}} = \frac{\partial \bar{\sigma}}{\partial \bar{\varepsilon}}\dot{\varepsilon} + \frac{\partial \bar{\sigma}}{\partial T}\dot{T} + \frac{\partial \bar{\sigma}}{\partial \xi}\dot{\xi} \qquad 6\text{-}2$$

Using tensors to represent the partial derivatives, Equation 6-2 can be written as Equation 6-3 (Liang & Rogers, 1990).

$$\dot{\bar{\sigma}} = D\dot{\bar{\varepsilon}} + \Theta\dot{T} + \Omega\dot{\xi} \qquad 6\text{-}3$$

Performing the integration with respect to time, the following equation is derived in relation to the initial values in a one-dimensional model:

$$\bar{\sigma} - \overline{\sigma_0} = D(\bar{\varepsilon} - \overline{\varepsilon_0}) + \Theta(T - T_0) + \Omega(\xi - \xi_0) \qquad 6\text{-}4$$

Looking at Equations 6-3 and 6-4, the constitutive model has three tensors: the stiffness tensor (D), the thermoelastic tensor (θ), and the transformation tensor (Ω). The stiffness tensor is derived from traditional mechanics using the associated moduli of elasticity and Poisson's ratios and the thermoelastic tensor is derived from traditional equations of thermoelasticity using the associated coefficients of thermal expansion. The transformation tensor, however, is unique to shape memory alloys. It accounts for the SMA's phase transformation and how it affects the stress experienced by the SMA. If the change in martensitic fraction is high, the transformation will play a large role in the overall stress analysis of the system. Assuming that both the transformation strain (ε^t)

and modulus of elasticity have linear relationships with the martensitic volume fraction in a one-dimensional model:

$$D = E^A + \xi(E^M - E^A) \quad 6\text{-}5$$

$$\varepsilon^t = \xi H^{cur}(\sigma) \quad 6\text{-}6$$

The transformation tensor can be presented as Equation 6-7 (Liang & Rogers, 1997):

$$\Omega = -DH^{cur}(\sigma) \quad 6\text{-}7$$

Assuming a linear relationship between the coefficient of thermal expansion and the martensite volume fraction in a one-dimensional model, the thermoelastic tensor can be presented as Equation 6-8:

$$\Theta = -D[\alpha^A + \xi(\alpha^M - \alpha^A)] \quad 6\text{-}8$$

Assuming the initial stress, strain, and martensitic fractions to be 0, Equations 6-5 to 6-8 can be substituted into Equation 6-4 to get Equation 6-9:

$$\sigma = [E^A + \xi(E^M - E^A)]\{\varepsilon - \xi H^{cur}(\sigma) - [\alpha^A + \xi(\alpha^M - \alpha^A)](T - T_0)\} \quad 6\text{-}9$$

Note that ε represents the total strain on the material, not just the strain solely induced by the stiffness tensor. Assuming that $\alpha^A \cong \alpha^M$, Equation 6-9 can be simplified to Equation 6-10:

$$\sigma = [E^A + \xi(E^M - E^A)][\varepsilon - \xi H^{cur}(\sigma) - \alpha(T - T_0)] \quad 6\text{-}10$$

The overall consistency condition for a shape memory alloy contains the stress rate, the temperature rate, and the martensite fraction rate; all with respect to time. The consistency condition is presented below as equation 6-11 and must be obeyed for any shape memory alloy model (Lagoudas, Khan, & Mayes, 2001).

$$\dot{\phi} = \frac{\partial \phi}{\partial \sigma}\dot{\sigma} + \frac{\partial \phi}{\partial T}\dot{T} + \frac{\partial \phi}{\partial \xi}\dot{\xi} = 0 \quad 6\text{-}11$$

6.2.4 One Way and Two Way Memory

SMAs can be programmed to either have one way or two way memory. In one way memory, the SMA has one programmed shape which is above the A_f temperature. When cooled below M_f, the alloy remains in its programmed shape. To deform it, a force or moment must be applied to the alloy. When reheated, the alloy returns to its austenite form and regains its programmed shape. This process is illustrated in a temperature-force-length diagram in Figure 6-6. With two way memory, the alloy has two programmed shapes: one above A_f and one below M_f. Essentially, it has a predetermined shape in its austenite phase and a separate one it its martensite phase. The advantage of two way memory is that a force is not needed to deform the martensite phase into a certain shape, it is programmed to deform on its own. The temperature-force-length diagram of a two way memory alloy is presented in Figure 6-7. The force axis of a two way memory alloy is non-existent thus making the third dimensional graph two dimensional.

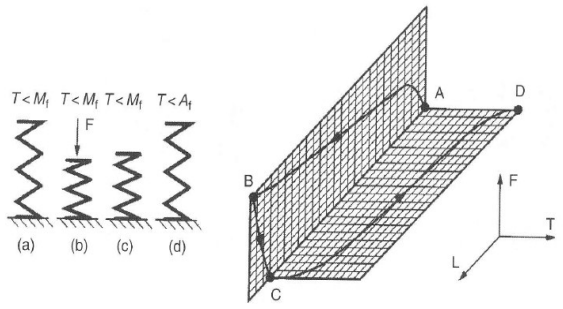

Figure 6-6: A Temperature-Force-Length Diagram of an SMA spring going through the one-way memory effect. Extracted from (Van Humbeeck, 2009)

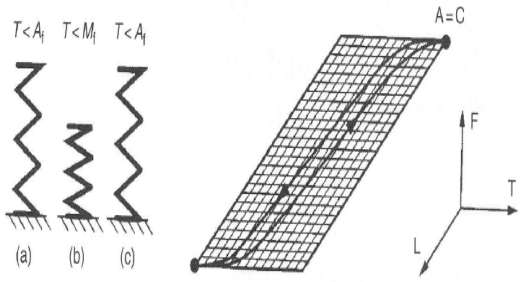

Figure 6-7: A Temperature-Force-Length Diagram of an SMA spring going through the two-way memory effect. Extracted from (Van Humbeeck, 2009)

To program the austenitic shape of an SMA, the alloy must be heat treated while constrained to its wanted shape. This is usually done in the final annealing step during fabrication (See Section 6.2.9). If an SMA has already gone through the final annealing step, one can still reprogram it using heat treatment techniques, but the alloy's material properties may be affected. The heating temperature and time are very important. Higher temperatures and longer times tend to decrease the SMA's strength, while lower temperatures and shorter times are inadequate to properly set the shape. Longer times

and certain temperatures have also been shown to increase the transition temperatures, a phenomenon known as aging (See Section 6.2.10.2). The heating times and temperatures generally have to be determined experimentally for the requirements of each desired part. Rapid cooling of some kind afterwards is preferred to avoid aging effects; a water quench is generally better than a rapid air cool. Table 6-3 gives shape setting instructions for nitinol from various sources. Using a consensus from these sources, it appears that a shape set temperature of around 500 °C is normally used with a heating time of around 10 minutes. However, it should be reiterated that the most appropriate guidelines for shape setting a specific SMA and design, must be obtained through experimentation.

Table 6-3: Nitinol Shape Set Instructions from Different Sources

Shape Set Instructions	Source
A heat treatment in the 500C range is adequate; the length of heat treatment varies with the equipment used for the heat treatment and the thermal mass of the shaping fixture. In a molten salt bath for example, the heat treatment time is generally between 2 and 5 minutes	(Memry Corporation, 2011)
Use a heating temperature of 500-550°C and bake in the oven for 1 minute	(Koga, 2009)
In general, temperatures as low as 400C and times as short as 1-2 minutes can set the shape, but generally one uses a temperature closer to 500C and times over 5 minutes	(Johnson Matthey Medical Components, 2011)
Place the part in a 550°C oven for approximately 15 minute Quench the part in a cold water bath.	(Voss, 2008)
The temperature should be in the range of 500-550°C with higher temperatures resulting in lower tensile strengths. Cooling should be rapid to avoid aging effects, a water quench is recommended	(Herring, 2010)
The shape setting is conventionally performed by exposing the NiTi elements fixed in various fixtures to high temperatures ~500C for several minutes	(Pilch, 2010)
Heat treat the part at 500C and water quench or fast cool it	(Donohue, 2009)

For two-way memory, the martensitic shape can be programmed using two methods: Shape Memory Effect (SME) training or Stress Induced Martensite (SIM) training (Ryhänen, 2000). In SME training, the alloy is cooled below M_f, bent to its desired shape, and heated above A_f. This process is repeated 20-30 times to condition the alloy

to perform this feature independently. In SIM training, the alloy is bent to its desired shape at a temperature just above M_s, cooled below M_f, and heated above A_f. Similar to SME training, this process is repeated 20-30 times to condition the alloy into performing the cycle independently. The two-way shape memory effect is a result of defects during training. These permanent defects create a residual internal stress state, thereby facilitating the formation of preferred martensitic variants when the SMA is cooled in the absence of external loads. In regards to two-way memory once programmed into an SMA, one must be careful not to heat the alloy beyond a certain point afterwards. Otherwise, the SMA may lose its ability to remember the martensitic programmed shape, a phenomenon appropriately known as amnesia.

6.2.5 Bias Force

As stated in the previous section, a force or moment must be applied to return a one-way SMA actuator back to its original position. When cooled below its M_f, the shape memory alloy changes from austenite to twinned martensite, but does not return to its starting position on its own. A force or moment is needed to de-twin the martensite phase and deform the SMA to its original position. This force or moment is generally known as a bias force. As outlined by Liang and Rogers (1997), there are generally three methods used to bias an SMA actuator. The first method uses a bias mass. Using a straight SMA wire attached to a bias mass as an example (See Figure 6-8a), when the SMA is heated, it transforms from detwinned martensite into austenite, consequently reducing its length, pulling the bias mass in the process. Once deactivated and cooled, the SMA would transform from austenite to twinned martensite, allowing the bias mass to de-twin the SMA's martensite structure, and bring the system back to its original position. For the example shown in Figure 6-8a, the stress can be substituted with W/A_{CS} in Equation 6-10 where W is the gravitational force of the object and A_{CS} is the cross-sectional area of the SMA wire:

$$\frac{W}{A_{CS}} = [E^A + \xi(E^M - E^A)][\varepsilon - \xi H^{cur}(\sigma) - \alpha(T - T_0)] \qquad 6\text{-}12$$

The second method uses a bias spring. Again using an SMA wire as an example (see Figure 6-8b); when activated, the SMA wire would shorten, displacing both an object (with a gravitational force of W) and extending the spring; when deactivated, both the weight of the object and the spring force will extend the SMA wire back to its original length. Typically a spring is used when the weight of the object is not sufficient to bring itself back to its original position. For the example shown in Figure 6-8b, the stress in Equation 6-10 can be substituted with $\left[{W}/{A_{CS}} + {kL\varepsilon}/{A_{CS}}\right]$, resulting in Equation 6-13 where k is the bias spring's stiffness and L is the original length of the bias spring. In Equation 6-13, it is assumed that at the actuator's original position, the weight is being completely supported by the SMA wire and the bias spring is at equilibrium.

$$\frac{W}{A_{CS}} + \frac{kL\varepsilon}{A_{CS}} = [E^A + \xi(E^M - E^A)][\varepsilon - \xi H^{cur}(\sigma) - \alpha(T - T_0)] \qquad 6\text{-}13$$

The third method uses two SMA actuators: one to move an object in one direction and the other to return the object to its original position. This type of SMA actuator is known as a differential SMA actuator. Figure 6-8c shows a differential SMA actuator using two SMA wires to raise and lower an object. The upper SMA wire raises the object when activated while the lower SMA wire is inactive; to lower the object, the upper SMA wire is deactivated, followed by activating the lower SMA wire. For the example shown in Figure 6-8c, Equation 6-10 can be rewritten as Equation 6-14 with the 1 and 2 subscripts denoting material properties belonging to the upper and lower SMA wires, respectively. Equation 6-14 assumes that the upper wire completely supports the weight of the object, W.

$$\frac{W}{A_{CS1}} + \left[{E_1}^A + \xi_1\left({E_1}^M - {E_1}^A\right)\right]\left[\varepsilon_1 - \xi_1 {H^{cur}}_1(\sigma) - \alpha_1(T_1 - T_{0_1})\right] = \left[{E_2}^A + \xi_2\left({E_2}^M - {E_2}^A\right)\right]\left[\varepsilon_2 - \xi_2 {H^{cur}}_2(\sigma) - \alpha_2(T_2 - T_{0_2})\right] \qquad 6\text{-}14$$

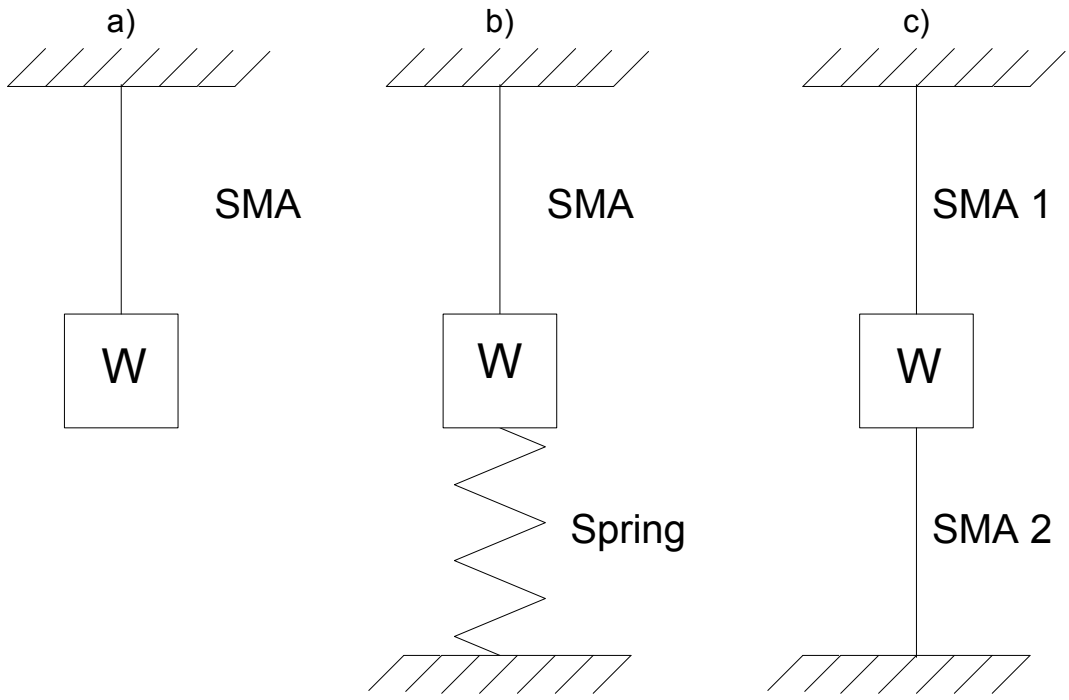

Figure 6-8: The three most used ways of biasing a one-way SMA: a) Using a Bias Mass, b) Using a Bias Spring, c) Using two SMA actuators, also known as a differential SMA force actuator

6.2.6 Cyclic Behavior

For SMA actuators meant to last for several cycles, it is important to first train the actuator so that its behavior becomes consistent. Training an SMA refers to a process of repeatedly loading the material following a cyclic thermomechanical loading path until the hysteretic response of the material stabilizes and the inelastic strain saturates (Kumar & Lagoudas, 2008). In other words, the strain-temperature relationship stabilizes and becomes consistent only after the actuator has been through a few cycles. SMA specimens that have been cycled multiple times, while under significant loading to cause plastic strain, will often exhibit less transformation strain than was shown before these cycles were applied (Hartl & Lagoudas, 2008). Extracted from Miller & Lagoudas (2000), Figure 6-9 shows the strain/temperature relationship of a NiTi shape memory alloy going through heating/cooling cycles at a constant load of 150 MPa. The alloy went through a total of 50 transformation cycles. The alloy went through a 0% to ~7.2% change in strain when first cooled from austenite to martensite, but when heated back to austenite the alloy returned to ~0.6%, indicating that some plastic deformation has

occurred. On the second cycle, the alloy went from ~0.6% to ~7.7% during cooling and from ~7.7% to ~1.2% during heating. These strains continued to rise after each cycle, but at smaller and smaller intervals until they converged to a set value at around 8.6% at the martensite phase and 2.6% at the austenite phase. Overall, the cycle put a 2.6% permanent strain on the austenite phase, but only a 1.4% permanent strain on the martensite phase, reducing the overall change in strain from 7.2% at the first cycle to a converged value of roughly 6% under cyclic loading. Essentially, the material is the strongest during the first loading cycle. Cyclic loading not only causes a permanent strain increase on the alloy, put also reduces the change in strain during the transformation. It is also common for the transformation temperatures to broaden (*i.e.* the difference between M_s and M_f, as well as A_s and A_f, increase). However, as the transformation strain values (and transformation temperatures) converge to a set value, SMA actuators can show consistency in their displacements, but only after the actuator has been under cyclic loading.

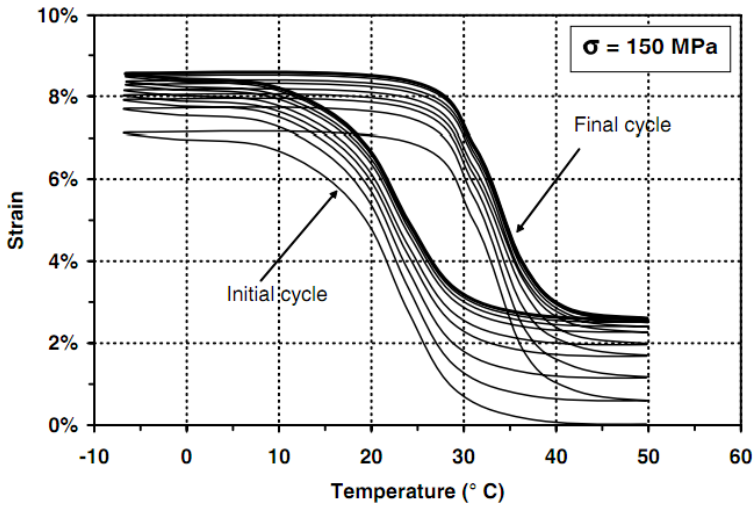

Figure 6-9: The thermal cyclic loading (50 cycles) of a NiTi shape memory alloy wire under a constant load of 150 MPa. Image extracted from (Miller & Lagoudas, 2000)

It has become apparent that cyclic loading is necessary for SMA actuators that are to be used multiple times. Studies have shown that in SMA actuators for multiple use, lower transformation strains (and lower loads) are more desirable as they increase fatigue life and decrease plastic strain development (Hartl & Lagoudas, 2008). However, if the

actuator is only to be used once, one can effectively use actuation strains near the first thermal cycle. These strains can be up to 8% for NiTi alloys (Hartl & Lagoudas, 2008).

6.2.7 Fatigue Strength

One of the most documented drawbacks to using shape memory alloys is their fatigue strength. Table 6-4 below highlights some of the various properties of certain shape memory alloys. The table suggests that both a greater shape recovery and thermal hysteresis causes the effective fatigue life to decrease overall. There are shape memory alloys that have excellent fatigue life such as Ni-Ti-Fe alloys, but the shape recovery is rather small. As many uses for shape memory alloys depend on a high shape memory strain, the Ni-Ti-Fe would not be suitable for these applications.

Table 6-4: Properties of Some Shape Memory Alloys. Data from (Culshaw, 1996)

Alloy	Structure of Low-Temp Phase	Thermal Hysteresis (K)	Shape Recovery Strain (%)	Fatigue Life (cycles)
Ni-Ti Ni-Ti-Fe	Rhombohedral	2-3	1	1,000,000
Ni-Ti-Cu	Orthorhombic	10-15	4-5	10,000
Ni-Ti	Monocline	20-40	6-8	<100

Overall, the fatigue behavior of an SMA depends on several conditions including the material processing (the fabrication process, heat treatment, surface finish, etc.), the loading conditions (applied stress, strain, temperature variations, etc.), and transformation induced microstructural modifications (*e.g.* defects on grain boundaries due to strain incompatibilities) (Kumar & Lagoudas, 2008). Providing that the deformation strains are low, the fatigue life can be substantially improved. Generally if the deformation is within 2%, the SMA may operate millions of times without losing its shape memory effect or being damaged due to fatigue (Liang & Rogers, 1997). However, in some cases, the material may be overloaded so that it causes stress-induced martensitic transformation at its supposed austenite phase. In such cases, the material fails considerably earlier in what is termed "transformation-induced low cycle fatigue", with a fatigue life of the order of thousands of cycles (Melton & Mercier, 1979). Fatigue life can also be improved under

conditions of partial transformation, transformations where the phase change does not completely transition from martensite to austenite and vice versa. In other words, the martensite volume fraction, ξ, is between 0 and 1. Kumar and Lagoudas (2008) show that a NiTiCu undergoing partial transformation under a fixed stress level of 200MPa, can improve the fatigue life by a factor of 7, but the amount of stable transformation strain is reduced by a factor of 3.

6.2.8 Material Selection for Actuators

Thus far, the only SMAs that have been discussed have primarily been NiTi based. This is because they have the best properties overall. Table 6-5 showcases several material properties of four different SMAs: NiTi, CuZnAl, CuAlNi, and FeNiCoTi. In comparison with other shape memory materials in Table 6-5, NiTi based alloys have larger transformation strains, larger fatigue life, larger fatigue strength, and excellent corrosion resistance. NiTi alloys also have a very high electrical resistivity, allowing them to be heated via electric current. Being quite biocompatible, NiTi alloys can effectively be placed inside the human body for biomedical applications such as heart stents, braces, or bone staples among other things. However, NiTi alloys can be 5-10 times more expensive and more difficult to machine than copper based alloys (Reynaerts & Van Brussel, 1998). Other disadvantages of NiTi alloys include its large hysteresis width and low transformation temperatures. If cost, machinability, high transformation temperature, or hysteresis are factors in the actuator's design, it may be favourable to choose an SMA other than NiTi.

Table 6-5: Several Material Properties for Four Different Shape Memory Alloys. Extracted from (Hesselback, 2007)

Alloy	NiTi	CuZnAl	CuAlNi	FeNiCoTi	Unit
Range of Transformation Temperature	-100 to +90	-200 to +100	-150 to 200	-150 to +550	°C
Hysteresis Width	30	15	20		K
Max. one-way effect	8	4	6	1	% Strain
Max. two-way effect	4	0.8	1	0.5	% Strain
Fatigue Strength	800…1000	400…700	700…800	600…900	N/mm^2
Admissible Stress for Actuator Cycling	150	75	100	250	N/mm^2
Typical Number of Cycles	>100 000	10 000	5 000	50	
Density	6450	7900	5000	50	kg/m^3
Electrical Resistivity	80…100	7…12	10…14		10^{-8} Ωm
Young's Modulus	50	70…100	80…100	170…190	GPa
Corrosion Resistance	Very good	Fair	Good	Bad	

6.2.9 Fabrication

The fabrication of SMAs is typically performed in three stages: the melting stage, the hot and cold working stage, and the shape setting stage. This section will briefly go through each stage to give the reader an understanding of the fabrication process and why each stage is necessary to produce the end product.

The melting stage is where the raw materials are fused together. This is usually done by vacuum induction melting (VIM) followed by vacuum arc melting (VAR). The VIM method first melts the raw materials together, while the VAR method improves the alloy chemistry, homogeneity, and structure. The VIM/VAR process ensures purity and quality and maintains the mechanical properties of the alloy (Thompson, 2000).

Materials prepared by the VIM/VAR process also tend to have a more uniform distribution of transformation temperatures along the ingot (Memry Corporation, 2011).

The hot and cold working stage is where the product is deformed into its desired shape. The hot working stage is typically performed at temperatures of 600-900°C as they are sufficient to lower the flow stresses to allow relatively large deformation steps (Pelton, Russel, & DiCello, 2003). Depending on the final shape, techniques such as press forging, rotary forging, extrusion, swaging, bar rolling, rod rolling, and sheet rolling may be used in the hot working stage. In addition to dimension reduction, these initial hot-deformation processes are effective in breaking up the as-cast microstructure, which has very little ductility & does not exhibit much shape memory, superelasticity, or resistance to fracture (Pelton, Russel, & DiCello, 2003). The cold working stage provides the final product's shape, surface finish, refined microstructure, and mechanical properties. As nitinol alloys work harden quite rapidly, the material must be fully annealed (at about 600-800°C) after cold working operations (Pelton, Russel, & DiCello, 2003). Generally, a series of cold-working and annealing steps are necessary to bring the material down to its final size. Nitinol wire and tube typically will have 30-40% cold work reduction during the last drawing steps, while sheet and strip products will typically have about 20% cold work reduction (NDC, 2011). The amount of cold work a material had prior to its shape set anneal is strongly correlated with the ultimate strength of the material.

For most applications, the as-drawn material does not exhibit the final desired properties after its cold-working or fully annealed conditions. To optimize its shape memory (or superelastic performance), the material must be partially heat treated after the final cold-working step. This final heat treatment controls the final properties of the SMA, including the shape, ultimate strength, and transition temperatures. After constraining the alloy into its desired set shape (*i.e.* the shape at its austenite phase), the alloy is heat treated in the temperature range of 450-550°C. When heated, the alloy will want to go to its previously set shape, but the constraints prevent it from doing so. The constraints force the alloy to deform to a new set shape. After annealing for a certain amount of time, the alloy will be programmed to deform at this new constrained shape. To shape set

straight wire, a process known as continuous strand annealing is used. As illustrated in Figure 6-10, as drawn-wire (wire that has gone through its final cold-working stage) is held under constant tension via spools and is fed through a furnace at constant speed to provide the wire with uniform properties. The tension sets the constraints to make the alloy's set-shape a straight wire. Straightness, mechanical properties, and the transition temperatures are all affected by the speed and temperature parameters of the continuous strand annealing process.

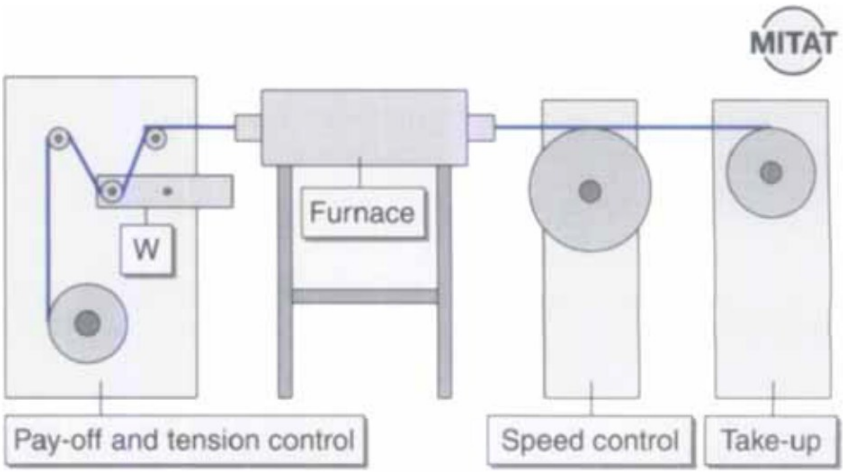

Figure 6-10: Schematic diagram of a continuous strand annealing equipment for optimized production of Nitinol wire. Extracted from (Pelton, DiCello, & Miyazaki, 2000)

6.2.10 Altering the Properties of Shape Memory Alloys

Depending on the particular design, an SMA may require certain properties. A situation may require specific transition temperatures, be strong enough to handle specific loading, or may require a certain amount of transformation strain. As already mentioned, nitinol alloys are the most popular SMA due to their high strength, transformation strain, and fatigue life; but they can also be manipulated to have specific transition temperatures, strengths, and hysteresis among other things. Two of the more popular methods to alter the properties of nitinol are to either add impurities to the alloy, or age the alloy by heating it for extended periods of time at the shape set fabrication stage. This section will go through both methods giving the reader an understanding of their affect on nitinol's mechanical and transformation properties.

6.2.10.1 ALLOY COMPOSITION

Depending on the desired transition temperature, the necessary control of the alloy's composition is between 0.01 and 0.1% (Reynaerts & Van Brussel, 1998). A 1% shift in the amount of either Ni or Ti can result in more than a 100°C change in the alloy's transformation temperatures. Altering the equiatomic composition of nickel and titanium (*i.e.* 50% Ni, 50% Ti) was first studied by Buehler and his colleagues at the Naval Ordnance Laboratory (Buehler, Gilfrich, & Wiley, 1963). They found that the equiatomic composition exhibits the maximum A_f temperature of all equiatomic compositions studied (120°C). They also found that decreasing the nickel atomic percentage below 50% does not change the transformation temperatures, but increasing the nickel atomic percentage above 50% causes a significant decrease in A_f (-40°C at 51% Nickel). In 1965, Buehler and his team started adding tertiary elements such as cobalt or iron, again noticing that the transition temperatures decreased (Wang, Buehler, & Pickart, 1965). Since then, numerous additives to nitinol have been thoroughly studied giving material scientists insight to how they affect nitinol's material properties.

Table 6-6 lists various tertiary elements that have been added to nickel-titanium alloys along with their affect on the alloy's transition temperature, strength, and ductility; the upwards, downwards, and horizontal arrows respectively represent an increase, decrease, and no change in the specific material property. Table 6-7 lists several nitinol alloys with varying nickel, titanium, and impurity atomic percentages along with their respective transition temperatures. Most of the elements listed in Table 6-6 cause a decrease in transformation temperature as they tend to react with titanium to form precipitates, resulting in an enrichment of nickel. Titanium particularly reacts with oxygen, nitrogen, or carbon to form oxides, nitrides, and carbides; it is therefore necessary to select melting methods to minimize their presence (Pelton, Russel, & DiCello, 2003). Chromium, cobalt, and iron substitute for nickel in the B2 lattice, having an additive effect in determining the transformation temperature (Pelton, Russel, & DiCello, 2003). In turn, most of the additives increase the alloy's strength while decreasing the alloy's ductility.

Table 6-6: A Schematic Table Illustrating the Effects of Various Impurities on Nitinol's properties. Extracted from (Pelton, Russel, & DiCello, 2003)

Impurity	O	N	H	C	Cu	Cr	Co	Fe	V	Nb
Transition Temperature	↓	↓	↓	↓	→	↓	↓	↓	↓	→
Strength	↑	↑	↑	↑	↘	↑	↑	↑	↑	↑
Ductility	↓	↓	↓	↓	→	↓	↓	↑	↓	→

Table 6-7: Representative transformation temperatures for SMAs with different compositions and heat treatments. Extracted from (Kumar & Lagoudas, 2008)

NiTi Based SMAs	M_f	M_s	A_s	A_f
$Ti_{50}Ni_{50}$	15	55	80	89
$Ti_{50.0}Ni_{50.0}$	-28	37.5	48.2	77.8
$Ti_{49.5}Ni_{50.5}$	-78	-19	9	53
$Ti_{49.1}Ni_{50.9}$	-115.8	-30.7	1.9	44.6
$Ti_{49}Ni_{51}$	-153	-114	-89	-40
$Ti_{48.5}Ni_{51.5}Cu_{10}$	14.4	37.5	42.6	60.0
$Ti_{49}Ni_{41}Cu_{10}$	8	30	35	50
$Ti_{50}Ni_{40}Cu_{10}$	21	41	53	67
$Ti_{44}Ni_{47}Nb_9$	-175	-90	-85	-35
$Ti_{42.2}Ni_{49.8}Hf_8$	50	69	111	142
$Ti_{40.7}Ni_{49.8}Hf_{9.5}$	61	90	118	159
$Ti_{40.2}Ni_{49.8}Hf_{10}$	103	128	182	198
$Ti_{35.2}Ni_{49.8}Hf_{15}$	95	136	140	210
$Ti_{30.2}Ni_{49.8}Hf_{20}$	127	174	200	276
$Ti_{48}Ni_{47}Zr_5$	20	65	75	138
$Ti_{43}Ni_{47}Zr_{10}$	45	100	113	165
$Ti_{38}Ni_{47}Zr_{15}$	100	175	175	230
$Ti_{33}Ni_{47}Zr_{20}$	205	275	265	330
$Ti_{50}Pd_{50}$	550	563	580	591
$Ti_{50}Ni_{20}Pd_{30}$	208	241	230	241
$Ti_{50}Ni_{10}Pd_{40}$	387	403	419	427
$Ti_{50}Ni_5Pd_{45}$	467	486	503	509
$Ti_{50}Ni_{45}Pt_5$	10	29	36	49
$Ti_{50}Ni_{40}Pt_{10}$	-8	18	-27	36
$Ti_{50}Ni_{30}Pt_{20}$	241	300	263	300
$Ti_{50}Ni_{20}Pt_{30}$	537	619	626	702

Although copper and niobium do not overly affect the alloy's transition temperatures or ductility, they have alternative functions not showcased in Table 6-6. Replacing a portion of nickel, copper is substituted to reduce the hysteresis of the SMA response at the expense of transformation strain. Generally, a 5.0 to 10.0 atomic percentage of copper is preferred as an atomic percentage higher than 10.0% tends to brittle the material (Kumar & Lagoudas, 2008). Alternatively, niobium is substituted to widen the hysteresis to show minimal response at wider temperature changes. This trait allows the

alloys to deform at low temperatures and yet be safely transported at ambient temperatures.

One trait that engineers found unfavourable about nitinol shape memory alloys was their limiting transition temperatures. Research into increasing the transition temperatures above 100°C started as early as 1970 (Donkersloot & Vucht, 1970). Labelled High Temperature Shape Memory Alloys (HTSMAs), adding elements such as palladium, platinum, hafnium, gold or zirconium to nitinol alloys can yield transition temperatures from 100 to 800°C (Lidquist & Wayman, 1990). However HTSMAs are limited in their transformation strains, having a magnitude of about 3% (Lidquist & Wayman, 1990).

6.2.10.2 AGING

Aging is the process in which the alloy is heated during the final treatment for an extended period of time. Aging an SMA increases its transition temperatures at the expense of decreasing the material's strength and actuation force. Higher treatment times and temperatures will increase the actuation temperature and often give a sharper thermal response (Johnson Matthey Medical Components, 2011). As with shape setting, aging temperature and times must be determined experimentally because they depend on the processing history of the material, the heating method, and temperature. It is also advisable to perform a water quench after aging to sharply define the heating time (Herring, 2010).

To visualize the effects of aging on a shape memory alloy, time-temperature transformation diagrams (TTT diagrams) are used to plot the changes in transition temperatures. Plotted by Pelton, DiCello, & Miyazaki (2000), Figure 6-11 shows a TTT diagram of $Ni_{50.8}Ti_{49.2}$ nitinol that initially had an A_f temperature of 11°C. Each line on the TTT graph represents a constant A_f temperature of an SMA alloy, representing the heating temperatures and times needed to produce said A_f temperature. The plot shows that a specific A_f temperature can be achieved by heating an SMA at any temperature between 300 and 600 °C by using different heating times. For example, if one wants to

increase the transition temperature to 20 °C, one can heat the alloy at 300 °C for about 100 minutes, at 450°C for about 1 minute, or at 510 °C for about 10 minutes. Likewise, different temperatures can produce the same A_f using the same heating time. If one wants to age the alloy to have an A_f of 20°C with a heating time of 10 minutes, one could heat it at either 330 or 510 °C. Looking at the TTT-diagram, it is apparent that the A_f temperature can be increased in less time at a temperature around 450 °C, but would take the longer at a temperature at around 525 °C. Another heating temperature one could use to increase the A_f temperature in a short amount of time is at around 575 °C. Although it would take 20-30 minutes for the A_f temperature to increase to 20 °C at a heating temperature of 575 °C as opposed to a time of 1 minute at a temperature of 450 °C; if one wanted to increase the A_f temperature to 40 °C, it would take less time using a heating temperature 575 °C in comparison to 450 °C. These patterns can be explained by looking at the precipitates that are formed during the ageing process.

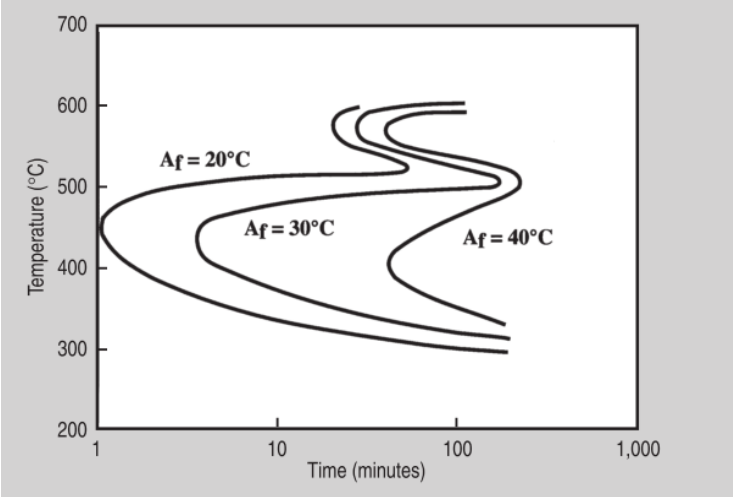

Figure 6-11: A time-temperature transformation diagram for Ti-50.8% Nitinol. Extracted from (Pelton, Russel, & DiCello, 2003)

At high temperatures, there is sufficient thermal energy to permit rapid diffusion of Ni and Ti atoms in the matrix, but it becomes more difficult for the atoms to form a precipitate as the temperature increases. However, at lower temperatures, higher precipitation rates will occur, but the rapid diffusion rates will be lower. These two processes are balanced at intermediate temperatures (*i.e.* around 450 °C) to achieve maximum precipitation rates. The precipitation that forms at this temperature is $Ni_{14}Ti_{11}$ (Pelton, DiCello, & Miyazaki, 2000). With these precipitates, the material becomes more

titanium enriched resulting in an increased A_f temperature. At higher temperatures (*i.e.* around 575°C), a similar phenomenon occurs, except the precipitate that forms is Ni_3Ti_2: a precipitate that requires an even greater amount of nickel than $Ni_{14}Ti_{11}$ (Pelton, DiCello, & Miyazaki, 2000). As a result, the A_f temperature will again increase at this higher heating temperature, but at a different rate in comparison to the intermediate temperature.

The aging temperature and time also have a profound impact on the material's strength. On the same nitinol grade, Pelton, DiCello, & Miyazaki (2000) found the ultimate tensile strength (UTS) using different ageing temperatures and times. Figure 6-12 shows a plot of the results. At lower to intermediate temperatures (300-450 °C), there was an increase in UTS with respect to time. Correlating with the precipitation of $Ni_{14}Ti_{11}$, it appears that this precipitate strengthens the material. However, higher temperatures (500-600 °C) showed a decrease in UTS with respect to time. Correlating with the precipitation of Ni_3Ti_2, it appears that this precipitate weakens the material.

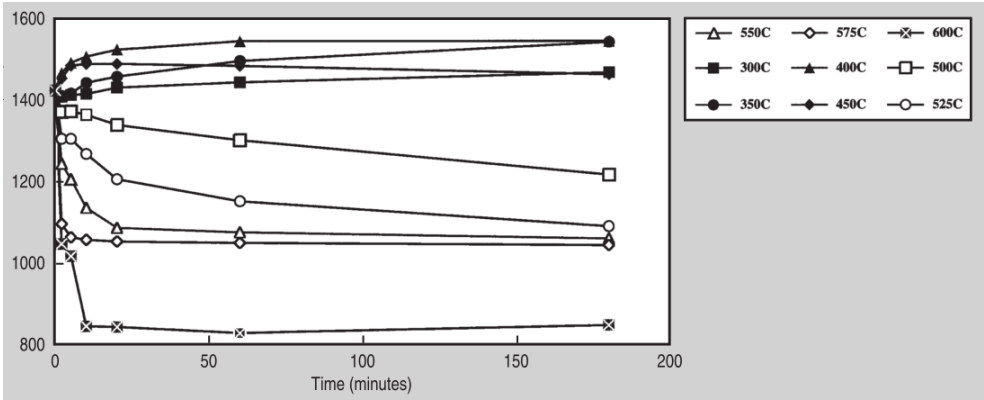

Figure 6-12: The effect of aging time and temperature on the ultimate tensile strength for $Ni_{50.8}Ti_{49.2}$ Nitinol. Aging temperatures between 350 and 450°C tend to increase the tensile strength due to precipitation hardening. Between 500 and 600°C, annealing effects dominate with a dramatic decrease in the strength. Image extracted from (Pelton, Russel, & DiCello, 2003)

Liu et al, 2008 performed a similar study using Ti-50.7 at% Ni nitinol with the aim of optimizing the thermal treatment parameters for fixing nitinol stent wires and achieving proper non-linear mechanical properties for medical applications at body temperature (Liu, Wang, Yang, & Qi, 2008). It was desired to find annealing properties that provided excellent shape-setting with only minor sacrifices to the material's properties. Like

Pelton et al, they found similar results with respect to the transition temperature and UTS. However, they added shape-setting a stent to their scope. Testing at annealing temperatures from 300 to 550 °C at times as long as 3 hours, the results show that the shape-setting results were stable when the wires were heat treated at 500 or 550 °C at times longer than 10 minutes. Overall, they recommended using 500 °C as it provided excellent shape-setting and had the least affect on the A_f temperature.

6.2.11 Transformation Shapes

As mentioned, an SMA can be programmed to be any shape imaginable, but some shapes are more useful than others to perform mechanical work. Some popular shapes for mechanical work include wires, bars, torsion springs, and helical springs. These shapes along with their respective maximum outputs are presented in Table 6-8. SMAs in wire form are the most popular as they are readily available, low cost, and relatively simple to shape set. SMA wires provide excellent recovery force, but not a lot of stroke. Dynalloy, Inc.'s Flexinol® wire will produce a recovery strain of about 4% when stressed to about 70 MPa using a dead weight bias. Flexinol® wires with diameters of 0.008" and 0.010" would therefore be able to lift about 230 g and 360 g, respectively with this recovery strain. The limited stroke can be improved by using mechanical amplification mechanisms such as levers or adjusting curvature as was done in Phillip Beezley's Hylozoic Ground (Beesley, Hylozoic Ground, 2010), but the mechanisms can end up requiring a lot of space and there is significant sacrifice in recovery force. For example, if the wire was to lift the shorter arm of a 5:1 lever, the stroke would be increased by 400%, but the recovery force would decrease to 20%. Even with these amplification mechanisms, at a recovery strain of 4%, a great length of wire is needed to provide adequate stroke magnitudes. Adequate space must therefore be provided for both the length of wire and amplification mechanisms.

One option to increase the stroke is to use helical springs. These springs can be made using straight wire with heat treatment techniques and do not require any amplification mechanisms. However, the downside to helical geometry is a decrease in the output force and a further worsening of the dynamic response and of the energy efficiency. This

is mainly due to the power exploitation, under torsional loading, of the material in the center of the solid section, which adds to the cooling time and to the power consumption without contributing to the strength (Spinella & Dragoni, 2009). To improve the energy efficiency, dynamic response, and cooling times, Spinella & Dragoni (2009) proposed using helical tube springs. They theoretically showed that by emptying the inefficient material from its center, the hollow section features a lower mass, lower cooling time, and lower heating energy than its solid counterpart for a given strength, stiffness, and deflection. However, it is quite difficult and expensive to machine these helical tubes. Spaggiari & Dragoni (2011) proposed making wave springs, whose advantages include a high electrical resistance and lower cooling times, the latter due to the high area to volume ratio. However, like the helical tube springs, the wave springs would be expensive and difficult to manufacture.

Table 6-8: The Outputs of 5 different SMA actuator Shapes. Extracted from (Hesselback, 2007)

Actuator Shape	Max. Force/Torque	Max. Stroke/Angle	Variables
Tension wire or bar, compression bar (round cross section)	$F_{Max} = \frac{\pi}{4} D^2 \sigma_{adm}$	$\Delta L_{Max} = \varepsilon_{adm} L$	F_{max} = Max. Force M_{max} = Max. Torque ΔL_{Max} = Max. Stroke $\Delta\phi_{Max}$ = Max. Angle σ_{adm} = Admissible Tensile Stress τ_{adm} = Admissible Shear Stress ε_{adm} = Admissible Strain γ_{adm} = Admissible Shear Strain D = Wire Diameter L = Wire Length D_m = Coil Diameter i_f = number of turns b, h = width & thickness of flat wires or bars
Tension wire or bar, compression bar (rectangular cross-section)	$F_{Max} = bh\sigma_{adm}$	$\Delta L_{Max} = \varepsilon_{adm} L$	
Torsion wire or bar (round cross section)	$M_{Max} = \frac{\pi}{16} D^3 \tau_{adm}$	$\Delta\phi_{Max} = \frac{2L}{D}\gamma_{adm}$	
Torsion Helical Spring	$M_{Max} = \frac{1}{6} bh^2 \sigma_{adm}$	$\Delta\phi_{Max} = 2\pi i_f \frac{D_m}{h} \varepsilon_{adm}$	
Coil Spring (Tension or Compression)	$F_{max} = \frac{\pi D^3}{8kD_m}\tau_{adm}$ $k = \frac{2D_m + D}{2D_m - D}$	$\Delta L_{max} = \pi i_f \frac{D_m^2}{D}\gamma_{adm}$	

Despite their drawbacks, SMA helical springs have been shown to be reliable mechanical actuators, providing that the load is not substantial. A helical spring's outputs: its recovery force, stroke, and reaction times, are all based on several factors including the spring diameter, wire diameter, number of turns, load, the transition temperatures and heating method. This study aims to experimentally show how these SMA helical spring properties affect the actuator's stroke and reaction times. The recovery force is outside the scope of these experiments.

6.2.12 Heat Treatments for Shape Programming Helical Springs

Taking cues from the kinetic dresses made by Berzowska's XS Lab, the author knew that helical SMA spring actuators could be programmed from straight SMA wire by wrapping the wire around a rod, constraining it, and heat treating it. Using the literature review presented in the previous subsections, the heat treat times and temperatures were estimated at 10 minutes and 500 °C, respectively. In literature, a 500 °C heat treat temperature at a 10 minute heat treat time has shown to adequately shape set the alloy without significantly changing the material's transition temperature and strength properties. However, it should be noted that these parameters are not completely agreed upon in the literature. By testing SMA spring performance at different annealing temperatures, Kim et al (2009) noticed two trends. Firstly, they noticed that the detwinning force decreases as the annealing temperature increases; second, springs annealed below 400 °C showed reasonable consistency on multiple trials, while springs annealed higher than 400 °C show more permanent deformation after multiple trials. Higher annealing temperatures also showed to increase the transition temperature. Figure 6-13 shows how the permanent deformation and transition currents varied in relation to the annealing temperature. From their research, it appears that lower transformation temperatures could in fact make the helical springs more reliable, but their article failed to mention the heating times. Judging from the significant changes in transition current, it is likely that the springs were in the oven for a significant amount of time. Nonetheless, the research by Kim et al (2009) demonstrates that to positively know what heating times and temperatures to use, one must determine them through

experimentation. However, experimenting with the annealing temperature is outside the scope of this thesis.

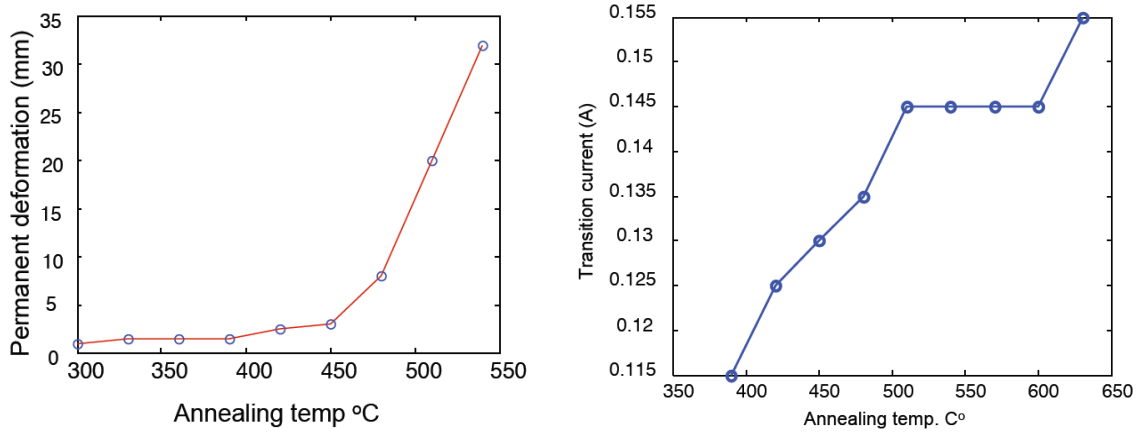

Figure 6-13: Helical SMA spring experiments performed by Kim et al (2009) showed an increased permanent deformation (Left) and aging (Right) at higher annealing temperatures. Images extracted from (Kim, Hawkes, Cho, Jolda, Foley, & Wood, 2009)

To constrain the wire to a rod, the author first constrained one end of a piece of straight Flexinol® wire to a rod using a C-clamp (See Figure 6-20), wrapped the wire around the rod, and then clamped the other end of the wire to the rod with an additional C-clamp. All the helical SMA springs were made using this method.

After already performing these experiments, the author found out about a new and more effective method to program helical SMA springs. Jee *et al.* (2008) first proposed and experimented with inverting the nitinol spring to greatly improve the stroke and recovery. They hypothesized that creating an initial tension on a spring would greatly improve the performance of the spring. Traditionally the method of creating an initial tension on a spring requires twisting the wire while winding. As the shape-setting heat treatment relaxes the initial tension, this twisting method would be ineffective. Alternatively, they proposed to give the spring an initial tension by inverting the coil orientation after the heat treatment. The results showed a perfect recovery with a greater amount of force (See Figure 6-14).

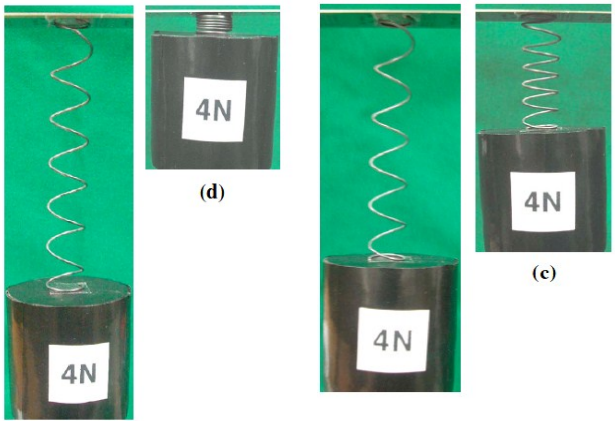

Figure 6-14: (Left) A Nitinol spring with inversion. (Right) A Nitinol spring without inversion. The inverted nitinol spring showed perfect recovery. Image extracted from (Jee, Han, Kim, Lee, & Jang, 2008)

One thing Jee *et al.* left out of their journal article was the method of inversion. Having read the article, Kim *et al.* (2009) experimented with two different inversion techniques. The first method (illustrated in Figure 6-15), the wrapping method, involves unwrapping the nitinol spring after heat treating followed by rewrapping the spring around the rod in the inverted direction. The second method (illustrated in Figure 6-16), the central tube method, involves heat treating the spring along a tube with a straight extension of the spring lying within the tube. After heat treating, the user would pull the extension through the tube, inverting the spring in the process. Kim *et al.* found that both methods not only improved the recovery (See Figure 6-17), but the reaction times as well. Overall, they preferred the central tube method; they did not find too much difference in

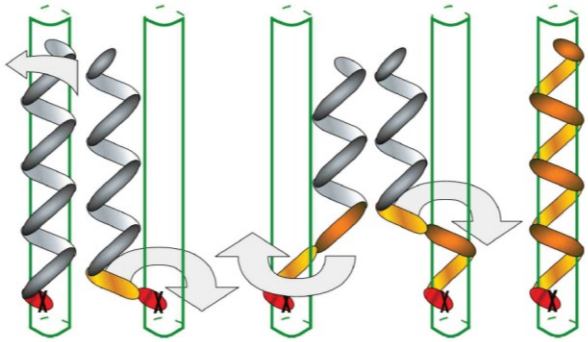

Figure 6-15: The wrapping inversion method. Image extracted from (Kim, Hawkes, Cho, Jolda, Foley, & Wood, 2009)

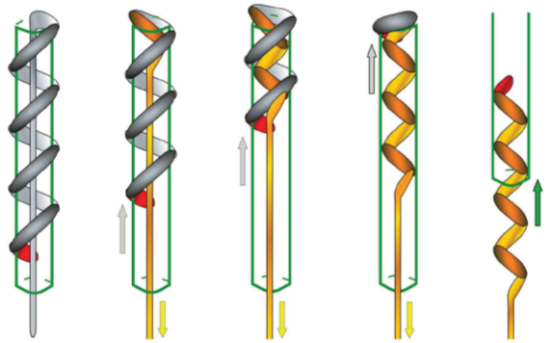

Figure 6-16: The central tube inversion method. Image extracted from (Kim, Hawkes, Cho, Jolda, Foley, & Wood, 2009)

performance between the two methods, but the central tube method is easier and faster to implement. Although inverting the spring was not explored in this thesis, it should be considered for future research in this area.

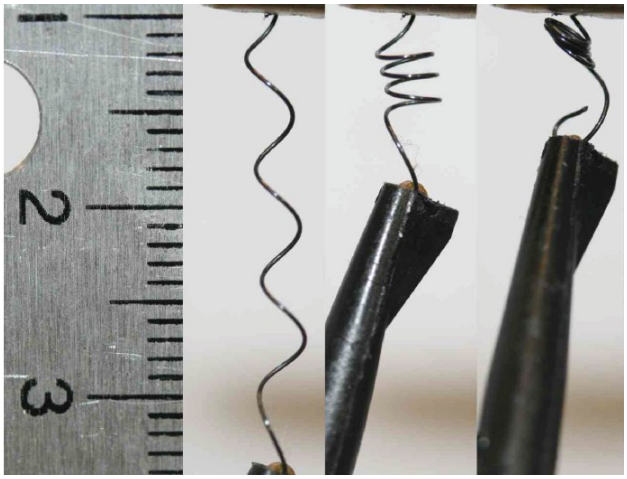

Figure 6-17: Kim et al. (2009) repeated the success of Jee et al. (2008) showing that inverting the spring greatly improves a nitinol spring's shape recovery. Image extractedfrom (Kim, Hawkes, Cho, Jolda, Foley, & Wood, 2009)

6.2.13 Heat Activation Mechanisms

SMAs are generally activated using one of two methods. The first method is by heating the alloy's surrounding environment, causing the alloy to heat to its transition temperature via convection. This can be done in various ways including blowing hot air onto the alloy or by submerging the alloy in hot water. The second method is by electric resistance heating. SMAs like Flexinol® have a high resistance in comparison to copper and other conductive materials, but still conductive enough to easily carry current. If the SMA is in wire form, electrical activation is highly favoured as it can be directly controlled, is instantaneous, and easy to implement. The electric current can be direct, alternating, or pulse-width modulated. However, Images SI, Inc. (2007) points out that pulse width modulation has distinct advantages. As it turns the current on and off quite quickly, the oscillating power allows the heat to flow to cold spots making for a more even heating. Additionally, the duty cycle of the square wave in pulse-width modulation can be varied from 100% to 0% providing improved proportional control. Images SI, Inc. (2007) argues that these factors provide better control for longer periods of time

without causing heat damage to the alloy's crystal lattice. Unfortunately, pulse-width modulation adds complexity to the modeling formulas. As direct current is easier to model, it will be used to activate the SMA wire.

6.3 MODELING HELICAL SHAPE MEMORY WIRE ACTUATORS

Part of the objectives of these experiments is to find a predictive model in relation to the SMA spring's stroke and heating times to compare with the experimental results. First presenting a predictive model for straight resistive wire, this section will then add shape memory parameters to this model, followed by the inclusion of mechanical spring parameters. Although the experiments only aim to find reaction times and stroke, temperature models are also presented in this section.

6.3.1 Straight Wire Modeling

After first presenting the heat transfer equations of resistive wire heating, this section will add elements exclusively found in SMAs to model a straight wire's temperature and reaction times. This will be followed by a section that presents models to predict a straight wire's stroke and recovery force.

6.3.1.1 REACTION TIMES AND TEMPERATURE

To predict the reaction times and temperature of a straight SMA wire, one must look at the electric heat transfer relationships in this particular situation. The rate at which energy is generated, $\dot{E}_g$, by passing a direct current, I, through a medium of electrical resistance, R_e, is expressed by:

$$\dot{E}_g = I^2 R_e \qquad 6\text{-}15$$

Expressing the equation in terms of the resistance per unit length, R_e', Equation 6-15 turns into:

$$\dot{E}_g = I^2 R_e' L \qquad 6\text{-}16$$

Providing that the power generation occurs uniformly through the medium of volume, V, the volumetric generation rate can be expressed as:

$$\frac{\dot{E}_g}{V} = \frac{I^2 R_e}{V} \quad 6\text{-}17$$

The basic laws of conservation of energy (*i.e.* the 1st law of thermodynamics) state that the total energy of the system is conserved, meaning that for a closed system (a region of fixed mass) the total energy stored, $\dot{E}_{st}$, is equivalent to the energy coming in, $\dot{E}_{in}$, and being generated,$\dot{E}_g$, minus the energy leaving the system, $\dot{E}_{out}$:

$$\dot{E}_{st} = \dot{E}_{in} - \dot{E}_{out} + \dot{E}_g \quad 6\text{-}18$$

For the case of resistive heating, the inflow is zero. The outflow is characterized by a combination of convection and radiation:

$$\dot{E}_{out} = \dot{E}_{conv} + \dot{E}_{rad} \quad 6\text{-}19$$

Because of the use of temperatures below 373 K, all radiation effects are assumed to be negligible. It is thus assumed that the outflow is completely due to convection and can be determined by the convection equation:

$$\dot{E}_{out} = \dot{E}_{conv} = hA_w(T(t) - T_\infty) = h(\pi dL)(T(t) - T_\infty) \quad 6\text{-}20$$

Where h, A_w, T(t), T_∞, d, and L respectively represent the convection coefficient, the wire's surface area, the temperature at a specific time, the ambient temperature, the wire's diameter, and the length of the wire. Assuming that the wire is the same temperature throughout its radius, the energy storage rate can be calculated as follows:

$$\dot{E}_{st} = \frac{dU_t}{dt} = \frac{d(\rho VcT(t))}{dt} = \rho Vc\frac{dT(t)}{dt} = \rho\left(\frac{\pi d^2 L}{4}\right)c\frac{dT(t)}{dt} \quad 6\text{-}21$$

Where U_t, ρ, V, and c respectively represent the internal energy stored, the material's density, the wire's volume, and the material's specific heat capacity. Substituting Equations 6-20 and 6-21 into Equation 6-18:

$$\rho\left(\frac{\pi d^2 L}{4}\right)c\frac{dT(t)}{dt} = I^2 R_e' L - h(\pi dL)(T(t) - T_\infty) \quad 6\text{-}22$$

Rearranging for dT(t)/dt gives the temperature's rate of change with respect to time:

$$\frac{dT(t)}{dt} = \frac{I^2 R_e' - h(\pi d)(T(t) - T_\infty)}{\rho\left(\frac{\pi d^2}{4}\right)c} \quad 6\text{-}23$$

To find the time needed to heat or cool to a specific temperature, *i.e.* the time it takes to get from an initial temperature, T_1, to a final temperature, T_2, one must rearrange and integrate Equation 6-23 to solve for t. Rearranging to get dt by itself:

$$dt = \rho\left(\frac{\pi d^2}{4}\right)c\frac{dT(t)}{I^2 R_e' - h(\pi d)(T(t) - T_\infty)} \quad 6\text{-}24$$

Followed by rearranging the denominator to get T(t) by itself:

$$dt = \frac{-\rho c d}{4h}\frac{dT(t)}{T(t) - \left(\frac{I^2 R_e'}{\pi d h} + T_\infty\right)} \quad 6\text{-}25$$

Integrating Equation 6-25 yields Equations 6-26 and 6-27 with the latter fully representing the total amount of time needed to change the temperature from T_1 to T_2

$$\int_0^{\Delta t} dt = \frac{-\rho c d}{4h}\int_{T_1}^{T_2}\frac{dT(t)}{T(t) - \left(\frac{I^2 R_e'}{\pi d h} + T_\infty\right)} \quad 6\text{-}26$$

$$\Delta t = \frac{-\rho c d}{4h} ln\frac{\left[T_2 - \left(\frac{I^2 R_e'}{\pi d h} + T_\infty\right)\right]}{\left[T_1 - \left(\frac{I^2 R_e'}{\pi d h} + T_\infty\right)\right]} \quad 6\text{-}27$$

If one wants to know the temperature of the wire after a time period, Equation 6-27 can be rearranged to yield T_2. First, the coefficients outside of the natural logarithm are brought over to the other side (Equation 6-28), followed by taking the exponential of both sides (Equation 6-29):

$$\frac{-4h\Delta t}{\rho c d} = ln\frac{\left[T_2 - \left(\frac{I^2 R_e'}{\pi d h} + T_\infty\right)\right]}{\left[T_1 - \left(\frac{I^2 R_e'}{\pi d h} + T_\infty\right)\right]} \quad 6\text{-}28$$

$$e^{\frac{-4h\Delta t}{\rho c d}} = \frac{\left[T_2 - \left(\frac{I^2 R_e{}'}{\pi d h} + T_\infty\right)\right]}{\left[T_1 - \left(\frac{I^2 R_e{}'}{\pi d h} + T_\infty\right)\right]} \quad 6\text{-}29$$

Rearranging Equation 6-29, one can find the formula for T_2:

$$T_2 = \frac{I^2 R_e{}'}{\pi d h} + T_\infty + \left[T_1 - \left(\frac{I^2 R_e{}'}{\pi d h} + T_\infty\right)\right] e^{\frac{-4h\Delta t}{\rho c d}} \quad 6\text{-}30$$

If one wants to know the steady state temperature, one can solve for it using Equation 6-23 knowing that at the steady state, $\frac{dT}{dt} = 0$:

$$I^2 R_e' L - h(\pi d L)(T_s - T_\infty) = 0 \quad 6\text{-}31$$

$$T_s = \frac{I^2 R_e'}{h(\pi d)} + T_\infty \quad 6\text{-}32$$

The steady state temperature, T_s, is therefore represented as Equation 6-32. The specific heat capacity is either the martensitic heat capacity or the austenitic heat capacity, depending on what phase the alloy is currently in. Due to the fact that a shape memory alloy changes phase during a transformation; a phenomenon that not only absorbs or releases energy, but can also change its specific heat capacity; the specific heat capacity generally cannot assume to be constant during a transformation. Reynaerts & Van Brussel (1998) represented the specific heat capacity in terms of the martensitic specific heat capacity, c_M, the austenitic specific heat capacity, c_A, and the transformation enthalpy, X_{AM}. The transformation enthalpy is essentially the total energy absorbed or released during the phase transformation. Reynaerts and Van Brussel argued that the averaged specific heat capacity during a transformation would be the average specific heat capacity of the martensite and austenite phases plus the transformation enthalpy divided by the temperature interval for the respective transformation. The specific heat capacities for both the martensite to austenite transformation, c_{MA}, and austenite to martensite transformation, c_{AM} can therefore be respectively shown as Equations 6-33 and 6-34:

$$c_{MA} = \frac{c_A + c_M}{2} + \frac{X_{MA}}{A_f - A_s} \quad 6\text{-}33$$

$$c_{AM} = \frac{c_A + c_M}{2} + \frac{X_{AM}}{M_s - M_f} \quad 6\text{-}34$$

As the martensite to austenite transformation is endothermic, X_{MA} will be a positive value; as the austenite to martensite transformation is exothermic, X_{AM} with be a negative value. As (A_f-A_s) will always be a positive value and (M_s-M_f) will always be a negative value, c_{MA} and c_{AM} will both always turn out positive. For the martensite to austenite transformation, one can use Equation 6-27 to calculate the time it takes for a transformation to take place. For the martensite to austenite transformation, where $T_1 = A_s$ and $T_2 = A_f$, the time interval, Δt_{MA}, can be presented as:

$$\Delta t_{MA} = \frac{-\rho c_{MA} d}{4h} ln \frac{\left[A_f - \left(\frac{I^2 R_e{}'}{\pi d h} + T_\infty\right)\right]}{\left[A_s - \left(\frac{I^2 R_e{}'}{\pi d h} + T_\infty\right)\right]} \quad 6\text{-}35$$

For the martensite to austenite transformation, where $T_1 = M_s$ and $T_2 = M_f$ and I = 0, the time interval, Δt_{AM}, can be presented as:

$$\Delta t_{Cool} = \frac{-\rho c_{AM} d}{4h} ln \frac{[M_f - T_\infty]}{[M_s - T_\infty]} \quad 6\text{-}36$$

Assuming that the applied direct current is sufficient to heat the wire from a martensite to the austenite phase, the total time to heat the wire from a martensite temperature, T_M, to an austenite temperature, T_A, can be calculated by combining Equations 6-27 and 6-35 with the appropriate variables:

$$\Delta t_{heat} = \frac{-\rho d}{4h} \left\{ c_M ln \frac{\left[A_s - \left(\frac{I^2 R_e{}'}{\pi d h} + T_\infty\right)\right]}{\left[T_M - \left(\frac{I^2 R_e{}'}{\pi d h} + T_\infty\right)\right]} + c_{MA} ln \frac{\left[A_f - \left(\frac{I^2 R_e{}'}{\pi d h} + T_\infty\right)\right]}{\left[A_s - \left(\frac{I^2 R_e{}'}{\pi d h} + T_\infty\right)\right]} + c_A ln \frac{\left[T_A - \left(\frac{I^2 R_e{}'}{\pi d h} + T_\infty\right)\right]}{\left[A_f - \left(\frac{I^2 R_e{}'}{\pi d h} + T_\infty\right)\right]} \right\} \quad 6\text{-}37$$

Likewise, the total time to cool down a wire from an austenite temperature, T_A, to a martensite temperature, T_M, can also be calculated:

$$\Delta t_{cool} = \frac{-\rho d}{4h}\left\{c_A ln\frac{[M_s - T_\infty]}{[T_A - T_\infty]} + c_{AM}\, ln\frac{[M_f - T_\infty]}{[M_s - T_\infty]} + c_M ln\frac{[T_M - T_\infty]}{[M_f - T_\infty]}\right\} \quad 6\text{-}38$$

If one wants to know the temperature of the wire after a certain heating or cooling time, one can rearrange Equations 6-37 and 6-38 in a similar manner to Equations 6-28 through 6-30. With reference to the heat time, rearranging Equation 6-37 to transfer the common coefficient to the left side yields:

$$\frac{-4h\Delta t_{heat}}{\rho d} = c_M ln\frac{\left[A_s - \left(\frac{I^2 R_e{}'}{\pi dh} + T_\infty\right)\right]}{\left[T_M - \left(\frac{I^2 R_e{}'}{\pi dh} + T_\infty\right)\right]} + c_{MA} ln\frac{\left[A_f - \left(\frac{I^2 R_e{}'}{\pi dh} + T_\infty\right)\right]}{\left[A_s - \left(\frac{I^2 R_e{}'}{\pi dh} + T_\infty\right)\right]} + c_A ln\frac{\left[T_A - \left(\frac{I^2 R_e{}'}{\pi dh} + T_\infty\right)\right]}{\left[A_f - \left(\frac{I^2 R_e{}'}{\pi dh} + T_\infty\right)\right]} \quad 6\text{-}39$$

Taking the exponential on both sides:

$$e^{\frac{-4h\Delta t_{heat}}{\rho d}} = \left\{\frac{\left[A_s - \left(\frac{I^2 R_e{}'}{\pi dh} + T_\infty\right)\right]}{\left[T_M - \left(\frac{I^2 R_e{}'}{\pi dh} + T_\infty\right)\right]}\right\}^{c_M} + \left\{\frac{\left[A_f - \left(\frac{I^2 R_e{}'}{\pi dh} + T_\infty\right)\right]}{\left[A_s - \left(\frac{I^2 R_e{}'}{\pi dh} + T_\infty\right)\right]}\right\}^{c_{MA}} + \left\{\frac{\left[T_A - \left(\frac{I^2 R_e{}'}{\pi dh} + T_\infty\right)\right]}{\left[A_f - \left(\frac{I^2 R_e{}'}{\pi dh} + T_\infty\right)\right]}\right\}^{c_A} \quad 6\text{-}40$$

Assuming the magnitude of the direct current is large enough to fully transform the wire into its austenite phase, Equation 6-40 can be rearranged to get the final temperature for the martensite to austenite transformation, T_A:

$$T_A = \frac{I^2 R_e{}'}{\pi d h} + T_\infty + \left(e^{\frac{-4h\Delta t_{heat}}{\rho d}} - \left\{ \frac{\left[A_s - \left(\frac{I^2 R_e{}'}{\pi d h} + T_\infty \right) \right]}{\left[T_M - \left(\frac{I^2 R_e{}'}{\pi d h} + T_\infty \right) \right]} \right\}^{c_M} - \left\{ \frac{\left[A_f - \left(\frac{I^2 R_e{}'}{\pi d h} + T_\infty \right) \right]}{\left[A_s - \left(\frac{I^2 R_e{}'}{\pi d h} + T_\infty \right) \right]} \right\}^{c_{MA}} \right)^{\frac{1}{c_A}} \left[A_f - \left(\frac{I^2 R_e{}'}{\pi d h} + T_\infty \right) \right] \quad 6\text{-}41$$

With reference to the cooling time, rearranging Equation 6-38 to get the common coefficients on the left side:

$$\frac{-4h\Delta t_{cool}}{\rho d} = \left\{ c_A ln \frac{[M_s - T_\infty]}{[T_A - T_\infty]} + c_{AM} ln \frac{[M_s - T_\infty]}{[M_f - T_\infty]} + c_M ln \frac{[T_M - T_\infty]}{[M_f - T_\infty]} \right\} \quad 6\text{-}42$$

Taking the exponential on both sides of Equation 6-42:

$$e^{\frac{-4h\Delta t_{cool}}{\rho d}} = \left\{ \frac{[M_s - T_\infty]}{[T_A - T_\infty]} \right\}^{c_A} + \left\{ \frac{[M_f - T_\infty]}{[M_s - T_\infty]} \right\}^{c_{AM}} + \left\{ \frac{[T_M - T_\infty]}{[M_f - T_\infty]} \right\}^{c_M} \quad 6\text{-}43$$

After rearranging Equation 6-43, the final temperature for an austenite to martensite transition, T_M, is found to be:

$$T_M = T_\infty + \left(e^{\frac{-4h\Delta t_{heat}}{\rho d}} - \left\{ \frac{[M_s - T_\infty]}{[T_A - T_\infty]} \right\}^{c_A} - \left\{ \frac{[M_f - T_\infty]}{[M_s - T_\infty]} \right\}^{c_{AM}} \right)^{\frac{1}{c_M}} [M_f - T_\infty] \quad 6\text{-}44$$

It must be noted, however, that all of these equations completely ignore superelasticity. When stress is applied to a SMA, the transformation temperatures proportionally increase. This phenomenon will most certainly affect the times and temperatures of the transformation. To account for superelastic effects, one would need to know the stress influence coefficients to recalculate the transition temperatures for the respective applied stress. The formulas used to calculate these new transition temperatures are presented in Chapter 7 as Equations 7-3 to 7-6.

6.3.1.2 STROKE AND RECOVERABLE FORCE

As presented in Section 6.2.3, shape memory alloys go through three different types of strain: elastic strain, ε^e, thermal strain, ε^{th} and transformation strain, $H^{cur}(\sigma)$. These strains are additive:

$$\varepsilon = \varepsilon^e + \varepsilon^{th} + \xi H^{cur}(\sigma) \tag{6-45}$$

As a wire is a 1-dimensional shape, Equation 6-45 can be rewritten as:

$$\varepsilon = \frac{\sigma}{E} + \alpha(T - T_0) + \xi H^{cur}(\sigma) \tag{6-46}$$

During a phase transformation, all three strain parameters will affect the overall change in strain. The most obvious one is the transformation strain. The transformation strain is only observed during a transformation. Providing that the transformation is complete, the total change in transformation strain will be $H^{cur}(\sigma)$ and is dependent on the stress level. The transformation strain generally has to be found through experimentation. As the austenite and martensite have different elastic and thermal properties, one must take this into account when calculating the overall strain change. With regards to the elastic strain, the modulus of elasticity changes from E^M to E^A or vice versa during a transformation. With regards to the thermal strain, the coefficient of thermal expansion would be α^M in the martensite phase, α^A during the austenite phase, and an average of the two coefficients during the transformation change. With reference to a martensite to austenite transformation, the change in elastic strain and thermal strain can therefore be formulated as Equations 6-47 and 6-48, respectively:

$$\Delta\varepsilon^e = \frac{\sigma}{E^A} - \frac{\sigma}{E^M} = \sigma\frac{E^M - E^A}{E^M E^A} \tag{6-47}$$

$$\Delta\varepsilon^{th} = \alpha^M(A_s - T_M) + \frac{\alpha^M + \alpha^A}{2}(A_f - A_s) + \alpha^A\left(T_A - A_f\right) \tag{6-48}$$

The total change in strain can therefore be modeled as:

$$\Delta\varepsilon = \sigma\frac{E^M - E^A}{E^M E^A} + \alpha^M(A_s - T_M) + \frac{\alpha^M + \alpha^A}{2}\left(A_f - A_s\right) + \alpha^A\left(T_A - A_f\right) - H^{cur}(\sigma) \tag{6-49}$$

Assuming that $\alpha^M \cong \alpha^A$, Equation 6-49 can be rewritten as:

$$\Delta\varepsilon = \sigma\frac{E^M - E^A}{E^M E^A} + \alpha^A(T_A - T_M) - H^{cur}(\sigma) \quad 6\text{-}50$$

With a wire of original length, L, the stroke, ΔL, can be expressed as:

$$\Delta L = \left(\sigma\frac{E^M - E^A}{E^M E^A} + \alpha^A(T_A - T_M) - H^{cur}(\sigma)\right)L \quad 6\text{-}51$$

A positive ΔL indicates an increase in length, whereas a negative ΔL indicates a decrease in length. If one measures the stroke, one could also solve for $H^{cur}(\sigma)$ by rearranging Equation 6-51 into:

$$H^{cur}(\sigma) = -\frac{\Delta L}{L} + \sigma\frac{E^M - E^A}{E^M E^A} + \alpha^A(T_A - T_M) \quad 6\text{-}52$$

Equation 6-52 thus represents the transformation strain after all elastic and thermal properties have been taken into account. Using the transformation strain and the universal 1-dimensional stress formulas, the recovery force, F_{rec}, can be represented as Equation 6-53 with A_{cs} representing the cross-sectional area of the wire (Hartl & Lagoudas, 2008).

$$F_{rec} = \sigma A_{cs} = [E^A H^{cur}(\sigma)]A_{cs} \quad 6\text{-}53$$

Equation 6-53 assumes that the wire has completely transformed from martensite to austenite. It should be noted, however, that it is important to not overstrain the material. In other words, the overall recovery stress should not be above the upper plateau yield stress (σ_{UPl}) as this will induce austenite to deform into martensite via superelasticity. For complete transformation to occur without permanent deformation, Equation 6-54 must be obeyed.

$$\sigma_{UPl} > \frac{F_{rec}}{A_{cs}} \quad 6\text{-}54$$

6.3.2 Helical Modeling

Now that the stroke, reaction times, temperature, and recovery forces have been established for straight wire, they must be translated into a helical spring wire. Unlike straight wire, helical springs are generally modeled with reference to their induced shear stress, τ, and shear strain, γ. Based on the multidimensional constitutive relations, Liang

and Rogers (1990) presented the derivative and integrated constitutive equations of a nitinol spring as Equations 6-55 and 6-56 with G representing the elastic shear modulus which can also be calculated using the respective elastic modulus and Poisson's ratio (shown in 6-57).

$$d\tau = Gd\gamma + \frac{\Omega}{\sqrt{3}}d\xi + \frac{\Theta}{\sqrt{3}}dT \qquad 6\text{-}55$$

$$\tau - \tau_0 = G(\gamma - \gamma_0) + \frac{\Omega}{\sqrt{3}}(\xi - \xi_0) + \frac{\Theta}{\sqrt{3}}(T - T_0) \qquad 6\text{-}56$$

$$G = \frac{E}{2(1+\upsilon)} \qquad 6\text{-}57$$

Using these constitutive relations for a helical spring, modeled equations for the stroke, reaction times, temperature, and recovery forces will be established.

6.3.2.1 TRADITIONAL SPRING MODELING

Before the shape memory transformation can be modeled, it is necessary to review spring mechanics. Liang and Rogers (1997) gives an excellent review of spring deformation by considering the deformation of an element of length, dx, cut from a wire of radius r (See Figure 6-18). Consider a line, ab, on the surface of the wire element, parallel to the spring axis; during a stress induced deformation by a constant force, the ab line will rotate through an angle, γ, and occupy a new position, line ac. Using Hooke's law for torsion, γ can be represented in relation to the maximum induced shear stress, τ_{max}, and modulus of rigidity. Additionally, τ can also be represented by the induced force (F), spring diameter (D) or radius (R), and wire diameter (d) or radius (r). These relations are shown in Equation 6-58.

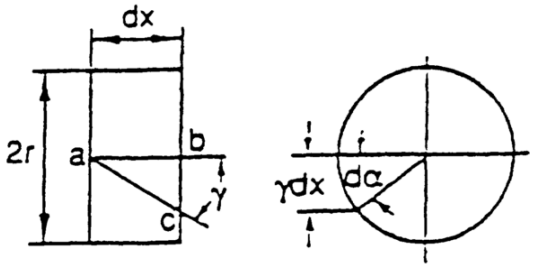

Figure 6-18: Cross-section element of a helical spring. Extracted from (Liang & Rogers, 1997)

$$\gamma = \frac{\tau_{max}}{G} = \frac{2FR}{\pi r^3 G} = \frac{8FD}{\pi d^3 G} \quad 6\text{-}58$$

To find the total deflection, one needs to find the total angular deflection, α_{def}. Angle $d\alpha_{def}$ through one section of the element rotates with respect to the other and can be modeled as:

$$d\alpha_{def} = \frac{\gamma(dx)}{r} \quad 6\text{-}59$$

Integrating 6-59, the angular deflection of one end of the spring wire with respect to the other is found:

$$\alpha_{def} = \int_0^{2\pi RN} \frac{\gamma}{r} dx = \frac{4FR^2N}{r^4 G} \quad 6\text{-}60$$

Where N is the number of the spring's active turns. The total deflection of the spring can therefore be represented as Equation 6-61 where k is the spring's stiffness:

$$\delta = \alpha_{def} R = \frac{4FR^3N}{r^4 G} = \frac{8FD^3N}{d^4 G} = \frac{F}{k} \quad 6\text{-}61$$

For springs undergoing static loading, the stress is generally multiplied by a factor, K_s, to get the maximum stress. K_s is dependent on the spring factor, C, which is the ratio between the spring diameter and wire diameter, (D/d). For a spring with a mass load, the maximum shear stress is

$$\tau_{max} = \frac{8(mg)D}{\pi d^3} K_s = \frac{8(mg)}{\pi d^3} C K_s \quad 6\text{-}62$$

Where K_s is:

$$K_s = 1 + \frac{0.615}{C} \quad 6\text{-}63$$

After some yielding has occurred, K_s can generally be assumed to be:

$$K_s = 1 + \frac{0.5}{C} = 1 + \frac{0.5d}{D} \quad 6\text{-}64$$

When using Equation 6-64, it is assumed that C is greater than 3 and that the pitch angle is less than 12°. There is also a normal force in the spring, put it is considered negligible providing that the pitch angle is less than 15° (Juvinall & Marshek, 2006). In all the equations presented in this chapter, the spring radius and spring diameter represents the diameter with reference to the wire's center, *i.e.* the average between the inner and outer spring radii or spring diameters.

6.3.2.2 REACTION TIMES AND TEMPERATURE

The reaction times and temperatures are found using the exact same formulas as the straight wire. For the reaction time and temperature formulas, one simply needs to refer to Section 6.3.1.1. However, it is again assumed that the transition temperatures do not change from superelastic effects.

6.3.2.3 STROKE AND RECOVERY FORCE

For a traditional spring, the deflection caused by a constant force was already presented as Equation 6-61. Looking solely at the change in elastic material properties during a transformation change, the deflections caused by a constant force at an SMA spring's austenite and martensite phases can be expressed as Equations 6-65 and 6-66

$$\delta_A = \frac{4FR^3N}{r^4G_A} = \frac{8FD^3N}{d^4G_A} = \frac{F}{k_A} \tag{6-65}$$

$$\delta_M = \frac{4FR^3N}{r^4G_M} = \frac{8FD^3N}{d^4G_M} = \frac{F}{k_M} \tag{6-66}$$

Based alone on the change in moduli of rigidity, one may tempt to model the stroke, $\Delta\delta$, as the change in elastic deflection:

$$\Delta\delta = \delta_M - \delta_A = F\frac{8D^3N}{d^4}\left(\frac{1}{G_M} - \frac{1}{G_A}\right) = F\frac{8D^3N(G_A - G_M)}{d^4G_MG_A} \tag{6-67}$$

Although some articles have stated that 6-67 can be used as stroke calculation [*e.g.* (Stevens, 1999)], this generally cannot be done as it negates the detwinning that occurs during the transformation process. As mentioned at the beginning of this chapter, when a

shape memory alloy is cooled to martensite, it is initially in its twinned form; applying stress to the alloy de-twins the alloy causing a change in length. During a stress-strain test, in data sheets, G_M represents the modulus of rigidity at detwinned martensite. G_M is needed to calculate the stroke, but an additional factor needs to be added to Equation 6-67 to take account of the transformation of twinned to detwinned martensite. Although fair to assume it to be negligible, Equation 6-67 also fails to take thermal strains into account.

Recalling the spring constitutive model (Equation 6-56), and assuming initial conditions of stress, strain, and martensitic fractions to be 0, the equation can be rewritten as:

$$\tau = G\gamma + \frac{\Omega}{\sqrt{3}}\xi + \frac{\Theta}{\sqrt{3}}T \qquad 6\text{-}68$$

Rearranging Equation 6-68 to get the shear strain by itself yields:

$$\gamma = \frac{\tau}{G} - \frac{\Omega}{G\sqrt{3}}\xi - \frac{\Theta}{G\sqrt{3}}T \qquad 6\text{-}69$$

Solving for the deflection in the same way as Equations 6-58 through 6-61, the total deflection can be modeled as Equation 6-70 (Liang & Rogers, 1997):

$$\delta = R\int_0^{2\pi RN}\frac{\gamma}{r}dx = \frac{2\pi R^2 N}{r}\left(\frac{\tau}{G} - \frac{\Omega}{G\sqrt{3}}\xi - \frac{\Theta}{G\sqrt{3}}T\right) \qquad 6\text{-}70$$

Substituting τ in Equation 6-70 with $\frac{2FR}{\pi r^3}$ yields Equation 6-71:

$$\delta = \frac{2\pi R^2 N}{r}\left(\frac{2FR}{G\pi r^3} - \frac{\Omega}{G\sqrt{3}}\xi - \frac{\Theta}{G\sqrt{3}}T\right) \qquad 6\text{-}71$$

Assuming a complete transformation, the total stroke from a martensite temperature to an austenite temperature, δ_{MA}, is modeled with three terms similar to the straight wire model. These terms are the deflection caused by elastic shear strain (γ^e), thermal shear strain (γ^{th}), and recovery shear strain (γ^{rec}):

$$\Delta\delta_{MA} = \frac{2\pi R^2 N}{r}(\gamma^e + \gamma^{th} + \gamma^{rec}) \qquad 6\text{-}72$$

Where:

$$\gamma^e = \frac{2FR}{G_A \pi r^3} - \frac{2FR}{G_M \pi r^3} = \frac{2FR}{\pi r^3} \frac{G_M - G_A}{G_M G_A} \quad 6\text{-}73$$

$$\gamma^{th} = \frac{\alpha^M E^M}{G_M \sqrt{3}} (A_s - T_M) + \frac{\alpha^M E^M + \alpha^A E^A}{(G_M + G_A)\sqrt{3}} (A_f - A_s) + \frac{\alpha^A E^A}{G_A \sqrt{3}} (T_A - A_f) \quad 6\text{-}74$$

$$\gamma^{rec} = \frac{\Omega}{G\sqrt{3}} \xi = -\frac{E^A H^{cur}(\sigma)}{G_A \sqrt{3}} = -\frac{2(1+\upsilon) H^{cur}(\sigma)}{\sqrt{3}} \quad 6\text{-}75$$

To transform $H^{cur}(\sigma)$ into a shear function, $H^{cur}(\tau)$, one can use the Von-Mises criterion which states that the shear stress would equal $\frac{\sigma}{\sqrt{3}}$ in a state of pure shear. The equivalent transformation in relation to the shear stress would therefore be $H^{cur}(\tau\sqrt{3})$. This states that providing one knows the transformation strain/stress relations, along with the induced shear stress, one would look up the transformation strain at a stress of $\sigma = \tau\sqrt{3}$. Substituting this information into Equation 6-75, one gets

$$\gamma^{rec} = -\frac{2(1+\upsilon) H^{cur}(\tau\sqrt{3})}{\sqrt{3}} \quad 6\text{-}76$$

If one assumes the thermal deflection to be negligible, then the total stroke can be expressed as Equation 6-77. Note that the stroke will turn out to be negative as G_M is always less than G_A and all the terms are positive.

$$\Delta\delta_{MA} = \frac{2\pi R^2 N}{r} \left(\frac{2FR}{\pi r^3} \frac{G_M - G_A}{G_M G_A} - \frac{2(1+\upsilon) H^{cur}(\tau\sqrt{3})}{\sqrt{3}} \right) \quad 6\text{-}77$$

The total stroke is thus dependent on two terms: the elastic stroke (the left term in 6-77) and the transformation stroke (the right term in Equation 6-77). Both terms add to the deflection thus making the overall deflection larger than the elastic stroke term alone. Like a straight wire, permanent deformation will occur when the induced stress reaches the upper plateau stress, σ_{UPl}, on the stress-strain diagram. Using Von-Mises criterion, the upper plateau stress is reached when the shear stress, τ, reaches $\frac{\sigma_{UPl}}{\sqrt{3}}$. Using the spring shear stress formula (Equation 6-58), the force needed to reach the upper plateau stress, F_{UPl}, is calculated to be:

$$F_{UPl} = \frac{\pi r^3 \sigma_{UPl}}{2\sqrt{3}R} = F_{rec} \quad 6\text{-}78$$

Equation 6-78 is thus the formula for the recovery force, F_{rec}. Using Equation 6-61, the austenitic deflection corresponding to this elastic stress limit, δ_{UPl}, is found to be:

$$\delta_{UPl} = \frac{2\pi N R^2 \sigma_{UPl}}{\sqrt{3} r G_A} \qquad 6\text{-}79$$

It should be mentioned that all of the formulas presented in this section assume that the spring diameter does not change during the transformation. This assumption is not realistic as the detwinning of martensite will likely encourage the spring diameter to decrease somewhat while the spring length increases during the austenite to martensite transformation. Kim et al (2009) address this issue by coming up with an effective stroke model:

$$\delta_{eff} = \delta_d + \delta_L + \delta_A = -\frac{\pi \gamma_d D^2 N}{d} - \frac{8 F D_{eff}^3 N}{G_M d^4} + \frac{8 F D^3 N}{G_A d^4} \qquad 6\text{-}80$$

Where δ_d represents the deflection from de-twinning the martensite, δ_L is the elastic deflection of the martensite after detwinning (*i.e.* the de-twinned martensite deflection), and δ_A is the deflection during the austenite phase. In the δ_M deflection, the γ_d represents the shear strain experienced by the spring during the de-twinning process which is based on the maximum transformation strain. In other words, γ_d is equivalent to γ^{rec} in Equation 6-76.

In the δ_L deflection, the D_{eff} represents the effective spring diameter after it has been reduced by de-twinning the martensite. D_{eff} can be represented as Equation 6-81 where θ is the angle between the spring wire and the horizontal plane:

$$D_{eff} = D \cos\theta \qquad 6\text{-}81$$

Substituting Equations 6-76 and 6-81 into Equation 6-80, one would get:

$$\delta_{eff} = -\frac{2\pi(1+\upsilon) H^{cur} \left(\tau\sqrt{3}\right) D^2 N}{d\sqrt{3}} - \frac{8 F (D\cos\theta)^2 N}{G_M d^4} + \frac{8 F D^3 N}{G_A d^4} \qquad 6\text{-}82$$

Although several stroke formulas have been presented in this thesis, the verification of a specific formula is outside the scope of this thesis. The overall experimental objectives will be presented in the next section.

6.4 EXPERIMENTAL OBJECTIVES & PREDICTIONS

As reviewed, many spring variables influence the output of a nitinol spring. These properties include the wire diameter, spring diameter, transition temperature, number of spring turns, bias mass, and direct current. These experiments aim to showcase how each variable influences the nitinol spring's performance in terms of its reaction times and stroke. These manipulated variables along with their respective experimental values, are listed in Table 6-9.

Table 6-9: The Manipulated Variables along with their Experimental Values

Variable	Units	# of Different Values	Values
Wire Diameter	Inches (mm)	4	0.006 (0.15), 0.008 (0.20), 0.010 (0.25), 0.015 (0.38)
Inner Spring Diameter	Inches (mm)	4	0.09375 (2.38),0.125 (3.175), 0.1875 (4.76),0.25 (6.35)
Transition Temperature	°C	2	70 and 90 at 3 different wire diameters
Number of Spring Turns	-	4	8, 12, 16, 20
Bias Mass	g	4	20, 30, 40, 50
Direct Current	A	4	0.3, 0.4, 0.5, 0.6

Table 6-10: The Values for each Property for each Manipulated Variable Experiment

Spring Properties	Units	Manipulated Variable Experiments					
		Wire Diameter	Inner Spring Diameter	Transition Temperature	Number of Spring Turns	Bias Mass	Direct Current
Wire Diameter	mm	0.15, 0.20, 0.25, 0.38	0.25	0.15, 0.20, 0.25,	0.25	0.25	0.25
Inner Spring Diameter	mm	3.175	2.38, 3.175, 4.76, 6.35	3.175	3.175	3.175	3.175
Transition Temperature	C	70	70	70 and 90	70	70	70
Number of Spring Turns	-	16	16	16	8,12, 16,20	16	16
Bias Mass	g	30	30	30	30	20,30, 40,50	30
Direct Current	A	0.55	0.55	0.55	0.55	0.55	0.45,0.5, 0.55,0.6

For repeatability purposes, at least three trials were performed for each experiment and every wire was activated on and off for 20 cycles. If one performs 3 trials for every possible property combination, one would have to perform more than 6, 000 trials. As this was not viable, the amount of manipulated experiments was reduced to 6, each one concentrating on manipulating only one variable to get a sense of how each variable relates to the spring's performance. With a minimum of 3 trials performed for each different value, the minimum amount of experimental trials reduces to 57. Each experiment was set up to be compared in relation to a nitinol spring of 0.25 mm wire diameter, 3.175 mm inner spring diameter, 70 °C transition temperature, 16 active spring turns, carrying a bias mass of 30 g, and activated with a 0.55 A direct current. A summary of the manipulated and controlled properties for all 6 experiments is presented as Table 6-10.

6.4.1 Predicted Results

Before the experiments took place, the heating and cooling reaction times were estimated. As only the transformation itself was being investigated, the heating and cooling times were estimated using equations 6-35 and 6-36, respectively. In other words, the starting and finishing temperatures of the nitinol are assumed to be the corresponding transition temperatures. The physical material properties used in these calculations were found from the manufacturer and are listed in Table 6-11. Shown as Figure 6-19, the transition temperatures for both the 70 °C and 90 °C Flexinol® wires were estimated from a temperature-strain graph from the manufacturer. The estimated transition temperatures are listed in Table 6-12.

Table 6-11: Material Properties of Flexinol® Wire

Property	Value	Source
Density, ρ	6.45 g/cm^3	(Dynalloy. Inc., 2011)
Specific Heat, $C_A = C_M$	837.36 J/kg/K (0.2 cal/g*°C)	
Melting Point	1300 C	
Latent Heat of Transformation, X_{AM}	24,190.4 J/kg (5.78 cal/g)	
Thermal Conductivity, k	0.18W/(cm*K)	
Thermal Expansion Coefficient, α **Martensite** **Austenite**	 6.6 x 10^{-6}/K 11.0 x 10^{-6}/K	
Electrical Resistivity (approx.), ρ_{res} **Martensite** **Austenite**	 80 micro-ohms*cm 100 micro-ohms*cm	
Modulus of Elasticity **Martensite, E_M** **Austenite, E_A**	 28-40 GPa 83 GPa	E-mail Correspondence with Erin Addison, from the University Research Department at Dynalloy, Inc. Note: 28 GPa was used in the martensite deflection calculations as it would give the best case scenario for stroke
Poisson's Ratio, ν (Estimated)	0.3	(Hartl & Lagoudas, 2008)

Table 6-12: The Estimated Transition Temperatures for both the 70 °C and 90 °C Flexinol® Wires

Transition Temperature	70 °C Flexinol® Wire	90 °C Flexinol® Wire
A_s	70	90
A_f	90	110
M_s	65	80
M_f	45	60

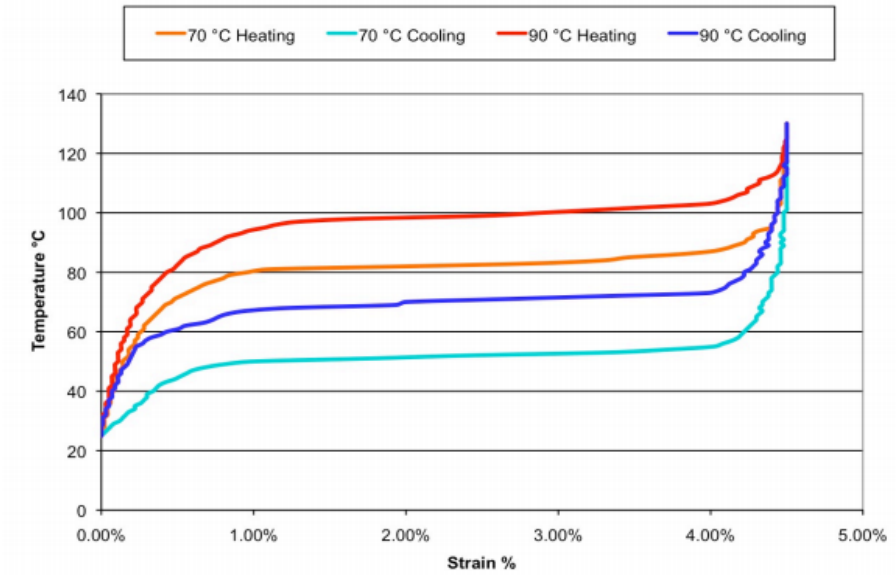

Figure 6-19: The Temperature-Strain Graphs for Flexinol®'s 70°C and 90°C wires. Extracted from (Dynalloy. Inc., 2011)

As Flexinol®'s transformation strains at varying stresses, *i.e.* $H^{cur}(\sigma)$, were not available from the manufacturer, a predicted estimate of the stroke was not performed; although it's hinted on their technical specifications that a maximum strain of nearly 5% is achievable at about 103 MPa or above (Dynalloy. Inc., 2011). Regardless, using the stroke equation (*i.e.* Equation 6-77), the stroke pattern was predicted based on increasing the respective manipulated variable. However, the experimental strokes are later compared with predicted results using Equation 6-67 to see if the transformation strain attributed to detwinning martensite (*i.e.* the rightmost term in Equation 6-77) can be ignored when estimating the stroke. From reasoning already discussed in Section 6.3.2.3, it is predicted that the strokes will be larger than what Equation 6-67 predicts as the act of detwinning the martensite should add to the overall martensite deflection.

To obtain more accurate performance predictions, measurements of the wire diameters, rod diameters, and bias masses were made. Using a scale with a resolution of 0.1g, all

bias masses were accurate to their manufactured specifications. However, the measured rod diameters and wire diameters had differences in comparison to their manufactured specifications. Using a micrometer with 0.00005" resolution, the wire diameters were all measured to be below their manufactured specifications, erring as high as 5.4%. The rod diameters were measured to be within 1.5% of their manufactured specifications. The measurements for both the wire diameters and rod diameters are presented as Table C-1 and Table C-2, respectively in APPENDIX C1: Wire and Rod Measurements. The measured rod and wire diameters were in turn used as measurements for the nitinol springs' inner diameters.

Using the measured rod and wire diameters, the heating times and cooling times were calculated using Equations 6-35 and 6-36. The convection coefficient was assumed to be 15 W/m^2 as this value was performed in numerous heat transfer examples in Incropera *et al.*'s Introduction to Heat Transfer, 5^{th} ed. (2007). The temperature of the room was not measured, but for the predictions, the room temperature is assumed to be 15 °C (288 K). All of the predicted times can be found in APPENDIX C2: Reaction Times and Stroke Predictions. Table 6-13 summarizes the predicted trends between heating time, cooling time, and stroke when the value of each manipulated variable is increased.

Table 6-13: Predicted Trends in Heating Time, Cooling Time, and Stroke in Relation to Increasing the Value of each Manipulated Variable

Manipulated Variable	Predicted Effect on Heating Time when Increased	Predicted Effect On Cooling Time When Increased	Predicted Effect on Stroke When Increased
Wire Diameter	Increase	Increase	Converged Decrease
Spring Diameter	No Change	No Change	Increase
Transition Temperature	Increase	Decrease	No Change
Number of Spring Turns	No Change	No Change	Increase
Bias Mass	No Change	No Change	Increase
Direct Current	Decrease	No Change	No Change

The next six subsections will briefly discuss the time and stroke predictions for each manipulated variable.

6.4.1.1 WIRE DIAMETER

As the wire diameter increases, the internal heat capacitance increases. An increased wire diameter would therefore require more heat to raise its temperature and would retain its heat better when forced to cool. The heating times and cooling times should therefore increase as the wire diameter increases. This was demonstrated in the predicted reaction times as the heating times and cooling times respectively increased from 0.56 s to 4.32 s and 10.8 s to 28.0 s as the wire diameter was increased from 0.145 mm to 0.375 mm. With regards to the stroke, looking at Equation 6-77, the stroke will decrease as the wire diameter increases providing that the bias mass does not exceed the recovery force. In fact, increasing the wire diameter should greatly decrease the stroke as it influences the elastic stroke to the negative fourth power and the transformation stroke will also decrease due to the fact that the shear stress decreases at increasing wire diameters; $H^{cur}(\tau)$ will thus decrease at larger wire diameters. The transformation stroke is also directly influence by the inverse of the wire diameter, causing a further decrease in stroke at increased wire diameters. The values of the controlled variables along with the predicted times and stroke patterns for the wire diameter manipulations are shown in Table C-3 and Table C-4 in APPENDIX C2: Reaction Times and Stroke Predictions.

6.4.1.2 SPRING DIAMETER

As the spring diameter does not have any effect on the thermal capacitance of the nitinol wire, there should not be any changes in reaction times when altered. This was shown in the predictions where all four spring diameters produced the same heating and cooling times, 1.75 s and 18.5 s respectively. However, the inner spring diameter should very much affect the stroke as Equation 6-77 dictates that it influences the elastic stroke to the third power. Equation 6-77 also dictates that the transformation stroke should also increase as an increased spring diameter increases the spring's shear stress; $H^{cur}(\tau)$ will thus increase as the spring diameter increases. The transformation stroke is also directly influenced by the square of the spring diameter, causing a further increase in stroke at larger spring diameters. The values of the controlled variables along with the predicted

times and stroke patterns for the spring diameter manipulations are presented in Table C-5 and Table C-6 respectively in APPENDIX C2: Reaction Times and Stroke Predictions.

6.4.1.3 TRANSITION TEMPERATURE

The transition temperature should have an impact on the reaction times. The heating times should be longer for the 90 °C wire as the wire must be heated an additional 20 °C before the martensite to austenite transformation can take place. Likewise, the cooling times should be longer for the 70 °C wire as the wire must cool an additional 20 °C before the austenite to martensite transformation can take place. This was shown in all predictions at the three different wire diameters that were tested. As for the stroke, the transition temperature is absent in Equation 6-77 and is therefore expected to not influence the spring's stroke. The values of the controlled variables along with the predicted times and stroke pattern for the transition temperature manipulations are presented in Table C-7 and Table C-8 in APPENDIX C2: Reaction Times and Stroke Predictions.

6.4.1.4 NUMBER OF SPRING TURNS

As the number of spring turns is absent from the reaction time equations, it is not expected to influence the reaction times. The predicted heating and cooling times were thus the same for all four active turn value, respectively at 1.75 s and 18.5 s. However, Equation 6-77 dictates that the number of active turns positively correlates with the stroke. In fact, as the number of turns is not a factor in the spring's shear stress, the transformation strain, $H^{cur}(\tau)$, should be the same for all four turn settings. This indicates that the relationship between the active turns and stroke should be linear. The values of the controlled variables along with the predicted times and stroke pattern for the number of spring turn manipulations are presented in Table C-9 and Table C-10 in APPENDIX C2: Reaction Times and Stroke Predictions.

6.4.1.5 BIAS MASS

As the bias mass is absent from the reaction time equations, it is not expected to affect the reaction times. Respectively predicted at 1.75 s and 18.5 s, the heating and cooling times were predicted to be the same for all bias masses. However, the bias mass is predicted to have an influence on the stroke based on Equation 6-77. As an applied force, Equation 6-77 dictates that the elastic stroke will linearly increase with an increasing bias mass. An increased bias mass will also increase the spring`s shear stress, therefore increasing $H^{cur}(\sigma)$ and the overall transformation stroke. The values of the controlled variables along with the predicted times and stroke pattern for the bias mass manipulations are presented in Table C-11 and Table C-12 in APPENDIX C2: Reaction Times and Stroke Predictions.

6.4.1.6 DIRECT CURRENT

As the direct current directly influences the amount of heat being transferred to the nitinol wire, it is very much expected to influence the heating time. A greater direct current increases the heat transfer rate thus allowing the wire to transform into its austenite phase faster. This is reflected in the predicted heat times of 2.83s to 1.44s as the direct current is increased from 0.45 A to 0.60 A. However, the cooling rate is not expected to be affected by the direct current because the nitinol wire cools without any applied direct current. Direct current is thus absent from the cooling time equation. This is reflected in the cooling time predictions; the cooling time is projected to be 18.5 s for all direct current values. The values for the controlled variables along with the predicted times and stroke pattern for the direct current manipulations are presented in Table C-13 and Table C-14 in APPENDIX C2: Reaction Times and Stroke Predictions.

6.5 TESTING APPARATUS AND PROCEDURES

This section will go through the various equipment used in these experiments along with the procedures taken. Divided into three subsections, the first subsection section goes through the shape-set heat treatments performed to produce the SMA helical springs, the

second subsection showcases the testing apparatus and the purpose of each piece of equipment, and the last subsection goes through the procedures taken to collect the data.

6.5.1 Heat Treatment and Connections

As mentioned in Section 6.2.12, the springs were made using straight Flexinol® wire by wrapping them around a steel rod. First, one end of the wire was constrained to the rod using a C-clamp; second, the wire was tightly wrapped around the rod so that it would be shape set as a completely compressed spring (See Figure 6-20); and the other end of the wire was constrained with an additional C-clamp. As the spring diameter is one of the manipulated variables in these experiments, rods of different diameters were used: 3/32", 1/8", 3/32", and 1/4". The wire/rod assemblies were then placed in a Lindberg™ oven (Pictured in Figure 6-21) at a temperature of 500 °C for 10 minutes. This was followed by a water quench (Pictured in Figure 6-22). After cutting the springs to a designated length, the wires were crimped to insulated electrical wires (Pictured in Figure 6-23) to later connect the spring to the variable power source and transistor.

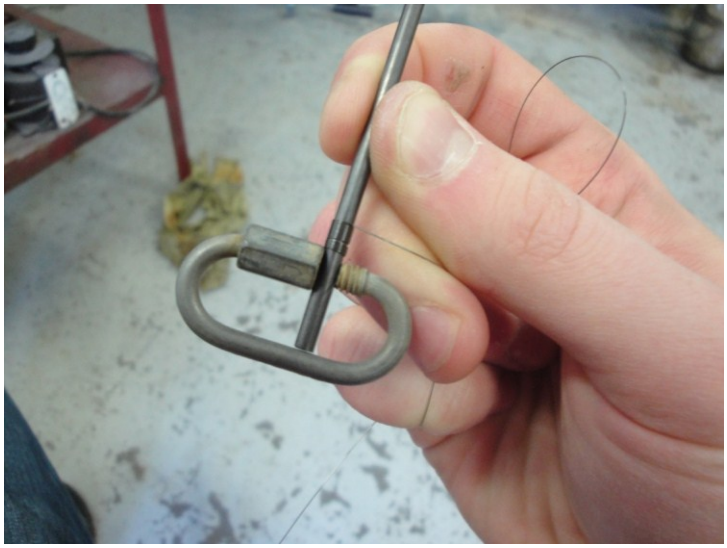

Figure 6-20: To constrain the Flexinol® wire to a helical spring, one end of the wire was clamped to a rod, followed by tightly wrapping the wire around the rod, and constraining the other end with an additional C-clamp

Figure 6-21: The wrapped wires were baked in a Lindberg™ oven (pictured left) at 500 °C for 10 minutes

Figure 6-22: After heat treating, the wires were water quenched

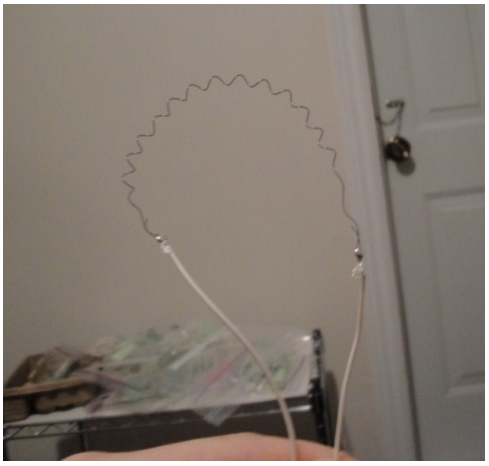

Figure 6-23: After going through the heat treatment, the springs were cut to their designated length and each end was crimped to an insulated electrical wire.

6.5.2 Testing Apparatus and Procedure

The testing apparatus consisted of several components, most of which are listed in Table 6-14. The overall testing apparatus is pictured in Figure 6-24. Figure 6-25 gives a close up of the electronic components that act as the central hub to connect everything together. A schematic of the electronic components can be found in APPENDIX C4: ELECTRONIC SCHEMATIC. The apparatus was controlled using an Arduino Duemillanove Microprocessor with code written on a computer. The code used can be found in APPENDIX C3: ARDUINO CODE.

Table 6-14: A List of Components in the Testing Apparatus Along with Their Function

Component	Function
SMA Helical Spring Crimped to insulated electrical wire	One of the manipulated variables in these experiments
Various Bias Masses	One of the manipulated variables in these experiments
Power Supply	Supplies the direct current needed to heat the SMA wires
Arduino Duemillanove Microprocessor	Controls the power supply via the transistor
Computer with Arduino Code	Gives the control code to the Arduino microprocessor and gives the Arduino microprocessor power
Parralax Ping))) Sensor	Senses the position of the bias mass to the let the microcontroller know when the SMA wire has finished transitioning
Electronic Breadboard	Connects the electronics to each other
Alligator Clips	Connects the SMA wires to the variable power supply
Transistor	Acts as a gate to allow or disallow the power supply to send current to the SMA wire
Ruler	Measures the position of the bias mass
Stand	Holds the ruler and top of SMA wire in place
0.1 µF Capacitor	Smoothes the power supply to the Parallax Ping))) Sensor
1kΩ Resistor	Limits current from the microprocessor to the transistor`s base to 5mA

As the Arduino microprocessor is only able to generate a maximum current of 50mA, an additional power source was needed to heat the SMA wire. The power source used had variable current settings, allowing the SMA wire to be activated at a constant electric current. The current was turned on and off using the microprocessor and a transistor. The transistor's base, collector, and emitter were respectively connected to the microprocessor, power source, and common ground. To activate the SMA wire, the microprocessor would simply turn the transistor base on high; to deactivate the SMA wire, the microprocessor would turn the base low. The code would be written to record

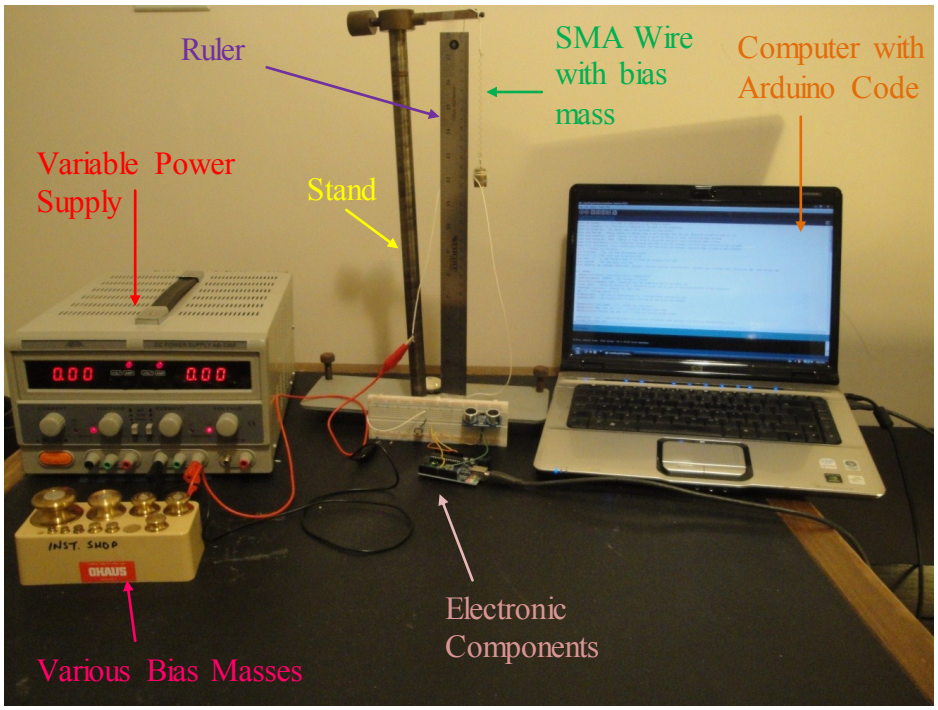

Figure 6-24: The Labelled Testing Apparatus for the SMA helical spring experiments

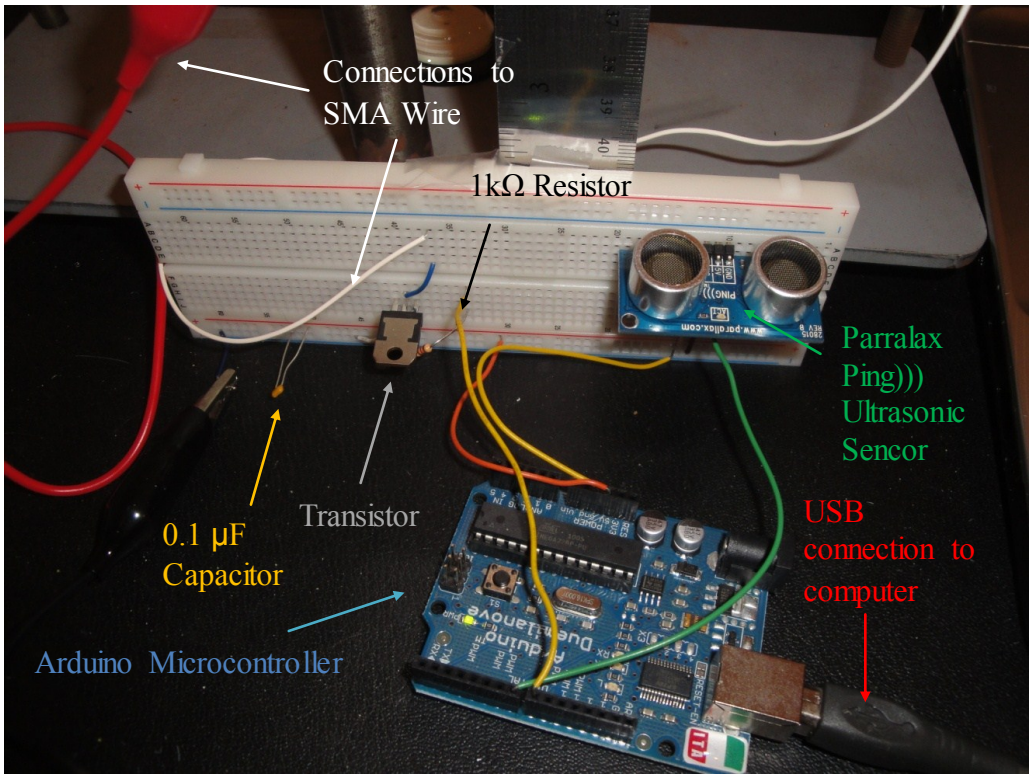

Figure 6-25: A close up of the electronic components

the time between transformations, thus recorded the heating and cooling times. To sense the position of the bias mass, a proximity sensor was used. When a transformation has ended, the bias mass will be at a constant height; it is stationary. Essentially, the Arduino code was written so that if the proximity sensor senses that the bias mass has become stationary, the microprocessor would switch its input to the transistor from high to low, or vice versa. For a more detailed explanation of the code, please refer to the notes in APPENDIX C3: ARDUINO CODE. For the control parameters used in each trial including the delay times and differential control parameters, please refer to APPENDIX C5: ARDUINO CODE CONTROL SETTINGS. Originally, the proximity sensor was sought to perform two functions: to sense when the bias mass has stopped moving and to record the height of the bias mass for deflection and stroke measurements. Two proximity sensors were tested: an ultrasonic sensor (the Parallax Ping))) sensor) and an infrared (IR) sensor (the Sharp GP2D120XJ00F). Both sensors were initially tested for accuracy. The ultrasonic sensor tended to underestimate the bias mass distance by about a centimeter, while the IR sensor's output tended to fluctuate and had a nonlinear relationship between the sensed distance and output voltage. As both sensors proved to be unreliable to sense the bias mass's stroke, it was decided to measure the stroke by eye. A ruler would be placed next to the bias mass, and the bias mass's activated and deactivated position would be recorded after each transformation to obtain the martensite length, austenite length, and stroke measurements. Although linear variable differential transducers (LVDT) have been used to measure an SMA's output stroke (Lee & Lee, 2000), the required LVDT would have compromised the bias mass parameters. The LVDT that would've been adequate for these experiments (one with a range of ±100mm) would've had an armature mass of 71g which would have to be added to the bias mass in the bias mass parameters. As 71g is a mass that is larger than the largest bias mass used in these experiments, an LVDT would not be viable to measure the SMA spring's stroke.

During a trial, the Arduino code would be activated. The transistor's base will be turned high, allowing the direct current from the power supply to go to the SMA wire. The wire will then activate and transform from its martensite form to its austenite form, *i.e.* the spring will compress (shown in the left image in Figure 6-26). Taking the data from the

Figure 6-26: Each time the wire was in its austenite phase (Left) and martensite phase (Right), the bias mass`s position on the ruler was recorded.

Ping))) ultrasonic sensor, the microprocessor will determine when the transformation is complete upon which the transistor's base will turn low, allowing the SMA wire to cool back to its martensite form, consequently elongating the spring (Shown in the right image in Figure 6-26). Keeping track of the elapsed time, the microprocessor will log the amount of time it took to heat the wire. When the wire has finished its austenite to martensite transformation as determined by the Ping))) ultrasonic sensor, the microprocessor will again turn the transistor's base to high, and the elapsed cooling time will be logged by the microprocessor. Each trial consisted of 20 cycles, giving 20 heating times, cooling times, martensite spring lengths, austenite spring lengths, and stroke measurements. As indicated earlier, the deflections were measured using the ruler. The SMA spring/bias mass connection was monitored relative to the ruler and the position was recorded for each transition. To obtain the austenite and martensite spring lengths, the distance at the top of the SMA spring in relation to the ruler was subtracted from the recorded bias mass position. The reason for doing 20 cycles is to not only to get repeatability of the results, but to also observe if the results change after each trial due to fatigue. If fatigue is a factor, the stroke would be expected to be highest during the first trial, and decreasing after each subsequent trial until the stroke converged to a set stroke.

One element that these experiments do not address is measuring the temperature of the wire. Although K-type thermocouples with very fine diameters (~0.012 mm) have been directly attached to SMA wires to sense the wire's temperature (Lee & Lee, 2000), the author felt it would inhibit the stroke of the SMA spring. Researchers tend to use IR thermometers to measure the temperature of SMA wires. However, the thermal emissivity of the IR thermometer needs to be adjusted as the emissivity of metal tends to be lower than carbon based materials. The thermal emissivity of carbon base materials tend to be around 0.95 (The Engineering Toolbox, 2012) while those of nitinol tend to be vary from 0.66 (Iadicola & Shaw, 2007) to 0.83 (Shaw & Kyriakides, 1997). Since accurate IR temperature measurement requires a sufficiently high emissivity (low reflectivity) of the wire surface, it may be necessary to paint the wire surface black (Churchill, Shaw, & Iadicola, 2009). Afraid that a coat of paint may also inhibit the performance of the nitinol wire, the author did not pursue this option. A small IR thermometer with adjustable emissivity settings was purchased to see if the temperature of the SMA wire could be accurately measured. When tested on a 70 °C Flexinol® wire in its activated and deactivated state, the measured temperature changed from 20 °C to 45 °C. As the SMA wire must be a temperature of at least 70 °C in its activated state, the IR thermometer was deemed incapable of accurately measuring the temperature of the Flexinol® wire. Measuring the temperature was therefore deemed to be outside of the scope of this investigation.

6.6 RESULTS and DISCUSSION

For each trial, the mean, median, standard deviation, and % standard deviation (in relation to the mean) were obtained for the twenty measurements taken during each trial. To get values for each setting as a whole, the results from the respective trials were combined to get the averaged mean, averaged median, and pooled standard deviation for each setting. The pooled standard deviation (s_p) was found using Equation 6-83 where k, n_i, and s_i represent the number of trials (generally three or four in this investigation), the number of measurements in a trial (*i.e.* 20 for all trials), and the standard deviation for a particular trial. By using a pooled standard deviation, it is assumed that the true variance

(*i.e.* precision) is the same for each set of measurements despite the fact that the means between sets could vary.

$$s_p = \left(\frac{\sum_{i=1}^{k} \left((n_i - 1) s_i^2 \right)}{\sum_{i=1}^{k} (n_i - 1)} \right)^{1/2} \qquad 6\text{-}83$$

The results from each trial and amalgamated results for each setting are presented in Table C-27 to Table C-56 in APPENDIX C6: TABULATED RESULTS.

Although most trials provided fairly consistent results, some had observable discrepancies. Some trials had quite high standard deviations. The author mainly attributes this to the control system put in place. For an example, on some occasions the control system would heat or cool the wire for extended periods of time before acknowledging the bias mass had become stationary. Likewise, there were times when the control system would switch the transistor on and off before the transformation was observably complete.

In relation to the type of measurement, Table 6-15 shows the percentage of measurements that had a pooled standard deviation of 20% or less. In total, 78.3 % of the measurements had a pooled standard deviation of 20% or less. However, if categorized by the type of measurement, one would notice that the reaction times had standard deviations that were significantly less than the deflection measurements. Respectively, 34.8% and 73.9% of the heating and cooling times had pooled standard deviations below 20%; compared respectively to 95.7%, 100%, and 87% in relation to the austenite lengths, martensite lengths, and strokes. If the control system more often erred by switching the transistor too quickly, the standard deviations for the deflection measurements would have been much larger as the strokes would be shorter if the transformations were not completed. This implies that the control system would more often err by allowing the wire to heat or cool more than necessary. If performed again, it would be recommended to add an override switch to the electronic components to allow the observer to override the control system to switch the transistor if the wires are observably being heated or cooled longer than necessary.

Table 6-15: The Percentage of Measurements with a Pooled Standard Deviation of 20% or Less with Respect to the Type of Measurement

	Heat Times	Cooling Times	Austenite Length	Martensite Length	Stroke	Total
% with a Pooled Standard Deviation of 20% or less	34.8	73.9	95.7	100.0	87.0	78.3

Between the heat times and cooling times, it was observed that the heat times had a higher relative pooled standard deviation; likely caused for two reasons. Firstly, the heat times were much shorter than the cooling times, thus making extended transformation times more significant when calculating a mean and standard deviation. Secondly, the bias mass was further away from the Ping))) sensor at the end of the heat time interval, thus making the bias mass more difficult to detect. Alternatively, the bias mass was closest to the Ping))) sensor at the end of the cooling cycle, thus making the bias mass easier to detect at the end of a cooling cycle. The extended heating times may have also directly contributed to extended cooling times as the wire would start the cooling time interval with a higher temperature, thus requiring more time for the wire to adequately cool and transform into martensite.

Because the extended heating and cooling times affected the averaged mean results, the author felt that the averaged median values would be a better reflection of the spring's output values. The averaged medians (both reaction times and deflections) would therefore be used for further analysis. The reaction times were compared with predicted values using Equations 6-35 and 6-36, while the austenite lengths, martensite lengths, and strokes were compared to models that ignore the transformation strain [*i.e.* Equation 6-61 plus the compressed spring length (wire diameter multiplied by the number of spring turns) for the austenite and martensite spring lengths, and Equation 6-67 for the stroke]. As expected, the stroke was much higher on all experimental results when compared to the predictions, demonstrating that the transformation strain cannot be overlooked when calculating the stroke. However, the author noticed that the predicted heating and cooling times did not accurately reflect the experimental results. Although this difference could be related to various experimental parameters such as the control system, estimated convection coefficient, or estimated ambient temperature, the author felt that it was

because the predicted results did not accurately account for the nitinol's superelasticity. As mentioned, an SMA's transition temperatures will linearly increase in relation to the applied stress. Using stress influence coefficients (C_A and C_M) of 7 MPa/°C, typical values that were previously present in Table 6-2, the new transition temperatures were calculated using Equations 7-19 to 7-22. These new transition temperatures were then used to re-evaluate the predicted heat and cooling times, again using Equations 6-35 and 6-36. Although the new predicted heat times did not improve much to accurately reflect the true heat times, the new predicted cooling times much better reflected the true cooling times. It became apparent that one cannot ignore superelasticity when calculating the cooling times for SMA springs.

It should be noted, however, that although the cooling time predictions greatly improved, there was some generalization in using Equations 7-19 to 7-22 as they only dictate the change in transition temperatures at the maximum shear stress which is located at the wire's outer surface. The shear stress is 0 MPa at the center; ignoring Wahl concentrations, the shear stress linearly increases from the center to the end of the wire radius. This indicates that the transition temperatures would also linearly increase from their original zero stress values (*i.e.* M_s, M_f, A_s, and A_f) to their stress-induced values (*i.e.* M_s^τ, M_f^τ, A_s^τ, and A_f^τ) from the wire's center to its outer surface. It may be fairer to have used the average shear stress when accounting for superelasticity which would have been two thirds of the maximum shear stress. If one uses the average shear stress as opposed to the maximum shear stress, the calculated heat times should decrease while the cooling times should increase as the new transition temperatures would be lower. After redoing the calculations using the average shear stress, the heat times did not noticeably change with decreases of 0% to 6.1%, but the cooling times did noticeable change with increases of 8.8% to 38.5% and did not correlate as well to the experimental values as the original calculations did. However, using different stress coefficients also affected the calculated reaction times. If one used the average shear stresses along with 5 MPa/°C stress influence coefficients as opposed to 7 MPa/°C, one would get reaction times quite similar to the original calculations; in relation, the heat times had decreases of 0% to 1.5% while the cooling times had increases of 1.9% to 8.3%. These recalculations indicate that it is

important to know the true stress influence coefficients when calculating the new transition temperatures along with an appropriate shear stress. Further study would be needed to both test the Flexinol® wire for its true stress influence coefficients and see if an averaged or maximum shear stress can be used for the reaction time calculations. Nonetheless, the results demonstrate that superelasticity cannot be ignored when calculating the cooling reaction times. For comparison purposes, the original calculations were used for the remainder of the discussion.

With regard to why the predicted heat times did not accurately reflect the true heat times, the author believes it has to do with the mechanical work the shape memory wire is performing on the bias mass. The equations don't take account of the fact that the recovery force is accelerating the bias mass, a feat that would no doubt require longer heat times to perform and would depend on the size of the bias mass. A smaller bias mass would accelerate more in comparison to a larger one and would thus take less time to move. If one wanted to investigate another predicted heat time equation, the applied acceleration onto the mass should no doubt play an important factor.

Divided further into 6 subsections, one for each manipulated variable, the remainder of this section will present and discuss the results from each manipulated variable experiment.

6.6.1 Wire Diameter

A total of four trials were performed at the various wire diameter settings for a total of 16 trials. The results for each trial are presented in Table C-27 through Table C-31; a summary of the results (*i.e.* the averaged median values and pooled % standard deviations) are presented in Table 6-16. In relation to the wire diameter, Figure 6-27 visually presents the experimental reaction times along with the predicted times with and without accounting for superelasticity, while Figure 6-28 visually presents the experimental austenite lengths, martensite lengths, and strokes along with the predicted results that ignore transformation strain. With reference to the predictions made in Table 6-13, the heating times and cooling times were expected to increase in relation to an

increased wire diameter. The predictions were confirmed as both the heat times and cooling times indeed increased upon each subsequent increase in wire diameter. However, as Table 6-16 shows, the predicted heat reaction times were greatly underestimated, with and without accounting for superelastic effects. The error of the superelastic heat time predictions ranged from -46.8% at the highest wire diameter (0.375 mm) to -76.7% at the lowest wire diameter (0.145 mm). The heat prediction model therefore inadequately represents the true heat times, especially at lower wire diameters.

Table 6-16: A Summary of the Results from the Wire Diameter Manipulation

Wire Diameter (Inches)/Measured Wire Diameter (mm)	0.006"/ 0.145 mm	0.008"/ 0.192 mm	0.010"/ 0.248 mm	0.015"/ 0.375 mm
Averaged Median Heat Time (s)	2.83	3.32	6.27	7.80
Pooled % Standard Deviation From Mean	82.8%	36.6%	25.9%	20.8%
% Error in Predicted Heat Time (Accounting for Superelasticity)	-76.7%	-67.2%	-71.5%	-46.8%
Averaged Median Cooling Time (s)	3.13	6.94	12.7	14.8
Pooled % Standard Deviation From Mean	14.7%	16.2%	16.9%	19.9%
% Error in Predicted Cooling Time (Accounting for Superelasticty)	-16.9%	-4.9%	6.3%	114.9%
Averaged Median Austenite Length (cm)	14.5	7.1	3.0	5.5
Pooled % Standard Deviation From Mean	2.8%	7.4%	7.1%	10.3%
Averaged Median Martensite Length (cm)	17.8	16.8	13.2	15.8
Pooled % Standard Deviation From Mean	0.3%	0.5%	4.3%	4.7%
Averaged Median Stroke (cm)	3.3	9.6	10.2	10.2
Pooled % Standard Deviation From Mean	12.3%	4.7%	5.3%	5.80%
Estimated Shear Stress (MPa)	823	355	167	50
Estimated Von-Mises Stress (MPa)	1426	614	290	87

The original cooling time prediction model greatly overestimated the cooling times, having % errors higher than 400%. However, the superelastic cooling time predictions showed very good correlation with the experimental results. The predicted results for the 0.145 mm, 0.192 mm, and 0.248 mm wires respectively had errors of -16.9%, -4.9%, and 6.3%, the latter two having errors within the standard deviation. However, the superelastic predicted cooling time for the largest wire, 0.375 mm, was greatly overestimated having an error of 115%. This may be attributed to the increased heat capacity of the larger diameter wire; the bias mass thus moved slower in comparison to the smaller diameters, making it easier for the control system to switch the transistor too hastily before the transformation had actually finished. Having said that, none of the measurements were remotely close to the predicted time of 31.8 seconds; the longest

cooling time measured was around 20 seconds. It is therefore unlikely that heat capacity is the cause for the overestimated cooling time for the 0.375 mm wire. It may have to do with limits in stroke, to be discussed next. To see if the cooling times continue to converge (*i.e.* if the heat times and cooling times converge or even decrease), the experiments should be further performed at larger wire diameters.

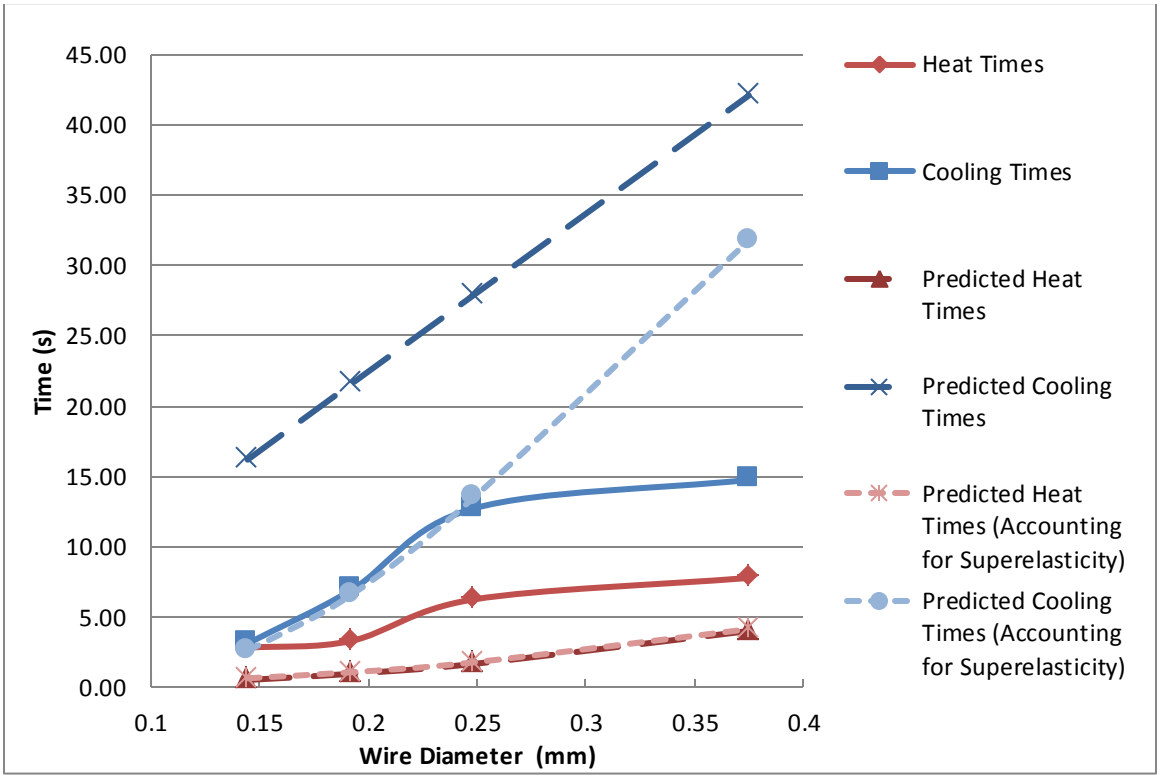

Figure 6-27: The Experimental and Predicted Heat and Cooling Times in relation to the SMA spring's wire diameter. Heating and cooling times are respectively presented as red and blue. Solid lines represent the experimental results, while the dashed lines represent the predicted results without accounting for superelasticity (darker hue with longer dashed lines) and with superelasticity (lighter hue with shorter dashed lines)

With regards to the predictions made in Table 6-13, the stroke was expected to decrease in relation to an increased wire diameter. This prediction did not correlate with the results. When increased from 0.145 mm to 0.192 mm, the stroke nearly tripled from 3.3 cm to 9.6 cm before converging to a set stroke value of 10.2 cm at subsequent wire diameters. The explanation for this result lies within the internal stresses and change in spring diameter. At the lowest wire diameter, the von-Mises stress is at 1426 MPa, a value that is well beyond the tensile yield strengths of both austenite and martensite (see

Table 6-1). The spring is therefore being forced to go beyond its elastic limit, causing permanent plastic deformation. This was demonstrated in the austenite length calculation as the results showed an austenite length that was almost 5 cm longer than the predicted austenite length. Also, there was a significant change in diameter during the austenite to martensite transformation. As the martensite de-twins from the stress applied by the bias mass, the spring diameter decreases. Looking at the deflection formulas, a decrease in spring diameter would significantly affect the deflections as they correlate with the spring diameter to the third power. This explains the low martensite length observed at 0.145 mm diameter wire.

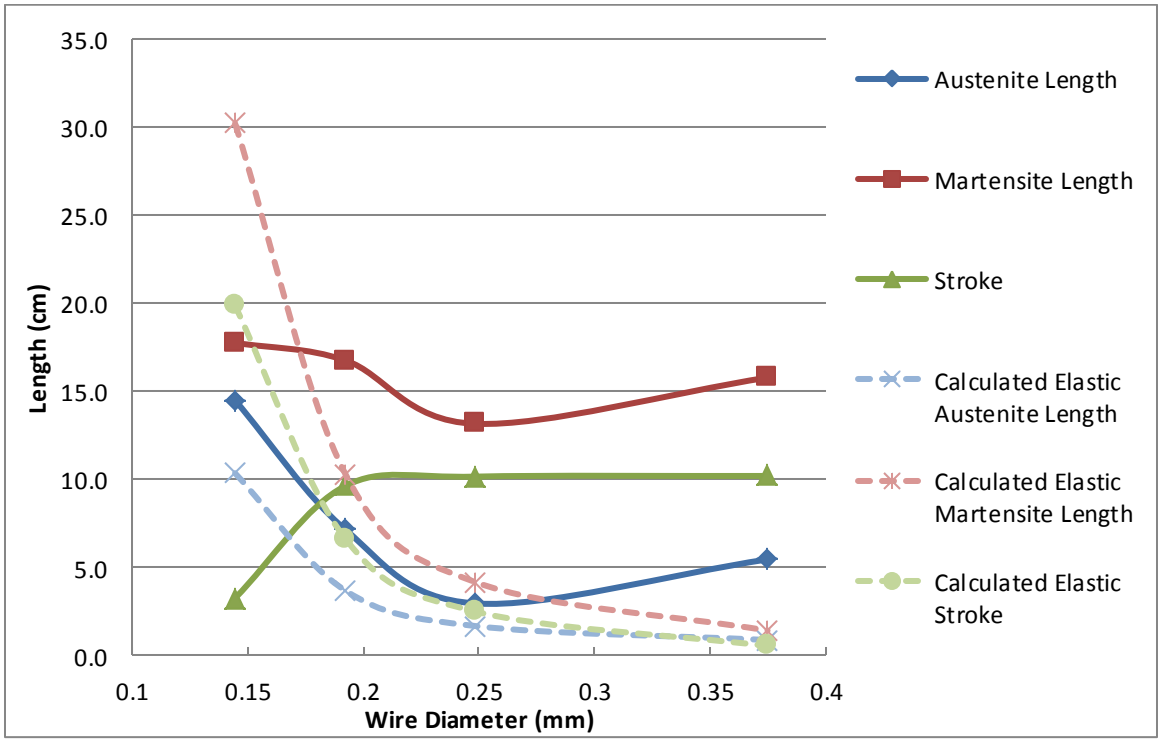

Figure 6-28: The Experimental Spring Lengths and Strokes of the Wire Diameter Manipulation those calculated from solely using the mechanical elastic properties (i.e. Equation 6-67). The Austenite Lengths, Martensite Lengths, and Strokes are respectively presented in blue, red, and green; while the experimental results and mechanical elastic property calculations are respectively presented as solid and dashed lines

In comparison to the predicted elastic strokes and deflections, the results support that these predictions are indeed unreliable as the stroke and martensite lengths are much longer than what the predictions dictate. These results demonstrate that the transformation strain cannot be overlooked when calculating the stroke and martensite lengths. The predictions also underestimated the true austenite lengths, but it should be

pointed out that the true austenite lengths decreased in a similar pattern to the predicted pattern (with exception of the 0.375 mm diameter wire). It is conceivable that the wrong modulus of rigidity was used in the predictions. If these experiments were to be done again, it would be recommended for the Flexinol® wire to go through a tensile test to get more accurate material properties.

What's interesting about the stroke results is the convergence to a value of 10.2 cm with increasing wire diameter. One possible explanation is that the bias force is large enough in all settings to fully de-twin the martensite (*i.e.* $H^{cur}(\sigma)$ is ε_L as presented in Equation 6-1), allowing for a maximum twisting angle for the wire diameter at larger diameters where the predicted elastic strokes are much lower and therefore more negligible. If this was the case, austenite would theoretically go through some cyclic permanent deformation as the maximum transformation strain has been surpassed. Permanent transformation deformation was indeed observed during the tests as the austenite length would generally be the lowest at the first reading, and gradually increase as it went through the twenty oscillations in a trial. In addition, when the bias mass was removed (from each trial), the SMA spring would not completely go back to its compressed spring length when activated, indicating that the maximum transformation strain was exceeded, and permanent transformation strain had occurred. Also supporting this convergence explanation is the maximum strain indicated by Dynalloy®. On Dynalloy™'s technical specifications of Flexinol® wire, they indicate that when the wire experiences a stress of 103 MPa or higher, its maximum transformation strain approaches 5%. This implies that once a certain stress has been reached, the maximum transformation strain has been reached. Looking at Table 6-16, it is shown that all of the wires except the 0.375 mm have an estimated Von-Mises stress above the maximum transformation stress of 103 MPa, implying that most of the wire diameters are in a state of stress where the maximum transformation strain has been surpassed and would thus limit the transformation stroke to a set value. Although the 0.375 mm did not pass the 103 MPa maximum transformation stress, it came quite close at an estimated value of 87 MPa. If one took account of the stress concentration factors highlighted in Equation 6-63, the estimated von-Mises stress would rise further to 94 MPa. With the change in spring diameter from

detwinning the martensite, the estimated stress would further increase indicating that it is conceivable for the maximum transformation stress to have been reached at this wire diameter.

Although the explanation of a maximum twisting angle seems conceivable, further experimentation is needed for support. The author would recommend repeating this experiment at different spring diameters to see if there is also a converged stroke value and also at larger wire diameters to see if the converging trend continues. The author believes that at a certain wire diameter, the internal stress would not be large enough to fully de-twin the martensite and the stroke would in turn decrease.

6.6.2 Spring Diameter

A total of four trials were performed for the 2.34 mm, 3.175 mm, and 4.80 mm inner spring diameters, while a total of three trials were performed for the 6.36 mm inner spring diameter. As one of the time trials was not recorded properly, there are only two time trials and three deflection trials for the 6.36 mm spring diameter manipulation. The results for each trial are presented in Table C-32 through Table C-36; a summary of the results are presented in Table 6-17. In relation to the spring diameter, Figure 6-29 visually presents the experimental reaction times along with the prediction times with and without accounting for superelasticity, while Figure 6-30 visually presents the experimental austenite lengths, martensite lengths, and strokes along with the predicted results that ignore transformation strain.

With reference to the predictions made in Table 6-13, the heating times and cooling times were not expected to change in relation to an increased spring diameter. This was because it was assumed that superelasticity was not a factor in determining the heat and cooling times. After re-evaluating the reaction times with superelasticity, it was found that the heat times did increase with increasing spring diameter (1.76 s, 1.79 s, 1.85 s, and 1.91 s), while the cooling times decreased with increasing spring diameter (15.4 s, 13.5 s, 10.9 s, and 9.1 s). Like the wire diameter manipulation, the predicted heat times for the spring diameter manipulation grossly underestimated the actual time with errors ranging

from -65.4% to -80.5%. However, the experimental heat times tended to rise with increasing spring diameter which was in line with the predicted results, but converged somewhat when increased from 4.80 mm to 6.36 mm. Like the wire diameter manipulation, the cooling time predictions correlated quite well with the results, having errors of -4.3% to 27.6%. Like the predictions, the actual cooling times decreased with respect to spring diameter; but unlike the predictions, increased at the largest spring diameter. The reason for this increase in time is unknown, but it should be noted that only two sets of reaction time data were obtained at the 6.36 mm spring diameter. Perhaps if more trials were performed, the averaged median may have been more in line with the predicted trend.

Table 6-17: A Summary of the Results from the Spring Diameter Manipulation

Measured Inner Spring Diameter (Rod Diameter)	2.34 mm	3.175 mm	4.80 mm	6.36 mm
Averaged Median Heat Time (s)	5.08	6.27	9.50	9.30
Pooled % Standard Deviation From Mean	9.3%	25.9%	21.5%	15.2%
% Error in Predicted Heat Time (Accounting for Superelasticity)	-65.4%	-71.5%	-80.5%	-79.5
Averaged Median Cooling Time (s)	16.1	12.7	8.54	10.6
Pooled % Standard Deviation From Mean	11.4%	16.9%	39.8%	36.2%
% Error in Predicted Cooling Time (Accounting for Superelasticity)	-4.3%	6.3%	27.6%	-14.2%
Averaged Median Austenite Length (cm)	1.7	3.0	8.1	15.9
Pooled % Standard Deviation From Mean	4.9%	7.1%	7.6%	6.1%
Averaged Median Martensite Length (cm)	7.5	13.2	23.4	31.8
Pooled % Standard Deviation From Mean	8.3%	4.3%	1.6%	0.5%
Averaged Median Stroke (cm)	5.8	10.2	15.2	15.8
Pooled % Standard Deviation From Mean	11.2%	5.3%	4.3%	6.1%
Estimated Shear Stress (MPa)	127	167	247	323
Estimated Von-Mises Stress (MPa)	219	290	427	559

With reference to the predictions made in Table 6-13, it was predicted that the strokes would increase with increasing spring diameter. The results did indeed show an increased stroke as the spring diameter increased from 2.34 mm, to 3.175 mm, and to 4.80 mm; but similar to the wire diameter manipulation, the stroke converged when increased to the final spring diameter, 6.36 mm. Although most likely coincidental, the converged value is quite close to the value predicted by the elastic model. One possible explanation for the convergence is the increased internal stress. At the 2.34 mm, 3.175 mm, 4.80 mm, and 6.36 mm spring diameters, the internal von-Mises stress respectively

increased from 219 MPa, to 290 MPa, to 427 MPa, and finally to 550 MPa. One explanation is that the maximum transformation strain ε_L was reached between 427 MPa and 550 MPa, thus limiting the twisting of the SMA wire; however, this explanation does not correlate with the results achieved from the wire diameter manipulations. The wire diameter manipulations showed a converged stroke as the internal stress decreased to a value as low as 87 MPa. Perhaps the yield stress is being reached as the spring diameter increases, thus causing permanent elastic strain rather than permanent transformation strain. During an austenite to martensite transformation, larger spring diameters are more prone to have their diameters reduced when the bias-mass de-twins the martensite as it better disperses the internal stress. If the total internal stress exceeds the austenite yield stress when the spring is activated back to its austenite phase, the spring will not be able to completely return to its original spring diameter and would thus have a larger austenite length than predicted. Looking at Figure 6-30, the austenite lengths did seem to increase more than expected, but this may be attributed to permanent transformation strain assuming that the maximum transformation strain was exceeded. With regards to the

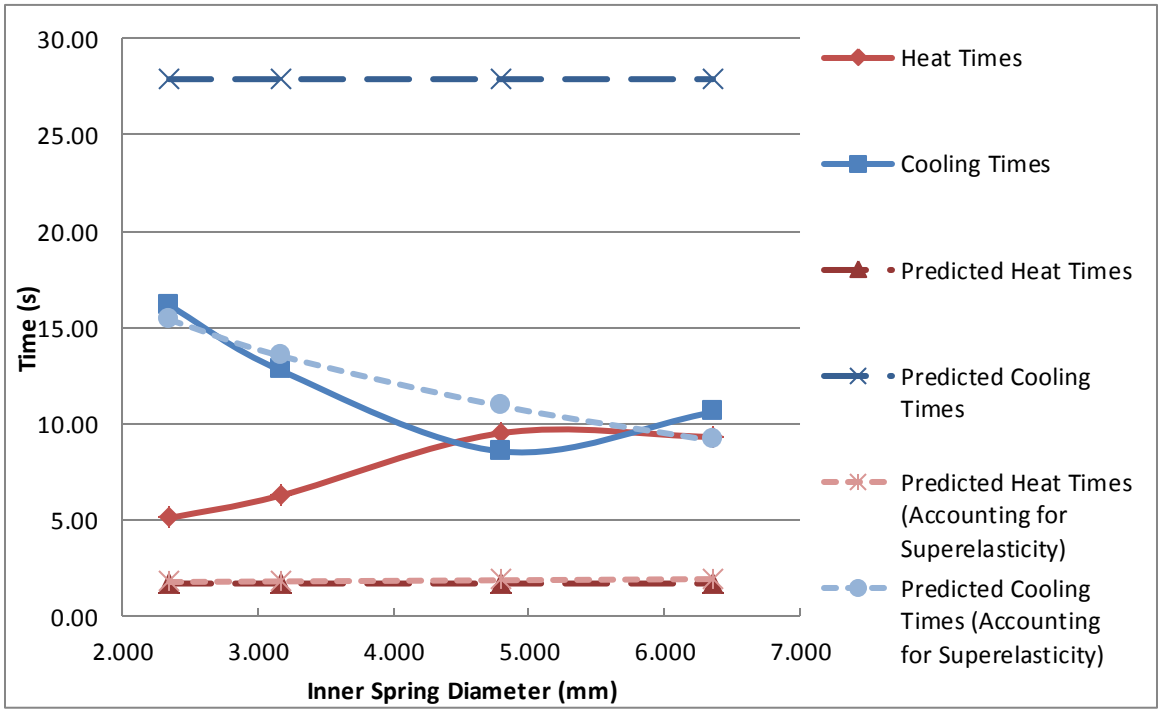

Figure 6-29: The Experimental and Predicted Heat and Cooling Times in Relation to the SMA spring's Inner Spring Diameter. Heating and Cooling Times are respectively presented as red and blue. Solid lines represent the experimental results, while the dashed lines represent the predicted results without accounting for superelasticity (darker hue with longer dashed lines), and with superelasticity (lighter hue with shorter dashed lines)

martensite length, Figure 6-30 also shows a less than expected martensite length. Although the author reiterates that the true martensite lengths should be larger than those predicted from the elastic model, the lengths should nonetheless increase in a similar pattern assuming that the martensite has been completely de-twinned in all trials. The martensite lengths should therefore increase in a concave up pattern, rather than the linear or concave down pattern shown in Figure 6-30. The author attributes this pattern to the decrease in spring diameter during the martensite phase. Looking at the spring deflection equation (Equation 6-61), a decrease in spring diameter would in turn decrease the overall martensite deflection. This decrease in martensite deflection also likely contributed to the converged stroke value.

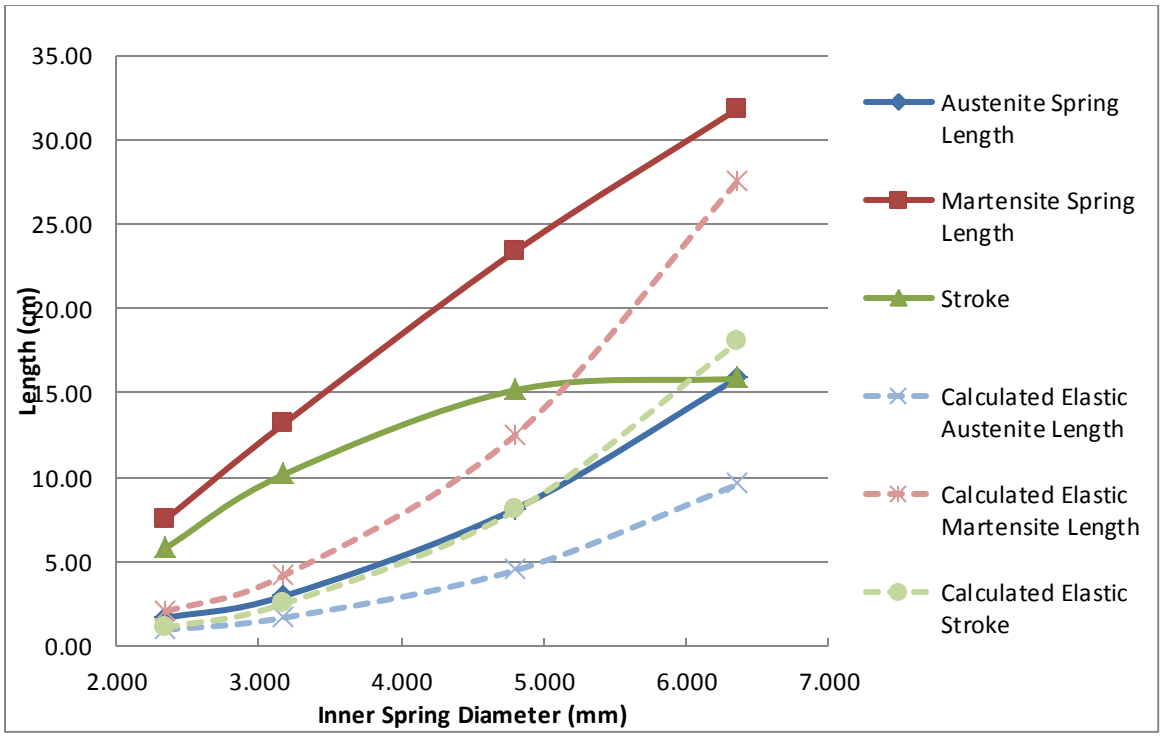

Figure 6-30: The Experimental Spring Lengths and Strokes of the Spring Diameter Manipulation and those calculated from solely using the mechanical elastic properties (i.e. Equation 6-67). The Austenite Lengths, Martensite Lengths, and Strokes are respectively presented in blue, red, and green; while the experimental results and mechanical elastic property calculations respectively presented as solid and dashed lines.

It would be recommended to attempt the experiments at higher spring diameters to see if the value still converges or if the stroke begins to decrease. The author would expect the stroke to decrease after a certain spring diameter as the martensitic spring diameter would be more inclined to decrease when loaded with a bias mass, thus increasing the internal

stresses and making it more difficult for the SMA spring to return to its original austenite spring diameter when activated.

From the results thus far obtained from the wire diameter and spring diameter manipulations, it appears that the internal stress is the underlying factor in achieving the maximum stroke at a certain variable. The internal stress must be large enough so that the maximum transformation strain can be achieved, but must be low enough to not cause plastic yielding when activated.

6.6.3 Transition Temperature

Using the 90°C Flexinol® wire, four trials were performed using 0.195 mm and 0.243 mm wire diameters while three trials were performed using 0.144 mm wire. The results for each trial are presented in Table C-37 through Table C-41; a summary of the results are presented in Table 6-18. In relation to the wire diameter, Figure 6-32 visually presents the experimental reaction times for both the 70 °C and 90 °C Flexinol® wire along with the predicted times with and without accounting for superelasticity, while Figure 6-31 visually presents the experimental austenite lengths, martensite lengths, and strokes along with the predicted results that ignore transformation strain.

Table 6-18: A Summary of the Results from Various Wire Diameters using 90°C Flexinol® Wire

Wire Diameter/ Measured Wire Diameter for the 90°C Transition Temperature	0.006"/ 0.144 mm	0.008"/ 0.195 mm	0.010"/ 0.243 mm
Averaged Median Heat Time (s)	2.21	2.98	5.84
Pooled % Standard Deviation From Mean	113.9%	63.6%	45.7%
% Error in Predicted Heat Time (Accounting for Superelasticity)	-69.7%	-61.4%	-69.9%
Averaged Median Cooling Time (s)	3.57	4.95	6.40
Pooled % Standard Deviation From Mean	43.8%	64.8%	35.6%
% Error in Predicted Cooling Time (Accounting for Superelasticity)	-32.8%	23.2%	68.8%
Averaged Median Austenite Length (cm)	17.4	15.0	10.7
Pooled % Standard Deviation From Mean	2.4%	6.7%	14.3%
Averaged Median Martensite Length (cm)	17.6	18.1	17.5
Pooled % Standard Deviation From Mean	0.3%	0.4%	1.8%
Averaged Median Stroke (cm)	0.1	3.1	6.7
Pooled % Standard Deviation From Mean	106.1%	22.6%	13.8%
Estimated Shear Stress (MPa)	823	355	167
Estimated Von-Mises Stress (MPa)	1426	614	290

With relation to the reaction times, it was predicted that the heat times and cooling times would respectively increase and decrease with an increased transition temperature. With regards to heat times, there was no noticeable difference between the 70 °C and 90 °C wires at all wire diameters. This is likely due to the fact that the heating happens rather rapidly using direct current; the predicted heating times were very close together as well. With regards to the cooling times, the predictions were generally correct; the 90 °C wires at 0.008" and 0.010" retracted faster, while there was no observable difference at the 0.006" wires. However, the predicted cooling times were not as accurate for the 90 °C wires; the % errors were -32.8%, 23.8%, and 68.8% which are less accurate than the 70 °C wires (16.9%, -4.9%, and 6.3%).

With relation to the reaction times, it was predicted that the heat times and cooling times would respectively increase and decrease with an increased transition temperature. With regards to heat times, there was no noticeable difference between the 70 °C and 90 °C wires at all wire diameters. This is likely due to the fact that the heating happens rather rapidly using direct current; the predicted heating times were very close together as well. With regards to the cooling times, the predictions were generally correct; the 90 °C wires at 0.008" and 0.010" retracted faster, while there was no observable difference at the 0.006" wires. However, the predicted cooling times were not as accurate for the 90 °C wires; the errors were -32.8%, 23.8%, and 68.8% which are less accurate than the 70 °C wires (16.9%, -4.9%, and 6.3%).

In relation to the stroke, it was predicted that the stroke would not change; this was not reflected in the results. The stroke decreased when the transition temperature was raised to 90 °C. Not only did the strokes decrease, but the wires observably suffered more from fatigue. For example, for the 0.006" wire made with 90°C Flexinol® wire, the stroke started at about 1.2 cm during the first activation, but decreased to 0.1 cm by the tenth activation. This fatigue provided very poor stroke statistics as the pooled standard deviations were quite large being 13.8%, 22.6%, and 106.1%. In fact, 46.7% of all the

standard deviations for the 90 °C Flexinol® wire (*i.e.* both reaction times and deflections) were over 20%. Fatigue is likely the cause for the poor statistics.

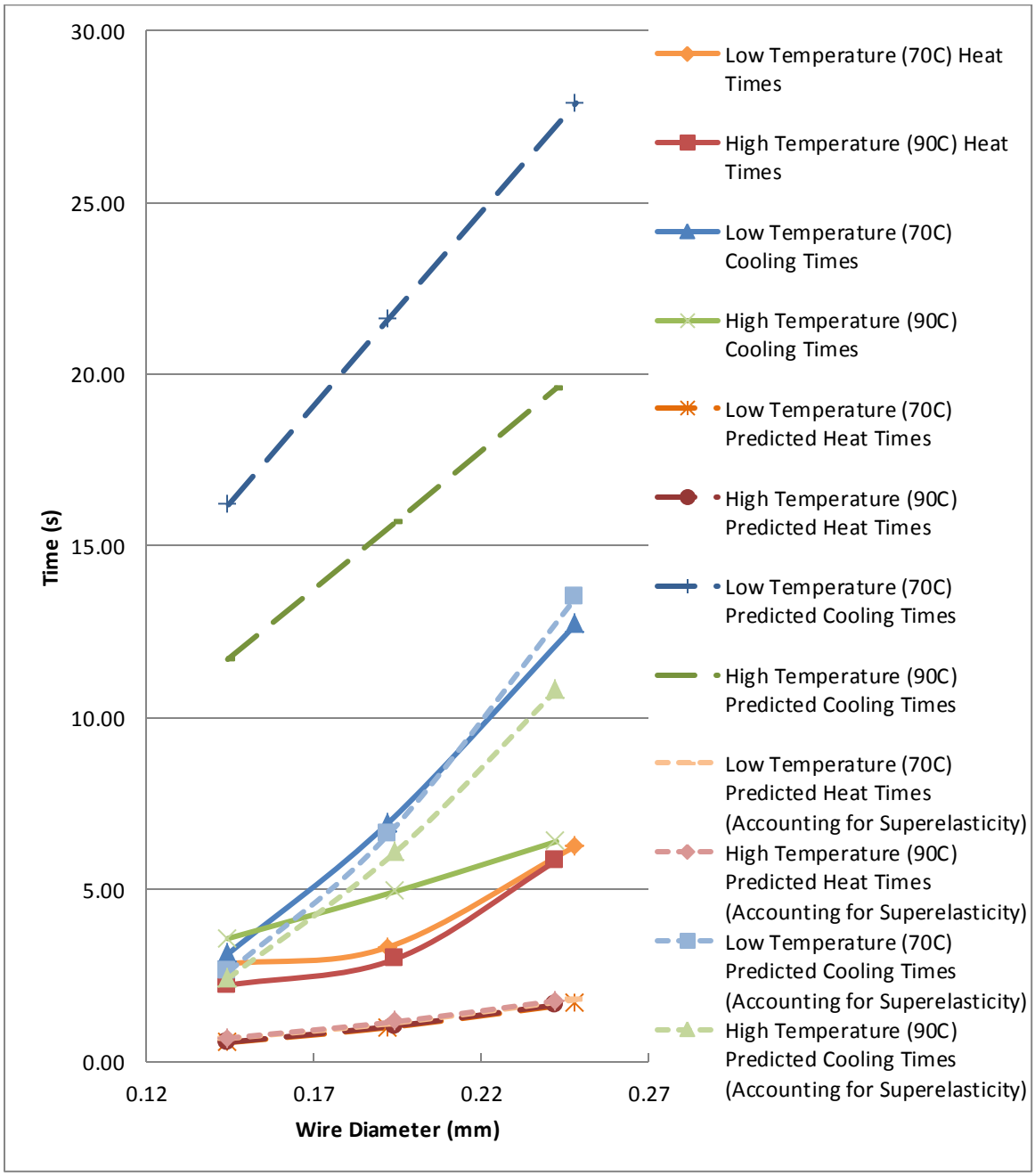

Figure 6-31: The Experimental Spring Lengths and Strokes of the Transition Temperature manipulation and those calculated from solely using the mechanical elastic properties (i.e. Equation 6-67). The Austenite Lengths, Martensite Lengths, and Strokes are respectively presented in blue, red, and green; the experimental results and mechanical elastic property calculations respectively presented as solid and dashed lines; and the 70 °C and 90 °C are respectively presented as darker and lighter hues.

Evidently, the 90 °C wire is not as strong as the 70 °C wire. This may be due to different additives in the 90 °C wire that were added by the manufacturer to increase its transition temperature. The additives may have inadvertently weakened the material's properties. However, recalling Section 6.2.10.1, additives are more likely to strengthen the material rather than weaken it. A more plausible explanation is that the Flexinol® wires were aged on purpose by the manufacturer to increase the transition temperature. As presented in Section 6.2.10.2, aging will increase the transition temperature, but at the expense of its strength properties including the upper plateau strength. A decreased upper plateau strength would in turn decrease the maximum transformation strain; this correlates with the experimental results.

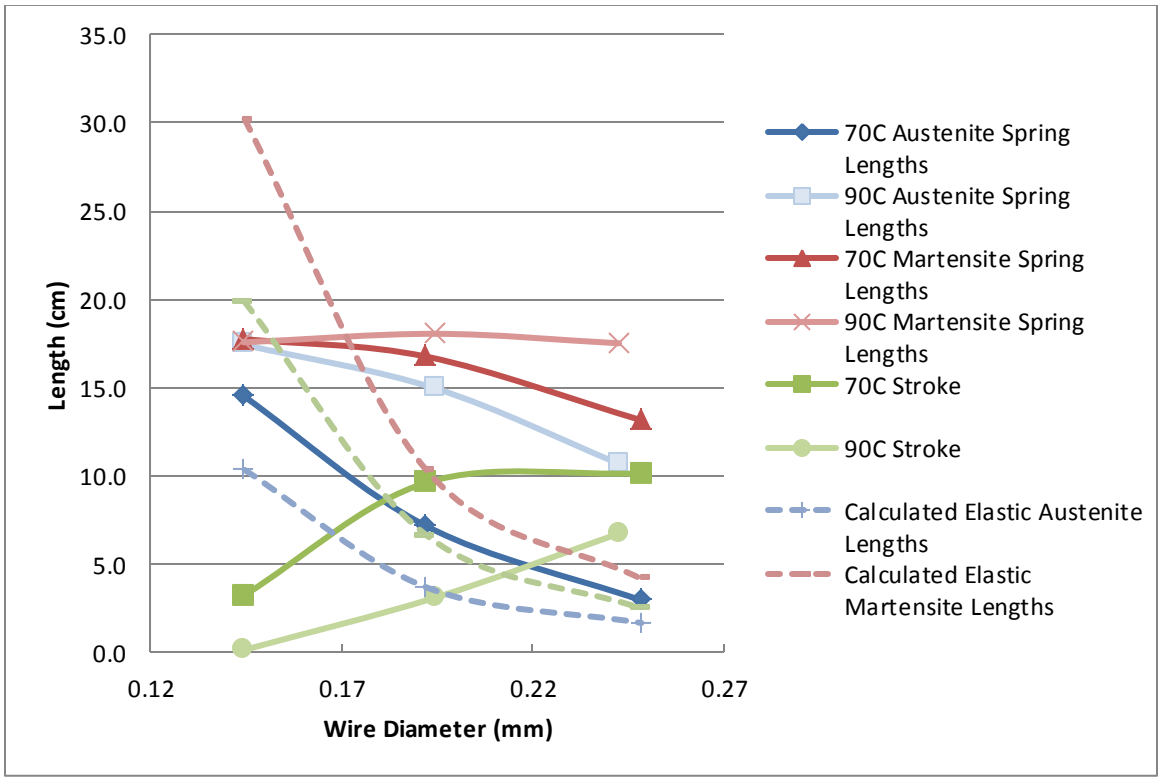

Figure 6-32: The Experimental and Predicted Heat and Cooling Times in Relation to the SMA spring's Transition Temperature and Wire Diameter. Heating and Cooling Times are respectively presented as orange (for 70 °C) and red (for 90 °C), and blue (for 70 °C) and green (for 90 °C). Solid lines represent the experimental results, while the dashed lines represent the predicted results without accounting for superelasticity (darker hue with longer dashed lines), and with superelasticity (lighter hue with shorter dashed lines)

6.6.4 Number of Spring Turns

A total of four trials were performed for each spring turn setting for a total of 16 trials. The results for each trial are presented in Table C-42 through Table C-46; a summary of the results are presented in Table 6-19. In relation to the number of turns, Figure 6-33 visually presents the experimental reaction times along with the predicted times with and without accounting for superelasticity, while Figure 6-34 visually presents the experimental austenite lengths, martensite lengths, and strokes along with the predicted results that ignore transformation strain.

Table 6-19: A Summary of the Results from the Number of Spring Turns Manipulation

Number of Spring Turns	8	12	16	20
Averaged Median Heat Time (s)	6.49	6.13	6.27	6.04
Pooled % Standard Deviation From Mean	13.9%	14.8%	25.9%	11.2%
% Error in Predicted Heat Time (Accounting for Superelasticity)	-72.4%	-70.8%	-71.5%	-70.4%
Averaged Median Cooling Time (s)	10.4	13.0	12.7	12.7
Pooled % Standard Deviation From Mean	12.0%	13.5%	16.9%	15.9%
% Error in Predicted Cooling Time (Accounting for Superelasticity)	29.8%	3.8%	6.3%	6.3%
Averaged Median Austenite Length (cm)	1.8	2.4	3.0	3.8
Pooled % Standard Deviation From Mean	9.3%	6.1%	7.1%	5.0%
Averaged Median Martensite Length (cm)	7.4	10.5	13.2	17.1
Pooled % Standard Deviation From Mean	2.3%	8.6%	4.3%	14.7%
Averaged Median Stroke (cm)	5.5	8.2	10.2	13.3
Pooled % Standard Deviation From Mean	4.0%	11.0%	5.3%	19.0%
Estimated Shear Stress (MPa)	167	167	167	167
Estimated Von-Mises Stress (MPa)	290	290	290	290

With reference to the reaction times, it was predicted that neither the heat times nor cooling times would change in relation to increasing the number of spring turns. These predictions turned out to be quite accurate overall. The heat times were all within 0.5 seconds of each other, while the three out of four of the cooling times were within 0.3 seconds of each other. All results had reasonable pooled standard deviations; the heat times ranged from 11.2% to 25.9% while the cooling times ranged from 12.0% to 16.9%. Like the previous manipulations, the predicted heat times greatly underestimated the actual heat times with % errors ranging from -70.4% to -72.4%, and the predicted cooling times that accounted for superelasticity were in great correlation with the experimental cooling times with three turn settings having an error of 3.8% to 6.3%. The one

exception was the 8 turn spring which had a cooling time with an error of 29.8% in relation to the predicted time. It is unclear why the 8 turn spring produced a reduced cooling time. One possible explanation is that the bias mass did not have far to move as the spring was shorter. The control system may have interpreted the bias mass as stationary when in fact the mass may still have been slowly moving.

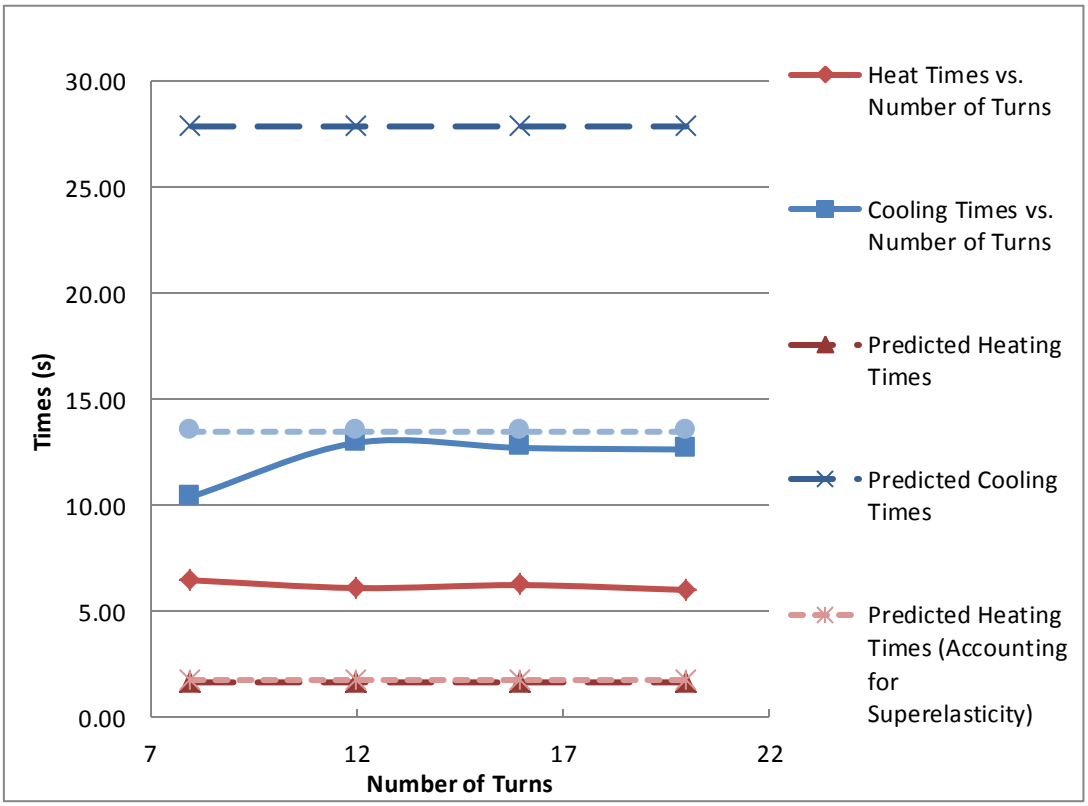

Figure 6-33: The Experimental and Predicted Heat and Cooling Times in Relation to the SMA spring's Number of Turns. Heating and Cooling Times are respectively presented as red and blue. Solid lines represent the experimental results, while the dashed lines represent the predicted results without accounting for superelasticity (darker hue with longer dashed lines), and with superelasticity (lighter hue with shorter dashed lines)

With reference to the stroke, it was predicted that not only the stroke would increase in relation to an increasing number of spring turns, it would increase in a linear fashion as the number of spring turns theoretically have no relation to the overall shear stress. As predicted, the stroke increased in a linear fashion. A linear regression was performed on the results with an R^2 value of 0.993 indicating that the results strongly correlate in a linear manner. Being quadruple the value, the experimental strokes were also much higher than the calculated elastic strokes; further supporting the fact that the

transformation strain cannot be overlooked when calculating the stroke of SMA helical spring actuators.

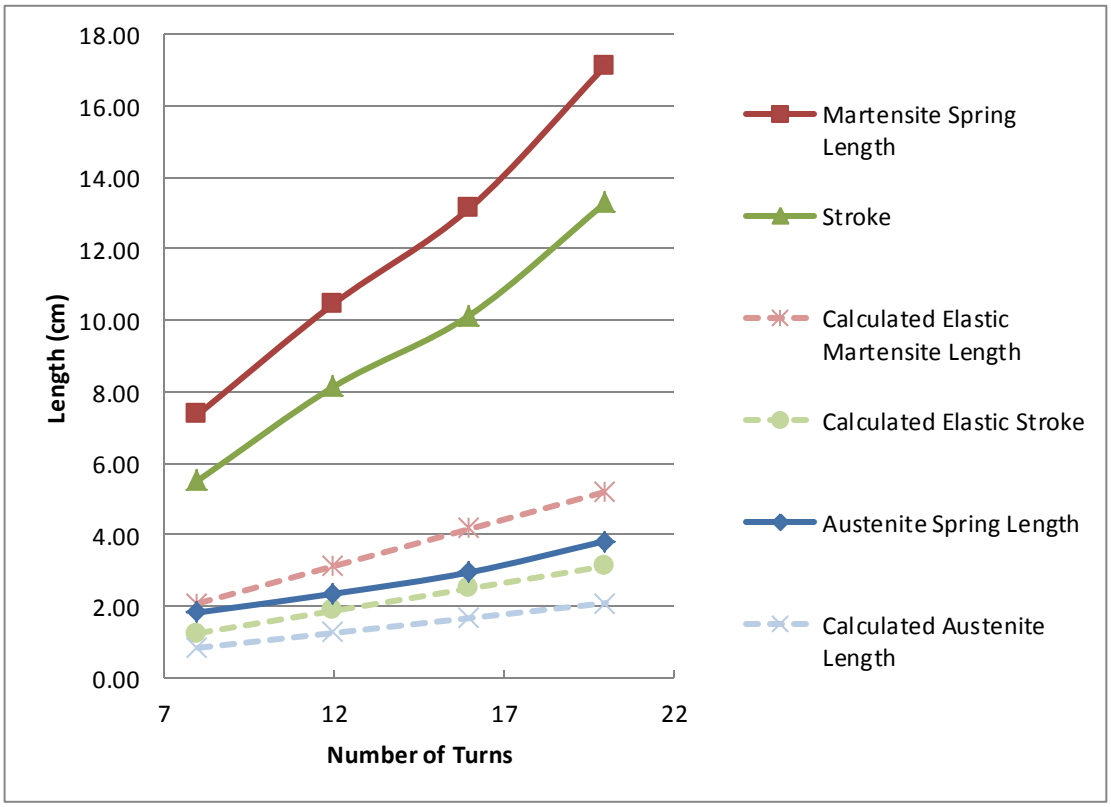

Figure 6-34: The Experimental Spring Lengths and Strokes of the Number of Spring Turns Manipulation and those calculated from solely using the mechanical elastic properties (i.e. Equation 6-67). The Austenite Lengths, Martensite Lengths, and Strokes are respectively presented in blue, red, and green; while the experimental results and mechanical elastic propery calculations respectively presented as solid and dashed lines.

6.6.5 Bias Mass

A total of four trials were performed for each bias mass setting for a total of 16 trials. The results for each trial are presented in Table C-47 through Table C-51; a summary of the results are presented in Table 6-20. In relation to the bias mass, Figure 6-35 visually presents the experimental reaction times along with the predicted times with and without accounting for superelasticity, while Figure 6-36 visually presents the experimental austenite lengths, martensite lengths, and strokes along with the predicted results that ignore transformation strain.

Table 6-20: A Summary of the Results from the Bias Mass Manipulation

Bias Mass	20 g	30 g	40 g	50 g
Averaged Median Heat Time (s)	4.90	6.27	8.63	11.3
Pooled % Standard Deviation From Mean	15.2%	25.9%	26.8%	24.7%
% Error in Predicted Heat Time (Accounting for Superelasticity)	-64.3%	-71.5%	-78.8%	-83.5%
Averaged Median Cooling Time (s)	18.0	12.7	10.9	10.4
Pooled % Standard Deviation From Mean	14.9%	16.9%	13.9%	17.0%
% Error in Predicted Cooling Time (Accounting for Superelasticity)	-9.4%	6.3%	5.5%	-2.9%
Averaged Median Austenite Length (cm)	2.23	2.95	3.9	5.3
Pooled % Standard Deviation From Mean	3.7%	7.1%	9.0%	13.5%
Averaged Median Martensite Length (cm)	10.3	13.2	14.0	15.3
Pooled % Standard Deviation From Mean	6.3%	4.3%	1.8%	1.5%
Averaged Median Stroke (cm)	8.1	10.2	10.1	10.0
Pooled % Standard Deviation From Mean	8.2%	5.3%	3.5%	6.2%
Estimated Shear Stress (MPa)	111	167	223	279
Estimated Von-Mises Stress (MPa)	193	290	386	483

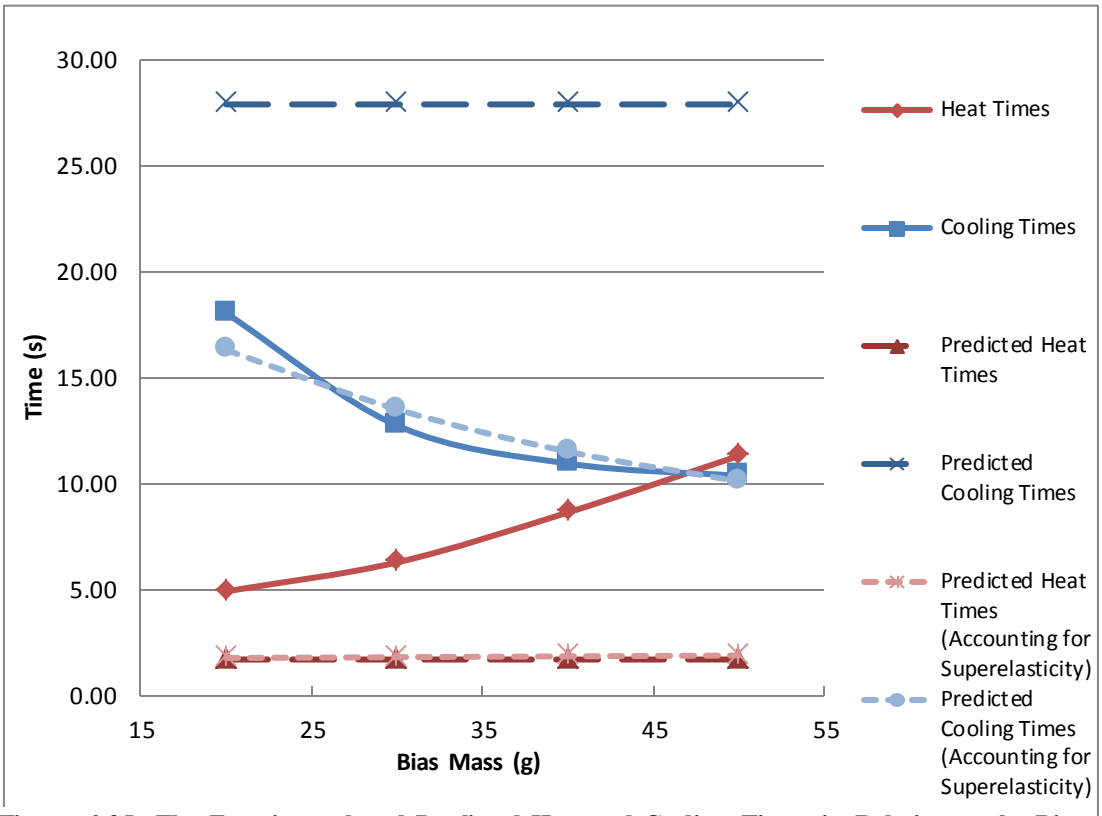

Figure 6-35: The Experimental and Predicted Heat and Cooling Times in Relation to the Bias Mass. Heating and Cooling Times are respectively presented as red and blue. Solid lines represent the experimental results, while the dashed lines represent the predicted results without accounting for superelasticity (darker hue with longer dashed lines), and with superelasticity (lighter hue with shorter dashed lines)

With reference to the reaction times, the original predictions foresaw the bias mass not having an effect on the reaction times. These original predictions, however, were based on ignoring superelasticity. After adjusting the transition temperatures to account for superelasticity, the new predictions foresaw increased heat times and decreased cooling times in relation to an increasing bias mass. These new predictions proved to be correct. Although the experimental heat times increased with an increasing bias mass as predicted, akin to the previous manipulations, the predicted heat times were much less than the actual heat times. The predicted heat times had errors ranging from -64.3% to -83.5%. The cooling time predictions accounting for superelasticity, however, had excellent correlation with the results; the predictions all had errors less than 10%.

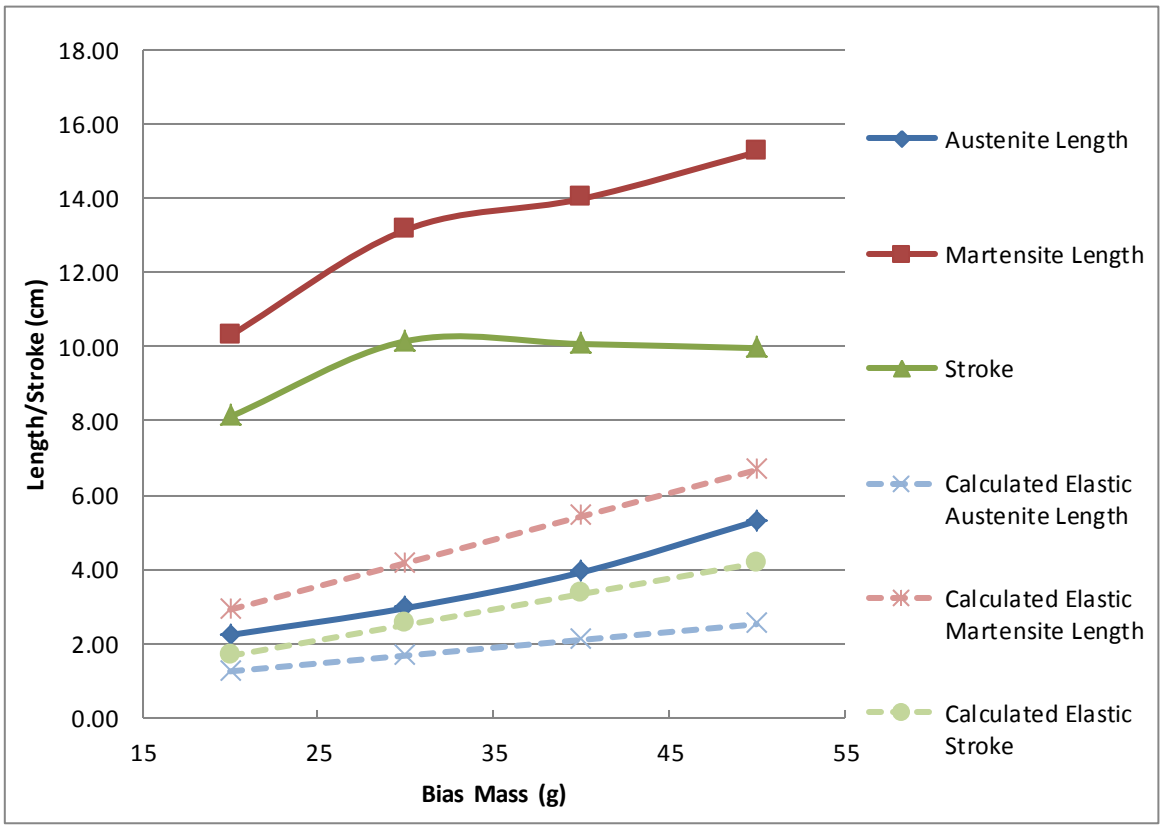

Figure 6-36: The Experimental Spring Lengths and Strokes of the Bias Mass Manipulation and those calculated from solely using the mechanical elastic properties (i.e. Equation 6-67). The Austenite Lengths, Martensite Lengths, and Strokes are respectively presented in blue, red, and green; while the experimental results and mechanical elastic propery calculations respectively presented as solid and dashed lines.

With reference to the stroke, it was predicted that the stroke would increase with an increasing bias mass. While the stroke did increase from roughly 8cm to 10cm when the

bias mass was increased from 20 g to 30 g, the stroke converged after increasing the bias mass to 40g and 50g. This is likely due to the increase in internal stresses as the bias mass was increased. Judging by the martensite lengths displayed in Figure 6-36, the 20 g bias mass did not give the helical spring an adequate stress to fully de-twin the martensite but the bias masses that were 30g or larger were sufficient to de-twin the martensite, allowing the maximum transformation strain to be achieved.

The converged value of the stroke is likely due to the decreased martensite diameter as mentioned earlier. At higher bias masses, the martensite diameter is more prone to decrease thus decreasing the overall martensite deflection as shown in the spring deflection equation (Equation 6-61). At higher bias masses, the spring would experience larger internal stresses, making it more difficult for the spring to fully return to its original austenite spring diameter when activated and in turn making the overall austenite deflection longer than predicted. Assuming that the transformation strain has been surpassed, the martensite and austenite lengths should have the same graphic slopes as the calculated elastic strokes, only the martensite lengths should be shifted vertically for the specific increase in length that is caused by de-twinning the martensite. Looking at Figure 6-36, one would observe that the trials where the transformation strain is assumed to be surpassed (*i.e.* 30 g, 40 g, and 50 g), the martensite length slope is less than the predicted elastic martensite slope while the austenite length slope is larger than the predicted elastic austenite slope. This indicates that the actual martensite lengths are smaller than predicted, while the austenite lengths are greater than predicted. This observation supports the hypothesis that the stroke is stagnating due to the decreased martensite diameter and increased internal stress, but it shouldn`t suggest that this is the only explanation. Other explanations for the different slopes include using inaccurate moduli of rigidity for the calculated elastic deflections and that the increase in austenite lengths may have been due to permanent transformation strain. Further experiments are needed to verify if the slope continues to converge or if this is in fact a peak. The author expects that at a certain increased bias mass, the stroke will begin to decline as the internal stress will continue to increase and the spring diameters will continue to decrease.

6.6.6 Direct Current

A total of three trials were performed for each direct current setting with the exception of the 0.55 A setting in which four trials were performed. The results for each trial are presented in Table C-52 through Table C-56; a summary of the results are presented in Table 6-21. In relation to the direct current, Figure 6-37 visually presents the experimental reaction times along with the predicted times with and without accounting for superelasticity, while Figure 6-38 visually presents the experimental austenite lengths, martensite lengths, and strokes along with the predicted results that ignore transformation strain.

With regards to the reaction times, it was predicted that the heat times and cooling times would respectively decrease and not change with respect to an increasing current. Both predictions proved correct; the heat times indeed decreased while the cooling times remained relatively constant with an increasing direct current. Like the other manipulations, the predicted heat times were greatly underestimated having errors that ranged from -68.9% to -81.9%. Also like the other manipulations, the predicted cooling times while accounting for superelasticity proved to be more reliable, having errors that ranged from 18.4% to 21.6%.

Table 6-21: A Summary of the Results from the Direct Current Manipulation

Direct Current	0.45A	0.50A	0.55A	0.60A
Averaged Median Heat Time (s)	16.2	9.47	6.27	4.69
Pooled % Standard Deviation From Mean	18.8%	31.5%	25.9%	15.7%
% Error in Predicted Heat Time (Accounting for Superelasticity)	-81.9%	-76.2%	-71.5%	-68.9%
Averaged Median Cooling Time (s)	11.1	11.4	12.7	11.0
Pooled % Standard Deviation From Mean	24.5%	18.4%	16.9%	15.8%
% Error in Predicted Cooling Time (Accounting for Superelasticity)	21.6%	18.4%	6.3%	22.7%
Averaged Median Austenite Length (cm)	6.0	3.2	3.0	2.8
Pooled % Standard Deviation From Mean	42.9%	6.0%	7.1%	5.3%
Averaged Median Martensite Length (cm)	14.0	13.2	13.2	12.7
Pooled % Standard Deviation From Mean	3.3%	3.1%	4.3%	3.2%
Averaged Median Stroke (cm)	7.8	10.0	10.2	9.9
Pooled % Standard Deviation From Mean	32.6%	5.1%	5.3%	5.0%
Estimated Shear Stress (MPa)	167	167	167	167
Estimated Von-Mises Stress (MPa)	290	290	290	290

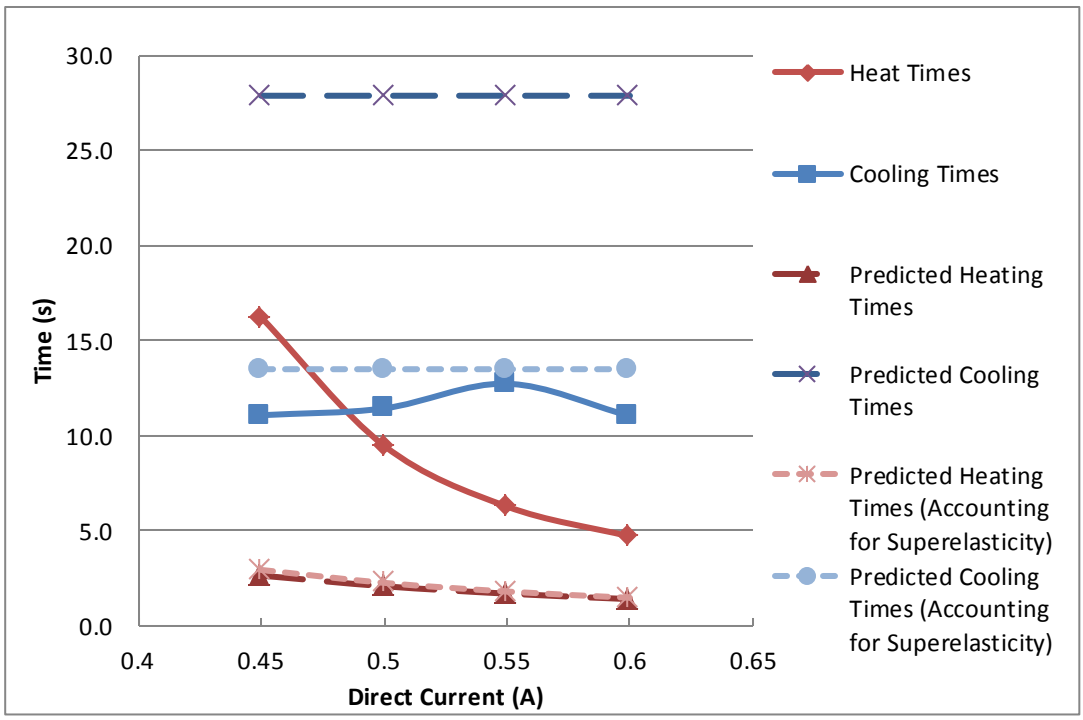

Figure 6-37: The Experimental and Predicted Heat and Cooling Times in Relation to the Bias Mass. Heating and Cooling Times are respectively presented as red and blue. Solid lines represent the experimental results, while the dashed lines represent the predicted results without accounting for superelasticity (darker hue with longer dashed lines), and with superelasticity (lighter hue with shorter dashed lines)

With regards to the strokes, it was predicted that the strokes would be unaffected by a change in direct current providing that the current is sufficient to induce the transformation. This prediction overall aligned with the experimental results as the median strokes for the 0.50 A, 0.55 A, 0.60 A were all around 10 cm. However, the 0.45 A trials produced a median stroke 0f 7.8 cm. The author attributes this to the control system. During the 0.45 A trials, the bias mass often moved quite slowly during the transformation; the control system would often mistake it for being stationary. At times when the control system allowed the spring to fully transform at 0.45 A, the stroke would generally be around 9 to 11 cm, but the control system would often cut this short as low as 4cm as it was moving rather slowly. This was reflected in the 0.45 A stroke's pooled standard deviation of 32.6%. Had the control system allowed the spring to completely transform, the true median stroke value would have been around 10 cm like the other direct current settings.

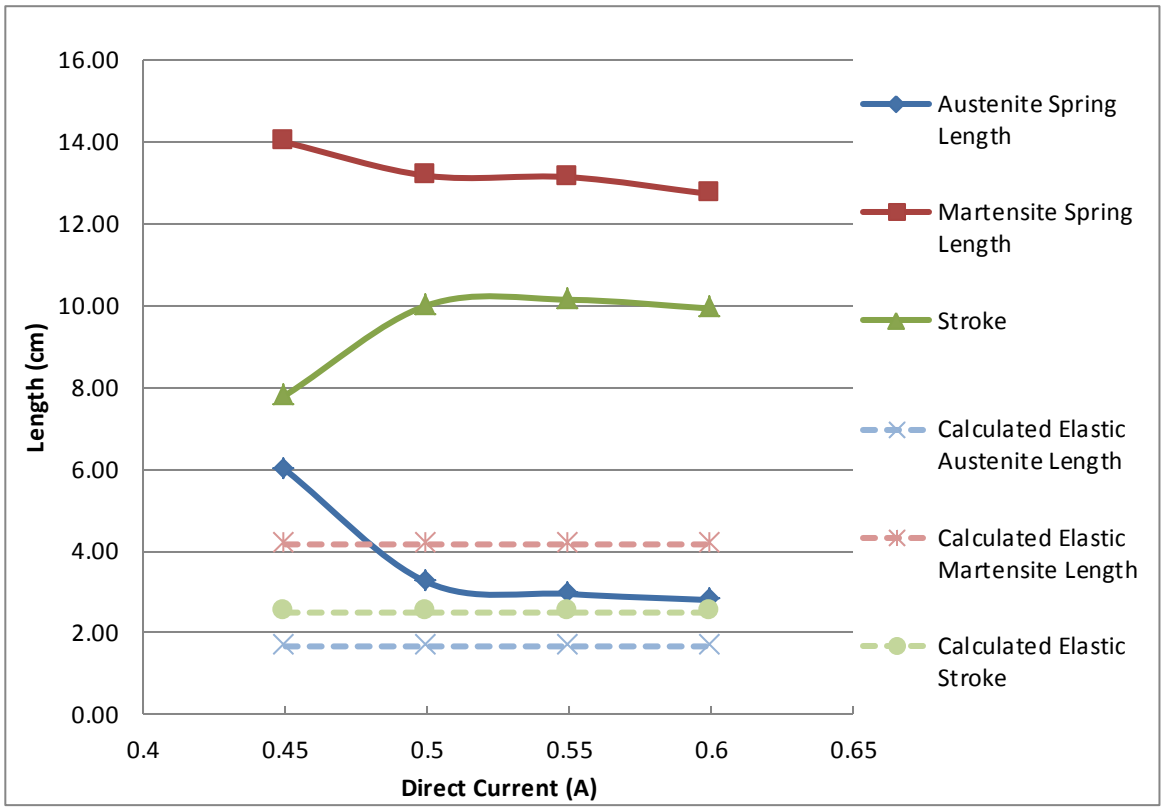

Figure 6-38: The Experimental Spring Lengths and Strokes of the Direct Current Manipulation and those calculated from solely using the mechanical elastic properties (i.e. Equation 6-67). The Austenite Lengths, Martensite Lengths, and Strokes are respectively presented in blue, red, and green; while the experimental results and mechanical elastic property calculations respectively presented as solid and dashed lines.

6.6.7 Cyclic Behavior Investigation

Although an SMA spring's cyclic behavior was not in the overall scope of the thesis, the author felt obligated to perform one trial to test a spring's stability over multiple cycles. After the last trial in the 0.375 mm diameter (70°C transition temperature) wire investigation, the spring was put through five more subsequent tests with each test requiring the SMA spring to undergo 20 more activation cycles. The median heat time, cool time, austenite spring length, martensite spring length, and stroke were then collected over each test to see if the outputs changed over subsequent tests. Figure 6-39 shows a graphic of the results. The heat times remained relatively constant throughout subsequent tests, but the cooling times showed a decrease in time. The largest decrease in cooling time was between the first and second tests where the median cooling time dropped from 14.7 seconds to 11.9 seconds. The cooling time continued to decrease until

converging to 10.2 seconds at the sixth test. The stroke also showed an overall decrease over subsequent tests. Like the cooling times, the largest decrease was between the first and second tests when the median stroke decreased from 10.5 cm to 9.35 cm. The stroke continued to decrease until converging to 8.25 cm at the sixth test; the author postulates that subsequent tests would produce similar stroke values judging by the small change between the fifth and sixth test, but further tests would be necessary for confirmation.

This cyclic behavior testing suggests that the results obtained throughout this thesis may decrease if used under extensive cyclic loading. If the experimental testing were to be done again, it would be recommended to put the SMA helical springs under cyclic loading to observe how they would perform under cyclic use. This would be especially important for applications like the flamenco stage set, where the springs are expected to perform consistently over a long period of time.

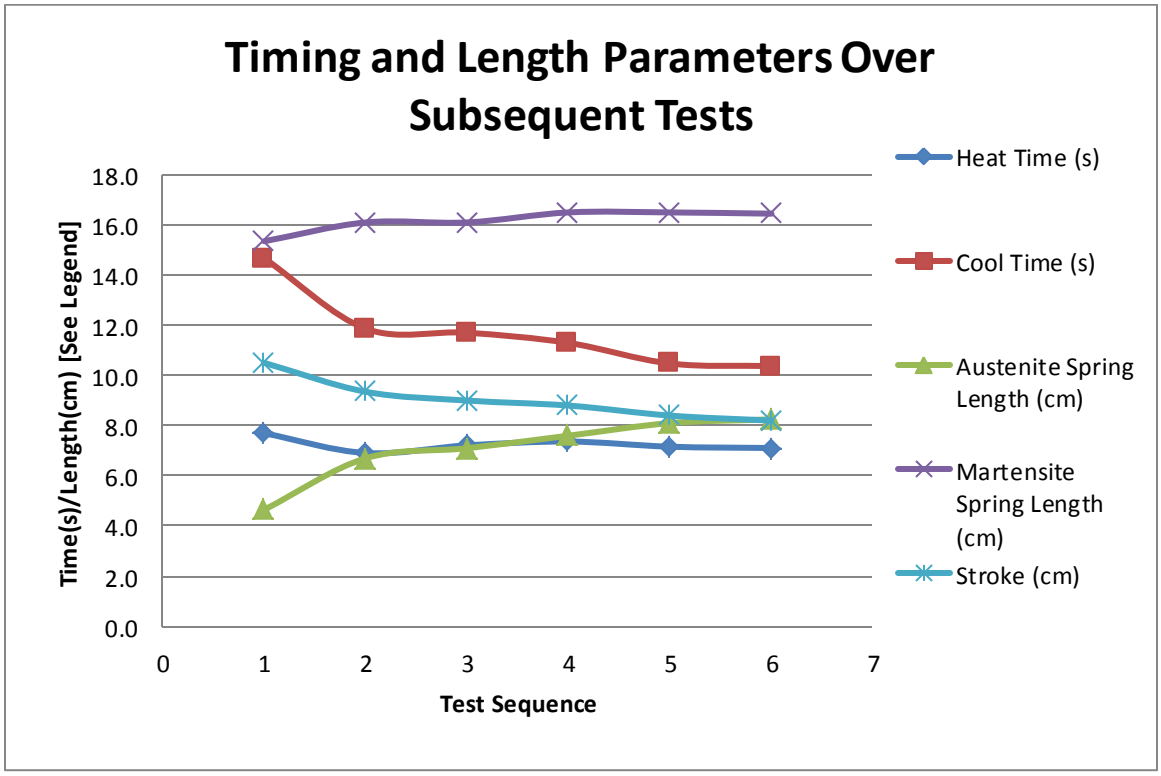

Figure 6-39: The Timing and Length Parameters of one of the 0.015" diameter wire springs under subsequent tests.

6.7 CONCLUSIONS AND RECOMMENDATIONS

Recalling the first objective, it was desired to find correlations between an SMA spring's parameters and their dynamic response. This investigation successfully tested how six variables (*i.e.* wire diameter, spring diameter, number of spring turns, transition temperature, direct current magnitude, and bias mass) affect the performance of SMA actuators in relation to their reaction times and strokes. It was found that four out of six variables affect the heating time, four out of six variables affect the cooling time, and all six variables affect the stroke. These experimental results will give helical SMA actuator designers a better understanding of how each parameter affects the actuator's resultant reaction times and strokes. Table 6-22 below showcases the experimental trends observed in the experimental results; Table 6-22 also presents the experimental trends in relation to the predictions previously presented in Table 6-13. As the experiments successfully found the correlations between all six variables and the SMA's dynamic response, the first objective was met.

Table 6-22: The Experimental Trends in relation to the Predicted Trends. The results in green font represent trends that were successfully predicted, the results in red represent trends that were not successfully predicted, and the results in blue font represent converging trends that were not foreseen

Manipulated Variable	Experimental Heating Times when Increased	Experimental Cooling Times When Increased	Experimental Strokes When Increased
Wire Diameter	Increase	Converged Increase	Converged Increase
Spring Diameter	Converged Increase	Converged Decrease	Converged Increase
Transition Temperature	No Change	Decrease	Decrease
Number of Spring Turns	No Change	No Change	Linear Increase
Bias Mass	Increase	Converged Decrease	Converged Increase
Direct Current	Converged Decrease	No Change	Converged Increase

The second objective was to catalogue the stroke and reaction times at different spring parameters for reference; the second objective was also met. As helical SMA actuators are not completely understood mechanically, it is often necessary to experimentally test their dynamic response as opposed to using equations to predict their behaviour. Additionally, custom made helical SMA actuators can be quite expensive in comparison to readily available SMA wire (such as Flexinol®). The catalogue made from these experimental results will not only enable helical SMA actuator designers to choose

appropriate parameters for projects that require certain reaction times or strokes, but will also allow them to use readily available, cost effective SMA wire to produce the helical SMA actuators as opposed to buying them custom made.

The remainder of this chapter will briefly list the conclusions made along with recommendations should this subject be pursued further.

6.7.1 Conclusions

In relation to the reaction times and an increasing variable, the following conclusions were made:

1. As the wire diameter increases, both the heat times and cooling times increase: trends that were predicted from the derived reaction time equations. Both values appeared to converge at the highest wire diameter: 0.375 mm
2. As the spring diameter increases, the heat times decrease while the cooling times decrease: trends that were predicted from the derived reaction time equations. Both values appeared to converge at the final spring diameter: 6.36 mm.
3. In comparison to the 70 °C Flexinol® wire, the 90 °C Flexinol® wire did not have any observable difference in heat time (a trend that was not predicted from the derived heat time queation), but had shorter cooling times (a trend that was predicted from the derived cooling time equation)
4. As the number of spring turns increases, the heat times and cooling times do not change: trends that were predicted from the derived reaction time equations
5. As the bias mass increases, the heat times increase while the cooling times decrease: trends that were predicted from the derived reaction time equations
6. As the direct current increases, the heat times decrease while the cooling times remain constant: trends that were predicted from the derived reaction time equations

In relation to the strokes, the following conclusions were made:

1. For the wire diameter manipulation, the stroke started out low at 0.145 mm but converged to around 10 cm for the 0.192 mm, 0.248 mm, and 0.375 mm wire diameters. This conflicted with the prediction of a decreased stroke with increasing spring diameter.
2. For the spring diameter manipulation, the stroke started out low at a spring diameter of 2.34 mm with a stroke of 5.8 cm, but appeared to converge at 15.8 cm at the final spring diameter, 6.36 mm. This somewhat conflicted with the prediction of an increased stroke with increasing spring diameter
3. For the transition temperature manipulation, the stroke from the 90°C wire was less than the 70°C wire for all three wire diameters. This conflicted with the prediction that stroke would not be affected by transition temperature.
4. The stroke linearly increased when increasing the number of spring turns: a trend that was predicted
5. When increasing the bias mass, the stroke started at 8.1cm using a 20 g bias mass, but converged to around 10 cm for the 30 g, 40 g, and 50 g bias masses. This somewhat conflicted with the prediction of an increased stroke with increasing bias mass
6. The stroke remained constant with an increasing direct current: a trend that was predicted

From the overall findings from this experiment, the following conclusions were made:

1. Superelasticity cannot be ignored when calculating the cooling times
2. The heat reaction time predictions were not accurate with the actual results
3. With the exception of the 90 °C Flexinol® wire, the cooling reaction time predictions that accounted for superelasticity predicted the actual cooling times quite well
4. The magnitude of stroke is likely caused from the spring`s internal stress. It is believed that the stress should be large enough so that the maximum transformation strain is achieved, but should not be larger than its yield stress as plastic deformation will develop. To keep permanent transformation strain to a

minimum, the spring should be strained only to its maximum transformation strain

5. It may not be valid to assume that the spring diameter does not change when calculating the stroke.
6. The stroke appears to converge at increasing parameters including wire diameter, spring diameter, and bias mass. Further testing is needed to see if the stroke is actually converging or if it has simply peaked at the larger values.
7. The springs experienced permanent transformation deformation resulting in a decrease in cooling time and stroke after subsequent cycles likely from surpassing the maximum transformation strain.

6.7.2 Recommendations

If one were to repeat these experiments, the author would make the following recommendations:

1. The springs should be tested at further parameter increases to see if the observed converging trends continue.
2. A tensile test should be performed on the wire while in its austenite phase to obtain accurate moduli of elasticity and yield strengths. This should be done before and after the shape setting process to see if the heat treatment has an effect on the material properties
3. A DSC should be performed to obtain the transition temperatures before and after heat treatment to see if the transition temperatures rose due to aging
4. The ambient temperature and convection coefficient should be monitored and recorded to get more accurate reaction time predictions
5. As the strokes tended to stabilize more towards the end of the twenty cycles due to cyclic behavior, it may be better to let the spring go through cyclic loading and have a stabilized stroke before taking measurements. If the actuation use needs to perform several cycles, it would be desired to know the stabilized output. The

standard deviation would be expected to be much smaller after the SMA wire has gone through cyclic loading

6. An override switch should be added to the electronic circuitry to allow the viewer to switch the transistor manually in the event that the microcontroller failed to accurately acknowledge when a transformation is complete

For further investigation, the author would recommend:

1. Performing a recovery strain test on the straight wire to see how much it recovers at certain stresses and applying this knowledge to a predicted stroke model.
2. Performing experiments at different annealing temperatures to find a temperature that allows the best recovery for Flexinol® wire
3. Finding the true value of the stress influence coefficients, C^A and C^M
4. Measuring the permanent strain after each test by activating the spring without a bias force, measuring the austenite length and subtracting the compressed spring length from the measurement.
5. Coming up with a more accurate heat time model, one that incorporates the mechanical work being performed on the bias mass
6. Coming up with a proper stroke model, one that would include the yield stress, permanent and maximum recovery strain, stress concentrations, and change in spring diameter
7. Performing these experiments using as-drawn wire as recommended by Dynalloy™ as opposed to using Flexinol®: an SMA wire that has already been through the annealing process

CHAPTER 7. MODELING AND TESTING THE STIFFNESS AND RESONANCE PROPERTIES OF HELICAL SUPERELASTIC NITINOL SPRINGS

7.1 SUPERELASTIC SHAPE MEMORY ALLOYS: AN OVERVIEW

Another feature of shape memory alloys that is often exploited is their uncanny reaction to applied stress. Essentially, when a stress is applied to an SMA, the characteristic transition temperatures linearly increase (See Figure 7-1). In light of this, the martenistic fraction curve shifts to the right (Shown in Figure 7-2). Martensite can therefore be induced when stress causes the austenitic forming temperatures to exceed the ambient temperature. This martensite is commonly known as stress induced martensite (SIM) and the phenomenon is known as superelasticity. Fundamentally, when enough stress is applied to austenite, it reverts back to its de-twinned martensite phase as shown in Figure 7-3. Providing that the applied stress does not exceed a certain value, the SMA will completely transform back to its austenite phase when the stress is removed, reverting back to its programmed shape. In summary, superelasticity enables physical austenite to experience physical deformation such as bending, only to return to its original shape when released. Superelastic nitinol can be strained 20 times more than stainless steel without being plastically deformed (Lombardi & Poncet, 2011). Superelasticity has been exploited in a wide range of commercial products including golf clubs, cell phone antennae, orthodontic archwires, bone staples, and even eyeglass frames (Jordan, 2011).

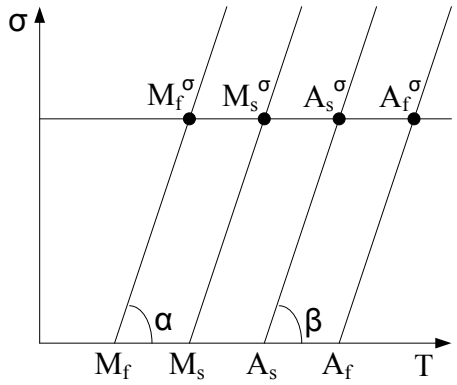

Figure 7-1: The presence of stress raises the critical phase change temperatures in a linear fashion.

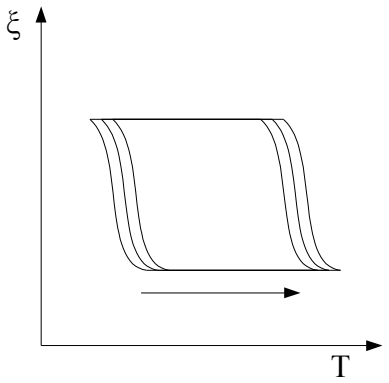

Figure 7-2: Applying Stress Causes the Martensitic Fraction Curve to shift to the right. Extracted from (Srinivasan & McFarland, Smart Structures: Analysis and Design, 2001)

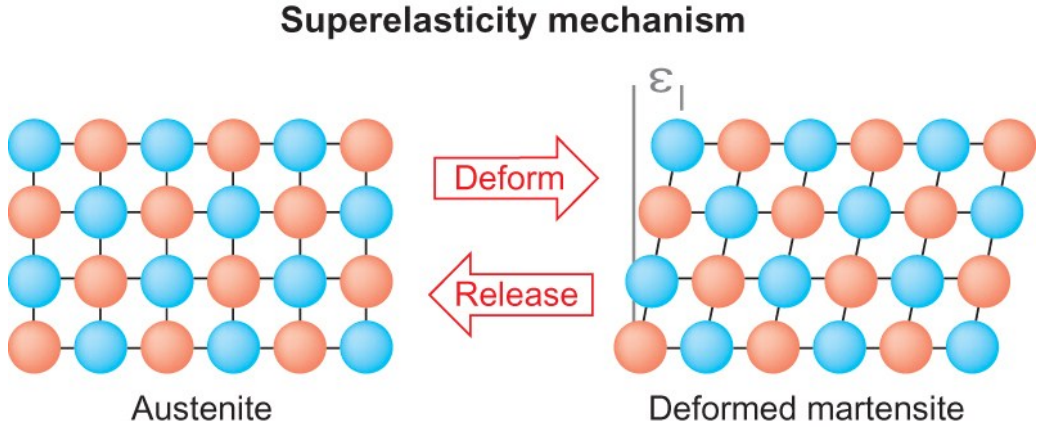

Figure 7-3: A superelastic SMA can be transformed into deformed (de-twinned) martensite through applying stress. Image extracted from (Lombardi & Poncet, 2011)

For superelasticity to occur, the SMA must be at a temperature above A_f and below M_d, the martensite deformation temperature. The M_d temperature is the upper temperature limit where superelasticity is not able to occur. In relation to the stress's magnitude, the transformation temperatures will linearly increase. The slopes of this linear relationship can be expressed in relation to angles α and β, as shown in Figure 7-1. Angle α represents the slope of the martensite transformation temperatures (*i.e.* M_f and M_s) while β represents the angle of the austenite transformation temperatures (*i.e.* A_s and A_f). The slopes are thus the tangents of these angles:

$$C_M = \tan \alpha \qquad 7\text{-}1$$

$$C_A = \tan\beta \qquad 7\text{-}2$$

In the event of a constant applied stress (as is the case shown in Figure 7-4), the zero-stress transition temperatures, M_f, M_s, A_s, and A_f, will respectively increase to M_s^σ, M_f^σ, A_s^σ, and A_f^σ. As the transition temperatures follow a linear relationship with the applied stress, they can be predicted using Equations 7-3 to 7-6.

$$M_s^\sigma = M_s + \frac{\sigma}{C^M} \qquad 7\text{-}3$$

$$M_f^\sigma = M_f + \frac{\sigma}{C^M} \qquad 7\text{-}4$$

$$A_s^\sigma = A_s + \frac{\sigma}{C^A} \qquad 7\text{-}5$$

$$A_f^\sigma = A_f + \frac{\sigma}{C^A} \qquad 7\text{-}6$$

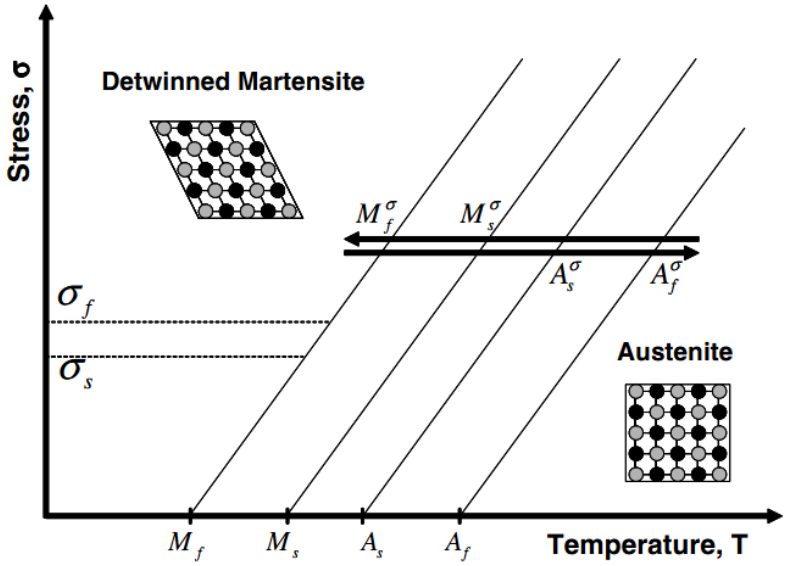

Figure 7-4: At a constant stress, the transition temperatures will linearly increase. The 0-stress transition temperatures, M_f, M_s, A_s, and A_f, will increase to M^σ_f, M^σ_s, A^σ_s, and A^σ_f, depending on the magnitude of applied stress. Image extracted from (Kumar & Lagoudas, 2008)

Assuming that during a martensite to austenite transformation, the martensitic volume fraction (ξ) linearly decreases with increasing temperature from A_s^σ to A_f^σ, ξ can be modelled as:

$$\xi = \frac{A_f^\sigma - T}{A_f - A_s} = \frac{A_f + \frac{\sigma}{C^A} - T}{A_f - A_s} \qquad 7\text{-}7$$

Likewise, assuming that during an austenite to martensite transformation, ξ linearly increases with decreasing temperature from M_s^σ to M_f^σ:

$$\xi = \frac{M_s^{\sigma} - T}{M_s - M_f} = \frac{M_s + \frac{\sigma}{C^M} - T}{M_s - M_f} \quad 7\text{-}8$$

In the event of a constant temperature (as is the case shown in Figure 7-5), the stresses required to change an SMA's transition temperatures also increase. These transition stresses, σ^{Af}, σ^{As} , σ^{Ms} , and σ^{Mf}, will respectively change the SMA's working temperature to $A_f^{\sigma^{Af}}$, $A_s^{\sigma^{As}}$, $M_s^{\sigma^{Ms}}$, and $M_f^{\sigma^{Mf}}$. At ambient temperatures above A_f, the SMA will begin its austenite to martensite transformation when the stress increases to σ^{Ms}, and will finish when increased to σ^{Mf}. Likewise, during a martensite to austenite transformation, austenite will first start to form when the applied stress is reduced to σ^{As}, and will finish when reduced to σ^{Af}. Using the linear relationship between applied stress and transition temperature, these transition stresses can be predicted using Equations 7-9 to 7-12:

$$\sigma^{Ms} = (T - M_s)C_M \quad 7\text{-}9$$

$$\sigma^{Mf} = (T - M_f)C_M \quad 7\text{-}10$$

$$\sigma^{As} = (T - A_s)C_A \quad 7\text{-}11$$

$$\sigma^{Af} = (T - A_f)C_A \quad 7\text{-}12$$

The stress-strain curves for austenite, reversible superelastic SMA, and reversible martensite are all illustrated in Figure 7-6. Austenite very much behaves like a traditional material having a linear elastic range with no sign of hysteresis. Conversely, both superelastic SMA and martensite have significant hysteresis but yet have dissimilar hysteresis loops. Superelastic SMA is able to return back to its original length during unloading, but martensite can only return to its original length after heating to austenite following unloading and then cooling back to its martensite phase. Figure 7-7 goes into further detail, showing both the elastic-plastic and reversible stress-strain curves of austenite, superelastic SMA, and martensite at various temperature ranges. The elastic-plastic curves for both superelastic SMA and martensite are quite similar, experiencing a small deformation in the elastic range followed by a dramatic increase in strain. Figure 7-7 also shows the stress-strain curve for martensite at a temperature much lower than M_f. Interestingly, at this temperature, the stress-strain curve behaves quite similarly to the austenite stress-strain curve.

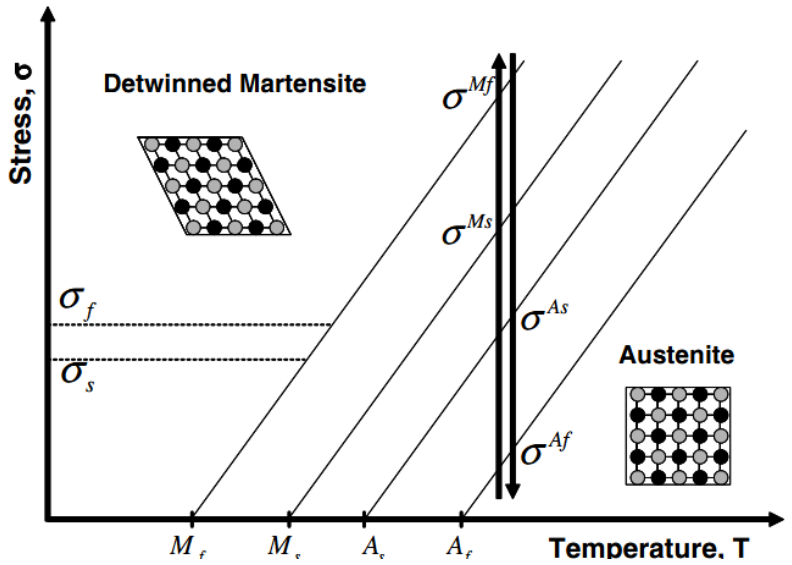

Figure 7-5: At a constant temperature, the stresses required to change the SMA's transition temperatures linearly increase. These "transition stresses", σ^{Af}, σ^{As}, σ^{Ms}, and σ^{Mf}, will change the SMA's working temperature to $A_f^{\sigma^{Af}}$, $A_s^{\sigma^{As}}$, $M_s^{\sigma^{Ms}}$, and $M_f^{\sigma^{Mf}}$. Transforming from martensite to austenite via applied stress, the SMA alloy will start to deform into austenite when the stress is reduced to σ^{As}, and finish when reduced to σ^{Af}. Likewise, transforming from austenite to martensite via applied stress, the SMA alloy will start to deform into martensite when the stress is increased σ^{Ms}, and finish when increased to σ^{Mf}. Image extracted from (Kumar & Lagoudas, 2008)

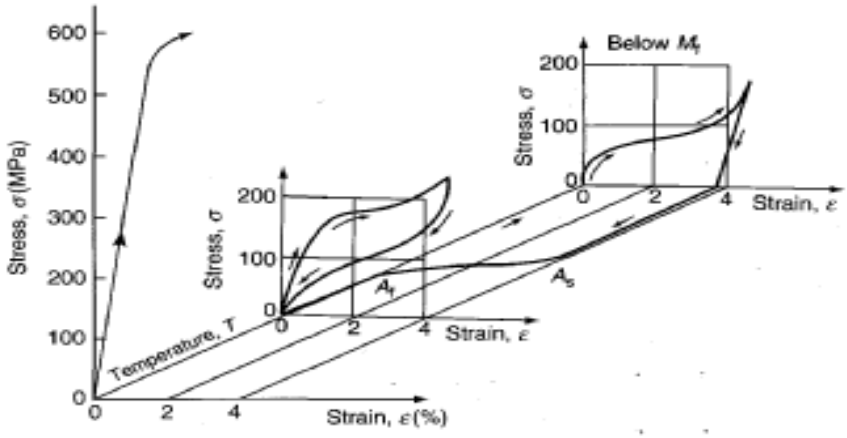

Figure 7-6: A three dimensional plot of stress, strain, and temperature with temperature decreasing into the page. The curve closest to the reader shows the elastic-plastic deformation of pure austenite which occurs at temperatures above M_d. The middle curve displays the elastic deformation of superelastic SMAs which takes place below M_d but above A_f. The curve furthest away from the reader displays the elastic deformation of martensite which takes place at a temperature below M_f. Extracted from (Wayman & Duerig, 1990)

When performing a monotonic stress test on superelastic SMAs, it is important to recall that heat will be released when transforming into martensite and absorbed when transforming into austenite. Although a monotonic test can be performed at constant ambient temperature, thermal energy can be added to the system during the exothermic stress-induced austenite to martensite transformation if the energy is not dissipated. It is thus important to perform the monotonic tests at low strain rates to allow convection and conduction to remove this additional heat without noticeably raising the specimen temperature. If loading or unloading too rapidly, the temperature will rise during loading and fall during unloading, violating any isothermal assumptions. For isothermal loading at any temperature, strain rates should not exceed 0.01-0.05 strain/second. (Hartl & Lagoudas, 2008).

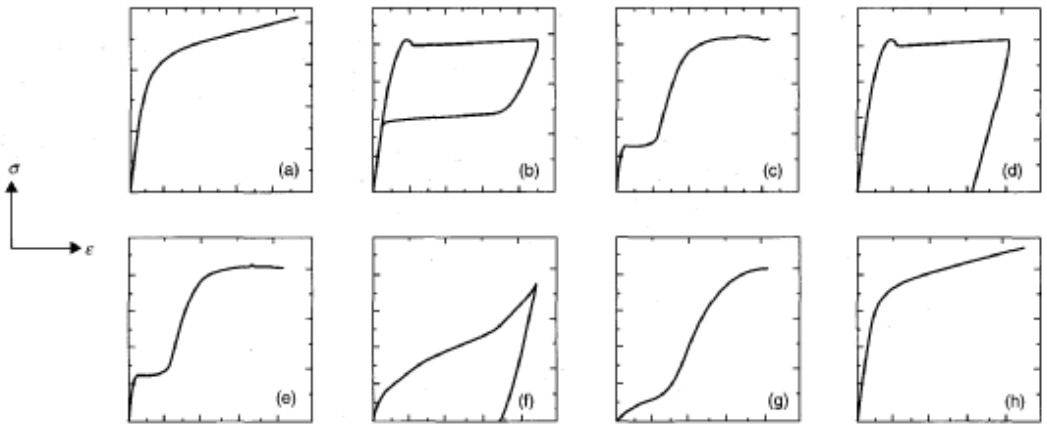

Figure 7-7: The Various Stress-Strain Curves for the various phases of SMAs. The characteristic temperature decreases from a-h. a) $T>M_d$ Austenite (Elastic-Plastic), b) $A_f<T<M_d$ (Reversible), c) $A_f<T<M_d$ SIM (Elastic-Plastic), d) $M_s<T<A_s$ SIM (Reversible),e) $M_s<T<A_s$ SIM (Elastic-Plastic), f) $T<M_f$ Martensite (Reversible), g) $T<M_f$ Martensite (Elastic-Plastic) Initial Strains through detwinning, h) $T<<M_f$ Martensite (Elastic-Plastic) where detwinning is not permissible. Extracted from (Barney & Bartning, 2009)

Figure 7-8 shows the monotonic loading of a superelastic SMA above its A_f transformation temperature with reference to the phase transformation points. Starting at a stress of 0 MPa where the SMA is in its austenite phase, the strain is increased at a constant rate and the resultant stress is recorded via force measurements and estimations of the decrease in cross-sectional area. At the start of the strain loading, the stress linearly increases with a slope that is equivalent to the austenite's modulus of elasticity,

E^A as previously introduced in Figure 6-5. However, after reaching a certain stress value, *i.e.* the upper plateau stress, the stress stays constant for a while. It's at this constant stress value where the austenite turns into stress induced martensite (*i.e.* detwinned martensite). If the stress is removed during this transition, the strain should be completely reversible and return to 0% strain. After reaching a certain strain (point 1 on Figure 7-8) the alloy has been completely transformed into stress-induced martensite and will start deforming via Hookian elasticity until it reaches its yield stress/elastic limit (point 2 on Figure 7-8). As previously mentioned in Section 6.2.2, if one decreases the stress before the yield stress, the stress-strain relationship will initially decrease linearly before converging into a lower constant stress value. This linear stress/strain relationship has a slope that is equivalent to the martensite modulus of elasticity (E^M), while the lower constant stress value is known as the lower plateau stress. As the strain continues to decrease at the lower plateau stress, the twinned martensite reverts back to austenite. The SMA fully transforms back into austenite when the strain decreases to the original austenite stress-strain curve. The strain then continues to decrease through Hookian elasticity until it returns back to a 0 stress-strain state. Similar to the temperature-strain relationship, the stress-strain curves of superelastic alloys have some hysteresis, an indicator of the energy dissipation and absorption during the austenite to martensite transformation and vice versa, respectively.

The plateau stresses are often exploited in the uses of superelastic SMAs as they indicate that a significant amount of strain can be applied at a constant force, something that does not happen with Hookian elasticity. A force corresponding to the upper plateau stress will typically strain the superelastic nitinol by about 5%. Once the upper plateau stress has been surpassed and transformed into martensite, if the applied force is removed, the superelastic nitinol will apply a constant force that corresponds to its lower plateau stress until the alloy de-strains by about 5%, returning to its austenite phase. The constant applied force during unloading is exploited in orthodontic archwires, for example. For optimum orthodontic tooth movement, a light continuous force is required. When the force level is maintained through treatment, there is a smooth progression of tooth movement resulting from direct bone resorption; and undesirable side effects, such as

loss of anchorage or damage to the periodontal tissues, are avoided (Nanda & Tosun, 2010). As superelastic SMAs can deliver a constant force over a wide range of deformation, it is the preferred first stage of orthodontic treatment. With reference to other alloys with superelastic properties, Ni-Ti alloys are the most biocompatible material and have excellent resistance to corrosion (Thompson, 2000).

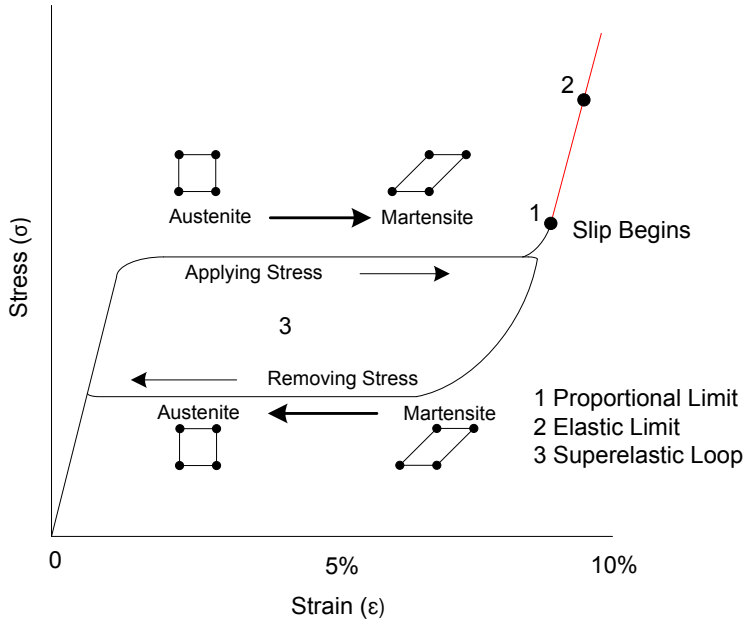

Figure 7-8: The Superelastic Nitinol Stress-Strain Curve with Associated Transformations. Extracted from (Memry Corporation, 2012)

Akin to the thermomechanical cyclic loading behavior previously presented in Section 6.2.6, a similar effect can be noticed for cyclic superelastic loading at a constant temperature above the A_f transition temperature. Figure 7-9 shows a superelastic nitinol alloy going through cyclic stress loading. After each cycle, the transformation strain, upper plateau stress, and lower plateau stress progressively decrease until converging to a set value. If a superelastic alloy is to be designed for continuous cyclic use, it is important to first put the alloy under said cyclic loading so that there are no inconsistencies in its final response.

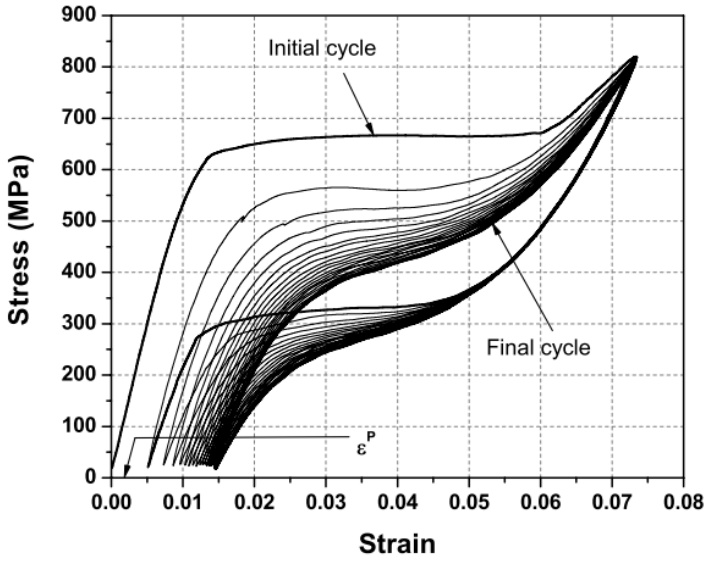

Figure 7-9: The Superelastic Cyclic Response of an as-received NiTi wire with an A_f of 65°C tested at 70°C after 20 cycles. After each cycle, the recoverable transformation strain, upper plateau stress, and lower plateau stress continued to decrease until converging to a set value. Image Extracted from (Kumar & Lagoudas, 2008)

7.2 SUPERELASTIC SMA WIRE AS A BIAS FORCE

After learning about the high strain deformation at a constant low force, the author thought it could effectively be used as a bias force for the SMA helical spring actuators in the flamenco stage set. Using 0.008" wire diameter, 0.09375" spring diameter SMA spring actuators, the author attached the actuators to the front of the fabric flap, while attaching superelastic nitinol wires to the back of the flap. When activated the SMA springs would contract, displacing the fabric in the process. When deactivated, the SMA springs would relax and the superelastic nitinol wires would bring the SMA spring and fabric back to its original position. Figure 7-10 shows a live action photo of one of the flaps when activated and deactivated. After experimenting with various superelastic wire lengths and diameters, the superelastic wires effectively acted as a bias force. The wire diameter that was found appropriate for the fabric flaps was found to be 0.017".

After the success of the fabric flaps, it was desired to better understand the superelastic forces exhibiting on and by the superelastic wire. One may be tempted to use cantilever beam equations like the ones presented in Section 4.3.2; however, as the wires go through much curvature when deflecting, one cannot make the assumption presented as Equation 4-3. The forces are thus not straightforward to calculate. In fact, in orthodontics, the forces aren't generally calculated, but compared relative to each other. Generally, each wire is assigned a cross sectional stiffness (CS) based on the wire's geometry, and material stiffness (MS) based on the material's modulus of elasticity; multiplication of these two values gives the total wire stiffness (WS). Essentially, an orthodontist would start his/her patient with a certain arch wire, and if the archwire was insufficient to effectively move their teeth, the archwire would be replaced with an archwire with higher stiffness.

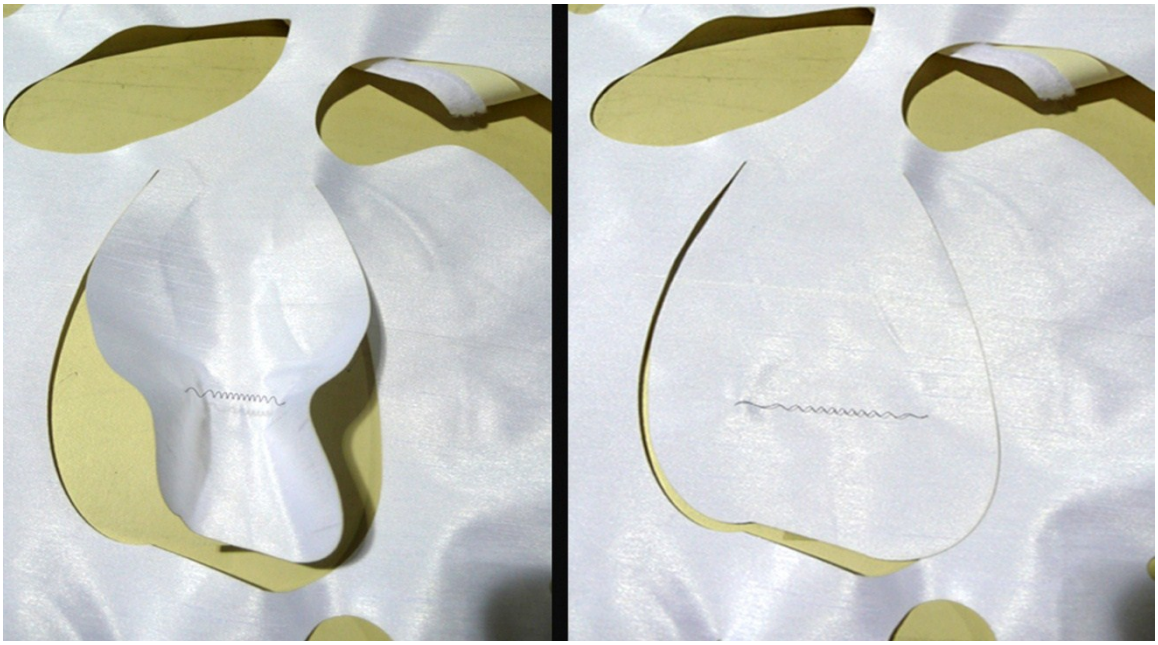

Figure 7-10: The nitinol spring actuators were tested on nitinol flaps using superelastic nitinol wire as a bias force. The nitinol spring, located on the front, would displace the fabric when activated

Originally, part of this thesis was to include possible formulas along with a database of the forces needed to bend superelastic wire along with the produced forces once released. Unfortunately, the forces were rather difficult to measure as they were quite small; too small to measure properly with a dynamometer. As the wires had circular cross sections, they were also quite prone to twist while measuring. Perhaps if the wires had a square or

rectangular cross-section, it may have been easier to measure as they have lower twisting angles. Fundamentally, to know what superelastic length or diameter wire to use, one should take cues from the orthodontic practice of archwires. Start with a wire with low stiffness; if the force is insufficient for the intended purpose, choose a wire with different properties or geometry. One can use the cantilever beam equation as a guideline to changing the stiffness. When one end of a cantilever beam is fixed and the other is supporting a downwards load, the overall stiffness (k) equation for a cantilever beam with circular cross-section can be represented as Equation 7-13 where P is the load, δ is the deflection, E is the modulus of elasticity, I is the moment of inertial, L is the total length of the beam, and d is the diameter of the beam's cross-section.

$$k = \frac{P}{\delta} = \frac{3EI}{L^3} = \frac{3\pi d^4 E}{64L^3} \qquad 7\text{-}13$$

Fundamentally the stiffness of the wire can be increased by increasing the wire diameter, increasing the modulus of elasticity, or decreasing the length. Proportional to the fourth power, the wire diameter has the strongest relation to the stiffness; proportional to the third power, the length has the next strongest influence on the stiffness; linearly proportional, the modulus of elasticity has the least influence on the stiffness.

7.3 SUPERELASTIC WIRE FOR A RESONANCE SPRING

For the HPLED jogging suit, the design team was looking for a mass-spring resonance system for power generation. Similar to some self-powered flashlights, a magnet would be used as the mass while a spring would cause the mass to resonate at a particular frequency. The magnet in turn would be surrounded by a wire coil which would translate the mechanical energy of the magnet into electrical energy used to power LEDs. An exploded view of the resonance shaker is shown in Figure 7-11. Using the spring-mass model (*i.e.* Equation 7-14) and assuming that the motion is periodic (*i.e.* Equation 7-15), the resonance frequency (ω_n) of the system can be shown to be Equation 7-16 by differentiating Equation 7-15 twice and substituting the result along with Equation 7-15 into Equation 7-14.

$$m\ddot{x}(t) + kx(t) = 0 \quad \text{7-14}$$

$$x(t) = A\sin(\omega_n t + \phi) \quad \text{7-15}$$

$$\omega_n = \sqrt{\frac{k}{m}} \quad \text{7-16}$$

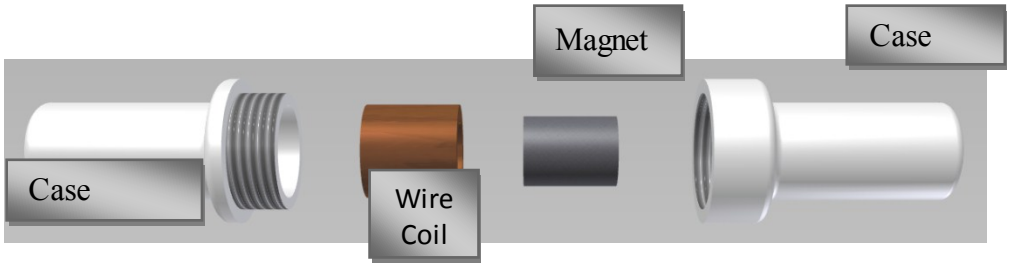

Figure 7-11: An Exploded View of the Resonant Shaker in the Human Powered LED Jogging Suit

Note that the resonant frequency as defined in Equation 7-16 is in rad/s. To get the resonant frequency in Hz, *i.e.* f_n, one must divide Equation 7-16 by 2π:

$$f_n = \frac{1}{2\pi}\sqrt{\frac{k}{m}} \quad \text{7-17}$$

For a human power system, the resonance frequency of the system should be on par with that of jogging. A typical jogging frequency would therefore be around 2 steps per second, or 2Hz. As the magnet would be a relatively low mass (around 25-40g) it was important for the spring to have a very low stiffness. As an example, for a 2 Hz resonance frequency and a 40g mass, the stiffness would need to be about 6.3N/m. Although this stiffness can indeed be manufactured using steel, it is not readily available; most steel springs have a much higher stiffness. Having worked with superelastic nitinol on the flamenco backdrop and seeing how much it can deform over low forces, the author suggested making springs made out of superelastic nitinol. The author was unsure if traditional resonant mechanics could be applied to superelastic nitinol springs, so several springs were made using gauge 19 superelastic nitinol wire at various spring diameters. The springs were then tested with the magnet attached to find a spring that would give the

required resonance. A suitable spring stiffness was indeed found, and the resonance shaker worked very well at a jogging frequency of about 2 Hz.

Wanting to know if traditional spring mechanics can indeed be applied to superelastic nitinol springs not just for resonance, but for overall spring stiffness, the author tested several superelastic nitinol springs at different wire diameters, spring diameters, and number of turns.

7.4 MODELING SUPERELASTIC NITINOL AS A HELICAL SPRING

7.4.1 Modeling the Stress-Induced Transition Temperatures and Shear Transition Stresses of Superelastic SMA Springs

Previously introduced as Equations 7-3 through 7-6, the transition temperatures linearly increase with applied stress. As springs experience stress when stretched, the transition temperatures increase when the springs are supporting a load. As helical springs undergo torsional deformation and shear stresses while the transition temperature equations are expressed in normal stress, Equations 7-3 through 7-6 need to be altered to account for shear stress. This is accomplished by using the Von Mises criterion at pure shear, *i.e.* Equation 7-18:

$$\tau\sqrt{3} = \sigma \tag{7-18}$$

By substituting Equation 7-18 into Equations 7-3 through 7-6, the transition temperatures can be expressed in terms of the applied shear stress:

$$M_s^\tau = M_s + \frac{\tau\sqrt{3}}{C^M} \tag{7-19}$$

$$M_f^\tau = M_f + \frac{\tau\sqrt{3}}{C^M} \tag{7-20}$$

$$A_s^\tau = A_s + \frac{\tau\sqrt{3}}{C^A} \tag{7-21}$$

$$A_f^\tau = M_f + \frac{\tau\sqrt{3}}{C^A} \tag{7-22}$$

During loading, if the applied shear stress causes the M_s^τ temperature to exceed the ambient temperature, stress-induced martensite will begin to deform. The alloy will have

completely transformed into stress-induced martensite providing that the stress is large enough for the M_f^τ transition temperature to exceed the ambient temperature. The martensitic volume fraction during an austenite to stress-induced martensite transformation can therefore be rewritten with reference to the applied shear stress as Equation 7-23 by substituting Equations 7-18, 7-19, and 7-20 into Equation 7-7. Likewise when unloading, the stress-induced martensite will begin reverting back into austenite when the shear stress is reduced to a value that produces an A_s^τ temperature that is less than ambient temperature, and will completely revert back to austenite when the shear stress is reduced to a value that produces an A_f^τ below ambient temperature. The martensitic volume fraction during a martensite to austenite transformation can therefore be rewritten with reference to the applied shear stress as Equation 7-24 by substituting Equations 7-18, 7-21, and 7-22 into Equation 7-8.

$$\xi = \frac{M_s^\tau - T}{M_s - M_f} = \frac{M_s + \frac{\tau\sqrt{3}}{C^M} - T}{M_s - M_f} \tag{7-23}$$

$$\xi = \frac{A_f^\tau - T}{A_f - A_s} = \frac{A_f + \frac{\tau\sqrt{3}}{C^A} - T}{A_f - A_s} \tag{7-24}$$

Likewise, the transition shear stresses of a superelastic SMA spring can be found by substituting the Von Mises criterion at pure shear into equations 7-9 through 7-12:

$$\tau^{Ms} = \frac{(T - M_s)C_M}{\sqrt{3}} \tag{7-25}$$

$$\tau^{Mf} = \frac{(T - M_f)C_M}{\sqrt{3}} \tag{7-26}$$

$$\tau^{As} = \frac{(T - A_s)C_A}{\sqrt{3}} \tag{7-27}$$

$$\tau^{Af} = \frac{(T - A_f)C_A}{\sqrt{3}} \tag{7-28}$$

It must be mentioned, however, that all the equations presented in this subsection only show the stress-induced transition temperatures, martensitic volume fractions, and shear stress at a certain shear stress. Ignoring Wahl factor stress concentrations, the shear stress

in a spring linearly increases from zero at the wire's center, to the maximum shear stress value at the wire's outer surface. Equations 7-19 through 7-28 therefore only represent the transition shear stresses at a certain radius along the wire, not the wire as a whole. To get the shear stress at a certain position along the wire's cross-section, one would take the ratio of the cross-section's radius to the wire's outer radius and multiply it by the maximum shear stress; one would then replace τ in Equations 7-19 through 7-28 with this new shear stress to get stress-induced properties at this particular radius.

7.4.2 Modeling The Stiffness Through Deflection

To model the force-deflection relationship of a superelastic SMA spring, one must not only take account of the two phase states, but must also take into account the areas in which the alloy changes phase. During its austenite phase, the austenite stiffness would be used; during its martensite phase, the martensite stiffness would be used; during a transformation, a transformation stiffness would be used.

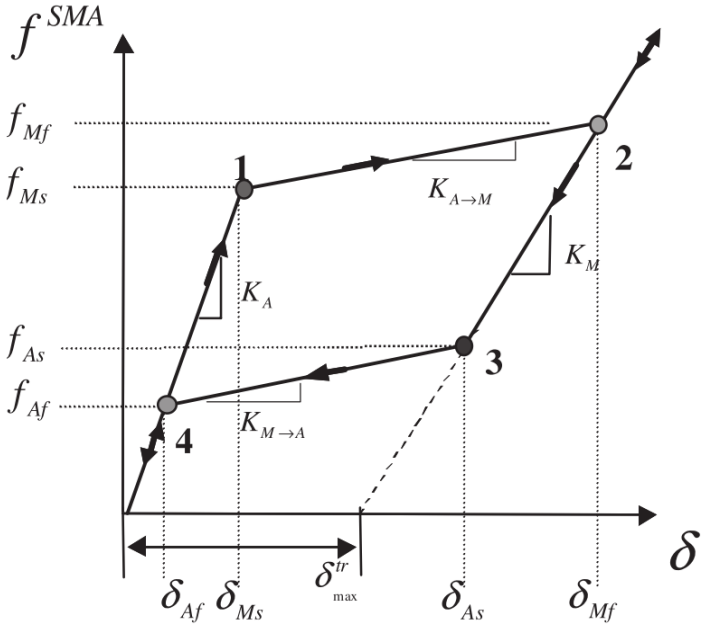

Figure 7-12: The Simplified Superelastic Spring Force-Displacement Model from Lagoudas, Khan, and Mayes (2001)

Shown in Figure 7-12, Lagoudas, Khan, and Mayes (2001) modeled a force-deflection graph of a superelastic spring similarly to a stress-strain graph of a superelastic alloy tension test. Starting in its pure austenite phase, at zero force at the spring's neutral position, the force would increase linearly with deflection until it reaches the force in

which stress-induced martensite begins to deform, F_{Ms}. The slope of this linear increase would correspond with the spring's austenite stiffness or:

$$K_A = \frac{F}{\delta} = \frac{d^4 G_A}{8D^3 N} \tag{7-29}$$

Substituting Equation 7-25 into the shear strain formula (Equation 6-58), F_{Ms} can be expressed as:

$$F_{Ms} = \frac{\pi \tau_{max}^{Ms} d^3}{8D} = \frac{\pi d^3 (T - M_s) C_M}{8D\sqrt{3}} \tag{7-30}$$

Using the deflection formula (Equation 6-61), the deflection imposed on the spring by F_{Ms} can therefore be expressed as:

$$\delta_{Ms} = \frac{8F_{Ms} D^3 N}{d^4 G_A} = \frac{\pi (T - M_s) C_M D^2 N}{d G_A \sqrt{3}} \tag{7-31}$$

Once the force has surpassed F_{Ms}, stress-induced martensite begins to form; the alloy will have completely transformed into stress-induced martensite when the force has increased to F_{Mf}. Like F_{Ms}, F_{Mf} can be found by substituting 7-26 into the shear strain formula:

$$F_{Mf} = \frac{\pi \tau_{max}^{Mf} d^3}{8D} = \frac{\pi d^3 (T - M_f) C_M}{8D\sqrt{3}} \tag{7-32}$$

When the force is increased or decreased past this point of loading, the slope of the force-deflection relationship is the stiffness of the spring in its martensite phase:

$$K_M = \frac{\Delta F}{\Delta \delta} = \frac{d^4 G_M}{8D^3 N} \tag{7-33}$$

Using the deflection formula, δ_{Mf} can be found using the martensite stiffness:

$$\delta_{Mf} = \frac{F_{Mf}}{k_M} + \delta_{max}^{tr} \tag{7-34}$$

δ_{max}^{tr} is the deflection that occurs during a transformation. It is directly proportional to the maximum shear strain that occurs during the transformation, γ_{max}^{tr}. Assuming that there is no change in spring diameter during the transition, δ_{max}^{tr} can be modeled as:

$$\delta_{max}^{tr} = \frac{\pi \gamma_{max}^{tr} D^2 N}{d} \tag{7-35}$$

Taking cues from Liang and Rogers (1990), previously presented as Equation 6-76, the shear strain could be modeled using the transformation strain at a particular stress level with reference to a straight wire going through a tensile test, *i.e.*:

$$\gamma^{tr} = \frac{2(1+\upsilon)H^{cur}(\sigma)}{\sqrt{3}} = \frac{2(1+\upsilon)H^{cur}(\tau\sqrt{3})}{\sqrt{3}} \quad 7\text{-}36$$

As γ_{max}^{tr} is when the alloy has completely turned into twinned martensite, the transformation strain has reached its maximum (*i.e.* $H^{cur} = \varepsilon_L$). γ_{max}^{tr} can therefore be represented as:

$$\gamma_{max}^{tr} = \frac{2(1+\upsilon)\varepsilon_L}{\sqrt{3}} \quad 7\text{-}37$$

Substituting Equation 7-37 into Equation 7-35, δ_{max}^{tr} can be rewritten as:

$$\delta_{max}^{tr} = \frac{2\pi(1+\upsilon)\varepsilon_L D^2 N}{d\sqrt{3}} \quad 7\text{-}38$$

And δ_{Mf} can be rewritten as:

$$\delta_{Mf} = \frac{\pi D^2 N(T-M_f)C_M}{d\,G_M\sqrt{3}} + \frac{2\pi(1+\upsilon)\varepsilon_L D^2 N}{d\sqrt{3}} \quad 7\text{-}39$$

Assuming that the force-deflection relationship is linear during a transformation, the stiffness during the austenite to martensite transformation, $K_{A\rightarrow M}$, can therefore be modeled as:

$$K_{AM} = \frac{F_{Mf} - F_{Ms}}{\delta_{Mf} - \delta_{Ms}} = \frac{d^4(M_s - M_f)}{8D^3 N\left[\frac{(T-M_f)}{G_M} + \frac{2(1+\nu)\varepsilon_L}{C_M} - \frac{(T-M_s)}{G_A}\right]} \quad 7\text{-}40$$

With reference to an alloy that is fully composed of stress-induced martensite, when the applied force is decreased to F_{As}, the alloy will begin transitioning to austenite. Using the shear strain formula, F_{As} can be expressed as:

$$F_{As} = \frac{\pi\tau_{max}^{As} d^3}{8D} = \frac{\pi d^3(T-A_s)C_A}{8D\sqrt{3}} \quad 7\text{-}41$$

Using the spring deflection formula, the deflection imposed on the spring, δ_{As}, can be expressed as:

$$\delta_{As} = \frac{\pi D^2 N(T-A_s)C_A}{dG_M\sqrt{3}} + \frac{2\pi(1+\upsilon)\varepsilon_L D^2 N}{d\sqrt{3}} \quad 7\text{-}42$$

The alloy will fully revert back to its austenite form when the force is decreased to F_{Af}. Using the shear strain formula, F_{Af} can be shown to be:

$$F_{Af} = \frac{\pi\tau_{max}^{Af} d^3}{8D} = \frac{\pi d^3(T-A_f)C_A}{8D\sqrt{3}} \quad 7\text{-}43$$

The deflection imposed by this force, δ_{Af}, can then be found using the austenite force-deflection relationship:

$$\delta_{Af} = \frac{8F_{Af}D^3N}{d^4G_A} = \frac{\pi(T - A_f)C_AD^2N}{dG_A\sqrt{3}} \quad 7\text{-}44$$

Like Equation 7-40, assuming that the force-deflection relationship is linear during a transformation, the stiffness during the martensite to austenite transformation, $K_{M\rightarrow A}$, can therefore be modeled as:

$$K_{MA} = \frac{F_{As} - F_{Af}}{\delta_{As} - \delta_{Af}} = \frac{d^4(A_f - A_s)}{8D^3N\left[\frac{(T - A_s)}{G_M} + \frac{2(1+\nu)\varepsilon_L}{C_A} - \frac{(T - A_f)}{G_A}\right]} \quad 7\text{-}45$$

Table 7-1 shows the force and deflection equations using the defined stiffnesses.

Table 7-1: The Force and Deflection Equations with Reference to the Defined Stiffnesses

Phase State	Conditions	Force Equations with Reference to Deflection	Deflection Equations with Reference to Applied Force
Pure Austenite	$0 < \delta \leq \delta_{Ms}$ $0 < F \leq F_{Ms}$	$F = K_A\delta$	$\delta = \frac{F}{K_A}$
Austenite to Martensite Transition	$\delta_{Ms} \leq \delta < \delta_{Mf}$ $F_{Ms} \leq F < F_{Mf}$	$F = K_{AM}(\delta - \delta_{Ms}) + F_{Ms}$	$\delta = \frac{F - F_{Ms}}{K_{AM}} + \delta_{Ms}$
Pure Stress-Induced Martensite	$\delta_{Mf} \leq \delta \leq \delta_{As}$ $F_{Mf} \leq F \leq F_{As}$	$F = K_M(\delta - \delta_{As}) + F_{As}$	$\delta = \frac{F - F_{As}}{K_M} + \delta_{As}$
Martensite to Austenite Transition	$\delta_{As} < \delta < \delta_{Af}$ $F_{As} < F < F_{Af}$	$F = K_{MA}(\delta - \delta_{Af}) + F_{Af}$	$\delta = \frac{F - F_{Af}}{K_{MA}} + \delta_{Af}$

It should be mentioned, however, that some of these equations were later shown to be invalid. In particular, it is not acceptable to assume that the stiffnesses during transformation (*i.e.* K_{AM} and K_{MA}) are constant. This will be further explained and explored in Section 7.7.

7.4.3 Modeling the Stiffness through Resonance

As previously mentioned, the resonance frequency of a spring-mass system can be found simply by taking the square root of the spring stiffness to mass ratio and dividing it by 2π. If one knows the mass's magnitude and obtains a value of the resonance frequency, one can obtain the spring's stiffness by using Equation 7-46:

$$k = 4\pi^2 f_n^2 m \qquad 7\text{-}46$$

The stiffness will not only depend on various spring properties such as the wire diameter, spring diameter, and number of turns, but will also depend on the spring's shear stress as it will change the alloy's phase after a certain level. Based on the linear system, if the shear stress is insufficient to produce stress-induced martensite, *i.e.* less than τ^{Ms}, one should expect the stiffness to be equivalent to K_A. If the shear stress is sufficient to produce stress-induced martensite, but insufficient to completely transform the alloy into stress-induced martensite, *i.e.* less than τ^{Mf} but greater than τ^{Ms}, one would expect the stiffness to be equivalent to $K_{A\rightarrow M}$. If the shear stress is large enough to completely transform the alloy into stress-induced martensite, *i.e.* greater than τ^{Mf}, one would expect the stiffness to be equivalent to K_M.

It should be noted, however, that the shear stress will change as the mass oscillates. It is therefore conceivable that the alloy may change phase while oscillating and therefore change stiffness. In the event this happens, the author is unsure how the resonant frequency may respond; there may be more than one resonant frequency. For this investigation, it was assumed that the stiffness will stay constant when oscillating at its natural frequency even though this assumption may not be valid.

To get the mass-spring system to resonate at its natural frequency, all one would need to do is apply an impulse force to the system. This can be verified mathematically. Equation 7-47 shows the spring-mass system with an implied impulse force, F_0:

$$m\ddot{x}(t) + k(x(t) - x_0) = F_0 \qquad 7\text{-}47$$

With zero initial conditions (*i.e.* $x_0 = 0$), and substituting the natural frequency, Equation 7-47 becomes Equation 7-48:

$$\ddot{x}(t) + \omega_n^2 x(t) = f_0 = \frac{F_0}{m} \quad 7\text{-}48$$

Assuming that the response follows a cosine pattern, *i.e.* x(t) = Xcos(ωt), differentiating the response twice and substituting into Equation 7-48 yields:

$$-\omega^2 X\, cos(\omega t) + \omega_n^2 X\, cos(\omega t) = 0 \quad 7\text{-}49$$

After canceling out the like terms, one will find that the oscillation frequency imposed on a mass system by an impulse force, is equivalent to the natural frequency:

$$\omega = \omega_n \quad 7\text{-}50$$

7.5 EXPERIMENTAL OBJECTIVES

As mentioned, the overall experimental objective was to see if traditional spring mechanics can be used to predict the behavior of superelastic nitinol springs. There were three main objectives to these experiments:

1. To see if the force-deflection relationship in a superelastic spring follows the linear relationship found in traditional springs or if it follows the proposed patterns discussed in Section 7.4.2
2. To see if a superelastic spring's geometry influences the spring's stiffness in a similar pattern as tradition spring mechanics (*i.e.* Equation 6-61)
3. To see if the spring's resonance frequency in a spring-mass system follows the traditional resonance frequency equation (*i.e.* Equation 7-17)

To accomplish the first objective, superelastic nitinol springs were made and forced to carry various mass loads. The resultant deflections were recorded and analyzed to see if they follow traditional spring mechanics, or those presented in Section 7.4.2.

For the second objective, superelastic nitinol springs were made with alternative geometries. These alternative geometries include two different wire diameters, four different spring diameters, and four different lengths (*i.e.* number of spring turns). Table 7-2 lists the spring geometries used for each manipulated variable experiment. The springs' stiffnesses were then compared with one another to see if the ratios correlate with the stiffness ratios predicted from traditional spring mechanics. Stiffness ratio comparisons were used as opposed to direct stiffness comparisons to minimize the effect

of inaccurate measurements. When one part of the spring's geometry is the controlled variable and was improperly measured, the improper measurement will cancel out when comparing two different manipulated variable results through ratios. For example, if the wire diameter was not measured correctly, the theoretical predictions could be quite different from the proper theoretical predictions; however, the stiffness ratios for both the proper and improper theoretical predictions will still be the same (when the wire diameter is a controlled variable) as the wire diameter measurements will cancel out. The theoretical and experimental stiffness ratios will therefore lessen the impact of inaccurate measurements. The moduli of elasticity were also calculated from each spring to see if they correspond to the austenite modulus of elasticity from the manufacturer. All moduli of elasticity should theoretically be the same for all springs providing that the springs are governed by traditional spring mechanics.

Table 7-2: The Spring Geometry Values for Each Manipulated Variable Experiment

Variable	Units	Manipulated Variable Experiment		
		Wire Diameter	Spring Diameter	# of Spring Turns
Wire Diameter	Inches [mm]	Gauge 19 (0.0359"), Gauge 22 (0.0254")	0.0254	0.0254
Spring Diameter	Inches	0.75	0.875, 0.75, 0.625, 0.5, 0.4375	0.75
Number of Spring Turns	Unitless	8	8	4, 8, 12, 16

For the third objective, the resonant frequency was found for each spring to see if resultant resonance frequencies match those predicted from traditional spring mechanics. Like the second objective, resultant stiffness ratios were found to be compared with the stiffness ratios found through traditional mechanics. The resultant moduli of elasticity will also be calculated to see how they correspond with the modulus of elasticity listed by the manufacturer.

7.6 PROCEDURE AND APPARATUS

7.6.1 Heat Treatment

Similar to the SMA spring actuators, the superelastic springs needed to be shape set in place using heat treatment techniques. This again involved wrapping superelastic nitinol wire around a rod and constraining it. However, because of the superelastic effect and the wire's inherent ability to return to its straight wire form, the superelastic nitinol would not permit the use of a smooth cylindrical rod or tube similar to the ones used in the SMA shape set treatments. Instead, the superelastic wire was constrained in place as it was being wrapped around the rod. This was accomplished by using power screws.

Five power screws were used, one for each spring diameter, and were initially put through a heat treatment to remove excess coating to prevent it from going on to the superelastic spring during heat treatment. Using a C-clamp, one end of the wire was clamped onto the power screw. The wires were then wrapped around the power screw while setting the wire within the grooves (See Figure 7-13). The other end of the wire was clamped to the power screw using an additional C-clamp. The power screw/superelastic spring assembly was then placed in an Inferno™ oven at a temperature of 500 °C (See Figure 7-14). The assembly was in the oven for 25 minutes instead of 10 minutes as previously performed on the SMA spring actuators; the extra time was needed as the springs were not completely shape set into a spring after 10 minutes. The assembly was then put through a water quench. The springs were then cut to their designated lengths.

Figure 7-13: A C-clamp was used to constrain one end of the superelastic wire to the power screw. The wire was then wrapped around the power screw within the grooves before constraining the other end of the wire to the power screw.

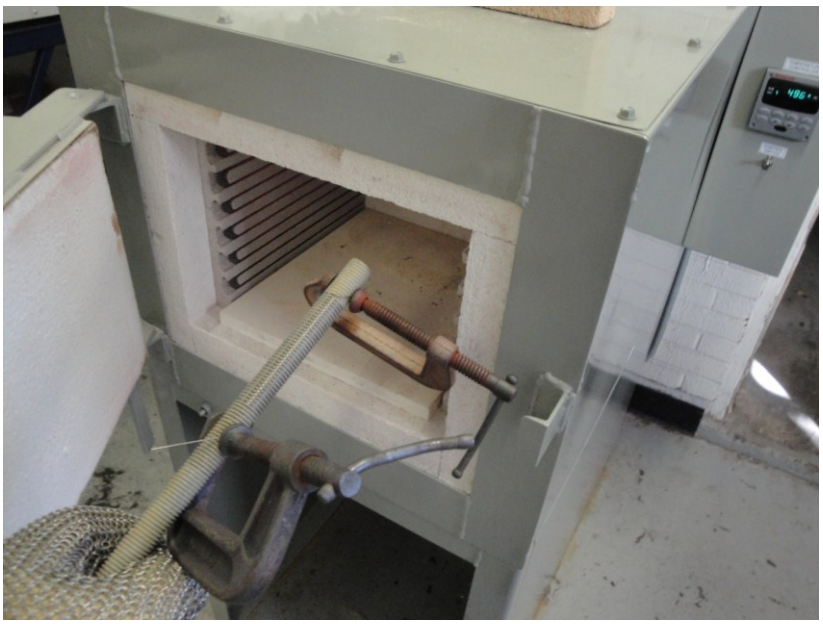

Figure 7-14: The Power Screw/Superelastic Spring Assembly was put in an Inferno™ oven for 25 minutes at a temperature of 500°C followed by a water quench

7.6.2 Geometry Measurements

After the heat treatment, the two wire diameters were measured with a micrometer with a 0.00005" resolution to obtain more accurate predictions. With 10 measurements each, the gauge 19 and gauge 22 wires had average measurements of 0.0349" (0.886 mm) and 0.0223" (0.566 mm) and standard deviations of 0.165% and 0.413%, respectively. Each spring's outer spring diameter was measured using a caliper with a 0.0005" resolution. Each spring's outer diameter was measured 5 times and the average was taken. All springs having the same wire diameter and supposed spring diameter, had measured spring diameters within 0.71% of each other. The outer spring measurements along with the differences in outer spring diameter can be found in APPENDIX D1: OUTER SPRING DIAMETER MEASUREMENTS.

7.6.3 Apparatus and Procedure

As both deflection and resonance frequency were to be found for each spring, it was beneficial to measure both outputs simultaneously rather than have two separate experiments; one for each output. The apparatus and procedure was therefore chosen to allow the simultaneous extraction of deflection and resonance frequency. Table 7-3 lists the various components used while Figure 7-15 shows a visual of the apparatus.

Each spring was constrained on one end to a stand, allowing the other end to freely resonate with a mass. A ruler was placed to the right of the spring to visually measure the spring lengths and deflections. Attached to the mass was a piezoelectric accelerometer, which would sense the impulse response of the mass when excited with an input force. The response was fed to the computer and Labview™ software was used to generate a fast-Fourier transform (FFT) of the response to obtain the system's natural frequency. A block diagram of the Labview™ program is shown in Appendix D2. Before attaching the mass/piezoelectric accelerometer system, a picture was taken of the spring's natural length to obtain the reference value to later calculate the spring's deflection.

Table 7-3: The Various Components Used in the Superelastic Spring Manipulations

Component	Function
Superelastic Nitinol Springs	The manipulated variable
Various Masses	Used to extend the spring to measure its deflection as well as influence the resonance frequency
Stand	Constrains one end of the superelastic spring, allowing the other to be free to resonate with the mass
Piezoelectric Accelerometer	Senses the bias masses movement for resonant frequency extraction
Computer/Labview™ Software	Analyzes the information sensed by the accelerometer into a fast Fourier transform to get the mass-spring's resonance frequency
Ruler	Used to measure the spring's deflection
Digital Camera	Used to take a picture of each deflection measurement
Power Supply/AD converter	Provides power to the accelerometer and translates the analog signal into a digital signal to be interpreted by the computer

Starting with a small mass, the mass/piezoelectric accelerometer system was attached to the spring's free end. The Labview™ program was initiated and then the user stretched the spring slightly to induce an impulse input. Over the course of a 16 second period, the Labview™ program would take the information from the piezoelectric accelerometer and produce a FFT of the magnitude vs. frequency at a resolution of 0.06 Hz. The peaked frequency was then extracted as the measured resonant frequency. Figure 7-16 shows one of the extracted FFT diagrams. The spring's movement was then allowed to naturally dissipate; after the spring became stationary, a picture was taken of the spring with reference to the ruler to later calculate its imposed deflection from the mass. For each spring and mass, three resonant frequency and deflection measurements were taken and averaged. When finished, the mass was removed and then replaced by a larger mass. Each spring was tested using at least six different masses, starting with the lowest mass and ending with the largest mass. When finished, the largest mass was removed and a picture was taken of the spring to see if any deformation had occurred during the trial that may have compromised the results. A total of three trials (*i.e.* three springs with the same geometrical properties) were performed for repeatability, and averaged.

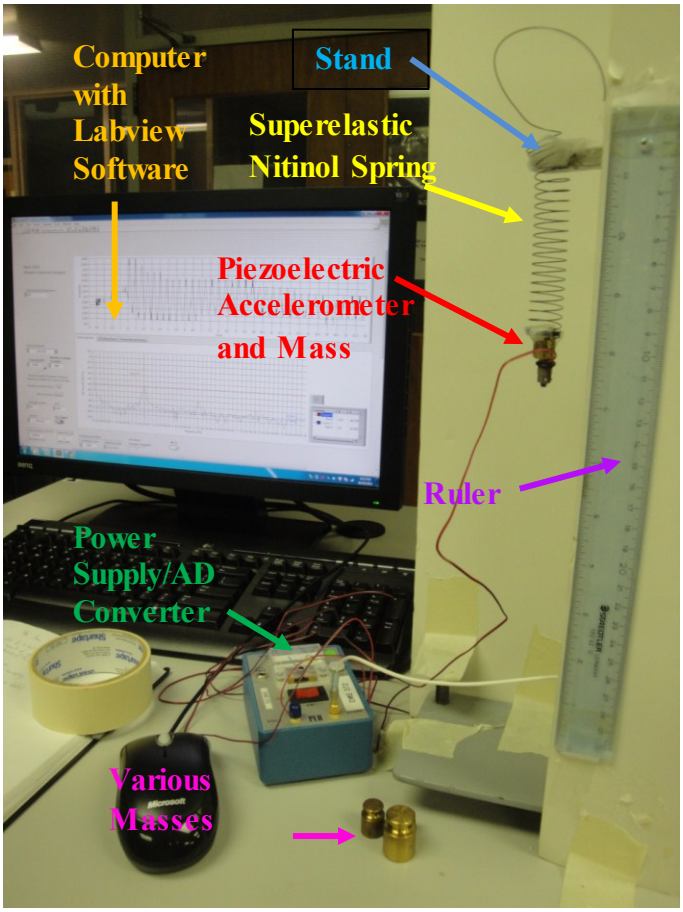

Figure 7-15: The experimental apparatus for the superelastic nitinol spring experiments with labelled components

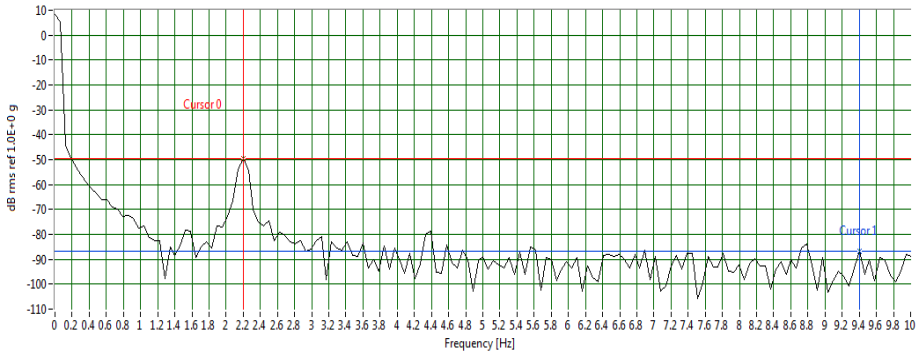

Figure 7-16: The resonance frequency was found by finding the peak on the FFT diagram. This particular FFT diagram was taken from a gauge 22 wire spring, made using a ¾" power screw, was 12 turns long, and was resonating with a 20g mass. The resultant peak was observed at 2.2Hz.

7.7 PREDICTIONS

Before analyzing the collected data from the experiments, predictions were made based on the models presented in Section 7.4. Made by Memry^{TM}, the listed properties of the superelastic wire was found on their company website and affiliated company websites and are listed in Table 7-4. The Poisson's ratio was assumed to be 0.33 as this is a typical value for nitinol (JM Medical Corp., 2012). The supplier was uncertain to what the transition temperature was; he believed the A_s transition temperature to be around 0 °C. As Memry^{TM} only produces superelastic alloys that have an A_s temperature of -5 °C to -15 °C, the author does not believe that the A_s would be 0 °C. A DSC would have to be performed to know the transition temperatures for certain, but this is outside the scope of this thesis.

Table 7-4: The Listed Properties of the Superelastic Nitinol Wire

Property	Value [Martensite (M)/Austenite (A)]	Source
Melting Point	1310	(Memry Corporation, 2012)
Density (g/cm^3)	6.5	
Electrical Resistivity (μΩ-cm)	76 (M)/ 82 (A)	
Thermal Expansion (10^{-6}/°C)	6.6 (M)/ 11 (A)	
Thermal Conductivity (W/m°C)	18	
Elastic Modulus (GPa)	40 (M)/ 75 (A)	
Assumed Poisson's Ratio	0.33	(JM Medical Corp., 2012)
Upper Superelastic Plateau Stress (MPa)	379	(SAES Getters Group, 2008)
Lower Superelastic Plateau Stress (MPa)	138	
Permanent Set after 10% Strain	0.10%	
Yield Strength of Martensite After Transition (MPa)	814	
Ultimate Tensile Strength (MPa)	1068	
Elongation to Failure	17.5%	
Maximum Strain Recovery	8%	

Extracted from SAES Getters Group (2008), the stress-strain curve for the superelastic alloy is shown in Figure 7-17. The upper plateau and lower plateau stresses are respectively 379 MPa and 138 MPa and the maximum strain recovery (ε_L) is 8% as listed in Table 7-4. As the alloy's transition temperatures are uncertain along with the room's ambient temperature, it was assumed for the predicted calculations that the upper plateau stress, lower plateau stress, and maximum strain recovery are those listed in Table 7-4.

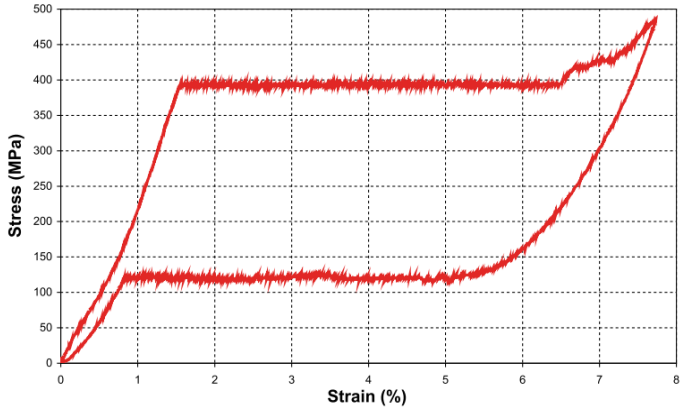

Figure 7-17: The Stress-Strain Curve of Memry's Superelastic Alloy [As = -10°C ±8°C (3σ), Af = +5 ± 16°C (3σ)]. Image extracted from (SAES Getters Group, 2008)

As there is no indication at what stresses the alloy begins and ends its stress-induced austenite to martensite transformation (*i.e.* σ^{Ms} or σ^{Mf}), the author assumed that the transformation begins and ends at the upper superelastic plateau stress (σ^{UP}) of 379 MPa. Using the Von Mises Criterion at pure shear, the maximum shear stress associated with the upper plateau stress is 218.8 MPa. Stress-induced martensite will therefore begin to form at this shear stress. If below this stress, the superelastic spring should completely be in its austenite phase, and the austenite modulus of elasticity should be used to calculate its deflection. Rearranging Equation 7-29, the deflection below a shear stress of 218.8 MPa is therefore predicted to be:

$$\delta^A = \frac{8FD^3N}{d^4G_A} \qquad 7\text{-}51$$

If the shear stress surpasses this value, the deflection will be the result of a combination of the austenite deflection limit (δ_{Ms}), the transformation deflection (δ^{tr}_{max}), and the twinned martensite deflection (δ^{TM}). Assuming that the maximum strain recovery (ε_L) is directly transferrable to a maximum shear strain (γ^{tr}_{max}) as shown in Equation 7-37, the resultant deflection after a transformation can be shown to be:

$$\delta^M = \delta_{Ms} + \delta_{max}^{tr} + \delta^{TM} = \frac{\pi\sigma^{UP}D^2N}{dG_A\sqrt{3}} + \frac{2\pi(1+\upsilon)\varepsilon_L D^2 N}{d\sqrt{3}} + \frac{8D^3N}{d^4G_M}\left(F - \frac{\pi\sigma^{UP}d^3}{8D\sqrt{3}}\right) \quad 7\text{-}52$$

Using Equations 7-51 and 7-52, predicted deflections were made for all geometrical manipulations.

For the resonance frequency predictions, it was assumed that the spring-mass model is still valid; therefore the resonance frequency would be a function of the spring's stiffness. Providing that the shear stress is below the critical shear stress value to form stress-induced martensite (*i.e.* 218.8 MPa), the stiffness was calculated based on the spring's geometry and austenitic modulus of rigidity. Using Equations 7-17 and 7-29, the resonance frequency while in its austenite phase (f_n^A) can be shown as:

$$f_n^A = \frac{1}{2\pi}\sqrt{\frac{d^4G_A}{m8D^3N}} \quad 7\text{-}53$$

For shear stresses surpassing the critical value of 218.8 MPa, the state of the spring was assumed to be stress-induced martensite; the stiffness was based on the spring's geometry along with the martensitic modulus of rigidity:

$$f_n^M = \frac{1}{2\pi}\sqrt{\frac{d^4G_M}{m8D^3N}} \quad 7\text{-}54$$

For the number of active turns manipulation, all of the estimated shear stresses were below 100 MPa; all of these springs were therefore assumed to still be in their austenite phase; only Equations 7-51 and 7-53 were needed as a result. The deflection and resonant frequency predictions for the number of active turn manipulation are presented in Table D-2 in Appendix D3. With a maximum estimated shear stress of 182 MPa, the wire diameter manipulations were also less than the critical shear stress of 218.8 MPa. Like the number of spring turns, only Equations 7-51 and 7-53 were used for the wire diameter manipulations. The deflection and resonant frequency predictions for the wire diameter manipulation are presented in Table D-12 in Appendix D4. For the spring diameter manipulation, some of the estimated shear stresses were above the critical shear

stress, therefore Equations 7-51 through 7-54 were used for the calculated predictions. The deflection and resonant frequency predictions for the spring diameter manipulation are presented in Table D-18 in Appendix D5.

When calculating the predicted deflections for deflections past the critical shear stress, the author realized that Equation 7-36 along with any equations that were derived using it were invalid for superelastic springs. Using Equation 6.37, the maximum recoverable shear strain was calculated to be 0.123. For the two spring diameters in which the critical shear stress was surpassed, the ones made with 0.5" and 0.4375" power screws, the transformation deflections were calculated to be 61.3 cm and 46.7 cm, respectively. The author knew these deflections were excessive for what was observed during the experiments. The author then realized that it was due to the wire's shear stress distribution. As the shear stress is linear, the stress-induced transition temperatures would vary linearly as well. The transition temperatures would radially increase in a linear fashion from M_S, M_f, A_s, and A_f at the wire's center to M_s^τ, M_f^τ, A_s^τ, and A_f^τ at the wire's outer surface. This implies that once the critical shear stress is exceeded, only the outside diameter will begin transforming into stress-induced martensite. As the shear stress continues to increase past the critical point, stress-induced martensite will form at closer areas to the center. For example, when the shear stress is increased 50% past its critical point, the area between the outer surface and two thirds of the wire's radius will have been transformed into stress-induced martensite while the remainder will still be austenite; when increased to twice the critical shear stress, the area between the outer surface and half of the wire's radius will have been transformed into stress-induced martensite while the remainder will be austenite. Because of the shear stress distribution, one cannot assume that when the critical shear stress has been reached, the whole specimen will have transformed into stress-induced martensite; only a portion of the specimen will have transformed. In summary, Equation 7-36 assumes that ξ is 1, indicating a complete transformation; this assumption is not valid.

Toi, Lee, & Taya (2004) gave an alternative way of looking at the shear stress constitutive equation for superelastic springs. As thermoelastic tensors can be assumed

to be negligible in isothermal conditions (*i.e.* $\theta = 0$), the shear stress constitutive equation can be presented as Equation 7-55:

$$\tau - \tau_0 = G_\tau(\gamma - \gamma_0) + \Omega_\tau(\xi_{S\tau} - \xi_{S\tau 0}) \quad 7\text{-}55$$

$\xi_{S\tau}$, G_τ, and Ω_τ respectively represent the stress-induced martensitic fraction, the modulus of rigidity at a particular shear stress, and the shear transformation constant. Toi, Lee, & Taya (2004) express $\Omega_\tau$as Equation 7-56 where γ_L is the maximum residual strain and is equivalent to ε_L:

$$\Omega_\tau = -\gamma_L G_\tau = -\varepsilon_L G_\tau \quad 7\text{-}56$$

G_τ is expressed as:

$$G_\tau = G_A + \xi_{S\tau}(G_M - G_A) \quad 7\text{-}57$$

While the spring is still in its austenite phase, $\xi_{S\tau}$ is 0 and the spring would thus follow traditional spring mechanics using its austenitic modulus of rigidity. However, as soon as stress-induced martensite forms, $\xi_{S\tau}$ is no longer 0. Using the beginning of the stress-induced transformation as initial conditions:

$$\tau_0 = \tau^{Ms}, \gamma_0 = \frac{\tau^{Ms}}{G_A}, \xi_{S\tau 0} = 0 \quad 7\text{-}58$$

Equation 7-55 can therefore be rewritten as:

$$\tau_{max} - \tau^{Ms} = G_\tau\left(\gamma^{tr} - \frac{\tau^{Ms}_{max}}{G_A}\right) + \Omega_\tau \xi_{S\tau} \quad 7\text{-}59$$

Substituting Equation 7-56 into Equation 7-59 and rearranging to solve for the transformation shear strain, γ^{tr}:

$$\gamma^{tr} = \frac{\tau_{max} - \tau^{Ms}}{G_A + \xi_{S\tau}(G_M - G_A)} + \frac{\tau^{Ms}_{max}}{G_A} + \varepsilon_L \xi_{S\tau} \quad 7\text{-}60$$

One can solve for the martinsitic volume fraction under the assumption there exists a critical radius where one side is austenite and the other is stress-induced martensite. The shear stress at this critical radius would thus be equivalent to τ^{Ms}. As the shear stress is linear from 0 at the wire's center to τ_{max} at the outer surface, the ratio of the critical radius to the wire radius would thus be equivalent to the ratio of τ_{max} to τ^{Ms}. The critical radius (r_{crit}) would thus be equivalent to:

$$r_{crit} = \frac{\tau^{Ms} * r}{\tau_{max}} \tag{7-61}$$

The stress-induced martensite volume fraction would thus be equivalent to:

$$\xi_{S\tau} = \frac{\pi(r^2 - r_{crit}^2)}{\pi r^2} = 1 - \left(\frac{r_{crit}^2}{r^2}\right) = 1 - \left(\frac{\tau^{Ms}}{\tau_{max}}\right)^2 \tag{7-62}$$

Substituting Equation 7-62 and 6-58 into Equation 7-60 yields the transformation shear strain:

$$\gamma = \frac{\tau_{max} - \tau^{Ms}}{G_A + \left[1 - \left(\frac{\tau^{Ms}}{\tau_{max}}\right)^2\right](G_M - G_A)} + \frac{\tau^{Ms}}{G_A} + \left[1 - \left(\frac{\tau^{Ms}}{\tau_{max}}\right)^2\right]\varepsilon_L \tag{7-63}$$

The total deflection caused by this transformation shear strain (δ^{tr}) is therefore:

$$\delta^{tr} = \frac{\pi D^2 N}{d}\left(\frac{\tau_{max} - \tau^{Ms}}{G_A + \left[1 - \left(\frac{\tau^{Ms}}{\tau_{max}}\right)^2\right](G_M - G_A)} + \frac{\tau^{Ms}}{G_A} + \left[1 - \left(\frac{\tau^{Ms}}{\tau_{max}}\right)^2\right]\varepsilon_L\right) \tag{7-64}$$

The absolute total deflection for a superelastic spring with stress-induced martensite would thus be the summation of the transformation deflection along with the austenite deflection limit:

$$\delta^{\tau} = \delta^{tr} + \delta_{Ms} \tag{7-65}$$

Using Equation 7-65, new deflection calculations were performed for the trials that surpassed the critical shear stress. Presented in Table D-18 in Appendix D5, these new predictions had values that ranged from 19% to 70.6% of their original calculations and thus were more in line with the overall observations. Although this deflection formula better depicts the nature of a superelastic spring, the values obtained still seemed higher than what was observed. When later compared to the actual results, they still overestimated the results by 157% to 277%. One reason for the overestimation is that this method essentially states that as soon as the spring goes into a stress-induced state, it has the calculated modulus of rigidity at its end state (*i.e.* when the spring reaches its final deflection); this statement is not valid. When stress-induced martensite starts to form when the stress limit has been reached, the modulus of rigidity will start at G_A and converge to $G_\tau$as it reaches its final deflection. To truly capture the end deflection, one

must therefore take an integrative approach or use a finite element method with reference to Equation 7-55: something that will not be explored in this thesis. Another reason for the observed error may be a decrease in the overall spring diameter which would in turn increase the overall stiffness and decrease the spring's overall deflection. If these experiments were to be performed again, it would be recommended to measure the spring's diameter when loaded to see if it indeed decreases.

Using the overall modulus of rigidity as defined in Equation 7-57, one can find the spring/mass systems resonant frequency by substituting the overall modulus of rigidity into Equation 7-54:

$$f_n^{\tau} = \frac{1}{2\pi}\sqrt{\frac{d^4 G_{\tau}}{m8D^3N}} = \frac{1}{2\pi}\sqrt{\frac{d^4\left[G_A + \left(1 - \left(\frac{\tau_{max}^{Ms}}{\tau_{max}}\right)^2\right)(G_M - G_A)\right]}{m8D^3N}} \qquad 7\text{-}66$$

Using Equation 7-66, new calculated predictions were made for trials having shear stresses above the critical shear stress limit. The new calculations are listed in Table D-18, located in Appendix D5.

7.8 RESULTS and DISCUSSION

Divided into three subsections, one for each spring manipulation, this section presents the results along with their respective calculated predictions. The three measurements from each trial were averaged and presented in graphs to calculate the overall stiffness of each spring using the deflection measurements and resonant frequency measurements. The slope of the force/deflection curves would be equivalent to the stiffness, while the slope of the resonant frequency/mass power curves would be equivalent to $2\pi k^{0.5}$. The resultant stiffness was then calculated using these slopes, followed by calculating the corresponding modulus of elasticity as indicated by Equations 6-57 and 6-61 to observe if it is similar to the moduli of elasticity listed by the manufacturer in Table 7-4. For comparison, at each trial the austenite and martensite spring stiffness, values were calculated for a spring with identical geometry.

7.8.1 Number of Spring Turns Manipulation

All of the data extracted from the number of spring turns manipulation can be found in Table D-3 through Table D-11 in Appendix D3. Figure 7-18 visually shows the force/deflection results from the number of spring turns manipulation along with the predicted results under the assumption that the alloy stays at its austenite phase, while Table 7-5 presents a summary of the stiffnesses extracted from Figure 7-18 along with the predicted austenite and martensite stiffnesses using the spring's geometry and listed moduli of elasticity. As mentioned, all springs were made from gauge 22 nitinol wire using the same 0.75" power screw. As shown in Table D-3, very little permanent transformation took place during this manipulation as two trials had no measured

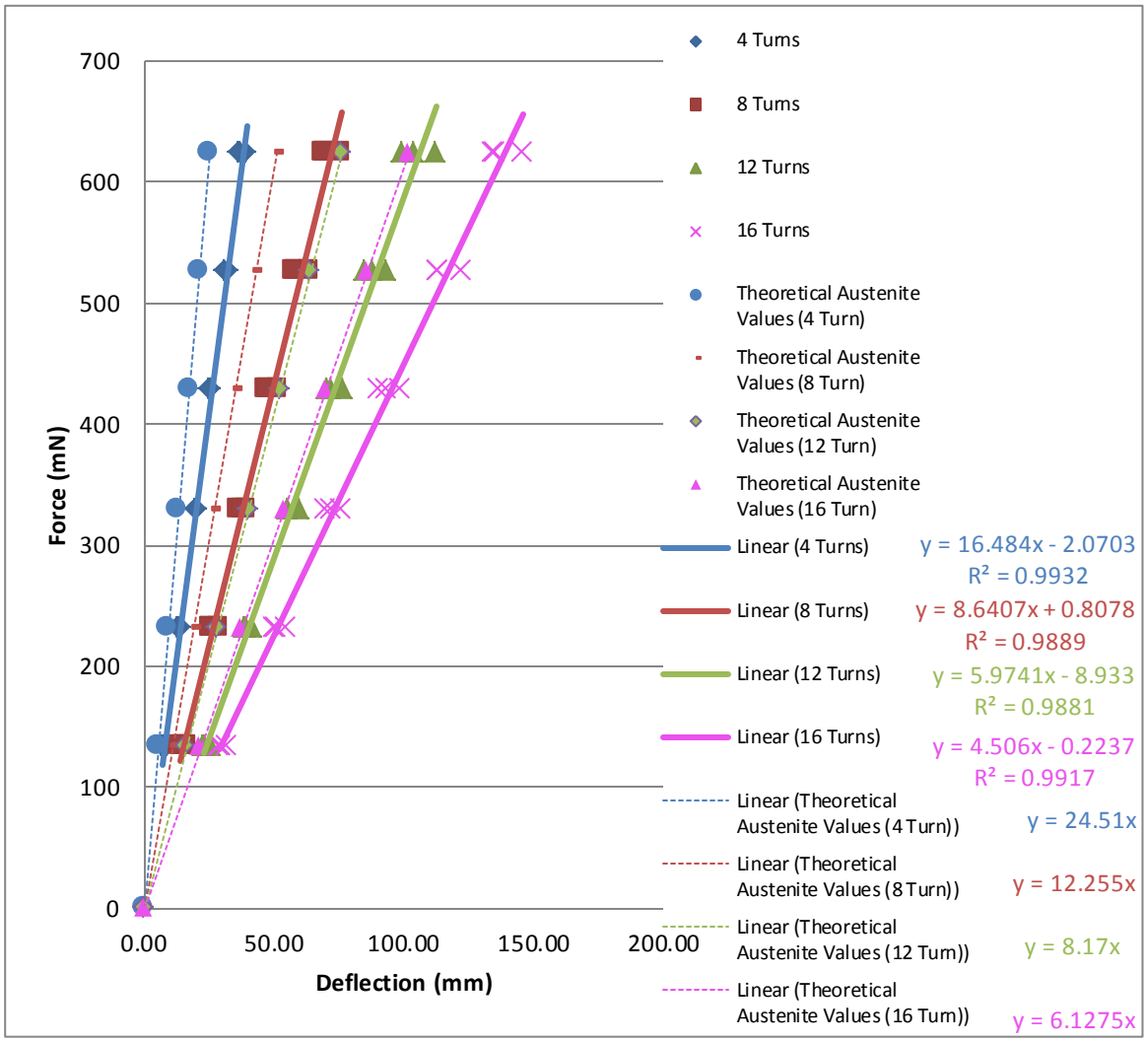

Figure 7-18: The Deflections for the Number of Spring Turn Manipulation with Reference to the Applied Force. Linear Trends and Regression Results are presented in the legend.

differences from the start and finish lengths and one trial only had a difference of 1mm. The measured deflections were therefore assumed to only have been caused by their respective applied forces rather than partially due to permanent transformation from a previously applied force.

Table 7-5: A Summary of the Stiffness Results for the Number of Spring Turns Manipulation with comparison to a superelastic spring that is completely austenite or martensite

Turns	Slope from Graph [*i.e.* Stiffness (N/m)]	R^2 Value	Stiffness Ratio in Comparison to 16 Turns		Calculated Modulus of Elasticity from Stiffness (GPa)	Calculated Austenite Stiffness (N/m)	Calculated Martensite Stiffness (N/m)
			Experimental	Theoretical			
4	16.48	0.9932	3.65	4	50.4	24.5	13.1
8	8.64	0.9889	1.92	2	52.9	12.3	6.54
12	5.97	0.9881	1.32	1.33	54.8	8.17	4.36
16	4.51	0.9917	1	1	55.2	6.13	3.27

The experimental results showed that there is indeed a linear relationship between the applied force and deflection as all spring turns had linear regression R^2 values between 0.9881 and 0.9932. This linear relationship was predicted as all of the trials had estimated shear stresses below the critical transformation shear stress of 218.8 MPa, indicating that they were all in their austenite phase and would have a constant modulus of rigidity as a result. The results also showed that there is a linear relationship between the stiffness and number of active turns as shown by the stiffness ratios. In comparison to a spring of 16 turns, the stiffness ratios should be 1, 1.33, 2, and 4 for springs with 16, 12, 8, and 4 turns, respectively. The test results revealed stiffness ratios of 1, 1.32, 1.92, and 3.65 which correspond to the theoretical ratios very well. The highest ratio error was from the 4 turn spring; the experimental ratio of 3.65 was 8.65% less than the theoretical ratio. This minor error is likely due to measurement resolution. As the 4 turn spring had lower deflections, estimating to the nearest mm may not have reflected the spring's true deflection.

Theoretically the calculated modulus of elasticity should be the same for each spring as they were constructed from the same wire. The calculated moduli of elasticity were

relatively close to one another having values of 50.4 GPa to 55.2 GPa which are within 9.5% of each other. However, these values did not correlate very well with the predicted austenite modulus of elasticity of 75 GPa; they were actually closer to the martensite modulus of elasticity of 40 GPa. From theory, the linear force-deflection pattern of the springs indicates that the modulus of rigidity is constant, indicating that the spring is not going through a transformation; the spring must therefore completely be in its austenite phase or martensite phase. It is possible that the listed modulus of elasticity from the manufacturer was not correct.

Figure 7-19 visually shows the resonant frequency results with respect to the resonating mass along with the predicted values at pure austenite, while Table 7-6 summarizes the numerical results, and calculated stiffnesses and moduli of elasticity. The results showed that there is a power relationship between the resonant frequency and the resonating mass

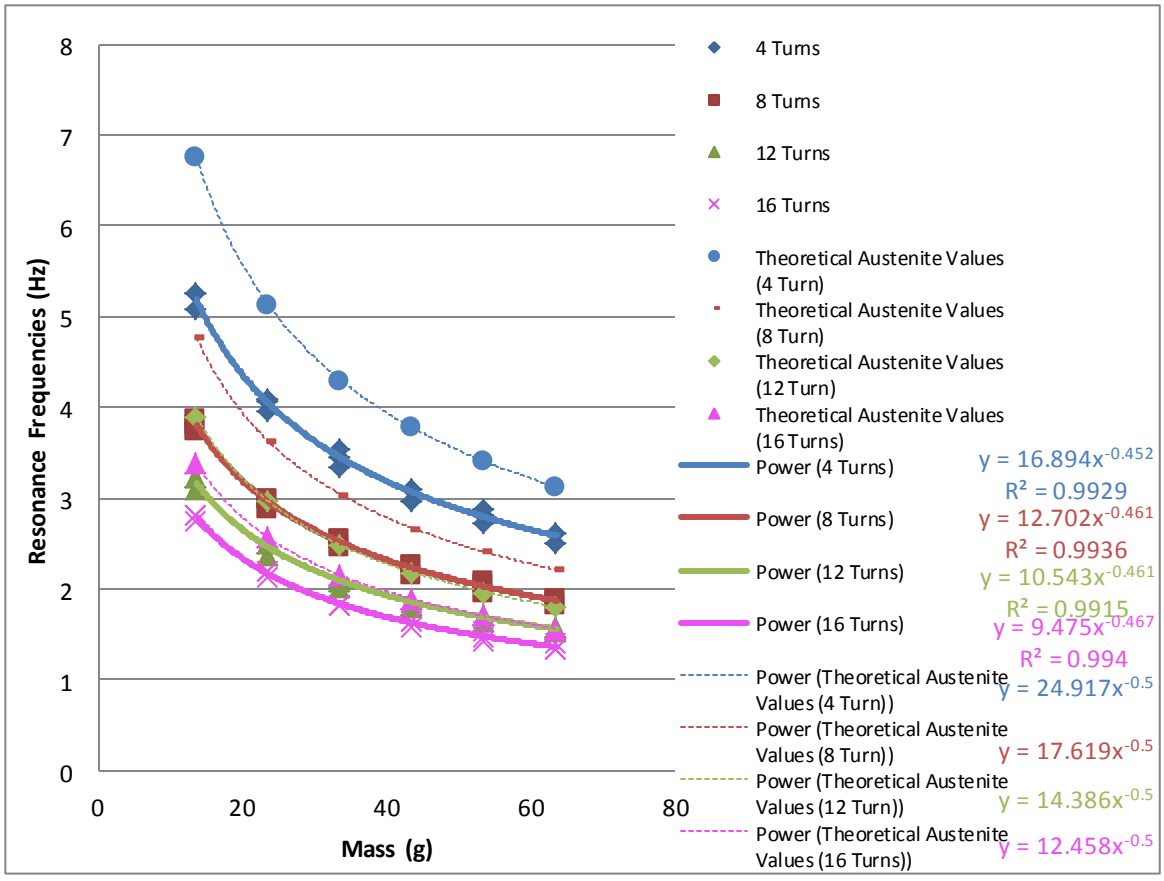

Figure 7-19: The Resonance Frequencies for the Number of Spring Turn Manipulations with Reference to the Mass. Power Trends and Regression Results are presented in the legend.

as indicated by Equation 7-46; the R^2 values were all above 0.99. However, the exponents, ranging from -0.452 and -0.467, fell short of the theoretical exponent of -0.5. Also, with errors ranging from 7.0% to 20.2%, the stiffness ratios did not correlate as well to the theoretical values in comparison with the force-deflection data. Like the force-deflection data, the biggest error was associated with the 4 turn spring. The calculated moduli of elasticity among all turns, varied from 34.5 GPa to 43.4 GPa, within 25.8% of each other. Not only were these moduli of elasticity less than those calculated from the force-deflection data, they were also more varied among spring turns. In comparison to the manufacturer's moduli of elasticity, those calculated from these experiments were more in line with the listed martensite value of 40 GPa than the predicted austenite modulus of elasticity of 75 GPa.

Table 7-6: A Summary of the Resonance Results for the Number of Spring Turns Manipulation with comparison to a superelastic spring that is completely austenite or martensite

Turns	Slope from Graph $[(N/m)^{1/2}]$	Exponent	R^2 Value	Calculated Stiffness from Slope (N/m), [Ratio to 16 Turns]	Calculated Modulus of Elasticity from Stiffness (GPa)	Calculated Austenite Stiffness (N/m)	Calculated Martensite Stiffness (N/m)
4	16.89	-0.452	0.9929	11.3 [3.10]	34.48	24.5	13.1
8	12.70	-0.461	0.9936	6.37 [1.8]	38.98	12.3	6.54
12	10.4	-0.461	0.9915	4.39 [1.24]	40.28	8.17	4.36
16	9.475	-0.467	0.994	3.54 [1]	43.38	6.13	3.27

From the data obtained from both experiments and the material properties from the manufacturer, it appears that the superelastic springs may be in their martensite phase as opposed to their austenite phase as originally thought. It is therefore conceivable that the transition temperatures may have risen during their heat treatment, allowing the martensite phase to form at lower ambient temperatures. This concept will be further investigated in Section 7.9.

7.8.2 Wire Diameter Manipulation

All of the data extracted from the wire diameter manipulation can be found in Table D-13 through Table D-17 in Appendix D4. Figure 7-20 shows the force/deflection results for the wire diameter manipulation, while Table 7-7 presents the stiffness values extracted from Figure 7-20 along with the calculated modulus of elasticity, and theoretical stiffnesses from an austenite and martensite spring of the same geometry. As mentioned, all springs were made using the same 0.75" diameter power screw and had 12 spring turns. As shown in Table D-13, the springs did not suffer from any permanent deformation during this manipulation; the deflections are therefore assumed to be solely from their respective applied force as opposed to being partially caused from a previously applied force.

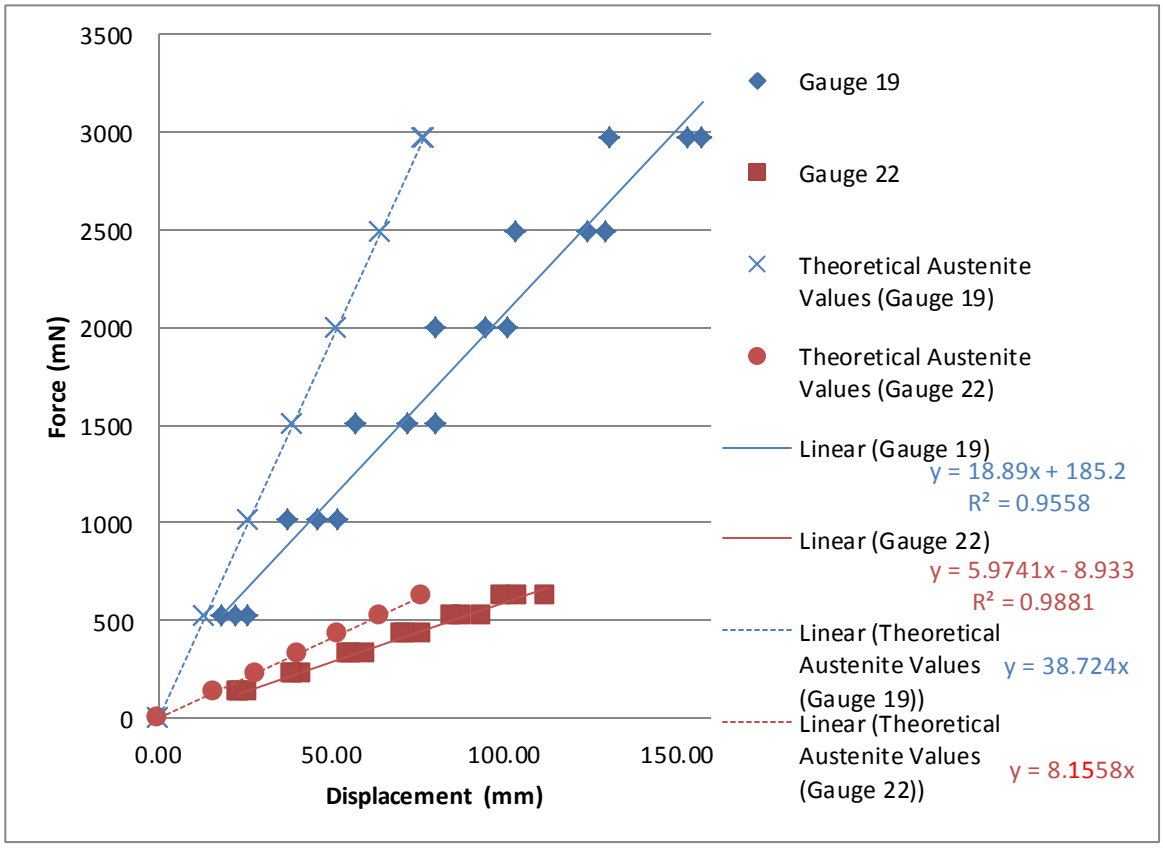

Figure 7-20: The Deflection Measurements with Respect to the Applied Force for the two wire diameters. Linear Trends and Regression Results are presented in the legend.

Overall, the experimental results support a linear relationship between force and deflection as predicted, however, the R^2 value of 0.9558 for the gauge 19 wire is not as

high as the R^2 value of 0.9881 for the gauge 22 wire. The lower R^2 value for the gauge 19 wire is due to the fact that one of the springs was observably stiffer than the other two and thus skewed the averaged stiffness. When comparing the experimental and theoretical stiffness ratios between the two wire diameters, one would notice that the experimental ratio is about two thirds of the theoretical ratio. The author believes that the difference in stiffness ratios may be due to inaccuracies in the wire diameter measurements. According to the micrometer, the gauge 19 and gauge 22 wires had diameters that were respectively 2.8% and 9.6% less than their supposed diameters. As the stiffness correlates with the wire diameter to the fourth power, an inaccurate wire diameter measurement will significantly alter the theoretical calculations. For example, if one assumed the wire diameters to be geometrically correct with their gauge specifications (*i.e.* 0.0359" and 0.0254" for gauge 19 and gauge 22 wires, respectively), the theoretical stiffness ratio would decrease to 3.55 which better correlates with the experimental stiffness ratio.

An inaccurate wire diameter may also be the reason for the observed difference in the calculated moduli of elasticity. Like the stiffness ratio, the calculated modulus of elasticity from the gauge 19 wire experiments (36.59 GPa) was about two thirds of the calculated modulus of elasticity from the gauge 22 wire experiments (54.84 GPa). However, if one recalculated the modulus of elasticity assuming that the wires have their intended gauge diameters, the calculated moduli of elasticity would change to 32.7 and 36.7 GPa for the gauge 19 and gauge 22 wires, respectively. In fact, if one recalculated the moduli of elasticity for the number of spring turns manipulation, one would get moduli of elasticity that ranged from 33.7 GPa and 36.9 GPa. An inaccurate wire diameter measurement could therefore compromise all of the modulus of elasticity calculations performed in these experiments. If one were to repeat these experiments, the author would recommend measuring the wire diameters using more than one micrometer to ensure that the measurement is accurate. Regardless of whether the wire diameter was not measured correctly, the moduli of elasticity were still much smaller than the listed austenite modulus of elasticity and more in line with the martensite modulus of elasticity as was seen in the number of spring turns manipulation.

Table 7-7: A Summary of the Stiffness Results for the Wire Diameter Manipulation with comparison to a superelastic spring that is completely austenite or martensite

Wire Diameter (mm)	Slope from Graph [*i.e.* Stiffness (N/m)]	Stiffness Ratio in Comparison to 0.583mm		Stiffness Ratio in Comparison to 16 Turns	Calculated Modulus of Elasticity from Stiffness (GPa)	Calculated Austenite Stiffness (N/m)	Calculated Martensite Stiffness (N/m)
		Experimental	Theoretical				
0.886	18.89	3.16	4.74	0.9558	36.59	38.7	20.7
0.583	5.97	1	1	0.9881	54.84	8.16	4.36

Figure 7-21 visually shows the experimental resonant frequencies with respect to the resonating mass, while Table 7-8 summarizes the numerical results, and calculated stiffness values and moduli of elasticity. The results support the theoretical power relationship between the resonance frequency and resonating mass with R^2 values of 0.983 and 0.992, but like the number of spring turns, all of the exponents were slightly less than the theoretical value of -0.5; the exponents were -0.461 and -0.469. The stiffness ratio, at 3.96, was closer to the predicted theoretical value of 4.74, but was

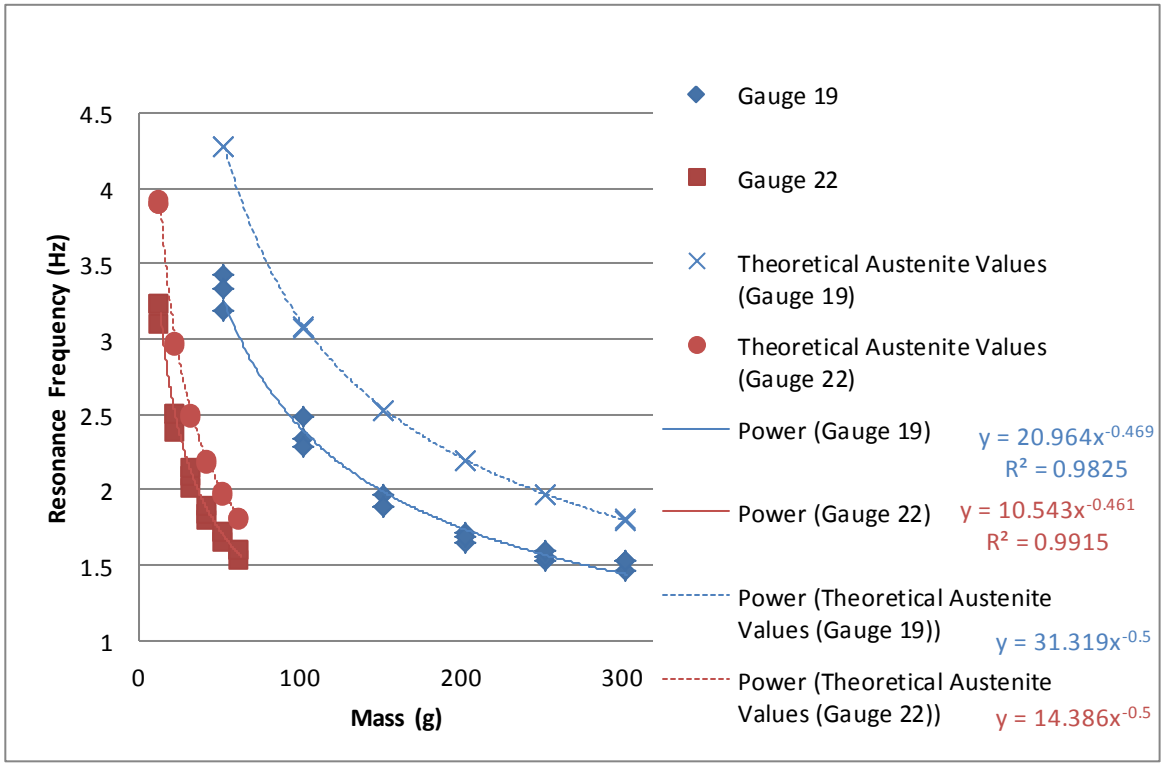

Figure 7-21: The Resonant Frequency Measurements with Respect to the mass for the two wire diameters. Power Trends and Regression Results are presented in the legend.

25.3% larger than the stiffness ratio from the force-deflection results. This conflicts with what was observed in the number of spring turns manipulation, where the stiffness ratios from the force-deflection data were higher than the resonance frequency data.

Table 7-8: A Summary of the Resonance Results for the Wire Diameter Manipulation with comparison to a superelastic spring that is completely austenite or martensite

Wire Diameter (mm)	Slope from Graph $[(N/m)^{1/2}]$	Exponent	R^2 Value	Calculated Stiffness from Slope (N/m) [Ratio to 0.583mm]	Calculated Modulus of Elasticity from Stiffness (GPa)	Calculated Austenite Stiffness (N/m)	Calculated Martensite Stiffness (N/m)
0.886	20.964	-0.469	0.983	17.4 [3.96]	33.60	38.7	20.7
0.583	10.543	-0.461	0.992	4.39 [1]	40.28	8.16	4.36

Like the number of spring turns manipulation, the calculated moduli of elasticity from the resonance results were lower than those calculated from the force-deflection results. With values of 33.6 GPa and 40.28 GPa for the gauge 19 and gauge 22 wires, respectively, the calculated moduli of elasticity were closer to a uniform value than the force-deflection measurements, but they were still well below the predicted austenite modulus of elasticity and more in line with the martensite modulus of elasticity. These results further support that the springs may be in their martensite phase as opposed to the presumed austenite phase.

7.8.3 Spring Diameter Manipulation

All of the data extracted from the spring diameter manipulation can be found in Table D-19 through Table D-29 in Appendix D5. As mentioned, all the springs used for the spring diameter manipulation were made from gauge 22 superelastic nitinol wire and had 8 turns. Figure 7-22 presents the force-deflection data from the spring diameter manipulation, while Table 7-9 summarizes the experimental stiffness and modulus of elasticity for each spring diameter along with their expected austenite or martensite stiffness for a spring with the same geometry. The start and end spring lengths (as shown in Table D-19) indicate that permanent strain may have occurred in some of the springs, the maximum being 2 mm in one of the 0.625" trials. However, as this permanent

deflection is quite minimal relative to the overall deflections imposed on the springs, it was assumed for this analysis that the resultant deflections were only caused by the associated applied force and not partially from previously applied forces.

Table 7-9: A Summary of the Stiffness Results for the Spring Diameter Manipulation with comparison to a superelastic spring that is completely austenite or martensite. Values in square parantheses represent the values when points that surpass the upper plateau stress are removed.

Spring Diameter (mm)	Slope from Graph [*i.e.* Stiffness (N/m)]	Stiffness Ratio in Comparison to 18.8mm Spring Diameter		R^2 Value	Calculated Modulus of Elasticity from Stiffness (GPa)	Calculated Austenite Stiffness (N/m)	Calculated Martensite Stiffness (N/m)
		Experimental	Theoretical				
18.8	5.41	1	1	0.9859	52.8	7.69	4.10
16.1	8.64	1.60	1.60	0.9889	52.9	12.3	6.54
13.4	14.5	2.68	2.78	0.9785	51.1	21.4	11.4
10.8	18.7	3.46 [4.66]	5.32	0.9735 [0.9971]	34.2 [46.2]	40.9	21.8
9.40	27.35	5.06 [7.50]	8.00	0.955 [0.9921]	33.3 [49.4]	61.5	32.8

The springs with larger diameters tended to have higher R^2 values indicating that a linear relationship between force and deflection was probable. However, as the spring diameters decreased to 10.8 mm and 9.40 mm, the higher forces tended to cause higher deflections than a linear relationship would predict; the R^2 at these spring diameters were lower as a result. Additionally, with regards to the stiffness ratios in relation to the 18.8 mm spring diameter, the 16.1 mm and 13.4 mm spring diameter had excellent correlation with their predictions with respective errors of 0.15% and 3.7%, but the 10.8 mm and 9.40 mm springs had poorer correlation with their predictions with errors of 35.0% and 36.8%, respectively. However, if one removes the data points caused by the largest three applied forces in the 10.8 mm spring as well as the data points caused by the largest two applied forces in the 9.40 mm spring, the stiffness ratios for the 10.8 mm and 9.40 mm springs increase to 4.66 and 7.50, decreasing the error with the theoretical values to 12.4% and 6.2%. Likewise the resultant moduli of elasticity for the 10.8 mm and 9.40 mm springs had respective values of 34.2 GPa and 33.3 GPa which are much less than the 18.8 mm, 16.1 mm, and 13.4 mm values of 52.8 GPa, 52.9 GPa, and 51.1 GPa,

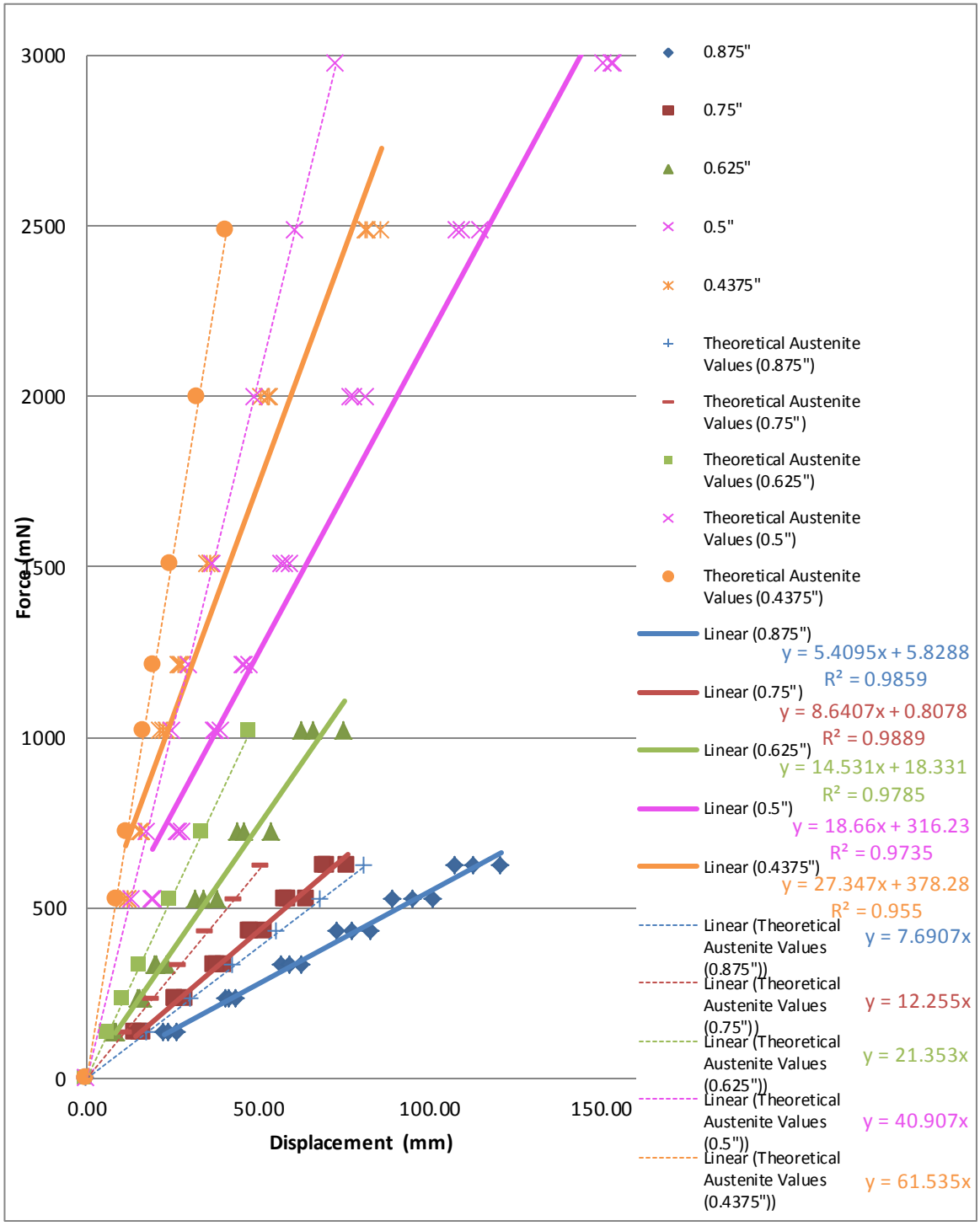

Figure 7-22: The Deflection Measurements with Respect to the Applied Force for the Spring Diameter Manipulation. Linear Trends and Regression Results are presented in the legend.

respectively. Taking the same data points away as the stiffness ratio example, the modulus of elasticity for the 10.8 mm and 9.40 mm springs falls more in line with the other spring diameters, having values of 46.2 GPa and 49.4 GPa. The removed data

points thus had different stiffness properties that changed the overall estimated stiffness in the linear regression analysis. All moduli of elasticity, nonetheless, are still less than the predicted austenite modulus of elasticity of 70 GPa and closer to the listed martensite modulus of elasticity of 45 GPa.

These trends indicate that the spring's stiffness was decreasing as the deflections got larger after a certain point. A likely explanation for this behavior is the formation of stress-induced martensite. Looking at the estimated shear stress values for each measurement (See Table D-18 in Appendix D5), the points that stray from the linear relationship (*i.e.* the highest three applied forces in the 10.8 mm spring diameter trials and the highest two applied forces in the 9.40 mm spring diameter trials) correlate with the points that theoretically cause the stress to exceed the critical shear stress and form stress-induced martensite. These observations therefore support the notion that the springs are in their austenite phase at ambient temperature despite the fact that their modulus of elasticity is considerably less than the austenite modulus of elasticity listed by the manufacturer.

Although the forming of stress-induced martensite is a plausible explanation for the observed force-deflection relationship, it is not the only one. It is possible that the spring's diameter may have decreased in response to the higher applied force. As the spring's stiffness is proportional to the spring diameter to the third power, a decrease in spring diameter could produce a significant decrease in stiffness. The stress-induced martensite explanation, however, seems more likely as observations indicated that the spring stiffness started to decrease only after the critical shear stress: an unlikely coincidence.

Figure 7-23 graphically depicts the results from the resonance frequency experiments in relation to the resonating mass, while Table 7-10 lists the results. Overall, the results supported the power relationship between the resonance frequency and resonating mass. With respective values of -0.503 and -0.501, the 18.8 mm and 13.4 mm spring diameters had exponents that were very close to the predicted value of -0.5; with respective values

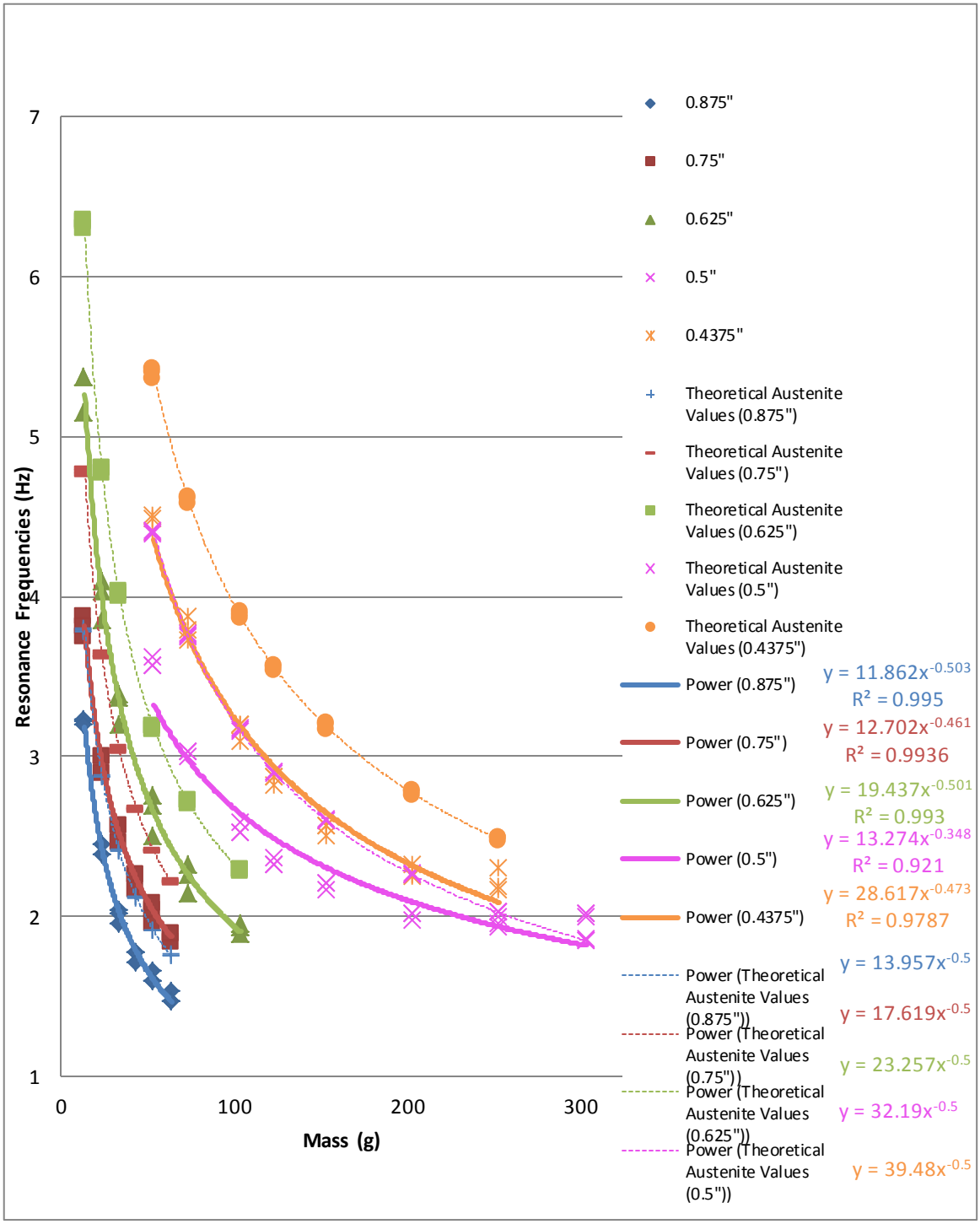

Figure 7-23: The Resonant Frequency Measurements with Respect to the Mass for the Spring Diameter Manipulation. Power Trends and Regression Results are presented in the legend.

of -0.461 and -0.47, the 16.1 mm and 9.40 mm spring diameters had exponents that were reasonably close to predicted value; the 10.8 mm spring diameter erred the most with an exponent of -0.348. With regards to the R^2 value, the larger spring diameters; 18.8 mm,

16.1 mm, and 13.4 mm; gave values larger than 0.993 indicating an excellent correlation with their calculated power function. The lower spring diameters, 10.8 mm and 9.40 mm, gave lower R^2 values of 0.921 and 0.9787, respectively which indicates less confidence in the resultant estimated power function. Likewise, having errors of 76.4% and 27.2%, the stiffness ratios for the two smaller spring diameters were greatly lower than their predicted ratios. Having an error of 28.2%, the 16.1 mm spring diameter also had a lower ratio than was predicted. The only spring diameter that had a stiffness ratio that was reasonably close to the predictions was the 13.4 mm spring with an error of 4.8%. The errors were then reflected in the moduli of elasticity calculations. The 18.8 mm and 13.4 mm springs had moduli of elasticity that were quite similar to those found in the force-deflection relationship (but still much less than the predicted austenite modulus of elasticity), while the spring diameters with larger deviations from their predicted stiffness ratio, had moduli of elasticity that were significantly less than those predicted. Interestingly, the spring diameter manipulation was the only manipulation with gauge 22 wire to produce similar stiffness results between the force-deflection and resonant frequency-mass relationships. For the resonant frequency-mass relationship, the stiffnesses found in the number of turns and wire diameter manipulations that used gauge 22 wire were all less than the stiffness values found in the force-deflection relationship. Recalling that only 16.1 mm spring diameters were used for both the number of turns and wire diameter manipulations, and that the 16.1 mm spring diameter trial in the spring diameter manipulation produced a resonant frequency stiffness that was lower than the force-deflection stiffness, there may have been something associated with the gauge 22 wire, 16.1 mm spring diameter spring trials that hampered with the resonant frequency results. It is not clear what the source of this error was.

Although it is unclear why the 16.1 mm springs had a stiffness ratio and modulus of elasticity that differed from the other large spring diameters, the deviations in the lower spring diameters are most likely due to their larger shear stresses as demonstrated earlier in the force-displacement results. At larger resonant masses, the spring's experience a larger shear stress; if said shear stress surpasses the critical shear stress, martensite will form, resulting in a decreased stiffness, and thus a lower resonant frequency. This

conflicts with the assumption of a constant stiffness as is required by the general resonant frequency equation for a spring-mass system.

Table 7-10: A Summary of the Resonance Results for the Spring Diameter Manipulation with comparison to a superelastic spring that is completely austenite or martensite

Spring Diameter (mm)	Slope from Graph $[(N/m)^{1/2}]$	Exponent	R^2 Value	Calculated Stiffness from Slope (N/m) [Ratio to 18.8mm]	Calculated Modulus of Elasticity from Stiffness (GPa)	Calculated Austenite Stiffness (N/m)	Calculated Martensite Stiffness (N/m)
18.8	11.86	-0.503	0.995	5.55[1]	54.17	7.69	4.10
16.1	12.7	-0.461	0.9936	6.37[1.15]	38.98	12.3	6.54
13.4	19.4	-0.501	0.993	14.7[2.65]	51.79	21.4	11.4
10.8	13.3	-0.348	0.921	6.96[1.25]	12.75	40.9	21.8
9.40	28.6	-0.47	0.9787	32.3[5.82]	39.40	61.5	32.8

Like the force-deflection results, if one removes the data points at which the estimated shear stress exceeds the critical shear stress, the stiffness ratios for the 10.8 mm and 9.40mm spring diameters increase to 4.0 and 10.77 resulting in errors of 24.8% and 34.8% and the moduli of elasticity increase to 40.9 GPa and 73.80 GPa, respectively. For the 10.8 mm spring diameter, removing the data points resulted in a stiffness ratio that better aligns with the predicted results and a modulus of elasticity that is closer to the other spring diameters. Although removing the two data points from the 9.40 mm spring diameter relation worsened the error in the stiffness ratio, it produced a calculated modulus of elasticity that was quite close to the austenite modulus of elasticity listed by the manufacturer. Regardless of the change in stiffness ratio or calculated modulus of elasticity, the removal of these data points produced power curves with much better R^2 values (0.988 for the 10.8 mm spring diameter and 0.998 for the 9.40 mm spring diameter), adding confidence that the data points with lower shear stresses better correlate with each other than the removed data points. The most plausible explanation for this is that the lower stresses had a constant stiffness; when the shear stress surpassed the critical stress, the spring's stiffness changed as a result of stress-induced martensite.

7.9 TENSILE TESTS

Throughout the experiments performed, there was much inconsistency with respect to the modulus of elasticity. Most of the experiments produced a resultant modulus of elasticity that was closer to the manufacturer's listed martensitic modulus of elasticity than the listed austenitic modulus of elasticity. This lead the author to believe that the transition temperatures may have risen during the heat treatment, allowing the alloy to be in its martensite state at ambient room temperature. Although the results from the spring diameter manipulation strongly suggested that the superelastic springs were indeed in their austenite phase at room temperature, the only way to be certain was to perform tensile tests as presented in Section 0. Tensile tests would therefore be performed on superelastic nitinol spring wires, before and after a heat treatment.

For the heat treatment, pieces of the gauge 19 wire were cut and placed inside a long brass tube with a small diameter to heat treat them as a straight wire. Like the superelastic springs, they were heat treated at 500 °C for 25 minutes followed by a water quench. Immediately after removal from the water quench, the author noticed that the wire's superelasticity was greatly reduced as the heat treated wires were not springing back as much in comparison to the untreated wires. However, the treated wires would completely return to their straight form once heated. It was evident that the second heat treatment had an effect on the superelastic wire's properties.

To perform the tensile tests, an Instron 8501 machine was used (See Figure 7-24). Taking cues from Liu, Wang, Yang, & Qi (2008), a low loading rate of 0.5 mm/min was used to minimize the thermal effects associated with the stress-induced transformation. All gauge lengths were approximately 45 mm, but were measured using a caliper to accurately calculate the strain rates. The wire diameters were also measured via micrometer, before loading. To get a stress-strain curve like the one provided by the manufacturer (See Figure 7-18), the wire was loaded up to roughly 7.75% strain, unloaded back down to 0% strain, and then reloaded until rupture, all at the specified loading rate of 0.5 mm/min. During loading and unloading, the machine would simultaneously record the wire's position along with the applied force. This information

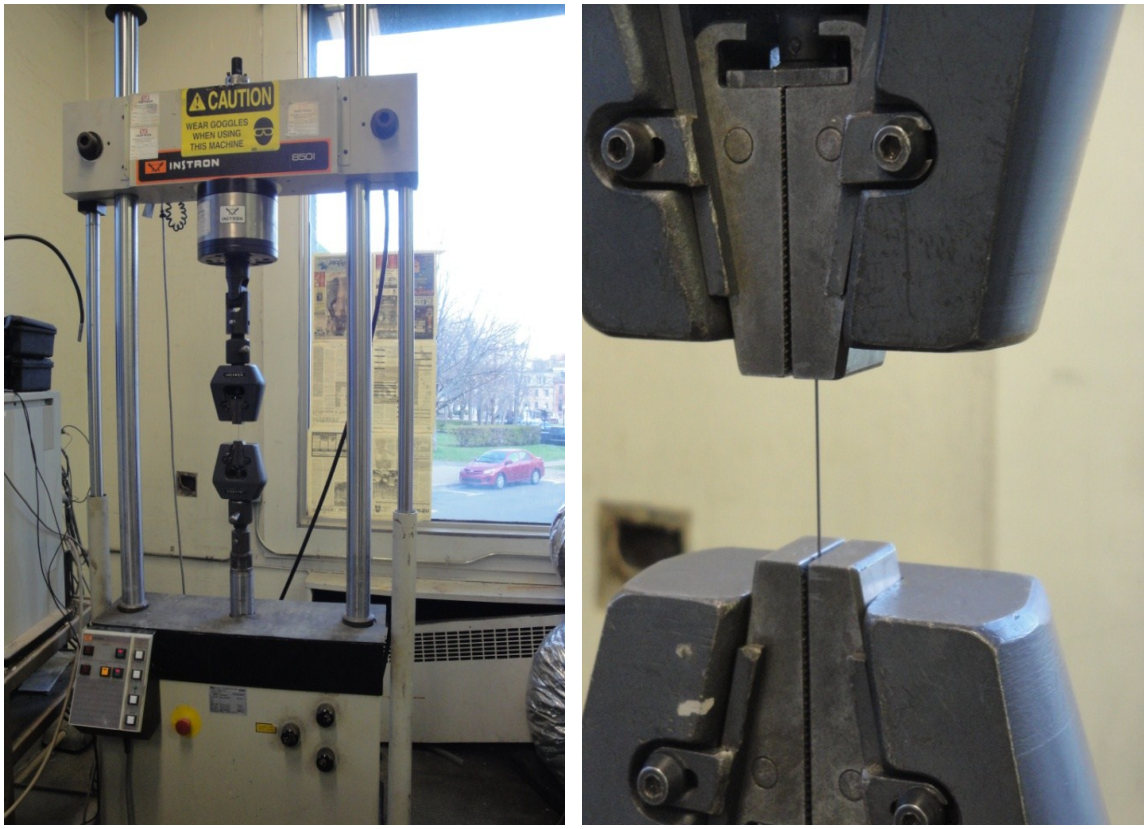

Figure 7-24: (Left) The Instron 8501 Tensile Testing Machine was used to obtain the stress-strain relationships for the superelastic nitinol wires. (Right) A closeup of the superelastic nitinol wire secured in the Instron machine's grippers.

was recorded onto a spreadsheet where the force and position would be translated into the resultant stress and strain. Using a Poisson's ratio of 0.33, the wire's cross-sectional area was appropriately changed in relation to the induced strain to get the appropriate cross-sectional area needed for the applied stress. As the wires started the loading scenario in buckling, the strain was appropriately translated in the stress strain graphs so that the strain was 0% when no force was being applied onto the wire.

Twelve tensile tests were performed: six using wires with no heat treatment and the other six with heat treatment. The austenite modulus of elasticity, upper plateau stress, and ultimate tensile stress were extracted from each stress-strain graph and are presented in Table 7-11 with corresponding averages and standard deviations. Unfortunately most of the martensitic moduli of elasticity were not retrievable as the specified maximum deflection, during the initial loading scenario, was not large enough to fully stress the

wire completely into its stress-induced martensite phase. This was likely due to the fact that the wires started in a buckling state and the maximum strain of 7.75% for the initial loading was not appropriately increased. As a result, only one acceptable martensite modulus of elasticity was found, having a value of 28.64 GPa. Figure 7-25 shows one of the stress-strain curves obtained from an unheated wire while Figure 7-26 shows one of the stress-strain curves obtained from a heated wire.

Table 7-11: A Summary of the Tensile Test Results

Wire	Austenite Modulus of Elasticity (GPa)		Upper Plateau Stress (MPa)		Ultimate Tensile Stress (MPa)	
	Untreated	Treated	Untreated	Treated	Untreated	Treated
1	27.11	31.83	296.9	199.5	1576	1322
2	32.27	20.18	315.9	210.7	1572	1455
3	30.91	35.88	317.9	202.7	1532	1412
4	31.08	23.25	290.5	268.9	1565	1470
5	24.81	27.04	307.3	226.4	1581	1403
6	21.43	30.37	313.6	261.7	1723	1508
Average	27.93	28.09	307.0	228.3	1592	1428
Std. Dev	4.25(15.2%)	5.78(20.6%)	11.1(3.62%)	30.2(13.2%)	66.8(4.2%)	64.9(4.5%)

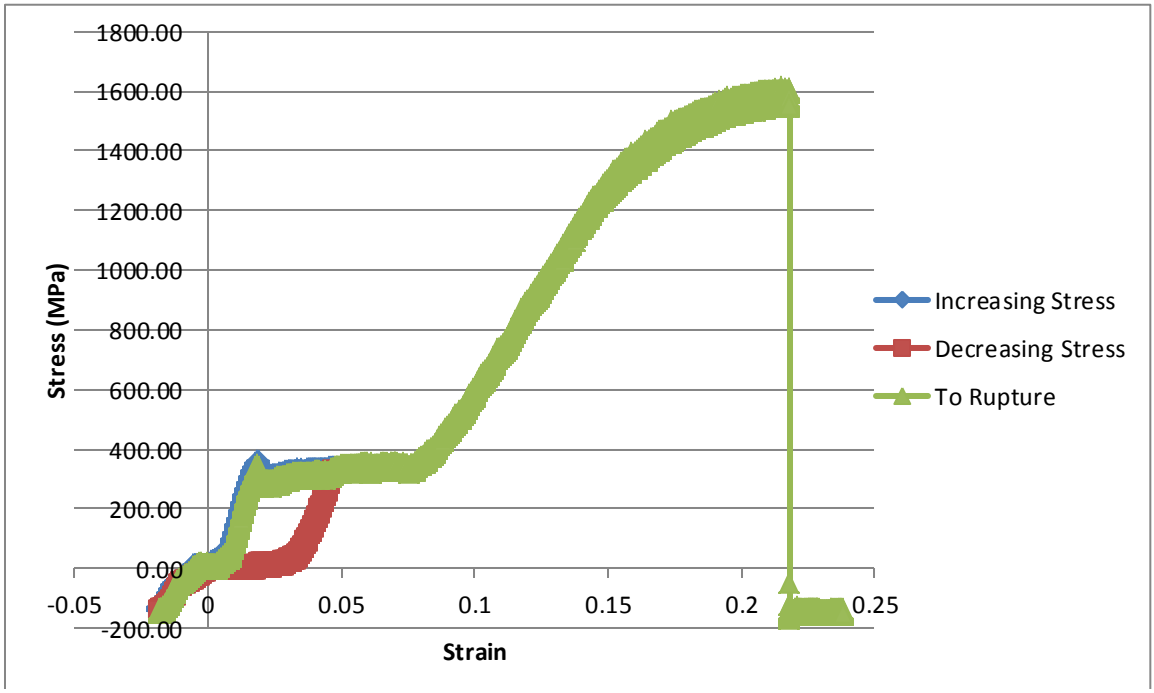

Figure 7-25: The Stress-Strain Curve of the Second Untreated Wire

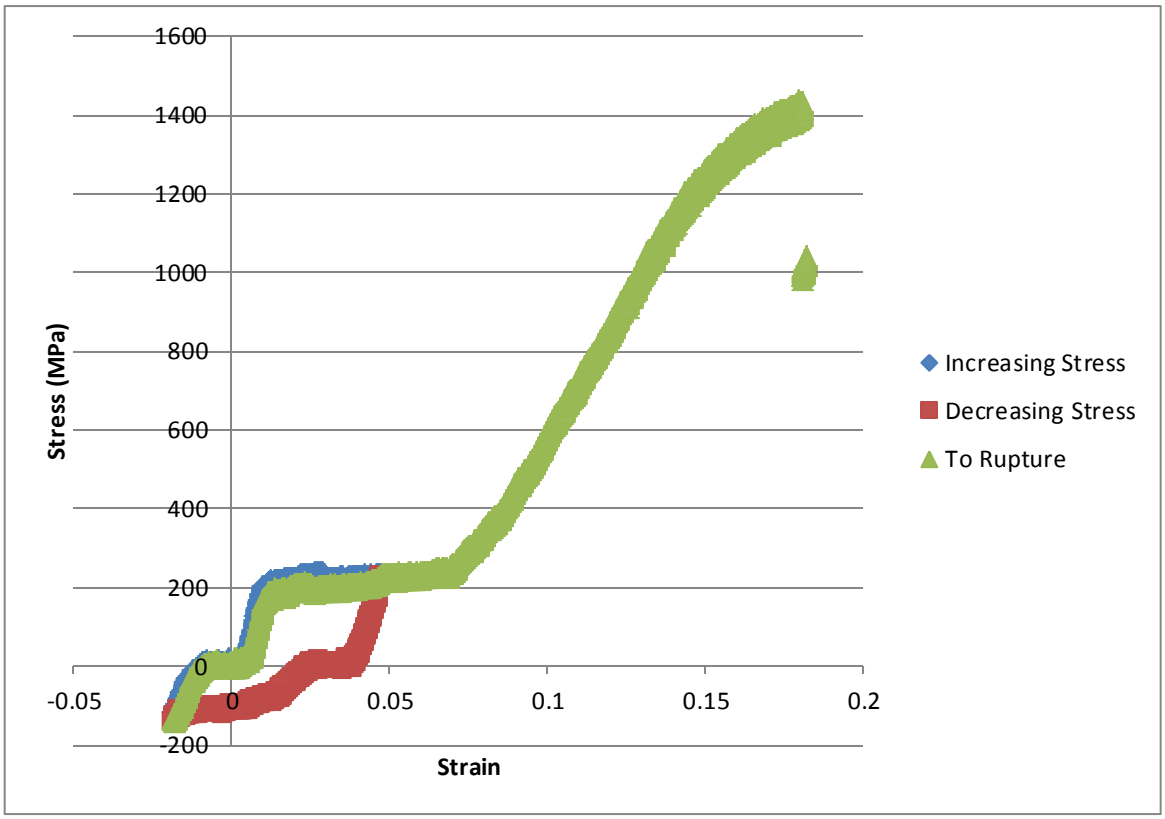

Figure 7-26: The Stress-Strain Curve of the Second Treated Wire

All of the stress-strain curves, both untreated and treated wires, were typical curves of superelastic alloys. During the initial loading, all curves had a linear stress-strain curve followed by a large strain transformation at a constant stress, the upper plateau stress; the wire went through mechanical strain deflection in its austenite phase followed by its transformation strain as it turns into stress-induced martensite. During unloading, the stress-strain curve would initially decrease before converging into another large transformation strain at constant stress, the lower plateau stress, and return back to 0% strain. During the second round of loading, the wire would again go through its initial stress-strain relationship and go to its corresponding upper plateau stress where it transforms into stress-induced martensite at a constant stress. When the transformation is complete, the stress-strain relationship would then be linear once more (at a different slope) and eventually plateau to its ultimate tensile stress where it would rupture. In summary, the stress-strain curves showed that the heat treated wires were still in their austenite phase at room temperature; the heat treatment thus did not raise the austenite transition temperatures above ambient room temperature.

With respective averaged values of 27.93 GPa and 28.09 GPa, the untreated and treated wires did not have any significant difference in their austenitic moduli of elasticity. It should be mentioned however that of the three properties extracted from the stress-strain curves, the austenitic moduli of elasticity had the most variance with standard deviations of 15.2% and 20.6% for the untreated and treated wires, respectively. The modulus of elasticity is therefore not overly consistent among trials.

However with regards to the upper plateau stress and ultimate tensile stress, there was a measurable difference between the untreated and treated wires. The treated wires had weaker upper plateau stresses and ultimate tensile stresses that were respectively 25.6% and 10.3% less than the untreated wires. As reviewed in Section 6.2.10.2, the literature shows that the ultimate tensile stress and plateau stresses decrease when aged due to precipitate formations. There was also a significant decrease in lower plateau stress. For the untreated wires' stress-strain curves (such as the one shown in Figure 7-25), the lower plateau stresses were barely above zero; for the treated wires' stress-strain curves (such as the one shown in Figure 7-26), the lower plateau stress was not only less than the untreated lower plateau stress, but did not have as much transformation strain recovery. The decreased transformation strain recovery explains the decreased springback in the heated wires that was observed after the water quench.

The tensile test results greatly differed than those listed by the manufacturer. As previously listed in Table 7-4, the manufacturer claimed the wire had an austenitic modulus of elasticity of 70 GPa, a martensitic modulus of elasticity of 45 GPa, an upper plateau stress of 379 MPa, a lower plateau stress of 138 MPa, and an ultimate tensile stress of 1068 MPa. The tension tests measured an austenitic modulus of elasticity that was 37% of the listed value, while the one successfully measured martensitic modulus of elasticity was 71.6% of the listed value. Looking back at the stress-strain curve extracted from the manufacturer (*i.e.* Figure 7-18), the author noticed that both the loading and unloading curves were almost parallel, suggesting that the austenitic and martensitic moduli of elasticity would be close in magnitude. Enlarging the photo, the author estimated the austenitic modulus and martensitic modulus to be 31.5 GPa and 28 GPa,

respectively which conflicts with what was listed in their material properties. As the estimated moduli of elasticity from Figure 7-18 are more in line with the experimental moduli of elasticity than the listed properties from the manufacturer's website, it is more likely that the true moduli of elasticity are the ones extracted from Figure 7-18. As for the differences in experimental and listed plateau stresses, it is conceivable that the stress-strain test in Figure 7-18 may have been performed at a lower ambient temperature which would result in a vertical shift in plateau stresses.

With the tensile testing results indicating that the heat treated wires are still in their austenite form at room temperature, having an austenitic modulus of elasticity of 28.09 GPa, it is apparent that the austenitic moduli of elasticity calculations are not accurate. As mentioned in the wire diameter manipulation section, inaccuracies in spring geometry measurements may be the cause. Another possibility is that the gauge 19 wire may have different properties than the gauge 22 wire. Recalling the wire diameter manipulation experiments for example, the gauge 19 springs had estimated austenitic moduli of elasticity of 36.59 GPa and 33.60 GPa from the force-deflection and resonance frequency experiments, respectively; while the gauge 22 springs had estimated austenitic moduli of elasticity of 54.84 GPa and 40.28 GPa. Recalling that only gauge 19 wires were used for the tensile tests, the tensile tests produced a modulus of elasticity that was more in line with the estimated moduli of elasticity obtained from the gauge 19 wire diameter experimental results. Perhaps if a tensile test was performed on the gauge 22 wire, it may have produced a modulus of elasticity more in line with the gauge 22 results. Another possibility is that traditional spring mechanics cannot be used to predict the behavior of superelastic nitinol springs even in its pure austenite form; however, the author finds this explanation unlikely as the springs exhibited a linear relationship between force and deflection, and most of the experimental austenite stiffness ratios were in good correlation with the stiffness ratios dictated by spring mechanics. The author believes the discrepancy is most likely from measurement errors in the spring geometry, particularly the wire diameter as the calculated modulus of elasticity is proportional to the wire diameter to the fourth power.

7.10 CONCLUSIONS

Recalling the first objective of these experiments, it was desired to see if the force-deflection relationship in a superelastic spring follows the linear relationship found in traditional springs or if it follows the patterns discussed in Section 7.4.2. Based on the results, the following conclusions were made in regards to this objective:

1. When in its austenite phase, superelastic springs show the linear force-deflection relationship, typical of traditional spring mechanics
2. At forces that exceeded the estimated critical shear stress, the deflections deviated from the linear relationship, having larger deformations than predicted. This is likely because the overall stiffness decreases as the amount of stress-induced martensite increases.
3. In recognition that the transformation deflection as proposed in Section 7.4.2 was unrealistically large, an alternative model was proposed. Although the alternative model better described the nature of the superelastic spring, the predictions were still much larger than the experimental results. A reliable model that accurately incorporates the transformation strain was thus not realized.

The second objective was to see if a superelastic spring's geometry influences the spring's stiffness in relation to tradition spring mechanics. Based on the results, the following conclusions were made in relation to this objective:

1. Looking at the stiffness ratios from the number of spring turns manipulation, the results indicate that the stiffness correlates linearly with the number of spring turns: a relationship shown in the traditional spring stiffness equation. The corresponding modulus of elasticity was relatively consistent for all spring turns. This relation seemed to hold providing that the shear stress was not large enough to produce stress-induced martensite.
2. The results from the wire diameter manipulation suggest that the stiffness is related to the wire diameter. A larger wire diameter produced a larger spring stiffness as seen in traditional springs. However, the experimental stiffness ratio was not as high as predicted, likely related to inaccurate wire diameter

measurements. The two wire diameters had different calculated moduli of elasticity as a result.

3. The stiffness ratios from the spring diameter manipulation showed strong correlation with the theoretical stiffness ratios, providing that the shear stress was below the estimated critical shear stress.
4. Overall, it appears that the spring stiffness equation in relation to the spring's geometry can be used to estimate a superelastic spring's stiffness, providing that the spring does not experience a load above its critical shear stress. However, one must ensure that accurate measurements are taken of the spring's geometry, particularly the wire diameter and spring diameter.

As for the third objective, it was desired to see if the spring's resonance frequency in a spring-mass system follows the traditional resonance frequency equation in spring mechanics. Based on the results, the following conclusions were made:

1. The high R^2 values at shear stresses below the estimated critical shear stress, suggest a strong power relationship between the resonating mass and resonance frequency when the superelastic spring is in its austenite phase. The exponents were within 10% of the predicted value of -0.5. Overall, the stiffness ratios correlated well with the predicted results, demonstrating that the traditional mass-spring resonance equation can be used for superelastic springs in their austenite phase
2. When the critical shear stress has been surpassed, the resonant frequencies can no longer be found using the traditional resonant frequency equation
3. Overall the calculated moduli of elasticity from the resultant stiffnesses tended to be less than those predicted from the force-deflection measurements. However, this was only noticed in springs with gauge 22 wire and 16.1 mm spring diameters; all other springs (while in their austenite phase) had resonant frequency stiffnesses that were quite similar to their force-deflection stiffnesses. There may have been an error when extracting the frequency information from these particular springs.

7.11 RECOMMENDATIONS

Although the stiffness ratios proved to be similar to those predicted, the resultant calculated moduli of elasticity were not on par with the actual modulus of elasticity of the superelastic nitinol wire. To improve the accuracy of the experiments, the author would make the following recommendations:

1. Tensile testing should be done on all wire diameters (both treated and untreated) before testing to ensure one has the correct material properties for more accurate predictions and that the heat treatment did not compromise the material properties
2. The wire diameters and spring diameters should be measured using more than one device for repeatability and accuracy
3. The spring diameters should be measured while carrying a load to ensure it does not change and compromise the calculated predictions
4. Use higher resolution when measuring the resonant frequencies

If one wanted to explore this investigation further, the author would recommend:

1. Testing superelastic springs while in their martensite phase
2. Finding formulas that more accurately predict the deflection and resonance frequency after surpassing the critical shear stress.
3. Placing superelastic springs directly on a Tensile Testing Machine to observe their complete force vs. deflection relationship with improved accuracy

CHAPTER 8. CONCLUSION

When designing responsive architectural and textile mechanical applications, as with any form of good engineering practice, this thesis has shown that one must take several measures to ensure that the applications are structurally secure and function for their intended use. The necessary measures are dependent on the application's objectives and design requirements. The measures can include wind load analysis as was done on the warming hut, torque specification as was done on the reactive ceiling, strength-to-weight ratio optimization and deflection minimization as was done on the flamenco stage set's collapsible tube mechanism, and strength enhancement as was done on the Cricket's joints. Although the aim of the project is to make the piece interactive and responsive to its user, the design must go through proper engineering analyses to ensure that the piece is structurally sound, mechanically reliable, and safe to use.

As smart materials are inherently responsive, it can be advantageous to use them in responsive architectural and textile mechanical applications. However, proper analyses of the smart material must be performed to effectively foresee its responsive potential to a particular need. This thesis has examined the potential use of smart materials in three mechanical applications.

As piezoelectric materials can be used to generate electricity via induced deformation, the author investigated if they would be a viable means of harvesting energy from human foot traffic. Through understanding the theory behind piezoelectric materials and piezoelectric harvesting and examining different types of transducers along with different methods of deforming said transducers, it was found that power can be harvested from human foot traffic using embedded floor tiles and shoe insoles. Unfortunately, the amount of power was found to be insufficient as a means for significant energy generation. The author also determined that piezoelectric harvesting is not a commercially viable means to generate sustainable energy.

From Berzowska *et al.*'s Kukkia and Vikas Dresses (2005), the @lab knew that SMA springs could be used to deform textiles but did not know the affects certain parameters had on its mechanical outputs such as the reaction times and strokes. By examining the theory behind SMA springs and experimentally testing them at varying parameters, the author was able to validate and disprove some preconceived relationships between said spring parameters and the dynamic response. It was shown that all six tested parameters (*i.e.* wire diameter, spring diameter, transition temperature, number of spring turns, bias mass, and direct current) affected the SMA spring's reaction times and/or stroke. Many of the relationships appeared to converge; something that the author did not anticipate. From the experimental results, a better understanding was developed on SMA spring actuator behavior; SMA spring actuators were successfully integrated into the flamenco backdrop as moveable flaps that were programmed to respond to music. As a result of this research, a catalog of reaction times and strokes at different parameters was produced. This catalog can be used as a reference for future use, but the catalog is limited based on the parameter magnitudes tested in these experiments. For the reaction times and strokes that appeared to converge with increasing parameters, it is recommended to perform additional experiments at further parameter increases to see if the converging trends continue.

Having previously used superelastic SMA wire on the flamenco backdrop as a bias force, the author postulated that the wire could effectively be used as helical springs for applications where low stiffness or low resonance is desired (*e.g.* the HPLED suit). However, it was uncertain if traditional spring mechanics could be used to predict a superelastic SMA spring's mechanical behavior. By experimentally finding the stiffnesses and resonant frequencies of several superelastic SMA spring-mass systems, it was found that traditional spring mechanics can be used to predict their behavior providing that the spring is not stressed past its upper plateau stress where stress-induced martensite begins to form. Superelastic springs can therefore effectively be used as low stiffness springs or for spring-mass resonance systems where a low resonant frequency is desired and spring mechanics can be used during the design process to predict their

behavior. Further study is needed to find an effective model for superelastic SMA springs that are stressed past their upper plateau stress.

These three investigations have shown that smart materials can be integral to making architectural and textile creations responsive to their environment. However, these investigations also emphasize the importance that their behaviour be properly understood to effectively predict their responsiveness. This understanding can come from a theoretical perspective as was done when evaluating the feasibility of extracting energy from human foot traffic via piezoelectric harvesting, but can more effectively come from experimental testing as was done on the SMA spring actuator and superelastic SMA spring investigations. Theoretical analysis can determine if the smart material can feasibly be used in a responsive setting, but experimental analysis will determine if the smart material can legitimately be used in a responsive setting.

BIBLIOGRAPHY

3V PR & Management. (2010, August 4). *TEEN CHOICE AWARDS TO DEBUT "GREEN CARPET"*. Retrieved March 22, 2012, from 3V PR & Management Facebook page: https://www.facebook.com/note.php?note_id=118108704904425

Acoustical Solutions, Inc. (2012). *Sonex™ One Foam Data Sheet*. Retrieved March 1, 2012, from Sonex™ Foam Web Site: http://www.sonexfoam.com/one_acou.php#!prettyPhoto[iframe]/2/

Active Materials Lab, UCLA. (2002). *Fiber Optic Sensors*. Retrieved May 31, 2011, from UCLA website: http://aml.seas.ucla.edu/research/areas/fiber-optic-sensors/overview.pdf

Active Materials Laboratory UCLA. (n.d.). *Magnetostriction and Magnetostrictive Materials*. Retrieved February 2, 2011, from Active Materials Laboratory UCLA: http://aml.seas.ucla.edu/research/areas/magnetostrictive/mag-composites/Magnetostriction%20and%20Magnetostrictive%20Materials.htm

Adams, J. (2009, February 1). *Power from the People*. Retrieved March 12, 2012, from Nightclub & Bar Magazine Web Site: http://www.nightclub.com/bar-management/power-people

Addington, M., & Schodek, D. (2005). *Smart Materials and Technologies for the Architecture and Design Professions*. Burlington, MA: Architectural Press.

ADV Engineering. (2012). *Thermoelectric materials on the basis of bismuth telluride Bi2Te3*. Retrieved February 25, 2012, from ADV Engineering Web Site: http://www.adv-engineering.com/production/bismuth%20telluride.html

Advanced Cerametrics Inc. (2009). *Piezoelectric Ceramic Fibers*. Lambertville, NJ: Advanced Cerametrics Inc.

Advanced Thermal Solutions, Inc. (2010). *Thermochromic Liquid Crystal Kit*. Retrieved December 23, 2010, from Advanced Thermal Solutions: http://www.qats.com/Products/Temperature-and-Velocity-Measurement/Liquid-Crystals/Thermochromic-Liquid-Crystal-Kit/2627.aspx

Aegerter, M. A., Avellaneda, C. O., Pawlicka, A., & Atik, M. (1997). Electrochromism in Materials Prepared by the Sol-Gel Process. *Journal of Sol-Gel Science and Technology , 8*, 689-696.

Agion Technologies. (2006). *How It Works*. Retrieved July 5, 2010, from Agion Technology: http://www.agion-tech.com/Technology.aspx?id=156

Aguiar, R. A., Savi, M. A., & Pacheco, P. M. (2010). Experimental and Numerical Investigations of Shape Memory Alloy Helical Springs. *Smart Materials and Structures* (19), 1-9.

Antaki, J. F., Bertocci, G. E., Green, E. C., Nadeem, A., Rintoul, T., Kormos, R. L., et al. (1995). A Gait-Powered Autologous Battery Charging System for Artificial Organs. *ASAIO Journal , 41*, M588-M595.

Anton, S. R., & Sodano, H. A. (2007). A review of power harvesting using piezoelectric materials (2003-2006). *Smart Materials and Structures* , R1-R21.

Anton, S. R., Erturk, A., & Inman, D. J. (2010). Multifunctional Self-Charging Structures using Piezoceramics and thin-film batteries. *Smart Materials and Structures* (19), 1-15.

APC International Ltd. (2011). *Soft Vs. Hard Ceramics*. Retrieved September 10, 2011, from APC International Ltd.: http://www.americanpiezo.com/knowledge-center/piezo-theory/soft-vs-hard-ceramics.html

APC International, Inc. (2012). *SPECIFICATIONS OF PMN-PT SINGLE CRYSTAL (PMN-32% PT)*. Retrieved April 23, 2012, from APC International, Inc. Web Site: http://www.americanpiezo.com/product-service/pmn-pt.html

APC International, Ltd. (2012). *Physical and Piezoelectric Properties of APC Materials*. Retrieved 03 16, 2012, from APC International Ltd. Web site: http://www.americanpiezo.com/apc-materials/piezoelectric-properties.html

Aron, J. (2011, August 23). *Metal Droplets could power your step*. Retrieved March 15, 2012, from NewScientist: http://www.newscientist.com/article/dn20822-metal-droplets-could-put-power-in-your-step.html

Badel, A., Guyomar, D., Lefeuvre, E., & Richard, C. (2005). Efficiency enhancement of a piezoelectric energy harvesting device in pulsed operation by synchronous charge inversion. *Journal of Intelligent Materials, Systems, and Structures , 16*, 889-901.

Baetens, R., Jelle, B. P., & Gustavsen, A. (2010). Properties, requirements and possibilities of smart windows for dynamic daylight and solar energy control in buildings: A state-of-the-art review. *Solar Energy Materials and Solar Cells , 94* (2), 87-105.

Baker, J., Roundy, S., & Wright, P. (2005). Alternative geometries for increasing power density in vibration energy scavenging for wireless sensor networks. *Proc. 3rd Int. Energy Conversion Engineering Conf.*, (pp. 959-970). San Francisco, CA.

Barberich, C. (2009, April 24). *Visionaire's Solar-Powered Issue Lights up our Lives*. Retrieved November 7, 2010, from refinery29.com: http://www.refinery29.com/visionaire-solar-powered.php

Bar-Cohen, Y. (2011, February 14). *Artificial Muscles*. Retrieved August 12, 2011, from WorldWide Electroactive Polymer Actuators Webhub: http://ndeaa.jpl.nasa.gov/nasa-nde/lommas/eap/EAP-web.htm

Bar-Cohen, Y. (2001). *ElectroActive Polymers - EAPs*. Retrieved February 25, 2012, from Azom.com: http://www.azom.com/article.aspx?ArticleID=885

Barney, M., & Bartning, M. (2009). On the Microstructural Mechanisms of SMEs. In M. Schwartz, *Smart Materials* (pp. 20.41-20.46). Boca Raton, FL: CRC Press.

Baz, A., Iman, K., & Mccoy, J. (1990). The Dynamics of Helical Shape Memory Actuators. *Journal of Intelligent Material Systems and Structures* , 105-133.

Beardmore, R. (2011, August 8). *Loaded Flat Plates*. Retrieved April 16, 2012, from RoyMech Web Site: http://www.roymech.co.uk/Useful_Tables/Mechanics/Plates.html

Bech, J. (n.d.). *Smart Materials*. Retrieved November 10, 2010, from Velkommen Til Teknologisk Institut: http://www.teknologisk.dk/9225,2

Beesley, P. (2009). *Canadian Pavillion Venice Biennale 2010 Hylozoic Ground.* Retrieved February 27, 2012, from Hylozoic Ground: http://www.hylozoicground.com/index.html

Beesley, P. (2010). *Hylozoic Ground.* Toronto, On: Riverside Architectural Press.

Bell, J. (2009). Smart Windows. In M. Schwartz, *Smart Materials* (pp. 14-17 - 14-33). Boca Raton, FL: CRC Press.

Bell, R. C. (2006, December 1). *Properties of Magnetorheological Fluids.* Retrieved January 29, 2011, from Richard C. Bell Personal Homepage: http://www.personal.psu.edu/faculty/r/c/rcb155/Research/R_MR_Fluids.htm

Berzowska, J., & Coelho, M. (2005). Kukkia and Vilkas: Kinetic Electronic Garments. *9th IEEE International Symposium on Wearable Computers.* Osake, Japan: ISWC.

Berzowska, J., Coelho, M., & Soder, H. (2005). *Kukkia and Vilkas Dresses*. Retrieved February 26, 2012, from XSLabs Web Site: http://xslabs.net/kukkia&vilkas/photo.php?photo=kukkia3

Berzowska, J., Mainstone, D., Bromley, M., Coelho, M., Gauthier, D., Raymond, F., et al. (2007). Skorpians: Kinetic Electronic Garments. *The 9th International Conference on Ubiquitous Computing*. Innsbruck, Austria: Ubicomp.

Bolton, W. (2008). *Mechatronics: A Multidisciplinary Approach*. Essex, England: Pearson Education Ltd.

Bonnemaison, S. (2008). *Architextile @lab Newsletter , 1* (1).

Bonnemaison, S., Berzowska, J., Macy, C., & Muller, R. (2011). *@LAB Architextile Laboratory: Electronic textiles in architecture*. Halifax: TUNS Press.

Bosartis. (2010, May 19). *Seiko AGS vintage*. Retrieved March 16, 2012, from Watch space We Site: http://watchspace.wordpress.com/2010/05/19/seiko-ags-vintage/

Brucker-Cohen, J. (2005). *Gizmodo Gallery: Elise Co*. Retrieved February 27, 2011, from Gizmodo: http://gizmodo.com/196926/gizmodo-gallery-elise-co

Buehler, W. J., Gilfrich, R. C., & Wiley, R. C. (1963). Effects of low-temperature phase changes on the mechanical properties of alloys near composition TiNi. *Journal of Applied Physics* (34), 1475.

Bullough, W. A. (2007). Electrorheological Fluid Actuators. In H. Janocha, *Adaptronics and Smart Structures* (pp. 163-184). Berlin: Springer.

Bullough, W. A. (2003). Smart Fluid Machines. In K. Worden, W. A. Bullough, & J. Haywood, *Smart Technologies* (pp. 193-219). Danvers, MA: World Scientific Publishing Co. Pte. Ltd.

Burkey, T. (2004). *Organic Synthesis; Organometallic Photochemistry*. Retrieved November 7, 2010, from University of Memphis: Department of Chemistry: http://www.chem.memphis.edu/people/faculty/Burkey/burkey_research.htm

Burle Industries Inc. *Fiber-optics: Theory and Applications*. Burle Industries.

Caceres, C. (2009, July 23). *Motionetics acquires M2E Power*. Retrieved March 18, 2012, from Vator News: http://vator.tv/news/2009-07-23-motionetics-acquires-m2e-power

Cao, W. (2007). Multifunctional Materials: The Basis for Adaptronics. In H. Janocha, *Adaptronics and Smart Structures* (pp. 29-53). Saarbrucken: Springer-Verlag Berlin Heidelberg.

Carlson, J. D. (2007). Magnetorheological Fluid Actuators. In H. Janocha, *Adaptronics and Smart Structures* (pp. 184-204). Berlin: Springer.

Carlson, J. D. (2009). Magnetorheological Fluids. In M. Schwartz, *Smart Materials* (pp. 17-1 to 17-8). Boca Raton, FL: CRC Press.

Casas, J. R., & Cruz, P. J. (2003). Fiber Optic Sensors for Bridge Monitoring. *Journal of Bridge Engineering , 8* (6), 362.

Case Western Reserve University. (2004). *Electric and Magnetic Field Effects*. Retrieved January 9, 2011, from External Influences on Liquid Crystals: http://plc.cwru.edu/tutorial/enhanced/files/lc/external/external.htm

Case Western Reserve University. (2004). *Twisted Nematic (TN) Displays*. Retrieved January 9, 2011, from Polymers and Liquid Crystals: http://plc.cwru.edu/tutorial/enhanced/files/lcd/tn/tn.htm

Centre of Molecular Materials for Photonics and Electronics. (2007). *Liquid Crystal Displays*. Retrieved January 14, 2011, from Research at CMMPE: http://www-g.eng.cam.ac.uk/CMMPE/displays2d.html

Centre of Molecular Materials for Photonics and Electronics. (2007). *Polymer Dispersed Liquid Crystals (PDLCs)*. Retrieved January 14, 2011, from Research at CMMPE: http://www-g.eng.cam.ac.uk/CMMPE/res_mat_pdlc.html

Cho, G. (2009). *Smart Clothing: Technology and Applications.* Boca Raton: CRC Press.

Chromatic Technologies, Inc. (CTI). (2009). *CTI Blog*. Retrieved November 7, 2010, from CTI: http://www.ctiinks.com/index.php

Churchill, C. B., Shaw, J. A., & Iadicola, M. A. (2009). Tips and Tricks for Characterizing Shape Memory Alloy Wire: Part 2- Fundamental Isothermal Responses. *Experimental Techniques* (January/February), 51-62.

Claeyssen, F., & Engdahl, G. (2007). Magnetorestrictive Actuators. In H. Janocha, *Adaptronics and Smart Structures* (pp. 126-145). Verlag: Springer.

Clark, W. M., & Mo, C. (2009). Piezoelectric Energy Harvesting for Bio-MEMS Applications. In P. Shashank, & D. J. Inman, *Energy Harvesting Technologies* (pp. 405-430). Boston, MA: Springer US.

Color Change Corporation. (2002). *Leuco Dyes*. Retrieved December 23, 2010, from Color Change Corporation: http://www.colorchange.com/

Color Change Corporation. (2002). *Liquid Crystals*. Retrieved December 23, 2010, from Color Change Corporation: http://www.colorchange.com/

Cook-Chennault, K. A., Thambi, N., Bitetto, M. A., & Hameyie, E. B. (2008). Piezoelectric Energy Harvesting: A Green and Clean Alternative for Sustained Power Production. *Bulletin of Science Technology & Society* (28), 496-509.

Coors Light. (2008, June 25). *Coors Light: Cold Alert Issued Across Canada*. Retrieved July 2, 2010, from Marketwire: http://www.marketwire.com/press-release/Coors-Light-Cold-Alert-Issued-Across-Canada-872989.htm

Crocker, T. (2011, January 19). *Electricity Generating Dance Floors and Other Miracles of Piezoelectricity*. Retrieved February 27, 2012, from HandMadeMusic: http://handmademusic.ning.com/forum/topics/piezo-power

Culshaw, B. (1996). *Smart Structures and Materials.* Norwood, MA: Artech House, Inc.

Cute Circuit. (2012). *Hug-Shirt*. Retrieved February 26, 2012, from Cute Circuit Company Web Site: http://www.cutecircuit.com/products/thehugshirt/

Danak, A. D., Yoon, H. S., & Washington, G. N. (2003). Optimization of electrical output in response to mechanical input in piezoceramic laminated shells. *Proc. ASME Int. Mechanical Engineering Congr.*, (pp. 309-315). Washington, DC.

Deb, S. K. (2008). Opportunities and challenges in science and technology of WO3 for. *Solar Energy Materials & Solar Cells , 92*, 245-258.

Deb, S. K. (1994). Reminiscences on the discovery of electrochromic. *Solar Energy Materials and Solar Cells , 39*, 191-201.

Desimpel, C. (2006). *The Basics About Liquid Crystals*. Retrieved January 8, 2011, from Liquid Crystals and Photonics Group: http://trappist.elis.ugent.be/ELISgroups/lcd/lc/lc2.php

Direct Industry. (2011). Retrieved January 17, 2011, from Direct Industry: The Virtual Industrial Exhibition: http://www.directindustry.com/prod/fludicon-gmbh/electrorheological-er-fluid-54863-362776.html

DMAC Electric. (2012). *FIBER OPTIC COLOR CHANGING CHANDELIERS*. Retrieved February 24, 2012, from DMAC Electric Company Website: http://www.dmac-electric.com/fiberopticchandeliers.php

Donelan, J. M., Li, Q., Naing, V., Hoffer, J. A., Weber, D. J., & Kuo, A. D. (2008). Biomechanical Energy Harvesting: Generating Electricity During Walking with Minimal User Effort. *Science , 319*, 807-810.

Donkersloot, H. C., & Vucht, V. (1970). Martensitic Transformatino in Au-Ti, Pd-Ti, and Pt-Ti alloys. *Journal of Less-Common Metals* (20), 83-91.

Donohue, B. (2009, March). Developing a Good Memory: Nitinol Shape Memory Alloy. *Today's Machining World* , 44-48.

Drake, J. (2001, February). The Greatest Shoe on Earth. *Wired* .

Duckworth, H. E. (1960). *Electricity and Magnetism*. New York: Holt, Rinehart and Winston.

Dynalloy. Inc. (2011). *FLEXINOL® Technical and Design Data - US Units*. Retrieved 5 14, 2010, from Dynalloy, Inc. Home Page: http://www.dynalloy.com/pdfs/TCF1140.pdf

Earthkeeper08. (2008, August 8). *POWERleap Feature Video*. Retrieved March 12, 2012, from YouTube: http://www.youtube.com/watch?v=tjy2wobhA9E

Elert, G. (2011). *Aerodynamic Drag*. Retrieved 14th 2011, July, from The Physics Hypertext Book: http://physics.info/drag/

Elert, G. (2005). *Coefficients of Friction for Aluminum*. Retrieved November 24, 2011, from The Physics FactBook: http://hypertextbook.com/facts/2005/aluminum.shtml

El-Sherif, M., Fidanboylu, K., El-Sherif, D., Gafsi, R., Yuan, J., Richards, K., et al. (2000). A Novel Fiber Optic System for Measuring the Dynamic Structural Behavior of Parachutes. *Journal of Intelligent Material Systems and Structures , 11*, 351.

Encyclopaedia Britannica Inc. (2012). *Peltier Effect*. Retrieved February 25, 2012, from Encyclopaedia Britannica Online: http://www.britannica.com/EBchecked/topic/449424/Peltier-effect

Encyclopædia Britannica Inc. (2012, February 23). *Thermoluminescence*. Retrieved February 23, 2012, from Encyclopædia Britannica Online: http://www.britannica.com/EBchecked/topic/591643/thermoluminescence

Environment Canada. (2011, June 1). *Halifax Historical Wind Speed*. Retrieved June 1, 2011, from http://halifax.weatherstats.ca/metrics/wind_speed.html

Erickson, B. (2009, April 6). *Self-Darkening Eyeglasses*. Retrieved November 7, 2010, from Chemical and Engineering News: http://pubs.acs.org/cen/science/87/8715sci5.html

Evans-Schultz, K. (2011, 1 19). *Hindsight Fashion: HyperColor*. Retrieved February 26, 2012, from Easy Mix Web Site: http://thehindsightletters.com/2011/01/19/hindsight-fashion-hypercolor/

Everything2 Media, LLC. (2002, January 30). *The Electric Shoe Company*. Retrieved March 20, 2012, from Everything2: http://everything2.com/title/The+Electric+Shoe+Company

Ewart, L. M., McLaughlin, E. A., & Gittings, K. D. (1999). *Investigation of the Compressive*. Newport, RI: Naval Undersea Warfare Center Division.

E-Z LOK. (2010). *AISI Type 303 Se Stainless Steel, cold drawn, bar, tested at RT*. Retrieved May 16th, 2010, from E-Z LOK Company Website: http://www.ezlok.com/TechnicalInfo/MPStainlessSteel.html

E-Z LOK. (2012). *Free-Cutting Brass, UNS C36000*. Retrieved March 16, 2012, from E-Z LOK Corporation Web Site: http://www.ezlok.com/TechnicalInfo/MPBrass.html

Fehrenbacher, J. (2006, February 19). *Super Smart Privacy Glass*. Retrieved November 14, 2010, from Inhabitat: http://www.inhabitat.com/2006/02/19/super-smart-privacy-glass/

Fehrenbacker, K. (2009, June 24). *Uncertain Times for M2E Power: Up for Sale, Looking to Vehicles*. Retrieved March 18, 2012, from GigaOM: http://gigaom.com/cleantech/uncertain-times-for-m2e-power-up-for-sale-looking-to-vehicles/

Fiber Bragg Gratings. (2002). Retrieved February 24, 2012, from http://www.immt.pwr.wroc.pl/~gasior/Researches/Optical_sensors/optical_sensors.htm#poczatek

Flashwear. (2012). *T-Qualizer - Chiller Equalizer Shirt*. Retrieved February 26, 2012, from The T-Qualizer Store: http://www.tqualizer.com/tqualizer/t-qualizer-flashing-equalizer-t-shirt-chiller.html

Fludicon. (2010). *RheOil*. Retrieved January 27, 2011, from Fludicon Products: http://www.fludicon.de/ER-fluids-electrorheological-fluids-ERF.52.0.html?&L=2

Freshman Seminar BioArt. (2009, September 30). *Hylozoic Soil*. Retrieved February 26, 2012, from Freshman Seminar BioArt: http://blog.lib.umn.edu/willow/bioart/2009/09/hylozoic-soil.html

Freudenrich, C. (2001, March 6). *How Fiber Optics Work*. Retrieved February 24, 2012, from HowStuffWorks.com: http://computer.howstuffworks.com/fiber-optic.htm

Freudenrich, C. (2010). *How OLEDs Work*. Retrieved November 10, 2010, from HowStuffWorks: http://electronics.howstuffworks.com/oled.htm

Fuhr, P. (2000, May 1). *Measuring with Light Part 2: Fiber-Optic Sensing-From Theory to Practice*. Retrieved February 24, 2012, from Sensors: http://www.sensorsmag.com/sensors/force-strain-load-torque/measuring-with-light-part-2-fiber-optic-sensing-from-theory--1082

Fuhr, P., Huston, D., Ambrose, T., & Barker, D. (1995). Embedded Sensor Results from the Winooski One Hydroelectric Dam. *Association of State Dam Safety Officials (ASDSO) Newsletter , 10* (3).

Fuller, B. (2009, May 13). *The Gleaning Power of Piezo*. Retrieved March 11, 2012, from Low-Power Engineering Community: http://chipdesignmag.com/lpd/blog/tag/powerleap/

Furukawa Electric Europe Ltd. (n.d.). *Materials-NiTi Alloys*. Retrieved April 2, 2010, from Furukawa Electric Europe Ltd Web Site: http://www.reapdesigns.co.uk/furukawa/nt.html

Galvañ, J., Sanchez, A., Casellas, C., Guilera, N., López, L., Pozo, C., et al. (2011). *Plastic Electronics and Its Introduction Into the Toy Sector*. Retrieved January 14, 2011, from Ides: The Plastic Web: http://www.ides.com/articles/design/2010/plastic-electronics.asp

gemong1. (2008, July 17). *Sustainable Dance Club*. Retrieved February 28, 2012, from YouTube: http://www.youtube.com/watch?v=xoewlHwI3U4&feature=related

Gil, I. (2010, Spring). *Power Move*. Retrieved March 21, 2012, from Mas Context Web Site: http://www.mascontext.com/issues/5-energy-spring-10/power-move/

Gonzalez, J. L., Rubio, A., & Moll, F. (2001). Human Powered Piezoelectric Batteries to Supply Power to Wearable Electronic Devices.

Green Energy. Green Home. (2012). *Solar Photovoltaic System*. Retrieved February 24, 2012, from Green Energy. Green Home: http://www.greenenergygreenhome.com/solar-photovoltaic-system

Guan, M. J., & Liao, W. H. (2008). Characteristics of Energy Storage Devices in Piezoelectric Energy Harvesting Systems. *Journal of Intelligent Material Systems and Structures , 19*, 671-679.

Guillon, O., Thiebaud, F., & Perreux, D. (2002). Tensile Fracture of Hard and Soft PZT. *International Journal of Fracture* (117), 235-246.

H.C. Materials Corporation. (2012). *Piezoelectric PMN-PT Single Crystal Products*. Retrieved April 23, 2012, from H.C. Materials Corporation Web Site: http://www.hcmat.com/Pmn_Products.html

Haga, Y., Makishi, W., Iwami, K., Totsu, K., Nakamura, K., & Esashi, M. (2005). Dynamic Braille display using SMA coil actuator and magnetic latch. *Sens. Actuat. A.* (119), 316-322.

Hammond Manufacturing. (2012). *D.C. Filter (153-159 Series)*. Retrieved March 27, 2012, from Hammond Manufacturing Corporation Web Site: http://www.hammondmfg.com/pdf/5c0032.pdf

Hande, A., Bridgelall, R., & Bhatia, D. (2009). Energy Harvesting for Active RF Sensors and ID Tags. In S. Priya, & D. J. Inman, *Energy Harvesting Technologies* (pp. 459-492). New York, NY: Springer Science+Business Media, LLC.

Hao, T. (2001). Electrorheological fluids. *Advanced Materials , 13*, 1847.

Harris, T., & Fenlon, W. (2002, January 31). *How Light Emitting Diodes Work*. Retrieved February 23, 2012, from HowStuffWorks.com: http://electronics.howstuffworks.com/led.htm

Hartl, D. J., & Lagoudas, D. C. (2008). Thermomechanical Characterization of Shape Memory Alloy Materials. In D. C. Lagoudas, *Shape Memory Alloys: Modelling and Engineering Applications* (pp. 53-119). New York, NY: Springer Science+Business Media, LLC.

Helke, G., & Lubitz, K. (2008). Piezoelectric PZT Ceramics. In W. Heywang, K. Lubitz, & W. Wersing, *Piezoelectricity: Evolution and Future of a Technology* (pp. 89-130). Heidelberg: Springer.

Herring, D. H. (2010, March 18). *Heat Treatment of Nitinol Alloys (Part 1)*. Retrieved September 12, 2011, from Heat Treat Industry News: http://www.houstonheattreat.com/news/March10/18.html

Hesselback, J. (2007). Shape Memory Actuators. In H. Janocha, *Adaptronics and Smart Structures, 2nd Ed.* (pp. 145-163). Berlin: Spinger.

Howells, C. A. (2009). Piezoelectric Energy Harvesting. *Energy Conversion and Management* (50), 1847-1850.

HowStuffWorks, Inc. (2000, July 14). *How do the battery testers on battery packages work?* Retrieved December 23, 2010, from HowStuffWorks.com: http://electronics.howstuffworks.com/question423.htm#

Hsu, Y.-H. (2006). *Basic Principles-Piezoelectric Effect*. Retrieved February 24, 2012, from Intravascular Ultrasound Image: http://bme240.eng.uci.edu/students/06s/yuhsianh/Piezoelctric%20effect.htm

Hu, M., Du, H., Ling, S.-F., Zhou, Z., & Li, Y. (2004). Motion Control of an Electrostrictive Actuator. *Mechatronics , 14*, 153-168.

Huang, W. (2002). On the selection of shape memory alloys for actuators. *Mater. Des.* (23), 11-19.

Hulkower, B. (2011, March 27). *San Francisco Nightclub's Sustainable Dance Floor Powered By Partiers*. Retrieved March 12, 2012, from TreeHugger.com: http://www.treehugger.com/green-architecture/san-francisco-nightclubs-sustainable-dance-floor-powered-by-partiers.html

Hutchison, J. (2009, August 12). *Hitachi's Dimming Film*. Retrieved January 28, 2011, from Jim On Light: http://www.jimonlight.com/2009/08/12/hitachis-dimming-film/

Hyposurface Corp. (2011). *Hyposurface Website*. Retrieved July 24, 2011, from http://hyposurface.org/

HypoSurface Corp. (2007, October 5). *HypoSurface*. Retrieved February 25, 2012, from Archimedes' Pool of Ideas: http://archimedespool.wordpress.com/2007/10/05/hyposurface/

HypoSurface Corp. (2007, July 30). *HYPOSURFACE*. Retrieved February 27, 2012, from YouTube: http://www.youtube.com/watch?v=Bbgo72EqfNc

Iadicola, M. A., & Shaw, J. A. (2007). An experimental method to measure initiation events. *Smart Materials and Structures , 16* (1), 155-169.

ICBS Inc. (2007). *Benefits of Massage*. Retrieved March 17, 2011, from Holistic Online: http://www.holisticonline.com/massage/mas_benefits.htm

Images SI, Inc. (2007). *Nitinol History*. Retrieved 4 25, 2010, from Images Scientific Instruments: http://www.imagesco.com/articles/nitinol/02.html

Incropera, F. P., Dewitt, D. P., Bergman, T. L., & Lavine, A. S. (2007). *Introduction to Heat Transfer, 5th ed.* Danvers, MA: John Wiley & Sons, Inc.

Inman, D. J. (2008). Harmonic Excitation of Undamped Systems. In D. J. Inman, *Engineering Vibration* (pp. 103-113). Upper Saddle River, NJ: Pearson Education, Inc.

Inman, M. (2008, February 7). *Knee device makes phone charging a walk in the park*. Retrieved March 12, 2012, from New Scientist: http://www.newscientist.com/article/dn13287-knee-device-makes-phone-charging-a-walk-in-the-park.html

Innovative Glass Corporation. (2006). *Features*. Retrieved October 17, 2010, from Innovative Glass: http://www.innovativeglasscorp.com/features.htm

InStep NanoPower, LLC. (2010). *Human gait energy scavenger*. Retrieved 15 2012, March, from InStep NanoPower Company Web site: http://www.instepnanopower.com/2_Technology/Technology.aspx

Intelligent Clothing. (2011, May 29). *Leah Buechley Reconfigurable Costume*. Retrieved February 27, 2012, from Crunchwear: http://www.crunchwear.com/leah-buechley-reconfigurable-costume/

International Shool of Photonics. (n.d.). *Fibre Optic Sensors*. Retrieved February 24, 2012, from International School of Photonics: http://www.photonics.cusat.edu/Research_Fiber%20Sensors_work%20at%20ISP.html

Introduction: the piezoelectric effect. (2007, July 21). Retrieved March 20, 2010, from Piezoelectric Materials: http://www.piezomaterials.com/index.htm

J.D. Lincoln Inc. (2010). *L-530 Product Data Sheet*. Retrieved May 17, 2010, from J.D. Lincoln Website: http://www.jdlincoln.com/L_530_Prepreg_1.html

Jalili, N. (2010). An Overview of Active Materials Utilized in Smart Structures. In N. Jalili, *Piezoelectric-Based Vibration Control* (pp. 115-128). New York, NY: Springer.

Jalili, N. (2010b). Physical Principles and Constitutive Models of Piezoelectric Materials. In N. Jalili, *Piezoelectric-Based Vibration Control* (pp. 129-158). New York, NY: Springer.

Japan Probe. (2008, October 18). *High tech shoe generates electricity*. Retrieved March 17, 2012, from Japan Probe Web Site: http://www.japanprobe.com/2008/10/18/high-tech-shoe-generates-electricity/

Jee, K. K., Han, J. H., Kim, Y. B., Lee, D. H., & Jang, W. Y. (2008). New Method for Improving Properties of SMA Coil Springs. *The European Physical Journal Special Topics* , 261-266.

Jenner, A. G., & Lord, D. G. (2003). Magnetostriction. In K. Worden, W. A. Bullough, & J. Haywood, *Smart Technologies* (pp. 171-192). New Jersey: World Scientific.

JM Medical Corp. (2012). *Nitinol Technical Properties*. Retrieved January 7, 2012, from JM Medical Corp. Web site: http://jmmedical.com/resources/221/Nitinol-Technical-Properties.html

Johnson Matthey Medical Components. (2011). *Setting Shapes in Nitinol*. Retrieved September 12, 2011, from Nitinol Shape Setting: http://jmmedical.com/resources/251/Nitinol-Shape-Setting.html

Jordan, C. (2011). *What Smart Metal!* Retrieved March 24, 2011, from http://www.ccmr.cornell.edu/education/modules/documents/Nitinol.pdf

JR East Group. (2008, 11 January). *Demonstration Experiment of the "Power-Generating Floor" at Tokyo Station*. Retrieved March 21, 2012, from JR East Group Web Site: http://www.jreast.co.jp/e/development/press/20080111.pdf

Julia. (2007, May 11). *Cute Circuit Hug Shirt – A hug for Mothers Day*. Retrieved February 26, 2012, from talk2myShirt: http://www.talk2myshirt.com/blog/archives/182

Juvinall, R. C., & Marshek, K. M. (2006). Springs. In R. C. Juvinall, & K. M. Marshek, *Fundamentals of Machine Component Design 4th ed.* (pp. 469-516). Hoboken, NJ: John Wiley & Sons.

Kalamkarov, A., Georgiades, A. V., MacDonald, D. O., & Fitzgerald, S. B. (2000). Pultruded Fiber Reinforced Polymer Reinforcements with Embedded Fibre Optic Sensors. *Canadian Journal of Civil Engineering , 27* (5), 972-984.

Katz, A. (2009, June 25). Lighting up the Dance Floor. (M. Farrell, Interviewer)

Kholkin, A. L., Kiselev, D. A., Kholkine, L. A., & Safari, A. (2009). Smart Ferromelectric Ceramics for Transducer Applications. In M. Schwartz, *Smart Materials* (pp. 9.1-9.12). Boca Raton, FL: CRC Press.

Kim, H., Priya, S., Stephanou, H., & Uchino, K. (2007). Consideration of Impedance Matching Techniques for Efficient Piezoelectric Energy Harvesting. *IEEE Transactions on Ultrasonics, Ferroelectrics, and Frequency Control , 54* (9), 1851-1859.

Kim, S., Clark, W. W., & Wang, Q. M. (2005). Piezoelectric energy harvesting using a bimorph circular plate: analysis. *Journal of Intelligent Materials, Systems, and Structures* (16), 847-854.

Kim, S., Hawkes, E., Cho, K., Jolda, M., Foley, J., & Wood, R. (2009). Micro artifical muscle fiber using NiTi spring for soft robotics. *The 2009 IEEE/RSJ International Conference on Intelligent Robots and Systems* (pp. 2228-2234). St. Louis, USA: IEEE Xplore.

KnitAmericas. (2002, Fall). *Adaptive Comfort*. Retrieved July 21, 2011, from FabricLink: http://www.fabriclink.com/Features/Assets/KA_Outlastfall02.pdf

Koga, M. (2009, February 13). *Shape Setting Nitinol for a Medical Device Prototype*. Retrieved September 13, 2010, from PADT Medical Blog: http://padtmedical.blogspot.com/2009/02/shape-setting-nitinol-for-medical.html

Kornbluh, R. D., Eckerie, J., & McCoy, B. (2011, July 18). *A scalable solution to harvest kinetic energy*. Retrieved March 12, 2012, from SPIE Newsroom: http://spie.org/x48868.xml

Kornbluh, R. D., Pelrine, R., Pei, Q., Heydt, R., Standford, S., Oh, S., et al. (2002). Electroelastomers: Applications of Dielectric Elastomers Transducers for Actuation, Generation, amd Smart Structures. *Smart Structures and Materials: Industrial and Commercial applications of Smart Structures Technologies* , 4698: 254-270.

Kroschwitz, J. (. (1992). *Encyclopedia or Chemical Technology*. New York, NY: John Wiley & Sons.

Kumar, P. K., & Lagoudas, D. C. (2008). Introduction to Shape Memory Alloys. In D. C. Lagoudas, *Shape Memory Alloys: Modeling and Engineering Applications* (pp. 1-51). New York, NY: Springer Science+Business Media, LLC.

Kymissis, J., Kendall, C., Paradiso, J., & Gershenfeld, N. (1998). Parasitic Power Harvesting in Shoes. *Second IEEE Int'l Conf. Wearable Computing* (pp. 132-139). Los Alamitos, CA: IEEE CS Press.

Lagoudas, D. C., Khan, M. M., & Mayes, J. J. (2001). Modelling of Shape Memory Alloy Springs for Passive Vibration Isolation. *2001 International Mechanical Engineering Congress and Exposition* (pp. 1-10). New York, NY, USA: ASME.

Lampert, C. M. (2004, March). Chromogenic Smart Materials. *Materials Today* , pp. 28-35.

LC Ceramics Laboratory. (2009). *Hard and soft ferroelectrics*. Retrieved 4 14, 2010, from ÉCOLE POLYTECHNIQUE FÉDÉRALE DE LAUSANNE: http://lc.epfl.ch/lc/Topics/Topic-hardsoft.html

Leckie, F. A., & Dal Bello, D. J. (2009). Composites. In F. A. Leckie, & D. J. Dal Bello, *Strength and Stiffness of Engineering Systems* (pp. 487-518). New York: Spring Science+Business Media, LLC.

Leckie, F. A., & Dal Bello, D. J. (2009). Smart Systems. In F. A. Leckie, & D. J. Dal Bello, *Strength and stiffness of engineering systems* (pp. 519-566). New York: Springer.

Lee, H. J., & Lee, J. J. (2000). Evaluation of the characteristics of a shape memory alloy spring actuator. *Smart Materials and Structures* , 817-823.

Lee, W. (2003, March 29). *SEIKO THERMIC: THE WORLD'S FIRST WATCH THAT DRIVEN BY BODY HEAT*. Retrieved March 15, 2012, from Roachman.com: http://www.roachman.com/thermic/

Lefeuvre, E., Badel, A., Richard, C., & Guyomar, D. (2005). Piezoelectric energy harvesting device optimization by synchronous charge extraction. *Journal of Intelligent Material Systems , 16*, 865-876.

Leo, D. J. (2007). Electroactive Polymer Materials. In D. J. Leo, *Engineering Analysis of Smart Material Systems* (pp. 346-384). New Jersey: John Wiley & Sons, Inc.

Leo, D. J. (2007). Introduction to Smart Material Systems. In D. J. Leo, *Engineering Analysis of Smart Material Systems* (pp. 1-23). Hoboken, NJ: John Wiley & Sons, Inc.

Leo, D. J. (2007). Piezoelectric Materials. In D. J. Leo, *Engineering Analysis of Smart Material Systems* (pp. 122-204). New Jersey: John Wiley & Sons, Inc.

Leo, D. J. (2007). Power Analysis for Smart Material Systems. In D. J. Leo, *Engineering Analysis of Smart Material Systems* (pp. 511-552). Hoboken, NJ: John Wiley & Sons, Inc.

Lester, G. (2005, September 8). *Penn Biologists Invent Power-Generating Backpack*. Retrieved March 16, 2012, from PureEnergySystems Web Site: http://pesn.com/2005/09/08/9600162_Power-Generating_Backpack/

Lewandowski, B. E., Kilgore, K. L., & Gustafson, K. J. (2009). Feasibility of an Implantable, Stimulated Muscle-Powered Piezoelectric Generator as a Power Source for Implanted Medical Devices. In S. Priya, & D. J. Inman, *Energy Harvesting Technologies* (pp. 389-404). Boston, MA: Springer US.

Lewis, R. W. (2003). Foreward. In X. Tao, *Smart Fibres, Fabrics and Clothing* (pp. xi-xii). Boca Raton, FL: Woodhead Publishing Ltd and CRC Press LLC.

Li, X.-F. (2007). Electroelasticity Problems of Piezoelectric Materials and a Full Solution of a Dielectric Crack. In P. L. Reece, *Smart Materials and Structures: New Research* (pp. 67-111). New York: Nova Science Publishers.

Liang, C., & Rogers, C. A. (1997). Design of Shape Memory Springs with Applications in Vibration Control. *Journal of Intelligent Material Systems and Structures , 8*, 314-322.

Liang, C., & Rogers, C. A. (1990). One-Dimensional Thermomechanical Constitutive Relations for Shape Memory Materials. *Journal of Intelligent Material Systems and Structure , 2* (1).

Lidquist, P. G., & Wayman, C. M. (1990). Shape memory and transformation behavior of martensitic Ti-Pd-Ni and Ti-Pt-Ni alloys. In T. W. Duerig, K. N. Melton, D. Stockel, & C. M. Wayman, *Engineering Aspects of Shape Memory Alloys* (pp. 58-68). London: Butterworth-Heinemann.

Lim, S. (2002). *Nike Sphere React : Never want to see you sweat*. Retrieved February 28, 2012, from FunkyGrad.com: http://www.funkygrad.com/lifestyle/displayarticle.php?artID=525&subcat=wear

Liquid Crystal Display. (2010, November 10). Retrieved November 10, 2010, from Wikipedia: http://en.wikipedia.org/wiki/LCD

Liu, X., Wang, Y., Yang, D., & Qi, M. (2008). The effect of ageing treatment on shape-setting and superelasticity of a nitinol stent. *Materials Characterization , 59*, 402-406.

Lloyd, P. A. (2007). Requirements for smart materials. *Proc. IMechE Vol. 221 Part G:* , 471-478.

Lombardi, S., & Poncet, P. (2011). *Metallurgical principles of Nitinol and its use in interventional devices*. Retrieved 9 20, 2011, from Controversies and Consensus in Imaging and Intervention: http://mail.c2i2.org/autumn2004/Metallurgical_principles_of_Nitinol.asp

Longhurst, C. (2011). *Ferrofluid or magneto-rheological fluid dampers - Audi Magnetic Ride*. Retrieved January 30, 2011, from The Suspension Bible: http://www.carbibles.com/suspension_bible_pg3.html

LORD Corporation. (2010). *LORD Magneto-Rheological (MR)*. Retrieved January 31, 2011, from LORD Corporation Home Page: http://www.lord.com/Products-and-Solutions/Magneto-Rheological.xml

Lumigram©. (2010). *Online Store*. Retrieved March 28, 2010, from Lumigram© Web site: http://www.lumigram.com/catalog/index.php?cPath=1

lx Innovations, LLC. (2010, August 17). *PocketPico at the… Teen Choice Awards?* Retrieved March 21, 2012, from lx Innovations, LLC: http://pocketpico.com/products/pocketpico-at-the%E2%80%A6-teen-choice-awards

M2E Power, I. (2008, August 25). *M2E Power, Inc. Taps into Everyday Motion to Charge Mobile Devices*. Retrieved March 18, 2012, from Business Wire Web Site: http://www.businesswire.com/portal/site/google/?ndmViewId=news_view&newsId=20080825005135&newsLang=en

Machado, L. G., & Lagoudas, D. C. (2008). Thermomechanical Constitutive Modeling of SMAs. In D. C. Lagoudas, *Shape Memory Alloys* (pp. 121-187). New York, NY, USA: Springer Science+Business Media, LLC.

Mateu, L., & Moll, F. (2005). Optimum Piezoelectric Bending Beam Structures for Energy Harvesting using Shoe Inserts. *Journal of Intelligent Material Systems and Structures , 16*, 835-845.

Matsui International Company, Inc. (2008). *Hydrochromic*. Retrieved December 17, 2010, from Matsui International Company, Inc Company Webpage: http://www.matsui-color.com/hydrochromic/

Mattila, H. R. (2006). *Intelligent textiles and clothing.* Boca Raton: CRC Press.

MatWeb, LLC. (2010). *Aluminum 6063-T832*. Retrieved May 17, 2010, from MatWeb Material Property Data.

McKnight, J. P. (2002). *Magnetostrictive Materials Background*. Retrieved February 2, 2011, from Active Materials Laboratory UCLA: http://aml.seas.ucla.edu/home.htm

Measures, R. M. (2001). *Structural Monitoring with Fiber Optic Technology*. San Diego: Academic Press.

Melton, K. N., & Mercier, O. (1979). Fatigue of NiTi thermoelastic martensites. *Acta Metallurgica , 27*, 137-144.

Memry Corporation. (2011). *Fabrication & Heat Treatment of Nitinol*. Retrieved August 11th, 2010, from Memry Corporation Website: http://www.memry.com/nitinol-iq/nitinol-fundamentals/fabrication-heat-treatment

Memry Corporation. (2012). *Physical Properties of Nitinol*. Retrieved January 14, 2012, from Memry Corporation's Company Website: http://www.memry.com/nitinol-iq/nitinol-fundamentals/physical-properties

Metallurgy for Dummies. (2011, December 20). *Smart Materials : Dielectric Elastomers*. Retrieved February 24, 2012, from Metallurgy for Dummies Web Site: http://metallurgyfordummies.com/smart-materials-dielectric-elastomers/

Metropolis Magazine. (2007, October 3). *Shaping the Future: Elizabeth Redmond Speaks @ ICFF 2007*. Retrieved March 19, 2012, from Metropolis Magazine Web Site: http://www.metropolismag.com/story/20071003/shaping-the-future-elizabeth-redmond-speaks-icff-2007

Michael, H.-K. (2001, May). Smart structures through embedding optical fibres strain sensing. *Smart Materials Bulletin* , 7-10.

MIDE Corp. (2012). *QP20w: Piezoelectric Sensor & Actuator*. Retrieved March 11, 2012, from MIDE Corporation Web Site: http://www.mide.com/products/qp/qp20w.php

Miller, D. A., & Lagoudas, D. C. (2000). Thermo-mechanical characterization of NiTiCu and NiTi SMA actuators: Influence of plastic strains. *Smart Materials and Structures , 5* (9), 640-652.

Minazara, E., Vasic, D., Costa, F., & Poulin, G. (2006). Piezoelectric diaphragm for vibration energy harvesting. *Proceedings of Ultrasonics International (UI'05) and World Congress on Ultrasonics* , (pp. e699–e703).

Mindstorm Ltd. (2011). *iBar®: brings bars to life*. Retrieved February 26, 2012, from Mindstorm Ltd. Web Site: http://www.mindstorm.com/products/ibar

Mo, C., Radziemski, L. J., & Clark, W. W. (2010a). Analysis of piezoelectric circular diaphragm energy harvesters for used in a pressure fluctuating system. *Smart Materials and Structures* (19).

Mo, C., Radziemski, L. J., & Clark, W. W. (2010b). Experimental validation of energy harvesting performance for pressure-loaded piezoelectroc circular diaphragms. *Smart Materials and Structures* .

Morell, D. (2007, November 14). *Turning Poetry into Material*. Retrieved March 19, 2012, from Metropolis Magazine: http://www.metropolismag.com/nextgen/ng_story.php?article_id=3041

Morgan, N. B., & Friend, C. M. (2003). Shape Memory Alloys - A Smart Technology? In K. Worden, W. A. Bullough, & J. Haywood, *Smart Technologies* (pp. 109-139). Danvers, MA: World Scientific Publishing Co. Pte. Ltd.

MTS Systems Corp. (n.d.). *Magnetostrictive Linear Position Sensors*. Retrieved February 2, 2011, from How They Work: http://www.sensorland.com/HowPage024.html

Nanda, R. S., & Tosun, Y. (2010). *Biomechanics in orthodontics : principles and practice*. Chicago: Quintessence Pub. Co.

Nave, C. R. (2009). *Magnetostriction: Why does the transformer hum?* Retrieved February 2, 2011, from Hyperphysics: http://hyperphysics.phy-astr.gsu.edu/hbase/solids/magstrict.html

NDC. (2011). *Nitinol Facts*. Retrieved September 12, 2011, from Nitinol University: http://www.nitinol.com/nitinol-university/nitinol-facts/

NEC-TOKIN. (2004). *Piezoelectric Devices 1*. Retrieved 3 8, 2010, from NEC-TOKIN: http://www.nec-tokin.com/english/product/piezodevaice1/index.html

Newport Adhesives and Composites, Inc. (2010). *Newport 301*. Retrieved May 7th, 2010, from Newport Adhesives and Composites, Inc.: http://www.newportad.com/pdf/PL.NB-301.090811.pdf

Niu, P., Chapman, P., Riemer, R., & Zhang, X. (2004). Evaliation of Motions and Actuation Methods for Biomechanical Energy Harvesting. *35th Annual IEEE Power Electronics Specialists Conference* , 2100-2106.

Nixon, A. (2008, March 15). *Outlook for heart stents improving*. Retrieved March 19, 2010, from Kalamazoo News Archive: http://blog.mlive.com/kzgazette/2008/03/outlook_for_heart_stents_impro.html

Nosowitz, D. (2008, December 13). *Self-Healing Paint Is Full of Magical Tiny Caulk Crystals*. Retrieved July 14, 2011, from Gizmodo: http://gizmodo.com/5109460/self+healing-paint-is-full-of-magical-tiny-caulk-crystals

NPG Asia Materials. (2008, October 10). *Mechanochromism: Gold Rush*. Retrieved November 10, 2010, from NPG Asia Materials: http://www.natureasia.com/asia-materials/highlight.php?id=286

NRC Ratings. (2009). *Noise Reduction Coefficient (NRC):*. Retrieved March 1, 2012, from NRC Ratings Web Site: http://www.nrcratings.com/

Orchard Farm Ltd. (2012). *Outlast Snuggle Bag*. Retrieved February 16, 2012, from Chariots All Terrain Push Chairs Website: http://www.pushchairs.co.uk/acatalog/outlast_snuggle.html

Outlast Technologies, Inc. (2010). *Phase Change Materials*. Retrieved July 4, 2010, from Outlast Adaptive Comfort: http://www.outlast.com/index.php?id=95&L=0

Ozcanli, O. C. (2010, June 8). *Turning Body Heat Into Electricity*. Retrieved March 15, 2012, from Forbes.com: http://www.forbes.com/2010/06/07/nanotech-body-heat-technology-breakthroughs-devices.html

panxut. (2006, October 4). *Sustainable Dance Club*. Retrieved February 27, 2012, from YouTube: http://www.youtube.com/watch?v=rzb3VFi3Sew

Paradiso, J. (2005, June). *Energy Harvesting for Mobile Computing*. Retrieved July 24, 2011, from Responsive Environments Group, MIT Media Lab: http://www4.dcu.ie/chemistry/asg//Workshop/EnergyHarvestingforMobileSystems-JParadiso.pdf

Pariyasamy, S., & Khanna, G. (2010). *Thermochromic Colours in textiles*. Retrieved November 7, 2010, from fibre2fashion.com: http://www.fibre2fashion.com/industry-article/9/804/thermochromic-colors-in-textiles1.asp

Parker, R. (2007, July 25). *New Solar Photovoltaic Cell Efficiency Record: 42.8%*. Retrieved February 24, 2012, from FuturePundit: http://www.futurepundit.com/archives/004418.html

Patrascu, D. (2009, July 20). *How Magnetorheological Suspension Works*. Retrieved January 30, 2011, from Autoevolution: http://www.autoevolution.com/news/how-magnetorheological-suspension-works-8947.html#image1

Pelton, A. R., DiCello, J., & Miyazaki, S. (2000). Optimisation of processing and properties of medical grade Nitinol wire. *Min Invas Ther & Allied Technol , 9* (1), 107-118.

Pelton, A. R., Russel, S. M., & DiCello, J. (2003, May). The Physical Metallurgy of Nitinol Medical Applications. *Journal of Metallurgy* , 33-37.

Peratech, Ltd. (2011). *Elektex*. Retrieved March 24, 2011, from Eleksen Website: http://www.eleksen.com/?page=technology/elektex.php

Performance Composites, Ltd. (2012). *Mechanical Properties of Carbon Fibre Composite Materials, Fibre / Epoxy resin (120°C Cure)*. Retrieved January 20, 2012, from Performance Composites Limited Website: http://www.performance-composites.com/carbonfibre/mechanicalproperties_2.asp

PI Ceramic GmbH. (2009). *Piezoelectric Ceramics / Piezo Materials*. Retrieved April 6, 2010, from PI Ceramic GmbH Web Site: http://www.piceramic.de/site/piezo.html

PI Ceramic GmbH. (2012). *PICeramic GmbH. Brochure.* Retrieved March 28, 2012, from PI Ceramic GmbH. Web Site: http://www.piceramic.com/pdf/piezo_material.pdf

Piccini, M. E., & Towe, B. C. (2012). A shape memory alloy microvalve with flow sensing. *Sensors & Actuators: A. Physical , 128* (2), 344-349.

Piezo Systems, Inc. (2012). *PIEZOCERAMIC MATERIALS & PROPERTIES*. Retrieved May 11, 2011, from Piezo Systems, Inc. Web Site: http://www.piezo.com/prodmaterialprop.html

Pilch, J. (2010). Behind the Shape Setting of NiTinol. *The International Conference on Shape Memory Superelastic Technologies.* Pacific Grove, California, USA: ASM.

Pira International. (2012). *About Smart Fabrics 2012*. Retrieved February 26, 2012, from Smart Fabrics Conference Web site: http://www.smartfabricsconference.com/about-Smart-Fabrics.aspx

Platt, S. R., Farritor, S., & Haider, H. (2005a). On low-frequency electric power generation with PZT ceramics. *IEEE/ASME Trans. Mechatronics , 10*, 240-252.

Platt, S. R., Farritor, S., & Haider, H. (2005b). The use of piezoelectric ceramics for electric power generation within orthopedic implants. *IEEE/ASME Trans. Mechatronics , 10*, 455-461.

Pobering, S., & Schwesinger, N. (2004). A Novel Hydropower Harvesting Device. *Proc. 2004 Int. Conf. on MEMS, NANO and Smart Systems*, (pp. 480-485). Banff, AL.

Power Leap. (2009, April 24). *POWERleap at GoGreen Expo*. Retrieved January 27, 2012, from Youtube: http://www.youtube.com/watch?v=8WZjTcwIRM8

POWERleap. (2012, March). *Buy/Rent*. Retrieved March 21, 2012, from POWERleap Web Site: http://powerleap.net/?page_id=22

POWERleap. (2012, March). *PowerFloor*. Retrieved March 21, 2012, from POWERleap Web Site: http://powerleap.net/?page_id=32

POWERleap. (2012). *POWERleap info*. Retrieved March 12, 2012, from Powerleap's facebook page: https://www.facebook.com/powerleap/info

POWERleap. (2012). *Product Page*. Retrieved 12 2012, March, from POWERleap Web Site: powerleap.net

POWERleap. (2012, March). *SmartFloor*. Retrieved March 21, 2012, from http://powerleap.net/?page_id=27: http://powerleap.net/?page_id=27

POWERleap Team. (2009, April 24). *POWERleap at GoGreen Expo*. Retrieved March 9, 2012, from YouTube: http://www.youtube.com/watch?v=8WZjTcwIRM8

POWERleap, Inc. (2010, September 2010). *POWERleap at the Teen Choice Awards 2010*. Retrieved March 12, 2012, from POWERleap, Inc. facebook page: https://www.facebook.com/media/set/?set=a.430305553406.198839.217715473406&type=3

POWERleap, Inc. (2010, August 9). *POWERleap facebook wall*. Retrieved March 12, 2012, from POWERleap facebook page: https://www.facebook.com/powerleap

Priya, S. (2007). Advances in energy harvesting using low profile piezoelectric transducers. *Journal of Electroceramics , 19*, 165-182.

Priya, S., Chen, C., Fye, D., & Zhand, J. (2005). Piezoelectric windmill: a novel solution to remote sensing. *Japan Journal of Applied Physics , 44*, L104-107.

Pulp Studio, Inc. (2001). *Specifications*. Retrieved January 15, 2011, from Switch Lite Privacy Glass: http://www.switchlite.com/specifications.html

Qiu, J., Jiang, H., Ji, H., & Zhu, K. (2009). Comparison between four piezoelectric energy harvesting circuits. *Front. Mech. Eng. China , 4* (2), 153-159.

Raja, S. (2007). Analysis of Hybrid Actuated Laminated Piezoelectric Sandwich Beams and Active Vibration Control Applications. In P. L. Reece, *Smart Materials and Structures* (pp. 113-159). New York: Nova Science Publishers Inc.

Rakuten Global Market. (2012). *The senior glass series that it is simple and is easy to wear*. Retrieved March 17, 2012, from Rakuten Global Market Web Site: http://global.rakuten.com/en/store/a-achi/item/ck-tp02/

Ramsey, M. (1990). Fiber Optic Cables. In *Fiber Optics Handbook*. New: McGraw-Hill.

RDP Electrosense. (2011, March 17). *DCTH Series DC to DC LVDT Displacement Transducer*. Retrieved September 15, 2011, from RDP Electrosense Website: http://www.rdpe.com/ex/dcth.htm

Redmond, E., Katz, A., & Trude, S. (2010, October 21). *POWERleap: Energy Generating Flooring*. Retrieved March 12, 2012, from The Buckminster Fuller Challenge: http://challenge.bfi.org/node/2286

Reece, P. L. (2007). *Smart Materials and Structures: New Research.* New York, NY: Nova Science Publishers.

Renaud, M., Sterken, T., Fiorini, P., Puers, R., Baert, K., & Van Hoof, C. (2005). Scavenging energy from human body: design of a piezoelectric transducer. *Proc. 13th Int. Conf. on Solid-State Sensors and Actuators and Microsystems*, (pp. 784-787). Seuol.

Research Frontiers Inc. (2011). *FAQs*. Retrieved January 16, 2011, from Research Frontiers Inc. SPD SmartGlass: http://www.refr-spd.com/faqs.asp

Research Frontiers, Inc. (2011). *SPD Brochure*. Retrieved January 16, 2011, from Research Frontiers Inc. SPD- SmartGlass: http://www.refr-spd.com/upload/Research_Frontiers_SPD_Brochure.pdf

Responsive Environments Group-MIT. (2006). *Parasitic Power Shoes Project*. Retrieved April 28, 2011, from Responsive Environments Group-MIT Web Site: http://resenv.media.mit.edu/power.html

Reynaerts, D., & Van Brussel, H. (1998). Design Aspects of Shape Memory Actuators. *Mechatronics 8* , 635-656.

Richter, D. (2007). Advantages and Limitations of Thermoluminescence Dating of Heated Flint from Paleolithic Sites. *Geoarchaeology: An International Journal , 22* (6), 671-683.

Ritter, A. (2007). *Smart materials in architecture, interior architecture and design.* Boston: Birkhäuser.

Rocha, J. G., Goncalves, L. M., Rocha, P. F., Silva, M. P., & Lanceros-Mendez, S. (2010). Energy Harvesting From Piezoelectric Materials. *IEEE TRANSACTIONS ON INDUSTRIAL ELECTRONICS , 57* (3), 813-819.

Rogers, A., Chandler, D., Mills, R., & Greencorn, M. (2010, April). *Design Final Term Report*. Retrieved March 10, 2012

Rome, L. C., Flynn, L., Goldman, E. M., & Yoo, T. D. (2005). *Science , 309*, 1725.

Rosenthal, E. (2008, October 23). *Partying Helps Power a Dutch Nightclub*. Retrieved February 27, 2012, from The New York Times: Europe: http://www.nytimes.com/2008/10/24/world/europe/24rotterdam.html?pagewanted=all

Roth, E. (2009, November 10). *Que Houxo*. Retrieved October 17, 2011, from Today and Tomorrow: http://www.todayandtomorrow.net/2009/11/10/que-houxo/

Rothmaier, M., Luong, M. P., & Clemens, F. (2008). Textile Pressure Sensor Made of Flexible Plastic Optical Fibers. *Sensors , 8*, 4318-4329.

Roundy, S., Wright, P. K., & Rabaey, J. (2003). A study of low level vibrations as a power source for wireless sensor nodes. *Comput. Commun.* , 1131-1144.

Ryhänen, J. (2000). *Fundamental characteristics of nickel-titanium shape memory alloy*. Retrieved March 16, 2010, from Biocompatibility evaluation of nickel-titanium shape memory metal alloy: http://herkules.oulu.fi/isbn9514252217/html/x317.html#AEN319

SAES Getters Group. (2008). SAES Smart Materials. Lainate, Italy. Retrieved from SAES Getters Corporation Website.

Sage Electrochromics, Inc. (2010). *FAQS*. Retrieved January 9, 2011, from Sage Glass: http://www.sage-ec.com/pages/faqs.html

SAGE Electrochromics, Inc. (2009). *HOW SAGEGLASS® TECHNOLOGY WORKS*. Retrieved January 3, 2011, from SAGE Electrocchromics, Inc.: http://www.sage-ec.com/pages/howworks.html

Sage Glass. (2010). *Sage Gallery*. Retrieved November 14, 2010, from Sage Electrochromics: http://www.sage-ec.com/pages/sagebldg.html

Sage Glass. (2010). *Switchable Technologies*. Retrieved November 14, 2010, from Sage Electrochromics: http://www.sage-ec.com/pages/sagebldg.html

Saint-Gobain. (2010). *Functional Glazing*. Retrieved January 3, 2011, from Saint-Gobain: http://www.saint-gobain-sekurit.com/en/?nav1=GC&fn=func_atmos_active.html

Sallard, S. (2008). *Research Interests*. Retrieved December 30, 2010, from Physikalisch-Chemisches Institut: http://www.uni-giessen.de/cms/fbz/fb08/chemie/physchem/smarsly/mitarbeiter-innen/dr-sebastien-sallard

Sanders, J. O., Sanders, A. E., More, R., & Ashman, R. B. (1993). A preliminary investigation of shape memory alloys in the surgical correction of scoliosis. *Spine , 18* (12), 1640-1646.

Schwartz, A. (2008, October 16). *Japanese Company Develops Electricity-Generating Shoes*. Retrieved March 16, 2012, from CleanTechnica.com: http://cleantechnica.com/2008/10/16/japanese-company-develops-electricity-generating-shoes/

Schwartz, M. (2009). *Smart Materials.* Boca Raton, FL: CRC Press.

Seeboth, A., Schneider, J., & Patzak, A. (2000). Materials for Intelligent Sun Protecting Glazing. *Solar Energy Materials & Solar Cells* , 263-277.

Seiko Watch Corporation. (2007). *Kinetic. A powerhouse of technological innovation.* Retrieved March 16, 2012, from Seiko Watch Corporation Web Site: http://www.seikowatches.com/technology/kinetic/index.html

SERN-TEX®. (2012). *SERN-TEX®*. Retrieved February 27, 2012, from SERN-TEX® Web Site: http://www.shangshanmo.com/english/smjs.asp

Sharaf, Y. (2012). *Shape Memory Alloys*. Retrieved May 4, 2012, from Smart structures wiki: http://smartstructures.wikispaces.com/smart+material+by+yunes+sharaf

Shaw, J. A., & Kyriakides, S. (1997). On the nucleation and propagation of phase . *Acta Materialia , 45* (2), 683-700.

Shenck, N. (1999). *A Demonstration of Useful Electric Energy Generation from Piezoceramics in a Shoe, MS Thesis.* Cambridge, Mass.: Dept. of Electrical Engineering and Computer Science, Massachusetts Institute of Technology.

Shenck, N. A., & Paradiso, J. A. (2001, May-June). Energy Scavenging with Shoe-Mounted Piezoelectrics. *IEEE Micro* , 30-42.

Shenzhen Star Spring Materials Co., L. (n.d.). *Knowledge*. Retrieved March 17, 2010, from Shenzhen Star Spring Materials Co., Ltd Web Site: http://www.starspring.com.cn/enzhishi.asp

Sinocera Corp. (2012). *PMN-PT Crystal*. Retrieved April 23, 2012, from Sinocera Corp. Web Site: http://www.sinocera.net/en/crystal_pmn.asp

Smart Technology Ltd. (2009). *Understanding ER Fluids and Their Properties.* Retrieved March 23, 2010, from ER Fluids: http://smarttec.co.uk/erf.htm

SmartGlass Medical Ltd. (2011). *SPD SmartGlass*. Retrieved January 15, 2011, from Smartglass medical: http://www.smartglassmedical.com/products-services/spd-smartglass

SmartLife. (2012). *Technology*. Retrieved February 27, 2012, from SmartLife Company Web Site: http://www.smartlifetech.com/technology/Health-Vest-/

Smith, C. R., Sabatino, D. R., & Praisner, T. J. (2001). Temperature Sensing with Thermochromic Liquid Crystals. *Experiments in Fluids , 20*, 190-201.

Snegidhi.com. (2009, October 27). *Samsung Flexible AMOLED | Unbreakable Foldable OLED Display*. Retrieved November 10, 2010, from Snegidhi.com: http://www.snegidhi.com/2009/27-10/samsung-flexible-amoled-display-video.html

Snyder, G. J. (2008, Fall). Small Thermoelectric Generators. *The Electrochemical Society Interface* , 54-56.

Sodano, H. A. (2009). Harvesting Energy from the Straps of a Backpack Using Piezoelectric Materials. In S. Priya, & D. J. Inman, *Energy Harvesting Technologies* (pp. 431-458). New York: Springer Science+Business Media, LLC.

Sodano, H. A., Inman, D. J., & Park, G. (2005). Generation and Storage of Electricity from Power Harvesting Devices. *Journal of Intelligent Material Systems and Structures , 16*, 67-75.

Spaggiari, A., & Dragoni, E. (2011). Multiphysics Modeling and Design of Shape Memory Alloy Wave Springs as Linear Actuators. *Journal of Mechanical Design , 133*, 061008-1 to 61008-8.

SPD Control Systems Corporation. (2010). *SPD Smart Glass*. Retrieved January 16, 2011, from SPD Control Systems Corporation: http://www.spdcontrolsystems.com/spdglass.htm

Spencer, B. F., Yang, G., Carlson, J. D., & Sain, M. K. (1998). "Smart" dampers for seismic protection of structures. *Proceedings of the Second World Conference on Structural Control*, (pp. 419-426). Kyoto, Japan.

Spinella, I., & Dragoni, E. (2009). Design equatinos for binary shape memory actuators under dissipative forces. *Journal of Mechanical Engineering Science* , 531-543.

Spinelli, M. (2007, January 22). *You Could Even Say it Glows: Phosphorescent Smart Art Project*. Retrieved August 18, 2011, from Jalopnik: http://jalopnik.com/katharina-sieverding/

SquidLondon. (2010). *London SkyLine*. Retrieved December 24, 2010, from SquidLondon: http://www.squidlondonshop.com/

Srinivasan, A. V., & McFarland, D. M. (2001). *Smart Structures: Analysis and Design*. New York, NY: Cambridge University Press.

Srinivasan, A. V., & McFarland, D. M. (2001). *Smart Structures: Analysis and Design*. New York, NY: Cambridge University Press.

Starner, T. (1996). Human Powered Wearable Computing. *IBM Systems Journal , 35* (No. 3 & 4), 618-629.

Stevens, C. G. (1999). Designing Shape Memory Alloy Springs for Linear Actuators. *Springs* , 24-35.

Steyn, J. L., & Hagood, N. W. (2003). *Development of a Solid-State Microhydraulic Energy Harvesting Mechanism for Heel Strike Power Harvesting*. Research Triangle Park, NC: U.S. Army Research Office.

Storr, W. (2012, March). *Electronics Tutorial about Full Wave Rectification*. Retrieved March 26, 2012, from Electronics-Tutorials.ws: http://www.electronics-tutorials.ws/diode/diode_6.html

Stratsys, Inc. (2011). *FORTUS FDM Thermoplastics Material Comparison*. Retrieved July 16, 2011, from Fortus 3D Production Systems: http://www.fortus.com/Materials/FDM-Material-Comparison.aspx

Streeter, A. (2008, September 5). *Eco-Club Wars: Dancers (Literally) Light Up Rotterdam's WATT, London's Club4Climate*. Retrieved February 26, 2012, from Treehugger: A Discovery Company: http://www.treehugger.com/culture/eco-club-wars-dancers-literally-light-up-rotterdams-watt-londons-club4climate.html

Sustainable Dance Club. (2011, June). *Sustainable Dance Floor*. Retrieved February 26, 2012, from Sustainable Dance Club: http://sustainabledanceclub.com/media/documents/pdf/16/Sustainable%20Dance%20Floor%20v1.0%20product%20sheet.pdf

Tang, H., MacLaren, D. C., & White, M. A. (2010). New insights concerning the mechanism of reversible thermochromic mixtures. *Canadian Journal of Chemistry , 88* (11), 1063-1070.

Tao, X. (2003). *Smart Fibres, Fabrics and Clothing*. Boca Raton, FL: Woodhead Publishing Ltd and CRC Press LLC.

TAXI : The Global Creative Network. (2011, August 3). *An Interactive Quilt to Bond Parent and Child*. Retrieved February 27, 2012, from TAXI : The Global Creative Network: http://designtaxi.com/news/35375/An-Interactive-Quilt-to-Bond-Parent-and-Child/

Technabob. (2008, December 4). *Marcus Tremento's EL Lamps Create 3D Illusions*. Retrieved February 23, 2012, from Technabob: http://technabob.com/blog/2008/12/04/marcus-tremonto-el-lamps-3d-illusions/

The Electricity Forum. (2012). *Solar Electricity Explained*. Retrieved February 24, 2012, from The Electricity Forum: http://www.electricityforum.com/solar-electricity.html

The Engineering Toolbox. (2012). *Emissivity Coefficients of some common Materials*. Retrieved February 6, 2012, from The Engineering Toolbox: http://www.engineeringtoolbox.com/emissivity-coefficients-d_447.html

The Green Microgym. (2012). Retrieved March 2, 2012, from The Green Microgym Web Site: http://thegreenmicrogym.com/

The Light Touch of a Cottom Swab. (2010, February 27). Retrieved November 10, 2010, from Beautiful Photochemistry: Chemistry under a new light:

http://beautifulphotochemistry.wordpress.com/2010/02/27/the-light-touch-of-a-cotton-swab/

The Science Channel. (2009, January 11). *Elizabeth Redmond of POWERLeap on piezo power for large cities*. Retrieved March 13, 2012, from YouTube: http://www.youtube.com/watch?v=-gb66Pm4-V8

The Sundance Channel. (2008, April 6). *Sundance Channel-The Green-Power Leap.* Retrieved March 12, 2012, from Dailymotion: http://www.dailymotion.com/video/x5o0uv_sundance-channel-the-green-power-le_shortfilms

Thermo Life® Energy Corp. (2008). *Thermo Life® Characteristics*. Retrieved March 15, 2012, from Thermo Life® Energy Corp. Web Site: http://www.poweredbythermolife.com/thermolife.htm

Thompson, S. A. (2000). An overview of nickel-titanium alloys used in dentistry. *International Endodontic Journal , 33*, 297-310.

ThorLabs. (2012). *Step-Index Multimode Patch Cables: SMA-SMA*. Retrieved February 24, 2012, from ThorLabs: http://www.thorlabs.com/newgrouppage9.cfm?objectgroup_id=351

Tier Cardiology Group, PC. (2011). *Pacemakers*. Retrieved March 19, 2012, from Cardiology Associates Web Site: http://www.cardioassoc.com/patient_pgs/procedures/pacemaker.asp

Ting, Y., Hariyanto, G., Hou, B. K., Ricky, S., Amelia, S., & Wang, C.-K. (2009). Investigation of Energy Harvest and Storage by Using Curve-shape Piezoelectric Unimorph. *IEEE International Symposium on Industrial Electronics*, (pp. 2047-2052). Seoul, Korea.

Toi, Y., Lee, J.-B., & Taya, M. (2004). Finite Element Analysis of Large Deformation Behavior of Shape Memory Alloy Helical Springs. *Computers and Structures , 82*, 1685-1693.

Torfs, T., Lennov, V., Van Hoof, C., & Gyselinckx, B. (2006). Body-Heat Powered Autonomous Pulse Oximeter. *5th IEEE Conference on Sensors.*

Tremont Electric, Inc. (2011). *Specifications*. Retrieved March 14, 2012, from nPowerPEG Web Site: http://www.npowerpeg.com/index.php/npower-peg/specifications

Tron Intelligent House. (n.d.). Retrieved May 25, 2011, from http://tronweb.super-nova.co.jp/tronintlhouse.html

TRS Technologies, Inc. (2010). *Electrostrictive Materials*. Retrieved February 2, 2011, from TRS Technologies: http://www.trstechnologies.com/Materials/electrostrictive_materials.php

Tsivgoulis. (1995). *New Photochromic Materials*. Retrieved November 7, 2010, from Marie Curie Fellowship Association: http://www.mariecurie.org/annals/volume1/tsivgoulis.pdf

Tyson, J. (2011). *How Stuff Works*. Retrieved January 9, 2011, from How LCDs Work: http://electronics.howstuffworks.com/lcd.htm

U.S. Natick Army Systems Center. (2002, May/June). *Adaptable 'skin'*. Retrieved April 16, 2011, from U.S. Natick Army Systems Center's Web Site: http://www.natick.army.mil/about/pao/pubs/warrior/02/mayjune/smartskin.htm

Uchino, K., & Ito, Y. (2009). Smart Ceramics: Transducers, Sensors, and Actuators. In M. Schwartz, *Smart Materials* (pp. 9.12-9.27). Boca Ranton, FL: CRC Press.

Udd, E. (2002). Overview of Fiber Optic Sensors. In F. T. Yu, & S. Yin, *Fiber Optic Sensors* (pp. 1-45). New York: Marcel Dekker, Inc.

University of Cambridge. (2007). *Liquid Crystals*. Retrieved January 9, 2010, from DoITPoMS Teaching and Learning Packages: http://www.doitpoms.ac.uk/tlplib/liquid_crystals/printall.php

Van Humbeeck, J. (2009). Shape Memory Alloys. In M. Schwartz, *Smart Materials* (pp. 20.28-20.36). Boca Raton, FL: CRC Press.

Vepa, R. (2010). Modelling and Analysis of a Piezoelectric Transducer. In R. Vepa, *Dynamics of Smart Structures* (pp. 34-38). West Sussex, United Kingdom: John Wiley & Sons Ltd.

vl Henkel, S. (2009). *MR Knee is a Step Up*. Retrieved January 30, 2011, from Sensors: Research and Development: http://archives.sensorsmag.com/articles/0101/14/index.htm

Voss, E. J. (2008, July 11). *Heat Treatment Training of NiTi*. Retrieved September 12, 2011, from The University of Wisconsin-Madison Materials Research Science and Engineering Center (UW MRSEC) Home Page: http://www.mrsec.wisc.edu/Edetc/nanolab/jig/index.html

Wagg, D., Bond, I., Weaver, P., & Friswell, M. (2007). *Adaptive Structures: Engineering Applications*. West Sussex, England: John Wiley & Sons Ltd.

Wang, F. E., Buehler, W. J., & Pickart, S. J. (1965). Crystal Structure and a unique "martensitic" transition of TiNi. *Journal of Applied Physics* (36), 3232-3239.

Wang, S.-H., Yao, W.-S., Laio, W.-S., & Tsai, M.-C. (2011). Design and Analysis of a unimorph piezoceramic generator with cantilever structure in a low-frequency environment. *Proceedings of the Institution of Mechanical Engineers, Part L: Journal of Materials Design and Applications , 225*, 11-21.

Wayman, C. M., & Duerig, T. W. (1990). An Introduction to Martensite and Shape Memory. In *Engineering Aspects of Shape Memory Alloys* (p. 3). London: Butterworth-Heineman.

Weinger, E. (2008, July 6). *Hypercolor is Hot Again*. Retrieved February 27, 2012, from Los Angeles Times: http://www.latimes.com/features/la-ig-hypercolor6-2008jul06,0,1781041.story

Weston, N. (2006, July 26). *iBar*. Retrieved February 26, 2012, from Luxist.com: http://www.luxist.com/2006/07/26/ibar/

What are Liquid Crystals. (2003). Retrieved December 23, 2010, from Introduction to Liquid Crystals: http://plc.cwru.edu/tutorial/enhanced/files/lc/intro.htm

Wilson, A. (2010, June 21). *High-Tech Glazing With Phase-Change Material*. Retrieved August 22, 2011, from Building Green, Inc. Company Website: http://www.buildinggreen.com/live/index.cfm/2010/6/21/HighTech-Glazing-With-PhaseChange-Material

Worden, K., Bullough, W. A., & Haywood, J. (2003). *Smart Technologies*. River Edge, NJ: World Scientific Publishing Co. Pte. Ltd.

XS Labs. (2006). *Accouphene*. Retrieved February 27, 2012, from Xs Labs: http://xslabs.net/accouphene/

XS Labs. (2010). *Captain Electric and Battery Boy*. Retrieved February 27, 2012, from XS Labs Web Site: http://www.captain-electric.net/

XS Labs. (2005). *INTIMATE MEMORY*. Retrieved February 27, 2012, from XS Labs Web Site: http://xslabs.net/work-pages/memory.html

Yoon, H.-S., Washington, G., & Danak, A. (2005). Modling, Optimization, and Design of Efficient Initially Curved Piezoceramic Unimorphs for Energy Harvesting Applications. *Journal of Intelligent Material Systems and Structures , 16*, 877-888.

Yoon, S. H., & Yeo, D. J. (2008). Experiment Investigation of Thermo-Mechanical Behaviors in Ni-Ti Shape Memory Alloy. *Journal of Intelligent Material Systems and Structures , 19*, 283-289.

Zhao, X., Yin, J., & Tang, H. (2007). New Advances in Design and Preparation of Electrorheological Materials and Devices. In P. L. Reece, *Smart Materials and Structures* (pp. 1-66). New York: Nova Science Publishers, Inc.

Zhou, Z., Huang, M., He, J., Chen, G., & Ou, J. (2010). Ice structure monitoring with an optical fiber sensing system. *Cold Regions Science and Technology* (61), 1-5.

Zhu, Z.-W., Liu, D.-Y., Yuan, Q.-Y., Liu, B., & Liu, J.-C. (2010). A novel distributed optic fiber transduser for landslides monitoring. *Optics and Lasers in Engineering , 49* (7), 1019-1024.

Zucker, G. (2011, March 29). *Sustainable Dance Floor*. Retrieved February 26, 2012, from Ecowizer: http://www.ecowizer.com/2011/03/sustainable-dance-floor/

APPENDIX A. CHAPTER 4 APPENDICES

APPENDIX A1: Flamenco Stage Set Tables

Table A-1: The Tube Diameters for the Three Situations

Situation	Dai	Dbi	Dci	Dao	Dbo	Dco
Sit 1	25.4	22.2	19.1	27.8	24.7	21.5
Sit 2	22.2	19.1	15.9	24.7	21.5	18.3
Sit 3	19.1	15.9	12.7	21.5	18.3	15.1

Table A-2: Calculated Ply Stresses and Safety Factors for Beam Weight Loading

D_{ai} (mm)	Maximum Stress (MPa)	σ_A in MPa, (Safety Factor)			σ_B in MPa, (Safety Factor)		
		σ_x	σ_y	τ	σ_x	σ_y	τ
25.4	6.50	-0.221 (**5620**)	0.824 (**72.9**)	0 (∞)	12.2 (**168**)	0.221 (**272**)	0 (∞)
22.2	7.13	-0.242 (**5120**)	0.904 (**66.5**)	0 (∞)	13.4 (**153**)	0.242 (**248**)	0 (∞)
19.1	7.88	-0.268 (**4640**)	0.999 (**60.2**)	0 (∞)	14.8 (**138**)	0.268 (**224**)	0 (∞)

Table A-3: The Mid-Diameters and Thicknesses used for the FEA Simulations

Situation	Situation 1 (mm)	Situation 2 (mm)	Situation 3 (mm)	Thickness (mm)
Dma	1.33	1.17	1.01	1.22 (0.048")
Dmab	1.25	1.09	0.934	2.44 (0.096")
Dmb	1.17	1.01	0.855	1.22 (0.048")
Dmbc	1.09	0.934	0.775	2.44 (0.096")
Dmc	1.01	0.855	0.696	1.22 (0.048")

Table A-4: FEA Results for Alumiunum Tubing

D_{ai} (mm)	Maximum Deflection (cm)		Maximum Stress [MPa] (Safety Factor)	
	0.5 cm^2 elements	0.3 cm^2 elements	0.5 cm^2 elements	0.3 cm^2 elements
25.4	15.9	15.6	40.4 **(6.67)**	42.7 **(6.30)**
22.2	24.0	23.3	52.0 **(5.18)**	54.6 **(4.92)**
19.1	38.7	37.2	70.0 **(3.85)**	72.6 **(3.71)**

Table A-5: FEA Results for Carbon Composite Tubing

D_{ai} (mm)	Maximum Deflection (cm)	Largest Global Stress (MPa)	Largest Local Stress-Fibre Direction [MPa] (Safety Factor)	Largest Local Stress-Transverse Direction [MPa] (Safety Factor)	Maximum Shear Stress (MPa)
0.5 cm² Elements					
25.4	10.6	48.2	68.8 **(29.7)**	2.92 **(20.6)**	33.7 **(2.70)**
22.2	14.9	59.9	85.5 **(23.8)**	3.43 **(17.5)**	41.9 **(2.17)**
19.1	22.0	77.8	111 **(18.4)**	3.42 **(17.6)**	54.5 **(1.67)**
0.3 cm² Elements					
25.4	10.4	48.9	69.7 **(29.3)**	2.87 **(21.0)**	34.2 **(2.67)**
22.2	14.5	60.8	86.8 **(23.5)**	3.00 **(20.1)**	42.6 **(2.14)**
19.1	21.3	79.1	113 **(18.1)**	3.90 **(15.4)**	55.4 **(1.64)**

APPENDIX A2: The Reactive Ceiling Dimensions and Results

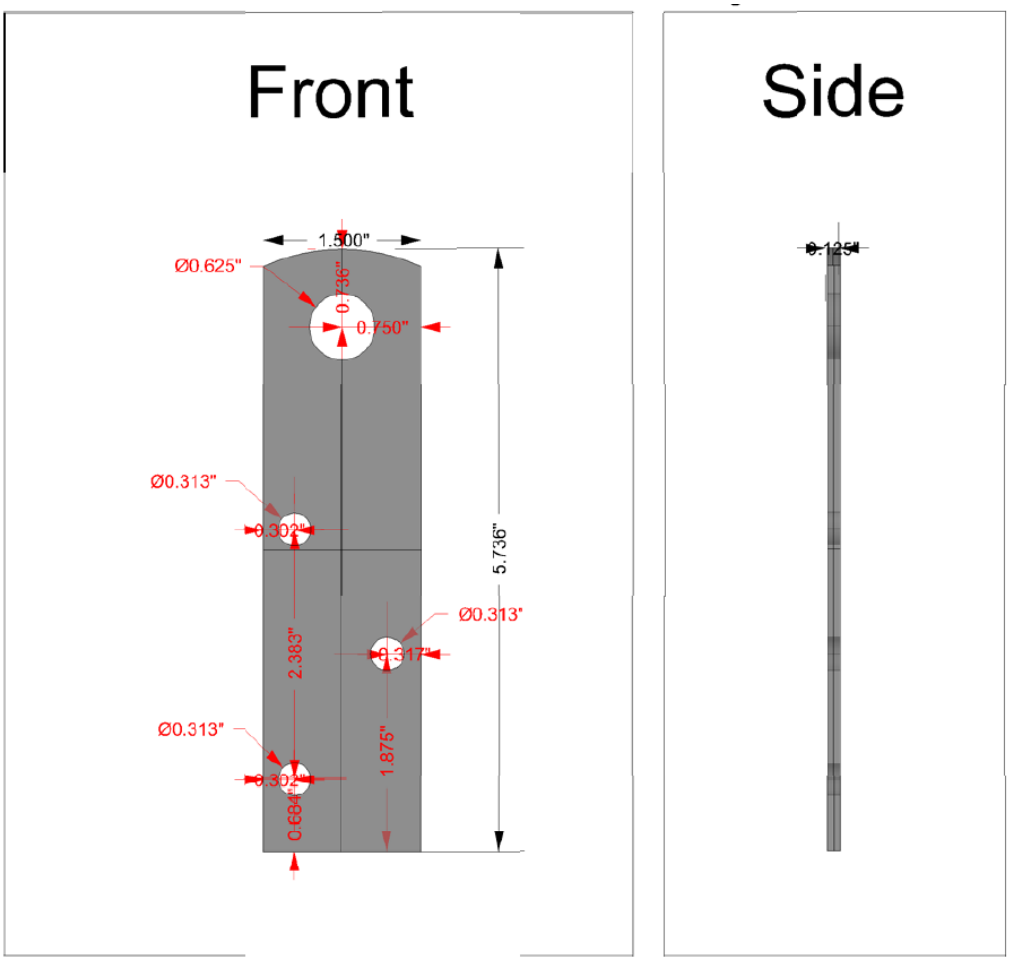

Figure A- 1: The Reactive Ceiling Lug Dimensions

Table A-6: Results From the Reactive Ceiling Lug Simulations

Cable A				
# Elements	Max Displacement (m)	Contact Stress (MPa)	Max Circumferential Stress (MPa)	Max Bending Stress (MPa)
378	2.75E-04	52.6	42.2	47.2
816	2.76E-04	92.9	46.0	47.8
1589	2.77E-04	143	48.0	48.8
2853	2.77E-04	150	47.9	49.6
6059	2.78E-04	249	50.0	49.9
22720	2.78E-04	413	51.8	50.5
Cable B				
378	3.92E-04	70.5	65.9	70.5
816	3.95E-04	116	69.6	72.2
1589	3.96E-04	162	74.9	74.1
2853	3.96E-04	184	74.8	75.4
6059	3.97E-04	277	78.2	76.1
22720	3.97E-04	413	81.1	77.3
Cable C				
378	3.83E-04	66.82	59.9	66.8
816	3.85E-04	110.90	66.4	68.0
1589	3.869E-04	159.00	70.7	69.7
2853	3.870E-04	185.60	70.7	71.1
6059	3.88E-04	276.70	73.5	71.8
22720	3.88E-04	481.80	76.1	72.8
Cable D				
378	2.98E-04	55.42	45.2	51.4
816	3.00E-04	97.47	50.0	52.0
1589	3.013E-04	155.60	52.2	53.0
2853	3.014E-04	160.50	52.3	53.8
6059	3.02E-04	239.50	54.1	54.2
22720	3.02E-04	421.60	56.1	54.8

APPENDIX B. CHAPTER 5 APPENDICES

APPENDIX B1: Chapter 5 Tables

Table B-1: Novel Piezoelectric Harvesting Devices and Their Properties. Extracted from (Cook-Chennault, Thambi, Bitetto, & Hameyie, 2008)

Material	Application	Dimensions	Power	Energy/ Power Density	Voltage	Load
PZT composite – d_{33} compressive loading of 39 MPa	Composite	-	-	12 mW/cm^3	-	-
PVF_2, d_{33} compressive load	Wind Mill Rotor Design	500µm x 90 mm x 70 mm	2.4 µW	0.76 µW/cm^3	1V	400 kΩ
PVDF bimorph, d_{31} mode	Shoe Insert	-	1.3 mW	-	18V	250 kΩ
PZT dimorph, d_{31} mode	Shoe Insert	-	8.4 mW	-	64.8V	500 kΩ
PVDF bimorph windmill. 12 cantilever bimorphs d_{31} loading	Windmill	Each bimorph 60 x 20 x 0.5 mm^3	10.2 mW	1.42 mW/cm^3	6.8V	4.6 kΩ
PZT-5A membrane, d_{31} loading from blood pressure	Biomedical	Surface area = 1 cm^2, thickness = 9µm	2.3 µW	2.6 mW/cm^3	-	-
PZT rectangular structure, knee implant, d_{33} compressive loading	Knee Implant	1.0 x 1.0 x 1.8 cm^3	4.8 mW	0.89 mW/cm^3	-	-
Unimorph membrane transducer subjected to shaker vibration	Low Power Sensors	Total radius = 20.5 mm, PZT radius = 12.5mm, PZT thickness = 230µm, brass thickness = 400µm	1.7 mW	0.106 mW/cm^3	9V	47 kΩ
PZT thin film d_{33} mode cantilever generator	MEMS	170 µm x 260 µm	1µW	0.74 mWh/cm^2	2.2V	5.2 MΩ
PZT thick film operating at 80 Hz	MEMS	20 µm thick layers	2 µW	-	0.816V	333 kΩ
PZT with 1.5 MPa lateral stress operating at 15 Hz	Autonomous wireless transmitter	Volume = 0.2 cm^3	1.2 mW	6 mW/cm^3	9V	-
PZT stacked generator- 164 layers at 1Hz subjected to 250 N	Power from activated muscle	5mm x 5mm x 8cm	690 µW	345 µW/cm^3	19.3V	540 kΩ
PZT thin film membrane generator coupled with heat engine	Hybrid	Surface area = 3 mm^2 Thickness = 3.4 µm	56 µW	5.5 W/cm^3	-	-
PZT cymbal device, d_{33} loading	Cymbal	Diameter = 29 mm Thickness = 3.4µm	29 mW	43.9 mW/cm^3	-	-
PMN-PT composite – d_{33} compressive loading of 40.4 MPa	Composite	-	-	22.1 mW/cm^3	-	-
PZT, steel and brass drum actuator subjected to cyclic stress of 0.7 N at 590 Hz	-	Volume = 0.51 cm^3	11 mW	21.57 mW/cm^3	14.07V	18 kΩ
Nanowire arrays of piezoelectric and semiconductive ZnO	Biosensors and self-powered electronics	300nm diameter wire Array dimensions 6.5 µm x 3.2 µm	~10-20 pW per wire	0.1-0.2 mW/cm^2	20 mV	-

Table B-2: Circular PE Discs that are readily available from APC International, Inc. Information extracted from (APC International, Ltd., 2012)

APCI Catalog Number	Substrate Diameter (mm)	Diameter of Ceramic (mm)	Total Thickness (mm)	Substrate Thickness (mm)	Ceramic Thickness (mm)	Maximum Number of Discs	
						Shoe Insole	Floor Tile
20-1330	8.9	6	0.11	0.05	0.06	360	1156
20-1200	10.5	7.5	0.14	0.07	0.07	250	841
20-1205	12	9	0.23	0.10	0.13	198	625
20-1210	15	11	0.23	0.10	0.13	126	400
20-1215	20	15	0.23	0.10	0.13	65	225
20-1240	27	20	0.45	0.22	0.23	40	121
20-1225	35	25	0.55	0.30	0.25	21	64
20-1230	41	25	0.23	0.10	0.13	12	49
20-1235	50	25	0.23	0.10	0.13	10	36

Table B-3: The Geometry Factors for all PE discs offered by APC International, Ltd with reference to their Substrate Diameter along with their power output on 1, 2, 4, and 8 Discs.

Substrate Diameter (mm)	Geometry Factor (mm^{-1})	Total Power on 1 Disc (W)	Total Power on 2 Discs (W)	Total Power on 4 Discs (W)	Total Power on 8 Discs (W)
8.9	2.12E-03	2.07E-05	1.03E-05	5.17E-06	2.58E-06
10.5	1.58E-03	1.54E-05	7.72E-06	3.86E-06	1.93E-06
12	2.04E-03	1.99E-05	9.95E-06	4.98E-06	2.49E-06
15	1.37E-03	1.33E-05	6.66E-06	3.33E-06	1.67E-06
20	7.36E-04	7.16E-06	3.58E-06	1.79E-06	8.96E-07
27	7.32E-04	7.13E-06	3.56E-06	1.78E-06	8.91E-07
35	5.09E-04	4.96E-06	2.48E-06	1.24E-06	6.20E-07
41	2.65E-04	2.58E-06	1.29E-06	6.45E-07	3.22E-07
50	2.65E-04	2.58E-06	1.29E-06	6.45E-07	3.22E-07

Table B-4: The Geometries of the Readily Available Bimorphs from Piezo Systems, Inc. along with their Calculates Geometry Factors for the Extension Deformation Mechanism

Bimorph	Width (mm)	Length (mm)	Total Thickness (mm)	Substrate Thickness (mm)	PE Layer Thickness (mm) ($t_p/2$)	Geometry Factor under constant stress (mm^3)
103	3.175	31.75	0.381	0.127	0.127	2.56E-08
			0.508		0.1905	3.84E-08
			0.6604		0.2667	5.38E-08
203	6.35	31.75	0.381		0.127	5.12E-08
			0.508		0.1905	7.68E-08
			0.6604		0.2667	1.08E-07
303	12.7	31.75	0.381		0.127	1.02E-07
			0.508		0.1905	1.54E-07
			0.6604		0.2667	2.15E-07
503	31.75	63.5	0.381		0.127	5.12E-07
			0.508		0.1905	7.68E-07
			0.6604		0.2667	1.08E-06

APPENDIX B2: The POWERleap™ Flooring System: A Closer Look

For her BFA 4th year design thesis at the University of Michigan School of Art and Design, Elizabeth Redmond designed the first prototype of what would become POWERleap™ in 2006. Essentially, POWERleap™ is a flooring system that harnesses the power of human foot traffic using PE materials. The original design had a glass top with grooves that in turn would bend a simply-supported rectangular PE transducer when stepped on. The transducer would then generate an electric displacement which was used to power green LEDs. At her presentation for the Metropolis Magazine's *Next Generation Design Competition*, Redmond presented an illustrated schematic of her tile (shown in Figure B-1); on this schematic, it is written that the tile generated a peak rating of 32 Volts and 5.2 Watts per step (Metropolis Magazine, 2007).

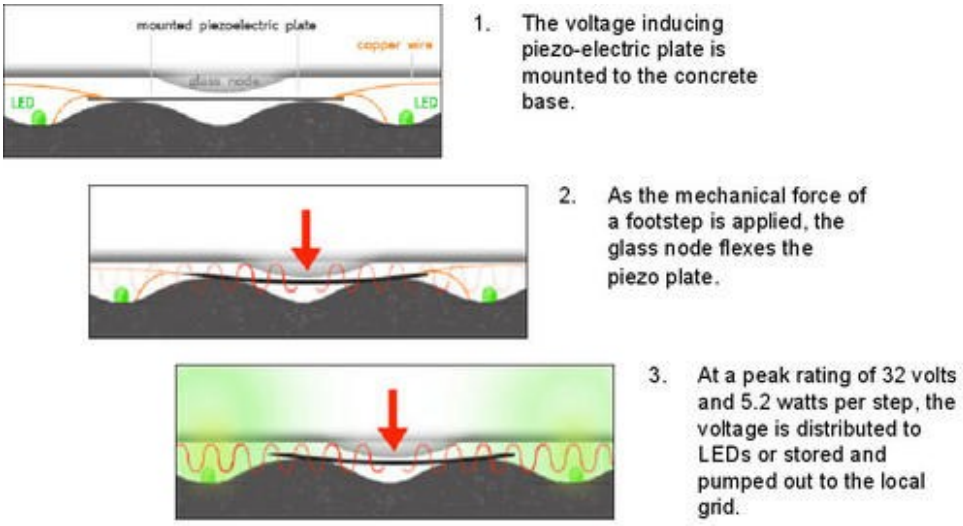

Figure B-1: Illustration of the original Power Leap Tile developed in 2006. Image extracted from (Metropolis Magazine, 2007)

Redmond would then go on to design 3 more generations of the POWERleap™ flooring system with the help of Andrew Katz (the Director of Business Development) and other staff. The second generation of POWERleap™ (shown in Figure B-2) consisted of black tiles that lit up surface-embedded white LEDs when stepped on to let the participant know that it works, supposedly. The excess energy would supposedly be transferred to a battery (battery is shown on bottom right corner

of Figure B-2). Based on demonstration videos Redmond did for the Sundance Channel's documentary series, "Big Ideas for a Small Planet" (The Sundance Channel, 2008) and for the series, "Next World" by the Science Channel (The Science Channel, 2009), the tiles appear to operate by using two rectangular PE transducers that are cantilevered; when the tile is stepped on, the free end of the cantilevered transducer would deform a few millimeters and convert the mechanical power into electricity. The body of the tile was made with SensiTile Terrazo (Morell, 2007). Figure B-3 shows Redmond demonstrating that the power is generated by the two rectangular PE plates. The third generation of POWERleap™ (shown in Figure B-4) appears to operate by using PE disc transducers. As PE discs are inexpensive and readily available, it is unsurprising that they were chosen for the next generation. As shown in a close-up of the 3rd generation tile in Figure B-4, the tile consists of 16 columns with a visible PE disc at the top of each column. When stepped on, the tile compresses (or bends) the PE discs which in turn generate an electric displacement which can be harvested as electrical energy. It is not certain whether each column consists of a stack of PE discs, or if there is solely one disc lying on top of a column; judging by the colour of the columns, the author speculates the latter.

Figure B-2: A bystander checking out the 2nd Generation POWERleap Prototype at Millennium Park in Chicago, IL on October 28, 2007 where it was being shot for the Sundance Channel`s "Big Ideas for a Small Planet" series. Image Extracted from (Morell, 2007)

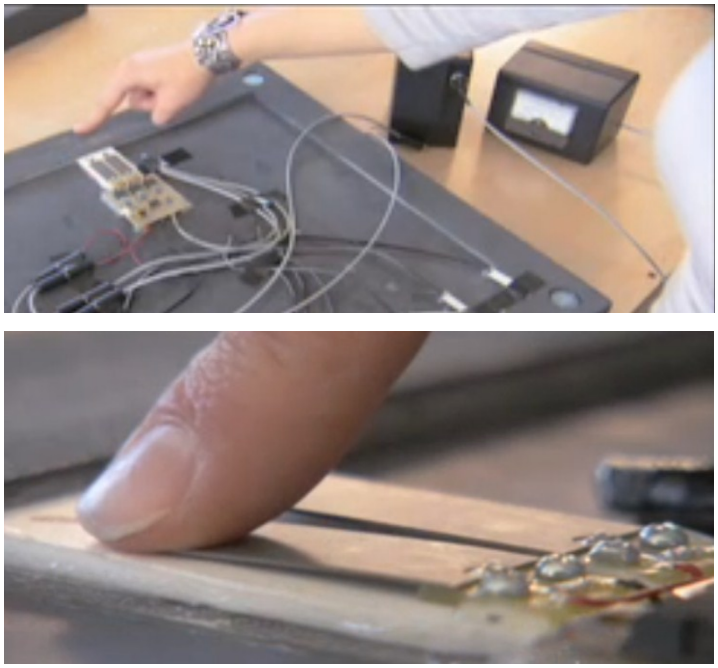

Figure B-3: The under side of the 2nd Generation POWERleap Prototype. (Top) Redmond pointing to the cantilevered PE transducers. (Bottom) Redmond bending a transducer to harvest mechanical energy. Image Extracted from (The Sundance Channel, 2008)

Figure B-4: (Left) Elizabeth Redmond presenting the 3rd Generation POWERleap Prototype at the World Energy Summit in Abu Dhabi, UAE that took place between January 18-21, 2010. (Right) A closeup of the prototype shows that the third generation consists of 16 columns with piezoceramic discs.Image Extracted from (Gil, 2010)

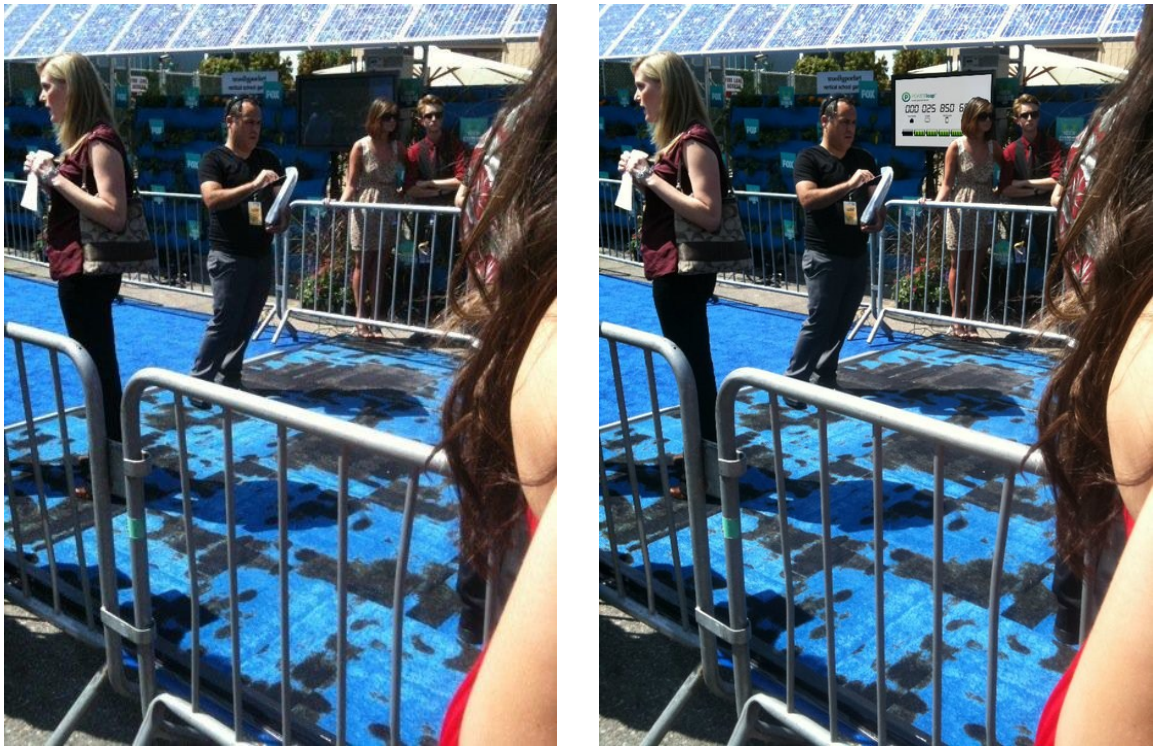

Figure B-5: The fourth generation of POWERleap tiles were used on the "green" carpet at the Teen Choice Awards on August 8th, 2010. Developed by lx Innovations, LLC, a PocketPico was used to measure the power output and an LCD screen was used to visually display the power output. The left image, where the display screen is off, was uploaded on POWERleap's facebook page on August 9th, 2010 while the right image, where the screen is on and displays a measured power output of 25.85 W, was uploaded to lx Innovations' web site on August 17th, 2010. Because of this discrepancy, the author believes that the right image was photoshopped.

The fourth generation came out in 2010 when POWERleap, Inc. got their first paying customer. Wanting to make a "green" carpet at the 2010 Teen Choice Awards (held on August 8th, 2010), Fox Broadcasting Corp. commissioned POWERleap, Inc. to make the first 10 feet of carpet out of energy harvesting floor tiles so that energy would be harvested as stars walked down the carpet (3V PR & Management, 2010). To measure power, POWERleap, Inc. used a PocketPico developed by lx Innovations, LLC and the amount of power was displayed on a screen monitor (lx Innovations, LLC, 2010). Figure B-5 shows two pictures taken of the "green" carpet along with the monitor in the background, the left picture was first uploaded to POWERleap, Inc.'s facebook wall on August 9th, 2010 (POWERleap, Inc., 2010) while the right picture was first uploaded to lx Innovations' website on August 17th, 2010 (lx Innovations, LLC, 2010). If one looks at both photos, one would see that they are identical minus the fact that the monitor screen is off on the left image, but displaying

the PocketPico software in the right image. It is evident that the right image was photoshopped either by lx Innovations, LLC or by POWERleap, Inc. Granted that the image was uploaded to lx Innovations' website first, but POWERleap, Inc. had no problem uploading the right image to their Teen Choice Awards' facebook photo album on September 30th, 2010 along with two other photos that show the background monitor displaying the PocketPico software (POWERleap, Inc., 2010). With evidence of one of the images being photoshopped, the images containing the monitor with the PocketPico software display are thus compromised and discredit the true amount of power harvested at the time the images were taken. It is uncertain if POWERleap, Inc. was responsible for photoshopping the image (or images), but it seems clear to the author that POWERleap, Inc. knew the image was altered, either by altering it themselves or by receiving a photo from lx Innovations, LLC that was different than the one they took. This discovery raised a red flag on POWERleap, Inc.'s integrity.

As for the supposed power that the POWERleap™ tiles can generate, the stated amount tended to fluctuate over time. On a YouTube video promoting the product in its 2nd generation (Earthkeeper08, 2008) , the video stated that each step generated milliwatts of energy: an amount that is generally on par with the literature review presented earlier given that only two rectangular PE transducers were being used. However, a year later her business partner, Andrew Katz, would state in a presentation at the 2009 Go Green Expo that the tiles generated 1 to 5 W/ft^2 (POWERleap Team, 2009). During an interview with Katz by Forbes magazine later that year, the power output would be reiterated as 1 to 5 $W\text{-}hr/ft^2$ (Katz, 2009). This value indicates that within a year, POWERleap™ improved on the power output by increasing it by 2 to 3 magnitudes. This power output immediately raised another red flag for the author as no device (that the author knows of) in literature has ever had this kind of power output for any type of piezoelectric harvesting. During this interview, Katz would go on to say that POWERleap, Inc. is currently researching ways to generate more electricity per footstep; Katz would say:

"*It's a matter of working with the actual material properties of the piezoelectric material right now…The things that are going on right now in terms of material properties in nanoengineering and nanotechnology, we see some light at the end of the tunnel that this material can generate significantly more electricity in terms of one or two hundred times the electricity its generating today*"

The interview would further state that Katz and Redmond believe that their energy harvesting floor can be both invisible and a viable alternative to solar energy and wind; something that the author finds hard to imagine.

More red flags came up when reviewing POWERleap's application for the Buckminster Fuller Challenge. Submitted on October 21, 2010 by Redmond, Katz, and Simon Trude (POWERleap's Director of Marketing and Sales), their application stated that they had developed two product lines: the Powerfloor and the Smartfloor (Redmond, Katz, & Trude, 2010). The Powerfloor is described as an electrical power source for densely populated urban environments while the Smartfloor is described as a self-powered wireless sensor network used to create more intelligent building automation systems (*e.g.* footsteps can be used to supply energy to the tile to send wireless signals to communicate with lighting, HVAC, or simply take occupancy data). On the application, Redmond, Katz, and Trude would go on to claim that:

"*Current tests show the Powerfloor is capable of generating 1 kwh of energy from a 50 m^2 area with at least 5,000 pedestrians passing by per hour…We estimate the initial cost to create this 1 kwh system will be under $500.*"

The first sentence in the above statement can be interpreted in two ways. The first way is that they tested the most recently built Powerfloor prototype and found that the maximum energy it can measurably generate is 1kwh over a 50 m^2 area. The second way is that they calculated how much energy can conceivably be extracted from a power harvesting floor using thermodynamic principles and said energy is 1kwh over a 50 m^2 area. The author speculates that POWERLeap, Inc. wanted the reader to interpret the statement the

first way, but would claim that they meant the second way if they were ever questioned about its meaning. Breaking down the above statement, the total amount of energy from a 50 m^2 Powerfloor would thus equate to 1.86 W-hr/ft^2 which is within the range of what Katz claimed in 2009. Assuming that each tile is 50 cm x 50 cm surface [*i.e.* the current Powerfloor surface (POWERleap, 2012)], and that the 5,000 pedestrians stepped on each tile once (which indicates that each pedestrian stepped on all 200 tiles), the total amount of energy harvested per step equates to 3.6 J.

POWERleap, Inc. would later update (likely in 2011) both its website and facebook page to state that the Powerfloor relied on electromagnetic harvesting. Their facebook page states that "Powerfloor generates up to 20 J per step with a unique electromagnetic technology" (POWERleap, 2012) while their website would be a bit more specific, stating that it "utilizes the principles of electromagnetic induction to generate roughly 10 Watts of energy per step with about 5-10 mm of movement" (POWERleap, 2012); the author extracted this information from their website on March 12, 2012. As the author has had experience with electromagnetic induction with the human powered LED jogging suit, the indicated power outputs may be conceivable (but still questionable). However, on the Buckminster Fuller Challenge application, there is no mention whatsoever of electromagnetic power generation. In fact, when asked on the application to present the critical success factors that must be in place for their project to achieve success, Redmond, Katz, and Trude responded by stating:

"The ultimate success of our product will depend on our ability to lower the cost and increase the power density. There are several ways to increase the power density. The first is to improve the design of the tiles to excite the piezoelectric material as much as possible. The second is to improve the piezoelectric material itself so that it generates the maximum amount of current per excitation. The final way is to improve the efficiency of the conditioning circuitry that carries the charge from the piezoelectric generator to the electrical application."

From the above statement, it is evident that at the time of submitting the funding application, POWERleap, Inc. had not intended on using electromagnetic harvesting and was not using electromagnetic harvesting in any of the previous prototypes. Redmond, Katz, and Trude thus used piezoelectric harvesting for all of the prototypes built up to its submission date and intended on creating a 50 m^2 Powerfloor that can generate 1 kwh using piezoelectric materials as its power source. As the 1^{st}, 2^{nd}, 3^{rd}, and 4^{th} generations were all completed by the date of submission, all of these prototypes were using piezoelectric materials to harvest their power. As for the estimated initial cost of under $500 to create the proposed 1 kWh system, one can see that it is a great underestimate by calculating the cost of the PE materials alone. Take the cheapest PE transducer for example: a PE disc. One can generally buy a PE disc for about two or three dollars, but if you order it directly, you could probably get them for about fifty cents each. Assuming that each tile is 50 cm x 50 cm, a total of 200 tiles would be needed for a 50 m^2 system, and that 16 PE discs were needed per tile as seen in the third generation of POWERleap™, the total cost for the 3200 needed PE discs would be $1600: a cost that is more than three times the initial estimated cost. Additionally, the $1600 does not include the cost for additional segments such as the harvesting electronic circuits or structural materials.

When the author went back to the POWERleap™ website on March 21, 2012, the company underwent a major website update and design change. In this update, POWERleap™ withdrew the statement that Powerfloor relied on electromagnetic induction, but added more specifications on the commercial product. These additional specifications would state that the tile had a 50 cm x 50 cm surface, was 8.5 cm in vertical height, would go through a 2-10 mm vertical displacement when stepped on, and would generate 5 Watt-seconds per step (POWERleap, 2012). The company would state, “In a day of growing urban population, Powerfloor is a no brainer for high-traffic urban environments where Powerfloor can generate kWh per day!”. As for the SmartFloor, the website update would state that its “core technology is a thin-film piezoelectric device that harvests energy from occupant footfall to power wireless sensors that save energy and collect data!” (POWERleap, 2012). The Smartfloor specifications would state that

the thin film used is 3mm in height, is built for a 20+ year lifespan, and can generate 500 μJ to 2 mJ per step. Judging from the literature examples presented earlier, the 0.5 mJ to 2 mJ per step are reasonable energy outputs for PE harvesting technologies.

The website update also came with an additional page where you can purchase a POWERleap™ Sample kit for $5000 that allows clients to test both the Powerfloor and Smartfloor capabilities (POWERleap, 2012). The Sample kit includes a POWERleap demo module; an integrated LED bar that flashes when the tile is stepped on; a wireless controls kit that can control surrounding objects such as lighting and also reports to a software piece that shows the number of steps recorded, the amount of data transferred, and the temperature in the room; a wireless multi-meter that displays the generated voltage on an iPhone, iPad app, or a custom Powerleap website; and a hard carry case. To describe the POWERleap™ demo module, POWERleap said the following:

"Measuring 50 x 50 cm and sitting 3cm tall, this module generates about 2 W of instantaneous energy or 500 μWs of electricity. The module moves about 2 mm under the foot to show the activity associated with the PowerFloor product and exhibit the natural occurring phenomena of piezoelectricity. This module utilized a patented piezoelectric technology that gives us a high voltage spike for instantaneous LED illumination, and granular data capture". Extracted from (POWERleap, 2012).

From this excerpt, it seems that the POWERleap™ demo module uses piezoelectricity to generate the 2W of instantaneous power or 500 μWs of electricity. Assuming that POWERleap, Inc. intended to say that the 500 μWs is continuous energy production, the average power generated from the tile would be 0.5 mW. From the literature review presented earlier, this amount of power generation is conceivable for piezoelectric harvesting. Recalling the PZT harvesting shoes made by Kymissis *et al.* (1998) and Shenck & Paradiso (2001), the continuous power outputs were 1.8 mW and 8.4 mW respectively; however, their maximum instantaneous power outputs were both around 80 mW. The instantaneous power output to average power output ratios for the PZT harvesting shoes developed by Kymissis *et al.* (1998) and Shenck & Paradiso (2001) are

respectively 44.4 and 9.52. Conversely, the instantaneous power output to average power output ratio for the demo module is 4000: two magnitudes higher than the ratio obtained from Kymissis *et al.* (1998). This significant shift in instantaneous to average power ratio causes the author to question the validity of the statement.

Additional findings on POWERleap, Inc. would produce additional red flags leading the author to fully question the validity of any statement POWERleap, Inc. makes about their products. Regardless or not that their current PowerFloor product produces the stated 5W power output, during their development, it seems evident that POWERleap, Inc. lied about their flooring system's power outputs on their funding applications, to media outlets, and to the general public. Looking at the stated outputs by Katz alone in 2009, it seems impossible to build a flooring system that generates 1-5 Whr of energy per square foot using PE harvesting based on the energy and power outputs found in the literature review.

APPENDIX C. CHAPTER 6 APPENDICES

APPENDIX C1: Wire and Rod Measurements

Table C-1: Diameter Measurements of Flexinol® Wires

Transition Temperature	Supposed Wire Diameter	Measured Wire Diameter (Average)	% Difference from Supposed Wire Diameter	Standard Deviation (in/ % of average)
70 °C	0.006"	0.00569" (0.145 mm)	-5.2%	2.2E-05/.39%
70 °C	0.008"	0.00757" (0.192 mm)	-5.4%	5.7E-05/0.75%
70 °C	0.010"	0.00978" (0.248 mm)	-2.25%	1.0E-04/1.07%
70 °C	0.015"	0.01476" (0.375 mm)	-1.6%	1.4E-04/0.97%
90 °C	0.006"	0.00568" (0.144 mm)	-5.3%	2.7E-05/0.48%
90 °C	0.008"	0.00766" (0.195 mm)	-4.3%	2.2E-05/0.29%
90 °C	0.010"	0.00955" (0.243 mm)	-4.5%	3.5E-05/0.37%

Table C-2: Rod Diameter Measurements

Supposed Rod Diameter	Measured Rod Diameter (Average)	% Difference from Supposed Wire Diameter	Standard Deviation (in/% of average)
3/32" (0.09375")	0.0923" (2.34 mm)	-1.5	4.18E-05/0.05%
1/8" (0.125")	0.1250" (3.175 mm)	0.0	8.4E-05/0.07%
3/16" (0.1875")	0.189" (4.80 mm)	0.92	7.6E-05/0.04%
1/4" (0.25")	0.25041" (6.36 mm)	0.16	2.3E-04/0.09%

APPENDIX C2: Reaction Times and Stroke Predictions

Table C-3: The Controlled Variables and their values for the Wire Diameter Manipulation

Controlled Variables	Value
Inner Spring Diameter/ Measured Inner Spring Diameter	0.125”/3.175 mm
Transition Temperature	70 °C
Number of Active Spring Turns	16
Bias Mass	30 g
Direct Current	0.55 A

Table C-4: The Predicted Reaction Times and Stroke Pattern for the Wire Diameter Manipulation

Wire Diameter	Measured Wire Diameter	Estimated Shear Stress (MPa)	Predicted Heating Time (s)	Predicted Cooling Time (s)	Predicted Stroke Pattern
0.006”	0.145 mm	823	0.54	16.2	Looking at the stroke equation, the stroke will decrease as the wire diameter increases providing that the bias mass does not exceed the recovery force. Note: the recovery force increases as wire diameter increases
0.008”	0.192 mm	355	0.98	21.6	
0.010”	0.248 mm	167	1.68	27.9	
0.015”	0.375 mm	50	4.02	42.1	

Table C-5: The Controlled Variables and their values for the Spring Diameter Manipulation

Controlled Variables	Value
Wire Diameter/ Measured Wire Diameter	0.01”/0.248 mm
Transition Temperature	70 °C
Number of Active Spring Turns	16
Bias Mass	30 g
Current	0.55 A

Table C-6: The Predicted Reaction Times and Stroke Pattern for the Spring Diameter Manipulation

Rod Diameter	Measured Rod Diameter	Estimated Shear Stress (MPa)	Predicted Heating Time (s)	Predicted Cooling Time (s)	Predicted Stroke Pattern
0.09375"	2.34 mm	127	1.68	27.9	Looking at the stroke equation, the stroke will increase with an increased spring diameter providing that the bias mass does not exceed the recovery force. Note: An increased diameter will decrease the recovery force
0.125"	3.175 mm	167	1.68	27.9	
0.1875"	4.80 mm	247	1.68	27.9	
0.25"	6.36 mm	323	1.68	27.9	

Table C-7: The Controlled Variables and their Values for the Transition Temperature Manipulation

Controlled Variables	Value
Inner Spring Diameter/ Measured Inner Spring Diameter (	0.125"/3.175 mm
Active Number of turns	16
Bias Mass	30 g
Current	0.55 A

Table C-8: The Predicted Reaction Times and Stroke Pattern for the Transition Temperature Manipulation

Transition Temperature	Wire Diameter/Measured Wire Diameter	Predicted Heating Time (s)	Predicted Cooling Time (s)	Predicted Stroke Pattern
70 °C	0.006"/0.145 mm	0.54	16.2	The transition temperature should not be a factor in stroke as it is not in the stroke equation.
	0.008"/0.192 mm	0.98	21.6	
	0.010"/0.248 mm	1.68	27.9	
90 °C	0.006"/0.144 mm	0.55	11.7	
	0.008"/0.195 mm	1.03	15.7	
	0.010"/0.243 mm	1.64	19.6	

Table C-9: The Controlled Variables and their Values for the Number of Spring Turn Manipulation

Controlled Variables	Value
Wire Diameter/ Measured Wire Diameter	0.01”/0.248 mm
Transition Temperature	70 °C
Inner Spring Diameter/ Measured Inner Spring Diameter	0.125”/0.1250
Bias Mass	30 g
Current	0.55 A

Table C-10: The Predicted Reaction Times and Stroke Pattern for the Number of Spring Turns Manipulation

Number of Active Spring Turns	Predicted Heating Time (s)	Predicted Cooling Time (s)	Predicted Stroke Pattern
8	1.68	27.9	From the stroke equation, the stroke will increase as the number of turns increase. As the number of turns is not a factor in the spring’s stress distribution, the stroke should increase in a linear fashion
12	1.68	27.9	
16	1.68	27.9	
20	1.68	27.9	

Table C-11: The Controlled Variables and their Values for the Bias Mass Manipulation

Controlled Variables	Value
Inner Spring Diameter/ Measured Inner Spring Diameter	0.125”/3.175 mm
Wire Diameter/ Measured Wire Diameter	0.01”/0.248 mm
Active Number of turns	16
Transition Temperature	70 °C
Current	0.55 A

Table C-12: The Predicted Reaction Times and Stroke Pattern for the Bias Mass Manipulation

Bias Mass	Estimated Shear Stress (MPa)	Predicted Heating Time (s)	Predicted Cooling Time (s)	Predicted Stroke Pattern
20 g	111	1.68	27.9	Looking at the stroke equation, an increased mass will cause an increase in stroke providing that the bias mass does not exceed the recovery force
30 g	167	1.68	27.9	
40 g	223	1.68	27.9	
50 g	279	1.68	27.9	

Table C-13: The Controlled Variables and their Values for the Direct Current Manipulation

Controlled Variables	Value
Inner Spring Diameter/ Measured Inner Spring Diameter (See Section 6.4.1.2)	0.125”/3.175 mm
Wire Diameter/ Measured Wire Diameter (See Section 6.4.1.1)	0.01”/0.248 mm
Active Number of turns	16
Transition Temperature	70 °C
Current	0.55 A

Table C-14: The Predicted Reaction Times and Stroke Pattern for the Direct Current Manipulation

Direct Current	Predicted Heating Time (s)	Predicted Cooling Time (s)	Predicted Stroke Pattern
0.45 A	2.63	27.9	Providing that the current is sufficient to heat the alloy to its austenite phase, the direct current should not affect the stroke. The stroke should be the same for all 4 currents
0.50 A	2.07	27.9	
0.55 A	1.68	27.9	
0.60 A	1.39	27.9	

Table C-15: The Predicted Reaction Times for the Wire Diameter Manipulation with Corrections for Superelasticity

Wire Diameter	Measured Wire Diameter	Predicted Heating Time (s)	% Difference	Predicted Cooling Time (s)	% Difference
0.006”	0.145 mm	0.66	22.2	2.6	-84.0
0.008”	0.192 mm	1.09	11.2	6.6	-69.4
0.010”	0.248 mm	1.79	6.5	13.5	-51.6
0.015”	0.375 mm	4.15	3.2	31.8	-24.5

Table C-16: The Predicted Reaction Times for the Spring Diameter Manipulation with Corrections for Superelasticity

Rod Diameter	Measured Rod Diameter	Predicted Heating Time (s)	% Difference	Predicted Cooling Time (s)	% Difference
0.09375”	2.34 mm	1.76	4.8	15.4	-44.8
0.125”	3.175 mm	1.79	6.5	13.5	-51.6
0.1875”	4.80 mm	1.85	10.1	10.9	-60.9
0.25”	6.36 mm	1.91	13.7	9.1	-67.4

Table C-17: The Predicted Reaction Times for the Transition Temperature Manipulation with Corrections for Superelasticity

Transition Temperature	Measured Wire Diameter	Predicted Heating Time (s)	% Difference	Predicted Cooling Time (s)	% Difference
70 °C	0.145 mm	0.66	22.2	2.6	-84.0
	0.192 mm	1.09	11.2	6.6	-69.4
	0.248 mm	1.79	6.5	13.5	-51.6
90 °C	0.144 mm	0.67	21.8	2.4	-79.5
	0.195 mm	1.15	11.7	6.1	-61.1
	0.243 mm	1.76	7.3	10.8	-44.9

Table C-18: The Predicted Reaction Times for the Number of Spring Turns Manipulation with Corrections for Superelasticity

Number of Spring Turns	Predicted Heating Time (s)	% Difference	Predicted Cooling Time (s)	% Difference
8	1.79	6.5	13.5	-51.6
12	1.79	6.5	13.5	-51.6
16	1.79	6.5	13.5	-51.6
20	1.79	6.5	13.5	-51.6

Table C-19: The Predicted Reaction Times for the Bias Mass Manipulation with Corrections for Superelasticity

Bias Mass	Predicted Heating Time (s)	% Difference	Predicted Cooling Time (s)	% Difference
20 g	1.75	4.2	16.3	-41.6
30 g	1.79	6.5	13.5	-51.6
40 g	1.83	8.9	11.5	-58.8
50 g	1.87	11.3	10.1	-63.8

Table C-20: The Predicted Reaction Times for the Direct Current Manipulation with Corrections for Superelasticity

Direct Current	Predicted Heating Time (s)	% Difference	Predicted Cooling Time (s)	% Difference
0.45 A	2.93	11.4	13.5	-51.6
0.50 A	2.25	8.7	13.5	-51.6
0.55 A	1.79	6.5	13.5	-51.6
0.60 A	1.46	5.0	13.5	-51.6

APPENDIX C3: ARDUINO CODE

```
const int pingPin = 7; //Pin that is connected to the Ping))) sensor
const int transpin = 8; //Pin that is connected to the base of the transistor
const int pingDelay = 100;//Delay time in milliseconds for ping sensor
const long maxtime = 30000; //Amount of maximum time in milliseconds that the wire should be allowed to heat or cool
const long heatdelay = 4000; //Amount of time delay to allow the spring to start contracting when heating
const long cooldelay = 9000; //Amount of time delay to allow the spring to start elongating when cooling
const float heatcontrol = 0.4; //Difference between last data point and average; indicates when contraction has finished
const float coolcontrol = 0.1; //Difference between last data point and average; indicates when elongation has finished
int j; //integer for averaging
long starttime; //The time when the program starts
long clock = 0; //The total time in milliseconds
long time = 0; //a time variable used to calculate the duration in a loop
long looptime; //The time spent in a loop
float duration, mm, startmm, deflection, average; //declare duration (microseconds), distance (mm), startmm (mm), deflection (mm), and average (mm)

void setup() {
 Serial.begin(9600); //Initialize Serial Communication
 pinMode(transpin, OUTPUT); //Set Transpin to Output
 digitalWrite(transpin, LOW); //Ensuring that the transistor pin is initially low
 delay (3000); //Delay the arduino for 3 seconds to allow time to open up the Serial Monitor to see everything
 starttime = millis(); //Record the start time
 mm = 0; //Get mm started at 0
 pinging(1500); //Get initial measurements for 3 seconds before heating the wire
 pinging(1500); //do pinging twice to get a start mm for the first heat reading

 Serial.print("Loop number \t"); //Print the loop number
 Serial.print("Heat Time (ms) \t"); //Print the Heating Time index
 Serial.println("Cooling Time (ms) \t"); //Print the Cooling Stroke index

 deflection = -1.0; //Deflection starts as a negative to indicate that the wire will first go through heating first
 for(int i=1; i<21; i++)
 {
  Serial.print(i); //prints the loop number
  Serial.print("\t"); //Print Tab
  digitalWrite(transpin, HIGH); //Turns on the SMA Wire
  pinging(maxtime); //Go to pinging function with max heat time
  Serial.print(looptime);
```

```
    Serial.print("\t");  //Print Tab

    digitalWrite(transpin, LOW);  //Turns off the SMA wire
    pinging(maxtime);  //Go to pinging function with max heat time
    Serial.println(looptime);  //Print Cooling Time

  }// Close For Loop
  pinging(10000);//  Keep program running for 10 seconds after everything is done
}//Close Setup


void loop()
{
}//void loop is not used as we only want to perform a set amount of measurements (i.e. not continuous)

void pinging(long pingtime)
{
  startmm = mm; //Makes startmm the mm measurement in the previous loop
  looptime = 0; //Make sure loop time is initially 0
  float first=1.0, second=2.0, third=3.0, fourth=4.0, fifth=5.0, sixth=6.0, seventh=7.0, eighth=8.0, ninth = 9.0, tenth = 10.0; //For averaging; started with arbitrary values
  j=1; //Index value always starts at 1
  while (looptime < pingtime)
  {
    time = millis();  //Set beginning time of the loop to be used to later measure the total time in the loop
    pinMode(pingPin, OUTPUT); //declare Ping pin as output
    digitalWrite(pingPin, LOW); //set as low for 2 microseconds to start pulse at definite low
    delayMicroseconds(2);
    digitalWrite(pingPin, HIGH); //Turn on pulse for 5 microseconds
    delayMicroseconds(5);
    digitalWrite(pingPin, LOW); //Bring pin back to low to analyze the pulse

    pinMode(pingPin, INPUT); //Change pingPin to input
    duration = pulseIn(pingPin, HIGH); //Read the Ping))) sensor to collect the time it took for the sound pulse to bounce back
    mm = microsecondsToCentimeters(duration)*10; //convert time into distance (mm) [Speed of sound is 340 m/s or 29.4 microseconds per centimeter]

    if(j%10==9){ //If Statements used to log the last ten measurements
    first = mm;
   }
    else if(j%10==8){
      second = mm;
```

```
    }
     else if(j%10==7){
      third = mm;
     }
      else if(j%10==6){
       fourth = mm;
      }
         else if(j%10==5){
         fifth = mm;
         }
          else if(j%10==4){
           sixth = mm;
          }
           else if(j%10==3){
            seventh =mm;
           }
            else if(j%10==2) {
             eighth = mm;
            }
             else if(j%10==1){
              ninth = mm;
             }
              else{
               tenth = mm;
              }
   average = (first+second+third+fourth+fifth+sixth+seventh+eighth+ninth+tenth)/10;
//Get the average reading of the last ten values
   if(abs(average-mm)< heatcontrol && looptime > heatdelay && deflection < 0) //if the
difference in the average value and mm is less
   //than the heatcontrol value, looptime is more than the heat delay value, and is heating,
break the loop
{
  break;
}
  else if(abs(average-mm)< coolcontrol && looptime > cooldelay && deflection > 0)// if
the difference in the average value and mm is less
  //than the coolcontrol value, looptime is more than the cooldelay value, and is cooling,
break the loop
{
 break;
}
   delay(pingDelay); //delay for designated ping delay
   looptime = looptime + millis() - time; //Gets the amount of time spent in the while
loop, final value is time spent while heating or cooling
   j=j+1; //Increase the index by 1
   }
```

```
   deflection = average-startmm; //Calculates the deflection
}

float microsecondsToCentimeters(float microseconds)
{
 // The speed of sound is 340 m/s or 29.4 microseconds per centimeter.
 // The ping travels out and back, so to find the distance of the
 // object we take half of the distance travelled.
 return microseconds / 29.4 / 2;
}
```

APPENDIX C4: ELECTRONIC SCHEMATIC

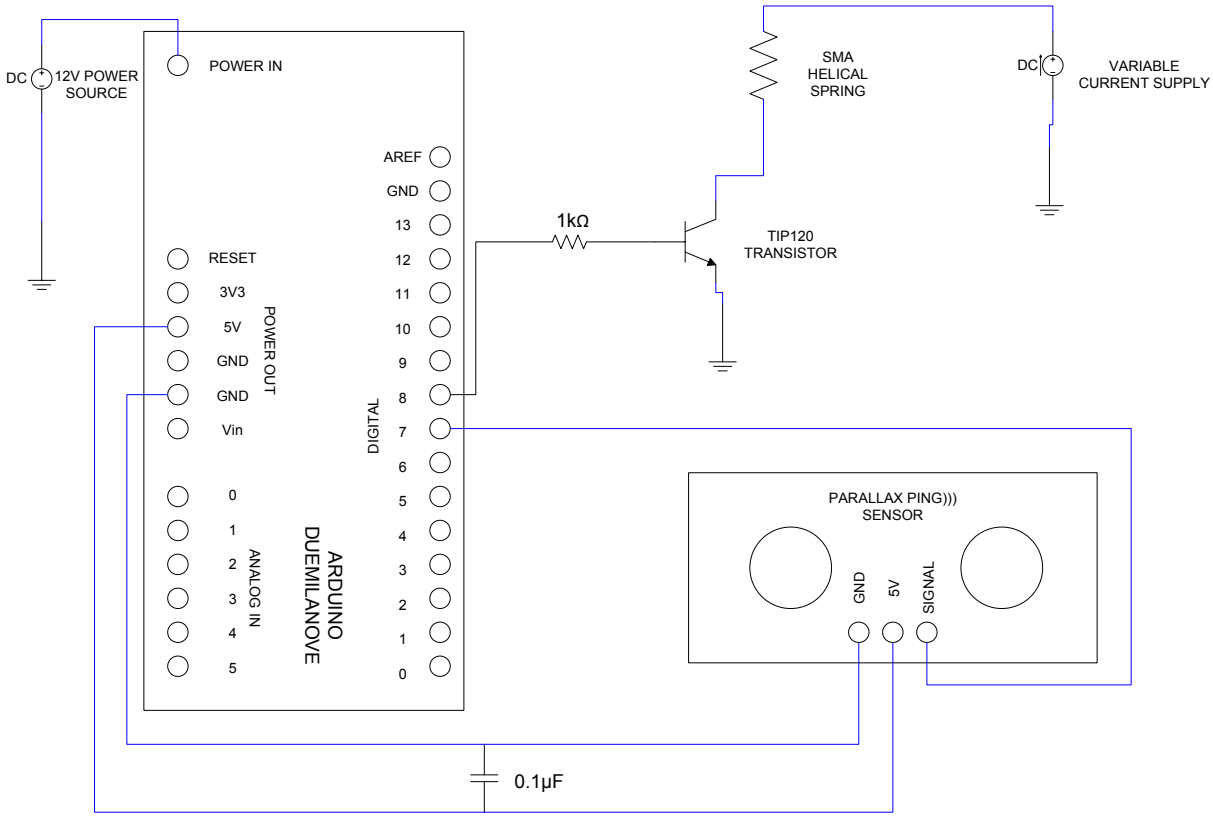

APPENDIX C5: ARDUINO CODE CONTROL SETTINGS

Table C-21: The Control Settings for the Wire Diameter Manipulation

Wire Diameter	Trial	Heat Control	Cool Control	Heat Time (ms)	Cool Time (ms)
0.145 mm	1	0.4	0.2	2500	3000
	2	0.4	0.2	2000	2000
	3	0.5	0.2	2000	2000
	4	0.5	0.2	2000	2000
0.192 mm	1	0.6	0.125	2500	6000
	2	0.6	0.125	2500	6000
	3	0.6	0.125	2500	6000
	4	0.6	0.125	2500	6000
0.248 mm	1	0.4	0.1	3000	7500
	2	0.4	0.15	3000	7500
	3	0.3	0.1	3000	9000
	4	0.4	0.15	3000	9000
0.375 mm	1	0.2	0.15	7000	10000
	2	0.2	0.15	7000	11000
	3	0.2	0.1	7000	10500
	4	0.2	0.1	7000	10500

Table C-22: The Control Settings for the Spring Diameter Manipulation

Rod Diameter	Trial	Heat Control	Cool Control	Heat Time (ms)	Cool Time (ms)
2.34 mm	1	0.4	0.125	4000	7500
	2	0.4	0.125	4000	9000
	3	0.4	0.125	4000	13000
	4	0.4	0.125	4000	11000
3.175 mm	1	0.6	0.125	2500	6000
	2	0.6	0.125	2500	6000
	3	0.6	0.125	2500	6000
	4	0.6	0.125	2500	6000
4.80 mm	1	0.25	0.125	6000	7500
	2	0.25	0.125	7000	7500
	3	0.25	0.125	7000	7500
	4	0.25	0.125	7000	7500
6.36 mm	1	0.25	0.125	7000	7500
	2	0.25	0.125	7000	7500
	3	0.25	0.125	7000	7500

Table C-23: The Control Settings for the Spring Diameter Manipulation

Transition Temperature	Wire Diameter	Trial	Heat Control	Cool Control	Heat Time (ms)	Cool Time (ms)
70 °C	0.145 mm	1	0.4	0.2	2500	3000
		2	0.4	0.2	2000	2000
		3	0.5	0.2	2000	2000
		4	0.5	0.2	2000	2000
	0.192 mm	1	0.6	0.125	2500	6000
		2	0.6	0.125	2500	6000
		3	0.6	0.125	2500	6000
		4	0.6	0.125	2500	6000
	0.248 mm	1	0.4	0.1	3000	7500
		2	0.4	0.15	3000	7500
		3	0.3	0.1	3000	9000
		4	0.4	0.15	3000	9000
	0.144 mm	1	0.5	0.2	2000	2000
		2	0.5	0.2	2000	2000
		3	0.5	0.2	2000	2000
90 °C	0.195 mm	1	0.25	0.125	2500	6000
		2	0.4	0.2	2500	3000
		3	0.4	0.2	2500	3000
		4	0.4	0.2	2500	3000
	0.243 mm	1	0.3	0.125	5000	6000
		2	0.25	0.125	4000	5000
		3	0.25	0.125	4000	5000
		4	0.25	0.125	4000	5000

Table C-24: The Control Settings for the Number of Turns Manipulation

Number of Spring Turns	Trial	Heat Control	Cool Control	Heat Time (ms)	Cool Time (ms)
8	1	0.4	0.125	5000	7500
	2	0.4	0.125	5000	7500
	3	0.4	0.125	5000	7500
	4	0.4	0.125	5000	7500
12	1	0.4	0.125	5000	7500
	2	0.4	0.125	5000	7500
	3	0.4	0.125	5000	7500
	4	0.4	0.125	5000	7500
16	1	0.4	0.1	3000	7500
	2	0.4	0.15	3000	7500
	3	0.3	0.1	3000	9000
	4	0.4	0.15	3000	9000
20	1	0.4	0.125	5000	7500
	2	0.4	0.125	5000	7500
	3	0.4	0.125	5000	7500
	4	0.4	0.125	5000	7500

Table C-25: The Control settings for the Bias Mass Manipulation

Bias Mass	Trial	Heat Control	Cool Control	Heat Time (ms)	Cool Time (ms)
20 g	1	0.4	0.05	3000	8000
	2	0.4	0.1	4000	7000
	3	0.4	0.1	3000	12000
	4	0.4	0.1	4000	9000
30 g	1	0.4	0.1	3000	7500
	2	0.4	0.15	3000	7500
	3	0.3	0.1	3000	9000
	4	0.4	0.15	3000	9000
40 g	1	0.15	0.2	5000	8000
	2	0.15	0.2	5000	8000
	3	0.15	0.2	5000	8000
	4	0.15	0.2	5000	8000

Table C-26: The Control Settings for the Direct Current Manipulation

Direct Current	Trial	Heat Control	Cool Control	Heat Time (ms)	Cool Time (ms)
0.45 A	1	0.1	0.1	13000	9000
	2	0.125	0.1	15000	9000
	3	0.125	0.1	15000	9000
0.50 A	1	0.1	0.125	5000	7500
	2	0.1	0.125	5000	7500
	3	0.1	0.125	5000	7500
0.55 A	1	0.4	0.1	3000	7500
	2	0.4	0.15	3000	7500
	3	0.3	0.1	3000	9000
0.60 A	1	0.4	0.125	4000	7500
	2	0.4	0.125	4000	7500
	3	0.4	0.125	4000	7500

APPENDIX C6: TABULATED RESULTS OF THE REACTION TIMES AND DISPLACEMENTS

Table C-27: The Heat Time Results for the Wire Diameter Manipulation

Wire Diameter/ Measured Wire Diameter	Values for each Trial	Trial 1	Trial 2	Trial 3	Trial 4	Averaged and Pooled Values From Trials	Value
0.006"/ 0.145 mm	Mean (s)	2.63	6.15	3.17	3.56	Averaged Mean (s)	3.88
	Median (s)	2.56	3.38	2.61	2.78	Averaged Median (s)	2.83
	Std Dev (s)	0.13	5.8	1.9	2.1	Pooled Std. Dev. (s)	3.2
	% Std. Dev	5.1	93.8	58.6	60.0	Pooled % Std. Dev	82.8%
0.008"/ 0.192 mm	Mean (s)	3.17	3.91	4.35	3.01	Averaged Mean (s)	3.61
	Median (s)	3.08	3.44	3.80	2.97	Averaged Median (s)	3.32
	Std Dev (s)	0.42	1.5	2.1	0.4	Pooled Std. Dev. (s)	1.3
	% Std. Dev	13.1	38.8	48.2	11.7	Pooled % Std. Dev	36.6%
0.010"/ 0.248 mm	Mean (s)	6.79	6.12	7.10	6.00	Averaged Mean (s)	6.50
	Median (s)	6.75	6.17	6.03	6.12	Averaged Median (s)	6.27
	Std Dev (s)	0.79	0.64	2.9	1.3	Pooled Std. Dev. (s)	1.7
	% Std. Dev	11.7	10.5	41.5	21.0	Pooled % Std. Dev	25.9%
0.015"/ 0.375 mm	Mean (s)	9.08	7.54	8.03	8.85	Averaged Mean (s)	8.37
	Median (s)	8.44	7.52	7.52	7.70	Averaged Median (s)	7.80
	Std Dev (s)	2.1	0.38	1.3	2.4	Pooled Std. Dev. (s)	1.7
	% Std. Dev	23.0	5.0	16.4	27.4	Pooled % Std. Dev	20.8%

Table C-28: The Cooling Time Results for the Wire Diameter Manipulation

Wire Diameter/ Measured Wire Diameter	Values for each Trial	Trial 1	Trial 2	Trial 3	Trial 4	Averaged and Pooled Values From Trials	Value
0.006"/ 0.145 mm	Mean (s)	3.31	3.30	3.22	3.08	Averaged Mean (s)	3.23
	Median (s)	3.27	3.07	3.22	2.97	Averaged Median (s)	3.13
	Std Dev (s)	0.15	0.87	0.20	0.29	Pooled Std. Dev. (s)	0.47
	% Std. Dev	4.6	26.2	6.3	9.4	Pooled % Std. Dev	14.7%
0.008"/ 0.192 mm	Mean (s)	7.30	7.39	7.92	6.45	Averaged Mean (s)	7.26
	Median (s)	7.06	7.32	7.23	6.15	Averaged Median (s)	6.94
	Std Dev (s)	0.92	0.87	1.9	0.48	Pooled Std. Dev. (s)	1.2
	% Std. Dev	12.6	11.7	24.2	7.5	Pooled % Std. Dev	16.2%
0.010"/ 0.248 mm	Mean (s)	11.6	13.8	11.5	14.4	Averaged Mean (s)	12.8
	Median (s)	11.1	14.1	11.9	13.8	Averaged Median (s)	12.7
	Std Dev (s)	2.4	1.7	2.3	2.1	Pooled Std. Dev. (s)	2.2
	% Std. Dev	21.1	12.1	20.1	14.9	Pooled % Std. Dev	16.9%
0.015"/ 0.375 mm	Mean (s)	13.3	16.6	15.4	15.1	Averaged Mean (s)	15.1
	Median (s)	12.5	16.2	15.7	14.7	Averaged Median (s)	14.8
	Std Dev (s)	2.0	2.6	2.8	4.2	Pooled Std. Dev. (s)	3.0
	% Std. Dev	14.9	15.7	17.9	28.0	Pooled % Std. Dev	19.9%

Table C-29: The Austenite Spring Length Results for the Wire Diameter Manipulation

Wire Diameter/ Measured Wire Diameter	Values for each Trial	Trial 1	Trial 2	Trial 3	Trial 4	Averaged and Pooled Values From Trials	Value
0.006"/ 0.145 mm	Mean (cm)	14.8	13.9	14.7	14.1	Averaged Mean (cm)	14.4
	Median (cm)	14.8	14.1	14.8	14.3	Averaged Median (cm)	14.5
	Std Dev (cm)	0.081	0.57	0.39	0.40	Pooled Std. Dev. (cm)	0.40
	% Std. Dev	0.55	4.1	2.7	2.8	Pooled % Std. Dev	2.8%
0.008"/ 0.192 mm	Mean (cm)	7.29	7.21	6.10	7.31	Averaged Mean (cm)	6.98
	Median (cm)	7.30	7.40	6.30	7.55	Averaged Median (cm)	7.14
	Std Dev (cm)	0.34	0.47	0.52	0.68	Pooled Std. Dev. (cm)	0.52
	% Std. Dev	4.6	6.5	8.5	9.3	Pooled % Std. Dev	7.4%
0.010"/ 0.248 mm	Mean (cm)	3.53	1.89	3.35	3.10	Averaged Mean (cm)	2.96
	Median (cm)	3.55	1.90	3.25	3.10	Averaged Median (cm)	2.95
	Std Dev (cm)	0.22	0.13	0.27	0.19	Pooled Std. Dev. (cm)	0.21
	% Std. Dev	6.4	6.6	8.1	6.2	Pooled % Std. Dev	7.1%
0.015"/ 0.375 mm	Mean (cm)	6.15	5.07	5.77	4.65	Averaged Mean (cm)	5.41
	Median (cm)	6.15	5.20	5.80	4.65	Averaged Median (cm)	5.45
	Std Dev (cm)	0.28	0.73	0.40	0.69	Pooled Std. Dev. (cm)	0.56
	% Std. Dev	4.6	14	6.9	15	Pooled % Std. Dev	10.3%

Table C-30: The Martensite Spring Length Results for the Wire Diameter Manipulation

Wire Diameter/ Measured Wire Diameter	Values for each Trial	Trial 1	Trial 2	Trial 3	Trial 4	Averaged and Pooled Values From Trials	Value
0.006"/ 0.145 mm	Mean (cm)	17.2	17.4	18.8	17.6	Averaged Mean (cm)	17.7
	Median (cm)	17.2	17.4	18.8	17.6	Averaged Median (cm)	17.8
	Std Dev (cm)	0.033	0.067	0.00	0.048	Pooled Std. Dev. (cm)	0.044
	% Std. Dev	0.19	0.39	0.00	0.27	Pooled % Std. Dev	0.3%
0.008"/ 0.192 mm	Mean (cm)	16.8	16.8	15.9	17.5	Averaged Mean (cm)	16.8
	Median (cm)	16.8	16.8	15.9	17.5	Averaged Median (cm)	16.8
	Std Dev (cm)	0.058	0.088	0.093	0.094	Pooled Std. Dev. (cm)	0.085
	% Std. Dev	0.34	0.52	0.59	0.54	Pooled % Std. Dev	0.5%
0.010"/ 0.248 mm	Mean (cm)	13.7	12.5	12.6	13.1	Averaged Mean (cm)	13.0
	Median (cm)	14.0	12.4	13.1	13.1	Averaged Median (cm)	13.2
	Std Dev (cm)	0.68	0.16	0.79	0.33	Pooled Std. Dev. (cm)	0.55
	% Std. Dev	5.0	1.3	6.3	2.5	Pooled % Std. Dev	4.3%
0.015"/ 0.375 mm	Mean (cm)	16.2	15.5	15.8	15.0	Averaged Mean (cm)	15.6
	Median (cm)	16.2	15.7	15.9	15.4	Averaged Median (cm)	15.8
	Std Dev (cm)	0.28	0.52	0.48	1.3	Pooled Std. Dev. (cm)	0.74
	% Std. Dev	1.7	3.3	3.0	8.5	Pooled % Std. Dev	4.7%

Table C-31: The Stroke Results from the Wire Diameter Manipulation

Wire Diameter/ Measured Wire Diameter	Values for each Trial	Trial 1	Trial 2	Trial 3	Trial 4	Averaged and Pooled Values From Trials	Value
0.006"/ 0.145 mm	Mean (cm)	2.29	3.52	4.11	3.44	Averaged Mean (cm)	3.34
	Median (cm)	2.40	3.30	4.00	3.30	Averaged Median (cm)	3.25
	Std Dev (cm)	0.074	0.59	0.39	0.40	Pooled Std. Dev. (cm)	0.41
	% Std. Dev	3.2	16.8	9.6	11.7	Pooled % Std. Dev	12.3%
0.008"/ 0.192 mm	Mean (cm)	9.52	9.59	9.81	10.1	Averaged Mean (cm)	9.76
	Median (cm)	9.50	9.40	9.65	9.95	Averaged Median (cm)	9.63
	Std Dev (cm)	0.34	0.43	0.45	0.59	Pooled Std. Dev. (cm)	0.46
	% Std. Dev	3.6	4.5	4.6	5.8	Pooled % Std. Dev	4.7%
0.010"/ 0.248 mm	Mean (cm)	10.1	10.6	9.31	10.0	Averaged Mean (cm)	10.0
	Median (cm)	10.3	10.6	9.60	10.1	Averaged Median (cm)	10.2
	Std Dev (cm)	0.66	0.19	0.70	0.40	Pooled Std. Dev. (cm)	0.53
	% Std. Dev	6.5	1.8	7.6	4.0	Pooled % Std. Dev	5.3%
0.015"/ 0.375 mm	Mean (cm)	10.0	10.3	9.98	10.2	Averaged Mean (cm)	10.1
	Median (cm)	10.0	10.3	9.95	10.5	Averaged Median (cm)	10.2
	Std Dev (cm)	0.37	0.29	0.37	1.0	Pooled Std. Dev. (cm)	0.58
	% Std. Dev	3.7	2.9	3.7	9.8	Pooled % Std. Dev	5.8%

Table C-32: The Heat Time Results for the Spring Diameter Manipulation

Measured Rod (Inner Spring) Diameter	Values for each Trial	Trial 1	Trial 2	Trial 3	Trial 4	Averaged and Pooled Values From Trials	Value
2.34 mm	Mean (s)	5.38	5.28	4.78	5.19	Averaged Mean (s)	5.16
	Median (s)	5.43	5.02	4.71	5.17	Averaged Median (s)	5.08
	Std Dev (s)	0.35	0.72	0.35	0.39	Pooled Std. Dev. (s)	0.48
	% Std. Dev	6.5	13.6	7.4	7.5	Pooled % Std. Dev	9.3%
3.175 mm	Mean (s)	6.79	6.12	7.10	6.00	Averaged Mean (s)	6.50
	Median (s)	6.75	6.17	6.03	6.12	Averaged Median (s)	6.27
	Std Dev (s)	0.79	0.64	2.9	1.3	Pooled Std. Dev. (s)	1.7
	% Std. Dev	11.7	10.5	41.5	21.0	Pooled % Std. Dev	25.9%
4.80 mm	Mean (s)	8.62	10.8	11.3	9.11	Averaged Mean (s)	9.96
	Median (s)	7.90	10.7	11.1	8.30	Averaged Median (s)	9.50
	Std Dev (s)	2.2	1.7	2.5	2.1	Pooled Std. Dev. (s)	2.1
	% Std. Dev	25.2	15.8	22.2	22.9	Pooled % Std. Dev	21.5%
6.36 mm	Mean (s)	9.47	10.0			Averaged Mean (s)	9.75
	Median (s)	8.77	9.83			Averaged Median (s)	9.30
	Std Dev (s)	1.4	1.6			Pooled Std. Dev. (s)	1.5
	% Std. Dev	14.8	15.5			Pooled % Std. Dev	15.2%

Table C-33: The Cooling Time Results for the Spring Diameter Manipulation

Measured Rod (Inner Spring) Diameter	Values for each Trial	Trial 1	Trial 2	Trial 3	Trial 4	Averaged and Pooled Values From Trials	Value
2.34 mm	Mean (s)	16.7	17.3	15.4	15.9	Averaged Mean (s)	16.3
	Median (s)	16.4	16.9	15.6	15.7	Averaged Median (s)	16.1
	Std Dev (s)	1.6	2.4	1.5	1.8	Pooled Std. Dev. (s)	1.9
	% Std. Dev	9.7	14.0	10.0	11.1	Pooled % Std. Dev	11.4%
3.175 mm	Mean (s)	11.6	13.8	11.5	14.4	Averaged Mean (s)	12.8
	Median (s)	11.1	14.1	11.9	13.8	Averaged Median (s)	12.7
	Std Dev (s)	2.4	1.7	2.3	2.1	Pooled Std. Dev. (s)	2.2
	% Std. Dev	21.1	12.1	20.1	14.9	Pooled % Std. Dev	16.9%
4.80 mm	Mean (s)	11.1	9.27	9.00	8.59	Averaged Mean (s)	9.50
	Median (s)	8.62	8.86	8.49	8.20	Averaged Median (s)	8.54
	Std Dev (s)	7.0	1.8	1.7	1.5	Pooled Std. Dev. (s)	3.78
	% Std. Dev	62.8	19.5	18.6	17.4	Pooled % Std. Dev	39.8%
6.36 mm	Mean (s)	9.84	13.3			Averaged Mean (s)	11.6
	Median (s)	9.65	11.5			Averaged Median (s)	10.6
	Std Dev (s)	1.2	5.8			Pooled Std. Dev. (s)	4.2
	% Std. Dev	12.5	43.6			Pooled % Std. Dev	36.2%

Table C-34: The Austenite Spring Length Results for the Spring Diameter Manipulation

Measured Rod (Inner Spring) Diameter	Values for each Trial	Trial 1	Trial 2	Trial 3	Trial 4	Averaged and Pooled Values From Trials	Value
2.34 mm	Mean (cm)	1.51	1.58	1.80	1.75	Averaged Mean (cm)	1.66
	Median (cm)	1.5	1.6	1.8	1.75	Averaged Median (cm)	1.66
	Std Dev (cm)	0.055	0.12	0.069	0.060	Pooled Std. Dev. (cm)	0.081
	% Std. Dev	3.7	7.7	3.8	3.5	Pooled % Std. Dev	4.9%
3.175 mm	Mean (cm)	3.53	1.89	3.35	3.10	Averaged Mean (cm)	2.96
	Median (cm)	3.55	1.90	3.25	3.10	Averaged Median (cm)	2.95
	Std Dev (cm)	0.22	0.13	0.27	0.19	Pooled Std. Dev. (cm)	0.21
	% Std. Dev	6.37	6.63	8.14	6.24	Pooled % Std. Dev	7.1%
4.80 mm	Mean (cm)	8.35	8.91	7.51	7.98	Averaged Mean (cm)	8.18
	Median (cm)	8.20	8.85	7.50	7.90	Averaged Median (cm)	8.11
	Std Dev (cm)	0.75	0.59	0.42	0.66	Pooled Std. Dev. (cm)	0.62
	% Std. Dev	9.0	6.6	5.6	8.3	Pooled % Std. Dev	7.6%
6.36 mm	Mean (cm)	15.6	15.8	16.1		Averaged Mean (cm)	15.8
	Median (cm)	15.6	16.3	15.7		Averaged Median (cm)	15.9
	Std Dev (cm)	0.66	0.98	1.2		Pooled Std. Dev. (cm)	0.97
	% Std. Dev	4.3	6.2	7.5		Pooled % Std. Dev	6.1%

Table C-35: The Martensite Spring Length Results for the Spring Diameter Manipulation

Measured Rod (Inner Spring) Diameter	Values for each Trial	Trial 1	Trial 2	Trial 3	Trial 4	Averaged and Pooled Values From Trials	Value
2.34 mm	Mean (cm)	7.54	7.44	6.81	7.79	Averaged Mean (cm)	7.39
	Median (cm)	7.55	7.75	6.70	7.95	Averaged Median (cm)	7.49
	Std Dev (cm)	0.25	0.76	0.64	0.69	Pooled Std. Dev. (cm)	0.62
	% Std. Dev	3.3	10.2	9.4	8.9	Pooled % Std. Dev	8.3%
3.175 mm	Mean (cm)	13.7	12.5	12.6	13.1	Averaged Mean (cm)	13.0
	Median (cm)	14.0	12.4	13.1	13.1	Averaged Median (cm)	13.2
	Std Dev (cm)	0.68	0.16	0.79	0.33	Pooled Std. Dev. (cm)	0.55
	% Std. Dev	5.0	1.3	6.3	2.5	Pooled % Std. Dev	4.3%
4.80 mm	Mean (cm)	23.0	24.8	22.2	23.1	Averaged Mean (cm)	23.3
	Median (cm)	23.3	24.9	22.2	23.1	Averaged Median (cm)	23.4
	Std Dev (cm)	0.62	0.11	0.26	0.27	Pooled Std. Dev. (cm)	0.37
	% Std. Dev	2.7	0.4	1.2	1.2	Pooled % Std. Dev	1.6%
6.36 mm	Mean (cm)	31.1	32.5	31.7		Averaged Mean (cm)	31.8
	Median (cm)	31.1	32.6	31.7		Averaged Median (cm)	31.8
	Std Dev (cm)	0.13	0.18	0.20		Pooled Std. Dev. (cm)	0.17
	% Std. Dev	0.4	0.5	0.6		Pooled % Std. Dev	0.5%

Table C-36: The Stroke Results from the Spring Diameter Manipulation

Measured Rod (Inner Spring) Diameter	Values for each Trial	Trial 1	Trial 2	Trial 3	Trial 4	Averaged and Pooled Values From Trials	Value
2.34 mm	Mean (cm)	6.04	5.89	5.05	6.08	Averaged Mean (cm)	5.76
	Median (cm)	6.00	6.10	4.90	6.20	Averaged Median (cm)	5.80
	Std Dev (cm)	0.27	0.77	0.71	0.71	Pooled Std. Dev. (cm)	0.65
	% Std. Dev	4.5	13.1	14.0	11.7	Pooled % Std. Dev	11.2%
3.175 mm	Mean (cm)	10.1	10.6	9.31	10.0	Averaged Mean (cm)	10.0
	Median (cm)	10.3	10.6	9.60	10.1	Averaged Median (cm)	10.2
	Std Dev (cm)	0.66	0.19	0.70	0.40	Pooled Std. Dev. (cm)	0.53
	% Std. Dev	6.5	1.8	7.6	4.0	Pooled % Std. Dev	5.3%
4.80 mm	Mean (cm)	14.7	16.0	14.7	15.1	Averaged Mean (cm)	15.1
	Median (cm)	14.8	16.0	14.7	15.1	Averaged Median (cm)	15.2
	Std Dev (cm)	0.79	0.61	0.41	0.75	Pooled Std. Dev. (cm)	0.66
	% Std. Dev	5.4	3.8	2.8	4.9	Pooled % Std. Dev	4.3%
6.36 mm	Mean (cm)	15.5	16.8	15.6		Averaged Mean (cm)	16.0
	Median (cm)	15.5	16.3	15.8		Averaged Median (cm)	15.8
	Std Dev (cm)	0.64	0.92	1.2		Pooled Std. Dev. (cm)	0.97
	% Std. Dev	4.1	5.5	8.0		Pooled % Std. Dev	6.1%

Table C-37: The Heat Time Results for the Transition Temperature Manipulation

Measured Wire Diameter (90°C Transition Temperature)	Values for each Trial	Trial 1	Trial 2	Trial 3	Trial 4	Averaged and Pooled Values From Trials	Value
0.144 mm	Mean (s)	2.64	4.56	3.93		Averaged Mean (s)	3.71
	Median (s)	2.30	2.10	2.23		Averaged Median (s)	2.21
	Std Dev (s)	0.85	6.5	3.2		Pooled Std. Dev. (s)	4.2
	% Std. Dev	32.0	142.9	81.9		Pooled % Std. Dev	113.9%
0.195 mm	Mean (s)	3.84	3.07	4.58	3.51	Averaged Mean (s)	3.75
	Median (s)	3.53	2.76	2.97	2.66	Averaged Median (s)	2.98
	Std Dev (s)	1.9	1.0	3.8	1.9	Pooled Std. Dev. (s)	2.4
	% Std. Dev	48.8	31.2	83.9	53.8	Pooled % Std. Dev	63.6%
0.243 mm	Mean (s)	6.10	6.06	7.61	5.68	Averaged Mean (s)	6.36
	Median (s)	5.63	5.74	6.30	5.68	Averaged Median (s)	5.84
	Std Dev (s)	1.2	1.4	5.4	1.0	Pooled Std. Dev. (s)	2.9
	% Std. Dev	20.4	23.1	71.1	18.2	Pooled % Std. Dev	45.7%

Table C-38: The Cooling Time Results for the Transition Temperature Manipulation

Measured Wire Diameter (90°C Transition Temperature)	Values for each Trial	Trial 1	Trial 2	Trial 3	Trial 4	Averaged and Pooled Values From Trials	Value
0.144 mm	Mean (s)	3.20	2.84	5.18		Averaged Mean (s)	3.74
	Median (s)	2.76	2.50	5.44		Averaged Median (s)	3.57
	Std Dev (s)	1.3	1.2	2.2		Pooled Std. Dev. (s)	1.6
	% Std. Dev	40.8	41.1	43.1		Pooled % Std. Dev	43.8%
0.195 mm	Mean (s)	10.6	4.35	4.23	4.95	Averaged Mean (s)	6.04
	Median (s)	6.49	4.40	4.14	4.75	Averaged Median (s)	4.95
	Std Dev (s)	7.7	0.35	0.51	1.1	Pooled Std. Dev. (s)	3.9
	% Std. Dev	72.6	8.2	12.0	21.6	Pooled % Std. Dev	64.8%
0.243 mm	Mean (s)	8.35	7.09	7.00	5.92	Averaged Mean (s)	7.09
	Median (s)	7.00	6.56	6.40	5.63	Averaged Median (s)	6.40
	Std Dev (s)	3.7	2.3	2.3	1.1	Pooled Std. Dev. (s)	2.5
	% Std. Dev	44.0	32.8	32.7	19.3	Pooled % Std. Dev	35.6%

Table C-39: The Austenite Spring Length Results for the Transition Temperature Manipulation

Measured Wire Diameter (90°C Transition Temperature)	Values for each Trial	Trial 1	Trial 2	Trial 3	Trial 4	Averaged and Pooled Values From Trials	Value
0.144 mm	Mean (cm)	16.2	18.1	17.5		Averaged Mean (cm)	17.3
	Median (cm)	16.4	18.2	17.7		Averaged Median (cm)	17.4
	Std Dev (cm)	0.41	0.41	0.42		Pooled Std. Dev. (cm)	0.41
	% Std. Dev	2.5	2.3	2.4		Pooled % Std. Dev	2.4%
0.195 mm	Mean (cm)	14.9	14.2	14.3	15.1	Averaged Mean (cm)	14.6
	Median (cm)	15.2	14.5	14.7	15.5	Averaged Median (cm)	15.0
	Std Dev (cm)	0.73	1.1	1.1	0.93	Pooled Std. Dev. (cm)	0.98
	% Std. Dev	4.9	7.8	7.8	6.2	Pooled % Std. Dev	6.7%
0.243 mm	Mean (cm)	12.7	8.21	10.0	10.5	Averaged Mean (cm)	10.3
	Median (cm)	12.6	8.70	10.5	11.0	Averaged Median (cm)	10.7
	Std Dev (cm)	0.36	1.8	1.7	1.6	Pooled Std. Dev. (cm)	1.5
	% Std. Dev	2.9	21.7	17.4	14.8	Pooled % Std. Dev	14.3%

Table C-40: The Martensite Spring Length Results for the Transition Temperature Manipulation

Measured Wire Diameter (90°C Transition Temperature)	Values for each Trial	Trial 1	Trial 2	Trial 3	Trial 4	Averaged and Pooled Values From Trials	Value
0.144 mm	Mean (cm)	16.5	18.3	17.9		Averaged Mean (cm)	17.6
	Median (cm)	16.5	18.3	17.9		Averaged Median (cm)	17.6
	Std Dev (cm)	0.046	0.049	0.037		Pooled Std. Dev. (cm)	0.044
	% Std. Dev	0.3	0.3	0.2		Pooled % Std. Dev	0.3%
0.195 mm	Mean (cm)	17.6	18.2	17.8	18.6	Averaged Mean (cm)	18.0
	Median (cm)	17.6	18.2	17.8	18.6	Averaged Median (cm)	18.1
	Std Dev (cm)	0.067	0.10	0.067	0.073	Pooled Std. Dev. (cm)	0.079
	% Std. Dev	0.4	0.6	0.4	0.4	Pooled % Std. Dev	0.4%
0.243 mm	Mean (cm)	18.1	16.3	17.8	17.5	Averaged Mean (cm)	17.4
	Median (cm)	18.1	16.5	18.0	17.6	Averaged Median (cm)	17.5
	Std Dev (cm)	0.051	0.44	0.37	0.25	Pooled Std. Dev. (cm)	0.31
	% Std. Dev	0.3	2.7	2.1	1.4	Pooled % Std. Dev	1.8%

Table C-41: The Stroke Results from the Transition Temperature Manipulation

Measured Wire Diameter (90°C Transition Temperature)	Values for each Trial	Trial 1	Trial 2	Trial 3	Trial 4	Averaged and Pooled Values From Trials	Value
0.144 mm	Mean (cm)	0.22	0.27	0.36		Averaged Mean (cm)	0.28
	Median (cm)	0.1	0.1	0.2		Averaged Median (cm)	0.13
	Std Dev (cm)	0.20	0.35	0.32		Pooled Std. Dev. (cm)	0.30
	% Std. Dev	91.7	133.7	88.1		Pooled % Std. Dev	106.1%
0.195 mm	Mean (cm)	2.67	3.91	3.46	3.42	Averaged Mean (cm)	3.36
	Median (cm)	2.40	3.75	3.15	3.15	Averaged Median (cm)	3.11
	Std Dev (cm)	0.63	0.81	0.83	0.76	Pooled Std. Dev. (cm)	0.76
	% Std. Dev	23.5	20.8	24.0	22.2	Pooled % Std. Dev	22.6%
0.243 mm	Mean (cm)	5.34	7.86	7.48	6.78	Averaged Mean (cm)	6.86
	Median (cm)	5.40	7.70	7.30	6.55	Averaged Median (cm)	6.74
	Std Dev (cm)	0.34	1.0	1.2	0.99	Pooled Std. Dev. (cm)	0.95
	% Std. Dev	6.3	13.3	15.8	14.7	Pooled % Std. Dev	13.8%

Table C-42: The Heat Time Results for the Number of Spring Turns Manipulation

Number of Spring Turns	Values for each Trial	Trial 1	Trial 2	Trial 3	Trial 4	Averaged and Pooled Values From Trials	Value
8	Mean (s)	6.15	6.10	6.87	7.34	Averaged Mean (s)	6.61
	Median (s)	6.04	6.00	6.81	7.12	Averaged Median (s)	6.49
	Std Dev (s)	0.74	0.78	1.1	1.0	Pooled Std. Dev. (s)	0.92
	% Std. Dev	12.1	12.8	16.2	13.5	Pooled % Std. Dev	13.9%
12	Mean (s)	5.94	6.66	6.33	5.87	Averaged Mean (s)	6.20
	Median (s)	6.04	6.35	6.24	5.88	Averaged Median (s)	6.13
	Std Dev (s)	0.62	1.3	1.0	0.49	Pooled Std. Dev. (s)	0.92
	% Std. Dev	10.4	20.2	15.4	8.4	Pooled % Std. Dev	14.8%
16	Mean (s)	6.79	6.12	7.10	6.00	Averaged Mean (s)	6.50
	Median (s)	6.75	6.17	6.03	6.12	Averaged Median (s)	6.27
	Std Dev (s)	0.79	0.64	2.9	1.3	Pooled Std. Dev. (s)	1.7
	% Std. Dev	11.7	10.5	41.5	21.0	Pooled % Std. Dev	25.9%
20	Mean (s)	6.05	5.91	6.43	6.15	Averaged Mean (s)	6.13
	Median (s)	5.77	5.83	6.17	6.38	Averaged Median (s)	6.04
	Std Dev (s)	0.79	0.66	0.74	0.51	Pooled Std. Dev. (s)	0.69
	% Std. Dev	13.1	11.2	11.6	8.3	Pooled % Std. Dev	11.2%

Table C-43: The Cooling Time Results for the Number of Spring Turns Manipulation

Number of Spring Turns	Values for each Trial	Trial 1	Trial 2	Trial 3	Trial 4	Averaged and Pooled Values From Trials	Value
8	Mean (s)	11.6	10.4	10.7	9.77	Averaged Mean (s)	10.6
	Median (s)	11.4	10.0	10.5	9.79	Averaged Median (s)	10.4
	Std Dev (s)	0.9	1.7	1.2	1.2	Pooled Std. Dev. (s)	1.3
	% Std. Dev	8.1	16.5	10.8	12.0	Pooled % Std. Dev	12.0%
12	Mean (s)	12.6	12.1	12.6	13.6	Averaged Mean (s)	12.7
	Median (s)	12.6	12.3	12.8	14.1	Averaged Median (s)	13.0
	Std Dev (s)	1.7	1.3	1.6	2.2	Pooled Std. Dev. (s)	1.7
	% Std. Dev	13.3	10.6	12.5	16.4	Pooled % Std. Dev	13.5%
16	Mean (s)	11.6	13.8	11.5	14.4	Averaged Mean (s)	12.8
	Median (s)	11.1	14.1	11.9	13.8	Averaged Median (s)	12.7
	Std Dev (s)	2.4	1.7	2.3	2.1	Pooled Std. Dev. (s)	2.2
	% Std. Dev	21.1	12.1	20.1	14.9	Pooled % Std. Dev	16.9%
20	Mean (s)	14.1	11.0	13.9	12.6	Averaged Mean (s)	12.9
	Median (s)	13.6	10.8	13.8	12.5	Averaged Median (s)	12.7
	Std Dev (s)	2.7	1.6	1.9	1.9	Pooled Std. Dev. (s)	2.0
	% Std. Dev	19.0	14.5	13.7	14.7	Pooled % Std. Dev	15.9%

Table C-44: The Austenite Spring Length Results for the Number of Spring Turns Manipulation

Number of Spring Turns	Values for each Trial	Trial 1	Trial 2	Trial 3	Trial 4	Averaged and Pooled Values From Trials	Value
8	Mean (cm)	1.98	1.81	1.67	1.79	Averaged Mean (cm)	1.81
	Median (cm)	2.00	1.80	1.70	1.80	Averaged Median (cm)	1.83
	Std Dev (cm)	0.15	0.17	0.16	0.19	Pooled Std. Dev. (cm)	0.17
	% Std. Dev	7.4	9.4	9.7	10.8	Pooled % Std. Dev	9.3%
12	Mean (cm)	2.34	2.18	2.53	2.38	Averaged Mean (cm)	2.36
	Median (cm)	2.35	2.10	2.55	2.40	Averaged Median (cm)	2.35
	Std Dev (cm)	0.15	0.11	0.19	0.12	Pooled Std. Dev. (cm)	0.14
	% Std. Dev	6.3	5.1	7.5	5.0	Pooled % Std. Dev	6.1%
16	Mean (cm)	3.53	1.89	3.35	3.10	Averaged Mean (cm)	2.96
	Median (cm)	3.55	1.90	3.25	3.10	Averaged Median (cm)	2.95
	Std Dev (cm)	0.22	0.13	0.27	0.19	Pooled Std. Dev. (cm)	0.21
	% Std. Dev	6.4	6.6	8.1	6.2	Pooled % Std. Dev	7.1%
20	Mean (cm)	3.79	3.07	4.32	4.07	Averaged Mean (cm)	3.81
	Median (cm)	3.80	3.10	4.25	4.15	Averaged Median (cm)	3.83
	Std Dev (cm)	0.18	0.15	0.22	0.21	Pooled Std. Dev. (cm)	0.19
	% Std. Dev	4.8	4.7	5.0	5.2	Pooled % Std. Dev	5.0%

Table C-45: The Martensite Spring Length Results for the Number of Spring Turns Manipulation

Number of Spring Turns	Values for each Trial	Trial 1	Trial 2	Trial 3	Trial 4	Averaged and Pooled Values From Trials	Value
8	Mean (cm)	7.88	6.99	7.32	7.21	Averaged Mean (cm)	7.35
	Median (cm)	7.90	7.10	7.30	7.20	Averaged Median (cm)	7.38
	Std Dev (cm)	0.08	0.29	0.07	0.13	Pooled Std. Dev. (cm)	0.17
	% Std. Dev	1.0	4.1	0.9	1.8	Pooled % Std. Dev	2.3%
12	Mean (cm)	10.4	10.8	10.7	10.4	Averaged Mean (cm)	10.6
	Median (cm)	10.1	10.5	10.8	10.5	Averaged Median (cm)	10.5
	Std Dev (cm)	1.3	1.3	0.31	0.22	Pooled Std. Dev. (cm)	0.91
	% Std. Dev	12.1	11.7	2.9	2.1	Pooled % Std. Dev	8.6%
16	Mean (cm)	13.7	12.5	12.6	13.1	Averaged Mean (cm)	13.0
	Median (cm)	14.0	12.4	13.1	13.1	Averaged Median (cm)	13.2
	Std Dev (cm)	0.68	0.16	0.79	0.33	Pooled Std. Dev. (cm)	0.55
	% Std. Dev	5.0	1.3	6.3	2.5	Pooled % Std. Dev	4.3%
20	Mean (cm)	17.3	15.5	18.8	18.1	Averaged Mean (cm)	17.4
	Median (cm)	17.5	14.4	18.4	18.3	Averaged Median (cm)	17.1
	Std Dev (cm)	0.87	4.4	2.2	1.1	Pooled Std. Dev. (cm)	2.6
	% Std. Dev	5.0	28.5	11.8	6.1	Pooled % Std. Dev	14.7%

Table C-46: The Stroke Results from the Number of Spring Turns Manipulation

Number of Spring Turns	Values for each Trial	Trial 1	Trial 2	Trial 3	Trial 4	Averaged and Pooled Values From Trials	Value
8	Mean (cm)	5.91	5.19	5.64	5.43	Averaged Mean (cm)	5.54
	Median (cm)	5.90	5.20	5.60	5.40	Averaged Median (cm)	5.53
	Std Dev (cm)	0.18	0.31	0.13	0.24	Pooled Std. Dev. (cm)	0.22
	% Std. Dev	3.0	5.9	2.3	4.4	Pooled % Std. Dev	4.0%
12	Mean (cm)	8.02	8.56	8.23	8.02	Averaged Mean (cm)	8.20
	Median (cm)	7.90	8.40	8.25	8.05	Averaged Median (cm)	8.15
	Std Dev (cm)	1.2	1.2	0.39	0.22	Pooled Std. Dev. (cm)	0.90
	% Std. Dev	15.3	14.5	4.8	2.8	Pooled % Std. Dev	11.0%
16	Mean (cm)	10.1	10.6	9.3	10.0	Averaged Mean (cm)	10.0
	Median (cm)	10.3	10.6	9.6	10.1	Averaged Median (cm)	10.2
	Std Dev (cm)	0.66	0.19	0.70	0.40	Pooled Std. Dev. (cm)	0.53
	% Std. Dev	6.5	1.8	7.6	4.0	Pooled % Std. Dev	5.3%
20	Mean (cm)	13.5	12.4	14.5	14.0	Averaged Mean (cm)	13.6
	Median (cm)	13.7	11.2	14.0	14.3	Averaged Median (cm)	13.3
	Std Dev (cm)	0.92	4.4	2.3	1.2	Pooled Std. Dev. (cm)	2.6
	% Std. Dev	6.8	35.6	15.5	8.2	Pooled % Std. Dev	19.0%

Table C-47: The Heat Time Results for the Bias Mass Manipulation

Bias Mass	Values for each Trial	Trial 1	Trial 2	Trial 3	Trial 4	Averaged and Pooled Values From Trials	Value
20 g	Mean (s)	5.07	4.72	4.99	4.97	Averaged Mean (s)	4.94
	Median (s)	5.37	4.50	4.76	4.95	Averaged Median (s)	4.90
	Std Dev (s)	0.77	0.84	0.90	0.40	Pooled Std. Dev. (s)	0.75
	% Std. Dev	15.11	17.88	17.96	8.09	Pooled % Std. Dev	15.2%
30 g	Mean (s)	6.79	6.12	7.10	6.00	Averaged Mean (s)	6.50
	Median (s)	6.75	6.17	6.03	6.12	Averaged Median (s)	6.27
	Std Dev (s)	0.79	0.64	2.94	1.26	Pooled Std. Dev. (s)	1.7
	% Std. Dev	11.67	10.47	41.50	20.98	Pooled % Std. Dev	25.9%
40 g	Mean (s)	8.61	9.39	9.06	9.22	Averaged Mean (s)	9.07
	Median (s)	8.22	9.30	8.02	8.96	Averaged Median (s)	8.63
	Std Dev (s)	1.50	2.37	3.57	1.75	Pooled Std. Dev. (s)	2.4
	% Std. Dev	17.43	25.28	39.40	18.96	Pooled % Std. Dev	26.8%
50 g	Mean (s)	15.84	9.81	11.78	10.46	Averaged Mean (s)	12.0
	Median (s)	15.22	9.66	10.91	9.40	Averaged Median (s)	11.3
	Std Dev (s)	4.55	0.68	2.50	2.77	Pooled Std. Dev. (s)	3.0
	% Std. Dev	28.73	6.92	21.23	26.45	Pooled % Std. Dev	24.7%

Table C-48: The Cooling Time Results for the Bias Mass Manipulation

Bias Mass	Values for each Trial	Trial 1	Trial 2	Trial 3	Trial 4	Averaged and Pooled Values From Trials	Value
20 g	Mean (s)	19.66	17.03	17.12	18.06	Averaged Mean (s)	18.0
	Median (s)	20.04	17.25	17.00	17.87	Averaged Median (s)	18.0
	Std Dev (s)	3.78	2.76	1.82	1.89	Pooled Std. Dev. (s)	2.7
	% Std. Dev	19.22	16.24	10.62	10.49	Pooled % Std. Dev	14.9%
30 g	Mean (s)	11.61	13.77	11.54	14.40	Averaged Mean (s)	12.8
	Median (s)	11.14	14.14	11.87	13.78	Averaged Median (s)	12.7
	Std Dev (s)	2.45	1.67	2.32	2.15	Pooled Std. Dev. (s)	2.2
	% Std. Dev	21.07	12.15	20.09	14.91	Pooled % Std. Dev	16.9%
40 g	Mean (s)	9.41	12.07	11.69	10.88	Averaged Mean (s)	11.0
	Median (s)	8.88	12.62	11.51	10.73	Averaged Median (s)	10.9
	Std Dev (s)	1.35	1.61	1.83	1.25	Pooled Std. Dev. (s)	1.5
	% Std. Dev	14.31	13.32	15.64	11.52	Pooled % Std. Dev	13.9%
50 g	Mean (s)	10.03	10.16	10.37	12.04	Averaged Mean (s)	10.7
	Median (s)	9.59	9.75	9.84	12.25	Averaged Median (s)	10.4
	Std Dev (s)	1.23	1.52	2.20	2.13	Pooled Std. Dev. (s)	1.8
	% Std. Dev	12.29	14.96	21.21	17.65	Pooled % Std. Dev	17.0%

Table C-49: The Austenite Spring Length Results for the Bias Mass Manipulation

Bias Mass	Values for each Trial	Trial 1	Trial 2	Trial 3	Trial 4	Averaged and Pooled Values From Trials	Value
20 g	Mean (cm)	2.42	2.45	2.18	1.79	Averaged Mean (cm)	2.21
	Median (cm)	2.40	2.50	2.20	1.80	Averaged Median (cm)	2.23
	Std Dev (cm)	0.11	0.08	0.08	0.03	Pooled Std. Dev. (cm)	0.082
	% Std. Dev	4.57	3.38	3.82	1.72	Pooled % Std. Dev	3.7%
30 g	Mean (cm)	3.53	1.89	3.35	3.10	Averaged Mean (cm)	2.96
	Median (cm)	3.55	1.90	3.25	3.10	Averaged Median (cm)	2.95
	Std Dev (cm)	0.22	0.13	0.27	0.19	Pooled Std. Dev. (cm)	0.21
	% Std. Dev	6.37	6.63	8.14	6.24	Pooled % Std. Dev	7.1%
40 g	Mean (cm)	4.17	3.68	3.88	3.87	Averaged Mean (cm)	3.90
	Median (cm)	4.20	3.75	3.80	3.90	Averaged Median (cm)	3.91
	Std Dev (cm)	0.16	0.30	0.52	0.32	Pooled Std. Dev. (cm)	0.35
	% Std. Dev	3.92	8.11	13.37	8.36	Pooled % Std. Dev	9.0%
50 g	Mean (cm)	5.05	5.12	5.61	5.47	Averaged Mean (cm)	5.31
	Median (cm)	5.15	5.25	5.50	5.30	Averaged Median (cm)	5.30
	Std Dev (cm)	0.71	0.33	0.92	0.77	Pooled Std. Dev. (cm)	0.72
	% Std. Dev	13.99	6.42	16.37	14.18	Pooled % Std. Dev	13.5%

Table C-50: The Martensite Spring Length Results for the Bias Mass Manipulation

Bias Mass	Values for each Trial	Trial 1	Trial 2	Trial 3	Trial 4	Averaged and Pooled Values From Trials	Value
20 g	Mean (cm)	10.58	11.17	9.91	9.13	Averaged Mean (cm)	10.2
	Median (cm)	10.70	11.30	9.90	9.30	Averaged Median (cm)	10.3
	Std Dev (cm)	0.28	1.16	0.06	0.47	Pooled Std. Dev. (cm)	0.64
	% Std. Dev	2.61	10.39	0.56	5.11	Pooled % Std. Dev	6.3%
30 g	Mean (cm)	13.70	12.48	12.62	13.11	Averaged Mean (cm)	13.0
	Median (cm)	14.00	12.40	13.10	13.10	Averaged Median (cm)	13.2
	Std Dev (cm)	0.68	0.16	0.79	0.33	Pooled Std. Dev. (cm)	0.55
	% Std. Dev	4.98	1.26	6.30	2.51	Pooled % Std. Dev	4.3%
40 g	Mean (cm)	13.99	13.98	13.79	14.13	Averaged Mean (cm)	14.0
	Median (cm)	13.95	13.90	13.90	14.20	Averaged Median (cm)	14.0
	Std Dev (cm)	0.25	0.21	0.27	0.27	Pooled Std. Dev. (cm)	0.25
	% Std. Dev	1.76	1.48	1.97	1.93	Pooled % Std. Dev	1.8%
50 g	Mean (cm)	15.46	14.79	15.44	15.28	Averaged Mean (cm)	15.2
	Median (cm)	15.50	14.80	15.40	15.30	Averaged Median (cm)	15.3
	Std Dev (cm)	0.16	0.18	0.26	0.28	Pooled Std. Dev. (cm)	0.23
	% Std. Dev	1.06	1.23	1.70	1.83	Pooled % Std. Dev	1.5%

Table C-51: The Stroke Results from the Bias Mass Manipulation

Bias Mass	Values for each Trial	Trial 1	Trial 2	Trial 3	Trial 4	Averaged and Pooled Values From Trials	Value
20 g	Mean (cm)	8.16	8.77	7.74	7.37	Averaged Mean (cm)	8.01
	Median (cm)	8.30	8.95	7.70	7.50	Averaged Median (cm)	8.11
	Std Dev (cm)	0.33	1.16	0.15	0.52	Pooled Std. Dev. (cm)	0.66
	% Std. Dev	4.00	13.21	1.93	7.09	Pooled % Std. Dev	8.2%
30 g	Mean (cm)	10.10	10.60	9.31	10.04	Averaged Mean (cm)	10.0
	Median (cm)	10.30	10.60	9.60	10.10	Averaged Median (cm)	10.2
	Std Dev (cm)	0.66	0.19	0.70	0.40	Pooled Std. Dev. (cm)	0.53
	% Std. Dev	6.50	1.84	7.57	4.03	Pooled % Std. Dev	5.3%
40 g	Mean (cm)	9.84	10.28	9.93	10.26	Averaged Mean (cm)	10.1
	Median (cm)	9.80	10.30	10.00	10.20	Averaged Median (cm)	10.1
	Std Dev (cm)	0.26	0.27	0.48	0.36	Pooled Std. Dev. (cm)	0.35
	% Std. Dev	2.60	2.63	4.81	3.48	Pooled % Std. Dev	3.5%
50 g	Mean (cm)	10.36	9.67	9.81	9.78	Averaged Mean (cm)	9.91
	Median (cm)	10.35	9.50	10.00	10.00	Averaged Median (cm)	10.0
	Std Dev (cm)	0.59	0.39	0.82	0.59	Pooled Std. Dev. (cm)	0.62
	% Std. Dev	5.74	4.07	8.35	6.03	Pooled % Std. Dev	6.2%

Table C-52: The Heat Time Results for the Direct Current Manipulation

Direct Current	Values for each Trial	Trial 1	Trial 2	Trial 3	Trial 4	Averaged and Pooled Values From Trials	Value
0.45 A	Mean (s)	17.5	16.4	17.1		Averaged Mean (s)	17.0
	Median (s)	16.7	15.8	16.1		Averaged Median (s)	16.2
	Std Dev (s)	4.0	2.7	2.7		Pooled Std. Dev. (s)	3.2
	% Std. Dev	23.1	16.3	15.7		Pooled % Std. Dev	18.8%
0.50 A	Mean (s)	12.1	9.25	9.10		Averaged Mean (s)	10.1
	Median (s)	11.4	9.15	7.82		Averaged Median (s)	9.47
	Std Dev (s)	3.2	2.7	3.6		Pooled Std. Dev. (s)	3.2
	% Std. Dev	26.7	28.8	39.8		Pooled % Std. Dev	31.5%
0.55 A	Mean (s)	6.79	6.12	7.10	6.00	Averaged Mean (s)	6.50
	Median (s)	6.75	6.17	6.03	6.12	Averaged Median (s)	6.27
	Std Dev (s)	0.79	0.64	2.9	1.3	Pooled Std. Dev. (s)	1.7
	% Std. Dev	11.7	10.5	41.5	21.0	Pooled % Std. Dev	25.9%
0.60 A	Mean (s)	4.94	5.07	4.77		Averaged Mean (s)	4.92
	Median (s)	4.66	4.80	4.60		Averaged Median (s)	4.69
	Std Dev (s)	0.72	0.75	0.85		Pooled Std. Dev. (s)	0.78
	% Std. Dev	14.5	14.9	17.8		Pooled % Std. Dev	15.7%

Table C-53: The Cooling Time Results for the Direct Current Manipulation

Direct Current	Values for each Trial	Trial 1	Trial 2	Trial 3	Trial 4	Averaged and Pooled Values From Trials	Value
0.45 A	Mean (s)	12.5	12.4	10.7		Averaged Mean (s)	11.8
	Median (s)	11.4	11.3	10.6		Averaged Median (s)	11.1
	Std Dev (s)	3.5	3.3	1.4		Pooled Std. Dev. (s)	2.9
	% Std. Dev	28.0	26.7	13.3		Pooled % Std. Dev	24.5%
0.50 A	Mean (s)	12.4	11.4	11.2		Averaged Mean (s)	11.6
	Median (s)	12.1	11.1	11.1		Averaged Median (s)	11.4
	Std Dev (s)	2.7	1.8	1.7		Pooled Std. Dev. (s)	2.1
	% Std. Dev	22.2	16.0	15.2		Pooled % Std. Dev	18.4%
0.55 A	Mean (s)	11.61	13.77	11.54	14.40	Averaged Mean (s)	12.8
	Median (s)	11.14	14.14	11.87	13.78	Averaged Median (s)	12.7
	Std Dev (s)	2.4	1.7	2.3	2.1	Pooled Std. Dev. (s)	2.2
	% Std. Dev	21.1	12.1	20.1	14.9	Pooled % Std. Dev	16.9%
0.60 A	Mean (s)	13.0	10.4	10.2		Averaged Mean (s)	11.2
	Median (s)	12.5	10.0	10.6		Averaged Median (s)	11.0
	Std Dev (s)	2.0	1.4	1.8		Pooled Std. Dev. (s)	1.8
	% Std. Dev	15.7	13.5	17.6		Pooled % Std. Dev	15.8%

Table C-54: The Austenite Spring Length Results for the Direct Current Manipulation

Direct Current	Values for each Trial	Trial 1	Trial 2	Trial 3	Trial 4	Averaged and Pooled Values From Trials	Value
0.45 A	Mean (cm)	6.08	4.55	7.51		Averaged Mean (cm)	6.05
	Median (cm)	5.60	4.00	8.35		Averaged Median (cm)	5.98
	Std Dev (cm)	3.2	1.4	2.8		Pooled Std. Dev. (cm)	2.6
	% Std. Dev	52.3	31.5	37.6		Pooled % Std. Dev	42.9%
0.50 A	Mean (cm)	3.22	3.18	3.19		Averaged Mean (cm)	3.19
	Median (cm)	3.30	3.20	3.20		Averaged Median (cm)	3.23
	Std Dev (cm)	0.14	0.24	0.18		Pooled Std. Dev. (cm)	0.19
	% Std. Dev	4.2	7.7	5.6		Pooled % Std. Dev	6.0%
0.55 A	Mean (cm)	3.53	1.89	3.35	3.10	Averaged Mean (cm)	2.96
	Median (cm)	3.55	1.90	3.25	3.10	Averaged Median (cm)	2.95
	Std Dev (cm)	0.22	0.13	0.27	0.19	Pooled Std. Dev. (cm)	0.21
	% Std. Dev	6.4	6.6	8.1	6.2	Pooled % Std. Dev	7.1%
0.60 A	Mean (cm)	2.82	2.70	2.86		Averaged Mean (cm)	2.79
	Median (cm)	2.80	2.70	2.90		Averaged Median (cm)	2.80
	Std Dev (cm)	0.081	0.15	0.18		Pooled Std. Dev. (cm)	0.15
	% Std. Dev	2.9	5.7	6.5		Pooled % Std. Dev	5.3%

Table C-55: The Martensite Spring Length Results for the Direct Current Manipulation

Direct Current	Values for each Trial	Trial 1	Trial 2	Trial 3	Trial 4	Averaged and Pooled Values From Trials	Value
0.45 A	Mean (cm)	13.8	13.9	13.8		Averaged Mean (cm)	13.9
	Median (cm)	13.9	14.3	13.8		Averaged Median (cm)	14.0
	Std Dev (cm)	0.29	0.65	0.33		Pooled Std. Dev. (cm)	0.45
	% Std. Dev	2.1	4.7	2.4		Pooled % Std. Dev	3.3%
0.50 A	Mean (cm)	13.1	13.7	12.9		Averaged Mean (cm)	13.2
	Median (cm)	13.1	13.8	12.7		Averaged Median (cm)	13.2
	Std Dev (cm)	0.30	0.41	0.50		Pooled Std. Dev. (cm)	0.41
	% Std. Dev	2.3	3.0	3.9		Pooled % Std. Dev	3.1%
0.55 A	Mean (cm)	13.7	12.5	12.6	13.1	Averaged Mean (cm)	13.0
	Median (cm)	14.0	12.4	13.1	13.1	Averaged Median (cm)	13.2
	Std Dev (cm)	0.68	0.16	0.79	0.33	Pooled Std. Dev. (cm)	0.55
	% Std. Dev	5.0	1.3	6.3	2.5	Pooled % Std. Dev	4.3%
0.60 A	Mean (cm)	12.7	12.9	12.9		Averaged Mean (cm)	12.8
	Median (cm)	12.6	12.8	12.9		Averaged Median (cm)	12.7
	Std Dev (cm)	0.44	0.36	0.42		Pooled Std. Dev. (cm)	0.41
	% Std. Dev	3.5	2.8	3.2		Pooled % Std. Dev	3.2%

Table C-56: The Stroke Results from the Direct Current Manipulation

Direct Current	Values for each Trial	Trial 1	Trial 2	Trial 3	Trial 4	Averaged and Pooled Values From Trials	Value
0.45 A	Mean (cm)	7.77	9.38	6.26		Averaged Mean (cm)	7.80
	Median (cm)	8.30	9.65	5.50		Averaged Median (cm)	7.82
	Std Dev (cm)	3.1	1.5	2.8		Pooled Std. Dev. (cm)	2.5
	% Std. Dev	39.9	15.7	44.3		Pooled % Std. Dev	32.6%
0.50 A	Mean (cm)	9.89	10.6	9.70		Averaged Mean (cm)	10.1
	Median (cm)	10.0	10.5	9.55		Averaged Median (cm)	10.0
	Std Dev (cm)	0.43	0.47	0.61		Pooled Std. Dev. (cm)	0.51
	% Std. Dev	4.4	4.5	6.3		Pooled % Std. Dev	5.1%
0.55 A	Mean (cm)	10.1	10.6	9.31	10.0	Averaged Mean (cm)	10.0
	Median (cm)	10.3	10.6	9.60	10.1	Averaged Median (cm)	10.2
	Std Dev (cm)	0.66	0.19	0.70	0.40	Pooled Std. Dev. (cm)	0.53
	% Std. Dev	6.5	1.8	7.6	4.0	Pooled % Std. Dev	5.3%
0.60 A	Mean (cm)	9.82	10.3	10.0		Averaged Mean (cm)	10.0
	Median (cm)	9.70	10.1	10.0		Averaged Median (cm)	9.93
	Std Dev (cm)	0.42	0.51	0.57		Pooled Std. Dev. (cm)	0.51
	% Std. Dev	4.3	5.0	5.7		Pooled % Std. Dev	5.0%

APPENDIX D. CHAPTER 7 APPENDICES

APPENDIX D1: OUTER SPRING DIAMETER MEASUREMENTS

Table D-1: Outer Spring Diameter Measurements

Wire Diameter	Coarse Threaded Screw Diameter /Pitch	Trial #	Winding Position on Screw	Outer Diameter Measurements (in)					Average		Rank Amongst Trials	% Difference Between Largest and Smallest
				1	2	3	4	5	(in)	(mm)		
Gauge 19	0.75	1	Beginning	0.6945	0.6925	0.693	0.6945	0.6935	0.6936	17.62	Medium	0.12
		2	Middle	0.6945	0.694	0.6935	0.6925	0.6915	0.6932	17.61	Smallest	
		3	End	0.6945	0.6925	0.695	0.694	0.694	0.694	17.63	Largest	
Gauge 22	0.875	1	Beginning	0.766	0.763	0.7585	0.762	0.759	0.7617	19.35	Smallest	0.27
		2	Middle	0.764	0.767	0.7605	0.7635	0.761	0.7632	19.39	Medium	
		3	End	0.768	0.765	0.76	0.761	0.7645	0.7637	19.40	Largest	
	0.75	1	End	0.6595	0.656	0.6575	0.6565	0.6545	0.6568	16.68	Medium	0.56
		2	Middle	0.658	0.6595	0.6565	0.6555	0.6605	0.658	16.71	Largest	
		3	Beginning	0.6545	0.6555	0.6535	0.652	0.657	0.6545	16.62	Smallest	
	0.625	1	End	0.551	0.5485	0.5475	0.5485	0.5485	0.5488	13.94	Medium	0.50
		2	Middle	0.549	0.55	0.548	0.548	0.547	0.5484	13.93	Smallest	
		3	Beginning	0.5525	0.552	0.5505	0.546	0.554	0.551	14.00	Largest	
	0.5	1	Beginning	0.4475	0.4475	0.4485	0.4475	0.446	0.4474	11.36	Largest	0.26
		2	Middle	0.447	0.4465	0.448	0.446	0.4465	0.4468	11.35	Medium	
		3	End	0.4455	0.4455	0.446	0.445	0.4495	0.4463	11.34	Smallest	
	0.4375	1	Beginning	0.393	0.3915	0.3905	0.403	0.394	0.3944	10.02	Largest	0.71
		2	Middle	0.3915	0.3925	0.3945	0.393	0.3875	0.3918	9.95	Smallest	
		3	End	0.393	0.3915	0.394	0.3915	0.3925	0.3925	9.97	Medium	

APPENDIX D2: LABVIEW™ BLOCK DIAGRAM FOR RESONANCE FREQUENCY EXTRACTION

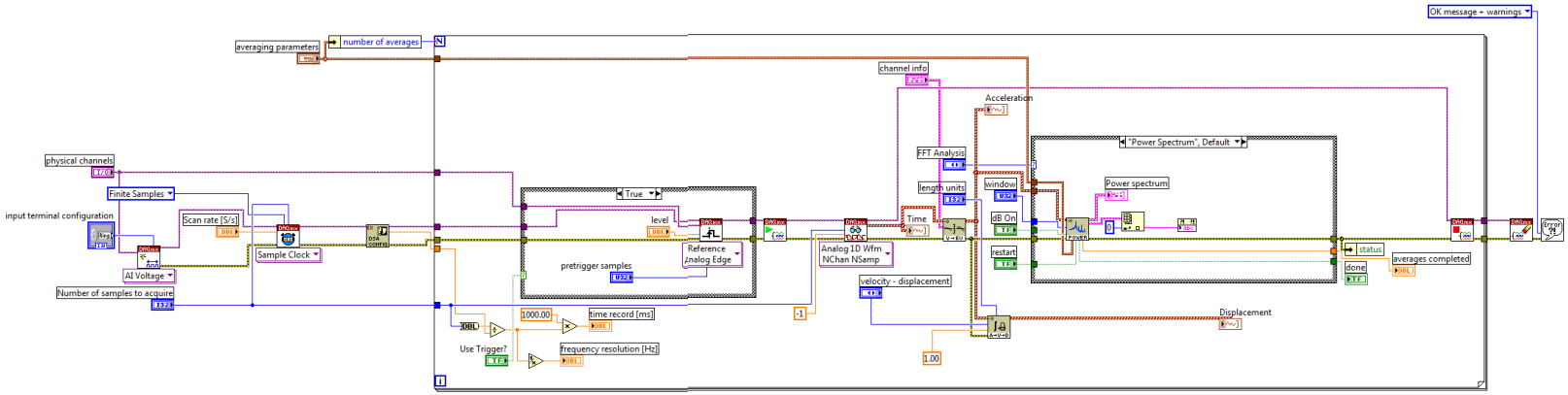

APPENDIX D3: DATA FROM THE NUMBER OF ACTIVE TURNS MANIPULATION

Table D-2: Predictions for the Number of Turns Manipulation (Gauge 22 Wire, 0.75" Power Screw)

Number of Spring Turns	Estimated Spring Stiffness (Austenite/ Martensite) (N/m)	Mass (g)	Estimated Shear Stress (MPa)	Predicted Deflection (mm)	Predicted Resonant Frequency (Hz)
4	24.5/13.1	13.6	27.5	5.44	6.76
		23.6	47.7	9.44	5.13
		33.6	67.9	13.43	4.30
		43.6	88.2	17.4	3.77
		53.6	108.4	21.4	3.40
		63.6	128.6	25.4	3.12
8	12.3/6.54	13.6	27.5	10.88	4.78
		23.6	47.7	18.9	3.63
		33.6	67.9	26.9	3.04
		43.6	88.2	34.9	2.67
		53.6	108.4	42.9	2.41
		63.6	128.6	50.9	2.21
12	8.17/4.36	13.6	27.5	16.3	3.90
		23.6	47.7	28.3	2.96
		33.6	67.9	40.3	2.48
		43.6	88.2	52.3	2.18
		53.6	108.4	64.3	1.96
		63.6	128.6	76.3	1.80
16	6.13/3.27	13.6	27.5	21.8	3.38
		23.6	47.7	37.7	2.56
		33.6	67.9	53.7	2.15
		43.6	88.2	69.7	1.89
		53.6	108.4	85.7	1.70
		63.6	128.6	101.7	1.56

Table D-3: The Start and Finish Lengths of the Superelastic Springs

Trial	Start Length (mm)	End Length (mm)	Difference (mm)
1	58	58	0
2	50	50	0
3	55	56	1

Table D-4: Deflection Data for the Superelastic Springs with 4 Active Turns

	Trial 1				Trial 2				Trial 3				Average Among Trials (mm)	Standard Deviation	
Loading Scenario	Measured Deflection (mm)			Average (mm)	Measured Deflection (mm)			Average (mm)	Measured Deflection (mm)			Average (mm)		(mm)	%
	1st	2nd	3rd		1st	2nd	3rd		1st	2nd	3rd				
Original Length (No Load)	11			11	11			11	11			11	11		
13.6 g	10	9	10	9.67	7	7	8	7.33	8	8	8	8	8.33	1.2	14.1
23.6 g	15	15	15	15	13	13	13	13	14	14	14	14	14.0	1.0	7.1
33.6 g	21	20	21	20.67	20	Bad Pic	20	20	21	21	21	21	20.6	0.36	1.7
43.6 g	27	26	26	26.33	26	26	26	26	25	25	25	25	25.8	0.28	1.1
53.6 g	33	33	33	33	31	32	32	31.67	31	31	31	31	31.9	0.71	2.2
63.6 g	39	40	39	39.33	37	37	38	37.33	37	36	38	37	37.9	1.0	2.7

Table D-5: Deflection Data for the Superelastic Springs with 8 Active Turns

	Trial 1				Trial 2				Trial 3				Average Among Trials (mm)	Standard Deviation	
Loading Scenario	Measured Deflection (mm)			Average (mm)	Measured Deflection (mm)			Average (mm)	Measured Deflection (mm)			Average (mm)		(mm)	%
	1st	2nd	3rd		1st	2nd	3rd		1st	2nd	3rd				
Original Length (No Load)	22			22	22			22	22			22	22		
13.6 g	16	17	17	16.67	14	14	14	14	16	15	16	15.67	15.4	1.3	8.7
23.6 g	29	29	29	29	Bad Pic	26	26	26	26	26	26	26	27.0	1.5	5.7
33.6 g	40	40	40	40	37	37	37	37	38	38	38	38	38.3	1.5	3.9
43.6 g	52	52	52	52	47	48	48	47.67	48	48	48	48	49.2	2.2	4.5
53.6 g	64	64	64	64	59	59	59	59	58	58	58	58	60.3	2.6	4.3
63.6 g	76	76	76	76	70	70	70	70	69	69	70	69.33	71.8	3.1	4.3

Table D-6: Deflection Data for the Superelastic Springs with 12 Active Turns

Loading Scenario	Trial 1				Trial 2				Trial 3				Average Among Trials (mm)	Standard Deviation	
	Measured Deflection (mm)			Average (mm)	Measured Deflection (mm)			Average (mm)	Measured Deflection (mm)			Average (mm)		(mm)	%
	1st	2nd	3rd		(mm)	(mm)	3rd		1st	2nd	3rd				
Original Length (No Load)	33			33	31			31	33			33	32.3		
13.6 g	26	26	27	26.33	23	23	23	23	24	24	23	23.67	24.3	1.7	6.9
23.6 g	41	42	42	41.67	39	40	40	39.67	39	39	39	39	40.1	1.1	2.6
33.6 g	60	60	60	60	56	56	56	56	55	55	56	55.33	57.1	2.1	3.6
43.6 g	76	77	77	76.67	72	72	72	72	71	71	70	70.67	73.1	2.4	3.3
53.6 g	94	93	94	93.67	88	88	88	88	85	85	85	85	88.9	3.0	3.4
63.6 g	112	113	112	112.33	104	104	104	104	100	100	99	99.67	105.3	4.5	4.2

Table D-7: Deflection Data for the Superelastic Springs with 16 Active Turns

Loading Scenario	Trial 1				Trial 2				Trial 3				Average Among Trials (mm)	Standard Deviation	
	Measured Deflection (mm)			Average (mm)	Measured Deflection (mm)			Average (mm)	Measured Deflection (mm)			Average (mm)		(mm)	%
	1st	2nd	3rd		1st	2nd	3rd		1st	2nd	3rd				
Original Length (No Load)	44			44	42			42	43			43	43		
13.6 g	32	32	32	32	30	30	30	30	29	30	29	29.33	30.4	1.1	3.5
23.6 g	54	55	55	54.67	51	51	51	51	50	50	50	50	51.9	1.9	3.7
33.6 g	76	75	76	76	72	72	72	72	70	70	70	70	72.7	2.1	2.9
43.6 g	100	98	99	99	94	93	94	93.67	90	91	90	90.33	94.3	2.9	3.1
53.6 g	122	122	122	122	113	113	114	113.33	113	113	113	113	116.1	4.4	3.8
63.6 g	146	145	146	145.67	135	135	136	135.33	134	135	135	134.67	138.6	5.3	3.8

Table D-8: Resonant Frequency Data for the Superelastic Springs with 4 Active Turns

Loading Scenario	Trial 1				Trial 2				Trial 3				Average Among Trials	Standard Deviation	
	Measured Resonant Frequency (Hz)			Average (Hz)	Measured Resonant Frequency (Hz)			Average (Hz)	Measured Resonant Frequency (Hz)			Average (Hz)			
	1st	2nd	3rd		1st	2nd	3rd		1st	2nd	3rd			(Hz)	%
13.6 g	5.13	5.07	5.07	5.09	5.25	5.25	5.25	5.25	5.25	5.25	5.25	5.25	5.20	0.081	1.6
23.6 g	3.97	3.91	3.97	3.95	4.09	4.09	4.03	4.07	4.09	4.09	4.09	4.09	4.04	0.062	1.5
33.6 g	3.36	3.36	3.3	3.34	3.48	3.48	3.42	3.46	3.54	3.54	3.54	3.54	3.45	0.066	1.9
43.6 g	2.99	2.99	2.93	2.97	3.11	3.11	3.05	3.09	3.11	3.11	3.11	3.11	3.06	0.062	2.0
53.6 g	2.75	2.75	2.69	2.73	2.81	2.81	2.81	2.81	2.87	2.87	2.87	2.87	2.80	0.044	1.6
63.6 g	2.5	2.5	2.5	2.5	2.62	2.62	2.62	2.62	2.62	2.62	2.62	2.62	2.58	0.061	2.4

Table D-9: Resonant Frequency Data for the Superelastic Springs with 8 Active Turns

Loading Scenario	Trial 1				Trial 2				Trial 3				Average Among Trials	Standard Deviation	
	Measured Resonant Frequency (Hz)			Average (Hz)	Measured Resonant Frequency (Hz)			Average (Hz)	Measured Resonant Frequency (Hz)			Average (Hz)			
	1st	2nd	3rd		1st	2nd	3rd		1st	2nd	3rd			(Hz)	%
13.6 g	3.78	3.72	3.72	3.74	3.91	3.85	3.85	3.87	3.85	3.78	3.78	3.8033	3.80	0.065	1.7
23.6 g	2.93	2.87	2.87	2.89	2.99	2.99	2.99	2.99	2.99	2.99	2.99	2.99	2.96	0.051	1.7
33.6 g	2.5	2.44	2.44	2.46	2.56	2.56	2.56	2.56	2.56	2.56	2.56	2.56	2.53	0.051	2.0
43.6 g	2.2	2.14	2.14	2.16	2.26	2.26	2.26	2.26	2.26	2.26	2.26	2.26	2.23	0.051	2.3
53.6 g	1.95	1.95	1.95	1.95	2.08	2.01	2.01	2.033	2.08	2.08	2.08	2.08	2.02	0.045	2.2
63.6 g	1.83	1.83	1.83	1.83	1.89	1.89	1.89	1.89	1.89	1.89	1.89	1.89	1.87	0.031	1.6

Table D-10: Resonant Frequency Data for the Superelastic Springs with 12 Active Turns

Loading Scenario	Trial 1				Trial 2				Trial 3				Average Among Trials	Standard Deviation	
	Measured Resonant Frequency (Hz)			Average (Hz)	Measured Resonant Frequency (Hz)			Average (Hz)	Measured Resonant Frequency (Hz)			Average (Hz)		(Hz)	%
	1st	2nd	3rd		1st	2nd	3rd		1st	2nd	3rd				
13.6 g	3.05	3.11	3.11	3.09	3.23	3.23	3.23	3.23	3.23	3.23	3.23	3.23	3.18	0.071	2.2
23.6 g	2.38	2.38	2.38	2.38	2.5	2.5	2.5	2.5	2.5	2.5	2.5	2.5	2.46	0.061	2.5
33.6 g	2.01	2.01	2.01	2.01	2.08	2.08	2.08	2.08	2.14	2.14	2.14	2.14	2.08	0.039	1.9
43.6 g	1.77	1.77	1.83	1.79	1.83	1.83	1.83	1.83	1.89	1.89	1.89	1.89	1.84	0.025	1.4
53.6 g	1.65	1.65	1.65	1.65	1.71	1.71	1.71	1.71	1.71	1.71	1.71	1.71	1.69	0.031	1.8
63.6 g	1.53	1.53	1.53	1.53	1.59	1.59	1.59	1.59	1.59	1.59	1.59	1.59	1.57	0.031	1.9

Table D-11: Resonant Frequency Data for the Superelastic Springs with 16 Active Turns

Loading Scenario	Trial 1				Trial 2				Trial 3				Average Among Trials	Standard Deviation	
	Measured Resonant Frequency (Hz)			Average (Hz)	Measured Resonant Frequency (Hz)			Average (Hz)	Measured Resonant Frequency (Hz)			Average (Hz)		(Hz)	%
	1st	2nd	3rd		1st	2nd	3rd		1st	2nd	3rd				
13.6 g	2.75	2.75	2.75	2.75	2.81	2.81	2.81	2.81	2.81	2.81	2.81	2.81	2.79	0.031	1.1
23.6 g	2.14	2.14	2.08	2.12	2.2	2.2	2.2	2.2	2.2	2.2	2.2	2.2	2.17	0.041	1.9
33.6 g	1.83	1.83	1.83	1.83	1.83	1.83	1.83	1.83	1.83	1.83	1.83	1.83	1.83	0.000	0.0
43.6 g	1.59	1.59	1.59	1.59	1.65	1.65	1.65	1.65	1.65	1.65	1.65	1.65	1.63	0.031	1.9
53.6 g	1.46	1.4	1.4	1.42	1.46	1.46	1.46	1.46	1.53	1.53	1.53	1.53	1.47	0.026	1.8
63.6 g	1.34	1.34	1.34	1.34	1.34	1.34	1.34	1.34	1.4	1.4	1.4	1.4	1.36	0.012	0.8

APPENDIX D4: DATA FROM THE WIRE DIAMETER MANIPULATION

Table D-12: Predictions for the Wire Diameter Manipulation (12 Spring Turns)

Averaged Measured Wire Diameter	Averaged Measured Spring Diameter	Estimated Spring Stiffness (Austenite/ Martensite) (N/m)	Mass (g)	Estimated Shear Stress (MPa)	Predicted Deflection (mm)	Predicted Resonant Frequency (Hz)
0.8865 mm	16.73 mm	38.7/20.7	53.6	32.1	13.6	4.28
			103.6	62.1	26.2	3.08
			153.6	92.1	38.9	2.53
			203.6	122.0	51.5	2.19
			253.6	152.0	64.2	1.97
			303.6	182.0	76.8	1.80
0.5835 mm	16.09 mm	8.17/4.36	13.6	27.5	16.3	3.90
			23.6	47.7	28.3	2.96
			33.6	67.9	40.3	2.48
			43.6	88.2	52.3	2.18
			53.6	108.4	64.3	1.96
			63.6	128.6	76.3	1.80

Table D-13: The Start and Finish Lengths of the Superelastic Springs

Wire Diameter	Trial	Start Length (mm)	End Length (mm)	Difference (mm)
Gauge 19 (0.0359")	1	47	45	0
	2	37	37	0
	3	39	39	0
Gauge 22 (0.0254")*	1	58	58	0
	2	50	50	0
	3	55	56	1

*Note: All of the Gauge 22 data was found in the "Number of Active Turns" Experiments

Table D-14: Deflection Data for the Superelastic Springs with Gauge 19 Wire

Loading Scenario	Trial 1				Trial 2				Trial 3				Average Among Trials (mm)	Standard Deviation	
	Measured Deflection (mm)			Average (mm)	Measured Deflection (mm)			Average (mm)	Measured Deflection (mm)			Average (mm)		(mm)	%
	1st	2nd	3rd		1st	2nd	3rd		1st	2nd	3rd				
Original Length (No Load)	32			32	30			30	30			30	30.7		
53.6 g	19	18	18	18.33	22	23	23	22.67	25	27	27	26.33	22.4	2.4	10.9
103.6 g	38	38	38	38	46	47	47	46.67	48	54	54	52	45.6	4.7	10.4
153.6 g	57	58	58	57.67	72	72	73	72.33	78	79	84	80.33	70.1	7.9	11.3
203.6 g	81	80	80	80.33	95	94	96	95	100	102	103	101.67	92.3	7.8	8.5
253.6 g	103	104	104	103.67	123	125	126	124.67	128	131	131	130	119.4	10.9	9.2
303.6 g	129	131	132	130.67	154	155	152	153.67	156	157	159	157.33	147.2	11.9	8.1

Table D-15: Deflection Data for the Superelastic Springs with Gauge 22 Wire

Loading Scenario	Trial 1				Trial 2				Trial 3				Average Among Trials (mm)	Standard Deviation	
	Measured Deflection (mm)			Average (mm)	Measured Deflection (mm)			Average (mm)	Measured Deflection (mm)			Average (mm)		(mm)	%
	1st	2nd	3rd		1st	2nd	3rd		1st	2nd	3rd				
Original Length (No Load)	33			33	31			31	33			33	32.33		
13.6 g	26	26	27	26.33	23	23	23	23	24	24	23	23.67	24.3	1.7	6.9
23.6 g	41	42	42	41.67	39	40	40	39.67	39	39	39	39	40.1	1.1	2.6
33.6 g	60	60	60	60	56	56	56	56	55	56	56	55.33	57.1	2.1	3.6
43.6 g	76	77	77	76.67	72	72	72	72	71	71	70	70.67	73.1	2.4	3.3
53.6 g	94	93	94	93.67	88	88	88	88	85	85	85	85	88.9	3.0	3.4
63.6 g	112	113	112	112.33	104	104	104	104	100	100	99	99.67	105.3	4.5	4.2

Table D-16: Resonant Frequency Data for the Superelastic Springs with Gauge 19 Wire

Loading Scenario	Trial 1				Trial 2				Trial 3				Average Among Trials	Standard Deviation	
	Measured Resonant Frequency (Hz)			Average (Hz)	Measured Resonant Frequency (Hz)			Average (Hz)	Measured Resonant Frequency (Hz)			Average (Hz)		(Hz)	%
	1st	2nd	3rd		1st	2nd	3rd		1st	2nd	3rd				
53.6 g	3.42	3.42	3.42	3.42	3.36	3.36	3.3	3.34	3.23	3.17	3.17	3.19	3.32	0.054	1.6
103.6 g	2.5	2.5	2.44	2.48	2.38	2.32	2.32	2.34	2.32	2.26	2.26	2.28	2.37	0.074	3.1
153.6 g	2.01	1.95	1.95	1.97	1.89	1.89	1.89	1.89	1.89	1.89	1.89	1.89	1.92	0.041	2.1
203.6 g	1.71	1.71	1.71	1.71	1.65	1.65	1.65	1.65	1.65	1.71	1.71	1.69	1.68	0.030	1.8
253.6 g	1.53	1.53	1.53	1.53	1.53	1.53	1.59	1.55	1.59	1.59	1.59	1.59	1.56	0.014	0.9
303.6 g	1.46	1.46	1.46	1.46	1.53	1.53	1.53	1.53	1.53	1.53	1.53	1.53	1.51	0.036	2.4

Table D-17: Resonant Frequency Data for the Superelastic Springs with Gauge 22 Wire

Loading Scenario	Trial 1				Trial 2				Trial 3				Average Among Trials	Standard Deviation	
	Measured Resonant Frequency (Hz)			Average (Hz)	Measured Resonant Frequency (Hz)			Average (Hz)	Measured Resonant Frequency (Hz)			Average (Hz)		(Hz)	%
	1st	2nd	3rd		1st	2nd	3rd		1st	2nd	3rd				
13.6 g	3.05	3.11	3.11	3.09	3.23	3.23	3.23	3.23	3.23	3.23	3.23	3.23	3.18	0.071	2.2
23.6 g	2.38	2.38	2.38	2.38	2.5	2.5	2.5	2.5	2.5	2.5	2.5	2.5	2.46	0.061	2.5
33.6 g	2.01	2.01	2.01	2.01	2.08	2.08	2.08	2.08	2.14	2.14	2.14	2.14	2.08	0.039	1.9
43.6 g	1.77	1.77	1.83	1.79	1.83	1.83	1.83	1.83	1.89	1.89	1.89	1.89	1.84	0.025	1.4
53.6 g	1.65	1.65	1.65	1.65	1.71	1.71	1.71	1.71	1.71	1.71	1.71	1.71	1.69	0.031	1.8
63.6 g	1.53	1.53	1.53	1.53	1.59	1.59	1.59	1.59	1.59	1.59	1.59	1.59	1.57	0.031	1.9

APPENDIX D5: DATA FROM SPRING DIAMETER MANIPULATION

Table D-18: Predictions for the Spring Diameter Manipulation (8 Spring Turns, Gauge 22 Wire). (Original predictions are in regular font, Revised Predictions are in Italics)

Averaged Measured Spring Diameter	Estimated Spring Stiffness (Austenite/ Martensite) (N/m)	Mass (g)	Estimated Shear Stress (MPa)	Predicted Deflection (mm)	Predicted Resonant Frequency (Hz)
18.79 mm	7.69/4.10	13.6	32.1	17.3	3.78
		23.6	55.7	30.1	2.87
		33.6	79.3	42.8	2.41
		43.6	103.0	55.6	2.11
		53.6	126.6	68.3	1.91
		63.6	150.2	81.0	1.75
16.09 mm	12.3/6.54	13.6	32.1	10.9	3.78
		23.6	55.7	18.9	2.87
		33.6	79.3	26.9	2.41
		43.6	103.0	34.9	2.11
		53.6	126.6	42.9	1.91
		63.6	150.2	50.9	1.75
13.37 mm	21.4/11.4	13.5	22.7	6.2	6.33
		23.6	39.7	10.8	4.79
		33.6	56.5	15.4	4.01
		53.6	90.1	24.6	3.18
		73.6	123.7	33.8	2.71
		103.6	174.1	47.5	2.28
10.77 mm	40.9/21.8	53.6	72.5	12.8	4.40
		73.6	99.6	17.6	3.75
		103.6	140.2	24.8	3.16
		123.6	167.2	29.6	2.90
		153.6	207.8	36.8	2.60
		203.6	275.4	744/*217*	1.65/*2.03*
		253.6	343.1	766/*419*	1.48/*1.71*
		303.6	410.7	789/*557*	1.35/*1.50*
9.40 mm	61.5/32.8	53.6	63.3	8.5	5.39
		73.6	86.9	11.7	4.60
		103.6	122.3	16.5	3.88
		123.6	145.9	19.7	3.55
		153.6	181.4	24.5	3.19
		203.6	240.4	558/*135*	2.62/*2.02*
		253.6	299.4	573/*251*	2.17/*1.81*

Table D-19: The Start and Finish Lengths of the Superelastic Springs from the Spring Diameter Experiments

Spring Diameter	Trial	Start Length (mm)	End Length (mm)	Difference (mm)
0.875”	1	36	36	0
	3	34	35	1
0.75”*	1	58	58	0
	2	50	50	0
	3	55	56	1
0.625”	1	35	37	2
0.5”	2	29	29	0
0.4375”	1	21	21	0
	3	24	23	-1

Table D-20: Deflection Data for the Superelastic Springs with 0.875" Spring Diameter

	Trial 1				Trial 2				Trial 3				Average Among Trials (mm)	Standard Deviation	
Loading Scenario	Measured Deflection (mm)			Average (mm)	Measured Deflection (mm)			Average (mm)	Measured Deflection (mm)			Average (mm)		(mm)	%
	1st	2nd	3rd		1st	2nd	3rd		1st	2nd	3rd				
Original Length (No Load)	24			24	21			21	23			23	22.67		
13.6 g	23	23	22	22.67	24	24	Bad Pic	24	26	26	27	26.33	24.3	0.9	3.6
23.6 g	40	41	41	40.67	42	41	42	41.67	43	44	44	43.67	42	0.7	1.6
33.6 g	57	57	57	57	59	59	60	59.33	63	63	63	63	59.8	1.5	2.5
43.6 g	73	74	73	73.33	77	78	78	77.67	84	83	82	83	78	2.6	3.3
53.6 g	89	90	89	89.33	93	97	96	95.33	101	100	102	101	95.2	3.4	3.6
63.6 g	106	109	107	107.33	114	113	112	113	120	122	No Pic	121	113.8	3.5	3.1

Table D-21: Deflection Data for the Superelastic Springs with 0.75" Spring Diameter*

Loading Scenario	Trial 1				Trial 2				Trial 3				Average Among Trials (mm)	Standard Deviation	
	Measured Deflection (mm)			Average (mm)	Measured Deflection (mm)			Average (mm)	Measured Deflection (mm)			Average (mm)		(mm)	%
	1st	2nd	3rd		1st	2nd	3rd		1st	2nd	3rd				
Original Length (No Load)	22			22	22			22	22			22	22		
13.6 g	16	17	17	16.67	14	14	14	14	16	15	16	15.67	15.4	1.3	8.7
23.6 g	29	29	29	29	Bad Pic	26	26	26	26	26	26	26	27	1.5	5.7
33.6 g	40	40	40	40	37	37	37	37	38	38	38	38	38.3	1.5	3.9
43.6 g	52	52	52	52	47	48	48	47.67	48	48	48	48	49.2	2.2	4.5
53.6 g	64	64	64	64	59	59	59	59	58	58	58	58	60.3	2.6	4.3
63.6 g	76	76	76	76	70	70	70	70	69	69	70	69.33	71.8	3.1	4.3

*Note: This data was found during the "Number of Active Turn" Experiments

Table D-22: Deflection Data for the Superelastic Springs with 0.625" Spring Diameter

Loading Scenario	Trial 1				Trial 2				Trial 3				Average Among Trials (mm)	Standard Deviation	
	Measured Deflection (mm)			Average (mm)	Measured Deflection (mm)			Average (mm)	Measured Deflection (mm)			Average (mm)		(mm)	%
	1st	2nd	3rd		1st	2nd	3rd		1st	2nd	3rd				
Original Length (No Load)	18			18	18			18	18			18	18		
13.6 g	8	8	8	8	8	8	8	8	9	9	8	8.67	8.2	0.1	1.5
23.6 g	15	15	15	15	15	15	16	15.33	16	17	No Pic	16.5	15.6	0.3	2.0
33.6 g	20	20	20	20	21	20	21	20.67	23	23	24	23.33	21.3	0.7	3.1
53.6 g	32	32	32	32	34	34	35	34.33	38	38	38	38	34.8	1.5	4.3
73.6 g	44	44	44	44	46	46	46	46	53	54	55	54	48	2.0	4.2
103.6 g	63	62	63	62.67	66	66	66	66	74	75	76	75	67.9	2.6	3.9

Table D-23: Deflection Data for the Superelastic Springs with 0.50" Spring Diameter

Loading Scenario	Trial 1				Trial 2				Trial 3				Average Among Trials (mm)	Standard Deviation	
	Measured Deflection (mm)			Average (mm)	Measured Deflection (mm)			Average (mm)	Measured Deflection (mm)			Average (mm)		(mm)	%
	1st	2nd	3rd		1st	2nd	3rd		1st	2nd	3rd				
Original Length (No Load)	15			15	15			15	16			16	15.33		
53.6 g	19	19	20	19.33	19	20	19	19.33	19	19	19	19	19.2	0.1	0.3
73.6 g	27	28	28	27.67	27	27	26	26.67	26	27	26	26.33	26.9	0.5	2.0
103.6 g	37	38	37	37.33	39	39	39	39	38	38	37	37.67	38	0.8	2.2
123.6 g	46	46	46	46	47	48	47	47.33	45	45	46	45.33	46.2	0.7	1.5
153.6 g	57	57	57	57	59	59	60	59.33	58	58	58	58	58.1	1.2	2.0
203.6 g	77	77	77	77	76	80	No Pic	78	79	82	83	81.33	78.8	0.9	1.1
253.6 g	105	109	110	108	100	112	117	109.67	110	116	119	115	110.9	1.5	1.3
303.6 g	151	155	155	153.67	142	153	158	151	141	157	162	153.33	152.7	1.3	0.9

Table D-24: Deflection Data for the Superelastic Springs with 0.4375" Spring Diameter

Loading Scenario	Trial 1				Trial 2				Trial 3				Average Among Trials (mm)	Standard Deviation	
	Measured Deflection (mm)			Average (mm)	Measured Deflection (mm)			Average (mm)	Measured Deflection (mm)			Average (mm)		(mm)	%
	1st	2nd	3rd		1st	2nd	3rd		1st	2nd	3rd				
Original Length (No Load)	14			14	14			14	14			14	14		
53.6 g	12	12	12	12	11	11	11	11	12	13	12	12.33	11.8	0.5	4.5
73.6 g	16	16	16	16	15	15	16	15.33	16	16	16	16	15.8	0.3	2.2
103.6 g	23	23	22	22.67	21	22	22	21.67	23	24	No Pic	23.5	22.6	0.6	2.5
123.6 g	28	27	27	27.33	26	27	28	27	27	28	28	27.67	27.3	0.2	0.7
153.6 g	37	36	36	36.33	35	35	36	35.33	36	36	36	36	35.9	0.5	1.4
203.6 g	52	54	55	53.67	50	52	No Pic	51	52	53	54	53	52.6	1.3	2.6
253.6 g	78	82	86	82	77	81	86	81.33	83	86	89	86	83.1	0.9	1.1

Table D-25: Resonant Frequency Data for the Superelastic Springs with a Spring Diameter of 0.875”

Loading Scenario	Trial 1				Trial 2				Trial 3				Average Among Trials	Standard Deviation	
	Measured Resonant Frequency (Hz)			Average (Hz)	Measured Resonant Frequency (Hz)			Average (Hz)	Measured Resonant Frequency (Hz)			Average (Hz)			
	1st	2nd	3rd		1st	2nd	3rd		1st	2nd	3rd			(Hz)	%
13.6 g	3.23	3.23	3.17	3.21	3.23	3.23	3.23	3.23	3.23	3.17	3.17	3.19	3.21	0.012	0.4
23.6 g	2.44	2.44	2.44	2.44	2.44	2.44	2.44	2.44	2.38	2.38	2.38	2.38	2.42	0.012	0.5
33.6 g	2.08	2.01	2.01	2.033	2.01	2.01	2.01	2.01	1.95	1.95	1.95	1.95	2.00	0.018	0.9
43.6 g	1.77	1.77	1.77	1.77	1.77	1.77	1.77	1.77	1.71	1.71	1.71	1.71	1.75	0.012	0.7
53.6 g	1.65	1.65	1.65	1.65	1.59	1.59	1.59	1.59	1.59	1.59	1.59	1.59	1.61	0.031	1.9
63.6 g	1.53	1.53	1.53	1.53	1.46	1.46	1.46	1.46	1.46	1.46	1.46	1.46	1.48	0.036	2.4

Table D-26: Resonant Frequency Data for the Superelastic Springs with a Spring Diameter of 0.75”*

Loading Scenario	Trial 1				Trial 2				Trial 3				Average Among Trials	Standard Deviation	
	Measured Resonant Frequency (Hz)			Average (Hz)	Measured Resonant Frequency (Hz)			Average (Hz)	Measured Resonant Frequency (Hz)			Average (Hz)			
	1st	2nd	3rd		1st	2nd	3rd		1st	2nd	3rd			(Hz)	%
13.6 g	3.78	3.72	3.72	3.74	3.91	3.85	3.85	3.87	3.85	3.78	3.78	3.8033	3.80	0.065	1.7
23.6 g	2.93	2.87	2.87	2.89	2.99	2.99	2.99	2.99	2.99	2.99	2.99	2.99	2.96	0.051	1.7
33.6 g	2.5	2.44	2.44	2.46	2.56	2.56	2.56	2.56	2.56	2.56	2.56	2.56	2.53	0.051	2.0
43.6 g	2.2	2.14	2.14	2.16	2.26	2.26	2.26	2.26	2.26	2.26	2.26	2.26	2.23	0.051	2.3
53.6 g	1.95	1.95	1.95	1.95	2.08	2.01	2.01	2.033	2.08	2.08	2.08	2.08	2.02	0.045	2.2
63.6 g	1.83	1.83	1.83	1.83	1.89	1.89	1.89	1.89	1.89	1.89	1.89	1.89	1.87	0.031	1.6

*Note: This data was found during the “Number of Active Turn” Experiments

Table D-27: Resonant Frequency Data for the Superelastic Springs with a Spring Diameter of 0.625”

Loading Scenario	Trial 1				Trial 2				Trial 3				Average Among Trials	Standard Deviation	
	Measured Resonant Frequency (Hz)			Average (Hz)	Measured Resonant Frequency (Hz)			Average (Hz)	Measured Resonant Frequency (Hz)			Average (Hz)		(Hz)	%
	1st	2nd	3rd		1st	2nd	3rd		1st	2nd	3rd				
13.6 g	5.37	5.37	5.37	5.37	5.37	5.37	5.37	5.37	5.19	5.13	5.13	5.15	5.30	0.042	0.8
23.6 g	4.09	4.09	4.09	4.09	4.03	4.03	4.03	4.03	3.85	3.85	3.85	3.85	3.99	0.050	1.3
33.6 g	3.42	3.36	3.36	3.38	3.36	3.36	3.36	3.36	3.23	3.17	3.17	3.19	3.31	0.036	1.1
53.6 g	2.75	2.75	2.75	2.75	2.69	2.69	2.69	2.69	2.5	2.5	2.5	2.5	2.65	0.052	2.0
73.6 g	2.32	2.32	2.32	2.32	2.26	2.26	2.26	2.26	2.14	2.14	2.14	2.14	2.24	0.042	1.9
103.6 g	1.95	1.95	1.95	1.95	1.95	1.95	1.89	1.93	1.89	1.89	1.89	1.89	1.92	0.014	0.7

Table D-28: Resonant Frequency Data for the Superelastic Springs with a Spring Diameter of 0.50”

Loading Scenario	Trial 1				Trial 2				Trial 3				Average Among Trials	Standard Deviation	
	Measured Resonant Frequency (Hz)			Average (Hz)	Measured Resonant Frequency (Hz)			Average (Hz)	Measured Resonant Frequency (Hz)			Average (Hz)		(Hz)	%
	1st	2nd	3rd		1st	2nd	3rd		1st	2nd	3rd				
53.6 g	3.66	3.6	3.6	3.62	3.6	3.54	3.54	3.56	3.6	3.54	3.54	3.56	3.58	0.031	0.9
73.6 g	3.05	3.05	2.99	3.03	2.99	2.99	2.99	2.99	3.05	3.05	2.99	3.03	3.02	0.020	0.7
103.6 g	2.62	2.56	2.56	2.58	2.56	2.5	2.5	2.52	2.56	2.5	2.5	2.52	2.54	0.031	1.2
123.6 g	2.32	2.32	2.32	2.32	2.38	2.32	2.38	2.36	2.32	2.32	2.32	2.32	2.33	0.021	0.9
153.6 g	2.2	2.2	2.2	2.2	2.2	2.14	2.14	2.16	2.2	2.2	2.2	2.2	2.19	0.020	0.9
203.6 g	1.95	1.95	2.01	1.97	2.01	2.01	2.01	2.01	2.01	2.01	2.01	2.01	2.00	0.020	1.0
253.6 g	1.89	1.95	1.95	1.93	1.95	1.95	1.95	1.95	1.95	2.01	2.01	1.99	1.96	0.014	0.7
303.6 g	2.01	2.01	2.01	2.01	1.95	2.01	2.01	1.99	1.95	2.01	2.08	2.0133	2.00	0.010	0.5

Table D-29: Resonant Frequency Data for the Superelastic Springs with a Spring Diameter of 0.4375”

Loading Scenario	Trial 1				Trial 2				Trial 3				Average Among Trials	Standard Deviation	
	Measured Resonant Frequency (Hz)			Average (Hz)	Measured Resonant Frequency (Hz)			Average (Hz)	Measured Resonant Frequency (Hz)			Average (Hz)			
	1st	2nd	3rd		1st	2nd	3rd		1st	2nd	3rd			(Hz)	%
53.6 g	4.46	4.39	4.33	4.3933	4.52	4.46	4.46	4.48	4.58	4.46	4.46	4.5	4.46	0.045	1.0
73.6 g	3.78	3.66	3.72	3.72	3.78	3.78	3.78	3.78	3.91	3.85	3.85	3.87	3.79	0.038	1.0
103.6 g	3.17	3.05	3.05	3.09	3.23	3.17	3.17	3.19	3.23	3.17	3.17	3.19	3.16	0.051	1.6
123.6 g	2.81	2.81	2.81	2.81	2.87	2.87	2.87	2.87	2.87	2.87	2.87	2.87	2.85	0.031	1.1
153.6 g	2.5	2.5	2.5	2.5	2.56	2.56	2.56	2.56	2.56	2.56	2.56	2.56	2.54	0.031	1.2
203.6 g	2.26	2.26	2.26	2.26	2.2	2.26	2.26	2.24	2.32	2.32	2.32	2.32	2.27	0.017	0.7
253.6 g	2.14	2.2	2.2	2.18	2.14	2.14	2.2	2.16	2.26	2.32	2.32	2.3	2.21	0.027	1.2